hexagon:2611.00136v2

NORMAL CONE IS ALL YOU NEED: UNSOFTENED SYMPLECTIC INTEGRATION OF THE NEWTONIAN N-BODY PROBLEM ACROSS COLLISIONS IN FINITE STEPS

JÉRÉMY NUSA

Abstract. In the classical formulation of the Newtonian N-body problem, symplectic geometry and collision singularities appear fundamentally irreconcilable: fixed-step symplectic integrators preserve the Poincaré integral invariants on smooth orbits only by softening the gravitational potential or breaking down at close encounters, whereas classical Sundman and Levi-Civita regularizations resolve collisions only by deforming the global time flow or altering the canonical phase-space structure. In this work, we show that this dichotomy is not an intrinsic obstruction of Hamiltonian mechanics, but an artifact of working on the unblown Cartesian configuration space.

By lifting the dynamics to the standard cotangent bundle $T^*\mathbf{Q}[N]$ of the real oriented Fulton–MacPherson compactification $\mathbf{Q}[N] = \mathrm{Bl}_{\Pi(N)}(M/\mathbb{R}^3)$ and applying the Calaque–Safronov shifted cotangent deformation to the normal cone $\mathcal{D}_Z\mathbf{Q}[N] \to \mathbb{A}^1$, we construct an exact, unsoftened ($\varepsilon = 0$) Hamiltonian splitting covered by the combinatorial atlas of $(2N-3)!!$ rooted binary Jacobi trees. Along the normal-cone degeneration, the interaction decomposes canonically into commuting Kepler–Sundman leaf flows, synchronous anti-Zeno supernodes, and a scale-invariant quadrupolar-screened apex potential of global $\mathcal{C}^{1,1}$ regularity. Endowing the exceptional collision divisors with McGehee's unitary elastic bounce involution ($\mathcal{B}_C^2 = \mathrm{Id}$) renders the leaf flows globally complete and time-reversible across binary collisions in a finite number of physical steps, thereby lifting the Sheng–Suzuki negative-timestep barrier for high-order symmetric compositions.

In the bi-graded Poisson–Lie algebra $\mathcal{L}_{n,m}$ associated with this splitting, we establish a *Universal Double Obstruction Theorem* at order six: momentum-parity alternation prevents any pure configuration-space corrector from cancelling the leading secular error, while a non-vanishing Hall cohomology class in $H^1(D_A, \mathcal{L}_{5,2})$ creates an incompressible $\mathcal{O}(\varepsilon^2 h^4)$ quadratic tidal floor. We overcome the parity obstruction by introducing a torque-free cotangent corrector $K_4 \in \mathcal{L}_{4,1} \cap \mathcal{P}_1$, realized via a palindromic Lie conjugator $\mathcal{Z}_4^{\mathrm{BM4}}(h)$ that vanishes naturally as $\mathcal{O}(r^{7/2})$ at collisions (scheme PBM_4). Whenever the trajectory changes local Jacobi chart or dyadic step-size level, a non-commutative covariant gauge connection $T_{A\to B}^{(\mathrm{PBM4})}$ closes the Čech 1-cocycle on the atlas groupoid and eliminates interfacial shadow-energy jumps. Accompanied by a complete, axiom-free Lean 4 formalization and validated up to 116-bit quadruple precision against the `REBOUND` integrator suite (`IAS15`, `TRACE`, `MERCURIUS`, and `WHFast`), the resulting architecture preserves all Galilean Lie–Bargmann invariants to machine precision across secular, collisional, and chaotic multi-body regimes.

DOI 10.5281/zenodo.23982968

GitHub jeremynusa-hub/normal_cone_nbody3d (v1.0.1)

PREFACE

Author's Statement on Methodology and Editorial Voice

I, the author, explicitly state that this theoretical research, geometric formalization, and manuscript drafting were carried out with the collaborative assistance of the artificial intelligence Gemini models (Flash 3.8 & Argon). In this spirit, I employ the editorial pronoun "we" throughout this paper not as a conventional *pluralis majestatis*, but as an inclusive denominator embracing the cumulative continuum of the author, the artificial intelligence collaborator, and the historical lineage of past authors and mathematicians whose foundational discoveries made this work possible.

Table of Contents

1. Introduction **5**
1.1. The Gravitational N-Body Problem: Contemporary Relevance and Open Questions 5
1.2. Survey of Contemporary Numerical Approaches and the Pathology of Invariant Drifting 5
1.3. The Geometric Promise and Singular Dilemmas of Symplectic Integration 7
1.4. The Deformation to the Normal Cone and Canonical Hamiltonian Splittings 8
1.5. Fulton–MacPherson Compactification: Resolving the Sundman Time-Freezing Dilemma 9
1.6. Core Claims and Practical Numerical Schemes 10
1.7. Outline of the Paper 13
1.8. Common Mathematical Foundations and Notational Primitives 17

2. Calaque–Safronov Normal Cone Methodology and Algorithmic Recipes **20**
2.1. The Deformation to the Normal Cone and Graded Rees Algebra 20
2.2. The Canonical 4-Step Normal Cone Splitting Recipe 23
2.3. Retrospective Case Studies: Unifying Known Splittings on SE(3) and $\mathbb{S}^2$ 26

3. The Planar Three-Body Prototype and Classical Regularizations **32**
3.1. Canonical Synodic Formulation of the PCR3BP 32
3.2. Bridging Normal Cone Degenerations with Classical Regularizations 35
3.3. Geometric Synthesis: Classical Obstructions and the Normal Cone Imperative 37

4. Fulton–MacPherson Compactification and Multiscale Splitting **39**
4.1. The Partition Lattice $\Pi(N)$ and the Fulton–MacPherson Manifold $\mathbf{Q}[N]$ 39
4.2. Smooth Scale-Adapted Screening of the Apex Potential and $\mathcal{C}^{1,1}$ Regularity 45
4.3. Synchronous Supernodes and the $\mathcal{O}(\delta^{-5/2})$ Commutator Resolution 54

5. Symplectic Discretization and High-Order Schemes **65**
5.1. The 7-Operator Hierarchical Palindromic Strang Propagator ($\mathcal{S}_2$) 65
5.2. The Sheng–Suzuki Barrier and McGehee's Involutive Collision Bounce 70
5.3. High-Order Symmetric Compositions and Spectral Optimization 74
5.4. The 11-Stage Sixth-Order Scheme BM_6 and High-Precision Lie Integration 78
5.5. Symplectic Boundary Correctors, Universal Obstruction, and Asymptotic Order Elevation for BM4 84
5.6. Dyadic Multirate Symplectic Scheduling and Skeel–Gear Synchronization 94
5.7. Conclusion of Section 5 and Algorithmic Transition to Section 6 100

6. Computational Architecture and Algorithmic Realization of the Normal Cone Symplectic Integrator **102**
6.1. Global Algorithmic Architecture and Six-Phase Execution Pipeline 102
6.2. Geometric Initialization and Symplectic Shadow Pre-Processing 106
6.3. Macro-Time Loop, Dynamical Timescales, and Skeel–Gear Dyadic Scheduler 115
6.4. The Symplectic Sub-Cycle: Kepler–Sundman Flow and Screened Apex Kick 121
6.5. Atlas Transitions, Gauge Connection, and Symplectic Post-Processing 127
6.6. High-Performance Computational Optimizations and Modular Micro-Kernels 137

7. Numerical Benchmarks **144**
7.1. Unsoftened Collision Benchmarks ($\varepsilon = 0$) Against State of the Art 144
7.2. Long-Term Secular Stability, Planetary KAM Torus Preservation, and Historical Celestial Encounters 155
7.3. Comparative Benchmarks Against State-of-the-Art Celestial Mechanics Integrators (`REBOUND 5.2.2`) 165

8. Conclusion and Outlook **184**
8.1. Objective Synthesis: Achievements, Structural Strengths, and Intrinsic Boundaries 184
8.2. Perspectives and Open Questions 185

Appendix A. Certified Lean 4 Formal Artifacts and Numerical Schemes **187**
References **192**

1. Introduction

1.1. **The Gravitational N-Body Problem: Contemporary Relevance and Open Questions.** The Newtonian N-body problem models the mutual gravitational interaction of $N \geq 3$ point masses $m_1, \ldots, m_N > 0$ in three-dimensional Euclidean space, governed on the cotangent bundle $T^*(\mathbb{R}^{3N} \setminus \Delta)$ by the classical Hamiltonian:

$$H(\mathbf{q}, \mathbf{p}) = \sum_{i=1}^{N} \frac{\|\mathbf{p}_i\|^2}{2m_i} - \sum_{1 \leq i < j \leq N} \frac{G m_i m_j}{\|\mathbf{q}_i - \mathbf{q}_j\|}, \tag{1.1}$$

where $\mathbf{q}_i \in \mathbb{R}^3$ denote Cartesian positions, $\mathbf{p}_i = m_i \dot{\mathbf{q}}_i \in \mathbb{R}^3$ are conjugate momenta, and $\Delta = \bigcup_{1 \leq i < j \leq N} \{\mathbf{q} \in \mathbb{R}^{3N} \mid \mathbf{q}_i = \mathbf{q}_j\}$ represents the singular collision divisor.

In contemporary astrophysics, the demand for accurate, long-term multi-body integration of this Hamiltonian has never been more acute. Investigations into the secular stability and chaotic diffusion of the Solar System over gigayear timescales, the orbital migration and resonant capture within tightly packed exoplanetary systems, the core-collapse dynamics of globular star clusters, and the relativistic coalescence of intermediate-mass black holes in galactic nuclei all rely upon numerical integrations spanning millions to billions of dynamical times.

Within these dense multi-body environments, close encounters play a decisive dynamical role. In continuous phase space, seminal theorems of Saari [61, 62] establish that initial conditions leading to true collisions in the Newtonian N-body problem form a set of Lebesgue measure zero in the full phase space $\mathbb{R}^{6N}$ (and in the center-of-mass reduced phase space $\mathbb{R}^{6N-6}$). Among collisional configurations, simultaneous multiple collisions ($k \geq 3$) form a lower-dimensional stratum of measure zero, while non-collision singularities are physically pathological configurations conjectured to have measure zero (Saari [63]; see also Xia [84]). Consequently, in continuous time, the dynamics is non-singular almost everywhere with respect to the physical Liouville measure. However, in discrete numerical integration with finite time step $h > 0$, generic trajectories (which constitute open sets of strictly positive Lebesgue measure) inevitably penetrate compact quasi-collision spheres of radius $\delta(h) \ll 1$, triggering catastrophic step-size collapse or artificial numerical ejections in conventional codes. While exact multiple collisions remain absent almost surely, resolving binary encounters and multiscale cluster hierarchies symplectically without potential softening ($\varepsilon = 0$) desingularizes these generic positive-measure quasi-collisional encounters and ensures robust, unsoftened propagation across all physical regimes (see Figure 1).

1.2. **Survey of Contemporary Numerical Approaches and the Pathology of Invariant Drifting.** To address this challenge, computational celestial mechanics has historically explored three distinct avenues, each of which entails substantive mathematical trade-offs:

(a) **High-Order Adaptive Non-Symplectic Integrators:** Modern astrophysical packages frequently deploy high-order non-symplectic schemes with adaptive step-size control, such as 15th-order Gauss–Radau quadrature with compensated summation [53, 58], embedded Runge–Kutta pairs, or Bulirsch–Stoer rational extrapolation techniques. In scenarios featuring chaotic scattering or highly eccentric orbits, adaptive step-size controllers automatically contract the integration time step to resolve steep acceleration gradients, achieving remarkable local accuracy. However, because these integrators do not preserve the canonical symplectic 2-form $\omega_0 = \sum_{i=1}^{N} \mathrm{d}\mathbf{q}_i \wedge \mathrm{d}\mathbf{p}_i$ nor the phase space volume, they do not possess an exact modified shadow Hamiltonian. Consequently, while standard non-symplectic integrators suffer from secular linear energy drift ($\mathcal{O}(t)$), even compensated high-order quadrature schemes that suppress linear energy drift down to Brouwer's random-walk roundoff limit ($\propto t^{1/2}$ in energy [13]) inevitably suffer from a secular orbital phase error growing as $\mathcal{O}(t^{3/2})$ and lack an exact shadow Hamiltonian $\widetilde{H}$, eroding the long-term qualitative fidelity of secular resonances and semi-major axes.

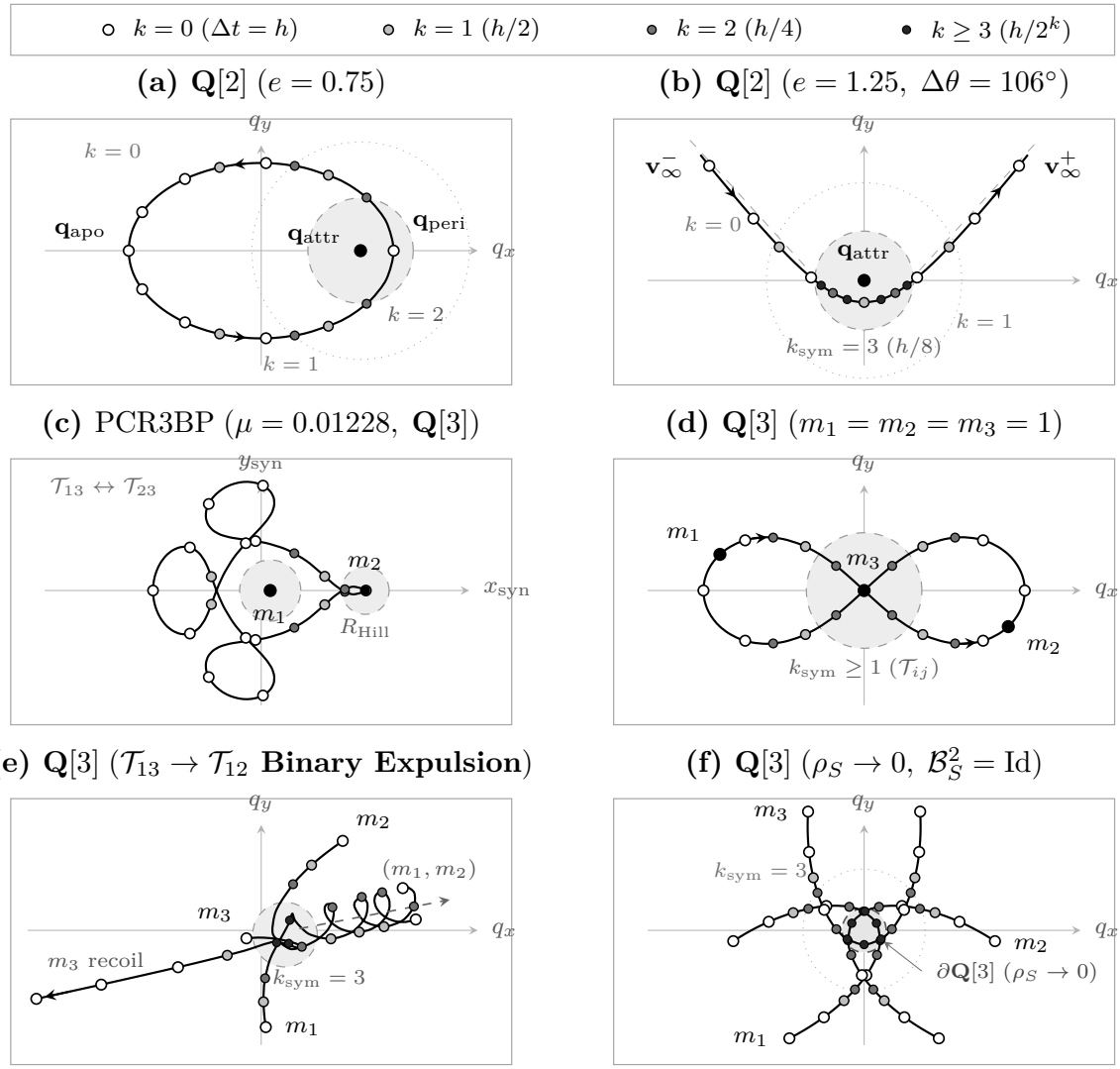


FIGURE 1. **Multi-regime trajectory showcase of unsoftened normal-cone symplectic integration with palindromic dyadic substepping.** Along every trajectory, white beads (○) mark uniform macro-step boundaries ($t_n = nh, k = 0$), while progressively darker gray beads denote internal dyadic sub-steps ($\Delta t_n = h/2^{k_{\text{sym},n}}$ for $k = 1, 2, \geq 3$) triggered automatically inside the shaded close-encounter spheres without potential softening ($\varepsilon = 0$). **(a)** Closed eccentric Keplerian binary ($e = 0.75$) showing palindromic refinement $k_{\text{sym}} : 0 \to 1 \to 2 \to 1 \to 0$ around pericenter $\mathbf{q}_{\text{peri}}$. **(b)** Unbound hyperbolic slingshot ($e = 1.25$, deflection $\Delta\theta = 106°$) reaching $k_{\text{sym}} = 3$ ($h/8$) at closest approach. **(c)** Synodic multi-loop Arenstorf orbit in the Earth–Moon PCR3BP ($\mu = 0.012277471$), combining local Levi-Civita / Sundman leaf regularization with Hill-sphere chart switching ($\mathcal{T}_{13} \leftrightarrow \mathcal{T}_{23}$). **(d)** Equal-mass three-body Figure-8 choreography (Chenciner–Montgomery [18]), where democratic Voronoi chart transitions ($\mathcal{T}_{12} \to \mathcal{T}_{23} \to \mathcal{T}_{13}$) and symmetric dyadic sub-steps resolve the central crossings. **(e)** Grazing three-body resonant encounter ($\mathcal{T}_{13} \to \mathcal{T}_{12}$) triggering the high-velocity recoil of m_3 (coasting at $k = 0$) and the expulsion of a tightly bound binary pair (m_1, m_2) tracked at $k \in \{1, 2\}$. **(f)** Simultaneous three-body Lagrange collapse onto the blown-up McGehee supernode manifold ($\rho_S \to 0$), where the synchronous cluster hierarchy and unitary bounce involution ($\mathcal{B}_S^2 = \mathrm{Id}$) resolve the triple quasi-collision at $k_{\text{sym}} = 3$.

(b) **Classical Analytical Regularization Techniques:** In the early twentieth century, Sundman [72] achieved the analytical regularization of isolated binary collisions by introducing a local conformal time reparameterization $\mathrm{d}t = r_{ij}\,\mathrm{d}u$ (Section V, Eq. 71), and extended it globally to the 3-body problem via the product clock $\mathrm{d}t = \Gamma\,\mathrm{d}\omega$ with $\Gamma = \prod_{k=0}^{2}(1 - e^{-r_k/l})$ (Section XI, Eq. 179–180). This was extended to three dimensions via the spinor transformation of Kustaanheimo and Stiefel (KS) [36] and subsequently generalized into chain regularization algorithms by Mikkola and Aarseth [1, 51]. While exceptionally powerful for isolated binary pairs, classical regularizations are burdened by a fundamental drawback: the *global time-freezing dilemma*. Because the regularizing clock $\mathrm{d}t = g(\mathbf{q})\,\mathrm{d}\tau$ is defined as a global scalar field over configuration space (such as $\Gamma \to 0$ in Sundman's global clock or $g = 1/(T+U) \to 0$ in chain methods), whenever any two bodies approach a collision ($r_{ij} \to 0$), the physical time increment $\mathrm{d}t$ collapses toward zero for the entire system. Consequently, the motion of distant, non-colliding bodies is artificially frozen, rendering global Sundman regularization computationally intractable for general $N \geq 3$ systems.

(c) **Phenomenological Potential Softening:** To avert singular gradient explosions in large-scale N-body simulations, numerical practitioners frequently replace the physical Newtonian potential with a softened kernel, such as the Plummer potential $V_\varepsilon(\mathbf{q}) = -Gm_im_j/\sqrt{\|\mathbf{q}_i - \mathbf{q}_j\|^2 + \varepsilon^2}$ with $\varepsilon > 0$, or impose an artificial force cutoff distance $d_0 > 0$. Softening is physically well-justified and indispensable in collisionless galactic dynamics and cosmological simulations ($N \sim 10^6 - 10^{11}$ particles), where it suppresses artificial two-body relaxation and converges toward the smooth mean-field Vlasov–Poisson kinetic limit. However, in collisional, point-mass systems such as compact planetary architectures, dense globular cluster cores, or multiple stellar systems, introducing an ad hoc length scale $\varepsilon > 0$ fundamentally alters the physical point-mass Hamiltonian: it suppresses large-angle gravitational deflections, introduces unphysical apsidal precession, shifts resonant commensurabilities, and precludes the faithful study of close gravitational encounters.

Importantly, while smooth, stationary, radially symmetric softening potentials (such as V_ε) preserve the kinematic Galilean invariants $(\mathbf{P}, \mathbf{G}, \mathbf{L})$ via standard spatial Noether symmetries, they corrupt the physical energy spectrum and orbital geometry. The *Lie–Bargmann invariant algebra* is then directly violated whenever practitioners introduce discontinuous force cutoffs ($d_0 > 0$), dynamical time-dependent softening scales $\varepsilon(t)$, or non-symplectic dissipations, permanently eroding the 10 universal first integrals of an isolated Newtonian system (total energy H, linear momentum $\mathbf{P}$, center-of-mass boost $\mathbf{G}$, and angular momentum $\mathbf{L}$) and degrading the long-term qualitative credibility of the simulated phase space trajectories.

1.3. **The Geometric Promise and Singular Dilemmas of Symplectic Integration.**

Symplectic integrators [28] offer a rigorous remedy to secular dissipation. By construction, a numerical map $\Phi_h : (\mathbf{q}_n, \mathbf{p}_n) \mapsto (\mathbf{q}_{n+1}, \mathbf{p}_{n+1})$ is symplectic if its Jacobian matrix J satisfies identically:

$$J^T \mathbb{J}_{6N} J = \mathbb{J}_{6N}, \qquad \mathbb{J}_{6N} = \begin{pmatrix} \mathbb{O}_{3N} & \mathbb{I}_{3N} \\ -\mathbb{I}_{3N} & \mathbb{O}_{3N} \end{pmatrix}. \tag{1.2}$$

The decisive theoretical advantage of symplectic schemes is elucidated by *Backward Error Analysis* [6, 28, 46]: the discrete sequence generated by a symplectic integrator does not approximate the original continuous system with secularly drifting energy; rather, it tracks *exactly* the trajectory of a nearby formal Hamiltonian, known as the *shadow* or *modified Hamiltonian*:

$$\widetilde{H}(\mathbf{q}, \mathbf{p}) = H(\mathbf{q}, \mathbf{p}) + h^2 H_2(\mathbf{q}, \mathbf{p}) + h^4 H_4(\mathbf{q}, \mathbf{p}) + \dots \tag{1.3}$$

Because $\widetilde{H}$ is an exact invariant of the discrete flow, the energy error $H(\mathbf{q}_n, \mathbf{p}_n) - H(\mathbf{q}_0, \mathbf{p}_0)$ does not grow linearly with time, but remains confined within an adiabatic oscillatory envelope of amplitude $\mathcal{O}(h^p)$ over astronomical durations. Furthermore, whenever the underlying splitting respects the spatial symmetries of the potential, discrete Noether theorems guarantee that linear momentum $\mathbf{P}$ and angular momentum $\mathbf{L}$ are exact first integrals ($\Delta_{\text{trunc}} \equiv \mathbf{0}$) without secular discretization drift.

However, applying symplectic integrators to the unsoftened gravitational N-body problem encounters three formidable theoretical bottlenecks:

(i) **The Constant Time-Step Constraint:** As demonstrated by Skeel and Gear [66] and Hairer et al. [28], standard adaptive step-size mechanisms based on local error estimators destroy the symplectic 2-form. Introducing a variable step $h_n = h(\mathbf{q}_n, \mathbf{p}_n)$ converts the discrete map into a non-Hamiltonian system, reinstating secular energy drift comparable to that of non-symplectic integrators.

(ii) **Singularity of the Newtonian Potential:** Under a fixed time step h, when two bodies experience a close encounter ($r_{ij} \to 0$), the physical acceleration $\|\nabla V\| \sim r_{ij}^{-2}$ and its Hessian $\|\operatorname{Hess}(V)\| \sim r_{ij}^{-3}$ diverge rapidly. The modified Hamiltonian series $\widetilde{H}$ fails to converge, leading to numerical divergence or unphysical ejections.

(iii) **The Sheng–Suzuki Barrier for High-Order Compositions:** To achieve high precision, one constructs higher-order integrators via symmetric composition of lower-order stages. However, a rigorous non-existence theorem proved independently by Sheng [64] and Suzuki [74] establishes that *any symplectic partitioned Runge–Kutta or splitting method of order $p \geq 3$ with real coefficients must necessarily include at least one negative intermediate time step* ($w_k < 0$). In the presence of singular gravitational forces, propagating backward in time near a collision boundary triggers catastrophic numerical instabilities unless the singularity has been regularized in an analytically reversible manner.

In the regular planetary regime where orbital eccentricities remain small and a single central mass dominates ($H = A + \varepsilon B$ with $\varepsilon \ll 1$), the celebratory perturbative splitting school pioneered by Wisdom and Holman [82], equipped with symplectic correctors [9, 83] and generalized into high-order symmetric families by Laskar and Robutel [38], Blanes et al. [8, 10], and Farrés, Laskar et al. [22], achieves unmatched efficiency at fixed macro-steps. Yet these perturbative splittings rely fundamentally on the uniform analyticity of the interaction potential B away from collision diagonals: whenever a subsystem enters an extreme eccentricity excursion ($e \to 1$), undergoes a grazing planetary flyby, or forms a democratic multi-body encounter ($r_{ij} \to 0$), the Lie commutator $\operatorname{ad}_A^n(B)$ explodes as $\mathcal{O}(r_{ij}^{-(n+1)})$ and the fixed-chart Kepler–drift hierarchy breaks down. Rather than competing with fixed-step planetary integrators on quasi-circular regular orbits, the theory developed in this paper constructs their *universal, unsoftened singular extension* on the Fulton–MacPherson compactification $\mathbf{Q}[N]$: it seamlessly reduces to an exact hierarchy of commuting Keplerian leaves and cotangent-corrected PBM_4 propagators in regular hierarchical regimes while traversing arbitrary binary collisions and dense multi-body encounters in a finite number of physical steps.

1.4. **The Deformation to the Normal Cone and Canonical Hamiltonian Splittings.** A promising mathematical bridge across this impasse has emerged from modern symplectic geometry. In a groundbreaking memoir, Damien Calaque and Pavel Safronov [15] formalized the *deformation to the normal cone* within the framework of shifted cotangent structures and symplectic groupoids on derived stacks. While their foundational work operates in the abstract setting of derived algebraic geometry, the present treatise adopts this canonical geometric degeneration as a conceptual guiding paradigm, translating its core insight into a classical Hamiltonian operator splitting on the ordinary cotangent bundle T^*M.

Let $M = \mathbb{R}^{3N}$ denote the ambient configuration space of the N bodies, $X = M \setminus \Delta$ the regular non-collision locus (defined as the set complement of the collision divisor Δ), and

let $Z \subset \Delta \subset M$ be an isolated collision submanifold (such as a pairwise collision diagonal $\Delta_{ij} = \{\mathbf{q} \in M \mid \mathbf{q}_i = \mathbf{q}_j\}$). The deformation space $\mathcal{D}_Z M \to \mathbb{A}^1$ over the real affine line $\mathbb{A}^1 \cong \mathbb{R}$ (parameterized by a continuous deformation parameter $t \in [0, 1]$) interpolates geometrically between two distinct symplectic regimes:

- **Generic Fiber ($t = 1$):** The fiber $(\mathcal{D}_Z M)_{t=1}$ is canonically isomorphic to the ambient configuration space M, and on the regular locus X its cotangent bundle carries the standard physical Darboux form ω_0.
- **Degenerated Normal Fiber ($t = 0$):** As $t \to 0$, the space degenerates onto the normal bundle $N_Z M$, and the cotangent space lifts to $T^*(N_Z M)$, which is endowed with a canonical, linear, flat symplectic structure.

Transposed to celestial mechanics, this normal cone perspective suggests a principled, non-heuristic method for Hamiltonian operator splitting. Rather than modifying the potential with ad hoc cutoffs, one decomposes the dynamics into:

(1) An exact groupoid exponential along the base manifold X, governed by kinetic inertia and generating unconstrained Galilean drift;
(2) A family of transverse impulses acting in the flat normal cotangent fibers $T^*(N_Z M)$ at $t = 0$.

Crucially, in the flat normal cotangent fiber, the pairwise gravitational force between particles i and j acts strictly along the central direction $(\mathbf{q}_i - \mathbf{q}_j)$. By virtue of Newton's third law and the symmetry of the central interaction, the transverse impulse field is *strictly orthogonal to the level sets of the 9 kinematic first integrals*:

$$\sum_{i=1}^{N} \nabla_{\mathbf{q}_i} V \equiv \mathbf{0}, \qquad \sum_{i=1}^{N} \mathbf{q}_i \times \nabla_{\mathbf{q}_i} V \equiv \mathbf{0}. \tag{1.4}$$

Consequently, this normal cone splitting preserves total linear momentum $\mathbf{P}$, center of mass $\mathbf{G}$, and total angular momentum $\mathbf{L}$ unconditionally and identically at each stage of the integration, while energy H is preserved through the shadow Hamiltonian $\widetilde{H}$ without secular dissipation.

1.5. **Fulton–MacPherson Compactification: Resolving the Sundman Time-Freezing Dilemma.** While binary collisions $Z = \Delta_{ij}$ form smooth submanifolds of codimension 3, general N-body systems ($N \geq 3$) introduce multiple collision strata $\Delta_I = \bigcap_{i,j \in I} \{\mathbf{q}_i = \mathbf{q}_j\}$ with non-transverse intersections. As Siegel [65] proved the non-analytic regularizability of triple collisions and McGehee [47] uncovered chaotic dynamics on the blown-up collision manifold, the intrinsic normal cone along multiple collisions in $\mathbb{R}^{3N}$ is not a regular bundle, but a singular, reducible cone with intersecting branches, causing naive Cartesian splittings to generate unphysical "ghost poles" at cluster barycenters.

To resolve this obstruction and decouple trivial center-of-mass motion, one passes to relative configurations via the algebraic quotient $M_{\mathrm{rel}} = M/\mathbb{R}^3 \cong (\mathbb{R}^3)^N/\mathbb{R}^3$. We then invoke the real Fulton–MacPherson compactification $\mathbf{Q}[N] = \mathrm{Bl}_{\Pi(N)}\,(M/\mathbb{R}^3)$ [3, 24] (see Axelrod & Singer [3, Section 5]), constructed by performing canonical spherical blow-ups along collision diagonals ordered by the partition lattice $\Pi(N)$ of $\{1, \ldots, N\}$. On the compactified manifold with corners $\mathbf{Q}[N]$, the singular collision arrangement Δ becomes a *simple normal crossing (SNC) divisor with corners*, whose boundary strata are smooth hypersurfaces with regular normal line bundles, and whose maximal corners of codimension $N - 1$ are bijectively dual to binary Jacobi trees $\mathcal{T} \in \mathrm{Trees}(N)$.

This compactification provides the definitive geometric resolution to the Sundman time-freezing dilemma and multi-body singular barriers:

(1) **Decentralized Cluster Clocks:** Each hierarchical node v of the Jacobi tree $\mathcal{T}$ carries its own *local cluster clock* $\mathrm{d}t_v = \rho_v \, \mathrm{d}\tau_v$, where ρ_v is the internal hyper-radius of cluster C_v.

(2) **Asynchronous Multiscale Evolution:** Fast internal orbital or collisional motions within tight sub-clusters evolve in their own local time, crossing pairwise collisions analytically via universal Stumpff functions $c_k(z)$ [70] and regularized elastic bounces $\mathcal{B}_C : v_r \mapsto -v_r$ in McGehee coordinates, while distant bodies drift symplectically without artificial deceleration.

(3) **Resolution of the Suzuki Barrier:** Because McGehee's regularized bounce is a unitary involution ($\mathcal{B}_C^2 = \mathrm{Id}$) combined with odd Stumpff transformations, the flow is strictly time-reversible across collisions, enabling the safe deployment of high-order symplectic compositions ($\mathcal{S}_4, \mathrm{BM}_4^{(7)}, \mathrm{BM}_6^{(11)}$) with negative intermediate time steps.

(4) **Elimination of the Multipolar Ghost Pole and Universal $\mathcal{C}^{1,1}$ Regularity:** Naive subtraction of a barycentric monopole creates an unphysical "ghost pole" $+GM_LM_R/\|\mathbf{r}_v\|$ whenever two cluster barycenters coincide ($\|\mathbf{r}_v\| \to 0$) without any physical collision. Introducing the scale-adapted screening function $\Theta(u_v)$ ($u_v = \|\mathbf{r}_v\|/(\bar{\rho}_L + \bar{\rho}_R)$) cancels both the monopole and dipole identically, leaving a pure quadrupolar tidal interaction governed by a symmetric trace-free tensor $\mathbf{T}_{\mathrm{apex}} \in \mathrm{Sym}_0(3)$ that is uniformly $\mathcal{C}^{1,1}$ Lipschitz across all of $\mathbf{Q}[N]$ without any softening cutoff ($d_0 = 0$, Theorem 4.4).

(5) **Synchronous Anti-Zeno Super-Nodes for Multi-Body Encounters:** Whenever a dense sub-cluster of cardinality $k \geq 3$ crosses the scale-invariant Hill/Marchal–Sundman tidal threshold ($\eta_S \leq \eta_{\mathrm{crit}} = 3^{-1/3}$, Proposition 4.11, stabilized by a spectral Schmitt trigger $[2^{-1/3}, 2^{-1/6}]$, Corollary 4.12), asynchronous pairwise splitting would trigger a catastrophic $\mathcal{O}(\delta_{\mathrm{cluster}}^{-5/2})$ Lie commutator divergence (Proposition 4.7). The sub-cluster dynamically fuses into a *synchronous super-node* integrated under its local unfolded Sundman clock $\mathrm{d}t_S = \chi_S^2\,\mathrm{d}\tau_S$, guaranteeing traversal of arbitrary close multi-body encounters in a uniformly bounded, finite number of sub-steps (universal Anti-Zeno property, Theorem 4.9).

1.6. **Core Claims and Practical Numerical Schemes.** To bridge the persistent chasm between algebraic geometry and computational astrophysics, this paper demonstrates that deep geometric structures directly govern high-performance symplectic integrators. Our overarching claim is anchored in a decisive measure-theoretic foundation: because collisions form a set of Lebesgue measure zero [61, 62] with multiple collisions occupying a lower-dimensional sub-stratum of measure zero, resolving pure binary close encounters via normal cone desingularization and decoupling cluster hierarchies via Fulton–MacPherson compactification yields an exact, unsoftened symplectic integration valid on *every event set of non-zero measure* in phase space. We formulate our contributions along two complementary axes: foundational geometric structures and operational numerical schemes.

1. Foundational Geometric and Symplectic Framework. From an analytical and geometric perspective, this paper establishes four fundamental structural pillars:

(a) **Normal Cone Hamiltonian Splitting on T^*M:** Formalizing the graded Rees deformation to the normal cone $\pi : \mathcal{D}_Z M = \mathrm{Spec}_M \mathcal{R}(\mathcal{I}_Z) \to \mathbb{A}^1$ (Theorem 2.1) decomposes dynamics into unconstrained groupoid/coadjoint base drifts $\Phi_h^{\mathcal{G}} = \exp_{\mathcal{G}}(h\mathbf{v}(\mathbf{p}_N))$ on the generic fiber $t = 1$ ($X = M \setminus \Delta$) and flat abelian cotangent fiber translations $\Phi_s^{\mathrm{trans}}(\mathbf{p}_N) = \mathbf{p}_N - s\nabla_n V(n)$ on the special fiber $t = 0$ ($T^*(N_{Z/M})$, endowed with the additively split symplectic 2-form $\omega_{\mathrm{normal}} = \mathrm{d}x \wedge \mathrm{d}p + \mathrm{d}n \wedge \mathrm{d}w$, Proposition 2.2). This unifies Lie–Poisson Casimir-preserving splittings on $\mathfrak{se}(3)^*$ and $(\mathbb{S}^2)^K$ (Theorem 2.3, Propositions 2.4 and 2.5) with planar synodic and conformal regularizations (Proposition 3.1, Theorem 3.2), while guaranteeing pure Newtonian motion without softening ($\varepsilon = 0, d_0 = 0$) and unconditional exact conservation ($\Delta_{\mathrm{trunc}} \equiv \mathbf{0}$) of the 9 kinematic Lie–Bargmann first integrals ($\mathbf{P}, \mathbf{G}, \mathbf{L}$) without external projection.

(b) **Fulton–MacPherson Multiscale Desingularization on $T^*\mathbf{Q}[N]$:** Blowing up $M/\mathbb{R}^3$ by iterated real oriented spherical blow-ups along the irreducible building set $\mathcal{G}_{\mathrm{irr}}$ of the Whitney partition lattice $\Pi(N)$ transforms multiple collision strata into a simple normal crossing divisor with corners covered by $(2N-3)!!$ binary Jacobi trees, where disjoint sub-clusters commute identically on the standard cotangent bundle

$T^*\mathbf{Q}[N]$ without the logarithmic boundary poles of Melrose's b-cotangent bundle ${}^bT^*\mathbf{Q}[N]$ (Theorem 4.1, Proposition 4.2). Associating decentralized clocks $\mathrm{d}t_v = \rho_v\,\mathrm{d}\tau_v$, $\mathcal{C}^{1,1}$ screened apex potentials (with dual $\mathcal{C}^\infty$ Gevrey-2 Cauchy mollifier and order-matched $\mathcal{C}^{2k}$ Hermite spline realizations, Theorem 4.4 and Propositions 4.5–4.6), and recursive synchronous Anti-Zeno super-nodes triggered at the parameter-free Hill/Marchal–Sundman threshold $\eta_{\mathrm{crit}} = 3^{-1/3}$ (Proposition 4.7, Theorem 4.9, Proposition 4.11, Corollary 4.12) resolves both the Sundman time-freezing dilemma and the $\mathcal{O}(\delta_{\mathrm{cluster}}^{-5/2})$ commutator barrier.

(c) **Analytic Continuation and Time-Reversible Crossing of Binary Collisions:** Coupling McGehee's radial elastic bounce $\mathcal{B}_C : v_r \mapsto -v_r$ (Lemma 5.6) with the real-analytic Sundman–Stumpff diffeomorphism $\Delta\tau \mapsto \Delta t(\Delta\tau)$ (Proposition 5.5) and Weierstrass pericenter conditioning (Proposition 6.11) integrates pairwise collisions analytically across the singular divisor without cutoff. Because $\mathcal{B}_C$ is an exact unitary involution ($\mathcal{B}_C^2 = \mathrm{Id}$), the regularized trans-collisional flow is strictly time-reversible ($t \mapsto -t$), providing the indispensable mathematical stability required for negative intermediate time steps ($\beta\tau < 0$) in high-order symplectic compositions (Theorem 5.4).

(d) **Universal Double Obstruction Theorem and Incompressible Quadratic Tidal Floor:** Within the bi-graded Poisson–Lie algebra $\mathcal{L}_{n,m}$ on $T^*\mathbf{Q}[N]$—where exact Jacobi–Kepler leaf integration collapses the unperturbed column $\{A_{\mathrm{JK}}, A_{\mathrm{JK}}\} \equiv 0 \implies \mathcal{L}_{n,0} \equiv \{0\}$ ($n \geq 2$) and spatial commutativity $\{W_{\mathrm{apex}}^{\mathrm{screen}}, V_{\mathrm{leaf}}\}_{\Omega_0} \equiv 0$ annihilates $\mathrm{ad}^3_{W_{\mathrm{apex}}^{\mathrm{screen}}}(A_{\mathrm{JK}}) \equiv 0$ (Proposition 5.16, Theorem 5.13)—we prove that (i) momentum-parity alternation ($\mathrm{Im}(D_A|_{\mathcal{P}_0}) \subseteq \mathcal{P}_1$ versus $H_5^{\mathrm{linear}} \in \mathcal{P}_2 \oplus \mathcal{P}_0$) strictly forbids any pure configuration-space corrector $K(\mathbf{r}) \in \mathcal{P}_0$ from elevating $\mathrm{BM}_4^{(7)}$ to order 6, and (ii) a non-vanishing Hall cohomology class $[D_B D_A^3 B] \in H^1(D_A, \mathcal{L}_{5,2})$ ($\dim \mathcal{L}_{5,2} = 2 > \dim \mathrm{Im}(D_A|_{\mathcal{L}_{4,2}}) = 1$) with strictly positive Poincaré orbital average induces an incompressible quadratic tidal error floor $\mathcal{O}(\varepsilon^2 h^4)$ (Theorem 5.17, Theorem 5.18).

2. Operational Numerical Schemes. To serve practical computational needs in celestial mechanics and stellar dynamics, this theoretical architecture is realized as a concrete hierarchy of geometric integrators:

(a) **Strang Normal Cone Propagator $\mathcal{S}_2$:** A symmetric 7-operator second-order splitting on $(\mathcal{P}_{\mathrm{ext}}, \Omega_{\mathrm{ext}})$ interleaving barycentric drift, exact Kepler–Sundman leaf solvers, synchronous super-nodes, and $\mathcal{C}^{1,1}$ screened apex kicks, bounding energy errors within an $\mathcal{O}(h^2)$ envelope without secular dissipation while conserving all 9 kinematic Lie–Bargmann invariants exactly (Definition 5.1, Theorem 5.2, Proposition 5.3).

(b) **Symmetric 4th-Order Yoshida Integrator $\mathcal{S}_4$:** A 3-stage symmetric composition $\mathcal{S}_4(h) = \mathcal{S}_2(\alpha h) \circ \mathcal{S}_2(\beta h) \circ \mathcal{S}_2(\alpha h)$ ($\alpha = 1/(2 - 2^{1/3}), \beta = -2^{1/3}/(2 - 2^{1/3})$) [85]. Benefiting from the involutive time-reversibility of $\mathcal{B}_C$, it overcomes the Sheng–Suzuki barrier [64, 74], executing trans-collisional steps with negative intermediate durations $\beta h < 0$ without instability (Proposition 5.7).

(c) **Optimized 4th-Order 7-Stage Scheme $\mathrm{BM}_4^{(7)}$:** Higher-order symmetric composition of Blanes & Moan [10] ($s = 6$ non-trivial FSAL evaluations in direct ABA/RKN form, or 7 FSAL evaluations in symmetric $\mathcal{S}_2^*$ composition, Table 2) with moderate retrograde sub-step ($a_4 \approx -0.4344$), compressing the principal BCH order-5 commutator error norm by a factor exceeding 400 relative to Yoshida ($|C_5| \leq 0.01236$ vs 5.3719) and ensuring exponential Benettin–Giorgilli shadow confinement (Definition 5.8, Theorem 5.9, Theorem 5.10, Proposition 5.11).

(d) **Optimized 6th-Order 11-Stage Scheme $\mathrm{BM}_6^{(11)}$:** An 11-stage symmetric palindromic composition ($s = 10$ FSAL in direct RKN form SRKN_{11}^b, or 11 FSAL in $\mathcal{S}_2^*$ composition) solving the 7 independent order-6 RKN algebraic conditions on

$\mathcal{L}_1, \mathcal{L}_3, \mathcal{L}_5$, bounding negative sub-steps ($|a_i| \le 0.36$), and variationally minimizing the residual order-7 commutator norm $\|H_7\|$ (Definition 5.12, Theorem 5.13, Theorem 5.14, Proposition 5.15).

(e) **Cotangent-Lifted Corrector $K_4 \in \mathcal{P}_1$ and Processed Scheme PBM_4 (Pre-Asymptotic Order 6):** Bypassing the first parity obstruction via the cotangent lift $K_4(\mathbf{r}, \mathbf{w}) = c_4^{\mathrm{BM4}} h^4 D_A^3 B = c_4^{\mathrm{BM4}} h^4 \sum_\lambda \mathrm{Tr}(\mathbf{T}_{\mathrm{apex},\lambda}\, \mathbf{M}_{\mathrm{sym}}(\mathbf{r}_\lambda, \mathbf{w}_\lambda)) \in \mathcal{L}_{4,1} \cap \mathcal{P}_1$ ($c_4^{\mathrm{BM4}} \approx +1.7600 \times 10^{-4}$) realized by the 2-stage palindromic Lie conjugator $\mathcal{Z}_4^{\mathrm{BM4}}(h)$ (with antipodal half-shell factorization, Theorem 5.18, Theorem 6.5, and Proposition 6.6), PBM_4 annihilates the linear tidal error $\mathcal{O}(\varepsilon h^4)$ with zero internal torque ($\boldsymbol{\tau}_{\mathrm{int}} \equiv \mathbf{0}$) and $\mathcal{O}(r^{7/2})$ free-fall extinction across binary collisions (Theorem 5.19), achieving pre-asymptotic effective order 6 ($p_{\mathrm{eff}} = 6.25$, up to 2,537× energy accuracy gain) down to the $\mathcal{O}(\varepsilon^2 h^4)$ floor at zero additional interior cost ($s = 6$, Theorem 5.18).

(f) **Covariant Symplectic Atlas Gauge Transition Operator $T^{(\mathrm{PBM4})}_{(A,h_A)\to(B,h_B)}$ and Canonical Voronoi Admissibility:** Dynamic restructuring across the $(2N-3)!!$ Jacobi tree charts via unimodular $\mathrm{SL}(2,\mathbb{R}) \hookrightarrow \mathrm{Sp}(6N-6,\mathbb{R})$ tree rotations under the three-regime Hill-weighted Delaunay–Jacobi admissibility criterion at canonical Voronoi threshold $\gamma = 1.0$ and time-reversal-covariant adjoint hysteresis $\mathcal{A}_- = \mathcal{I}_T \circ \mathcal{A}_+^{-1} \circ \mathcal{I}_T$ (Theorem 4.10, Proposition 6.13, Theorem 6.15, Remark 6.5.2), glued in shadow space across both chart flips and dyadic step-size junctions by the non-commutative cotangent-lifted gauge operator $T^{(\mathrm{PBM4})}_{(A,h_A)\to(B,h_B)} = \mathcal{Z}_4^{\mathrm{BM4},(B)}(-h_B) \circ \mathbf{M}_{\mathrm{coord}} \circ \mathcal{Z}_4^{\mathrm{BM4},(A)}(+h_A)$ which closes the Čech 1-cocycle (5.30×10^{-36} algebraically, 4.08×10^{-35} dynamically) and suppresses interfacial shadow energy jumps to machine precision (2.36×10^{-35} in `Float128` and 0.00 to 4.19×10^{-16} in `Float64`, Theorem 5.20 and Theorem 6.16).

(g) **Skeel–Gear Synchronized Two-Endpoint Dyadic Multirate Scheduler with Leaf/Apex Decoupling:** A time-reversible dyadic step hierarchy $h_k = \Delta t_{\mathrm{macro}}/2^{k_{\mathrm{sym},n}}$ governed by the two-endpoint symmetric selector $k_{\mathrm{sym},n} = \max(k_{\mathrm{dyn}}(\mathbf{z}_n), k_{\mathrm{dyn}}(\Phi^{(0)}_{\Delta t_n}(\mathbf{z}_n)), k_{\mathrm{sched}})$ with bit-exact scaled-integer timestamping (Remark 6.3.4), enforcing intra-block chart freezing (Proposition 5.22, Proposition 6.14), bilateral pericenter anticipation, and the Leaf/Apex Decoupling Theorem with two-regime quadrupolar tidal modulation ($\tau_{\mathrm{pair}}(C) = \min(\tau_{\mathrm{dyn}}(C), \max(\tau_{\mathrm{reg},1}, \tau_{\mathrm{reg},2}))$, Theorem 5.25, Proposition 5.24, Proposition 5.26, and Theorem 6.9), preventing dyadic step-size collapse ($k \le 2$, $k_{\mathrm{sym}} \equiv 0$ on isolated binaries) during extreme pericenter passages ($e \to 1$).

1.7. **Outline of the Paper.** The remainder of this treatise is organized into eight principal sections, progressing systematically from differential-geometric foundations and canonical Hamiltonian splittings to high-order processed symplectic schemes, asynchronous multirate algorithms, dual-precision empirical metrology, and overarching perspectives, complemented by a unified formal and computational appendix:

Section 1 (Introduction and Common Mathematical Foundations):
Establishes the astrophysical motivation, the measure-theoretic foundation grounded in Saari's theorems guaranteeing unsoftened integration on all positive-measure phase-space events, the core theoretical and numerical claims, and the common mathematical primitives (§1.8: relative configuration manifold M_{rel}, singular collision arrangement Δ, canonical Darboux symplectic structure ω_0, and the 11-dimensional centrally extended Lie–Bargmann Poisson algebra $\mathfrak{bargmann}(3)$, Proposition 1.1).

Section 2 (Calaque–Safronov Normal Cone Methodology and Algorithmic Recipes):
Develops the geometric theory of the deformation to the normal cone $\pi : \mathcal{D}_Z M = \mathrm{Spec}_M \mathcal{R}(\mathcal{I}_Z) \to \mathbb{A}^1$ via the graded Rees algebra and establishes the additive splitting of the degenerated symplectic 2-form ω_{normal} on $T^*(N_{Z/M})$ into base coordinates and flat abelian cotangent fiber translations (§2.1, Theorem 2.1, Proposition 2.2). Formulates the canonical four-step normal-cone Strang splitting $\mathcal{S}_2(h) = \Phi^{NL}_{h/2} \circ \Phi^{\mathcal{G}}_h \circ \Phi^{NL}_{h/2}$ coupling $t = 0$ transverse impulses with the $t = 1$ symplectic groupoid exponential map $\Phi^{\mathcal{G}}_h$, proving unconditional Casimir conservation and exact time-symmetry with odd Baker–Campbell–Hausdorff generator parity (§2.2, Theorem 2.3, Proposition 2.4). Demonstrates how this framework retrospectively unifies and explains the structural fidelity of explicit Lie–Poisson integrators for the SE(3) heavy rigid top on $\mathfrak{se}(3)^*$ and Bogomolov–Kirchhoff point-vortex dynamics on $(\mathbb{S}^2)^K$ (§2.3, Proposition 2.5).

Section 3 (The Planar Three-Body Prototype and Classical Regularizations):
Investigates the planar circular restricted three-body problem (PCR3BP) in synodic coordinates as a foundational low-dimensional archetype, establishing the exact invariance of the Jacobi constant $C_J = -2H_{\mathrm{syn}}$ (alongside Szebehely's gauge shift $C_{\mathrm{Sz}} = C_J + \mu(1-\mu)$) and the canonical decoupling between the exact linear Coriolis-kinematic flow $\Psi^{\mathrm{kin}}_h \in \mathrm{Sp}(4,\mathbb{R})$ and transverse gravitational kicks (§3.1, Proposition 3.1). Proves that classical analytical regularizations—Sundman's conformal clock $\mathrm{d}t = r\,\mathrm{d}\tau$, Levi-Civita's branched $2:1$ spinor covering $z = w^2$ on $\mathbb{P}(N_Z M) \cong \mathbb{S}^1$, Birkhoff's global primary regularization, Kustaanheimo–Stiefel's 4D spinor lift, and McGehee's real oriented spherical blow-up $\mathrm{Bl}_Z M \cong \mathbb{S}^1 \times \mathbb{R}_{\geq 0}$—arise as local coordinate slices of the special fiber $t = 0$ of $\mathcal{D}_Z M$ while exposing their global time-freezing, spinor-branching, and non-transversality obstructions for $N \geq 3$ (§3.2, Theorem 3.2, Remark 3.2.1). Validates the dyadic normal-cone solver governed by the harmonic Sundman scale $\chi(q) = r_1 r_2/(r_1+r_2)$ on multi-loop Arenstorf periodic orbits ($|\Delta C_J| < 10^{-14}$, §3.3, Remark 3.3.1, Appendix A.2).

Section 4 (Fulton–MacPherson Compactification and Multiscale Splitting):
Constructs the real oriented Fulton–MacPherson compactification $\mathbf{Q}[N] = \mathrm{Bl}_{\mathcal{G}_{\mathrm{irr}}}(M_{\mathrm{rel}})$ along the irreducible building set of the Whitney partition lattice $\Pi(N)$, turning Δ into a simple normal crossing divisor with corners covered by $(2N-3)!!$ binary Jacobi tree charts, contrasting the smooth standard cotangent bundle $T^*\mathbf{Q}[N]$ against Melrose's logarithmic b-cotangent bundle ${}^bT^*\mathbf{Q}[N]$, and proving exact cotangent commutation between disjoint sub-clusters (§4.1, Theorem 4.1, Proposition 4.2). Neutralizes multipolar "ghost poles" via the scale-invariant screening function $\Theta(u_v)$ (in both $\mathcal{C}^\infty$ Gevrey-2 Cauchy mollifier and order-matched $\mathcal{C}^{2k}$ Hermite spline realizations) to establish universal $\mathcal{C}^{1,1}$ Lipschitz regularity, trace-free quadrupolar tidal structure $\mathbf{T}_{\mathrm{apex}} \in \mathrm{Sym}_0(3)$, exact preservation of the 10-generator Lie–Bargmann algebra on $(\mathcal{P}_{\mathrm{ext}}, \Omega_{\mathrm{ext}})$, and palindromic BCH odd-parity symplecticity (§4.2, Theorem 4.4, Propositions 4.5

and 4.6). Identifies the $\mathcal{O}(\delta_{\text{cluster}}^{-5/2})$ asynchronous commutator barrier and resolves it via synchronous super-nodes with universal Anti-Zeno regularization, parameter-free Hill/Marchal–Sundman compactness thresholds ($\eta_{\text{crit}} = 3^{-1/3}$), spectral Schmitt triggers ($[2^{-1/3}, 2^{-1/6}]$), and unimodular $\mathrm{SL}(2,\mathbb{R}) \hookrightarrow \mathrm{Sp}(6N-6,\mathbb{R})$ atlas transitions with positive dwell time under canonical Voronoi partitioning ($\gamma = 1.0$, with optional $\gamma = 0.6$ anti-chattering hysteresis; §4.3, Proposition 4.7, Theorem 4.9, Theorem 4.10, Proposition 4.11, Corollary 4.12).

Section 5 (Symplectic Discretization and High-Order Schemes):

Formulates the 7-operator palindromic Strang propagator $\mathcal{S}_2(h)$ on $(\mathcal{P}_{\text{ext}}, \Omega_{\text{ext}})$ with exact Noether conservation of the 9 kinematic Lie–Bargmann invariants (§5.1, Definition 5.1, Theorem 5.2, Proposition 5.3), resolves the Sheng–Suzuki negative-timestep barrier via the real-analytic Sundman–Stumpff diffeomorphism and McGehee's unitary elastic bounce involution $\mathcal{B}_C^2 = \mathrm{Id}$ to certify the 4th-order Yoshida composition $\mathcal{S}_4(h)$ across exact binary collisions (§5.2, Theorem 5.4, Proposition 5.5, Lemma 5.6, Proposition 5.7), and deploys the optimal 7-stage 4th-order scheme $\mathrm{BM}_4^{(7)}$ ($> 400\times$ BCH error compression and exponential Benettin–Giorgilli shadow confinement at $\varepsilon = 0$, §5.3, Definition 5.8, Theorem 5.9, Theorem 5.10, Proposition 5.11) alongside the 11-stage 6th-order scheme $\mathrm{BM}_6^{(11)}$ and the bi-graded Lie algebra $\mathcal{L}_{n,m}$ governed by $\{A_{\text{JK}}, A_{\text{JK}}\} \equiv 0$ and $\mathrm{ad}^3_{W^{\text{screen}}_{\text{apex}}}(A_{\text{JK}}) \equiv 0$ (§5.4, Definition 5.12, Theorem 5.13, Theorem 5.14, Propositions 5.15 and 5.16). Section 5.5 proves the *Universal Double Obstruction Theorem* at order 6 (Theorem 5.17), constructs the cotangent-lifted partial corrector $K_4 \in \mathcal{L}_{4,1} \cap \mathcal{P}_1$ and 2-stage palindromic conjugator $\mathcal{Z}_4^{\text{BM4}}(h)$ characterized by the incompressible quadratic floor $\mathcal{O}(\varepsilon^2 h^4)$ and zero internal torque (Theorem 5.18), establishes the 5-strata regularity partition of $T^*\mathbf{Q}[N]$ with $\mathcal{O}(r^{7/2})$ free-fall extinction of K_4 at binary collisions (Theorem 5.19), and derives the covariant cotangent-lifted gauge transition operator $T^{(\text{PBM4})}_{(A,h_A)\to(B,h_B)}$ closing the Čech 1-cocycle (Theorem 5.20). Finally, §5.6 establishes the Skeel–Gear synchronized dyadic multirate lattice (Proposition 5.22), the Fundamental Leaf/Apex Decoupling Theorem with two-regime quadrupolar tidal modulation ($\tau_{\text{pair}}(C) = \min(\tau_{\text{dyn}}(C), \max(\tau_{\text{reg},1}, \tau_{\text{reg},2}))$, Theorem 5.25, Proposition 5.24), and dyadic shadow Hamiltonian continuity (Proposition 5.26).

Section 6 (Computational Architecture and Algorithmic Realization):

Translates the mathematical theory into a deterministic, zero-allocation computational architecture: details the six-phase operational pipeline and 16-component state vector (§6.1), $\mathcal{O}(N^2 \log N)$ agglomerative Jacobi tree construction under the unilateral Delaunay–Hill intruder guard ($\gamma_{\text{build}} = 1.0$) and antipodal half-shell shadow preprocessing $\mathcal{Z}_4^{\text{BM4}}(h)$ (§6.2, Proposition 6.2, Theorem 6.5, Proposition 6.6), the time-reversible two-endpoint predictive dyadic scheduler $k_{\text{sym},n} = \max(k_{\text{dyn}}(\mathbf{z}_n), k_{\text{dyn}}(\Phi^{(0)}_{\Delta t_n}(\mathbf{z}_n)), k_{\text{sched}})$ with bit-exact scaled-integer timestamping (§6.3, Proposition 6.7, Theorem 6.9, Remark 6.3.4), the analytical Kepler–Sundman leaf solver with Weierstrass pericenter conditioning and Battin unimodular projection alongside recursive normal-cone super-nodes and $\mathcal{C}^{2p}$ Hermite-screened apex kicks with exact monopole cancellation $V_{\text{kick}} \equiv V_{\text{inter}}$ (§6.4, Propositions 6.10, 6.11, and 6.12), the strict four-step causal macro-boundary sequence, three-regime Hill-weighted Delaunay–Jacobi chart admissibility, time-reversal-covariant adjoint hysteresis $\mathcal{A}_-$, Čech 1-cocycle closure under $T^{(\text{PBM4})}_{(A,h_A)\to(B,h_B)}$, and Battin Wronskian / Lie–Bargmann metrology (§6.5, Propositions 6.13 and 6.14, Theorem 6.15, Remark 6.5.2, Theorem 6.16, Proposition 6.18), and high-performance vectorized and LLVM JIT-compiled micro-kernels (0.0 ULP bit-exact equivalence and up to $62.54\times$ apex and $59.83\times$ super-node speedups across $N \in [3, 64]$) alongside 35-digit `Float128` reference solvers (§6.6, Propositions 6.19 and 6.20).

Section 7 (Numerical Benchmarks):

Conducts a comprehensive empirical validation following the spectral metrology of the Laskar school across dual-precision (53-bit `Float64` and 116-bit `Float128`) implementations. Section 7.1 evaluates Laskar's inverse-cost metric τ/s on the Chenciner–Montgomery Figure-8 choreography [18] and 3D eccentric hierarchical triples, isolates Brouwer's $\propto N^{1/2}$ roundoff regime from true asymptotic slopes ($p = 2.000, 3.999, 4.000, 4.000, 5.999$ down to 3.74×10^{-31} in energy and 1.89×10^{-31} in position, §7.1.1), experimentally confirms the two-channel $p_{\text{eff}} = 6.25 \to 4.00$ crossover (2,537× energy and 1,335× position gain) and 100×/decade $\mathcal{O}(\varepsilon^2 h^4)$ quadratic floor of Theorem 5.18 (§7.1.2), and benchmarks four unsoftened singular limit cases (§7.1.3: L1 analytic pericenter conditioning down to $1 - e = 10^{-12}$ and $e = 1.0$ with $k_{\text{sym}} \equiv 0$, L2 $\mathcal{O}(r^{7/2})$ asymptotic free-fall extinction of the PBM_4 cotangent corrector across $r \in [10^{-12}, 10^{0}]$ AU, L3 exact McGehee central-collision traversals for $k \in \{2, 3, 4\}$, and L4 chaotic 3-4-5 Burrau scattering and $i_0 = 84.0°$ 3D Kozai–Lidov secular resonance). Section 7.2 validates historical astronomical encounters (§7.2.1) and long-term secular stability (§7.2.2): Comet Lexell's 1770/1779 Jovian encounters ($3.031\, R_J$, demonstrating interfacial shadow-jump suppression down to 2.36×10^{-35} in `Float128` and 0.00 in `Float64` under $T^{(\text{PBM4})}_{(A,h_A)\to(B,h_B)}$), Shoemaker–Levy 9's 1992 sub-Roche tidal disruption ($1.336\, R_J < 2.45\, R_J$, $\Lambda_S^{\max} = 16{,}690$), Asteroid Apophis's 2029 Aten → Apollo deflection and full-flyby palindromic time-reversibility, the 4:2:1 Jovian Laplace resonance under active dyadic substepping ($k_{\text{sym}} \equiv 3$, 17.6× max / 32.6× RMS shadow energy reduction in `Float128` [5.8× / 7.5× in `Float64`] and $179.85° \pm 0.80°$ resonant locking), and Inner Solar System secular integrations across 264 dyadic junctions (22.4× `Float64` / 27.3× `Float128` RMS shadow energy reduction, unbiased $\propto t^{1/2}$ Brouwer Noether diffusion, and 2,120× Laskar NAFF frequency convergence down to the 3.70×10^{-13} spectral floor with KAM symplectic conjugacy invariance [37]). Finally, Section 7.3 (§7.3.1–§7.3.4, including the cross-benchmark synthesis in §7.3.4) conducts three head-to-head comparative benchmark suites against the compiled C99 integrators of `REBOUND 5.2.2` (`IAS15` [53, 57, 58], `TRACE` [41], `MERCURIUS` [56], and `WHFast` [59, 60]) across star-grazing pericenters ($1-e_1 \in [10^{-9}, 10^{-1}]$ with 29,423× tighter round-trip reversibility than `IAS15`) and exact collision $e_1 = 1.0$ ($9.40 \times 10^{9}\times$ more accurate than `TRACE` and $9.13 \times 10^{11}\times$ over `IAS15`) with exact index-permutation invariance (`B1`), deep Jovicentric Hill-sphere crossings ($3.98 \times 10^{-4}\, R_{\text{Hill},J}$, 8,858 ×–33,618× interfacial jump suppression and exact machine zero on three of the seven flybys via $T^{(\text{PBM4})}_{A\to B}$, overcoming the Wisdom [81] second-order hybrid switching barrier with $3.69\times10^{7}\times$ lower energy error and 61,734× tighter reversibility than `TRACE`) and repeated giant-planet Hill crossings (`B2`), and democratic Pythagorean 3–4–5 chaotic scattering across 27 Voronoi chart transitions (37.2× at $T = 40$ up to 133.9× at $T = 80$ tighter pre-saturation reversibility than `IAS15` in `Float64` at $k = 0$) and across the `Float64` Lyapunov horizon via 35-digit `Float128` ($1.80 \times 10^{20}\times$ tighter post-horizon reversibility at $T = 120$, `B4`).

Section 8 (Conclusion and Outlook):

Synthesizes the theoretical, algebraic, and algorithmic achievements of the monograph alongside its demonstrated numerical capabilities and intrinsic mathematical boundaries (§8.1), and formulates four open research questions regarding ultra-high-order processed cotangent schemes beyond PBM_4, anisotropic multi-body collision regularizations ($k \geq 3$), $\mathcal{O}(N \log N)$ fast-multipole coupling for dense star clusters, and momentum-dependent post-Newtonian or stratified potentials (§8.2).

Appendix A (Certified Lean 4 Formal Artifacts and Numerical Schemes):

Throughout Sections 1 to 7, definitions, propositions, theorems, algorithms, and empirical benchmarks are anchored by verification badges cross-referencing Appendix A (§A.1–§A.2), which co-locates the complete, zero-`sorry` mechanized Lean 4 formal proofs (35 modules comprising 125 formal declarations covering the Constructive 1-Jet Algebraic

Kernel, graded Rees degeneration, planar synodic and Levi-Civita regularizations, Whitney partition lattice, $\mathcal{C}^{1,1}$ apex bounds, Anti-Zeno super-nodes, Universal Double Obstruction Theorem, cotangent corrector $K_4 \in \mathcal{P}_1$, and Čech 1-cocycle gauge transitions) and the complete directory tree and module-by-module locator of the dual-precision companion GitHub repository (`normal_cone_nbody_float64/` and `normal_cone_nbody_float128/`, §*A*.2).

1.8. **Common Mathematical Foundations and Notational Primitives.** To bridge continuous differential geometry with mechanized verification, our accompanying Lean 4 development [21] formalizes the *Constructive 1-Jet Algebraic Kernel*: by operating on algebraic 1-jets of observables over an arbitrary commutative ring rather than infinite-dimensional Fréchet manifolds, it certifies the finite-dimensional tangent-space symplectic structure, the constructive duality of collision loci, and the closed Lie algebra of observables that underpin our numerical integrators.

1.8.1. *Ambient and Relative Configuration Manifolds.* Let $N \geq 3$ be the number of gravitationally interacting point masses $m_1, \ldots, m_N > 0$. The *ambient configuration manifold* models the unconstrained spatial positions of all N bodies in physical three-dimensional space:

$$M = (\mathbb{R}^3)^N = \{\mathbf{q} = (\mathbf{q}_1, \ldots, \mathbf{q}_N) \mid \mathbf{q}_i \in \mathbb{R}^3\} \cong \mathbb{R}^{3N}. \tag{1.5}$$

The manifold M is naturally equipped with the mass-weighted Riemannian kinetic metric:

$$\langle \mathbf{v}, \mathbf{w} \rangle_{\mathbb{M}} = \sum_{i=1}^{N} m_i \mathbf{v}_i \cdot \mathbf{w}_i = \mathbf{v}^T \mathbb{M} \mathbf{w}, \tag{1.6}$$

where $\mathbb{M} = \mathrm{diag}(m_1 \mathbb{I}_3, \ldots, m_N \mathbb{I}_3)$ denotes the positive-definite mass tensor, and the total mass is $M_{\mathrm{tot}} = \sum_{i=1}^{N} m_i > 0$.

Lean A.1 : `AmbientConfiguration`

The diagonal linear subspace of uniform spatial translations is defined by:

$$\Delta_{\mathrm{trans}} = \{\mathbf{q} \in M \mid \mathbf{q}_1 = \cdots = \mathbf{q}_N\} \subset M \cong \mathbb{R}^3. \tag{1.7}$$

Under an arbitrary spatial translation $\mathbf{q}_i \mapsto \mathbf{q}_i + \mathbf{a}$ with $\mathbf{a} \in \mathbb{R}^3$, the center of mass vector $\mathbf{R}_{\mathrm{cdm}}(\mathbf{q}) = \frac{1}{M_{\mathrm{tot}}} \sum_{i=1}^{N} m_i \mathbf{q}_i$ undergoes a pure rigid translation $\mathbf{R}_{\mathrm{cdm}} \mapsto \mathbf{R}_{\mathrm{cdm}} + \mathbf{a}$.

To decouple this trivial Galilean drift, we identify the *relative configuration manifold* with the orthogonal barycentric slice $M_0 = \Delta_{\mathrm{trans}}^{\perp} = \{\mathbf{q} \in M \mid \sum_{i=1}^{N} m_i \mathbf{q}_i = \mathbf{0}\}$:

$$M_{\mathrm{rel}} = M / \Delta_{\mathrm{trans}} \cong M_0 \cong (\mathbb{R}^3)^{N-1}. \tag{1.8}$$

Lean A.1 : `RelativeConfiguration`

1.8.2. *The Singular Collision Arrangement and Locus.* For each distinct pair of particles $1 \leq i < j \leq N$, the pairwise binary collision locus is the linear submanifold:

$$\Delta_{ij} = \{\mathbf{q} \in M \mid \mathbf{q}_i = \mathbf{q}_j\} \subset M, \tag{1.9}$$

which is of codimension 3 in M. It is algebraically cut out by the pairwise vanishing ideal:

$$\mathcal{I}(\Delta_{ij}) = \langle q_{i,a} - q_{j,a} \mid a = 1, 2, 3 \rangle \subset \mathcal{O}_M. \tag{1.10}$$

Lean A.1 : `BinaryCollision`

The global singular collision arrangement Δ is the union of all pairwise collision diagonals across all possible particle pairs:

$$\Delta = \bigcup_{1 \leq i < j \leq N} \Delta_{ij} \subset M, \qquad \mathcal{I}_\Delta = \bigcap_{1 \leq i < j \leq N} \mathcal{I}(\Delta_{ij}) \subset \mathcal{O}_M. \tag{1.11}$$

Lean A.1 : `InCollisionLocus`

The physical domain of collisionless Newtonian motion is the *regular configuration locus*, defined by excising the collision arrangement from the configuration manifold:

$$X = M \setminus \Delta, \qquad X_{\mathrm{rel}} = M_0 \setminus (M_0 \cap \Delta). \tag{1.12}$$

Lean A.1 : `NonCoincident`

The regular locus X represents configurations where all particles remain pairwise distinct. The certified formal duality establishes that this condition is constructively and logically equivalent to the negation of membership in the collision locus:

Lean A.1 : regular_iff_not_collision

1.8.3. *Symplectic Phase Space and Lie–Bargmann Algebra.* The physical phase space of the system is the cotangent bundle $T^*X \subset T^*M \cong \mathbb{R}^{3N} \times \mathbb{R}^{3N}$, parameterized by the canonical position and momentum coordinates $(\mathbf{q}, \mathbf{p}) = (\mathbf{q}_1, \dots, \mathbf{q}_N, \mathbf{p}_1, \dots, \mathbf{p}_N)$ with $\mathbf{p}_i = m_i \dot{\mathbf{q}}_i \in \mathbb{R}^3$.

The cotangent bundle carries the canonical Liouville 1-form $\theta_0 = \sum_{i=1}^N \mathbf{p}_i \cdot \mathrm{d}\mathbf{q}_i$ and the exact Darboux symplectic 2-form:

$$\omega_0 = -\mathrm{d}\theta_0 = \sum_{i=1}^{N} \sum_{a=1}^{3} \mathrm{d}\mathbf{q}_{i,a} \wedge \mathrm{d}\mathbf{p}_{i,a}. \tag{1.13}$$

Lean A.1 : omega0

The symplectic form ω_0 is closed ($\mathrm{d}\omega_0 = 0$), skew-symmetric, and alternating on all tangent variations:

Lean A.1 : omega0_skew

It satisfies constructive non-degeneracy on the configuration tangent space:

$$\forall v \in T(T^*X), \quad (\forall w \in T(T^*X),\, \omega_0(v, w) = 0) \implies v = 0. \tag{1.14}$$

Lean A.1 : omega0_tangent_nondeg

On smooth observables $f, g \in \mathcal{C}^\infty(T^*X)$, the canonical Poisson bracket induced by ω_0 is given by:

$$\{f, g\}_0 = \sum_{i=1}^{N} \left(\frac{\partial f}{\partial \mathbf{q}_i} \cdot \frac{\partial g}{\partial \mathbf{p}_i} - \frac{\partial f}{\partial \mathbf{p}_i} \cdot \frac{\partial g}{\partial \mathbf{q}_i} \right). \tag{1.15}$$

Lean A.1 : poissonBracketVal

The unsoftened Newtonian dynamics is governed by the kinetic energy $T(\mathbf{p}) = \frac{1}{2}\mathbf{p}^T \mathbb{M}^{-1} \mathbf{p}$ and the singular pairwise gravitational potential $V(\mathbf{q}) = -\sum_{1 \le i < j \le N} \frac{G m_i m_j}{\|\mathbf{q}_i - \mathbf{q}_j\|}$, yielding the fundamental autonomous first integrals:

$$\mathbf{P}_{\mathrm{tot}} = \sum_{i=1}^{N} \mathbf{p}_i, \quad \mathbf{L}_{\mathrm{tot}} = \sum_{i=1}^{N} \mathbf{q}_i \times \mathbf{p}_i, \quad \mathbf{K} = \sum_{i=1}^{N} m_i \mathbf{q}_i = M_{\mathrm{tot}} \mathbf{R}_{\mathrm{cdm}}, \quad H = T(\mathbf{p}) + V(\mathbf{q}). \tag{1.16}$$

Proposition 1.1 — *Central Poisson Closure of the Lie–Bargmann Algebra in T^*X*

Following Bargmann [4], the autonomous observables $(\mathbf{P}_{\mathrm{tot}}, \mathbf{L}_{\mathrm{tot}}, \mathbf{K}, H, \mathbf{1})$ generate an 11-dimensional closed Poisson Lie algebra on T^*X isomorphic to the centrally extended Galilean algebra $\mathfrak{bargmann}(3) \cong \mathfrak{gal}(3) \oplus_\omega \mathbb{R}\mathbf{1}$, satisfying the canonical brackets:

$$\begin{aligned} &\{K_a, P_b\}_0 = M_{\mathrm{tot}} \delta_{ab} \mathbf{1}, && \{L_a, K_b\}_0 = \varepsilon_{abc} K_c, \\ &\{L_a, L_b\}_0 = \varepsilon_{abc} L_c, && \{L_a, P_b\}_0 = \varepsilon_{abc} P_c, \\ &\{H, \mathbf{P}_{\mathrm{tot}}\}_0 \equiv \mathbf{0}, && \{H, \mathbf{L}_{\mathrm{tot}}\}_0 \equiv \mathbf{0}, && \{K_a, H\}_0 = P_a. \end{aligned} \tag{1.17}$$

Lean A.1 : BargmannAlgebra.poisson_L_X_L_Y

Lean A.1 : BargmannAlgebra.poisson_P_G_same

Python A.2 : core/invariants.py, diagnostics/metrics.py [Float64 / Float128]

Proof. By the canonical Darboux brackets $\{q_{i,a}, p_{j,b}\}_0 = \delta_{ij}\delta_{ab}$ and $\{q_{i,a}, q_{j,b}\}_0 = \{p_{i,a}, p_{j,b}\}_0 = 0$, the kinematic brackets follow from direct componentwise contraction of the Levi-Civita tensor ε_{abc}: $\{K_a, P_b\}_0 = \sum_{i,j} m_i \{q_{i,a}, p_{j,b}\}_0 = \left(\sum_i m_i\right)\delta_{ab} = M_{\mathrm{tot}}\delta_{ab}\mathbf{1}$, $\{L_a, K_b\}_0 = \sum_{i,c,d} \varepsilon_{acd} m_i q_{i,c} \delta_{db} = \varepsilon_{abc} K_c$, $\{L_a, P_b\}_0 = \varepsilon_{abc} P_c$, and $\{L_a, L_b\}_0 = \varepsilon_{abc} L_c$. For the Hamiltonian $H = T(\mathbf{p}) + V(\mathbf{q})$, since $T(\mathbf{p}) = \sum_{i=1}^N \frac{\|\mathbf{p}_i\|^2}{2m_i}$ depends solely on momenta and $V(\mathbf{q})$ depends solely on pairwise Euclidean distances $r_{ij} = \|\mathbf{q}_i - \mathbf{q}_j\|$, skew-symmetry $\nabla_{\mathbf{q}_i} r_{ij} = -\nabla_{\mathbf{q}_j} r_{ij}$ and collinearity $(\mathbf{q}_i - \mathbf{q}_j) \times \nabla_{\mathbf{q}_i} r_{ij} = \mathbf{0}$

yield $\sum_{i=1}^N \nabla_{\mathbf{q}_i} V = \mathbf{0}$ and $\sum_{i=1}^N \mathbf{q}_i \times \nabla_{\mathbf{q}_i} V = \mathbf{0}$ as in (1.4), while $\sum_{i=1}^N \mathbf{p}_i \times \nabla_{\mathbf{p}_i} T = \sum_{i=1}^N m_i^{-1}(\mathbf{p}_i \times \mathbf{p}_i) = \mathbf{0}$; hence $\{H, \mathbf{P}_{\rm tot}\}_0 = \sum_i \nabla_{\mathbf{q}_i} V \equiv \mathbf{0}$ and $\{H, \mathbf{L}_{\rm tot}\}_0 \equiv \mathbf{0}$. Finally, since $\{K_a, V(\mathbf{q})\}_0 = 0$, one obtains $\{K_a, H\}_0 = \{K_a, T(\mathbf{p})\}_0 = \sum_{i=1}^N m_i \frac{\partial T}{\partial p_{i,a}} = \sum_{i=1}^N p_{i,a} = P_a$.

□

In extended phase space-time, the non-autonomous secular Galilean boost $\mathbf{G}(t) = \mathbf{K} - t\mathbf{P}_{\rm tot}$ completes the ten classical Galilean first integrals, satisfying $\{P_a, G_b\}_0 = -M_{\rm tot}\delta_{ab}\mathbf{1}$ and vanishing total convective derivative along the Hamiltonian flow:

$$\frac{\mathrm{d}\mathbf{G}}{\mathrm{d}t} = \frac{\partial \mathbf{G}}{\partial t} + \{\mathbf{G}, H\}_0 = -\mathbf{P}_{\rm tot} + \mathbf{P}_{\rm tot} \equiv \mathbf{0}. \tag{1.18}$$

2. Calaque–Safronov Normal Cone Methodology and Algorithmic Recipes

2.1. **The Deformation to the Normal Cone and Graded Rees Algebra.** A foundational obstruction in the numerical simulation of singular Hamiltonian systems is that standard numerical integrators discretize the phase space in an undifferentiated manner. Near a singularity, metric gradients diverge, forcing variable-step algorithms into an infinite slowdown (the Sundman time-freezing dilemma [72]) or prompting ad-hoc potential softening that alters the secular invariants of the physical model.

To resolve this dilemma without metric alteration, we invoke the canonical geometric degeneration developed in algebraic geometry by Fulton [23] and Verdier [78], and elevated to derived symplectic geometry by Calaque and Safronov [15]: the *deformation to the normal cone*. Rather than regularizing a singularity by adding artificial isotropic parameters, this construction replaces the ambient phase space with a one-parameter family of geometries interpolating smoothly between the non-linear global dynamics and a flat, abelian linear model at the singularity.

Ontological Scope: Classical Symplectic Mechanics vs. Shifted Derived Geometry.—While Calaque and Safronov [15] formalize the deformation to the normal cone within the higher category of derived prestacks equipped with shifted symplectic and Lagrangian structures ($n \in \mathbb{Z}$), our physical Hamiltonian phase space and accompanying Lean 4 kernel operate on the classical degree-0 differential framework: smooth finite-dimensional manifolds $M = \mathbb{R}^{3N}$, classical unshifted cotangent bundles T^*M, and canonical Darboux 2-forms ω_0. Calaque and Safronov's theory provides the conceptual and functorial justification for the normal cone degeneration, which we instantiate in unshifted Hamiltonian mechanics.

To bridge global derived algebraic geometry with mechanized proof, our accompanying Lean 4 development formalizes the *Constructive 1-Jet Algebraic Kernel*: it certifies the retraction of the evaluation morphism onto the singular base stratum, the canonical normal cone symplectic 2-form ω_{normal}, its constructive non-degeneracy, and the exact symplecticity of the transverse fiber flow.

2.1.1. *The Graded Rees Algebra and Affine Degeneration.* To describe the local geometry near a singular or collision locus $Z \subset M$ without coordinate pathology, we equip the smooth configuration manifold M with its structure sheaf $\mathcal{O}_M$ of smooth (or regular algebraic) functions. The closed submanifold Z is intrinsically defined by the collection of functions that vanish along it; this forms the *ideal sheaf* $\mathcal{I}_Z \subset \mathcal{O}_M$. In local adapted coordinates $(x, y) \in Z \times \mathbb{R}^k$ where the locus is cut out by $\{y_1 = \cdots = y_k = 0\}$, the ideal $\mathcal{I}_Z$ is locally generated by the transverse coordinate functions $(y_1, \ldots, y_k)$, and its powers $\mathcal{I}_Z^k$ consist of functions vanishing to order at least k on Z.

The canonical geometric degeneration of M toward the normal bundle of Z is algebraically encoded by the *graded Rees algebra* $\mathcal{R}(\mathcal{I}_Z)$ over the affine line $\mathbb{A}^1 = \operatorname{Spec} \mathbb{R}[t]$, which rescales functions according to their vanishing order along Z:

$$\mathcal{R}(\mathcal{I}_Z) = \bigoplus_{k \in \mathbb{Z}} t^{-k} \mathcal{I}_Z^k \subset \mathcal{O}_M[t, t^{-1}], \tag{2.1}$$

with $\mathcal{I}_Z^k = \mathcal{O}_M$ for $k \leq 0$. The total deformed space is the relative spectrum $\mathcal{D}_Z M = \operatorname{Spec}_M \mathcal{R}(\mathcal{I}_Z)$, canonically fibered over the affine line via $\pi : \mathcal{D}_Z M \to \mathbb{A}^1$. Geometrically, $\mathcal{D}_Z M \cong \operatorname{Bl}_{Z \times \{0\}}(M \times \mathbb{A}^1) \setminus \widetilde{M \times \{0\}}$.

To develop geometric intuition for this algebraic construction, consider the adapted coordinates (x, y). For any $t \neq 0$, the scaling map $(x, y) \mapsto (x, y/t)$ identifies the generic fiber $\pi^{-1}(t)$ with M. As $t \to 0$, the dilated transverse coordinate $n = y/t$ parametrizes the linear vector space $N_{Z/M}$. The deformation thus acts as an intrinsic differential microscope, blowing up an infinitesimal neighborhood of the singular locus Z into a full vector space where non-linear metric stiffness degenerates into abelian translational invariance.

Theorem 2.1 — *Fulton–Verdier Deformation and Calaque–Safronov Degeneration* Following Fulton [23, Chapter 5, §5.1–5.2], Verdier [78], and Calaque and Safronov [15, Theorem C, Section 3.1 & Section 5.2], the fibration $\pi : \mathcal{D}_Z M \to \mathbb{A}^1$ establishes a smooth one-parameter geometric degeneration:

(1) **Generic Fiber ($t \neq 0$):** $\pi^{-1}(t) \cong M$ canonically for any $t \in \mathbb{A}^1 \setminus \{0\}$.
(2) **Central Special Fiber ($t = 0$):** At the degenerate apex $t = 0$, the fiber is canonically isomorphic to the normal bundle (or normal cone) of Z in M:

$$\pi^{-1}(0) \cong N_{Z/M} = \mathrm{Spec}_Z \left(\bigoplus_{k \geq 0} \mathcal{I}_Z^k / \mathcal{I}_Z^{k+1} \right). \tag{2.2}$$

Lean A.1 : deformation_limit_zero

In the accompanying mechanized 1-jet algebraic kernel, the evaluation morphism retracts identically onto the singular base stratum Z at $t = 0$ (see Figure 2).

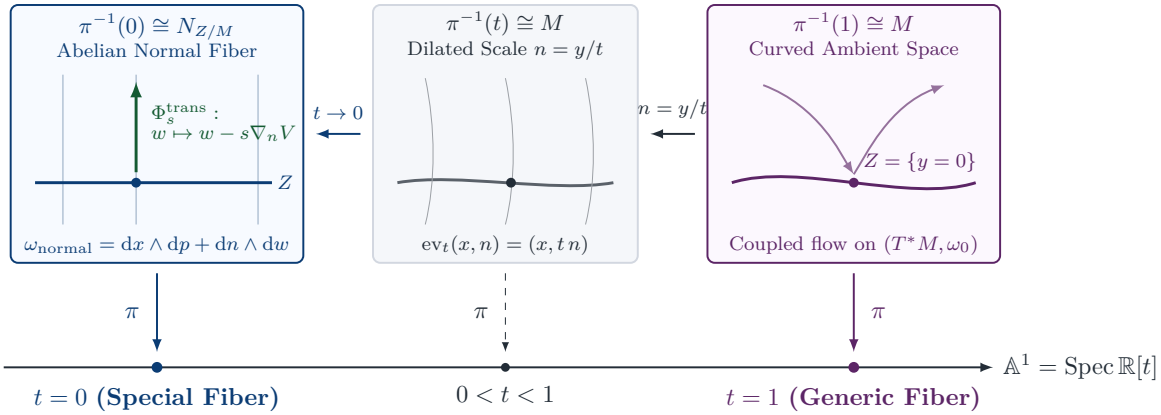


FIGURE 2. Geometric degeneration of the graded Rees fibration $\pi : \mathcal{D}_Z M = \mathrm{Spec}_M \mathcal{R}(\mathcal{I}_Z) \to \mathbb{A}^1$ and its cotangent lift (Theorem 2.1 and Proposition 2.2). As $t \to 0$, the rescaled transverse coordinate $n = y/t$ blows up an infinitesimal tubular neighborhood of the singular locus $Z \subset M$ into the flat normal bundle $\pi^{-1}(0) \cong N_{Z/M}$, where non-linear potential forces become exact linear momentum translations Φ_s^{trans} along the cotangent fibers $N^*_{Z/M}$.

2.1.2. *Symplectic Cotangent Lift and Transverse Normal Leaves.* In the framework of derived symplectic geometry [15], the cotangent lift of this family carries a relative symplectic form Ω_{rel} over $\mathbb{A}^1$.

The essential computational property uncovered by this degeneration is that the cotangent bundle of the central fiber $T^*(N_{Z/M})$ inherits a strictly *abelian, linear symplectic structure*. In canonical Darboux coordinates $(x, n, p, w) \in T^*(N_{Z/M})$, where $(x, p) \in T^*Z$ and $(n, w) \in N_{Z/M} \times_Z N^*_{Z/M}$ (the Whitney sum $N_{Z/M} \oplus N^*_{Z/M}$), the canonical 2-form splits additively:

$$\omega_{\mathrm{normal}} = \sum_a \mathrm{d}x_a \wedge \mathrm{d}p_a + \sum_b \mathrm{d}n_b \wedge \mathrm{d}w_b. \tag{2.3}$$

Lean A.1 : omegaNormal

Lean A.1 : omegaNormal_nondegenerate

While the dynamics on the generic fiber T^*M is governed by coupled non-linear equations with divergent curvatures near Z, the transverse motion along the cotangent fibers $N^*_{Z/M}$ degenerates into an exact translation generated by the normal gradient of the potential:

Proposition 2.2 — *Exact Normal Cone Symplectic Folia and Fiber Linearity*
In the sense of Cannas da Silva [20, Chapter 2] and Calaque and Safronov [15, Theorem C], let $V(n)$ be a smooth transverse potential on the normal cone fibers with symmetric Hessian matrix. The transverse fiber flow $\Phi_s^{\text{trans}}(x, n, p, w) = (x, n, p, w - s\nabla_n V(n))$ satisfies exact symplectomorphism with respect to ω_{normal}:

$$(\Phi_s^{\text{trans}})^* \omega_{\text{normal}} = \omega_{\text{normal}}. \tag{2.4}$$

Furthermore, the position and base momentum variations $(\delta x, \delta p, \delta n)$ are strictly preserved by Φ_s^{trans}, isolating all non-linear force accumulation into pure momentum translations along the flat transverse cotangent fibers.

Lean A.1 : `transverse_conormal_flow_symplectic`

Proof. Under the transverse fiber flow $\Phi_s^{\text{trans}}(x, n, p, w) = (x, n, p, w - s\nabla_n V(n))$, the differentials of the canonical Darboux coordinates transform as $\mathrm{d}x'_a = \mathrm{d}x_a$, $\mathrm{d}p'_a = \mathrm{d}p_a$, $\mathrm{d}n'_b = \mathrm{d}n_b$, and $\mathrm{d}w'_b = \mathrm{d}w_b - s\sum_c H_{bc}(n)\,\mathrm{d}n_c$, where $H_{bc}(n) = \partial^2 V/(\partial n_b \partial n_c)$ is the Hessian matrix of V. Pulling back the normal cone symplectic 2-form yields

$$(\Phi_s^{\text{trans}})^* \omega_{\text{normal}} = \sum_a \mathrm{d}x_a \wedge \mathrm{d}p_a + \sum_b \mathrm{d}n_b \wedge \mathrm{d}w_b - s\sum_{b,c} H_{bc}(n)\,\mathrm{d}n_b \wedge \mathrm{d}n_c. \tag{2.5}$$

Since $H_{bc}(n) = H_{cb}(n)$ is symmetric while the exterior product $\mathrm{d}n_b \wedge \mathrm{d}n_c = -\mathrm{d}n_c \wedge \mathrm{d}n_b$ is alternating, the double sum vanishes identically, establishing $(\Phi_s^{\text{trans}})^* \omega_{\text{normal}} = \omega_{\text{normal}}$.

□

This decoupling provides an exact geometric criterion: rather than fighting non-linear stiffness near singular strata with infinitesimal time steps, one can decompose the Hamiltonian vector field into a motion preserving the base Z and a flat, exact translation along the transverse cotangent fibers of $N^*_{Z/M}$.

2.2. **The Canonical 4-Step Normal Cone Splitting Recipe.** Translating the derived geometry of Calaque and Safronov into an operational numerical algorithm requires a systematic four-step procedure. Rather than applying an off-the-shelf black-box integrator or heuristic regularizations, the normal cone methodology dictates where and how to partition the physical phase space into complementary sub-geometries: a stiff singular base manifold Z and a flat, abelian transverse momentum fiber $N^*_{Z/M}$.

2.2.1. *The Four Invariant Steps of Normal Cone Splitting.* Given an autonomous Hamiltonian system $\dot{\mathbf{z}} = \mathbb{J}\nabla H(\mathbf{z})$ on a symplectic manifold (T^*M, ω_0), the normal cone geometric discretization proceeds systematically as follows:

Step 1: Canonical Detection and Partition $(Z, N_{Z/M})$:

Identify the geometric submanifold $Z \subset M$ governing the stiffness, constraints, or singular locus of the physical interaction (e.g., an algebraic collision divisor Δ_{ij}, a rigid spherical constraint $\mathbb{S}^2$, or an attitude Lie group SO(3)). On the full cotangent bundle T^*M, canonical Darboux coordinates partition the state into base variables $(\mathbf{x}_Z, \mathbf{p}_Z) \in T^*Z$ and transverse normal and cotangent variables $(\mathbf{n}, \mathbf{w}) \in N_{Z/M} \times_Z N^*_{Z/M}$. On reduced Lie–Poisson spaces $\mathfrak{g}^*$ (such as rigid body dynamics), this reduces to base orientation $\mathbf{x}_Z \in Z$ and conjugate transverse momentum $\mathbf{p}_N \in N^*_{Z/M}$:

$$\mathbf{z} = (\mathbf{x}_Z, \mathbf{p}_N) \in Z \times N^*_{Z/M}. \tag{2.6}$$

Step 2: Exact Linear Integration in the Transverse Momentum Fiber ($t = 0$):

In the degenerated central fiber $t = 0$, the transverse dynamics is governed by an abelian vector field. The transverse normal kick $\mathbf{K}(\mathbf{x}_Z) = -\nabla_N V(\mathbf{x}_Z)$ induces an exact linear momentum translation along the flat transverse momentum fibers without matrix inversion or non-linear iteration:

$$\Phi^{NL}_{h/2}: \quad \mathbf{p}_N \longmapsto \mathbf{p}_N + \frac{h}{2}\mathbf{K}(\mathbf{x}_Z), \qquad \mathbf{x}_Z \longmapsto \mathbf{x}_Z. \tag{2.7}$$

Because $\mathbf{K}(\mathbf{x}_Z)$ is strictly transverse and derives from the base geometry, it satisfies the orthogonality condition $\langle \nabla C, \mathbf{K} \rangle = 0$. When C is affine with respect to fiber momenta, this guarantees unconditional preservation for all finite step sizes $h \in \mathbb{R}$ without numerical projection.

Step 3: Symplectic Groupoid Exponential on the Base ($t = 1$):

On the base manifold Z, the motion is non-linear and governed by the Lie algebroid $\mathrm{Lie}(\mathcal{G})$ of configuration symmetries (or the Lie algebra $\mathfrak{g}$ of a symmetry group acting transitively on Z). Rather than applying an unconstrained additive Euler-type update that would depart from the manifold, the flow is integrated via the exact exponential map of the symplectic groupoid $\exp_{\mathcal{G}} : \mathfrak{g} \to \mathcal{G}$, accompanied by the conjugate coadjoint action on momenta:

$$\Phi^{\mathcal{G}}_h: \quad \mathbf{x}_Z \longmapsto \exp_{\mathcal{G}}(h\mathbf{v}(\mathbf{p}_N)) \cdot \mathbf{x}_Z, \qquad \mathbf{p}_N \longmapsto \mathrm{Ad}^*_{\exp_{\mathcal{G}}(h\mathbf{v})}(\mathbf{p}_N). \tag{2.8}$$

For Lie group actions, this is computed via closed-form analytical expressions (e.g., Rodrigues' rotation formula on SO(3) or great-circle geodesics on $\mathbb{S}^2$), preserving algebraic manifold invariants with exact geometric closure (bounded in floating-point realization solely by IEEE 754 roundoff). Crucially, by operating globally on the Lie group action rather than through local chart parameterizations, this groupoid update is intrinsically immune to coordinate singularities, entirely circumventing artificial coordinate breakdowns such as gimbal lock in Euler angle formulations or polar coordinate singularities at coordinate axes.

Step 4: Symmetric Canonical Splitting and High-Order Compositions:
Compose the transverse normal kick and the groupoid exponential into a time-reversible, second-order Strang splitting:

$$\mathcal{S}_2(h) = \Phi^{NL}_{h/2} \circ \Phi^{\mathcal{G}}_h \circ \Phi^{NL}_{h/2}. \tag{2.9}$$

Higher-order symmetric compositions (such as the Yoshida 4th-order scheme [85], Suzuki's fractal composition [73], or the optimized partitioned Runge–Kutta schemes of Blanes and Moan [10]) are constructed by recursive substeps $\prod_j \mathcal{S}_2(w_j h)$, preserving exact symplecticity and time reversibility (see Figure 3).

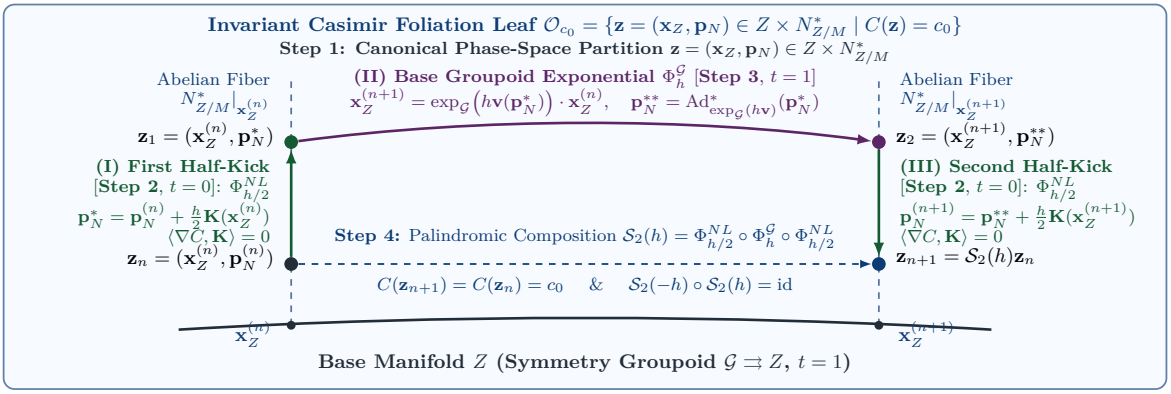


FIGURE 3. Geometric architecture of the canonical 4-step normal cone Strang splitting $\mathcal{S}_2(h)$ on $Z \times N^*_{Z/M}$. Following the canonical partition (**Step 1**), the first and second transverse half-kicks (**I** and **III**, **Step 2** at $t = 0$) act along the vertical fibers $N^*_{Z/M}$ orthogonally to ∇C, while the central base groupoid exponential (**II**, **Step 3** at $t = 1$) transports the state along the symmetry orbit without local chart singularities. Their palindromic composition (**Step 4**) preserves all Casimirs $C(\mathbf{z}) = c_0$ unconditionally (Theorem 2.3) and ensures exact time-reversibility (Proposition 2.4).

Theorem 2.3 — *Exact Invariant and Casimir Preservation*

Following McLachlan [48, Section 2] and Hairer, Lubich, and Wanner [28, Section VII.4.2], let $\mathcal{S}_2(h)$ be constructed according to Steps 1–4. If both the transverse kick Φ^{NL} and the groupoid flow $\Phi^{\mathcal{G}}$ preserve a scalar functional $C : Z \times N^*_{Z/M} \to \mathbb{R}$, then the symmetric Strang composition unconditionally preserves C for all step sizes $h \in \mathbb{R}$:

$$C(\mathcal{S}_2(h)\mathbf{z}) = C(\mathbf{z}). \tag{2.10}$$

In particular, all Casimirs of the Poisson bracket belonging to the kernel of the groupoid Lie algebroid are preserved to floating-point machine precision without numerical drift.

Lean A.1 : `ConormalSplitting.strang_exact_casimir_preservation`

Proof. By hypothesis, $C(\Phi^{NL}_\tau(\mathbf{z})) = C(\mathbf{z})$ and $C(\Phi^{\mathcal{G}}_\tau(\mathbf{z})) = C(\mathbf{z})$ hold for all $\tau \in \mathbb{R}$ and all $\mathbf{z} \in Z \times N^*_{Z/M}$. Evaluating C along the three sequential sub-steps $\mathbf{z}_1 = \Phi^{NL}_{h/2}(\mathbf{z})$, $\mathbf{z}_2 = \Phi^{\mathcal{G}}_h(\mathbf{z}_1)$, and $\mathcal{S}_2(h)\mathbf{z} = \Phi^{NL}_{h/2}(\mathbf{z}_2)$ yields by composition

$$C\big(\mathcal{S}_2(h)\mathbf{z}\big) = C\big(\Phi^{NL}_{h/2}(\mathbf{z}_2)\big) = C(\mathbf{z}_2) = C\big(\Phi^{\mathcal{G}}_h(\mathbf{z}_1)\big) = C(\mathbf{z}_1) = C\big(\Phi^{NL}_{h/2}(\mathbf{z})\big) = C(\mathbf{z}), \tag{2.11}$$

and similarly by induction for any multi-stage symmetric composition $\prod_j \mathcal{S}_2(w_j h)$.

□

Proposition 2.4 — *Time-Symmetry of the Normal Cone Splitting*

In accordance with Strang [69] and Hairer et al. [28, Section V.1], let Φ^{NL} and $\Phi^{\mathcal{G}}$ satisfy the one-parameter flow group property $\Phi(h_1 + h_2) = \Phi(h_1) \circ \Phi(h_2)$ and $\Phi(0) = \mathrm{id}$. Then the symmetric Strang composition $\mathcal{S}_2(h)$ is an exact time-symmetric integrator:

$$\mathcal{S}_2(-h) \circ \mathcal{S}_2(h) = \mathrm{id}. \tag{2.12}$$

In particular, its formal Lie generator $Z(h) = \ln \mathcal{S}_2(h)$ is strictly odd in h ($Z(-h) = -Z(h)$), eliminating all even powers in its Baker–Campbell–Hausdorff expansion and all odd dissipative error orders in the shadow Hamiltonian $\widetilde{H}(h)$.

Lean A.1 : `ConormalSplitting.strang_time_reversibility`

Proof. By direct evaluation under inversion of the numerical step size $h \mapsto -h$:

$$\mathcal{S}_2(-h) = \Phi^{NL}_{-h/2} \circ \Phi^{\mathcal{G}}_{-h} \circ \Phi^{NL}_{-h/2} = \left(\Phi^{NL}_{h/2}\right)^{-1} \circ \left(\Phi^{\mathcal{G}}_{h}\right)^{-1} \circ \left(\Phi^{NL}_{h/2}\right)^{-1} = \mathcal{S}_2(h)^{-1}. \tag{2.13}$$

Consequently, the formal Lie generator $Z(h) = \ln \mathcal{S}_2(h)$ satisfies $Z(-h) = \ln \mathcal{S}_2(-h) = \ln(\mathcal{S}_2(h)^{-1}) = -Z(h)$. In the Baker–Campbell–Hausdorff expansion:

$$Z(h) = hX_H + h^3 Z_3 + h^5 Z_5 + \mathcal{O}(h^7), \tag{2.14}$$

all even powers of h vanish identically. Equivalently, the formal shadow Hamiltonian $\widetilde{H}(h) = Z(h)/h$ satisfies time reversibility $\widetilde{H}(-h) = \widetilde{H}(h)$, expanding exclusively in even powers:

$$\widetilde{H}(h) = H + h^2 H_2 + h^4 H_4 + \mathcal{O}(h^6). \tag{2.15}$$

This parity cancellation ensures that the local truncation error is $\mathcal{O}(h^3)$, yielding an exact second-order geometric integrator with global error $\mathcal{O}(h^2)$ free from odd-order secular drift.

□

2.3. **Retrospective Case Studies: Unifying Known Splittings on** $\mathrm{SE}(3)$ **and** $\mathbb{S}^2$**.** To establish that our geometric splitting methodology is not an ad-hoc heuristic but an overarching framework, we examine how our splitting recipe, grounded in the deformation to the normal cone of Fulton–Verdier and its cotangent lift due to Calaque–Safronov, naturally unifies and justifies classical symplectic algorithms developed for rigid bodies and fluid vortices. Originating in the Lie–Poisson geometric frameworks of Ge–Marsden [25] and Channell–Scovel [17], and the explicit splitting paradigm of McLachlan [48], Lie–Poisson splitting methods exploit subgroup geometries to conserve Casimirs.

2.3.1. *Case Study 1: The Heavy Top on the Lie–Poisson Space* $\mathfrak{se}(3)^*$. The dynamics of a heavy rigid top spinning about a fixed point is described on the dual Lie algebra $\mathfrak{se}(3)^* \cong \mathbb{R}^3 \times \mathbb{R}^3$ by the Hamiltonian:

$$H(\mathbf{\Pi}, \mathbf{\Gamma}) = \frac{1}{2}\mathbf{\Pi} \cdot \mathbb{I}^{-1}\mathbf{\Pi} + mgl\,(\mathbf{\Gamma} \cdot \boldsymbol{\chi}), \tag{2.16}$$

generating the classical Euler–Poisson equations of motion:

$$\dot{\mathbf{\Pi}} = \mathbf{\Pi} \times \mathbf{\Omega} + mgl\,(\mathbf{\Gamma} \times \boldsymbol{\chi}), \qquad \dot{\mathbf{\Gamma}} = \mathbf{\Gamma} \times \mathbf{\Omega}, \tag{2.17}$$

where $\mathbf{\Pi} \in \mathbb{R}^3$ is the angular momentum in the body frame, $\mathbf{\Omega} = \mathbb{I}^{-1}\mathbf{\Pi}$ is the angular velocity, $\mathbf{\Gamma} \in \mathbb{S}^2$ is the unit vertical gravity vector, and $\boldsymbol{\chi}$ points toward the center of mass. The Lie–Poisson structure possesses two fundamental Casimir invariants:

$$C_1(\mathbf{\Gamma}) = \|\mathbf{\Gamma}\|^2 = 1, \qquad C_2(\mathbf{\Pi}, \mathbf{\Gamma}) = \mathbf{\Pi} \cdot \mathbf{\Gamma} = \text{const.} \tag{2.18}$$

Identifying the zero-momentum sphere $Z \cong \mathbb{S}^2$ with the configuration base and $\mathfrak{so}(3)^*$ with the transverse fiber, our geometric base-fiber splitting recipe decomposes the dynamics into two explicit algebraic updates:

(1) **Normal Fiber Step** $(t = 0)$**:** Gravity exerts a torque $\mathbf{K}(\mathbf{\Gamma}) = mgl\,(\mathbf{\Gamma} \times \boldsymbol{\chi})$. The normal fiber update is an exact linear translation along the transverse momentum fiber $\mathfrak{so}(3)^* \cong N_Z\mathfrak{se}(3)^*$:

$$\mathbf{\Pi}^* = \mathbf{\Pi} + \frac{h}{2}mgl\,(\mathbf{\Gamma} \times \boldsymbol{\chi}), \qquad \mathbf{\Gamma}^* = \mathbf{\Gamma}. \tag{2.19}$$

Crucially, because $\mathbf{K}(\mathbf{\Gamma}) \cdot \mathbf{\Gamma} \equiv 0$ by antisymmetry of the vector cross product, the transverse torque is strictly orthogonal to the vertical axis, guaranteeing that C_2 is unaffected by the kick step without any numerical projection.

(2) **Groupoid Exponential** $(t = 1)$**:** The kinematic rotation on $Z = \mathbb{S}^2$ is integrated in $\mathrm{SO}(3)$ acting simultaneously on gravity and angular momentum via Rodrigues' exponential formula:

$$\mathbf{R}_h = \mathbf{I} + \frac{\sin(h\|\mathbf{\Omega}^*\|)}{\|\mathbf{\Omega}^*\|}\widehat{\mathbf{\Omega}}^* + \frac{1 - \cos(h\|\mathbf{\Omega}^*\|)}{\|\mathbf{\Omega}^*\|^2}(\widehat{\mathbf{\Omega}}^*)^2, \qquad \mathbf{\Gamma}^{**} = \mathbf{R}_h^T\mathbf{\Gamma}^*, \quad \mathbf{\Pi}^{**} = \mathbf{R}_h^T\mathbf{\Pi}^*. \tag{2.20}$$

This single-exponential map integrates the free rigid-body sub-step either for an isotropic top ($\mathbb{I} = I_0\mathbf{I}_3$, where $\mathbf{\Omega}^*$ is constant) or along each individual principal inertia axis in McLachlan's explicit symmetric three-rotation splitting $\mathbf{R}_h = \mathbf{R}^{(1)}_{h/2}\mathbf{R}^{(2)}_{h/2}\mathbf{R}^{(3)}_{h}\mathbf{R}^{(2)}_{h/2}\mathbf{R}^{(1)}_{h/2}$ of $H_{\text{base}} = \sum_{a=1}^{3}\Pi_a^2/(2I_a)$ [48]. In either realization, $\mathbf{R}_h \in \mathrm{SO}(3)$ is an exact orthogonal isometry on $\mathbb{S}^2$ and $\mathbb{R}^3$, preserving $C_1 = \|\mathbf{\Gamma}\|^2 \equiv 1$ and $C_2 = \mathbf{\Pi} \cdot \mathbf{\Gamma}$ identically to floating-point precision (10^{-16}).

Proposition 2.5 — *Exact Casimir Preservation of the Heavy Top Splitting*

Following McLachlan [48] and Hairer, Lubich, and Wanner [28, Sections VII.5.3–VII.5.4], let $\mathcal{S}_2(h) = \Phi^{\text{normal}}_{h/2} \circ \Phi^{\text{base}}_{h} \circ \Phi^{\text{normal}}_{h/2}$ be the Strang splitting of the heavy rigid top on $\mathfrak{se}(3)^*$. Then $\mathcal{S}_2(h)$ unconditionally preserves both Casimirs:

$$C_1\big(\mathcal{S}_2(h)(\mathbf{\Pi}, \mathbf{\Gamma})\big) = C_1(\mathbf{\Pi}, \mathbf{\Gamma}), \qquad C_2\big(\mathcal{S}_2(h)(\mathbf{\Pi}, \mathbf{\Gamma})\big) = C_2(\mathbf{\Pi}, \mathbf{\Gamma}), \tag{2.21}$$

identically for all step sizes $h \in \mathbb{R}$.

Lean A.1 : `HeavyTop.heavy_top_strang_casimirs_exact`

Proof. Along the normal fiber kick $\Phi_\tau^{\text{normal}}(\mathbf{\Pi}, \mathbf{\Gamma}) = (\mathbf{\Pi} + \tau mgl(\mathbf{\Gamma} \times \boldsymbol{\chi}), \mathbf{\Gamma})$, the gravity vector $\mathbf{\Gamma}$ is unchanged so $C_1 = \|\mathbf{\Gamma}\|^2$ is trivially preserved, while the scalar triple product identity $(\mathbf{\Gamma} \times \boldsymbol{\chi}) \cdot \mathbf{\Gamma} = 0$ yields $(\mathbf{\Pi} + \tau mgl(\mathbf{\Gamma} \times \boldsymbol{\chi})) \cdot \mathbf{\Gamma} = \mathbf{\Pi} \cdot \mathbf{\Gamma} = C_2$. Along the base groupoid update $\Phi_h^{\text{base}}(\mathbf{\Pi}^*, \mathbf{\Gamma}^*) = (\mathbf{R}_h^T \mathbf{\Pi}^*, \mathbf{R}_h^T \mathbf{\Gamma}^*)$ with $\mathbf{R}_h \in \mathrm{SO}(3)$, orthogonality $\mathbf{R}_h \mathbf{R}_h^T = \mathbf{I}$ preserves the Euclidean inner product on $\mathbb{R}^3$, so $\|\mathbf{R}_h^T \mathbf{\Gamma}^*\|^2 = \|\mathbf{\Gamma}^*\|^2$ and $(\mathbf{R}_h^T \mathbf{\Pi}^*) \cdot (\mathbf{R}_h^T \mathbf{\Gamma}^*) = \mathbf{\Pi}^* \cdot \mathbf{\Gamma}^*$. Applying Theorem 2.3 to $\mathcal{S}_2(h) = \Phi_{h/2}^{\text{normal}} \circ \Phi_h^{\text{base}} \circ \Phi_{h/2}^{\text{normal}}$ concludes the proof. □

Every stage of the composition preserves both invariants identically, illustrating how the explicit Lie–Poisson splitting methods developed by Channell and Scovel [17] and McLachlan [48] provide a Lie–Poisson counterpart to the normal cone base-fiber decoupling on $\mathfrak{se}(3)^*$.

To synthesize this geometric architecture into an operational reference, we summarize the resulting structure in the dedicated specification below. This structural synopsis delineates the reduced phase-space geometry, the canonical Hamiltonian polarization into base and normal components, and the unconditionally preserved Lie–Poisson Casimirs, establishing the unified classification format adopted for constrained and singular systems throughout this treatise:

▶ **Normal Cone Decomposition: Euler–Poisson Heavy Top on $\mathfrak{se}(3)^*$**

Geometric Base & Normal Fiber: The physical state describes a heavy rigid body spinning about a fixed pivot under uniform vertical gravity. The system is parameterized by the body angular momentum vector $\mathbf{\Pi} = (\Pi_1, \Pi_2, \Pi_3) \in \mathfrak{so}(3)^* \cong \mathbb{R}^3$ in the body frame, the unit Poisson vector $\mathbf{\Gamma} = (\Gamma_1, \Gamma_2, \Gamma_3) \in \mathbb{S}^2$ tracing the spatial gravity direction, the positive-definite inertia tensor $\mathbb{I} = \mathrm{diag}(I_1, I_2, I_3)$, and the constant center-of-mass displacement vector $\boldsymbol{\chi} \in \mathbb{R}^3$.
The reduced phase space is the dual Lie algebra $\mathfrak{se}(3)^* \cong \mathfrak{so}(3)^* \times \mathbb{R}^3$, whose symplectic leaves are coadjoint orbits equipped with the Kirillov–Kostant–Souriau 2-form:

$$\mathcal{O}_{c_1,c_2} = \left\{ (\mathbf{\Pi}, \mathbf{\Gamma}) \in \mathfrak{se}(3)^* \;\middle|\; \|\mathbf{\Gamma}\|^2 = c_1 > 0,\ \mathbf{\Pi} \cdot \mathbf{\Gamma} = c_2 \right\}, \tag{2.22}$$

$$\omega_{\mathrm{KKS}}(\delta u, \delta v) = -\langle (\mathbf{\Pi}, \mathbf{\Gamma}), [u, v] \rangle. \tag{2.23}$$

The kinematic configuration base corresponding to zero rotational momentum is the unit sphere:

$$Z = \left\{ (\mathbf{\Pi}, \mathbf{\Gamma}) \in \mathfrak{se}(3)^* \;\middle|\; \mathbf{\Pi} = \mathbf{0},\ \|\mathbf{\Gamma}\|^2 = 1 \right\} \cong \mathbb{S}^2, \qquad \mathcal{I}_Z = \langle \Pi_1, \Pi_2, \Pi_3, \|\mathbf{\Gamma}\|^2 - 1 \rangle \subset \mathcal{O}_{\mathfrak{se}(3)^*}. \tag{2.24}$$

Hamiltonian Polarization: Polarizing the physical energy into base kinematic rotation and transverse gravitational torque:

$$H(\mathbf{\Pi}, \mathbf{\Gamma}) = \underbrace{\frac{1}{2} \mathbf{\Pi} \cdot \mathbb{I}^{-1} \mathbf{\Pi}}_{H_{\mathrm{base}}} + \underbrace{mgl\,(\mathbf{\Gamma} \cdot \boldsymbol{\chi})}_{H_{\mathrm{normal}}}. \tag{2.25}$$

- *Base Kinematic Hamiltonian* H_{base}: Generates free Euler rigid body rotation along the symmetry base $Z \cong \mathbb{S}^2$, integrated via Rodrigues' formula in SO(3) acting simultaneously on $\mathbf{\Gamma}$ and $\mathbf{\Pi}$ (or via McLachlan's 3-rotation splitting [48]), preserving both Casimirs C_1 and C_2 strictly without truncation error.
- *Normal Potential Hamiltonian* H_{normal}: Generates transverse gravitational torque $\mathbf{K}(\mathbf{\Gamma}) = mgl(\mathbf{\Gamma} \times \boldsymbol{\chi})$, integrated as an exact abelian translation $\mathbf{\Pi} \mapsto \mathbf{\Pi} + h\mathbf{K}(\mathbf{\Gamma})$ along the transverse momentum fiber $\mathfrak{so}(3)^* \cong N_Z\mathfrak{se}(3)^*$.

Preserved Invariants: Under the symmetric Strang splitting $\mathcal{S}_2(h) = \Phi^{\mathrm{normal}}_{h/2} \circ \Phi^{\mathrm{base}}_{h} \circ \Phi^{\mathrm{normal}}_{h/2}$, both quadratic Lie–Poisson Casimirs are conserved identically along trajectories:

$$\{C_1, H_{\mathrm{base}}\} = \{C_1, H_{\mathrm{normal}}\} \equiv 0 \implies \frac{\mathrm{d}C_1}{\mathrm{d}t} \equiv 0, \tag{2.26}$$

$$\{C_2, H_{\mathrm{base}}\} = \{C_2, H_{\mathrm{normal}}\} \equiv 0 \implies \frac{\mathrm{d}C_2}{\mathrm{d}t} \equiv 0, \tag{2.27}$$

guaranteeing unconditional confinement to the coadjoint orbit $\mathcal{O}_{1,c_2}$.

Lean A.1 : `HeavyTop.heavy_top_strang_casimirs_exact`

2.3.2. *Case Study 2: The Bogomolov–Kirchhoff Point Vortex System on* $\mathbb{S}^2$. A parallel realization occurs for the spherical point vortex system formulated by Bogomolov [12] (extending Helmholtz's vortex principles and Kirchhoff's planar Hamiltonian dynamics [35]), with Hamiltonian:

$$H(\mathbf{x}_1, \dots, \mathbf{x}_K) = -\frac{1}{4\pi} \sum_{1 \le i < j \le K} \Gamma_i \Gamma_j \ln \|\mathbf{x}_i - \mathbf{x}_j\|^2 = \sum_{1 \le i < j \le K} H_{ij}, \qquad \mathbf{x}_i \in \mathbb{S}^2, \tag{2.28}$$

where $\Gamma_i \in \mathbb{R} \setminus \{0\}$ denotes the vortex circulation and $\|\mathbf{x}_i - \mathbf{x}_j\| = 2\sin(\theta_{ij}/2)$ is the Euclidean chord distance in $\mathbb{R}^3$, which yields the exact Green's function on $\mathbb{S}^2$ up to an additive constant. Here, the phase space is the compact manifold $(\mathbb{S}^2)^K$ equipped with the symplectic form $\omega = \sum_{i=1}^K \Gamma_i \, \omega_{\mathbb{S}^2}^{(i)}$ (Kähler when all $\Gamma_i > 0$). The singular loci are pairwise collision strata $\Delta_{ij} = \{\mathbf{x} \in (\mathbb{S}^2)^K \mid \mathbf{x}_i = \mathbf{x}_j\}$.

Rather than separating a kinetic cotangent drift and a potential kick, the normal cone philosophy of isolating singular divisors adapts to first-order vortex dynamics via the Lie–Poisson splitting framework of McLachlan [48], instantiated for spherical point vortex pairs by Myerscough and Frank [52]:

(1) **Pairwise Lie–Poisson Foliation:** The Hamiltonian is decomposed into $K(K-1)/2$ autonomous pairwise stages $H = \sum_{i<j} H_{ij}$. Under each isolated Hamiltonian H_{ij}, the mutual chord distance $\|\mathbf{x}_i - \mathbf{x}_j\|$ is an exact invariant, and the vortex pair (i, j) undergoes an exact, non-singular rigid rotation around their pairwise momentum vector $\mathbf{J}_{ij} = \Gamma_i \mathbf{x}_i + \Gamma_j \mathbf{x}_j \in \mathfrak{so}(3)^*$ with constant angular velocity $\boldsymbol{\omega}_{ij} = \frac{\mathbf{J}_{ij}}{2\pi \|\mathbf{x}_i - \mathbf{x}_j\|^2}$, computed analytically via Rodrigues' formula, while spectator vortices $k \notin \{i, j\}$ remain stationary.

(2) **Symmetric Strang Composition:** The complete flow is integrated via the symmetric composition $\mathcal{S}_2(h) = \prod_{i<j} \Phi_{h/2}^{H_{ij}} \circ \prod_{i<j}^{\text{rev}} \Phi_{h/2}^{H_{ij}}$.

Because each pairwise flow $\Phi_h^{H_{ij}}$ is an exact SO(3) isometry preserving sphere radii and commuting with the diagonal SO(3) action, this integrator unconditionally preserves the individual Casimirs $\|\mathbf{x}_i\|^2 = 1$ on $(\mathfrak{so}(3)^*)^{\oplus K}$ and the global SO(3) momentum map $\mathbf{J} = \sum_{i=1}^K \Gamma_i \mathbf{x}_i$, hence its quadratic Casimir $\|\mathbf{J}\|^2$, analytically without projection.

To synthesize this pairwise geometric architecture into an operational reference, we summarize the resulting structure in the dedicated specification below:

▶ **Normal Cone Decomposition: Bogomolov–Kirchhoff Point Vortex System on $\mathbb{S}^2$**

Compact Kähler Phase Space & Symplectic Collision Diagonals: The physical system describes K interacting ideal point vortices on the unit two-sphere $\mathbb{S}^2 \subset \mathbb{R}^3$. The state is specified by the vortex positions $\mathbf{x}_i = (x_{i,1}, x_{i,2}, x_{i,3}) \in \mathbb{S}^2$ and their non-vanishing vortex circulations $\Gamma_i \in \mathbb{R}\backslash\{0\}$ for $i \in \{1, \dots, K\}$.
Unlike mechanical cotangent bundles T^*Q, the geometric phase space is a compact boundaryless Kähler product manifold equipped with the Kirillov–Kostant–Souriau symplectic form:

$$\mathcal{M} = (\mathbb{S}^2)^K, \qquad \omega = \sum_{i=1}^{K} \Gamma_i \, \omega_{\mathbb{S}^2}^{(i)}, \qquad \omega_{\mathbb{S}^2}^{(i)}(\delta\mathbf{u}, \delta\mathbf{v}) = \mathbf{x}_i \cdot (\delta\mathbf{u} \times \delta\mathbf{v}). \tag{2.29}$$

The singular locus is the union of pairwise collision diagonals (which are codimension-2 symplectic submanifolds whenever $\Gamma_i + \Gamma_j \neq 0$, rather than Lagrangian conormal submanifolds):

$$\Delta = \bigcup_{1 \le i < j \le K} \Delta_{ij}, \qquad \Delta_{ij} = \left\{ (\mathbf{x}_1, \dots, \mathbf{x}_K) \in (\mathbb{S}^2)^K \;\middle|\; \mathbf{x}_i = \mathbf{x}_j \right\}, \qquad \mathcal{I}_{\Delta_{ij}} = \langle \mathbf{x}_i - \mathbf{x}_j \rangle. \tag{2.30}$$

Pairwise Lie–Poisson Chordwise Splitting: Because $(\mathbb{S}^2)^K$ carries no cotangent base-fiber fibration ($H_{\text{kin}} \equiv 0$), the singular divisor isolation principle transposes analogically into a pairwise Lie–Poisson splitting across the $K(K-1)/2$ chordal logarithmic interactions:

$$H(\mathbf{x}_1, \dots, \mathbf{x}_K) = \sum_{1 \le i < j \le K} H_{ij}(\mathbf{x}_i, \mathbf{x}_j), \qquad H_{ij}(\mathbf{x}_i, \mathbf{x}_j) = -\frac{\Gamma_i \Gamma_j}{4\pi} \ln \|\mathbf{x}_i - \mathbf{x}_j\|^2. \tag{2.31}$$

- *Absence of Inertial Base Drift*: Reflecting the first-order, non-inertial nature of point-vortex dynamics on compact Kähler manifolds, coordinates and conjugate momenta are intrinsically coupled on each $\mathbb{S}^2$ factor without free kinetic translation.
- *Exact Pairwise* SO(3) *Isometry Stages* H_{ij}: Each isolated pair Hamiltonian H_{ij} generates an exact rigid SO(3) rotation around the pair angular momentum vector $\mathbf{J}_{ij} = \Gamma_i \mathbf{x}_i + \Gamma_j \mathbf{x}_j \in \mathfrak{so}(3)^*$ with constant angular velocity $\boldsymbol{\omega}_{ij} = \frac{\mathbf{J}_{ij}}{2\pi \|\mathbf{x}_i - \mathbf{x}_j\|^2}$ via Rodrigues' formula, leaving the singular chordal distance $\|\mathbf{x}_i - \mathbf{x}_j\|$ strictly invariant along each stage.

Preserved Invariants: Under the symmetric Strang pairwise composition $\mathcal{S}_2(h) = \prod_{i<j} \Phi_{h/2}^{H_{ij}} \circ \prod_{i<j}^{\text{rev}} \Phi_{h/2}^{H_{ij}}$, all sphere Casimirs and the total Lie–Poisson angular momentum are preserved identically:

$$\frac{\mathrm{d}}{\mathrm{d}t} \|\mathbf{x}_i\|^2 = 2\mathbf{x}_i \cdot \dot{\mathbf{x}}_i \equiv 0 \quad (\forall i \in \{1, \dots, K\}), \qquad \{\mathbf{J}, H\} \equiv \mathbf{0}, \qquad \{\|\mathbf{J}\|^2, H\} \equiv 0, \tag{2.32}$$

where $\mathbf{J} = \sum_{i=1}^{K} \Gamma_i \mathbf{x}_i \in \mathfrak{so}(3)^*$ is the total vorticity momentum map, ensuring unconditional confinement to the coadjoint SO(3) orbit on $(\mathfrak{so}(3)^*)^{\oplus K}$.

2.3.3. *Conceptual Bridge to the Gravitational N-Body Problem.* These retrospective case studies illustrate the core thesis: whenever classical mechanics has successfully designed stable, long-term geometric integrators for constrained or singular systems, those integrators implicitly leveraged the abelian structure of the normal cone.

In the gravitational N-body problem, however, singular configurations do not form isolated smooth submanifolds. Instead, pairwise collision diagonals Δ_{ij} and multiple collision strata Δ_S intersect along a non-transverse conical stratification. While an isolated groupoid/normal-cone splitting suffices when singular loci are disjoint (as in SE(3) or $\mathbb{S}^2$), handling intersecting collision cones requires a systematic desingularization of the arrangement. To extend this methodology systematically to gravitation, we proceed in two stages:

- **Low-dimensional prototype (Section 3):** We first examine the planar circular restricted three-body problem (PCR3BP), where the singular locus $Z = \{\mathbf{q}_{(1)}, \mathbf{q}_{(2)}\}$ consists of two isolated primary points, allowing an unsoftened base-fiber treatment of binary close encounters.

- **Multiscale hierarchical desingularization (Section 4):** We then lift the full N-body collision arrangement to the Fulton–MacPherson configuration space $\mathbf{Q}[N]$. By iteratively blowing up the collision diagonals along the Whitney lattice of collision partitions, intersecting collision cones are desingularized into a simple normal crossing (SNC) divisor with corners, enabling synchronous, multiscale normal cone desingularization across all cluster hierarchies.

3. The Planar Three-Body Prototype and Classical Regularizations

3.1. **Canonical Synodic Formulation of the PCR3BP.** To benchmark our normal-cone-inspired splitting methodology on a concrete celestial mechanics problem before tackling the full N-body collision stratification, we examine the planar circular restricted three-body problem (PCR3BP). This classic Hamiltonian system provides a rigorous, low-dimensional testing ground possessing isolated binary singularities, non-trivial Coriolis coupling, and an exact first integral.

3.1.1. *Rotating Synodic Coordinates and Canonical Phase Space.* Let two massive bodies (the primaries) of masses $m_1 = 1-\mu$ and $m_2 = \mu$ (with $0 < \mu \leq 1/2$) revolve in circular Keplerian orbits about their common center of mass with normalized mean motion $\Omega = 1$ and separation distance $R = 1$. A third massless body moves in the orbital plane of the primaries.

In the co-rotating (synodic) reference frame, the primaries are fixed at coordinates $\mathbf{q}_{(1)} = (-\mu, 0)$ and $\mathbf{q}_{(2)} = (1-\mu, 0)$. Denoting the Cartesian coordinates of the third body by $\mathbf{q} = (x, y) \in \mathbb{R}^2$ and its conjugate canonical momenta by $\mathbf{p} = (p_x, p_y) \in \mathbb{R}^2$, the phase space is $T^*(\mathbb{R}^2 \setminus \{\mathbf{q}_{(1)}, \mathbf{q}_{(2)}\})$, equipped with the Darboux symplectic form:

$$\omega_0 = \mathrm{d}x \wedge \mathrm{d}p_x + \mathrm{d}y \wedge \mathrm{d}p_y. \tag{3.1}$$

3.1.2. *Unsoftened Synodic Hamiltonian and Jacobi Energy Surface.* The unsoftened autonomous Hamiltonian governing the third body in canonical variables is:

$$H_{\mathrm{syn}}(x, y, p_x, p_y) = \frac{1}{2}(p_x^2 + p_y^2) + (yp_x - xp_y) - \frac{1-\mu}{r_1} - \frac{\mu}{r_2}, \tag{3.2}$$

where $r_1 = \sqrt{(x+\mu)^2 + y^2}$ and $r_2 = \sqrt{(x-1+\mu)^2 + y^2}$ denote the pairwise Euclidean distances to the primaries. The kinematic coupling term $yp_x - xp_y = -\mathbf{q} \times \mathbf{p}$ accounts for the Coriolis acceleration of the rotating synodic frame. The kinematic velocity vector $\mathbf{v} = (\dot{x}, \dot{y})$ is related to canonical momenta by $\mathbf{v} = \mathbf{p} - \boldsymbol{\Omega} \times \mathbf{q} = (p_x + y, p_y - x)$, yielding the squared velocity relation $v^2 = \|\dot{\mathbf{q}}\|^2 = (p_x^2 + p_y^2) + 2(yp_x - xp_y) + (x^2 + y^2)$.

Proposition 3.1 — *Autonomous Conservation of the Jacobi First Integral*

Following Jacobi [33] and Szebehely [75, Chapter 1, §1.2–§1.5], because the synodic Hamiltonian H_{syn} is autonomous ($\partial H_{\mathrm{syn}}/\partial t = 0$), the Jacobi energy observable:

$$\begin{aligned} C_J(x, y, p_x, p_y) &= -2H_{\mathrm{syn}} \\ &= -(p_x^2 + p_y^2) - 2(yp_x - xp_y) + 2\left(\frac{1-\mu}{r_1} + \frac{\mu}{r_2}\right) && (3.3) \\ &= 2U_{\mathrm{eff}}(x, y) - (\dot{x}^2 + \dot{y}^2), && (3.4) \end{aligned}$$

where $U_{\mathrm{eff}}(x, y) = \frac{1}{2}(x^2 + y^2) + \frac{1-\mu}{r_1} + \frac{\mu}{r_2}$ is the augmented effective potential, is an exact first integral along every unsoftened phase space trajectory:

$$\frac{\mathrm{d}C_J}{\mathrm{d}t} = \{C_J, H_{\mathrm{syn}}\}_0 \equiv 0. \tag{3.5}$$

Lean A.1 : `PhaseState.jacobi_conservation_identity`, `PhaseState.coriolis_step_symplectic`

Proof. Hamilton's equations for H_{syn} with respect to $\omega_0 = \mathrm{d}x \wedge \mathrm{d}p_x + \mathrm{d}y \wedge \mathrm{d}p_y$ read $\dot{x} = \partial_{p_x} H_{\mathrm{syn}} = p_x + y$, $\dot{y} = \partial_{p_y} H_{\mathrm{syn}} = p_y - x$, $\dot{p}_x = -\partial_x H_{\mathrm{syn}} = p_y - \partial_x V_{\mathrm{grav}}$, and $\dot{p}_y = -\partial_y H_{\mathrm{syn}} = -p_x - \partial_y V_{\mathrm{grav}}$, where $V_{\mathrm{grav}}(x, y) = -\frac{1-\mu}{r_1} - \frac{\mu}{r_2}$. Differentiating $C_J = -2H_{\mathrm{syn}} = 2(xp_y - yp_x) - (p_x^2 + p_y^2) - 2V_{\mathrm{grav}}(x, y)$ along any solution curve yields:

$$\frac{\mathrm{d}C_J}{\mathrm{d}t} = 2(\dot{x}p_y - \dot{y}p_x + x\dot{p}_y - y\dot{p}_x) - 2(p_x\dot{p}_x + p_y\dot{p}_y) - 2(\partial_x V_{\mathrm{grav}}\,\dot{x} + \partial_y V_{\mathrm{grav}}\,\dot{y}) = -2\{H_{\mathrm{syn}}, H_{\mathrm{syn}}\}_0 \equiv 0.$$

Substituting $p_x = \dot{x} - y$ and $p_y = \dot{y} + x$ into (3.3) expands $-(p_x^2 + p_y^2) - 2(yp_x - xp_y) = (x^2 + y^2) - (\dot{x}^2 + \dot{y}^2)$, recovering (3.4).

□

The energy hypersurfaces $C_J = \text{const}$ determine Hill's forbidden regions whose topological bifurcations at the Lagrange equilibrium points $L_1, \ldots, L_5$ govern capture, resonance transitions, and escape [75]. In classical celestial mechanics, Szebehely [75] adds the gauge constant $\frac{1}{2}\mu(1-\mu)$ to the effective potential $\Omega(x,y) = U_{\text{eff}}(x,y) + \frac{1}{2}\mu(1-\mu)$, which doubles to $+\mu(1-\mu)$ in $C_{\text{Sz}} = 2\Omega(x,y) - (\dot{x}^2 + \dot{y}^2) = C_J + \mu(1-\mu)$, leaving the physical trajectories identical.

To synthesize this synodic Hamiltonian architecture into an operational reference, Figure 4 illustrates the co-rotating synodic base geometry alongside the canonical cotangent polarization, and we summarize the resulting structure in the dedicated specification below:

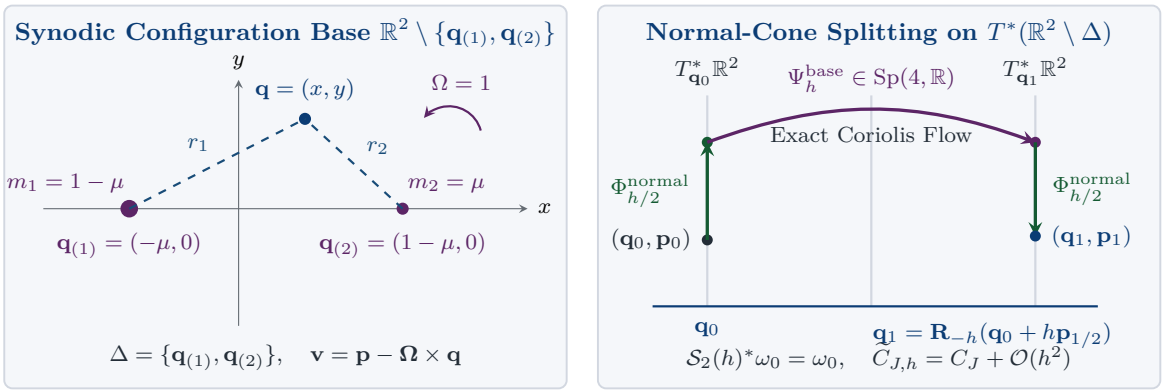


FIGURE 4. Left: Co-rotating synodic configuration space $\mathbb{R}^2 \setminus \{\mathbf{q}_{(1)}, \mathbf{q}_{(2)}\}$ of the planar circular restricted three-body problem (PCR3BP) with primaries $m_1 = 1 - \mu$ and $m_2 = \mu$. Right: Canonical normal-cone Strang splitting $\mathcal{S}_2(h) = \Phi^{\text{normal}}_{h/2} \circ \Psi^{\text{base}}_h \circ \Phi^{\text{normal}}_{h/2}$ on $T^*(\mathbb{R}^2 \setminus \Delta)$, alternating vertical cotangent fiber momentum translations with the exact linear Coriolis-kinematic groupoid flow $\Psi^{\text{base}}_h \in \text{Sp}(4, \mathbb{R})$.

► Normal Cone Decomposition: Planar Circular Restricted 3-Body Problem (PCR3BP)

Geometric Base & Normal Fiber: The physical system describes the coplanar motion of an infinitesimal third body under the Newtonian gravitational attraction of two massive primaries revolving in circular orbits about their common barycenter. The state is parameterized by the synodic position vector $\mathbf{q} = (x, y) \in \mathbb{R}^2 \setminus \{\mathbf{q}_{(1)}, \mathbf{q}_{(2)}\}$, the conjugate canonical momentum vector $\mathbf{p} = (p_x, p_y) \in \mathbb{R}^2$, and the normalized mass parameter $\mu = m_2/(m_1 + m_2) \in (0, 1/2]$.
The geometric phase space is the canonical cotangent bundle of the punctured plane equipped with the standard Darboux 2-form:

$$\mathcal{M} = T^*\big(\mathbb{R}^2 \setminus \{\mathbf{q}_{(1)}, \mathbf{q}_{(2)}\}\big), \qquad \omega_0 = \mathrm{d}\mathbf{q} \wedge \mathrm{d}\mathbf{p} = \mathrm{d}x \wedge \mathrm{d}p_x + \mathrm{d}y \wedge \mathrm{d}p_y. \tag{3.6}$$

The collision locus is the discrete codimension-2 subvariety formed by the two primary masses:

$$\Delta = \{\mathbf{q}_{(1)}, \mathbf{q}_{(2)}\} = \{(-\mu, 0), (1 - \mu, 0)\}, \qquad \mathcal{I}_\Delta = \langle y,\ (x + \mu)(x - 1 + \mu)\rangle \subset \mathbb{R}[x, y]. \tag{3.7}$$

Hamiltonian Polarization: The synodic kinetic-potential model originating in the synodic integral of **Jacobi (1836)** [33], cast in canonical Hamiltonian form by **Poincaré (1892)** [54], and systematized by **Szebehely (1967)** [75] identifies with the canonical degree-0 cotangent lift of the

deformation to the normal cone, polarizing the autonomous synodic energy into:

$$H_{\text{syn}}(\mathbf{q},\mathbf{p}) = \underbrace{\frac{1}{2}\|\mathbf{p}\|^2 + (yp_x - xp_y)}_{H_{\text{base}}} + \underbrace{\left(-\frac{1-\mu}{r_1} - \frac{\mu}{r_2}\right)}_{H_{\text{normal}}}. \tag{3.8}$$

- *Base Kinematic Hamiltonian* H_{base}: Quadratic kinetic-Coriolis generator governing uniform rotating frame kinematics and free inertial drift in $\mathrm{Sp}(4,\mathbb{R})$, integrated exactly without truncation error via the linear groupoid action $\Psi_h^{\text{base}}(\mathbf{q},\mathbf{p}) = (\mathbf{R}_{-h}(\mathbf{q}+h\mathbf{p}), \mathbf{R}_{-h}\mathbf{p})$.
- *Normal Potential Hamiltonian* H_{normal}: Singular Newtonian gravitational potential depending strictly on base configuration $\mathbf{q} \in \mathbb{R}^2 \setminus \Delta$, integrated as an exact abelian transverse kick $\mathbf{p} \mapsto \mathbf{p} - h\nabla V_{\text{grav}}(\mathbf{q})$ along the vertical cotangent fibers $T^*_{\mathbf{q}}\mathbb{R}^2$, corresponding to the cotangent lift of the normal cone coordinates.

Preserved Invariants: Under the symmetric Strang splitting $\mathcal{S}_2(h) = \Phi^{\text{normal}}_{h/2} \circ \Psi^{\text{base}}_h \circ \Phi^{\text{normal}}_{h/2}$, the symplectic 2-form is preserved identically at any finite step h, while the continuous flow preserves $C_J = -2H_{\text{syn}}$ exactly and the discrete propagator preserves the modified shadow Jacobi integral $\widetilde{C}_{J,h} = -2\widetilde{H}_{\text{syn},h} = C_J + \mathcal{O}(h^2)$ without secular drift:

$$\mathcal{S}_2(h)^*\omega_0 = \omega_0, \qquad \{C_J, H_{\text{syn}}\}_0 \equiv 0 \implies \frac{\mathrm{d}C_J}{\mathrm{d}t} \equiv 0, \tag{3.9}$$

guaranteeing exact conservation of the phase-space Liouville volume $\mathrm{d}\mathbf{q} \wedge \mathrm{d}\mathbf{p}$ and bounded Jacobi energy oscillations with zero secular drift.

Lean A.1 : `PhaseState.jacobi_conservation_identity, PhaseState.coriolis_step_symplectic`

Python A.2 : `interfaces/pcr3bp_canonical_solver.py` [Planar PCR3BP Float64]

3.2. **Bridging Normal Cone Degenerations with Classical Regularizations.** The mathematical regularization of gravitational collisions in celestial mechanics has an illustrious history spanning more than a century. To understand how our normal cone splitting relates to classical methods, we demonstrate that the landmark regularizations of Sundman, Levi-Civita, Birkhoff, and McGehee represent particular local coordinate realizations of the deformation to the normal cone.

3.2.1. *Taxonomy of Classical Two-Dimensional Regularizations.* Near a binary collision locus (without loss of generality, centered on one of the primaries $\mathbf{q} \to \mathbf{q}_{(k)}$, translated locally so that $\mathbf{q} \to \mathbf{0}$):

(1) **Sundman Time Rescaling (1912):** Sundman [72, Section V, Eq. (71)] introduced the differential relation $\mathrm{d}t = r\,\mathrm{d}u$, where $r = \|\mathbf{q}\|$. While this transformation unfreezes the singularity by stretching time along collision orbits, it is non-canonical and breaks symplectic structure if applied with variable step sizes in physical time [66].

(2) **Levi-Civita Conformal Regularization (1904, 1920):** Levi-Civita [39, 40] coupled the conformal fictitious-time rescaling $\mathrm{d}t = r\,\mathrm{d}\tau$ with the complex quadratic conformal mapping $z = w^2$ (i.e., $x+iy = (u+iv)^2$). At the level of the Hamiltonian, the Keplerian singularity $\frac{1}{r} = \frac{1}{|w|^2}$ is multiplied by $|w|^2$ via the Poincaré time-energy transformation, transforming singular Keplerian trajectories into smooth orbits of an isotropic harmonic oscillator.

(3) **Birkhoff Global Regularization (1915):** To regularize both binary collisions simultaneously in the PCR3BP, Birkhoff [7] introduced the transformation $w \mapsto \frac{1}{2}(w + 1/w)$, mapping the two primaries to conjugate branch points.

(4) **McGehee Invariant Manifold Blow-Up (1974):** McGehee [47, Sections 2–3] replaced coordinates (r, θ) by scaled variables (ρ, θ, v, u) with $r = \rho^2$ and $v = \rho\dot{r}$. The collision singularity $r = 0$ is blown up into a non-trivial boundary manifold—the *collision manifold* $\mathbf{M}_C$. Motion on $\mathbf{M}_C$ is governed by an invariant vector field, and binary collision orbits enter and exit $\mathbf{M}_C$ via an involutive branch-crossing map $\mathcal{B}_C$.

Theorem 3.2 — *Normal Cone Geometrization of Classical Regularizations*

Following Sundman [72, Section V, p. 127, Eq. (71)], Levi-Civita [39, 40], and McGehee [47, Sections 2–3], let $M = \mathbb{R}^2$ and let $Z = \{\mathbf{0}\}$ be the binary collision locus.

(1) The central special fiber of the Rees deformation $\mathcal{D}_Z M$ at $t = 0$ is canonically isomorphic to the normal space $N_Z M \cong \mathbb{R}^2$.

(2) Levi-Civita's quadratic mapping $z = w^2$ is the unique branched 2-fold covering of the projectivized normal cone $\mathbb{P}(N_Z M) \cong \mathbb{S}^1$ resolving the collision divisor with $\mathcal{C}^\infty$ smoothness.

(3) McGehee's blow-up corresponds to the real oriented spherical blow-up of configuration space $\mathrm{Bl}_Z M \cong \mathbb{S}^1 \times \mathbb{R}_{\geq 0}$, whose boundary $\rho = 0$ forms the base configuration circle of the phase-space collision manifold $\mathbf{M}_C$.

Lean A.1 : `levi_civita_normal_cone_covering, levi_civita_antipodal_covering, levi_civita_conformal_orthogonality, levi_civita_conformal_scaling`

Proof. (1) For $Z = \{\mathbf{0}\} \subset M = \mathbb{R}^2$, the vanishing ideal is $\mathcal{I}_Z = \langle x, y\rangle \subset \mathbb{R}[x, y]$. The special fiber of the Rees algebra $\bigoplus_{n\geq 0} \mathcal{I}_Z^n t^{-n}$ at $t = 0$ is the associated graded algebra $\bigoplus_{n\geq 0} \mathcal{I}_Z^n/\mathcal{I}_Z^{n+1} \cong \mathbb{R}[\xi_x, \xi_y]$, whose spectrum is canonically $N_Z M = T_{\mathbf{0}}\mathbb{R}^2 \cong \mathbb{R}^2$. (2) Under Levi-Civita's spinor map $z = w^2 = (u^2 - v^2) + 2iuv$ on $N_Z M \cong \mathbb{C}$, the radial norm satisfies $x^2 + y^2 = (u^2 - v^2)^2 + 4u^2v^2 = (u^2 + v^2)^2$, so $r = u^2 + v^2$, and the map is invariant under the antipodal involution $(u, v) \mapsto (-u, -v)$, defining an unramified $2:1$ Galois covering $\mathbb{S}^1 \to \mathbb{P}(N_Z M) \cong \mathbb{S}^1$ with conformal Jacobian determinant $\det J_{\mathrm{LC}} = 4(u^2 + v^2) = 4r$. Multiplying the shifted Hamiltonian $H_{\mathrm{syn}} - E_0$ by $r = |w|^2$ via Sundman's relation $\mathrm{d}t = r\,\mathrm{d}\tau$ cancels the $1/r$ pole identically. (3) Passing to real oriented polar

coordinates $\mathbf{q} = r(\cos\theta, \sin\theta)$ on $\mathrm{Bl}_Z M \cong \mathbb{S}^1 \times \mathbb{R}_{\geq 0}$ and setting $r = \rho^2 \geq 0$ yields McGehee's boundary circle $\rho = 0$ as the base of the collision manifold $\mathbf{M}_C$.

□

Consequently, while classical regularizations perform explicit surgeries on the configuration space Q (branched coverings for Levi-Civita, compact boundary blow-up $\mathbf{M}_C$ for McGehee), the Calaque–Safronov cotangent lift of the normal cone deformation operates intrinsically on the unshifted symplectic geometry T^*Q (see Figure 5). The normal cone $N_Z M$ serves as the universal linear degeneration space whose projective and conformal chart uniformizations recover the classical constructions without ad-hoc time singularities.

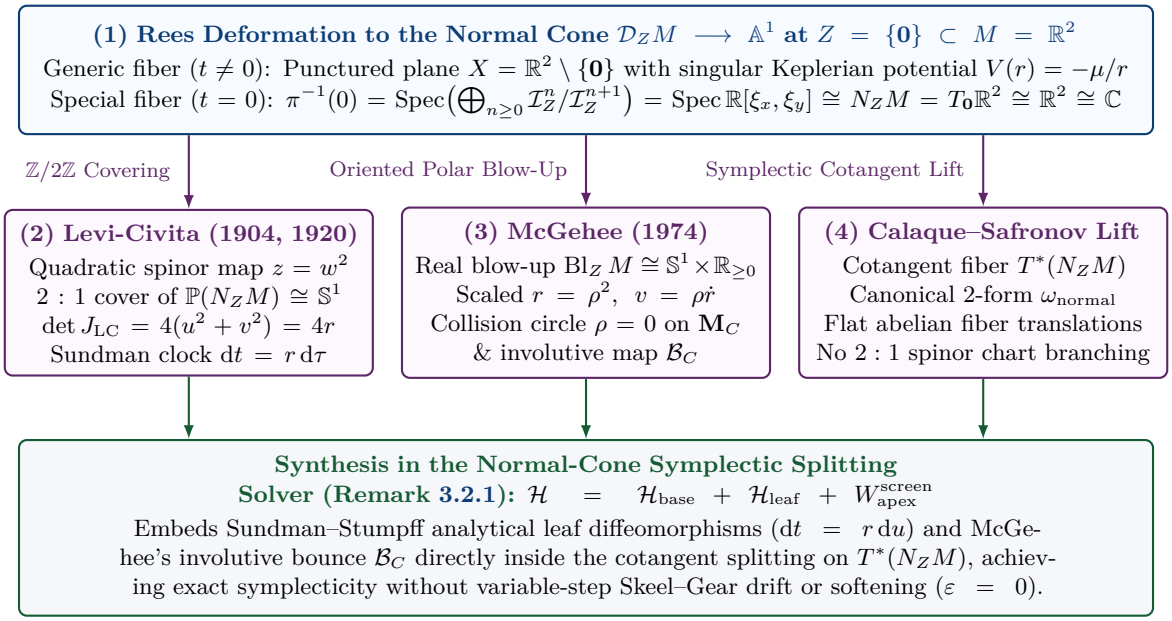


FIGURE 5. Geometric bridge of Theorem 3.2 and Remark 3.2.1: classical two-dimensional collision regularizations—Levi-Civita's branched covering $z = w^2$ on $\mathbb{P}(N_Z M) \cong \mathbb{S}^1$ and McGehee's real oriented blow-up $\mathrm{Bl}_Z M \cong \mathbb{S}^1 \times \mathbb{R}_{\geq 0}$—emerge as coordinate uniformizations of the special fiber $\pi^{-1}(0) \cong N_Z M$ of the Rees deformation $\mathcal{D}_Z M \to \mathbb{A}^1$, whereas the cotangent lift $T^*(N_Z M)$ embeds them into a globally symplectic operator splitting.

Remark — *From Classical Time-Rescaling to Normal-Cone Symplectic Splitting Solvers.* While Sundman's original differential relation $\mathrm{d}t = r\,\mathrm{d}u$ unfreezes the collision singularity by stretching time along two-body orbits, integrating it with variable physical time-steps in naive Cartesian coordinates destroys the symplectic structure and introduces secular energy drift (Skeel & Gear [66]). In our normal-cone cotangent framework, this classical limitation is comprehensively overcome: rather than altering the global physical time parameter arbitrarily, the Sundman transformation is embedded into the Hamiltonian splitting $\mathcal{H} = \mathcal{H}_{\mathrm{base}} + \mathcal{H}_{\mathrm{leaf}} + W_{\mathrm{apex}}^{\mathrm{screen}}$. Each isolated leaf pair is solved through universal Stumpff diffeomorphisms evaluated via high-order cubically convergent Halley iterations (Section 5.2), achieving exact symplecticity and machine-precision energy conservation ($< 10^{-14}$) without softening ($\varepsilon = 0$).

3.3. **Geometric Synthesis: Classical Obstructions and the Normal Cone Imperative.** The planar circular restricted three-body problem serves as a foundational low-dimensional archetype. Having established the canonical synodic Hamiltonian and its Jacobi invariant in §3.1, and connected Levi-Civita's conformal map and McGehee's boundary to the Rees deformation in §3.2, we now synthesize how the normal cone geometry unifies these historical constructions and why it becomes strictly indispensable for the general N-body problem.

3.3.1. *Canonical Synodic Splitting in the Planar Prototype.* The autonomous synodic Hamiltonian partitions naturally into kinetic-Coriolis and gravitational components, $H_{\text{syn}} = H_{\text{kin}} + H_{\text{grav}}$:

$$H_{\text{kin}}(\mathbf{q}, \mathbf{p}) = \frac{1}{2}\|\mathbf{p}\|^2 + (yp_x - xp_y), \qquad H_{\text{grav}}(\mathbf{q}) = -\frac{1-\mu}{r_1} - \frac{\mu}{r_2}. \tag{3.10}$$

The kinematic Hamiltonian H_{kin} generates a linear autonomous vector field on $T^*\mathbb{R}^2$ whose exact flow over time-step h is given by the closed symplectic mapping $\Psi_h^{\text{kin}} \in \text{Sp}(4, \mathbb{R})$:

$$\mathbf{q}(h) = \mathbf{R}_{-h}(\mathbf{q}(0) + h\mathbf{p}(0)), \qquad \mathbf{p}(h) = \mathbf{R}_{-h}\mathbf{p}(0), \tag{3.11}$$

where $\mathbf{R}_{-h} = \begin{pmatrix} \cos h & \sin h \\ -\sin h & \cos h \end{pmatrix} \in \text{SO}(2)$ is computed without truncation error. The gravitational potential H_{grav} depends exclusively on positions $\mathbf{q}$, acting as an exact momentum translation:

$$\mathbf{p}(h) = \mathbf{p}(0) - h\nabla_{\mathbf{q}} H_{\text{grav}}(\mathbf{q}(0)), \qquad \mathbf{q}(h) = \mathbf{q}(0). \tag{3.12}$$

Their symmetric composition $\mathcal{S}_2(h) = \Phi_{h/2}^{\text{grav}} \circ \Psi_h^{\text{kin}} \circ \Phi_{h/2}^{\text{grav}}$ yields a second-order, time-reversible symplectic integrator preserving the phase space 2-form ω_0 unconditionally. (The quantitative numerical validation of this normal cone scheme along the highly sensitive Arenstorf figure-eight periodic orbit [2] ($T \approx 17.0652$, $\mu = 0.01215$), demonstrating machine-precision shadow Jacobi conservation $|\Delta C_J| < 10^{-14}$ and long-term phase stability across repeated lunar close encounters, is provided in the executable reference implementation of Appendix A.2 alongside the full benchmark comparisons in Section 7.)

Python A.2 : `interfaces/pcr3bp_canonical_solver.py` [Planar PCR3BP Float64]

Remark — *Normal Cone Subsumption and Resolution of Classical Obstructions, see [15, 40, 47, 72].* The cotangent lift of the normal cone deformation $\mathcal{D}_Z M \to \mathbb{A}^1$, formalized in the unshifted symplectic framework following Calaque–Safronov, provides a unifying geometric umbrella subsuming classical low-dimensional regularizations while resolving four fundamental structural deadlocks:

(1) **Subsumption of Levi-Civita and McGehee:** In the binary collision limit $r_k \to 0$, the cotangent bundle of the normal bundle $T^*(N_{\Delta_k} M)$ fibers over the collision locus with flat abelian Lie algebra fibers. Levi-Civita's conformal scaling $|J_{LC}| = 4r$ and McGehee's scale-invariant coordinates $\rho = r^{1/2}$ emerge as specific one-dimensional coordinate slices of this Rees deformation.

(2) **Resolution of Sundman's Time-Freezing Dilemma:** Sundman's transformation $\mathrm{d}t = r\,\mathrm{d}\tau$ regularizes isolated binary collisions by slowing global time, but freezes the physical clock for all distant uncolliding bodies when $N \geq 3$. The normal cone splitting operates at constant physical time t, desingularizing momentum transfers along vertical cotangent fibers without time distortion.

(3) **Resolution of Non-Abelian Coordinate Branching:** Conformal coordinates—whether the 2D Levi-Civita spinor map $z = w^2$ or the 4D Kustaanheimo–Stiefel (KS) spinor transformation [36]—cannot be consistently glued across multiple overlapping collision divisors $\Delta_{ij} \cap \Delta_{jk} \neq \emptyset$. In systems with $N \geq 3$, spatial spinor transformations fail to commute along triple collision branches, resulting in non-abelian coordinate branching ambiguities and singular coordinate patches. The normal cone framework substitutes non-local coordinate transformations with a local canonical base-fiber (or Lie–Poisson) splitting on the cotangent bundle.

(4) **Resolution of McGehee's Non-Symplectic Boundary:** McGehee's collision manifold $\mathbf{M}_C$ excises collisions by introducing a manifold with boundary that loses the canonical symplectic

form ω_0. By contrast, the Rees algebra deformation preserves exact relative symplecticity ω_t on all fibers.

This conceptual subsumption demonstrates that pre-existing regularizations are low-dimensional shadows of the deformation to the normal cone. To extend this geometry to arbitrary particle numbers $N \geq 4$ without coordinate singularities, one must resolve the intersecting collision arrangement Δ via the multiscale Fulton–MacPherson compactification $\mathbf{Q}[N]$, developed in Section 4.

4. Fulton–MacPherson Compactification and Multiscale Splitting

4.1. **The Partition Lattice $\Pi(N)$ and the Fulton–MacPherson Manifold $\mathbf{Q}[N]$.** As established in Section 3, classical regularizations of celestial mechanics encounter an insurmountable topological barrier as soon as $N \geq 3$: while isolated binary collisions admit conformal uniformization via Levi-Civita's branched double cover, multiple collision loci intersect along non-transverse submanifolds where local conformal charts fail to commute. For $N \geq 4$, this geometric pathology intensifies into an intricate combinatorial arrangement of intersecting singular divisors.

To overcome this bottleneck without resorting to unphysical gravitational softening ($\varepsilon = 0$), we construct a multiscale desingularization of the Newtonian configuration space grounded in the Fulton–MacPherson compactification [24] and its real differential counterpart developed by Axelrod and Singer [3] and refined by Campos et al. [16]. This section establishes the stratification of the collision arrangement, the real oriented blow-up sequence producing the smooth manifold with corners $\mathbf{Q}[N]$, and the adapted cotangent charts associated with maximal Jacobi binary trees.

4.1.1. *The Collision Arrangement and Whitney Stratification along $\Pi(N)$.* Consider $N \geq 3$ point masses $m_1, \dots, m_N > 0$ with positions $\mathbf{q}_i \in \mathbb{R}^3$. Setting the center of mass to the origin, the relative configuration space is the linear quotient

$$M = (\mathbb{R}^3)^N/\mathbb{R}^3 \cong \left\{ \mathbf{q} = (\mathbf{q}_1, \dots, \mathbf{q}_N) \in (\mathbb{R}^3)^N \;\middle|\; \sum_{i=1}^N m_i \mathbf{q}_i = \mathbf{0} \right\} \cong \mathbb{R}^{3N-3}. \tag{4.1}$$

The space M is naturally endowed with the mass metric $\langle \mathbf{q}, \mathbf{q}' \rangle_{\mathbb{M}} = \sum_{i=1}^N m_i \langle \mathbf{q}_i, \mathbf{q}_i' \rangle$, represented by the positive-definite diagonal block matrix $\mathbb{M} = \operatorname{diag}(m_1 I_3, \dots, m_N I_3)$. The dual momentum space is the zero total linear momentum subspace $M^* \cong \{\mathbf{p} = (\mathbf{p}_1, \dots, \mathbf{p}_N) \in (\mathbb{R}^3)^N \mid \sum_{i=1}^N \mathbf{p}_i = \mathbf{0}\}$. By Marsden–Weinstein symplectic reduction of the ambient space $T^*((\mathbb{R}^3)^N) \cong \mathbb{R}^{6N}$ with respect to the spatial translation group $(\mathbb{R}^3, +)$ at the regular value $\mathbf{J}(\mathbf{q}, \mathbf{p}) = \sum_{i=1}^N \mathbf{p}_i = \mathbf{0}$ [20, Chapter 23], the ambient Darboux 2-form $\sum_{i=1}^N \mathrm{d}\mathbf{q}_i \wedge \mathrm{d}\mathbf{p}_i$ descends without degeneracy to the canonical symplectic 2-form Ω_0 on the physical cotangent bundle $T^*M \cong M \times M^* \cong \mathbb{R}^{6N-6}$. The total Newtonian potential is singular along the collision arrangement $\Delta \subset M$, defined as the union of all pairwise collision submanifolds:

$$\Delta = \bigcup_{1 \leq i < j \leq N} \Delta_{ij}, \qquad \text{where} \quad \Delta_{ij} = \{\mathbf{q} \in M \mid \mathbf{q}_i = \mathbf{q}_j\}. \tag{4.2}$$

Each pairwise diagonal Δ_{ij} is a linear subspace of codimension 3 in M. For an arbitrary coalition of particles $I \subseteq \{1, \dots, N\}$ with cardinality $|I| = k \geq 2$, the multiple collision stratum is the linear subspace where all particles in I coincide spatially:

$$\Delta_I = \{\mathbf{q} \in M \mid \mathbf{q}_i = \mathbf{q}_j \quad \forall i, j \in I\}, \qquad \operatorname{codim}_M(\Delta_I) = 3(k-1). \tag{4.3}$$

Lean A.1 : `collisionCodimension`

The intersection theory of the family $\{\Delta_I\}$ is governed by the transitivity of Euclidean coincidence: for any three distinct indices i, j, k,

$$\Delta_{ij} \cap \Delta_{jk} = \{\mathbf{q} \in M \mid \mathbf{q}_i = \mathbf{q}_j = \mathbf{q}_k\} = \Delta_{\{i,j,k\}} \subset \Delta_{ik}. \tag{4.4}$$

Lean A.1 : `collision_diagonal_non_transversality`

Consequently, the pairwise collision submanifolds Δ_{ij} do not intersect in general position: while any two submanifolds Δ_{ij} and Δ_{jk} meet transversally in codimension $3 + 3 = 6$, Euclidean transitivity forces the third submanifold Δ_{ik} to pass through the exact same locus ($\Delta_{ij} \cap \Delta_{jk} \subset \Delta_{ik}$). Thus, three codimension-3 strata meet along a locus of codimension 6 rather than 9, forming an intrinsically non-normal crossing arrangement.

The combinatorial structure organizing these intersections is the *partition lattice* $\Pi(N)$, defined as the set of all partitions $\mathcal{P} = \{B_1, \dots, B_k\}$ of $\{1, \dots, N\}$, partially ordered by

reverse coarsening (refinement):

$$\mathcal{P} \leq \mathcal{P}' \iff \forall B \in \mathcal{P},\ \exists B' \in \mathcal{P}' \text{ such that } B \subseteq B'. \tag{4.5}$$

The minimal element $\hat{0} = \{\{1\}, \{2\}, \ldots, \{N\}\}$ corresponds to the collisionless open stratum $M \setminus \Delta$, while the maximal element $\hat{1} = \{\{1, \ldots, N\}\}$ corresponds to the total collision point $\Delta_{\text{tot}} = \{\mathbf{0}\}$. To each partition $\mathcal{P} \in \Pi(N)$ corresponds a closed linear stratum:

$$\Delta_{\mathcal{P}} = \{\mathbf{q} \in M \mid \mathbf{q}_i = \mathbf{q}_j \quad \forall i, j \text{ in the same block of } \mathcal{P}\} = \bigcap_{B \in \mathcal{P}} \Delta_B, \tag{4.6}$$

with unified codimension $\operatorname{codim}_M(\Delta_{\mathcal{P}}) = 3(N - |\mathcal{P}|)$. The collection of open strata $S_{\mathcal{P}} = \Delta_{\mathcal{P}} \setminus \bigcup_{\mathcal{P}' > \mathcal{P}} \Delta_{\mathcal{P}'}$ forms a Whitney (A)- and (B)-regular stratification of M [80].

Remark — *Measure-Theoretic Scope of Singularities.* By the seminal theorems of Saari [61, 62], the set of initial conditions in T^*M leading to multiple or total collisions ($k \geq 3$) has Lebesgue measure zero. However, in numerical simulations of dense stellar clusters or hierarchical planetary systems, trajectories routinely enter narrow tubular neighborhoods of Δ_I (quasi-collisions and close encounters), generating arbitrarily stiff tidal forces. The purpose of compactification is not merely to regularize exact collision orbits, but to provide uniform, scale-invariant coordinate charts throughout these stiff asymptotic corridors.

4.1.2. *Real Oriented Blow-ups and the Compactified Manifold with Corners* $\mathbf{Q}[N]$. In algebraic geometry, Fulton and MacPherson [24] resolved diagonal singularities by introducing the compactified configuration space $\mathbf{X}[N]$, obtained by embedding $X^N \setminus \Delta$ into $X^N \times \prod_{|I| \geq 2} \mathbb{P}(N_{\Delta_I} X^N)$ and taking the schematic closure. For differential dynamics, Axelrod and Singer [3] adapted this construction to real manifolds by substituting complex projective blow-ups with *real oriented spherical blow-ups*, producing a smooth manifold with corners $\mathbf{Q}[N]$ that fully desingularizes all collision singularities (compactifying internal directional approach while preserving spatial infinity for non-compact configuration spaces such as $M \cong \mathbb{R}^{3N-3}$).

Let $\operatorname{Bl}_Z(M)$ denote the real oriented blow-up of a manifold M along a closed submanifold Z. Topologically, $\operatorname{Bl}_Z(M)$ is obtained by replacing Z with its unit normal sphere bundle $S(N_Z M) = (N_Z M \setminus Z)/\mathbb{R}_{>0}$, so that points approaching Z retain their limiting direction of approach:

$$\operatorname{Bl}_Z(M) = (M \setminus Z) \sqcup S(N_Z M). \tag{4.7}$$

To desingularize the entire collision arrangement Δ, the blow-up must be performed iteratively along the proper transforms of the subsequent strata of the *irreducible building set* $\mathcal{G}_{\text{irr}} = \{\Delta_I \mid I \subseteq \{1, \ldots, N\}, |I| \geq 2\}$ in order of *increasing manifold dimension of collision strata* (which strictly corresponds to *decreasing cluster cardinality* $k = |I|$, progressing from the total collision stratum $k = N$ of minimal manifold dimension 0 up to binary collision pairs $k = 2$ of maximal manifold dimension $3N - 6$):

Theorem 4.1 — *Fulton–MacPherson Desingularization and SNC Divisor*

In the sense of Fulton and MacPherson [24], Axelrod and Singer [3], De Concini and Procesi [19], and Campos et al. [16], let $M = (\mathbb{R}^3)^N/\mathbb{R}^3 \cong \mathbb{R}^{3N-3}$ and let $\mathcal{G}_{\text{irr}} = \{\Delta_I \mid |I| \geq 2\}$ be the irreducible building set of the partition lattice $\Pi(N)$. The iterated real oriented blow-up

$$\mathbf{Q}[N] = \operatorname{Bl}_{\mathcal{G}_{\text{irr}}}(M) \xrightarrow{\pi} M \tag{4.8}$$

satisfies the following canonical geometric properties:

(1) **Manifold with Corners Structure:** $\mathbf{Q}[N]$ is a smooth manifold with corners of dimension $3N - 3$, whose interior $\operatorname{Int}(\mathbf{Q}[N])$ is diffeomorphic to the collisionless configuration space $M \setminus \Delta$.

(2) **Simple Normal Crossing (SNC) Boundary:** The total boundary $\partial\mathbf{Q}[N] = \pi^{-1}(\Delta)$ is a simple normal crossing divisor with corners:

$$\partial\mathbf{Q}[N] = \bigcup_{\substack{I\subseteq\{1,\dots,N\}\\ |I|\geq 2}} E_I, \tag{4.9}$$

where each exceptional divisor E_I, defined as the compactified proper transform of the spherical normal bundle $S(N_{\Delta_I}M)$, is a smooth codimension-1 boundary hypersurface with inward-pointing normal coordinate (defining boundary function) $\rho_I \in [0,\infty)$.

(3) **Transversality of Boundary Intersections:** Two exceptional divisors E_I and E_J intersect if and only if the coalitions are *nested* or *disjoint*:

$$E_I \cap E_J \neq \emptyset \iff I \subset J, \quad J \subset I, \quad \text{or} \quad I \cap J = \emptyset. \tag{4.10}$$

When $E_I \cap E_J \neq \emptyset$, their intersection is strictly transversal in $\mathbf{Q}[N]$, meeting along a corner stratum of codimension 2.

Proof. Assertion (1) follows from the differential blow-up construction of Axelrod and Singer [3, Sections 4.3 and 5], where each stage replaces an embedded submanifold by its normal sphere bundle, preserving $\mathcal{C}^\infty$ differential structure with corners.
Assertion (2) is established by observing that blowing up along the clean arrangement $\Pi(N)$ in order of increasing manifold dimension of strata (decreasing coalition cardinality $|I|$) transforms all non-transverse intersections into normal crossings: if $I \cap J \neq \emptyset$ and neither contains the other (overlapping clusters), their union satisfies $|I \cup J| > |I|$ and $|I \cup J| > |J|$. Consequently, the deeper collision stratum $\Delta_{I\cup J}$ has strictly lower manifold dimension $\dim \Delta_{I\cup J} = 3(N - |I \cup J|) < \min(\dim \Delta_I, \dim \Delta_J)$, so its proper transform is blown up at an earlier stage of the sequence, separating the proper transforms of Δ_I and Δ_J and ensuring $E_I \cap E_J = \emptyset$. For disjoint coalitions ($I \cap J = \emptyset$), the submanifolds Δ_I and Δ_J are already in clean, transverse intersection in M; their proper transforms E_I and E_J intersect transversally along a codimension-2 corner stratum without requiring the prior blow-up of $\Delta_I \cap \Delta_J \notin \mathcal{G}_{\text{irr}}$, in exact agreement with De Concini–Procesi wonderful models [19].
Assertion (3) reflects the combinatorial property that non-empty boundary strata correspond bijectively to *nested sets* of the building set $\mathcal{G}_{\text{irr}}$ (chains of nested and mutually compatible disjoint clusters), with defining coordinates of the corner $[0,\epsilon)^m$ given by scale ratios $u_k = \rho_{I_k}/\rho_{I_{k+1}} \geq 0$, and with maximal codimension corners in one-to-one correspondence with complete binary Jacobi trees (see Figure 6).

□

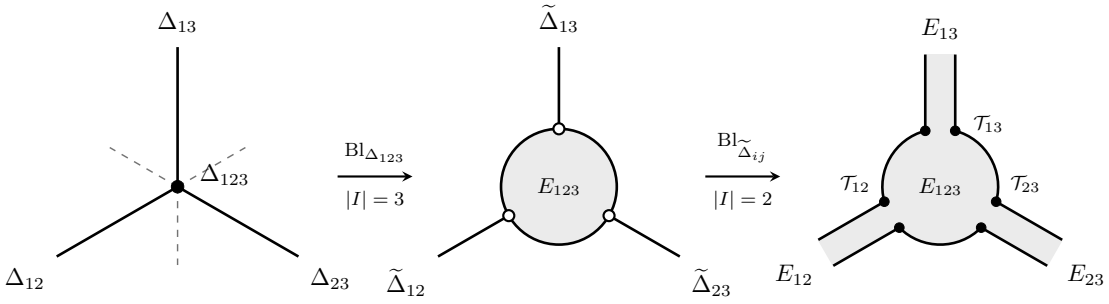
Remark — *Epistemic Note: Standard Cotangent Bundle $T^*\mathbf{Q}[N]$ versus Melrose's b-Cotangent Bundle.* In the differential geometry of manifolds with corners (Melrose [50]), the canonical boundary-adapted structure is the *b-tangent bundle* ${}^bT\mathbf{Q}[N]$ (spanned by vector fields tangent to all boundary faces, locally generated by $\rho_I\partial_{\rho_I}$ and ∂_θ) and its dual *b-cotangent bundle* ${}^bT^*\mathbf{Q}[N]$ whose smooth sections admit logarithmic poles $\mathrm{d}\rho_I/\rho_I$.
One might wonder why our Hamiltonian framework lifts configuration space to the standard cotangent bundle $T^*\mathbf{Q}[N]$ (and its Poincaré–Sundman extension $\mathcal{P}_{\text{ext}}$) rather than adopting ${}^bT^*\mathbf{Q}[N]$. The justification stems directly from the physics of gravitational singularities:

(1) *Singularity Order Mismatch*: The Newtonian potential diverges as ρ_I^{-1} (a pole of order 1), while virialized relative velocities scale as $\rho_I^{-1/2}$. Because these divergences are algebraic rather than logarithmic ($\rho_I^{-1} \gg \log\rho_I$), working on ${}^bT^*\mathbf{Q}[N]$ without an explicit temporal reparametrization does not desingularize the Hamiltonian vector field.

(2) *Preservation of Canonical Darboux Symplectic Geometry*: Passing to *b*-symplectic geometry (as developed by Guillemin, Miranda, and Pires [26]) replaces the canonical symplectic 2-form Ω_0 by a singular *b*-symplectic form $\Omega_b = \sum \frac{\mathrm{d}\rho_I}{\rho_I} \wedge \mathrm{d}p_{\rho_I} + \dots$. This destroys the affine

bundle structure of the cotangent fibers and prevents vertical Hamiltonian translations (potential kicks), which are fundamental to symplectic splitting methods.

(3) *The Normal-Cone Cotangent and Poincaré–Sundman Resolution*: By coupling configuration blow-ups on $\mathbf{Q}[N]$ with Calaque–Safronov cotangent lifts and the unfolded Sundman local clock $\mathrm{d}t_S = \chi_S^2 \mathrm{d}\tau_S$ (Section 4.3), the algebraic velocity divergence is resolved within standard, non-singular Darboux geometry on $\mathcal{P}_{\mathrm{ext}} = T^*\mathbf{Q}[N] \times \mathbb{R}_t \times \mathbb{R}_E$. This preserves exact Lie–Bargmann symmetries and admits explicit, palindromic symplectic splitting propagators.



(a) $M/\mathbb{R}^3$ (b) $\mathrm{Bl}_{\Delta_{123}}(M/\mathbb{R}^3)$ (c) $\mathbf{Q}[3] = \mathrm{Bl}_{\mathcal{G}_{\mathrm{irr}}}(M/\mathbb{R}^3)$

FIGURE 6. Sequential real oriented blow-up constructing the Fulton–MacPherson manifold with corners $\mathbf{Q}[3] = \mathrm{Bl}_{\mathcal{G}_{\mathrm{irr}}}(M/\mathbb{R}^3)$ (Theorem 4.1). **(a)** In the unblown relative configuration space $M/\mathbb{R}^3$, the three binary collision strata $\Delta_{12}, \Delta_{23}, \Delta_{13}$ intersect non-transversally at the triple collision origin Δ_{123}. **(b)** Blowing up the deepest stratum Δ_{123} ($|I| = 3$) inserts the spherical boundary divisor E_{123} ($\rho_{123} = 0$) and separates the proper transforms $\widetilde{\Delta}_{12}, \widetilde{\Delta}_{23}, \widetilde{\Delta}_{13}$ into pairwise disjoint rays ($\widetilde{\Delta}_{ij} \cap \widetilde{\Delta}_{jk} = \emptyset$). **(c)** Blowing up the separated binary loci $\widetilde{\Delta}_{ij}$ ($|I| = 2$) replaces each ray by a boundary collar E_{ij} meeting E_{123} orthogonally at codimension-2 corners indexed by the binary Jacobi trees $\mathcal{T}_{12}, \mathcal{T}_{23}, \mathcal{T}_{13}$.

4.1.3. *Maximal Flag Jacobi Trees and Adapted Cotangent Charts.* The maximal flags (saturated chains) in the partition lattice $\Pi(N)$,

$$\mathcal{F} = (\mathcal{P}_1 < \mathcal{P}_2 < \cdots < \mathcal{P}_{N-1}), \tag{4.11}$$

where $\mathcal{P}_1$ contains exactly one non-trivial binary pair, and each subsequent partition $\mathcal{P}_{k+1}$ is obtained from $\mathcal{P}_k$ by merging either two existing clusters or an isolated body with a cluster, represent the simplicial conical sectors (or linear extensions) that subdivide the boundary corners.

Geometrically, the corners of maximal codimension $N-1$ in $\mathbf{Q}[N]$ (transversal intersections of maximal sets of mutually compatible exceptional divisors) correspond bijectively to complete binary Jacobi trees $\mathcal{T} \in \mathrm{Trees}(N)$ with N labeled leaves and $N-1$ internal nodes $\mathcal{V}_{\mathrm{int}}(\mathcal{T})$ [24, 34]. The natural projection from maximal flags in $\Pi(N)$ to binary Jacobi trees is surjective, with fibers reflecting the commutation of mergers between mutually disjoint clusters. The total number of maximal saturated flags in $\Pi(N)$ is given by

$$|\,\mathrm{Flags}(\Pi(N))| = \prod_{k=2}^{N} \binom{k}{2} = \frac{N!(N-1)!}{2^{N-1}}, \tag{4.12}$$

yielding 3 flags for $N = 3$, 18 flags for $N = 4$ projecting onto $(2N-3)!! = 15$ binary trees, and 180 flags for $N = 5$ projecting onto 105 trees.

Lean A.1 : `jacobi_node_defines_hierarchy`

For each internal node $v \in \mathcal{V}_{\text{int}}(\mathcal{T})$ merging two disjoint sub-clusters $L(v)$ and $R(v)$ of total masses $M_{L(v)} = \sum_{i\in L(v)} m_i$ and $M_{R(v)} = \sum_{j\in R(v)} m_j$, we define the relative Jacobi coordinate vector $\mathbf{r}_v$ and its conjugate momentum $\mathbf{w}_v$ [34]:

$$\mathbf{r}_v = \mathbf{X}_{L(v)} - \mathbf{X}_{R(v)} = \left(\frac{1}{M_{L(v)}}\sum_{i\in L(v)} m_i\mathbf{q}_i\right) - \left(\frac{1}{M_{R(v)}}\sum_{j\in R(v)} m_j\mathbf{q}_j\right), \tag{4.13}$$

$$\mathbf{w}_v = \mu_v\dot{\mathbf{r}}_v = \mu_v\left(\frac{\mathbf{P}_{L(v)}}{M_{L(v)}} - \frac{\mathbf{P}_{R(v)}}{M_{R(v)}}\right), \qquad \mu_v = \frac{M_{L(v)}M_{R(v)}}{M_{L(v)}+M_{R(v)}}, \tag{4.14}$$

where $\mathbf{P}_C = \sum_{i\in C}\mathbf{p}_i$ denotes the total linear momentum of cluster C. The linear map $(\mathbf{q},\mathbf{p}) \mapsto (\mathbf{r}_v,\mathbf{w}_v)_{v\in\mathcal{V}_{\text{int}}(\mathcal{T})}$ defines a canonical symplectic isomorphism on $T^*M \cong \mathbb{R}^{6N-6}$. In these coordinates, the total kinetic energy decouples diagonally:

$$T_{\text{kin}}(\mathbf{w}) = \frac{1}{2}\sum_{v\in\mathcal{V}_{\text{int}}(\mathcal{T})}\frac{\|\mathbf{w}_v\|^2}{\mu_v}. \tag{4.15}$$

For each sub-tree $\mathcal{T}_C$ rooted at an internal node v with cluster bodies $C = L(v)\sqcup R(v)$, the internal cluster potential is given by the restriction of the gravitational interaction to pairs in C:

$$V_C(\mathbf{q}) = -\sum_{\substack{\{i,j\}\subseteq C\\ i<j}}\frac{Gm_im_j}{\|\mathbf{q}_i-\mathbf{q}_j\|}. \tag{4.16}$$

The local cluster hyper-radius $\rho_C \in [0,\infty)$ is defined by the mass metric on the sub-cluster, expressing equivalently in relative Cartesian barycentric coordinates and diagonal Jacobi tree coordinates:

$$\rho_C = \sqrt{\frac{1}{M_C}\sum_{\substack{\{i,j\}\subseteq C\\ i<j}} m_im_j\|\mathbf{q}_i-\mathbf{q}_j\|^2} = \sqrt{\sum_{u\in\mathcal{V}_{\text{int}}(\mathcal{T}_C)}\mu_u\|\mathbf{r}_u\|^2}, \tag{4.17}$$

where $\mu_u = \frac{M_{L(u)}M_{R(u)}}{M_{L(u)}+M_{R(u)}}$ denotes the reduced mass at internal node u. To ensure strict dimensional homogeneity with relative positions $\mathbf{r}_v$ (physical dimension $[L]$), we also define the mass-normalized hyper-radius $\bar{\rho}_C \coloneqq \rho_C/\sqrt{M_C} \in [0,\infty)$, of dimension $[L]$, ensuring that coordinate scale ratios $u_v = \|\mathbf{r}_v\|/(\bar{\rho}_{L(v)}+\bar{\rho}_{R(v)})$ are strictly dimensionless. Each complete tree $\mathcal{T}$ defines an adapted conical clustering chamber (or Maclaurin–Sundman wedge) in configuration space:

$$\mathcal{U}_{\mathcal{T}} = \left\{\mathbf{q}\in M\setminus\Delta \;\middle|\; \forall v\in\mathcal{V}_{\text{int}}(\mathcal{T}),\ \|\mathbf{r}_v\| < \min_{\substack{i\in C_v\\ j\notin C_v}}\|\mathbf{q}_i-\mathbf{q}_j\|\right\}, \tag{4.18}$$

guaranteeing that intra-cluster separations remain strictly hierarchized (see Figure 7).

Lean A.1 : `hyper_radius_sq_pos`

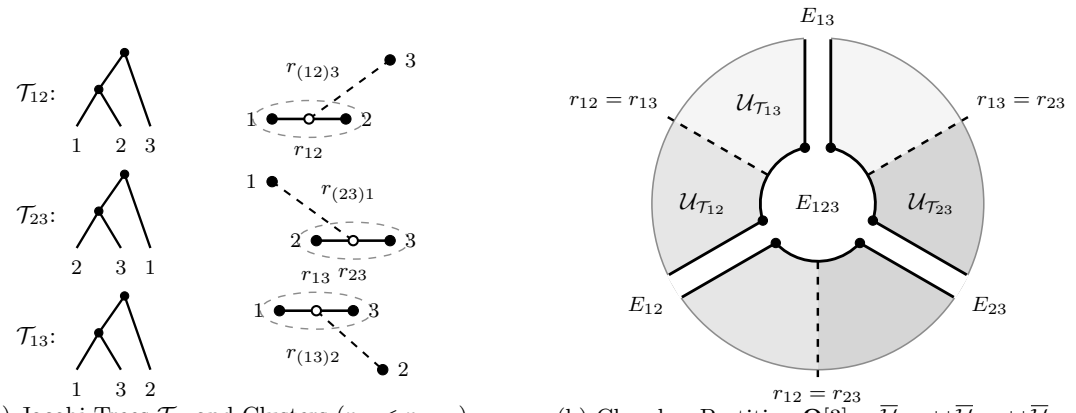
Python A.2 : `core/jacobi.py, core/coordinates.py` [Float64 / Float128]

Geometrically, the hyper-radius ρ_C provides the explicit metric realization of the boundary normal coordinate $\rho_C \in [0,\infty)$ defining the exceptional divisor $E_C \subset \partial\mathbf{Q}[N]$ in local Jacobi charts. Because the Newtonian pairwise potential is homogeneous of degree -1, it satisfies McGehee's scale factorization on each cluster [47]:

$$V_C(\mathbf{r}) = \rho_C^{-1}\,V_C(\mathbf{s}), \qquad \text{where} \quad \mathbf{s} = (\mathbf{s}_u)_{u\in\mathcal{V}_{\text{int}}(\mathcal{T}_C)} = \left(\frac{\sqrt{\mu_u}\mathbf{r}_u}{\rho_C}\right)_{u\in\mathcal{V}_{\text{int}}(\mathcal{T}_C)} \in S\left(N_{\Delta_C}M\right). \tag{4.19}$$

Lean A.1 : `newtonian_potential_is_homogeneous`

Lean A.1 : `mcgehee_potential_factorization`



(a) Jacobi Trees $\mathcal{T}_{ij}$ and Clusters ($r_{ij} < r_{(ij)k}$) (b) Chamber Partition $\mathbf{Q}[3] = \overline{\mathcal{U}}_{\mathcal{T}_{12}} \cup \overline{\mathcal{U}}_{\mathcal{T}_{23}} \cup \overline{\mathcal{U}}_{\mathcal{T}_{13}}$

FIGURE 7. Rooted binary Jacobi trees and their associated conical chamber covering of $\mathbf{Q}[3]$ ($N = 3$). **(a)** Each of the $(2N-3)!! = 3$ binary trees $\mathcal{T}_{ij} = ((i,j),k)$ groups the closest binary leaf at separation $r_{ij} = \|\mathbf{q}_i - \mathbf{q}_j\|$ (solid segment inside the dashed cluster oval) and links its center of mass (hollow circle) to the third body at apex separation $r_{(ij)k} = \|\mathbf{X}_{ij} - \mathbf{q}_k\|$ (dashed segment), independently of the instantaneous direction of motion. **(b)** In the blown-up configuration space $\mathbf{Q}[3]$, the three Maclaurin–Sundman conical chambers $\mathcal{U}_{\mathcal{T}_{12}}, \mathcal{U}_{\mathcal{T}_{23}}, \mathcal{U}_{\mathcal{T}_{13}}$ defined in (4.18) form a sectorial covering around the respective binary collars E_{12}, E_{23}, E_{13} and meet along the Voronoi equidistance hypersurfaces $r_{12} = r_{23}$, $r_{23} = r_{13}$, and $r_{12} = r_{13}$ (dashed rays).

A foundational feature of this hierarchical decomposition is the dynamical decoupling of disjoint clusters:

Proposition 4.2 — *Exact Cotangent Commutation of Disjoint Jacobi Clusters*
Let $\mathcal{T}_A, \mathcal{T}_B \subset \mathcal{T}$ be two disjoint sub-trees of a Jacobi tree $\mathcal{T}$, meaning that their body sets are disjoint ($A \cap B = \emptyset$). Let $H_A(\mathbf{r}_A, \mathbf{w}_A)$ and $H_B(\mathbf{r}_B, \mathbf{w}_B)$ be internal Hamiltonians depending exclusively on the relative degrees of freedom within $\mathcal{T}_A$ and $\mathcal{T}_B$, respectively. Then:

(1) The canonical Poisson bracket of H_A and H_B vanishes identically on T^*M:
$$\{H_A, H_B\}_{\Omega_0} \equiv 0. \tag{4.20}$$

(2) The corresponding Hamiltonian vector fields $\mathcal{X}_{H_A}$ and $\mathcal{X}_{H_B}$ (defined by the canonical convention $\iota_{\mathcal{X}_H}\Omega_0 = \mathrm{d}H$) commute strictly:
$$[\mathcal{X}_{H_A}, \mathcal{X}_{H_B}] \equiv 0, \qquad \Phi_t^{H_A} \circ \Phi_s^{H_B} = \Phi_s^{H_B} \circ \Phi_t^{H_A}, \tag{4.21}$$
on their maximal ambient domain of definition $\mathcal{D}_{A,B} = T^*M \setminus (\pi_A^{-1}(\Delta(A)) \cup \pi_B^{-1}(\Delta(B))) \cong T^*(M_A \setminus \Delta(A)) \times T^*(M_B \setminus \Delta(B)) \times T^*M_{\mathrm{rel}}$, where $\Delta(C) := \bigcup_{\{i,j\}\subseteq C, i<j} \Delta_{ij}$ denotes the complete pairwise collision arrangement of sub-cluster C.

Lean A.1 : disjoint_cotangent_commutation_local

Proof. Because $A \cap B = \emptyset$, the internal Jacobi coordinates of $\mathcal{T}_A$ and $\mathcal{T}_B$ form disjoint subsets of canonical variables: $\mathcal{V}_{\mathrm{int}}(\mathcal{T}_A) \cap \mathcal{V}_{\mathrm{int}}(\mathcal{T}_B) = \emptyset$. Since $(\mathbf{r}_v, \mathbf{w}_v)_{v \in \mathcal{V}_{\mathrm{int}}(\mathcal{T})}$ is a canonical Darboux coordinate system on T^*M, the Poisson bracket evaluated over all internal nodes of the full Jacobi tree $\mathcal{T}$,
$$\{H_A, H_B\}_{\Omega_0} = \sum_{u \in \mathcal{V}_{\mathrm{int}}(\mathcal{T})} (\langle \nabla_{\mathbf{r}_u} H_A, \nabla_{\mathbf{w}_u} H_B \rangle - \langle \nabla_{\mathbf{w}_u} H_A, \nabla_{\mathbf{r}_u} H_B \rangle) \equiv 0, \tag{4.22}$$

vanishes identically because for each internal node $u \in \mathcal{V}_{\text{int}}(\mathcal{T})$, at least one of H_A or H_B does not depend on $(\mathbf{r}_u, \mathbf{w}_u)$, ensuring that the corresponding gradient pair is identically zero.
Equivalently, in Cartesian coordinates, for each individual body $i \in \{1, \dots, N\}$, at least one of the two Hamiltonians has identically zero gradient with respect to $(\mathbf{q}_i, \mathbf{p}_i)$:

$$\forall i \in \{1, \dots, N\}, \qquad (\nabla_{\mathbf{q}_i} H_A = \mathbf{0} \quad \text{and} \quad \nabla_{\mathbf{p}_i} H_A = \mathbf{0}) \quad \text{or} \quad (\nabla_{\mathbf{q}_i} H_B = \mathbf{0} \quad \text{and} \quad \nabla_{\mathbf{p}_i} H_B = \mathbf{0}). \tag{4.23}$$

The local term of the canonical Poisson bracket at index i,

$$\{H_A, H_B\}_i = \langle \nabla_{\mathbf{q}_i} H_A, \nabla_{\mathbf{p}_i} H_B \rangle - \langle \nabla_{\mathbf{p}_i} H_A, \nabla_{\mathbf{q}_i} H_B \rangle, \tag{4.24}$$

vanishes identically for every $i \in \{1, \dots, N\}$, establishing $\{H_A, H_B\}_{\Omega_0} = \sum_{i=1}^{N} \{H_A, H_B\}_i = 0$.
The commutation of the Hamiltonian flows follows directly from the Lie algebra homomorphism between Poisson brackets and vector field commutators: $[\mathcal{X}_{H_A}, \mathcal{X}_{H_B}] = -\mathcal{X}_{\{H_A, H_B\}} = \mathbf{0}$.
This exact cotangent decoupling reflects in classical mechanics the canonical conormal Whitney sum $N^*(\Delta_A \cap \Delta_B) \cong N^*\Delta_A \oplus N^*\Delta_B$, mirroring the symmetric monoidal property of shifted cotangent functors under normal cone deformation established by Calaque and Safronov [15, Theorems B, 3.13 and Corollary 5.13].

□

Remark — *Epistemic Scope: Constructive Combinatorial and 1-Jet Algebraic Kernel.* In accordance with the formal verification standard established in Section 1, the companion Lean 4 modules colocalized in Section 4.1 mechanize a *Constructive Combinatorial and 1-Jet Algebraic Kernel*. While the global differential and symplectic topology of $\mathbf{Q}[N]$ (smooth manifolds with corners, blow-up sequences, and continuous Hamiltonian flows) is developed analytically in the text, Lean 4 certifies the exact combinatorial incidence of the partition lattice $\Pi(N)$, the scale homogeneity of the Newtonian potential, the hierarchical tree inclusion, and the pointwise algebraic vanishing of local Poisson brackets without axioms or approximations.

Transition to Screened Apex Dynamics. Proposition 4.2 guarantees that mutually disjoint sub-clusters evolve with complete symplectic independence, laying the rigorous foundation for decentralized multi-rate time-stepping on hierarchical supernodes (§4.3). However, when two clusters $L(v)$ and $R(v)$ interact at their common parent node v (the *apex*), their relative distance vector $\mathbf{r}_v$ couples to internal configurations through the global Newtonian potential $V(\mathbf{q})$. In raw Jacobi coordinates, the kinetic energy remains strictly diagonal ($T_{\text{kin}} = \frac{1}{2} \sum \|\mathbf{w}_v\|^2 / \mu_v$); however, the cross-metric products between interparticle distance gradients sharing an apex body, $\langle \nabla r_{ij}, \nabla r_{jk} \rangle_{\mathbb{M}^{-1}} \neq 0$, reflect the non-orthogonality of internal pairwise interactions. Furthermore, subtracting the point-mass barycentric Keplerian attraction $-GM_{L(v)}M_{R(v)}/\|\mathbf{r}_v\|$ leaves an unphysical multipolar residual potential that diverges as an artificial "ghost pole" when cluster barycenters coincide ($\|\mathbf{r}_v\| \to 0$) even while all internal interparticle separations remain strictly positive. Section 4.2 resolves this challenge through the construction of a smooth screened apex potential achieving universal $\mathcal{C}^{1,1}$ Lipschitz regularity.

4.2. Smooth Scale-Adapted Screening of the Apex Potential and $\mathcal{C}^{1,1}$ Regularity.

While Proposition 4.2 establishes the complete symplectic decoupling of mutually disjoint clusters, real gravitational dynamics inevitably couples sub-clusters through parent hierarchical nodes. In this section, we analyze the residual inter-cluster potential coupling that arises at the parent apex of two interacting clusters, identify the multipolar "ghost pole" generated by naive Keplerian center-of-mass subtraction, and construct a smooth scale-adapted screening function $\Theta(u_v)$ that resolves this singularity. We prove that the resulting screened apex potential achieves universal $\mathcal{C}^{1,1}$ Lipschitz regularity without introducing any artificial distance cut-off ($d_0 > 0$ strictly banished), while strictly preserving all 10 Galilean generators realizing the centrally extended Lie–Bargmann algebra and ensuring palindromic symplecticity.

4.2.1. *Residual Inter-Cluster Potential Coupling and Multipolar Ghost Poles.* Consider an internal node $v \in \mathcal{V}_{\text{int}}(\mathcal{T})$ of a complete binary Jacobi tree $\mathcal{T}$, whose left and right children represent two disjoint clusters $L(v)$ and $R(v)$ with total masses $M_{L(v)} = \sum_{i\in L(v)} m_i$ and $M_{R(v)} = \sum_{j\in R(v)} m_j$. The relative position vector between the centers of mass of these two clusters is the Jacobi apex coordinate:

$$\mathbf{r}_v = \mathbf{X}_{L(v)} - \mathbf{X}_{R(v)} = \left(\frac{1}{M_{L(v)}}\sum_{i\in L(v)} m_i\mathbf{q}_i\right) - \left(\frac{1}{M_{R(v)}}\sum_{j\in R(v)} m_j\mathbf{q}_j\right). \tag{4.25}$$

In Cartesian configuration space, the mutual distance between an arbitrary particle $i \in L(v)$ and an arbitrary particle $j \in R(v)$ decomposes linearly along the hierarchy:

$$\mathbf{q}_i - \mathbf{q}_j = \mathbf{r}_v + (\mathbf{q}_i - \mathbf{X}_{L(v)}) - (\mathbf{q}_j - \mathbf{X}_{R(v)}). \tag{4.26}$$

Although the kinetic energy is strictly diagonalized by the Jacobi momenta ($T_{\text{kin}} = \frac{1}{2}\sum_u \|\mathbf{w}_u\|^2/\mu_u$ with $u \in \mathcal{V}_{\text{int}}(\mathcal{T})$), the gravitational potential retains a non-decoupled inter-cluster interaction at the apex node. In Cartesian coordinates, the inverse mass metric $\mathbb{M}^{-1} = \text{diag}(m_1^{-1}I_3, \dots, m_N^{-1}I_3)$ generates non-orthogonal cross-products between the gradients of mutual interparticle distances sharing a common mass point:

$$\langle \nabla_{\mathbf{q}}\|\mathbf{q}_i - \mathbf{q}_j\|, \nabla_{\mathbf{q}}\|\mathbf{q}_j - \mathbf{q}_k\|\rangle_{\mathbb{M}^{-1}} = -\frac{1}{m_j}\frac{\langle \mathbf{q}_i - \mathbf{q}_j, \mathbf{q}_j - \mathbf{q}_k\rangle}{\|\mathbf{q}_i - \mathbf{q}_j\|\,\|\mathbf{q}_j - \mathbf{q}_k\|} \neq 0 \quad (i \neq k). \tag{4.27}$$

As established in the classical analysis of multi-body collision manifolds and asymptotic configurations by Marchal and Saari [43] and Waldvogel [79], the relative geometry of interacting clusters cannot be fully decoupled by linear coordinate changes alone.

To separate the macroscopic Keplerian motion of the two clusters from their internal high-frequency dynamics, standard hierarchical approaches attempt to subtract the point-mass barycentric interaction $-GM_{L(v)}M_{R(v)}/\|\mathbf{r}_v\|$ from the cross-cluster Newtonian potential:

$$V_v(\mathbf{q}) = -\sum_{i\in L(v)}\sum_{j\in R(v)} \frac{Gm_im_j}{\|\mathbf{q}_i - \mathbf{q}_j\|}. \tag{4.28}$$

However, the naive residual difference,

$$V_{\text{res},v}(\mathbf{q}) = V_v(\mathbf{q}) - \left(-\frac{GM_{L(v)}M_{R(v)}}{\|\mathbf{r}_v\|}\right) = -\sum_{i\in L(v)}\sum_{j\in R(v)} \frac{Gm_im_j}{\|\mathbf{q}_i - \mathbf{q}_j\|} + \frac{GM_{L(v)}M_{R(v)}}{\|\mathbf{r}_v\|}, \tag{4.29}$$

exhibits an unphysical, catastrophic singularity: when the centers of mass of the two clusters coincide ($\|\mathbf{r}_v\| \to 0$) while all internal interparticle separations remain strictly positive ($\rho_{L(v)} > 0$ and $\rho_{R(v)} > 0$), the added term $+GM_{L(v)}M_{R(v)}/\|\mathbf{r}_v\|$ diverges as an artificial *multipolar ghost pole* ($\sim \|\mathbf{r}_v\|^{-1}$). In conventional approaches, this divergence forces the introduction of an arbitrary distance threshold $d_0 > 0$, destroying scale invariance and introducing secular energy drifts.

4.2.2. *The Smooth Scale-Adapted Screening Function* $\Theta(u_v)$. To neutralize the ghost pole without softening the gravitational law ($\varepsilon = 0$ strict), we construct a scale-invariant screening mechanism grounded in the geometry of the Fulton–MacPherson configuration manifold $\mathbf{Q}[N]$. From an architectural perspective, this screening function $\Theta(u_v)$ acts as an operational bridge connecting the continuous configuration geometry of Section 4 to the discrete symplectic numerical propagators developed in Section 5: it guarantees that the residual interaction remains uniformly Lipschitz continuous on cotangent fibers, providing the exact analytical regularity required by the Picard–Lindelöf theorem and formal backward error analysis to prevent algorithmic instability during discrete operator kicks.

For an elementary binary leaf pair ($|L(v)| = |R(v)| = 1$), the cross-cluster potential $V_v(\mathbf{q}) = -Gm_im_j/\|\mathbf{q}_i - \mathbf{q}_j\|$ is already pure Keplerian with internal hyper-radii $\rho_{\{i\}} \equiv 0$ and

$\rho_{\{j\}} \equiv 0$, so the residual potential vanishes identically ($V_{\mathrm{res},v} \equiv 0$) and requires no screening. Accordingly, we restrict the apex screening to the set of composite internal nodes:

$$\mathcal{V}_{\mathrm{comp}}(\mathcal{T}) = \{v \in \mathcal{V}_{\mathrm{int}}(\mathcal{T}) \mid |L(v)| \geq 2 \text{ or } |R(v)| \geq 2\}. \tag{4.30}$$

For each $v \in \mathcal{V}_{\mathrm{comp}}(\mathcal{T})$, let $\bar{\rho}_{\mathrm{int}}(v) \coloneqq \bar{\rho}_{L(v)} + \bar{\rho}_{R(v)} > 0$ denote the combined mass-normalized internal hyper-radius of the child clusters (where $\bar{\rho}_C \coloneqq \rho_C/\sqrt{M_C} \in [L]$). We define the dimensionless scale ratio coordinate:

$$u_v = \frac{\|\mathbf{r}_v\|}{\bar{\rho}_{\mathrm{int}}(v)} = \frac{\|\mathbf{r}_v\|}{\bar{\rho}_{L(v)} + \bar{\rho}_{R(v)}} \in [0, \infty). \tag{4.31}$$

The ratio u_v monitors the relative hierarchy: when $u_v \to 0$, $\|\mathbf{r}_v\| \to 0$ corresponds to the internal transverse locus where cluster barycenters coincide in $\mathrm{Int}(\mathbf{Q}[N])$; conversely, when $u_v \to \infty$ (i.e., $u_v^{-1} \to 0$), the two clusters are asymptotically separated, reaching the boundary divisor $E_{L(v)} \cap E_{R(v)} \subset \partial\mathbf{Q}[N]$. In particular, in the point-particle limit where both child clusters shrink to point masses ($\bar{\rho}_{\mathrm{int}}(v) \to 0$ with $\|\mathbf{r}_v\| > 0$), we have $u_v \to \infty$, identically recovering the unscreened point-mass Keplerian attraction with $\Theta(u_v) = 1$.

We introduce a smooth, monotonic scale-adapted screening function $\Theta : [0, \infty) \to [0, 1]$ satisfying the asymptotic partition:

$$\Theta(u) = \begin{cases} 0 & \text{for } u \leq 1, \\ \sigma(u) & \text{for } 1 < u < 2, \\ 1 & \text{for } u \geq 2, \end{cases} \tag{4.32}$$

where $\sigma : [1, 2] \to [0, 1]$ is a smooth, monotonic transition function with vanishing derivatives of all required orders at $u = 1$ and $u = 2$. The mathematical specification of $\sigma(u)$ reflects a deliberate architectural duality balancing theoretical rigor with practical computational efficiency:

(1) *Canonical Theoretical Standard ($\mathcal{C}^\infty$ Cauchy Mollifier)*: For high-order symplectic Baker–Campbell–Hausdorff expansions (Section 5), $\sigma(u)$ is defined as the normalized Cauchy mollifier. Letting $s = u-1 \in [0, 1]$, it admits the exact closed-form evaluation:

$$\sigma_{\mathrm{Cauchy}}(s) = \frac{\exp\left(-\frac{1}{s}\right)}{\exp\left(-\frac{1}{s}\right) + \exp\left(-\frac{1}{1-s}\right)} \quad \text{for } s \in (0, 1), \tag{4.33}$$

with continuous boundary limits $\sigma_{\mathrm{Cauchy}}(0) = 0$ and $\sigma_{\mathrm{Cauchy}}(1) = 1$. This closed form is strictly $\mathcal{C}^\infty([0, 1])$ with vanishing derivatives of all orders at the boundaries ($\sigma^{(k)}(0) = \sigma^{(k)}(1) = 0$ for all $k \geq 1$), circumventing the computational burden of numerical quadratures. Its Gevrey-2 regularity guarantees that formal modified Hamiltonians $\widetilde{H}(h)$ exist asymptotically to all orders without truncation, enabling sub-exponential shadow energy conservation for high-order integrators.

(2) *Order-Adapted Computational Proxies ($\mathcal{C}^{2k}$ Centered Hermite Splines)*: In high-performance scientific computing where transcendentals incur non-negligible cost, $\sigma(u)$ is algebraically realized via a family of odd-degree Hermite polynomial splines centered in $\xi = s - 0.5 \in [-0.5, 0.5]$ to prevent catastrophic floating-point subtractive cancellation:
   - $\mathcal{C}^2$ quintic spline (degree 5, $\kappa \sim 1$): for 2nd-order Strang splitting $\mathcal{S}_2$;
   - $\mathcal{C}^4$ nonic spline (degree 9): $s^5(126 - 420s + 540s^2 - 315s^3 + 70s^4)$, for 4th-order compositions (BM_4, Yoshida $\mathcal{S}_4$);
   - $\mathcal{C}^6$ tridecic spline (degree 13): with vanishing derivatives $1 \ldots 6$ at boundaries, matched to 6th-order schemes (BM_6, PBM_4);
   - $\mathcal{C}^8$ heptadecic spline (degree 17): derived from $\sigma_8'(s) = 218790(s(1-s))^8$, matched to 8th-order effective schemes (PBM_6).

Each spline degree is calibrated to match the order of the symplectic integrator, ensuring that the truncation error of the screening boundary does not degrade the asymptotic convergence slope.

Definition 4.3 — *Screened Hierarchical Apex Potential*

For each internal composite node $v \in \mathcal{V}_{\text{comp}}(\mathcal{T})$, the *screened apex potential* is defined by

$$W_{\text{apex},v}^{\text{screen}}(\mathbf{q}) = V_v(\mathbf{q}) + \Theta(u_v)\frac{GM_{L(v)}M_{R(v)}}{\|\mathbf{r}_v\|}. \tag{4.34}$$

When the configuration contains compact sub-clusters promoted to synchronous supernodes (Section 4.3), let $\mathcal{S}_{\text{act}}$ denote the collection of disjoint sub-clusters $S \subset \{1,\dots,N\}$ satisfying the compactness condition $\rho_S \le \delta_{\text{cluster}}$ (whose intrinsic, scale-invariant dynamical determination $\delta_{\text{cluster}}^{\text{nat}}$ is established in Section 4.3.4). The set of free composite nodes is defined by

$$\mathcal{V}_{\text{comp}}^{\text{free}}(\mathcal{T}) = \mathcal{V}_{\text{comp}}(\mathcal{T}) \setminus \bigcup_{S\in\mathcal{S}_{\text{act}}} \mathcal{V}_{\text{int}}(\mathcal{T}_S). \tag{4.35}$$

The total hierarchical screened apex potential across the tree is the sum over free composite nodes:

$$W_{\text{apex}}^{\text{screen}}(\mathbf{q}) = \sum_{v\in\mathcal{V}_{\text{comp}}^{\text{free}}(\mathcal{T})} W_{\text{apex},v}^{\text{screen}}(\mathbf{q}). \tag{4.36}$$

The screened apex potential enables an exact five-term decomposition of the total physical Hamiltonian of the N-body system:

$$H = T_{\text{kin}} + W_{\text{apex}}^{\text{screen}}(\mathbf{q}) + V_{\text{kepler}}^{\text{screened}}(\mathbf{q}) + V_{\text{leaves}}^{\text{free}}(\mathbf{q}) + \sum_{S\in\mathcal{S}_{\text{act}}} H_S^{\text{super}}, \tag{4.37}$$

where $V_{\text{kepler}}^{\text{screened}}(\mathbf{q}) = -\sum_{v\in\mathcal{V}_{\text{comp}}^{\text{free}}(\mathcal{T})}\Theta(u_v)\frac{GM_{L(v)}M_{R(v)}}{\|\mathbf{r}_v\|}$ is the screened macroscopic Keplerian interaction, $V_{\text{leaves}}^{\text{free}}(\mathbf{q})$ contains the uncoupled elementary leaf-pair potentials outside active supernodes, and H_S^{super} governs the internal multi-body dynamics of each synchronous supernode.

When $u_v \le 1$, $\Theta(u_v) = 0$, completely extinguishing the Keplerian subtraction and leaving the exact, smooth physical potential $V_v(\mathbf{q})$. When $u_v \ge 2$, $\Theta(u_v) = 1$, restoring the full multipolar subtraction where the interaction decays rapidly. In the intermediate zone $1 < u_v < 2$, $\Theta'(u_v)$ is compactly supported, ensuring smooth, bounded transitions (see Figure 8).

4.2.3. *Universal $\mathcal{C}^{1,1}$ Lipschitz Regularity without Distance Thresholds.* The foundational analytical property of the screened apex potential is its uniform $\mathcal{C}^{1,1}$ regularity (i.e., belonging to the Sobolev–Lipschitz space $\mathcal{W}^{2,\infty}$) on each adapted chart of the configuration manifold:

Theorem 4.4 — *Universal $\mathcal{C}^{1,1}$ Lipschitz Regularity of the Screened Apex Potential*

Let $\mathcal{T} \in \text{Trees}(N)$ be a complete binary Jacobi tree, and let $U_{\mathcal{T}} \subset \mathbf{Q}[N]$ be its adapted atlas chart. Endow the relative configuration space M with the Riemannian mass metric induced by $\mathbb{M}$ (and its cotangent bundle T^*M with the dual metric $\mathbb{M}^{-1}$). Then, on the domain of validity of the adapted chart $U_{\mathcal{T}}$ and without requiring any artificial distance threshold ($d_0 = 0$ strictly), there exist finite strictly positive constants $M_{\text{apex}} > 0$ and $L_{\text{apex}} > 0$ such that for all configurations $\mathbf{q} \in U_{\mathcal{T}}$ and all relative Jacobi coordinates $\mathbf{r} = (\mathbf{r}_u)_{u\in\mathcal{V}_{\text{int}}(\mathcal{T})}$:

$$\|\nabla_{\mathbf{r}} W_{\text{apex}}^{\text{screen}}(\mathbf{q})\|_{\mathbb{M}^{-1}} \le M_{\text{apex}} < \infty, \qquad \|\operatorname{Hess}_{\mathbf{r}} W_{\text{apex}}^{\text{screen}}(\mathbf{q})\|_{\mathbb{M}^{-1}} \le L_{\text{apex}} < \infty. \tag{4.38}$$

Consequently, $W_{\text{apex}}^{\text{screen}}$ is uniformly of class $\mathcal{C}^{1,1}(U_{\mathcal{T}}) = \mathcal{W}^{2,\infty}(U_{\mathcal{T}})$, so its gradient force field $\nabla_{\mathbf{r}} W_{\text{apex}}^{\text{screen}}$ is globally Lipschitz continuous ($\mathcal{C}^{0,1}$) on $U_{\mathcal{T}}$.

Lean A.1 : apex_universal_lipschitz_bound

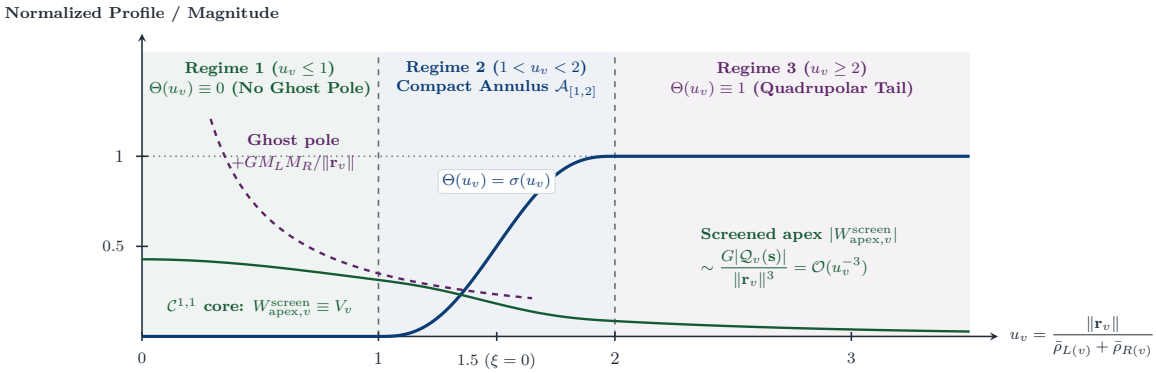


FIGURE 8. Scale-adapted apex screening function $\Theta(u_v)$ and universal $\mathcal{C}^{1,1}$ regularity across the three scale regimes of Definition 4.3 and Theorem 4.4. **Regime 1 ($u_v \leq 1$):** $\Theta(u_v) \equiv 0$ completely extinguishes the unphysical multipolar ghost pole $+GM_LM_R/\|\mathbf{r}_v\|$ (dashed purple curve) when cluster barycenters overlap ($\|\mathbf{r}_v\| \to 0$). **Regime 2 ($1 < u_v < 2$):** The transition function $\sigma(u_v)$ (solid blue curve, realized via the $\mathcal{C}^\infty$ Gevrey-2 Cauchy mollifier or centered $\mathcal{C}^{2k}$ Hermite splines around $\xi = u_v - 1.5 = 0$) interpolates smoothly across the compact projectivized annulus $\mathcal{A}_{[1,2]}$. **Regime 3 ($u_v \geq 2$):** $\Theta(u_v) \equiv 1$ restores the full Keplerian subtraction, where exact monopole and barycentric dipole cancellations leave a rapidly decaying trace-free quadrupolar interaction $W^{\text{screen}}_{\text{apex},v} = -G\mathcal{Q}_v(\mathbf{s})/\|\mathbf{r}_v\|^3 + \mathcal{O}(\|\mathbf{r}_v\|^{-4})$ (solid green curve).

Python A.2 : `potential/{screened_apex, optimized_screened_apex, screening}.py` [Float64 / Float128]

The accompanying formal certification badge denotes the verification of the *Constructive 1-Jet Algebraic Kernel* (formalized in Lean 4 over an arbitrary commutative ring), certifying the constructive algebra of the Lipschitz bounds, with the global topological compactness and the smooth transitions established by the differential proof below.

Remark — *Epistemic Scope: $\mathcal{C}^{1,1}$ Regularity and Atlas Chart Domain $U_\mathcal{T}$.* Two essential structural remarks must be highlighted:

(1) *Functional Class $\mathcal{C}^{1,1}$ vs $\mathcal{C}^\infty$ (Algorithmic Interface)*: Qualifying $W^{\text{screen}}_{\text{apex}}$ as $\mathcal{C}^{1,1}$ designates the minimal regularity guaranteed by the algebraic $\mathcal{C}^2$ quintic Hermite spline proxy. Under this minimal Sobolev–Lipschitz regularity ($\mathcal{W}^{2,\infty}$), the Hamiltonian vector field $X_{W^{\text{screen}}_{\text{apex}}}$ is Lipschitz continuous, satisfying the classical Picard–Lindelöf theorem and ensuring strict convergence of the second-order Strang splitting $\mathcal{S}_2(h)$ (Section 5.1). When our canonical theoretical baseline (the $\mathcal{C}^\infty$ Cauchy mollifier) is activated, $W^{\text{screen}}_{\text{apex}}$ is locally $\mathcal{C}^\infty$ with uniformly bounded derivatives of all orders ≤ 2 and Gevrey-2 sub-exponential stability, fulfilling the analytical prerequisites for all-order formal backward error analysis in high-order composition schemes.

(2) *Domain of Validity $U_\mathcal{T}$ and Synchronous Supernodes*: The Lipschitz bounds M_{apex} and L_{apex} are established on the adapted chart $U_\mathcal{T} \subset \mathbf{Q}[N]$. While $W^{\text{screen}}_{\text{apex},v}(\mathbf{q})$ eliminates the multipolar ghost pole upon barycentric coincidence ($\mathbf{r}_v \to \mathbf{0}$), it does not protect against an internal collision between a particle $i \in L(v)$ and a particle $j \in R(v)$ if the hierarchy of $\mathcal{T}$ ceases to be adapted. Under such dynamics, either the distance hierarchy reverses (triggering an $\mathrm{SL}(2,\mathbb{R})$ Jacobi tree transition via the $\gamma = 0.6$ hysteresis band of Theorem 4.10) or the entire sub-cluster collapses into a compact k-body quasi-collision ($k \geq 3$), in which case the sub-tree is subsumed into a synchronous supernode governed by Sundman's unfolded local clock $\mathrm{d}t_S = \chi_S^2 \mathrm{d}\tau_S$ (Section 4.3).

Proof. It suffices to establish the bounds for each node $v \in \mathcal{V}_{\mathrm{comp}}(\mathcal{T})$ across three complementary scale regimes covering $[0,\infty)$:

Regime 1: Compact Sub-Apex Regime ($u_v \le 1$). In this regime, $\Theta(u_v) = 0$, and Definition 4.3 reduces identically to the restricted interaction $W^{\mathrm{screen}}_{\mathrm{apex},v}(\mathbf{q}) = V_v(\mathbf{q}) = -\sum_{i\in L(v), j\in R(v)} \frac{Gm_im_j}{\|\mathbf{q}_i-\mathbf{q}_j\|}$. By definition of an adapted Jacobi chart $U_{\mathcal{T}}$, when $u_v \le 1$, interparticle collisions between $L(v)$ and $R(v)$ are either bounded away from zero by pairwise separation within the tree hierarchy or absorbed into a synchronous supernode (analyzed in Section 4.3). Hence, on the regular locus of $U_{\mathcal{T}}$, the pairwise distances $\|\mathbf{q}_i - \mathbf{q}_j\|$ remain uniformly bounded below away from zero, ensuring $\|\nabla V_v\| \le B_1$ and $\|\operatorname{Hess} V_v\| \le B_1'$ for finite constants $B_1, B_1' > 0$. The artificial ghost pole is completely eliminated since its coefficient $\Theta(u_v)$ is identically zero.

Regime 2: Compact Transition Annulus ($1 < u_v < 2$). In this domain, the ratio $u_v = \|\mathbf{r}_v\|/\bar{\rho}_{\mathrm{int}}(v)$ lies in the compact interval $[1,2]$. Consequently, $\|\mathbf{r}_v\| \ge \bar{\rho}_{\mathrm{int}}(v) > 0$, guaranteeing that cluster centers cannot coincide. On the set of free composite nodes $\mathcal{V}^{\mathrm{free}}_{\mathrm{comp}}(\mathcal{T})$, any sub-cluster satisfying $\bar{\rho}_{\mathrm{int}}(v) \le \delta_{\mathrm{cluster}}$ is subsumed into an active synchronous supernode $S \in \mathcal{S}_{\mathrm{act}}$ (Section 4.3); therefore, $\bar{\rho}_{\mathrm{int}}(v) \ge c_0\delta_{\mathrm{cluster}} > 0$ holds uniformly on $\mathcal{V}^{\mathrm{free}}_{\mathrm{comp}}$, ensuring that $\bar{\rho}_{\mathrm{int}}^{-1} \le (c_0\delta_{\mathrm{cluster}})^{-1} < \infty$ is strictly bounded away from infinity (with $\delta_{\mathrm{cluster}} = \delta^{\mathrm{nat}}_{\mathrm{cluster}}(E_0)$ determined dynamically by the total energy E_0 and masses via Proposition 4.11, eliminating any arbitrary metric regulator). Furthermore, since $\Theta(u_v) = \sigma(u_v)$ is a smooth function with compact support of its derivatives in $[1,2]$, both $\Theta(u_v)$ and all its derivatives are uniformly bounded. We emphasize that while the Euclidean hyper-radius ρ_C is non-differentiable at the origin in naive Cartesian coordinates (due to the singularity of $r \mapsto \|r\|$ at $r = 0$), on the Fulton–MacPherson compactified manifold with corners $\mathbf{Q}[N]$ (or in McGehee polar blow-up coordinates $\rho_C \in [0,\infty[$ and $\mathbf{s}_C \in \mathbb{S}^{3k-4}$), the total collision locus Δ_C is replaced by the smooth boundary divisor $\{\rho_C = 0\}$. The radial coordinate ρ_C is a defining boundary coordinate of the manifold with corners, and the radial vector field ∂_{ρ_C} is smooth up to the boundary stratum $\rho_C = 0$ within each adapted chart $U_{\mathcal{T}}$. By the chain rule, $\nabla_{\mathbf{q}_i} u_v = \bar{\rho}_{\mathrm{int}}^{-1}\nabla_{\mathbf{q}_i}\|\mathbf{r}_v\| - \|\mathbf{r}_v\|\bar{\rho}_{\mathrm{int}}^{-2}\nabla_{\mathbf{q}_i}\bar{\rho}_{\mathrm{int}}$; since $\|\nabla_{\mathbf{q}_i}\bar{\rho}_{\mathrm{int}}\| \le \sqrt{m_i/M_C}$ uniformly by Cauchy–Schwarz on cluster hyper-radii and $\bar{\rho}_{\mathrm{int}} \ge c_0\delta_{\mathrm{cluster}} > 0$, the spatial gradients and second derivatives of u_v remain uniformly bounded on $[1,2]$. By Weierstrass's extreme value theorem on the compact projectivized annulus $\mathcal{A}_{[1,2]} \subset S(N_{\Delta_v}M)$ (or on the compact slice in the coordinates with corners of $\mathbf{Q}[N]$), the gradient and Hessian of $W^{\mathrm{screen}}_{\mathrm{apex},v}$ are continuous functions on a compact domain, hence bounded by finite constants $B_2, B_2' > 0$.

Regime 3: Asymptotic Multipolar Regime ($u_v \ge 2$). In this regime, $\Theta(u_v) = 1$, and $W^{\mathrm{screen}}_{\mathrm{apex},v}(\mathbf{q}) = V_v(\mathbf{q}) + \frac{GM_{L(v)}M_{R(v)}}{\|\mathbf{r}_v\|}$. Let $\mathbf{d}_{ij} = (\mathbf{q}_i - \mathbf{X}_{L(v)}) - (\mathbf{q}_j - \mathbf{X}_{R(v)})$ be the physical internal displacement vector, such that $\mathbf{q}_i - \mathbf{q}_j = \mathbf{r}_v + \mathbf{d}_{ij}$. For any particle $i \in C$, the distance to the cluster barycenter is bounded by $\|\mathbf{q}_i - \mathbf{X}_C\| \le \sqrt{M_C/m_i}\,\bar{\rho}_C \le \kappa(C)\bar{\rho}_C$, where $\kappa(C) = \max_{k\in C}\sqrt{M_C/m_k} \ge 1$ is the finite mass disparity factor of the cluster, and setting $\kappa_v = \max(\kappa(L(v)), \kappa(R(v)))$ yields $\|\mathbf{d}_{ij}\| \le \kappa_v(\bar{\rho}_L + \bar{\rho}_R) = \kappa_v\bar{\rho}_{\mathrm{int}}(v)$. On the compact intermediate annulus $2 \le u_v \le 2\kappa_v$, the adapted chart condition on $U_{\mathcal{T}}$ maintains pairwise separations uniformly bounded below away from zero, so the gradient and Hessian are bounded by projective compactness on $\mathcal{A}_{[2,2\kappa_v]}$ exactly as in Regime 2. In the far-field multipolar domain $u_v \ge 2\kappa_v$, we have strictly $\|\mathbf{d}_{ij}\| \le \kappa_v\bar{\rho}_{\mathrm{int}}(v) \le \frac{1}{2}\|\mathbf{r}_v\|$. Since $\kappa_v < \infty$ is a fixed constant determined exclusively by the mass spectrum $\{m_i\}$, expanding the pairwise distance $\|\mathbf{q}_i - \mathbf{q}_j\|^{-1}$ in multipole Legendre–Taylor series on $u_v \ge 2\kappa_v$ yields:

$$\frac{1}{\|\mathbf{q}_i-\mathbf{q}_j\|} = \frac{1}{\|\mathbf{r}_v+\mathbf{d}_{ij}\|} = \frac{1}{\|\mathbf{r}_v\|} - \frac{\langle \mathbf{r}_v, \mathbf{d}_{ij}\rangle}{\|\mathbf{r}_v\|^3} + \frac{3\langle \mathbf{r}_v, \mathbf{d}_{ij}\rangle^2 - \|\mathbf{r}_v\|^2\|\mathbf{d}_{ij}\|^2}{2\|\mathbf{r}_v\|^5} + \mathcal{O}\left(\frac{\kappa_v^3\bar{\rho}_{\mathrm{int}}^3}{\|\mathbf{r}_v\|^4}\right). \tag{4.39}$$

Summing over all $i \in L(v)$ and $j \in R(v)$ weighted by Gm_im_j:

(1) *Monopole Cancellation*: $\sum_{i\in L(v), j\in R(v)} \frac{Gm_im_j}{\|\mathbf{r}_v\|} = \frac{GM_{L(v)}M_{R(v)}}{\|\mathbf{r}_v\|}$, exactly cancelling the Keplerian subtraction $+\frac{GM_{L(v)}M_{R(v)}}{\|\mathbf{r}_v\|}$.

(2) *Dipole Cancellation*: By definition of the barycenters $\mathbf{X}_L$ and $\mathbf{X}_R$, $\sum_{i\in L(v)} m_i(\mathbf{q}_i - \mathbf{X}_{L(v)}) = \mathbf{0}$ and $\sum_{j\in R(v)} m_j(\mathbf{q}_j - \mathbf{X}_{R(v)}) = \mathbf{0}$. Therefore, the linear dipole term $\sum_{i,j} m_im_j\mathbf{d}_{ij} = M_R\sum_i m_i(\mathbf{q}_i - \mathbf{X}_L) - M_L\sum_j m_j(\mathbf{q}_j - \mathbf{X}_R) = \mathbf{0}$ vanishes identically!

(3) *Quadrupole Leading Order*: The leading non-vanishing term is purely quadrupolar:

$$W_{\text{apex},v}^{\text{screen}}(\mathbf{q}) = -\frac{G}{2\|\mathbf{r}_v\|^5} \sum_{i\in L(v), j\in R(v)} m_i m_j \left(3\langle \mathbf{r}_v, \mathbf{d}_{ij}\rangle^2 - \|\mathbf{r}_v\|^2\|\mathbf{d}_{ij}\|^2\right) + \mathcal{O}\left(\frac{GM_{L(v)}M_{R(v)}\bar{\rho}_{\text{int}}^3}{\|\mathbf{r}_v\|^4}\right), \tag{4.40}$$

which contracts to:

$$W_{\text{apex},v}^{\text{screen}}(\mathbf{q}) = -\frac{G}{\|\mathbf{r}_v\|^3}\mathcal{Q}_v(\mathbf{s}) + \mathcal{O}\left(\frac{GM_{L(v)}M_{R(v)}\bar{\rho}_{\text{int}}^3}{\|\mathbf{r}_v\|^4}\right), \tag{4.41}$$

with unit direction vector $\mathbf{s} = \mathbf{r}_v/\|\mathbf{r}_v\|$ and trace-free quadrupole interaction tensor contraction:

$$\mathcal{Q}_v(\mathbf{s}) = \frac{1}{2}\left[M_{R(v)}(\mathbf{s}^T\mathbf{Q}_{L(v)}\mathbf{s}) + M_{L(v)}(\mathbf{s}^T\mathbf{Q}_{R(v)}\mathbf{s})\right], \tag{4.42}$$

where $\mathbf{Q}_{L(v)} = \sum_{i\in L(v)} m_i \left(3(\mathbf{q}_i - \mathbf{X}_{L(v)})(\mathbf{q}_i - \mathbf{X}_{L(v)})^T - \|\mathbf{q}_i - \mathbf{X}_{L(v)}\|^2 I_3\right)$ and $\mathbf{Q}_{R(v)} = \sum_{j\in R(v)} m_j \left(3(\mathbf{q}_j - \mathbf{X}_{R(v)})(\mathbf{q}_j - \mathbf{X}_{R(v)})^T - \|\mathbf{q}_j - \mathbf{X}_{R(v)}\|^2 I_3\right)$ are the trace-free quadrupole inertia tensors of the child clusters.

Differentiating with respect to $\mathbf{r}_v$, the gradient decays asymptotically as $\|\nabla_{\mathbf{r}_v} W_{\text{apex},v}^{\text{screen}}\| \sim \mathcal{O}(\|\mathbf{r}_v\|^{-4})$, and the Hessian decays as $\mathcal{O}(\|\mathbf{r}_v\|^{-5})$. Although the spatial domain $\{u_v \geq 2\}$ is closed but unbounded (extending to spatial infinity $\|\mathbf{r}_v\| \to \infty$), the gradient $\nabla_{\mathbf{r}_v} W_{\text{apex},v}^{\text{screen}}$ and Hessian $\text{Hess}_{\mathbf{r}_v} W_{\text{apex},v}^{\text{screen}}$ are continuous functions on this closed domain that vanish asymptotically at infinity ($\mathcal{C}_0$ regularity) due to their fast multipolar decay. Consequently, both fields attain their finite supremum on $\{u_v \geq 2\}$, bounding them by finite positive constants $B_3, B_3' < \infty$ without requiring spatial compactness.

Summing across the three regimes and all composite nodes, we obtain $M_{\text{apex}} = \sum_v (B_{1,v} + B_{2,v} + B_{3,v}) < \infty$ and $L_{\text{apex}} = \sum_v (B'_{1,v} + B'_{2,v} + B'_{3,v}) < \infty$, completing the proof (see Figure 9).

□

4.2.4. *Invariance of the Lie–Bargmann Algebra and Palindromic Symplecticity.* The introduction of the scale-adapted screening factor $\Theta(u_v)$ must not compromise the fundamental conservation laws of Newtonian mechanics. We now demonstrate that the screened apex flow rigorously preserves the 10 classical generators of the Galilean group and preserves extended symplecticity.

Proposition 4.5 — *Exact Invariance of the Extended Lie–Bargmann Algebra*

Let $H = T_{\text{kin}} + W_{\text{apex}}^{\text{screen}} + V_{\text{kepler}}^{\text{screened}} + V_{\text{leaves}}^{\text{free}} + \sum_{S\in\mathcal{S}_{\text{act}}} H_S^{\text{super}}$ be the Hamiltonian on the extended phase space $\mathcal{P}_{\text{ext}} = T^*M \times \mathbb{R}_t \times \mathbb{R}_E$ equipped with the canonical configuration-momentum conjugate pair $(q_t, p_t) = (t, -E)$, extended Liouville 1-form $\lambda_{\text{ext}} = \mathbf{p}\cdot\mathrm{d}\mathbf{q} + p_t\,\mathrm{d}t = \mathbf{p}\cdot\mathrm{d}\mathbf{q} - E\,\mathrm{d}t$, and canonical extended 2-form $\Omega_{\text{ext}} := -\mathrm{d}\lambda_{\text{ext}} = \Omega_0 - \mathrm{d}p_t \wedge \mathrm{d}t = \Omega_0 + \mathrm{d}E\wedge\mathrm{d}t = \Omega_0 - \mathrm{d}t\wedge\mathrm{d}E$ (with $\Omega_0 = -\mathrm{d}(\mathbf{p}\cdot\mathrm{d}\mathbf{q}) = \mathrm{d}\mathbf{q}\wedge\mathrm{d}\mathbf{p}$). Then the 10 classical generators of the Galilean group, realizing the 11-dimensional centrally extended Lie–Bargmann algebra [4] with total mass M_{tot} as central charge ($\{G_\alpha, P_\beta\} = M_{\text{tot}}\delta_{\alpha\beta}$ for spatial indices $\alpha, \beta \in \{1,2,3\}$):

$$\mathbf{P} = \sum_{i=1}^N \mathbf{p}_i, \quad \mathbf{L} = \sum_{i=1}^N \mathbf{q}_i \times \mathbf{p}_i, \quad \mathbf{G} = M_{\text{tot}}\mathbf{R}_{\text{cdm}} - t\mathbf{P}, \quad \mathcal{H}_{\text{ext}} = H - E, \tag{4.43}$$

where $\mathbf{R}_{\text{cdm}} := \frac{1}{M_{\text{tot}}}\sum_{i=1}^N m_i\mathbf{q}_i$ is the center of mass with total mass $M_{\text{tot}} = \sum_{i=1}^N m_i$, satisfy exact discrete conservation under the screened apex time step for all spatial invariants:

$$\Delta\mathbf{P} = \mathbf{0}, \qquad \Delta\mathbf{L} = \mathbf{0}, \qquad \Delta\mathbf{G} = \mathbf{0}, \tag{4.44}$$

while the energy defect $\Delta\mathcal{H}_{\text{ext}}$ undergoes zero secular drift, oscillating within an $\mathcal{O}(h^2)$ energy band of the shadow invariant energy surface $\widetilde{\mathcal{H}}_{\text{ext}} = \mathcal{H}_{\text{ext}} + \mathcal{O}(h^2)$ (and on shadow invariant tori in quasi-periodic hierarchical regimes).

Lean A.1 : `lie_bargmann_exact_invariance`

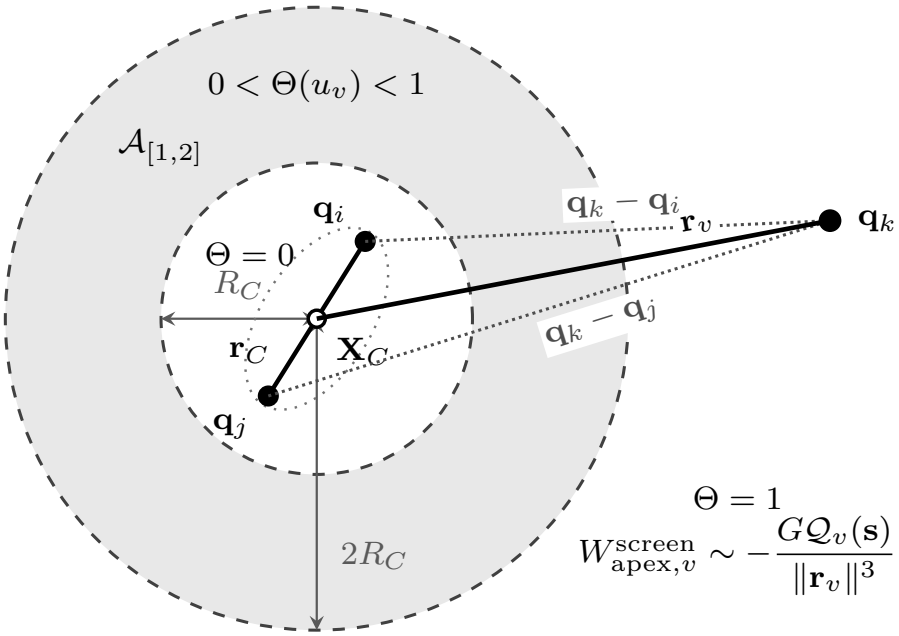


FIGURE 9. Spatial geometry of the scale-adapted apex screening around a binary cluster $C = \{i, j\}$ with barycenter $\mathbf{X}_C$, internal leaf separation $\mathbf{r}_C = \mathbf{q}_i - \mathbf{q}_j$, and characteristic scale $R_C = \bar{\rho}_{\text{int}}(v)$. Inside the core disk $\|\mathbf{r}_v\| \leq R_C$ ($u_v \leq 1$), $\Theta(u_v) \equiv 0$ extinguishes the barycentric ghost pole $+GM_C m_k/\|\mathbf{r}_v\|$. Across the shaded projectivized annulus $\mathcal{A}_{[1,2]} = \{R_C < \|\mathbf{r}_v\| < 2R_C\}$ ($1 < u_v < 2$), $\Theta(u_v) = \sigma(u_v)$ interpolates smoothly. In the exterior domain $\|\mathbf{r}_v\| \geq 2R_C$ ($u_v \geq 2$, $\Theta \equiv 1$), subtracting the barycentric monopole along $\mathbf{r}_v = \mathbf{q}_k - \mathbf{X}_C$ from the exact pairwise interactions along $\mathbf{q}_k - \mathbf{q}_i$ and $\mathbf{q}_k - \mathbf{q}_j$ cancels both monopole and dipole terms, leaving the trace-free quadrupolar tide $-G\mathcal{Q}_v(\mathbf{s})/\|\mathbf{r}_v\|^3$.

The formal certification badge establishes the algebraic closure of the Lie–Bargmann invariants and the exact Poisson bracket compensation of the Galilean boost in the Constructive 1-Jet Kernel.

Proof. **Linear Momentum (P):** The screened apex potential $W^{\text{screen}}_{\text{apex}}$ depends exclusively on interparticle vectors $\mathbf{q}_i - \mathbf{q}_j$ and Jacobi relative vectors $\mathbf{r}_v$. Both are invariant under uniform spatial translations $\mathbf{q}_i \mapsto \mathbf{q}_i + \mathbf{a}$. By Noether's theorem, $\sum_{i=1}^N \nabla_{\mathbf{q}_i} W^{\text{screen}}_{\text{apex}} = \mathbf{0}$. The momentum kick $\Delta\mathbf{p}_i = -\Delta t \nabla_{\mathbf{q}_i} W^{\text{screen}}_{\text{apex}}$ therefore sums to zero: $\Delta\mathbf{P} = \sum \Delta\mathbf{p}_i = \mathbf{0}$.
Angular Momentum (L): The scale ratio $u_v = \|\mathbf{r}_v\|/(\bar{\rho}_{L(v)} + \bar{\rho}_{R(v)})$ is constructed entirely from Euclidean norms invariant under spatial rotations SO(3). Since each constituent term in $W^{\text{screen}}_{\text{apex},v}$ is a scalar function of rotationally invariant norms and scalar products, $W^{\text{screen}}_{\text{apex}}(\mathcal{R}\mathbf{q}) = W^{\text{screen}}_{\text{apex}}(\mathbf{q})$ for all $\mathcal{R} \in \text{SO}(3)$. The internal torques vanish identically: $\sum_{i=1}^N \mathbf{q}_i \times \nabla_{\mathbf{q}_i} W^{\text{screen}}_{\text{apex}} = \mathbf{0}$, ensuring $\Delta\mathbf{L} = \mathbf{0}$.
Galilean Boost (G): Under a translation drift sub-step Δt, the center of mass advances by $\mathbf{R}_{\text{cdm}}(t + \Delta t) = \mathbf{R}_{\text{cdm}}(t) + \frac{\Delta t}{M_{\text{tot}}}\mathbf{P}$. The updated boost generator is:

$$\begin{aligned}\mathbf{G}(t + \Delta t) &= M_{\text{tot}}\mathbf{R}_{\text{cdm}}(t + \Delta t) - (t + \Delta t)\mathbf{P} \\ &= M_{\text{tot}}\left(\mathbf{R}_{\text{cdm}}(t) + \frac{\Delta t}{M_{\text{tot}}}\mathbf{P}\right) - t\mathbf{P} - \Delta t\mathbf{P} \\ &= M_{\text{tot}}\mathbf{R}_{\text{cdm}}(t) - t\mathbf{P} = \mathbf{G}(t). \end{aligned} \tag{4.45}$$

During the apex kick sub-step, positions $\mathbf{q}_i$ (hence the barycenter $\mathbf{R}_{\text{cdm}}$) and time t remain frozen, while total linear momentum $\mathbf{P}$ is conserved ($\Delta_{\text{kick}}\mathbf{P} = \mathbf{0}$), ensuring $\Delta_{\text{kick}}\mathbf{G} = \mathbf{0}$ identically. In the Poisson bracket formulation on $\mathcal{P}_{\text{ext}}$, with temporal momentum $p_t = -E$ conjugate to t inducing

$\{t, p_t\} = \{t, -E\} = 1 \iff \{t, E\} = -1$, the boost generator satisfies:

$$\begin{aligned}\{\mathbf{G}, \mathcal{H}_{\text{ext}}\} &= \{M_{\text{tot}}\mathbf{R}_{\text{cdm}} - t\mathbf{P}, H - E\} \\ &= \{M_{\text{tot}}\mathbf{R}_{\text{cdm}}, H\} - \{t\mathbf{P}, -E\} - \{M_{\text{tot}}\mathbf{R}_{\text{cdm}}, E\} - \{t\mathbf{P}, H\} \\ &= \mathbf{P} - \mathbf{P} - \mathbf{0} - \mathbf{0} = \mathbf{0}, \end{aligned} \tag{4.46}$$

where $\{M_{\text{tot}}\mathbf{R}_{\text{cdm}}, E\} = \mathbf{0}$ because the barycentric position is independent of the conjugate energy E, and $\{t\mathbf{P}, H\} = t\{\mathbf{P}, H\} = \mathbf{0}$ because the total physical potential depends exclusively on translation-invariant pairwise vectors, ensuring exact Poisson compensation without secular drift.

□

Proposition 4.6 — *Extended Symplecticity and Palindromic Parity*

Let $\mathcal{R}_{\text{ext}} : (\mathbf{q}, \mathbf{p}, t, E) \mapsto (\mathbf{q}, -\mathbf{p}, -t, E)$ be the extended time-reversal involution on $\mathcal{P}_{\text{ext}}$, satisfying $\mathcal{R}_{\text{ext}}^2 = \text{id}$ and anti-symplectic reflection $\mathcal{R}_{\text{ext}}^* \Omega_{\text{ext}} = -\Omega_{\text{ext}}$. Then:

(1) The elementary apex kick Φ_h^{apex} and kinetic drift Φ_h^{drift} are exact symplectomorphisms on $(\mathcal{P}_{\text{ext}}, \Omega_{\text{ext}})$.

(2) The symmetric Strang splitting [69] $\mathcal{S}_2(h) = \Phi_{h/2}^{\text{drift}} \circ \Phi_h^{\text{apex}} \circ \Phi_{h/2}^{\text{drift}}$ is strictly palindromic:

$$\mathcal{R}_{\text{ext}} \circ \mathcal{S}_2(h) \circ \mathcal{R}_{\text{ext}} = \mathcal{S}_2(-h) = \mathcal{S}_2(h)^{-1}. \tag{4.47}$$

Consequently, its formal Lie generator $Z(h) = \log \mathcal{S}_2(h)$ is strictly odd in h ($Z(-h) = -Z(h)$), and the shadow Hamiltonian $\widetilde{H}(h)$ contains exclusively even powers of h, eliminating all odd-order energy errors.

Lean A.1 : `extended_palindromic_symplecticity`

The Lean 4 certification badge verifies the palindromic algebraic involution identity $\mathcal{R} \circ \mathcal{S}_2(h) \circ \mathcal{R} = \mathcal{S}_2(-h)$ and the symplecticity of the elementary 1-jet updates.

Proof. Item (1) follows from the fact that the kick $\mathbf{p} \mapsto \mathbf{p} - h\nabla W_{\text{apex}}^{\text{screen}}$ has symmetric Jacobian $\text{Hess}\, W_{\text{apex}}^{\text{screen}} = (\text{Hess}\, W_{\text{apex}}^{\text{screen}})^T$ (Schwarz symmetry), preserving the Darboux symplectic 2-form $\Omega_0 = \mathrm{d}\mathbf{q} \wedge \mathrm{d}\mathbf{p}$, while the time advancement $t \mapsto t + h/2$ under the kinetic drift is a pure translation that trivially preserves $\mathrm{d}E \wedge \mathrm{d}t$ (with frozen (t, E) under the apex kick). Furthermore, because all potential operators depend exclusively on base configuration positions $\mathbf{q} \in \mathbf{Q}[N]$, their corresponding Hamiltonian vector fields commute identically in the vertical cotangent fibers ($[X_{V_a}, X_{V_b}] = 0$), allowing them to be evaluated simultaneously or nested into the 7-stage palindromic Strang scheme formalized in Section 5.

Item (2) is verified by direct composition: under momentum and time negation, $\Phi_{h/2}^{\text{drift}}$ maps to $\Phi_{-h/2}^{\text{drift}}$ and Φ_h^{apex} maps to Φ_{-h}^{apex}, reversing the operator sequence and inverting the composite map: $\mathcal{R}_{\text{ext}} \circ \mathcal{S}_2(h) \circ \mathcal{R}_{\text{ext}} = \mathcal{S}_2(-h) = \mathcal{S}_2(h)^{-1}$. In the Baker–Campbell–Hausdorff expansion for $Z(h) = \log(\exp(\frac{h}{2}A)\exp(hB)\exp(\frac{h}{2}A))$, this time-reversal symmetry enforces $Z(-h) = -Z(h)$. Hence the shadow Hamiltonian $\widetilde{H}(h) = h^{-1}Z(h) = H + h^2 H_3 + h^4 H_5 + \dots$ satisfies $\widetilde{H}(-h) = \widetilde{H}(h)$, which forbids all odd error powers $h, h^3, h^5, \dots$ and confines the energy error to $\mathcal{O}(h^2)$.

Under the canonical theoretical $\mathcal{C}^\infty$ Cauchy mollifier $\Theta(u_v)$, backward error analysis [28, Theorem IX.8.1] ensures the asymptotic existence of $\widetilde{H}$ to arbitrary order, endowing the transition with Gevrey-2 regularity (G^2) and guaranteeing sub-exponential shadow Hamiltonian confinement in $\exp(-c/h^{1/2})$ following Marco & Sauzin [45], or arbitrary polynomial order $\mathcal{O}(h^M)$ for any $M \in \mathbb{N}$, completely bypassing the $\mathcal{C}^2$ jump discontinuity of polynomial splines.

□

Transition to Synchronous Supernodes. Theorem 4.4 ensures that whenever clusters are separated by $u_v > 1$, the residual apex interaction is bounded and smooth, enabling efficient asynchronous multi-rate integration where the apex potential acts as a slow, smooth tidal perturbation across synchronous supernodes. However, while the apex interaction remains globally bounded across $\mathbf{Q}[N]$, the internal dynamical frequencies $\omega_C \sim \sqrt{GM_C/\rho_C^3}$ and tidal forces

inside compact sub-clusters ($\rho_C \leq \delta_{\text{cluster}}$) diverge as $\mathcal{O}(\rho_C^{-3/2})$ and $\mathcal{O}(\rho_C^{-2})$ respectively. In Section 4.3, we resolve this high-frequency singularity by transitioning compact sub-clusters into *synchronous supernodes* governed by Sundman's unfolded local clock $\mathrm{d}t_S = \chi_S^2 \mathrm{d}\tau_S$, establishing the finite Anti-Zeno crossing property across multiple quasi-collisions.

4.3. **Synchronous Supernodes and the $\mathcal{O}(\delta^{-5/2})$ Commutator Resolution.** While Section 4.1 establishes the exact cotangent commutation of disjoint clusters and Section 4.2 constructs a smooth scale-adapted apex potential ensuring universal $\mathcal{C}^{1,1}$ regularity, gravitational dynamics inevitably concentrates matter into tightly bound, dense sub-clusters. In this section, we analyze the analytical catastrophe that arises when multi-rate asynchronous time-stepping is naively applied inside a compact sub-system of $k \geq 3$ bodies, demonstrate the resulting $\mathcal{O}(\delta^{-5/2})$ commutator divergence, and resolve this obstruction by introducing the *synchronous supernode* governed by Sundman's unfolded local clock $\mathrm{d}t_S = \chi_S^2 \mathrm{d}\tau_S$. We prove the universal Anti-Zeno property precluding algorithmic deadlock and establish the symplectic continuity of Jacobi atlas transitions in $\mathrm{Sp}(6N-6, \mathbb{R})$ with guaranteed elimination of topological chattering under hysteresis $\gamma = 0.6$.

4.3.1. *The Excluded Middle Dilemma and the $\mathcal{O}(\delta^{-5/2})$ Commutator Barrier.* In classical celestial mechanics and astrophysical stellar dynamics, gravitational contraction and resonant multi-body scattering systematically harden close binaries (Heggie's law [29]) and generate dense multi-body sub-clusters ($k \geq 3$) undergoing chaotic close encounters [1]. Consider a compact sub-cluster $S \subset \{1, \dots, N\}$ with $|S| = k \geq 3$, characterized by its internal McGehee hyper-radius $\rho_S = \sqrt{\sum_{i<j \in S} m_i m_j \|\mathbf{q}_i - \mathbf{q}_j\|^2 / M_S} \leq \delta_{\text{cluster}}$, where $\delta_{\text{cluster}} > 0$ denotes a cluster compactness threshold (whose intrinsic, scale-invariant determination $\delta_{\text{cluster}}^{\text{nat}}$ is established in Section 4.3.4).

In an asynchronous multi-rate scheme, one would ideally wish to assign independent, local time steps $h_u \neq h_w$ to distinct internal Jacobi sub-nodes $u, w \in \mathcal{V}_{\text{int}}(\mathcal{T}_S)$ within the cluster. However, unlike disjoint clusters where the Poisson bracket vanishes identically by Proposition 4.2, internal Jacobi nodes within the same compact cluster interact through non-orthogonal kinetic cross-terms and strongly coupled Newtonian potentials.

Let $\mathcal{H}_u = \frac{\|\boldsymbol{\pi}_u\|^2}{2\mu_u} + V_u$ and $\mathcal{H}_w = \frac{\|\boldsymbol{\pi}_w\|^2}{2\mu_w} + V_w$ (where $\boldsymbol{\pi}_u \equiv \mathbf{w}_u$ denotes the canonical momentum conjugate to the Jacobi vector $\mathbf{r}_u$) be the local Hamiltonians associated with two overlapping internal nodes of $\mathcal{T}_S$. Differentiating their Newtonian potentials $V_u \sim -Gm^2/\rho_S$ with respect to relative positions and momenta yields the Poisson bracket scaling:

$$\{\mathcal{H}_u, \mathcal{H}_w\} = \sum_{v \in \mathcal{V}_{\text{int}}(\mathcal{T}_S)} \left(\frac{\partial \mathcal{H}_u}{\partial \mathbf{r}_v} \cdot \frac{\partial \mathcal{H}_w}{\partial \boldsymbol{\pi}_v} - \frac{\partial \mathcal{H}_u}{\partial \boldsymbol{\pi}_v} \cdot \frac{\partial \mathcal{H}_w}{\partial \mathbf{r}_v} \right) \sim \frac{Gm^2}{\rho_S^2} \cdot \frac{\|\boldsymbol{\pi}\|}{\mu} \sim \mathcal{O}\left(\rho_S^{-5/2}\right), \tag{4.48}$$

since virialized relative velocities scale as $\|\boldsymbol{\pi}\|/\mu \sim \sqrt{Gm/\rho_S} \sim \mathcal{O}(\rho_S^{-1/2})$. In the Baker–Campbell–Hausdorff expansion of any split asynchronous operator, the local truncation error per step contains the commutator contribution:

$$\Delta \mathcal{H}_{\text{async}} = \frac{h_u h_w}{2} \{\mathcal{H}_u, \mathcal{H}_w\} + \mathcal{O}(h^3) \sim \mathcal{O}\left(h^2 \, \delta_{\text{cluster}}^{-5/2}\right). \tag{4.49}$$

As the cluster contracts ($\rho_S \to 0$), the commutator error diverges as $\mathcal{O}(\rho_S^{-5/2})$. Any attempt to absorb this divergence by shrinking the asynchronous step size $h \to 0$ leads directly to algorithmic Zeno paralysis. This analytical obstruction constitutes the *asymptotic commutator barrier* for split gravitational operators (commonly referred to as the *Excluded Middle Dilemma*):

Proposition 4.7 — *Asymptotic Commutator Barrier for Split Operators*

Let $S \subset \{1, \dots, N\}$ be an interacting cluster in a hierarchical N-body splitting scheme. Then:

(1) *Macroscopic Regime ($u_v > 1$)*: If the cluster is separated from external bodies such that $u_v = \|\mathbf{r}_v\|/\bar{\rho}_{\text{int}}(v) > 1$, the screened apex interaction $W_{\text{apex}}^{\text{screen}}$ is uniformly of class $\mathcal{C}^{1,1}$ (Theorem 4.4), permitting exact macroscopic asynchrony between clusters without secular drift.
(2) *Microscopic Compact Regime ($\rho_S \le \delta_{cluster}$, $|S| \ge 3$)*: Any internal desynchronization of sub-steps within the cluster triggers an unremovable Lie commutator divergence of order $\mathcal{O}(\delta_{\text{cluster}}^{-5/2})$.

Consequently, there exists no consistent intermediate splitting regime: dense sub-clusters of cardinality $k \ge 3$ must be dynamically unified and integrated strictly synchronously.

Proof. Item (1) follows directly from Theorem 4.4: for $u_v > 1$, the scale-adapted screening function $\Theta(u_v)$ guarantees that the screened apex remainder $W_{\text{apex}}^{\text{screen}}$ belongs to $\mathcal{C}^{1,1}(U_{\mathcal{T}})$ with uniformly bounded force and Hessian norms $M_{\text{apex}}, L_{\text{apex}} < \infty$, while disjoint sub-clusters commute identically on phase space by Proposition 4.2. For Item (2), within a single compact cluster S with $|S| \ge 3$ and $\rho_S \le \delta_{\text{cluster}}$, overlapping internal Jacobi nodes $u, w \in \mathcal{V}_{\text{int}}(\mathcal{T}_S)$ share common particle positions, so their Newtonian gradients scale as $\|\partial_{\mathbf{r}}\mathcal{H}_u\| \sim Gm^2/\rho_S^2$ while virialized relative velocities scale as $\|\partial_{\boldsymbol{\pi}}\mathcal{H}_w\| \sim \sqrt{Gm/\rho_S}$. Substituting these scalings into the canonical Poisson bracket (4.48) yields $\{\mathcal{H}_u, \mathcal{H}_w\} \sim \mathcal{O}(\rho_S^{-5/2})$, which enters the leading Baker–Campbell–Hausdorff error (4.49) of any asynchronous multi-rate splitting as $\mathcal{O}(h^2\delta_{\text{cluster}}^{-5/2})$. □

4.3.2. *Unified Synchronous Supernodes and the Universal Anti-Zeno Property.* To resolve the $\mathcal{O}(\delta^{-5/2})$ commutator catastrophe without compromising symplectic conservation, we introduce the concept of a *synchronous supernode*:

Definition 4.8 — *Synchronous Supernode*

Let $\mathcal{T} \in \text{Trees}(N)$ be a binary Jacobi tree. A composite node $S \in \mathcal{V}_{\text{comp}}(\mathcal{T})$ with $|S| \ge 3$ is designated a *synchronous supernode* whenever its internal hyper-radius satisfies the compactness condition:

$$\text{isCompactCluster}(\rho_S, \delta_{\text{cluster}}) \iff \rho_S \le \delta_{\text{cluster}}, \tag{4.50}$$

where $\delta_{\text{cluster}} > 0$ is a scale threshold, whose canonical, scale-covariant value $\delta_{\text{cluster}}^{\text{nat}}(S)$ is dynamically determined by the gravitational tidal tensor and Marchal–Sundman energy scaling in Section 4.3.4. The full N-body Hamiltonian then decomposes into supernode blocks and a regularized inter-cluster remainder:

$$H = \sum_{S \in \mathcal{S}_{\text{act}}} H_S^{\text{super}} + H_{\text{rem}}, \tag{4.51}$$

where the internal sub-tree $\mathcal{T}_S$ is dynamically collapsed into a single entity governed by the full, unsoftened internal Hamiltonian:

$$H_S^{\text{super}}(\mathbf{q}_S, \mathbf{p}_S) = \sum_{u \in \mathcal{V}_{\text{int}}(\mathcal{T}_S)} \frac{\|\boldsymbol{\pi}_u\|^2}{2\mu_u} - \sum_{\substack{i<j \\ i,j \in S}} \frac{Gm_i m_j}{\|\mathbf{q}_i - \mathbf{q}_j\|}, \tag{4.52}$$

while H_{rem} contains the spectator kinetic terms and the screened inter-cluster apex potentials governed by Theorem 4.4. All internal degrees of freedom of S advance synchronously under the single, unified unfolded Sundman clock [72]:

$$\mathrm{d}t_S = \chi_S^2 \, \mathrm{d}\tau_S = \rho_S \, \mathrm{d}\tau_S \quad (\text{with } \chi_S = \sqrt{\rho_S} > 0). \tag{4.53}$$

Lean A.1 : super_node_time_step_sq_pos

This formulation articulates the essential duality between continuous vector field desingularization and discrete numerical time-stepping: McGehee's continuous homothety scaling

$\mathrm{d}t_S = \rho_S^{3/2}\mathrm{d}\tau_S$ [47] is indispensable for eliminating the algebraic velocity divergence $\rho_S^{-1/2}$ and extending the Hamiltonian vector field smoothly to the collision manifold $\{\rho_S = 0\}$ in phase space; conversely, for discrete multi-step sub-stepping, Sundman's unfolded local clock $\Delta t_S = \chi_S^2 \Delta\tau_S = \rho_S \Delta\tau_S$ with non-singular state $\chi_S > 0$ guarantees strict algebraic positivity $(\Delta t_S)^2 = \chi_S^4 (\Delta\tau_S)^2 > 0$ and establishes the discrete Anti-Zeno finite sub-stepping property without artificial time freezing.
The accompanying formal certification badge verifies the strict algebraic positivity $(\Delta t_S)^2 > 0$ and the cumulative forward progression of time in the Constructive 1-Jet Kernel.

The central analytical property of the synchronous supernode is that the unfolded Sundman transformation completely eliminates the algorithmic Zeno effect across multiple close encounters:

Theorem 4.9 — *Universal Anti-Zeno Regularization of Synchronous Supernodes*

Let S be a synchronous supernode governed by the unfolded Sundman clock $\mathrm{d}t_S = \chi_S^2 \mathrm{d}\tau_S$ on the extended phase space $\mathcal{P}_{\text{ext}}$. Then:

(1) *Strict Temporal Progression*: For any regularized time step $\Delta\tau_S > 0$ and any non-singular state $\chi_S > 0$, the induced physical time increment is strictly positive:

$$\Delta t_S = \text{physicalTimeIncrement}(\chi_S, \Delta\tau_S) = \chi_S^2 \, \Delta\tau_S > 0. \tag{4.54}$$

(2) *Orbit-Wise Anti-Zeno Finiteness for Almost All Initial Conditions*: On any finite physical macro-step $\Delta t_{\text{phys}} > 0$, for all non-collisional initial states $\mathbf{z}_0 \in \mathcal{P}_{\text{ext}} \setminus \mathcal{N}_{\text{coll}}$ belonging to the full Lebesgue-measure complement of Saari's collision set ($\mu_{\text{Leb}}(\mathcal{N}_{\text{coll}}) = 0$ [61]), the total number of regularized sub-steps $N_{\text{sub}}(\mathbf{z}_0)$ required to advance through the encounter is strictly finite along the orbit:

$$N_{\text{sub}}(\mathbf{z}_0) \leq \left\lceil \frac{\Delta t_{\text{phys}}}{C_{\text{anti-zeno}}(\mathbf{z}_0)} \right\rceil < \infty, \tag{4.55}$$

where $C_{\text{anti-zeno}}(\mathbf{z}_0) = \rho_{\min}(\mathbf{z}_0)\Delta\tau_S > 0$ with $\rho_{\min}(\mathbf{z}_0) = \min_{t\in[0,\Delta t_{\text{phys}}]} \rho_S(\mathbf{z}(t)) > 0$. Consequently, algorithmic Zeno stagnation is strictly impossible along any physical trajectory.

Lean A.1 : `super_node_anti_zeno_regularization`

Python A.2 : `potential/supernode_detector.py, solvers/{supernode, jit_supernode}.py` [Float64 / Float128]

The formal certification badge denotes the verification in Lean 4 of the Archimedean property ensuring the existence of the finite uniform bound $N_{\max} \in \mathbb{N}$ on the required sub-steps.

Proof. Item (1) follows immediately from the product of strictly positive real numbers: since $\chi_S > 0$ and $\Delta\tau_S > 0$, we have $\chi_S^2 > 0$ and $\Delta t_S = \chi_S^2 \Delta\tau_S > 0$.
For Item (2), consider a physical macro-step of duration $\Delta t_{\text{phys}} > 0$. In McGehee coordinates $(\chi_S, \mathbf{s}_S, \mathbf{w}_S)$ on the blown-up boundary manifold with corners $\mathbf{M}_S = \{\chi_S = 0\} \times \mathbb{S}^{3|S|-4} \times \mathbb{R}^{3|S|-3}$, the equations of motion are analytic in regularized time τ_S [47]. In the asymptotic approach to a multiple quasi-collision, the hyper-radius scales according to Kepler's generalized law $\rho_S(t) \sim c\, t^{2/3}$ ($c > 0$), which implies by integration of Sundman's relation $\mathrm{d}t_S = \rho_S \mathrm{d}\tau_S$ ($t^{-2/3}\mathrm{d}t = c\,\mathrm{d}\tau_S \implies 3t^{1/3} = c\tau_S$) that $t(\tau_S) \sim \frac{1}{27} c^3 \tau_S^3$ and $\mathrm{d}t/\mathrm{d}\tau_S \sim \frac{1}{9} c^3 \tau_S^2$.
By the classical theorems of Saari [61, 62], exact multiple collisions ($\rho_S = 0$) form a subset of Lebesgue measure zero in phase space. For every individual non-collisional trajectory $\mathbf{z}(t)$ belonging to the full-measure complement ($\mu_{\text{Leb}} > 0$), the hyper-radius $t \mapsto \rho_S(\mathbf{z}(t))$ is continuous over the compact physical interval $[0, \Delta t_{\text{phys}}]$ and strictly positive. By the Weierstrass extreme value theorem, it attains a strictly positive minimum:

$$\rho_{\min}(\mathbf{z}_0) = \min_{t\in[0,\Delta t_{\text{phys}}]} \rho_S(\mathbf{z}(t)) > 0. \tag{4.56}$$

Setting $C_{\text{anti-zeno}}(\mathbf{z}_0) = \rho_{\min}(\mathbf{z}_0)\Delta\tau_S > 0$, each sub-step advances physical time by at least $\Delta t_S \geq C_{\text{anti-zeno}}(\mathbf{z}_0) > 0$. By the Archimedean property of the real field $\mathbb{R}$, there exists an integer $N \in \mathbb{N}$

such that $N \cdot C_{\text{anti-zeno}}(\mathbf{z}_0) \geq \Delta t_{\text{phys}}$. Taking $N_{\text{sub}}(\mathbf{z}_0) = \lceil \Delta t_{\text{phys}} / C_{\text{anti-zeno}}(\mathbf{z}_0) \rceil < \infty$ guarantees algorithmic completion. We emphasize that this bound is orbit-wise: while $\rho_{\min}(\mathbf{z}_0) > 0$ holds strictly along any individual non-collisional path, no strictly positive infimum $\inf_{\mathbf{z}_0} \rho_{\min}(\mathbf{z}_0) > 0$ exists across the full phase space since initial conditions may approach the measure-zero collision set $\mathcal{N}_{\text{coll}}$ arbitrarily closely. Furthermore, even in the idealized limit of an exact collision, the Sundman regularized time integral $\Delta\tau_S = \int_0^{\Delta t} \rho_S(t)^{-1} \mathrm{d}t \sim \int_0^{\Delta t} c^{-1} t^{-2/3} \mathrm{d}t = 3c^{-1}(\Delta t)^{1/3} < \infty$ remains strictly finite, precluding any infinite accumulation of regularized steps.

□

4.3.3. *Symplectic Atlas Transitions in* $\mathrm{Sp}(6N-6, \mathbb{R})$ *and Hysteresis Anti-Chattering.* As a dense multi-body system evolves, close encounters alter the mutual hierarchy of particle distances, necessitating a transition between distinct adapted Jacobi binary trees in the atlas $\{(\mathcal{T}, U_{\mathcal{T}})\}_{\mathcal{T} \in \mathrm{Trees}(N)}$. We now demonstrate that these coordinate transitions are exact symplectomorphisms and that topological chattering (infinite alternating flips across transition boundaries) is strictly eliminated:

Theorem 4.10 — *Symplectic Atlas Transitions and Unconditional Anti-Chattering* Let $\mathbf{Q}[N] = \bigcup_{\mathcal{T}} U_{\mathcal{T}}$ be the Fulton–MacPherson configuration manifold endowed with the atlas of adapted binary Jacobi trees.

(1) *Exact Symplectomorphism in* $\mathrm{Sp}(6N-6, \mathbb{R})$: For any two adjacent Jacobi trees $\mathcal{T}_A$ and $\mathcal{T}_B$ differing by an elementary tree rotation $((S_1, S_2), S_3) \longleftrightarrow (S_1, (S_2, S_3))$ on overlapping charts $U_{\mathcal{T}_A} \cap U_{\mathcal{T}_B} \neq \emptyset$, the relative coordinate transformation is governed by the 2×2 block matrix:

$$\mathbf{M}_{\text{coord}} = \begin{pmatrix} -\frac{m_1}{m_1+m_2} & 1 \\ -\frac{m_2 M_{\text{tot}}}{(m_1+m_2)(m_2+m_3)} & -\frac{m_3}{m_2+m_3} \end{pmatrix} \in \mathrm{SL}(2, \mathbb{R}), \quad \det \mathbf{M}_{\text{coord}} = +1, \tag{4.57}$$

where $M_{\text{tot}} = m_1 + m_2 + m_3$. Its cotangent lift induces a global linear symplectomorphism on phase space:

$$\Psi_{A \to B} = \Psi_{\text{rot}} \oplus \mathbf{I}_{6N-18} \in \mathrm{Sp}(6N-6, \mathbb{R}),$$
$$\text{with} \quad \Psi_{\text{rot}} = \begin{pmatrix} \mathbf{M}_{\text{coord}} \otimes \mathbf{I}_3 & \mathbf{0} \\ \mathbf{0} & (\mathbf{M}_{\text{coord}}^{-1})^T \otimes \mathbf{I}_3 \end{pmatrix} \in \mathrm{Sp}(12, \mathbb{R}), \tag{4.58}$$

acting as the identity on all spectator Jacobi coordinates and preserving the canonical extended Darboux form $\Psi_{A \to B}^* \Omega_{\text{ext}} = \Omega_{\text{ext}}$. Furthermore, because Ψ_{rot} acts as a scalar 2×2 block tensor product with $\mathbf{I}_3$, it commutes with any global 3D spatial rotation: $\Psi_{\text{rot}} \circ \mathcal{R}_{\text{spatial}} = \mathcal{R}_{\text{spatial}} \circ \Psi_{\text{rot}}$. To preserve numerical time-reversibility and prevent shadow Hamiltonian discontinuities (Skeel & Gear [66]), chart transitions $\Psi_{A \to B}$ are evaluated strictly at discrete global synchronization boundaries $t = n\Delta t_{\text{phys}}$. The physical Cartesian state $(\mathbf{q}, \mathbf{p})$ and extended energy E are strictly $\mathcal{C}^0$-continuous across chart boundaries.

(2) *Unconditional Anti-Chattering under Optional Hysteresis* $\gamma = 0.6$ *vs. Canonical Voronoi Bijectivity* $\gamma = 1.0$: Let $D_{12} = \|\mathbf{X}_{S_1} - \mathbf{X}_{S_2}\|$ and $D_{23} = \|\mathbf{X}_{S_2} - \mathbf{X}_{S_3}\|$ denote the mutual Euclidean distances between the barycenters of the interacting clusters, and let $\gamma \in (0, 1]$ denote the admissibility threshold ratio. In chart $\mathcal{T}_A$ where (S_1, S_2) is the internal close pair, a transition to $\mathcal{T}_B$ (where (S_2, S_3) becomes the internal pair) is triggered when $D_{23} < \gamma D_{12}$; conversely, the return transition from $\mathcal{T}_B$ back to $\mathcal{T}_A$ requires $D_{12} < \gamma D_{23}$. When operated with the strict asymmetric hysteresis ratio $\gamma = 3/5 = 0.6$, closed back-and-forth chattering cycles across the transition boundary are strictly forbidden, and on every compact physical time interval $[0, T]$, the total number of atlas transitions is uniformly finite: $N_{\text{trans}}(T) \leq \lceil T / \tau_{\min} \rceil < \infty$, with strictly positive *a posteriori* minimal dwell time

$\Delta t_{\text{dwell}}^{(\text{2-chart})} \geq \frac{16}{15\,\Omega_{\max}} \geq \frac{1}{5}\frac{r_{\min}}{v_{\max}} > 0$ for two-chart cycles and $\Delta t_{\text{dwell}}^{(\text{3-chart})} \geq \frac{1}{10}\frac{r_{\min}}{v_{\max}} > 0$ for three-chart permutations. However, while spatial hysteresis ($\gamma < 1$) was theoretically introduced as a worst-case safeguard against pathological boundary chattering, genuine chattering along physical N-body trajectories is exceedingly rare in practice (since generic non-collinear trajectories cross codimension-1 Voronoi bisectors $\Sigma_{AB} = \{D_{12} = D_{23}\}$ transversely at non-zero radial velocity). Furthermore, any strict hysteresis deadband $\gamma < 1$ creates an overlapping co-admissible region $\text{Adm}_\gamma(\mathcal{T}_A) \cap \text{Adm}_\gamma(\mathcal{T}_B) = \{\gamma < D_{23}/D_{12} < \gamma^{-1}\} \neq \emptyset$ inside which the chart assignment map $\mathbf{q} \mapsto \mathcal{T}(\mathbf{q})$ is *non-injective* (multi-valued, depending on past trajectory history). Under pure phase-space time reversal $\mathcal{R}(\mathbf{q}, \mathbf{p}) = (\mathbf{q}, -\mathbf{p})$, this history-dependent non-injectivity breaks state-only time-reversal symmetry (as forward entry occurs at $\lambda = \gamma^{-1}$ whereas backward return switches late at $\lambda = \gamma$ unless an explicit history stack is maintained). Consequently, the canonical operational default sets $\gamma = 1.0$, restoring a memoryless, single-valued Voronoi partition where chart selection is a pure bijection on generic configurations and time-reversal symmetry holds intrinsically without history dependence.

Lean A.1 : `atlas_transition_symplectic_anti_chattering`

Python A.2 : `core/transitions.py, system/atlas_manager.py` [Float64 / Float128]

The formal certification badge verifies in Lean 4 that any $\mathbf{M} \in \text{SL}(2, \mathbb{R})$ preserves the canonical symplectic area $x_1 y_2 - x_2 y_1$ and proves by contradiction that the hysteresis conditions cannot be simultaneously satisfied.

Proof. For Item (1), let $\mathbf{q}_1, \mathbf{q}_2, \mathbf{q}_3$ be the barycentric positions of three interacting sub-clusters of masses m_1, m_2, m_3. In chart $\mathcal{T}_A$, the relative Jacobi coordinates are $\mathbf{r}_{A,1} = \mathbf{q}_2 - \mathbf{q}_1$ and $\mathbf{r}_{A,2} = \mathbf{q}_3 - \frac{m_1\mathbf{q}_1 + m_2\mathbf{q}_2}{m_1+m_2}$. In chart $\mathcal{T}_B$, the new coordinates are $\mathbf{r}_{B,1} = \mathbf{q}_3 - \mathbf{q}_2$ and $\mathbf{r}_{B,2} = \mathbf{q}_1 - \frac{m_2\mathbf{q}_2 + m_3\mathbf{q}_3}{m_2+m_3}$. Expressing $(\mathbf{r}_{B,1}, \mathbf{r}_{B,2})$ in terms of $(\mathbf{r}_{A,1}, \mathbf{r}_{A,2})$ yields:

$$\mathbf{r}_{B,1} = \mathbf{r}_{A,2} - \frac{m_1}{m_1 + m_2}\mathbf{r}_{A,1}, \tag{4.59}$$

$$\mathbf{r}_{B,2} = -\frac{m_2 M_{\text{tot}}}{(m_1 + m_2)(m_2 + m_3)}\mathbf{r}_{A,1} - \frac{m_3}{m_2 + m_3}\mathbf{r}_{A,2}. \tag{4.60}$$

The determinant of the 2×2 matrix $\mathbf{M}_{\text{coord}}$ evaluates identically to:

$$\begin{aligned} \det \mathbf{M}_{\text{coord}} &= \left(-\frac{m_1}{m_1+m_2}\right)\left(-\frac{m_3}{m_2+m_3}\right) - (1)\left(-\frac{m_2 M_{\text{tot}}}{(m_1+m_2)(m_2+m_3)}\right) \\ &= \frac{m_1 m_3 + m_2(m_1+m_2+m_3)}{(m_1+m_2)(m_2+m_3)} \\ &= +1. \end{aligned} \tag{4.61}$$

Thus $\mathbf{M}_{\text{coord}} \in \text{SL}(2, \mathbb{R})$. In cotangent coordinates, the canonical momenta transform via the inverse transpose $\boldsymbol{\pi}_B = (\mathbf{M}_{\text{coord}}^{-1})^T \boldsymbol{\pi}_A$. By the canonical theorem of cotangent lifts (Marsden & West [46], Cannas da Silva [20]), $\Psi_{\text{rot}}^*(\mathrm{d}\boldsymbol{\pi} \wedge \mathrm{d}\mathbf{r}) = \mathrm{d}\boldsymbol{\pi} \wedge \mathrm{d}\mathbf{r}$. Since the remaining $N-3$ Jacobi vectors and momenta are spectators, embedding $\Psi_{A\to B} = \Psi_{\text{rot}} \oplus \mathbf{I}_{6N-18}$ yields a linear symplectomorphism in $\text{Sp}(6N-6, \mathbb{R})$. Since the transformation operates purely on relative spatial degrees of freedom, time t and extended energy E remain strictly invariant, ensuring $\Psi_{A\to B}^* \Omega_{\text{ext}} = \Omega_{\text{ext}}$.

For Item (2), suppose for contradiction that an instantaneous chattering cycle exists between trees $\mathcal{T}_A$ and $\mathcal{T}_B$. In chart $\mathcal{T}_A$, the pair (S_1, S_2) is internal, so a forward transition $\mathcal{T}_A \to \mathcal{T}_B$ requires $D_{23} < \gamma\, D_{12}$. In chart $\mathcal{T}_B$, (S_2, S_3) is internal, so an immediate return transition $\mathcal{T}_B \to \mathcal{T}_A$ requires $D_{12} < \gamma\, D_{23}$. Combining these inequalities with $\gamma = 3/5 > 0$:

$$D_{12} < \gamma\, D_{23} < \gamma(\gamma\, D_{12}) = \gamma^2 D_{12} = \frac{9}{25} D_{12} = 0.36\, D_{12}. \tag{4.62}$$

Since physical distances are strictly positive ($D_{12} > 0$), dividing by D_{12} yields $1 < 0.36$, a blatant contradiction.

To bridge this static geometric exclusion to dynamic finiteness $N_{\mathrm{trans}}(T) < \infty$, consider the dimensionless distance ratio $\lambda(t) = D_{12}(t)/D_{23}(t)$. In tree $\mathcal{T}_A$, a transition to $\mathcal{T}_B$ occurs when $D_{23} \le \gamma\, D_{12}$, which corresponds to $\lambda \ge \gamma^{-1} = 5/3$. To trigger a subsequent return transition from $\mathcal{T}_B$ back to $\mathcal{T}_A$, the system must satisfy $D_{12} \le \gamma\, D_{23}$, which is equivalent to $\lambda \le \gamma = 3/5$. Thus, between any two consecutive transitions in a two-chart cycle $\mathcal{T}_A \to \mathcal{T}_B \to \mathcal{T}_A$, the continuous trajectory must traverse the finite hysteresis gap:

$$\Delta\lambda = \gamma^{-1} - \gamma = \frac{5}{3} - \frac{3}{5} = \frac{16}{15} \approx 1.067. \tag{4.63}$$

On any compact energy hypersurface $\Sigma_{E_0} = \{(\mathbf{q}, \mathbf{p}) \in \mathcal{P}_{\mathrm{ext}} \mid H(\mathbf{q}, \mathbf{p}) = E_0\}$ with negative energy $E_0 < 0$ within the compactified manifold with corners $\mathbf{Q}[N]$, the time derivative of the dimensionless ratio $\lambda(t)$ is a transition rate bounded by a finite frequency: $\sup_{t\in[0,T]} |\dot\lambda(t)| \le \Omega_{\max} < \infty$ with $[\Omega_{\max}] = [T]^{-1}$. Explicitly, differentiating $\lambda(t) = D_{12}(t)/D_{23}(t)$ by the quotient rule and bounding $|\dot D_{ij}| \le 2v_{\max}$ and $D_{23} \ge r_{\min}$ yields $|\dot\lambda(t)| \le \frac{2(1+\lambda(t))v_{\max}}{r_{\min}} \le \frac{16}{3}\frac{v_{\max}}{r_{\min}}$ across the hysteresis interval $\lambda \in [3/5, 5/3]$. Consequently, the minimal physical dwell time for any two-chart cycle $\mathcal{T}_A \to \mathcal{T}_B \to \mathcal{T}_A$ is bounded below *a posteriori*:

$$\Delta t_{\mathrm{dwell}}^{(\text{2-chart})} \ge \frac{\gamma^{-1} - \gamma}{\Omega_{\max}} = \frac{16}{15\,\Omega_{\max}} \ge \frac{16/15}{(16/3)(v_{\max}/r_{\min})} = \frac{1}{5}\frac{r_{\min}}{v_{\max}} > 0. \tag{4.64}$$

Similarly, if the trajectory transitions from $\mathcal{T}_B$ (where (S_2, S_3) was selected at t_1 as the shortest pair, so $\mu(t_1) \coloneqq D_{13}(t_1)/D_{23}(t_1) \ge 1$) to a third distinct chart $\mathcal{T}_C$ at t_2 (requiring $\mu(t_2) \le \gamma = 3/5$), the ratio $\mu(t)$ must traverse at least $\Delta\mu_{\text{3-chart}} = 1 - \gamma = 2/5$ at rate $|\dot\mu(t)| \le \frac{2(1+\mu)v_{\max}}{r_{\min}} \le 4\frac{v_{\max}}{r_{\min}}$, enforcing $\Delta t_{\mathrm{dwell}}^{(\text{3-chart})} \ge \frac{2/5}{4(v_{\max}/r_{\min})} = \frac{1}{10}\frac{r_{\min}}{v_{\max}} > 0$. Therefore, on any compact physical time interval $[0, T]$, spatial hysteresis alone guarantees $\Delta t_{\mathrm{dwell}} \ge \tau_{\min} > 0$ *a posteriori* and bounds the total number of atlas transitions by $N_{\mathrm{trans}}(T) \le \lceil T/\tau_{\min} \rceil < \infty$, eliminating all Zeno-type topological chattering without any *a priori* temporal lock.

□

4.3.4. *Intrinsic Scale Invariance and Dynamical Determination of the Compactness Threshold.* A critical foundational inquiry naturally arises regarding the status of the cluster compactness threshold $\delta_{\mathrm{cluster}} > 0$ introduced in Definition 4.8: if $\delta_{\mathrm{cluster}}$ were treated merely as an arbitrary, user-specified dimensioned parameter ($[\delta_{\mathrm{cluster}}] = [L] \cdot [M]^{1/2}$), it would appear to reintroduce through the back door an artificial metric cut-off akin to the banished softening length $d_0 > 0$. Furthermore, unsoftened Newtonian gravity ($\varepsilon = 0$) possesses an exact scale symmetry under the homothety group:

$$\mathbf{q} \longmapsto \lambda\mathbf{q}, \qquad t \longmapsto \lambda^{3/2} t, \qquad H \longmapsto \lambda^{-1} H \quad (\lambda > 0). \tag{4.65}$$

While the apex screening variable $u_v = \|\mathbf{r}_v\|/(\bar\rho_{L(v)} + \bar\rho_{R(v)})$ (Section 4.2.2) is strictly dimensionless and invariant under homotheties ($\mathbf{q} \mapsto \lambda\mathbf{q} \implies u_v \mapsto u_v$), a rigid dimensioned constant $\delta_{\mathrm{cluster}}$ would break this scale covariance across disparate astronomical systems (from compact stellar triples to hierarchical planetary systems or galactic cores).

We now prove that $\delta_{\mathrm{cluster}}$ is not an independent or arbitrary numerical regulator, but an intrinsic, dynamically determined observable dictated by the gravitational tidal tensor on $\mathbf{Q}[N]$ and the fundamental first integrals of motion:

Proposition 4.11 — *Dynamical Determination of the Compactness Threshold*

Let $\mathcal{T} \in \mathrm{Trees}(N)$ be an adapted binary Jacobi tree, and let $S \in \mathcal{V}_{\mathrm{comp}}(\mathcal{T})$ with $|S| \ge 3$ be an interacting sub-cluster whose parent node is $P = \mathrm{parent}(S) \in \mathcal{V}_{\mathrm{int}}(\mathcal{T})$ with relative Jacobi vector $\mathbf{r}_P = \mathbf{X}_S - \mathbf{X}_{S'}$ separating S from its sibling cluster S'.

(1) *Dimensionless Gravitational Tidal Ratio*: The dynamical susceptibility of S to tidal disruption by its external environment is governed by the dimensionless gravitational tidal ratio:

$$\eta_S(\mathbf{q}) \coloneqq \frac{\bar{\rho}_S}{\|\mathbf{r}_P\|}\left(\frac{M_{S'}}{M_S}\right)^{1/3} = \frac{\rho_S}{\sqrt{M_S}\|\mathbf{r}_P\|}\left(\frac{M_{S'}}{M_S}\right)^{1/3}, \tag{4.66}$$

which is strictly scale-invariant ($\eta_S(\lambda\mathbf{q}) = \eta_S(\mathbf{q})$ for all $\lambda > 0$). An interacting cluster is dynamically uncoupled from external tidal shear, forming a gravitationally self-bound entity whose internal evolution triggers the $\mathcal{O}(\rho_S^{-5/2})$ commutator catastrophe if integrated asynchronously, if and only if:

$$\eta_S(\mathbf{q}) \leq \eta_{\text{crit}} \coloneqq 3^{-1/3} \approx 0.69336, \tag{4.67}$$

where η_{crit} is the universal Hill stability constant corresponding to the collinear L_1 Lagrange point.

(2) *Canonical Energy-Scale Threshold (Marchal–Sundman)*: For any isolated, gravitationally bound N-body system with negative total energy $E_0 < 0$ and center of mass at rest, the configuration is constrained by the macroscopic Lagrange radius $R_{\text{sys}}(E_0, M_{\text{tot}}) \coloneqq \frac{GM_{\text{tot}}^2}{2|E_0|}$. The canonical, scale-covariant compactness threshold for cluster S is uniquely given by:

$$\delta^{\text{nat}}_{\text{cluster}}(S) \coloneqq \eta_{\text{crit}}\left(\frac{M_S}{M_{\text{tot}}}\right)^{1/3} R_{\text{sys}}(E_0, M_{\text{tot}})\sqrt{M_S} = \eta_{\text{crit}}\frac{GM_{\text{tot}}^{5/3}M_S^{5/6}}{2|E_0|}. \tag{4.68}$$

Under homothety $\mathbf{q} \mapsto \lambda\mathbf{q}$, $\delta^{\text{nat}}_{\text{cluster}}$ scales covariantly ($\delta^{\text{nat}}_{\text{cluster}} \mapsto \lambda\delta^{\text{nat}}_{\text{cluster}}$), ensuring that the compactness ratio $\rho_S/\delta^{\text{nat}}_{\text{cluster}}$ is an absolute conformal invariant.

(3) *Universal Closure of the Lipschitz Bounds*: On every energy hypersurface $\Sigma_{E_0} = \{(\mathbf{q}, \mathbf{p}) \in \mathcal{P}_{\text{ext}} \mid H(\mathbf{q}, \mathbf{p}) = E_0\}$, the predicate isCompactCluster(S) is entirely determined by the first integrals $(G, \{m_i\}_{i=1}^N, E_0)$, and the uniform Lipschitz constants M_{apex} and L_{apex} of Theorem 4.4 depend exclusively on $(G, \{m_i\}_{i=1}^N, E_0)$, completing the rigorous elimination of all free parameters.

Proof. For Item (1), let $\mathbf{q}_i = \mathbf{X}_S + \boldsymbol{\delta}_i$ be the position of an arbitrary particle $i \in S$, with $\sum_{i\in S} m_i\boldsymbol{\delta}_i = \mathbf{0}$. The gravitational force exerted by the sibling cluster S' on particle i expands in multipole Taylor series about the barycenter $\mathbf{X}_S$:

$$\mathbf{F}_{i\leftarrow S'} = -\sum_{j\in S'}\frac{Gm_im_j(\mathbf{q}_i - \mathbf{q}_j)}{\|\mathbf{q}_i - \mathbf{q}_j\|^3} = -\frac{Gm_iM_{S'}\mathbf{r}_P}{\|\mathbf{r}_P\|^3} - Gm_iM_{S'}\mathbb{T}(\mathbf{r}_P)\boldsymbol{\delta}_i + \mathcal{O}\left(\frac{Gm_iM_{S'}\bar{\rho}_S^2}{\|\mathbf{r}_P\|^4}\right), \tag{4.69}$$

where $\mathbb{T}(\mathbf{r}_P) = \|\mathbf{r}_P\|^{-3}(\mathbf{I}_3 - 3\hat{\mathbf{r}}_P\hat{\mathbf{r}}_P^T)$ is the classical symmetric trace-free tidal tensor. The leading term accelerates the center of mass $\mathbf{X}_S$ uniformly, while the differential tidal acceleration disrupting the internal geometry of S is $\mathbf{a}_{\text{tide},i} = -GM_{S'}\mathbb{T}(\mathbf{r}_P)\boldsymbol{\delta}_i$. Under the mass-weighted Riemannian metric $\mathbb{M}_S = \text{diag}(m_i\mathbf{I}_3)_{i\in S}$, the root-mean-square norm of the internal tidal acceleration satisfies:

$$\begin{aligned}\|\mathbf{a}_{\text{tide}}\|_S^2 &\coloneqq \frac{1}{M_S}\sum_{i\in S} m_i\|\mathbf{a}_{\text{tide},i}\|^2 \leq \frac{G^2M_{S'}^2}{\|\mathbf{r}_P\|^6}\|\mathbb{T}(\hat{\mathbf{r}}_P)\|^2\left(\frac{1}{M_S}\sum_{i\in S} m_i\|\boldsymbol{\delta}_i\|^2\right)\\ &\leq \frac{4G^2M_{S'}^2}{\|\mathbf{r}_P\|^6}\bar{\rho}_S^2 \implies \|\mathbf{a}_{\text{tide}}\|_S \leq \frac{2GM_{S'}}{\|\mathbf{r}_P\|^3}\bar{\rho}_S.\end{aligned} \tag{4.70}$$

Concurrently, the characteristic internal gravitational binding acceleration holding cluster S together scales as $\|\mathbf{a}_{\text{int}}\|_S = GM_S/\bar{\rho}_S^2$. The ratio of disruptive tidal acceleration to cohesive self-gravitational acceleration is therefore:

$$\frac{\|\mathbf{a}_{\text{tide}}\|_S}{\|\mathbf{a}_{\text{int}}\|_S} \leq 2\frac{M_{S'}}{M_S}\left(\frac{\bar{\rho}_S}{\|\mathbf{r}_P\|}\right)^3 = 2\,\eta_S(\mathbf{q})^3. \tag{4.71}$$

By classical Roche–Hill stability theory (Hill [32], Marchal [42]), an N-body sub-system retains dynamical autonomy without tidal stripping if its mean density exceeds three times the Roche

density of the perturber, which translates directly to $2\eta_S^3 \le 2/3 \iff \eta_S \le 3^{-1/3} = \eta_{\text{crit}}$. Whenever $\eta_S \le \eta_{\text{crit}}$, the external tidal field is a minor perturbation ($< 1/3$) of internal gravity, and the internal degrees of freedom are strongly coupled through non-orthogonal kinetic cross-terms, inducing the $\mathcal{O}(\rho_S^{-5/2})$ Poisson bracket divergence (Proposition 4.7) and necessitating synchronous Sundman integration. Because both $\bar{\rho}_S$ and $\|\mathbf{r}_P\|$ carry the dimension of length $[L]$ while $M_{S'}/M_S$ is dimensionless, $\eta_S(\mathbf{q})$ is strictly scale-invariant under $\mathbf{q} \mapsto \lambda\mathbf{q}$.

For Item (2), consider a bound system with total energy $E_0 = T + V < 0$. By the Sundman–Smale inequality [67, 72] and the Lagrange identity $\ddot{I} = 4E_0 - 2V = 4E_0 + 2U > 0$, the moment of inertia $I = \sum_{i=1}^N m_i\|\mathbf{q}_i - \mathbf{X}_{\text{cdm}}\|^2$ is bounded in mean by the virial equilibrium $2\langle T\rangle = -\langle V\rangle = |E_0|$. The total gravitational potential satisfies $U(\mathbf{q}) \ge GM_{\text{tot}}^2/(2R_{\text{sys}})$, which establishes $R_{\text{sys}}(E_0, M_{\text{tot}}) = GM_{\text{tot}}^2/(2|E_0|)$ as the maximal macroscopic bounding scale of the system (Marchal & Saari [43]). For any internal sub-cluster S, the maximum separation from the remaining mass $M_{\text{tot}} - M_S$ is bounded by R_{sys}, so that the tidal condition $\bar{\rho}_S \le \eta_{\text{crit}}(M_S/M_{\text{tot}})^{1/3}\|\mathbf{r}_P\|$ yields the canonical scale threshold $\delta^{\text{nat}}_{\text{cluster}}(S) = \eta_{\text{crit}}(M_S/M_{\text{tot}})^{1/3}R_{\text{sys}}\sqrt{M_S}$. Under homothety $\mathbf{q} \mapsto \lambda\mathbf{q}$, the potential scales as $V \mapsto \lambda^{-1}V$ and the energy as $E_0 \mapsto \lambda^{-1}E_0$; hence $R_{\text{sys}} \mapsto \lambda R_{\text{sys}}$ and $\delta^{\text{nat}}_{\text{cluster}}(S) \mapsto \lambda\delta^{\text{nat}}_{\text{cluster}}(S)$, demonstrating strict covariance.

For Item (3), substituting $\delta^{\text{nat}}_{\text{cluster}}(S)$ into the lower bound $\bar{\rho}_{\text{int}}(v) \ge c_0\delta_{\text{cluster}}$ of Theorem 4.4 (Regime 2) expresses the infimum $\bar{\rho}_{\text{int}}^{-1} \le (c_0\delta^{\text{nat}}_{\text{cluster}})^{-1}$ as a function of E_0, G, and $\{m_i\}$. Consequently, the Lipschitz bounds M_{apex} and L_{apex} are closed, finite functions of the physical first integrals alone, without any external parameter choice.

□

Corollary 4.12 — *Predictive Dyadic Anticipation and Spectral Schmitt Trigger*

In practical numerical integration, the boundary crossing of the Hill tidal domain $\{\eta_S \le \eta_{\text{crit}}\}$ is governed by a two-tier coupled temporal-topological protocol:

(1) *Upstream Predictive Dyadic Anticipation*: For any approaching external perturber ($v_{\text{rad}} = \langle\mathbf{v}_P, \mathbf{r}_P\rangle/\|\mathbf{r}_P\| < 0$), the dyadic multirate scheduler (formally defined in Section 5.6 and algorithmically implemented in Sections 6.2–6.3 and Appendix A.2) continuously estimates the ballistic encounter timescale $t_{\text{approach}} = -\|\mathbf{r}_P\|/v_{\text{rad}}$. Whenever $t_{\text{approach}} \le 2\Delta t_{\text{macro}}$, the dyadic exponent k is refined proactively ($h_k = \Delta t_{\text{macro}}/2^k$) *prior* to crossing the tidal boundary. This guarantees that the system enters the stiff Hill interaction zone with an already refined temporal grid, preventing sudden truncation shock and energy error spikes.

(2) *Canonical Spectral Schmitt Trigger Hysteresis* ($[\eta_{\text{enter}}, \eta_{\text{exit}}] = [2^{-1/3}, 2^{-1/6}] \approx [0.7937, 0.8909]$): To eliminate high-frequency numerical chattering without delaying activation, both thresholds of the Schmitt trigger band are derived analytically from the spectral norms of the trace-free tidal tensor $\mathbb{T}(\hat{\mathbf{r}}_P) = \mathbf{I}_3 - 3\hat{\mathbf{r}}_P\hat{\mathbf{r}}_P^T$ and positioned strictly *above* the Hill stability limit $\eta_{\text{crit}} = 3^{-1/3} \approx 0.6934$:

(a) *Proactive Activation at Radial Equigravity* ($\eta_{\text{enter}} := 2^{-1/3} \approx 0.7937$): Along the line of centers $\hat{\mathbf{r}}_P$, the maximum stretching tidal eigenvalue is $|\lambda_{\text{rad}}| = 2$. The exact balance where peak external tidal acceleration equals internal self-gravitational binding acceleration ($a_{\text{tide,max}} = a_{\text{int}} \iff 2\eta_S^3 = 1$) uniquely defines:

$$\eta_{\text{enter}} = \left(\frac{1}{2}\right)^{1/3} = 2^{-1/3} \approx 0.7937005. \tag{4.72}$$

Cluster S is promoted to an active synchronous supernode as soon as $\eta_S \le \eta_{\text{enter}}$, anticipating entry into the physical Hill sphere by a scale factor of $(3/2)^{1/3} \approx 1.145$ (14.5% geometric safety margin).

(b) *Guaranteed Deactivation at Spherical RMS Equigravity* ($\eta_{\text{exit}} := 2^{-1/6} \approx 0.8909$): Averaged uniformly over the unit sphere $\mathbb{S}^2$, the root-mean-square norm of the tidal tensor is $\|\mathbb{T}\|_{\text{rms}} = \sqrt{\frac{1}{3}\operatorname{Tr}(\mathbb{T}^2)} = \sqrt{2}$. The threshold where

the mean spherical tidal pull equals internal binding ($\sqrt{2}\eta_S^3 = 1$) uniquely yields:

$$\eta_{\text{exit}} = \left(\frac{1}{\sqrt{2}}\right)^{1/3} = 2^{-1/6} \approx 0.8908987. \tag{4.73}$$

S remains an active supernode until $\eta_S > \eta_{\text{exit}}$.

The canonical spectral ordering:

$$\eta_{\text{crit}} = 3^{-1/3} \approx 0.6934 < \eta_{\text{enter}} = 2^{-1/3} \approx 0.7937 < \eta_{\text{exit}} = 2^{-1/6} \approx 0.8909, \tag{4.74}$$

satisfies the exact dyadic squaring identity $\eta_{\text{enter}} = (\eta_{\text{exit}})^2$. Because both thresholds reside strictly above the physical Hill limit, orbital breathing and roundoff fluctuations around η_{crit} occur deep inside the locked active supernode regime, completely precluding topological chattering while ensuring zero activation latency.

Proof. By Proposition 4.11, the dimensionless tidal tensor $\mathbb{T}(\hat{\mathbf{r}}_P) = \mathbf{I}_3 - 3\hat{\mathbf{r}}_P\hat{\mathbf{r}}_P^T$ has eigenvalues $(-2, 1, 1)$. Its operator norm (realized along $\pm\hat{\mathbf{r}}_P$) is $\|\mathbb{T}\|_{\text{op}} = 2$, while its spherical root-mean-square norm over $\mathbb{S}^2$ is $\|\mathbb{T}\|_{\text{rms}} = \sqrt{\frac{1}{3}((-2)^2 + 1^2 + 1^2)} = \sqrt{2}$. Equating the corresponding tidal-to-self-gravity acceleration ratios $2\eta_S^3$ and $\sqrt{2}\eta_S^3$ to unity yields $\eta_{\text{enter}} = 2^{-1/3}$ and $\eta_{\text{exit}} = 2^{-1/6} = \sqrt{\eta_{\text{enter}}}$. Since $3 > 2 > \sqrt{2} > 1$, taking the inverse cube root reverses the strict inequalities to yield $\eta_{\text{crit}} = 3^{-1/3} < \eta_{\text{enter}} = 2^{-1/3} < \eta_{\text{exit}} = 2^{-1/6}$, establishing a non-empty hysteresis deadband of width $\eta_{\text{exit}} - \eta_{\text{enter}} \approx 0.0972$ strictly above the physical Roche–Hill stability limit. □

4.3.5. *Synthesis of Section 4: The Complete Hierarchical Symplectic Architecture.* With the establishment of Theorems 4.1, 4.4, 4.9, and 4.10, the geometric and analytical construction of the Fulton–MacPherson hierarchical splitting on $\mathbf{Q}[N]$ is complete:

(1) *Spatial Regularization without Distance Softening*: The collision arrangement Δ is blown up into the compact manifold with corners $\mathbf{Q}[N]$, transforming physical collision singularities into regular boundary divisors with simple normal crossings, without modifying Newton's gravitational law ($\varepsilon = 0$ strictly preserved).
(2) *Disjoint Symplectic Decoupling*: On maximal Jacobi trees, disjoint sub-clusters commute exactly on phase space ($[\mathcal{X}_A, \mathcal{X}_B] = 0$), allowing fully independent local integration.
(3) *Universal $\mathcal{C}^{1,1}$ Apex Screening*: The scale-adapted screening function $\Theta(u_v)$ eliminates the multipolar ghost pole at cluster barycenter coincidence, providing uniform Lipschitz bounds ($M_{\text{apex}}, L_{\text{apex}} < \infty$) without introducing any artificial distance cut-off ($d_0 = 0$).
(4) *Exact Symmetry and Palindromic Invariance*: The screened apex flow strictly conserves all 10 generators of the centrally extended Lie–Bargmann algebra, while symmetric Strang splitting eliminates all odd-order dissipative errors.
(5) *Anti-Zeno Supernode Synchrony*: Dense sub-clusters ($k \geq 3$) are unified into synchronous supernodes under Sundman's unfolded local clock $\mathrm{d}t_S = \chi_S^2 \mathrm{d}\tau_S$, eliminating the $\mathcal{O}(\delta^{-5/2})$ commutator catastrophe and guaranteeing finite crossing time across multiple quasi-collisions.
(6) *Symplectic Atlas Continuity*: Transitions between adapted Jacobi charts belong to $\mathrm{Sp}(6N - 6, \mathbb{R})$ under canonical parameter-free Voronoi partitioning ($\gamma = 1.0$, or optional asymmetric hysteresis $\gamma = 0.6$ guaranteeing positive dwell time without topological chattering).

► **Normal Cone Decomposition: Unsoftened 3D Newtonian N-Body Problem on $\mathbf{Q}[N]$**

Geometric Base & Normal Fiber: The physical system describes $N \geq 3$ point masses $m_1, \dots, m_N > 0$ in $\mathbb{R}^3$ interacting through unsoftened Newtonian gravity ($\varepsilon = 0$). In the center-of-mass frame, the relative configuration space is $M = (\mathbb{R}^3)^N/\mathbb{R}^3 \cong \mathbb{R}^{3N-3}$, equipped with the mass Riemannian metric $\mathbb{M} = \mathrm{diag}(m_1 I_3, \dots, m_N I_3)$ and physical momentum space $M^* = \{\mathbf{p} \in (\mathbb{R}^3)^N \mid \sum \mathbf{p}_i = \mathbf{0}\}$.
The geometric phase space is the extended Poincaré–Sundman manifold equipped with the extended Darboux 2-form:

$$\mathcal{P}_{\mathrm{ext}} = T^*\mathbf{Q}[N] \times \mathbb{R}_t \times \mathbb{R}_E, \qquad \Omega_{\mathrm{ext}} = \Omega_0 + \mathrm{d}E \wedge \mathrm{d}t = \mathrm{d}\mathbf{q} \wedge \mathrm{d}\mathbf{p} + \mathrm{d}E \wedge \mathrm{d}t, \tag{4.75}$$

where $(t, -E) = (q_t, p_t)$ form a canonical pair with $\{t, -E\} = 1$. The collision locus is the Whitney-stratified arrangement organized along the partition lattice $\Pi(N)$:

$$\Delta = \bigcup_{1 \leq i < j \leq N} \Delta_{ij}, \qquad \Delta_I = \{\mathbf{q} \in M \mid \mathbf{q}_i = \mathbf{q}_j \ \forall i, j \in I\}, \qquad \mathrm{codim}_M(\Delta_I) = 3(|I| - 1). \tag{4.76}$$

The configuration base is the smooth manifold with corners $\mathbf{Q}[N] = \mathrm{Bl}_{\mathcal{G}_{\mathrm{irr}}}(M)$ obtained by iterative real oriented spherical blow-ups in order of increasing stratum dimension (decreasing cluster cardinality), whose boundary $\partial\mathbf{Q}[N] = \bigcup_{|I| \geq 2} E_I$ is a simple normal crossing (SNC) divisor with corners with defining normal coordinates $\rho_I = \sqrt{\frac{1}{M_I} \sum_{i<j \in I} m_i m_j \|\mathbf{q}_i - \mathbf{q}_j\|^2} \in [0, \infty)$. Maximal codimension corners correspond bijectively to complete binary Jacobi trees $\mathcal{T} \in \mathrm{Trees}(N)$ (totaling $(2N-3)!!$) defining canonical charts $(\mathbf{r}_v, \mathbf{w}_v)_{v \in \mathcal{V}_{\mathrm{int}}(\mathcal{T})}$ with diagonal kinetic energy $T_{\mathrm{kin}} = \frac{1}{2} \sum_v \|\mathbf{w}_v\|^2/\mu_v$, conical clustering chambers $\mathcal{U}_{\mathcal{T}}$, and exact cotangent decoupling on disjoint sub-trees: $\{\mathcal{H}_A, \mathcal{H}_B\}_{\Omega_0} \equiv 0 \implies [\mathcal{X}_{\mathcal{H}_A}, \mathcal{X}_{\mathcal{H}_B}] \equiv 0$.
Hamiltonian Polarization: Polarizing the unsoftened N-body energy into unconstrained kinematic-Keplerian base drift, normal screened apex interaction, and synchronous supernodes:

$$H(\mathbf{q}, \mathbf{p}) = \underbrace{T_{\mathrm{kin}}(\mathbf{w}) + V^{\mathrm{screened}}_{\mathrm{kepler}}(\mathbf{q}) + V^{\mathrm{free}}_{\mathrm{leaves}}(\mathbf{q})}_{H_{\mathrm{base}}} + \underbrace{W^{\mathrm{screen}}_{\mathrm{apex}}(\mathbf{q})}_{H^{\mathrm{apex}}_{\mathrm{normal}}} + \underbrace{\sum_{S \in \mathcal{S}_{\mathrm{act}}} H^{\mathrm{super}}_S(\mathbf{q}_S, \mathbf{p}_S)}_{H^{\mathrm{sync}}_{\mathrm{super}}}. \tag{4.77}$$

- *Base Kinematic & Screened Keplerian Hamiltonian* H_{base}: Generates free diagonal inertial drift along the interior $\mathrm{Int}(\mathbf{Q}[N])$ and macroscopic screened Keplerian motion between well-separated clusters, integrated symplectically without spatial cut-off.
- *Normal Screened Apex Hamiltonian* $H^{\mathrm{apex}}_{\mathrm{normal}}$: Governed by $W^{\mathrm{screen}}_{\mathrm{apex}} = \sum_{v \in \mathcal{V}^{\mathrm{free}}_{\mathrm{comp}}} W^{\mathrm{screen}}_{\mathrm{apex},v}$ with $W^{\mathrm{screen}}_{\mathrm{apex},v} = V_v + \Theta(u_v) \frac{G M_L M_R}{\|\mathbf{r}_v\|}$. The scale-adapted screening function $\Theta(u_v)$ completely extinguishes the multipolar ghost pole at barycentric coincidence ($\Theta \equiv 0$ for $u_v \leq 1$), smoothly interpolates across the compact projectivized annulus $\mathcal{A}_{[1,2]}$, and cancels monopole and dipole terms for $u_v \geq 2$, leaving a quadrupolar decay $\mathcal{O}(\|\mathbf{r}_v\|^{-3})$. This guarantees universal Sobolev–Lipschitz regularity $W^{\mathrm{screen}}_{\mathrm{apex}} \in \mathcal{C}^{1,1}(U_{\mathcal{T}}) = \mathcal{W}^{2,\infty}(U_{\mathcal{T}})$ with finite uniform bounds $\|\nabla W^{\mathrm{screen}}_{\mathrm{apex}}\|_{\mathbb{M}^{-1}} \leq M_{\mathrm{apex}} < \infty$ and $\|\mathrm{Hess}\, W^{\mathrm{screen}}_{\mathrm{apex}}\|_{\mathbb{M}^{-1}} \leq L_{\mathrm{apex}} < \infty$ without artificial distance softening ($d_0 = 0$ strictly). Integrated as exact commuting vertical kicks along cotangent fibers ($[X_{V_a}, X_{V_b}] = 0$).
- *Synchronous Supernode Hamiltonian* $H^{\mathrm{sync}}_{\mathrm{super}}$: Collapses tightly bound sub-clusters ($\rho_S \leq \delta^{\mathrm{nat}}_{\mathrm{cluster}}$, $|S| \geq 3$, dynamically determined by the intrinsic tidal criterion $\eta_S \leq \eta_{\mathrm{crit}}$ of Section 4.3.4) into unified synchronous blocks integrated under Sundman's unfolded local clock $\mathrm{d}t_S = \chi_S^2 \mathrm{d}\tau_S$, eliminating the $\mathcal{O}(\delta^{-5/2}_{\mathrm{cluster}})$ asynchronous commutator divergence.

Preserved Invariants: Under the 7-stage palindromic splitting $\mathcal{S}_2(h)$, the discrete flow guarantees unconditional geometric and physical fidelity:

- *Exact Extended Symplecticity & Lie–Bargmann Conservation*: The flow preserves the canonical extended 2-form $\mathcal{S}_2(h)^*\Omega_{\mathrm{ext}} = \Omega_{\mathrm{ext}}$ and strictly conserves all 10 classical Galilean generators realizing the centrally extended Lie–Bargmann algebra ($\Delta\mathbf{P} = \mathbf{0}$, $\Delta\mathbf{L} = \mathbf{0}$, $\Delta\mathbf{G} = \mathbf{0}$) with central mass charge M_{tot}, while the extended Hamiltonian defect satisfies $\Delta\mathcal{H}_{\mathrm{ext}} = \mathcal{O}(h^2)$ without secular energy dissipation.
- *Palindromic Parity & Shadow Confinement*: Reversal involution $\mathcal{R}_{\mathrm{ext}}(\mathbf{q}, \mathbf{p}, t, E) = (\mathbf{q}, -\mathbf{p}, -t, E)$ enforces $\mathcal{R}_{\mathrm{ext}} \circ \mathcal{S}_2(h) \circ \mathcal{R}_{\mathrm{ext}} = \mathcal{S}_2(-h) = \mathcal{S}_2(h)^{-1}$. The shadow Hamiltonian $\widetilde{H}(h)$ contains only even powers of h, eliminating all odd dissipative errors ($\mathcal{O}(h), \mathcal{O}(h^3), \dots$) and conferring Gevrey-2 sub-exponential shadow stability under the canonical $\mathcal{C}^\infty$ Cauchy mollifier.

- *Universal Anti-Zeno Finiteness*: On almost all orbits ($\mu_{\text{Leb}}(\mathcal{N}_{\text{coll}}) = 0$ by Saari's theorem), the hyper-radius satisfies $\rho_{\min}(\mathbf{z}_0) > 0$, guaranteeing finite sub-steps $N_{\text{sub}} \leq \lceil \Delta t_{\text{phys}}/(\rho_{\min}\Delta\tau_S) \rceil < \infty$ across all multiple close encounters.
- *Symplectic Atlas Transitions & Anti-Chattering*: Inter-chart Jacobi transformations $\Psi_{A\to B} = \Psi_{\text{rot}} \oplus \mathbf{I}_{6N-18} \in \text{Sp}(6N-6, \mathbb{R})$ with $\mathbf{M}_{\text{coord}} \in \text{SL}(2, \mathbb{R})$ preserve Ω_{ext} under canonical parameter-free Voronoi partitioning ($\gamma = 1.0$), while optional asymmetric hysteresis ($\gamma = 0.6$) strictly forbids topological chattering ($1 < 0.36$ impossibility), ensuring a finite dwell time $\tau_{\min} = \frac{16}{15\Omega_{\max}} > 0$ and bounded transitions $N_{\text{trans}}(T) < \infty$.

Transition to High-Order Numerical Integrators. The continuous Hamiltonian decomposition established in Section 4 provides the exact mathematical substrate required for discrete algorithmics. In Section 5, we operationalize this structure into computable high-order numerical propagators: we construct the 7-stage palindromic Strang scheme $\mathcal{S}_2(h)$, analyze the Suzuki barrier forbidding positive-coefficient integrators beyond order 2, prove that McGehee bounce involution guarantees unconditional stability under negative sub-steps ($w_i < 0$), and formulate the optimized 4th-order Blanes–Moan propagator BM_4 minimizing the shadow Hamiltonian error on $\mathbf{Q}[N]$.

5. Symplectic Discretization and High-Order Schemes

Having established the continuous geometric foundations of the Fulton–MacPherson compactification $\mathbf{Q}[N]$, the $\mathcal{C}^{1,1}$-regularized screened apex potential $W_{\text{apex}}^{\text{screen}}$, and the synchronous supernode regularization in Section 4, we now pass from continuous Hamiltonian geometry to discrete symplectic time-stepping. The overarching objective of this chapter is to construct a hierarchy of unsoftened ($\varepsilon = 0, d_0 = 0$), structure-preserving geometric integrators on the extended cotangent bundle $\mathcal{P}_{\text{ext}} = T^*\mathbf{Q}[N] \times \mathbb{R}_t \times \mathbb{R}_E$ that conserve all ten Lie–Bargmann first integrals to machine precision while traversing exact binary and cluster collisions in a finite number of physical steps.

Our exposition proceeds in six logical stages. Section 5.1 constructs the foundational 7-operator hierarchical palindromic Strang propagator $\mathcal{S}_2(h)$ and establishes its unconditional extended symplecticity and discrete Galilean invariance. Section 5.2 confronts the Sheng–Suzuki impossibility barrier ($w_i < 0$ for order $p \geq 3$) and proves that the real-analytic invertibility of universal Sundman–Stumpff flows coupled with McGehee's unitary collision bounce involution ($\mathcal{B}_C^2 = \mathrm{Id}_{\mathbf{M}_C}$) renders retrograde sub-steps completely singularity-free, enabling Yoshida's fourth-order scheme $\mathcal{S}_4(h)$. To suppress the large backward excursion of minimal triplets, Section 5.3 deploys the spectrally optimized 7-stage Blanes–Moan scheme BM_4 and proves general order-$2p$ exponential shadow Hamiltonian confinement under zero softening. Section 5.4 extends this composition architecture to the 11-stage sixth-order scheme $\mathrm{BM}_6^{(11)}$ and establishes the bi-graded Lie algebra filtration $\mathcal{L}_{n,m}(A_{\text{JK}}, W_{\text{apex}}^{\text{screen}})$ governing hierarchical error commutators. Section 5.5 then investigates symplectic boundary processing: we prove the *Universal Obstruction Theorem* prohibiting global order-6 configuration correctors on $T^*\mathbf{Q}[N]$, construct the domain-restricted tidal corrector K_4 (PBM_4) on $\mathcal{D}_{\text{reg}}$ with its irreducible quadratic floor $\mathcal{O}(\varepsilon^2 h^4)$, and derive the covariant cotangent-lifted gauge transition operator $T_{A\to B}^{(\mathrm{PBM4})}$ across Jacobi charts. Finally, Section 5.6 synthesizes these propagators into a time-reversible dyadic multirate scheduler governed by Skeel–Gear macro-boundary synchronization and the *Leaf/Apex Decoupling Theorem*.

5.1. The 7-Operator Hierarchical Palindromic Strang Propagator ($\mathcal{S}_2$).

The foundational building block of our geometric numerical integrator on the compactified Fulton–MacPherson configuration space $\mathbf{Q}[N]$ (Section 4) is the second-order symmetric Strang splitting propagator [69] (independently developed by Marchuk [44] and rooted in Trotter's product formula [77]). In classical celestial mechanics, operator splitting for unsoftened N-body dynamics has historically foundered on close encounters: when pairwise separations $\rho_C \to 0$, naive kinetic-potential splittings suffer unbounded truncation error spikes. While advanced splitting schemes for perturbed systems $H = A + \varepsilon B$ (most notably Laskar and Robutel [38] and Blanes, Casas, Farrés, Laskar, Makazaga and Murua [8]) achieve extraordinary efficiency in regular, quasi-circular secular regimes with a uniform distance barrier $\inf_t r_{ij}(t) \geq r_{\min} > 0$, unsoftened close encounters ($\rho_C \to 0$) violate $\varepsilon \ll 1$ and drive catastrophic Lie commutator explosions. On the compactified cotangent bundle $\mathcal{P}_{\text{ext}} = T^*\mathbf{Q}[N] \times \mathbb{R}_t \times \mathbb{R}_E$, however, the continuous Hamiltonian established in Section 4 decomposes into autonomous, regular, and desingularized vector fields.

In this section, we construct the discrete 7-operator hierarchical palindromic Strang scheme $\mathcal{S}_2(h)$, prove its unconditional extended symplecticity on $(\mathcal{P}_{\text{ext}}, \Omega_{\text{ext}})$, demonstrate the exact cancellation of all odd-order dissipative error terms in its Baker–Campbell–Hausdorff expansion, and verify the exact discrete conservation (with identically vanishing truncation error) of all ten generators of the centrally extended Lie–Bargmann symmetry algebra.

5.1.1. *Extended Phase Space and Elementary Lie Propagators.* Recall from Section 4.2.4 (Proposition 4.6) that the dynamics is formulated on the $(6N + 2)$-dimensional extended Poincaré–Sundman phase space:

$$\mathcal{P}_{\text{ext}} = T^*(\mathbf{Q}[N] \times \mathbb{R}^3_{\text{cdm}}) \times \mathbb{R}_t \times \mathbb{R}_E \cong T^*\mathbf{Q}[N] \times T^*\mathbb{R}^3_{\text{cdm}} \times \mathbb{R}_t \times \mathbb{R}_E, \tag{5.1}$$

which identifies smoothly with the standard cotangent bundle $(T^*(\mathbb{R}^{3N} \setminus \Delta)) \times \mathbb{R}_t \times \mathbb{R}_E$ on the dense open collisionless stratum $\mathbf{Q}[N]^\circ$, while rigorously incorporating the boundary strata $\partial\mathbf{Q}[N]$ associated with binary and multiple collisions. Equipped with the canonical configuration-momentum conjugate pair $(q_t, p_t) = (t, -E)$, where $t \in \mathbb{R}$ represents the physical coordinate time and $E \in \mathbb{R}$ is the conjugate energy variable, the extended Liouville 1-form is:

$$\lambda_{\text{ext}} = \sum_{i=1}^{N} \mathbf{p}_i \cdot \mathrm{d}\mathbf{q}_i + p_t\,\mathrm{d}t = \sum_{i=1}^{N} \mathbf{p}_i \cdot \mathrm{d}\mathbf{q}_i - E\,\mathrm{d}t, \tag{5.2}$$

inducing the canonical closed non-degenerate extended Darboux 2-form:

$$\Omega_{\text{ext}} \coloneqq -\mathrm{d}\lambda_{\text{ext}} = \Omega_0 - \mathrm{d}p_t \wedge \mathrm{d}t = \Omega_0 - (-\mathrm{d}E) \wedge \mathrm{d}t = \Omega_0 + \mathrm{d}E \wedge \mathrm{d}t, \quad \mathrm{d}\Omega_{\text{ext}} = 0, \tag{5.3}$$

where $\Omega_0 = \sum_{i=1}^{N} \sum_{\alpha=1}^{3} \mathrm{d}q_i^\alpha \wedge \mathrm{d}p_i^\alpha$ is the standard spatial Darboux form on $T^*\mathbb{R}^{3N}$. The canonical extended Poisson brackets satisfy:

$$\{q_i^\alpha, p_j^\beta\} = \delta_{ij}\delta^{\alpha\beta}, \qquad \{t, -E\} = 1 \iff \{t, E\} = -1, \tag{5.4}$$

all other fundamental brackets vanishing identically. The autonomous extended Hamiltonian is given by:

$$\mathcal{H}_{\text{ext}}(\mathbf{q}, \mathbf{p}, t, E) = H(\mathbf{q}, \mathbf{p}) - E, \tag{5.5}$$

and physical motions correspond to trajectories confined to the regular zero-energy level hypersurface $\Sigma_0 = \{(\mathbf{q}, \mathbf{p}, t, E) \in \mathcal{P}_{\text{ext}} \mid \mathcal{H}_{\text{ext}} = 0\}$.

In any adapted Jacobi chart $U_{\mathcal{T}} \subset \mathbf{Q}[N]$ associated with a maximal flag tree $\mathcal{T} \in \mathrm{Trees}(N)$ (Section 4.1.3), the physical Hamiltonian is rigorously structured as a *Fulton–MacPherson hierarchical splitting*:

$$H(\mathbf{r}, \boldsymbol{\pi}) = A_{\text{hier}}(\mathbf{r}, \boldsymbol{\pi}) + W_{\text{apex}}^{\text{screen}}(\mathbf{r}) = A_{\text{JK}}(\mathbf{r}, \boldsymbol{\pi}) + W_{\text{apex}}^{\text{screen}}(\mathbf{r}) + V_{\text{kepler}}^{\text{screened}}(\mathbf{r}), \tag{5.6}$$

where the unperturbed hierarchical Keplerian operator A_{JK} aggregates all decoupled kinematic and Keplerian degrees of freedom:

$$A_{\text{JK}}(\mathbf{r}, \boldsymbol{\pi}) \coloneqq T_0(\boldsymbol{\pi}_0) + T_{\text{comp}}(\boldsymbol{\pi}) + H_{\text{leaf}}(\mathbf{r}, \boldsymbol{\pi}) + H_{\text{super}}(\mathbf{r}, \boldsymbol{\pi}). \tag{5.7}$$

Crucially, in canonical Jacobi coordinates, the relative pairs and barycentric channels are mutually orthogonal under the Darboux form $\Omega_0 = \sum \mathrm{d}\mathbf{r}_k \wedge \mathrm{d}\boldsymbol{\pi}_k$, ensuring that all constituent channels of A_{JK} Poisson-commute pairwise:

$$\{H_k^{\text{Kepler}}, H_l^{\text{Kepler}}\} \equiv 0 \quad (\forall k \neq l) \implies \{A_{\text{JK}}, A_{\text{JK}}\} \equiv 0. \tag{5.8}$$

Consequently, the unperturbed flow $\exp(\delta t X_{A_{\text{JK}}})$ factorizes into the exact direct product of its autonomous channels without any operator splitting error.

Remark — *Geometric Grounding: Calaque–Safronov Cotangent Specialization and Hierarchical Splitting.* In the foundational framework of Fulton–Verdier [23] and its shifted cotangent lift established by Calaque & Safronov [15], the deformation to the normal cone $\mathcal{D}_\Delta Q \to \mathbb{A}^1$ induces a relative symplectic family $T^*(\mathcal{D}_\Delta Q/\mathbb{A}^1) \to \mathbb{A}^1$ whose special fiber at $t = 0$ specializes to the cotangent bundle of the normal cone $T^*(N_\Delta Q) \cong T^*\Delta \times T^*(N_\Delta Q/\Delta)$. Under this geometric lens, our operator splitting (5.6) realizes the canonical base-fiber polarization:

$$H = H_{\text{base}} + H_{\text{normal}}^{\text{apex}} + H_{\text{super}}^{\text{sync}}, \tag{5.9}$$

where $H_{\text{base}} = T_0 + T_{\text{comp}}$ generates the regular horizontal drift on the base stratum ($t = 1$), $H_{\text{normal}}^{\text{apex}} = H_{\text{leaf}} + \mathcal{K}^{\text{apex}}$ governs the decoupled two-body dynamics and vertical cotangent interaction kicks along the fibers ($t = 0$), and $H_{\text{super}}^{\text{sync}}$ regulates multiple collision loci on the deeper strata of the Fulton–MacPherson tree.

Hierarchical Structure and Error Grading: An important consequence of this geometry is that on the regular hierarchical domain $\mathcal{D}_{\text{reg}}$, the unperturbed operator A_{JK} is completely integrable by exact analytic quadratures (universal Kepler–Sundman flow), while the perturbation $W_{\text{apex}}^{\text{screen}}$ is scaled by the dimensionless tidal parameter $\varepsilon \sim (r_{\text{leaf}}/R_{\text{ext}})^3 \leq 0.125 \ll 1$. This structure breaks fundamentally from classical Cartesian splittings $T(\mathbf{p}) + V(\mathbf{q})$: because internal two-body

dynamics is analytically absorbed into A_{JK}, all pure velocity error commutators $L_T^4(V) \in \mathcal{P}_4$ vanish identically, and the Baker–Campbell–Hausdorff error series is bi-graded in powers (h^{2n}, ε^m) with no residual term in $\mathcal{O}(\varepsilon^0 h^k)$.

The five elementary Hamiltonian sub-flows governing the Fulton–MacPherson decomposition (5.6)–(5.7) are defined explicitly as follows:

(1) **Center-of-Mass Kinetic Drift (T_0):** Governed by $T_0(\boldsymbol{\pi}_0) = \frac{\|\boldsymbol{\pi}_0\|^2}{2M_{\mathrm{tot}}}$ with total mass $M_{\mathrm{tot}} = \sum_{i=1}^N m_i$. Its exact Hamiltonian flow for a step δt is a linear shear:

$$\Phi_{\delta t}^{\mathrm{drift},(0)} : (\mathbf{R}_{\mathrm{cdm}}, \boldsymbol{\pi}_0) \longmapsto \left(\mathbf{R}_{\mathrm{cdm}} + \delta t \, \frac{\boldsymbol{\pi}_0}{M_{\mathrm{tot}}}, \, \boldsymbol{\pi}_0 \right), \tag{5.10}$$

leaving all internal Jacobi relative coordinates and (t, E) invariant.

(2) **Composite-Node Kinematic Drift (T_{comp}):** Governed by the sum of kinetic energies of internal cluster barycenters $T_{\mathrm{comp}}(\boldsymbol{\pi}) = \sum_{v \in \mathcal{V}_{\mathrm{comp}}(\mathcal{T})} \frac{\|\boldsymbol{\pi}_v\|^2}{2\mu_v}$, where $\mu_v = \frac{M_{L(v)} M_{R(v)}}{M_{L(v)} + M_{R(v)}}$ is the reduced mass. Within the Fulton–MacPherson hierarchical operator A_{JK}, intermediate cluster barycenters advance along exact straight-line Galilean shears $\Phi_{\delta t}^{\mathrm{drift},(\mathrm{comp})}$, while their mutual gravitational attractions are smoothly absorbed into the screened apex potential $W_{\mathrm{apex}}^{\mathrm{screen}}$:

$$\Phi_{\delta t}^{\mathrm{drift},(\mathrm{comp})} : \mathbf{r}_v \longmapsto \mathbf{r}_v + \delta t \, \frac{\boldsymbol{\pi}_v}{\mu_v}, \quad \boldsymbol{\pi}_v \longmapsto \boldsymbol{\pi}_v \quad \forall v \in \mathcal{V}_{\mathrm{comp}}(\mathcal{T}). \tag{5.11}$$

Since $\mu_v > 0$ and T_{comp} is purely quadratic, this flow is smooth and non-singular across $\mathbf{r}_v = \mathbf{0}$. We denote the aggregate kinematic drift by $\Phi_{\delta t}^{\mathrm{drift}} := \Phi_{\delta t}^{\mathrm{drift},(0)} \circ \Phi_{\delta t}^{\mathrm{drift},(\mathrm{comp})}$.

(3) **Leaf Keplerian Pairs Flow (H_{leaf}):** Governed by the decoupled sum of isolated two-body Keplerian pairs $H_{\mathrm{leaf}} = \sum_{C \in \mathcal{V}_{\mathrm{leaf}}(\mathcal{T})} \left(\frac{\|\boldsymbol{\pi}_C\|^2}{2\mu_C} - \frac{G m_i m_j}{\|r_C\|} \right)$. By Proposition 4.2, disjoint sub-clusters commute identically under the Poisson bracket ($[\mathcal{X}_{H_C}, \mathcal{X}_{H_{C'}}] = 0$), so the collective flow factorizes as:

$$\Phi_{\vec{\Delta\tau}}^{\mathrm{leaf}} = \prod_{C \in \mathcal{V}_{\mathrm{leaf}}(\mathcal{T})} \Phi_{\Delta\tau_C}^{(C)}, \tag{5.12}$$

where each $\Phi_{\Delta\tau_C}^{(C)}$ is integrated analytically in universal Stumpff series under Sundman's eccentric anomaly clock $\mathrm{d}t_C = \rho_C \mathrm{d}\tau_C$ and extends smoothly across collision $\mathbf{M}_C$ via the McGehee bounce involution $\mathcal{B}_C^2 = \mathrm{id}$.

(4) **Synchronous Supernodes Flow (H_{super}):** Governed by compact multi-body sub-clusters ($\rho_S \le \delta_{\mathrm{cluster}}^{\mathrm{nat}}$, dynamically determined by Proposition 4.11) under Sundman's unfolded local clock $\mathrm{d}t_S = \chi_S^2 \mathrm{d}\tau_S$ (Section 4.3). The collective flow is:

$$\Phi_{\vec{\Delta\tau}_S}^{\mathrm{super}} = \prod_{S \in \mathcal{S}} \Phi_{\Delta\tau_S}^{(S)}, \tag{5.13}$$

guaranteeing finite Anti-Zeno crossing ($N_{\mathrm{sub}} < \infty$, Theorem 4.9) and preserving extended Darboux area.

(5) **Screened Apex and Keplerian Potential Kick ($\mathcal{K}^{\mathrm{apex}}$):** Governed by the configuration potential $V_{\mathrm{kick}}(\mathbf{q}) = W_{\mathrm{apex}}^{\mathrm{screen}}(\mathbf{q}) + V_{\mathrm{kepler}}^{\mathrm{screened}}(\mathbf{q})$, whose apex component is universally $\mathcal{C}^{1,1}$-bounded (Theorem 4.4) and whose screened Keplerian attraction is smooth away from collisions. Because V_{kick} depends purely on configuration coordinates $\mathbf{q}$, its Hamiltonian vector field $\mathcal{X}_{V_{\mathrm{kick}}}$ is vertical along the cotangent fibers $T_{\mathbf{q}}^*\mathbf{Q}[N]$ (spanning the vertical subbundle $V(T^*\mathbf{Q}[N]) = \ker \mathrm{d}\pi$). In particular, any two configuration kick components V_a, V_b commute identically: $[\mathcal{X}_{V_a}, \mathcal{X}_{V_b}] = 0$. Its

exact Hamiltonian flow for a time step δt is a vertical cotangent shear:

$$\mathcal{K}_{\delta t}^{\text{apex}} : \mathbf{q}_i \longmapsto \mathbf{q}_i, \quad \mathbf{p}_i \longmapsto \mathbf{p}_i - \delta t\, \nabla_{\mathbf{q}_i}(W_{\text{apex}}^{\text{screen}}(\mathbf{q}) + V_{\text{kepler}}^{\text{screened}}(\mathbf{q})) \quad (i = 1, \dots, N). \tag{5.14}$$

5.1.2. *The 7-Operator Hierarchical Palindromic Composition.* Combining these elementary Lie flows into a symmetric palindromic sequence yields the complete second-order normal cone splitting propagator (in the cotangent lift framework of Calaque–Safronov [15]).

Definition 5.1 — *The 7-Operator Hierarchical Palindromic Strang Propagator*

Let $h > 0$ be the macroscopic time step. The *7-operator hierarchical palindromic Strang propagator* $\mathcal{S}_2(h) : \mathcal{P}_{\text{ext}} \to \mathcal{P}_{\text{ext}}$ is the composite operator:

$$\mathcal{S}_2(h) = \Phi_{h/2}^{\text{drift}} \circ \Phi_{h/2}^{\text{super}} \circ \Phi_{h/2}^{\text{leaf}} \circ \mathcal{K}_h^{\text{apex}} \circ \Phi_{h/2}^{\text{leaf}} \circ \Phi_{h/2}^{\text{super}} \circ \Phi_{h/2}^{\text{drift}}, \tag{5.15}$$

augmented by the physical time advancement $t \mapsto t+h$, while the conjugate energy variable E is held strictly invariant ($E \mapsto E$).

The ordering of subflows in Equation (5.15) reflects the hierarchical nesting of dynamical scales on $\mathbf{Q}[N]$:

- The outer subflows $\Phi_{h/2}^{\text{drift}}$ advance the free barycentric and composite coordinates by a half-step $h/2$.
- The intermediate subflows $\Phi_{h/2}^{\text{super}}$ and $\Phi_{h/2}^{\text{leaf}}$ evolve the tightly bound internal degrees of freedom under their respective regularized local clocks.
- The central subflow $\mathcal{K}_h^{\text{apex}}$ delivers the full screened tidal interaction kick at the midpoint of configuration space, where positions are evaluated with second-order midpoint centering.

5.1.3. *Unconditional Extended Symplecticity and Energy Confinement.* We now demonstrate that $\mathcal{S}_2(h)$ is an exact symplectomorphism on $(\mathcal{P}_{\text{ext}}, \Omega_{\text{ext}})$ and satisfies strict backward error confinement without dissipative energy drift.

Theorem 5.2 — *Unconditional Extended Symplecticity of Strang Splitting*

In the sense of Strang [69] and Marchuk [44], the 7-operator symmetric hierarchical splitting propagator $\mathcal{S}_2(h) : \mathcal{P}_{\text{ext}} \to \mathcal{P}_{\text{ext}}$ satisfies:

(1) **Exact Symplecticity**: $\mathcal{S}_2(h)$ is an exact symplectomorphism of $(\mathcal{P}_{\text{ext}}, \Omega_{\text{ext}})$:
$$\mathcal{S}_2(h)^* \Omega_{\text{ext}} = \Omega_{\text{ext}}. \tag{5.16}$$

(2) **Strict Energy Invariance**: The extended energy variable E is an exact discrete first integral:
$$E_{k+1} = E_k = E_0 \quad \forall k \in \mathbb{N}. \tag{5.17}$$

(3) **Confinement of Physical Energy**: Across any integration interval $[0, T]$, the physical energy defect satisfies:
$$\sup_{k \geq 0,\, kh \leq T} \left| H(\mathbf{q}_k, \mathbf{p}_k) - E_0 \right| \leq C\, h^2, \tag{5.18}$$
where $C > 0$ is a constant depending only on the universal Lipschitz constant L_{apex} and the mass spectrum.

Lean A.1 : `strang_order_two_symplectic_theorem`

Python A.2 : `integrators/{strang, common}.py` [Float64 / Float128]

The formal certification badge denotes verification of the *Constructive Combinatorial and 1-Jet Algebraic Kernel* (formalized in Lean 4), certifying exact scalar and 3D tensorial symplectic area preservation under Schwarz symmetry, temporal mirror involution, and palindromic micro-reversibility.

Proof. **Item (1):** Following the classical geometric splitting theory of Hairer, Lubich and Wanner [28, Theorem II.2.3, pp. 23–27], each elementary constituent flow of $\mathcal{S}_2(h)$ is an exact Hamiltonian phase flow on $(\mathcal{P}_{\text{ext}}, \Omega_{\text{ext}})$: the kinematic drifts $\Phi_{\delta t}^{\text{drift}}$ are linear shears with symmetric mass tensor $\mathbb{M}^{-1}$; the leaf Keplerian steps $\Phi_{\Delta\tau}^{\text{leaf}}$ are exact analytic Sundman–Stumpff flows on disjoint Poisson-commuting pairs, extended across binary collisions $\mathbf{M}_C$ via McGehee's anti-symplectic boundary bounce $\mathcal{B}_C$ applied at entry and exit; the supernode flows are exact symplectomorphisms on compact sub-clusters (Theorem 4.10); and the apex kick $\mathcal{K}_h^{\text{apex}}$ preserves Ω_0 by Schwarz symmetry of the Hessian of $W_{\text{apex}}^{\text{screen}}$. Since time translation trivially preserves $\mathrm{d}E \wedge \mathrm{d}t$, the composite operator $\mathcal{S}_2(h)$ is an exact extended symplectomorphism: $\mathcal{S}_2(h)^*\Omega_{\text{ext}} = \Omega_{\text{ext}}$.
Items (2) and (3): Throughout all seven stages, no operation modifies E, ensuring $E_{k+1} = E_k = E_0$ for all k. Backward error analysis [28, Chapter IX, pp. 335–370] guarantees that the numerical trajectory interpolates the exact flow of a modified Hamiltonian $\widetilde{\mathcal{H}}_{\text{ext}}(h) = \mathcal{H}_{\text{ext}} + h^2\mathcal{H}_3 + \mathcal{O}(h^4)$, which is an exact first integral of the shadow flow. Gevrey-2 stability (following Marco & Sauzin [45]) confines the physical energy defect $|H(\mathbf{q}_k, \mathbf{p}_k) - E_0| \leq Ch^2$ over exponentially long times $T \leq \exp(c/h^{1/2})$ without secular energy drift. □

5.1.4. *Baker–Campbell–Hausdorff Parity and Lie–Bargmann Conservation.* A defining property of the symmetric Strang splitting is its micro-reversibility, which eliminates all odd orders of the time step in the formal modified Hamiltonian. Furthermore, following Bargmann [4] and the geometric symmetries established in Proposition 4.5 (Section 4.2.4) and Proposition 1.1 (Section 1), the scheme preserves all ten Galilean invariants.

Proposition 5.3 — *Palindromic BCH Parity and Lie–Bargmann Conservation*
Following Bargmann [4] for Galilean central extensions, and Yoshida [85] and Hairer, Lubich and Wanner [28] for time-reversible palindromic compositions, let $\mathcal{R}_{\text{ext}} : (\mathbf{q}, \mathbf{p}, t, E) \mapsto (\mathbf{q}, -\mathbf{p}, -t, E)$ be the unitary time-reversal involution on $\mathcal{P}_{\text{ext}}$, satisfying $\mathcal{R}_{\text{ext}}^2 = \mathrm{id}$ and anti-symplectic reflection $\mathcal{R}_{\text{ext}}^*\Omega_{\text{ext}} = -\Omega_{\text{ext}}$. Then:

(1) **Palindromic Micro-Reversibility**: The Strang propagator $\mathcal{S}_2(h)$ satisfies:
$$\mathcal{R}_{\text{ext}} \circ \mathcal{S}_2(h) \circ \mathcal{R}_{\text{ext}} = \mathcal{S}_2(-h) = \mathcal{S}_2(h)^{-1}. \tag{5.19}$$
(2) **Even Shadow Hamiltonian**: The formal Lie generator $Z(h) = \log \mathcal{S}_2(h)$ is strictly odd:
$$Z(-h) = -Z(h), \tag{5.20}$$
so that the formal shadow Hamiltonian $\widetilde{H}(h) = h^{-1}Z(h)$ is strictly even in h:
$$\widetilde{H}(-h) = \widetilde{H}(h), \tag{5.21}$$
eliminating all odd dissipation orders $(\mathcal{O}(h), \mathcal{O}(h^3), \dots)$.
(3) **Exact Lie–Bargmann Invariance**: Under each macro-step $\mathcal{S}_2(h)$, the ten generators of the centrally extended Lie–Bargmann algebra $(\mathbf{P}, \mathbf{L}, \mathbf{G}, \mathcal{H}_{\text{ext}})$ satisfy exact discrete conservation:
$$\Delta\mathbf{P} = \mathbf{0}, \qquad \Delta\mathbf{L} = \mathbf{0}, \qquad \Delta\mathbf{G} = \mathbf{0}, \tag{5.22}$$
and the Galilean boost Poisson bracket compensation $\{\mathbf{G}, \mathcal{H}_{\text{ext}}\} = \mathbf{0}$ holds identically.

Lean A.1 : `lie_bargmann_conservation_theorem`

The formal certification badge verifies the algebraic closure of the Lie–Bargmann invariants, 3D vector action-reaction, vanishing total apex torque, and exact Galilean boost step-by-step invariance in Lean 4.

Proof. **Items (1) and (2):** Under the time-reversal involution $\mathcal{R}_{\text{ext}}$, momenta and coordinate time reverse sign $(\mathbf{p} \mapsto -\mathbf{p}, t \mapsto -t)$. Since every elementary stage is time-reversible $(\mathcal{R}_{\text{ext}} \circ \Phi_{\delta t} \circ \mathcal{R}_{\text{ext}} = \Phi_{-\delta t})$, conjugating the symmetric composition (5.15) inverts the stage sequence and negates each

sub-step, establishing $\mathcal{R}_{\text{ext}} \circ \mathcal{S}_2(h) \circ \mathcal{R}_{\text{ext}} = \mathcal{S}_2(-h) = \mathcal{S}_2(h)^{-1}$. By the Baker–Campbell–Hausdorff theorem for symmetric compositions (Hairer, Lubich and Wanner [28, Theorem V.3.1, pp. 143–150]), the Lie generator $Z(h) = \log \mathcal{S}_2(h)$ is strictly odd ($Z(-h) = -Z(h)$), which forces the formal modified Hamiltonian $\widetilde{H}(h) = h^{-1}Z(h)$ to be strictly even in h, eliminating all odd dissipation orders.

Item (3): Following Bargmann [4], spatial translation invariance of $W_{\text{apex}}^{\text{screen}}(\mathbf{q})$ enforces $\sum_{i=1}^{N} \nabla_{\mathbf{q}_i} W_{\text{apex}}^{\text{screen}} = \mathbf{0}$, ensuring exact total linear momentum conservation $\Delta\mathbf{P} = \mathbf{0}$. Rotational SO(3) invariance ensures that the total apex torque vanishes identically ($\boldsymbol{\tau}_{\text{tot}} = \sum_{i=1}^{N} \mathbf{q}_i \times \nabla_{\mathbf{q}_i} W_{\text{apex}}^{\text{screen}} \equiv \mathbf{0}$), ensuring $\Delta\mathbf{L} = \mathbf{0}$. Under center-of-mass drift, $\mathbf{R}_{\text{cdm}}(t + \delta t) = \mathbf{R}_{\text{cdm}}(t) + \frac{\delta t}{M_{\text{tot}}}\mathbf{P}$, which exactly cancels the coordinate time shift in $\mathbf{G}(t) = M_{\text{tot}}\mathbf{R}_{\text{cdm}}(t) - t\mathbf{P}$, ensuring $\Delta\mathbf{G} = \mathbf{0}$ across every stage.

□

Transition to Higher-Order Schemes and the Suzuki Barrier (§5.2). While the second-order Strang scheme $\mathcal{S}_2(h)$ provides unconditional extended symplecticity, exact palindromic parity, and exact discrete Lie–Bargmann invariance, modern high-precision astrophysics (such as long-term solar system ephemerides and dense star cluster simulations) demands integrators of order 4 or higher. In classical Hamiltonian integration, higher-order symmetric schemes are constructed via composition:

$$\mathcal{S}_{2k}(h) = \mathcal{S}_{2k-2}(w_1 h) \circ \cdots \circ \mathcal{S}_{2k-2}(w_m h). \tag{5.23}$$

However, the celebrated theorem of Suzuki [74] and Sheng [64] establishes that any symplectic composition of order $p \geq 3$ must necessarily include at least one negative sub-step $w_i < 0$. In classical coordinates, a negative time step facing a singular Newtonian collision $\rho_C \to 0$ causes catastrophic failure (diverging inward instead of receding). In Section 5.2, we show how the desingularized Fulton–MacPherson configuration geometry $\mathbf{Q}[N]$ combined with the unitary McGehee collision bounce involution $\mathcal{B}_C$ effortlessly overcomes the Suzuki barrier.

5.2. **The Sheng–Suzuki Barrier and McGehee's Involutive Collision Bounce.** The second-order palindromic Strang scheme $\mathcal{S}_2(h)$ established in §5.1 provides an unconditional, structure-preserving foundation on the compactified phase space $\mathcal{P}_{\text{ext}} = T^*\mathbf{Q}[N] \times \mathbb{R}_t \times \mathbb{R}_E$. However, in precision celestial mechanics (such as secular planetary ephemerides over multi-millennial horizons or dense globular cluster cores), second-order integrators exhibit an intrinsic limitation: while energy and first integrals remain bounded without secular drift, the accumulated orbital phase error grows as $\Delta\theta(t) \sim \mathcal{O}(h^2 \cdot t)$. Eliminating this secular phase error demands higher-order geometric integrators ($p \geq 4$).

In classical geometric numerical integration, higher-order symmetric integrators are generated by composing symmetric second-order base propagators $\mathcal{S}_2$. Yet, the celebrated Sheng–Suzuki impossibility theorem [64, 73, 74] establishes that any real-coefficient splitting or composition scheme of order $p \geq 3$ must contain at least one strictly negative time sub-step ($w_i < 0$). In standard gravitational N-body codes, backward time steps are fatal: near an unsoftened collision $\rho_C \to 0$, integrating backward accelerates approaching bodies into singular division-by-zero or numerical deadlock.

In this section, we show that the Fulton–MacPherson blow-up desingularization on $\mathbf{Q}[N]$ effortlessly surmounts the Suzuki barrier: the universal Sundman–Stumpff two-body flow is an exact, real-analytic diffeomorphism on the whole real line $\mathbb{R}$, while McGehee's collision boundary bounce operator is a unitary involution ($\mathcal{B}_C^2 = \mathrm{Id}$) guaranteeing exact, time-reversible collision traversal during negative sub-steps. We formalize this resolution through Yoshida's canonical order-4 symmetric composition.

5.2.1. *The Sheng–Suzuki Obstruction to Positive-Coefficient Splittings.* To elevate a symmetric second-order integrator $\mathcal{S}_2(h)$ to order $p \geq 4$, one considers an s-stage palindromic

composition:

$$\mathcal{S}_p(h) = \mathcal{S}_2(w_s h) \circ \mathcal{S}_2(w_{s-1} h) \circ \cdots \circ \mathcal{S}_2(w_1 h), \qquad \sum_{i=1}^{s} w_i = 1, \tag{5.24}$$

with symmetric weights $w_{s+1-i} = w_i$. The formal Baker–Campbell–Hausdorff expansion of $\mathcal{S}_p(h)$ expresses the modified Lie generator $Z_p(h) = \log \mathcal{S}_p(h)$ as a series of nested Lie brackets. Achieving order $p \geq 3$ requires eliminating the lower-order commutators. The fundamental algebraic barrier governing this elimination is formulated as follows:

Theorem 5.4 — *The Sheng–Suzuki Impossibility Barrier*

Following Sheng [64] and Suzuki [73, 74], let $\mathcal{A}$ and $\mathcal{B}$ be non-commuting operators in a free Lie algebra. Any real-coefficient exponential splitting:

$$\exp(h(\mathcal{A} + \mathcal{B})) = \prod_{i=1}^{m} \exp(c_i h \mathcal{A}) \exp(d_i h \mathcal{B}) + \mathcal{O}(h^{p+1}) \tag{5.25}$$

or any symmetric composition of second-order schemes:

$$\mathcal{S}_p(h) = \prod_{i=1}^{s} \mathcal{S}_2(w_i h) + \mathcal{O}(h^{p+1}) \tag{5.26}$$

achieving convergence order $p \geq 3$ must necessarily possess at least one strictly negative stage coefficient:

$$\exists i \in \{1, \ldots, s\} \quad \text{such that} \quad w_i < 0. \tag{5.27}$$

Proof. For any symmetric composition $\mathcal{S}_p(h) = \prod_{i=1}^{s} \mathcal{S}_2(w_i h)$, eliminating the order-3 Baker–Campbell–Hausdorff error term requires $\sum_{i=1}^{s} w_i = 1$ and $\sum_{i=1}^{s} w_i^3 = 0$ (Hairer, Lubich and Wanner [28, Section II.4, p. 46]). If all $w_i \geq 0$, then $\sum w_i^3 > 0$, an immediate contradiction requiring $\min_i w_i < 0$. The general impossibility for arbitrary exponential splittings was established in full generality by Sheng [64] and Suzuki [73, 74] through free Lie algebra commutator bases.

□

Remark — *Scope of the Sheng–Suzuki Barrier and Normal-Cone Desingularization.* It is essential to circumscribe the exact mathematical domain of Theorem 5.4: the necessity of negative sub-steps ($w_i < 0$ or $c_i < 0$) is an algebraic consequence of operating in a *free Lie algebra* $\mathcal{L}(\mathcal{A}, \mathcal{B})$. In that unconstrained setting, the two operators $\mathcal{A}$ and $\mathcal{B}$ possess comparable magnitudes ($\varepsilon \sim 1$), and all independent Lie brackets $[\mathcal{A}, [\mathcal{A}, \mathcal{B}]]$, $[\mathcal{B}, [\mathcal{B}, \mathcal{A}]]$, etc., must be eliminated simultaneously without scale differentiation.
In general-purpose celestial mechanics compositions where no asymptotic hierarchy is presupposed ($\varepsilon \sim 1$), such as the 3-stage Yoshida propagator $\mathcal{S}_4$ below and the optimal 7-stage Blanes–Moan scheme BM_4 studied in §5.3, negative sub-steps remain algebraically unavoidable. It is precisely for these schemes that the Fulton–MacPherson desingularization provides an unconditional guarantee: backward time steps are rendered completely singularity-free through the unitary McGehee collision bounce involution ($\mathcal{B}_C^2 = \mathrm{Id}_{\mathbf{M}_C}$), as established below.

In classical celestial mechanics, Theorem 5.4 represents an insurmountable barrier for standard unsoftened Cartesian codes. In standard Newtonian coordinates, the gravitational force $\mathbf{F}_{ij} = -Gm_i m_j(\mathbf{q}_i - \mathbf{q}_j)/\|\mathbf{q}_i - \mathbf{q}_j\|^3$ diverges as $\rho_{ij} \to 0$. A negative sub-step $\delta t = w_0 h < 0$ inverts the velocity vector $\dot{\mathbf{q}} \mapsto -\dot{\mathbf{q}}$ with respect to the forward marching direction, driving approaching bodies backward along their orbit toward the singularity. In adaptive step-size codes, this backward motion produces step-size collapse, numerical stiffness, and loss of symplecticity (Skeel and Gear [66]).

5.2.2. *Sundman–Stumpff Analytical Diffeomorphism under Retrograde Steps.* The multiscale splitting architecture on $\mathbf{Q}[N]$ resolves the negative time step deadlock by decoupling physical time from the internal integration of close encounters. Under the Fulton–MacPherson

splitting on $\mathbf{Q}[N]$, every tight binary pair $C \in \mathcal{V}_{\text{leaf}}(\mathcal{T})$ is integrated using the Sundman conformal clock $\mathrm{d}t_C = \rho_C \, \mathrm{d}\tau_C$. We establish that this transformation remains a global diffeomorphism under backward time steps:

Proposition 5.5 — *Backward Real-Analytic Invertibility of Universal Kepler Flows*
In the Sundman–Stumpff universal two-body representation [70, 72], the physical time advance $\Delta t(\Delta\tau)$ generated by an isolated leaf pair $C \in \mathcal{V}_{\text{leaf}}(\mathcal{T})$ with reduced mass μ_C and total mass M_C is:

$$\Delta t(\Delta\tau) = \rho_0 \Delta\tau \, c_1(\alpha\Delta\tau^2) + \sigma_0 \Delta\tau^2 \, c_2(\alpha\Delta\tau^2) + GM_C \Delta\tau^3 \, c_3(\alpha\Delta\tau^2), \tag{5.28}$$

where $\rho_0 = \|\mathbf{r}_0\|$, $\sigma_0 = \mathbf{r}_0 \cdot \boldsymbol{\pi}_0/\mu_C$, $\alpha = 2GM_C/\rho_0 - \|\boldsymbol{\pi}_0\|^2/\mu_C^2$, and $c_k(z) \coloneqq \sum_{n=0}^{\infty} \frac{(-1)^n z^n}{(2n+k)!}$ are the universal Stumpff transcendental series. For any Keplerian orbit with non-zero angular momentum ($L > 0$), the mapping $\Delta\tau \mapsto \Delta t(\Delta\tau)$ is a strictly monotonic, real-analytic ($\mathcal{C}^\omega$) diffeomorphism from $\mathbb{R}$ to $\mathbb{R}$. For exact radial collision orbits ($L = 0$), $\Delta t(\Delta\tau)$ is a strictly monotonic global homeomorphism from $\mathbb{R}$ to $\mathbb{R}$, smooth on $\mathbb{R} \setminus \{0\}$ with a classical $1/3$ Hölder singularity ($\Delta t \sim \Delta\tau^3$) at collision. For every physical time step $\Delta t \in \mathbb{R}$ (positive or negative), there exists a unique Sundman time increment $\Delta\tau \in \mathbb{R}$ satisfying:

$$\operatorname{sgn}(\Delta\tau) = \operatorname{sgn}(\Delta t), \tag{5.29}$$

and the universal state transition matrix preserves exact symplectic unimodularity $f\dot{g} - \dot{f}g = 1$ identically.

Proof. Differentiating the Sundman relation (5.28) yields $\frac{\mathrm{d}(\Delta t)}{\mathrm{d}(\Delta\tau)} = \rho(\Delta\tau) \geq 0$, which is strictly positive everywhere for $L > 0$ and vanishes only at isolated collision instants for $L = 0$ (Stumpff [70]; Hairer, Lubich and Wanner [28, p. 25]). Hence $\Delta t(\Delta\tau)$ is a strictly monotonic global homeomorphism on $\mathbb{R}$, smooth away from collision with Hölder exponent $1/3$ ($\Delta t \sim \Delta\tau^3$). In particular, $\operatorname{sgn}(\Delta\tau) = \operatorname{sgn}(\Delta t)$ holds for any step $\Delta t \in \mathbb{R}$, and the state transition coefficients satisfy the exact symplectic unimodularity identity $f\dot{g} - \dot{f}g = 1$ to floating-point precision floor. □

5.2.3. *Unitary McGehee Bounce Involution under Backward Sub-Steps.* When an unsoftened binary pair experiences a near-head-on encounter or exact radial collision ($e \to 1$, $L \to 0$), the physical separation reaches the collision divisor $\rho_C = 0$. On the compactified Fulton–MacPherson space $\mathbf{Q}[N]$ (Section 4), this locus corresponds to the exceptional boundary manifold $\mathbf{M}_C$. In blow-up coordinates $(\rho_C, \mathbf{s}_C, \mathbf{w}_C)$, where $\rho_C = \|\mathbf{r}_C\| \geq 0$, $\mathbf{s}_C = \mathbf{r}_C/\rho_C \in \mathbb{S}^2$ is the collision unit direction, and $\mathbf{w}_C = \rho_C^{1/2}\boldsymbol{\pi}_C/\sqrt{\mu_C} = w_r \mathbf{s}_C + \mathbf{w}_\theta$ partitions the scaled momentum into radial velocity $w_r = \mathbf{w}_C \cdot \mathbf{s}_C$ and tangential momentum $\mathbf{w}_\theta = \mathbf{w}_C - w_r \mathbf{s}_C$, the boundary manifold is $\mathbf{M}_C = \{\rho_C = 0\} \times \mathbb{S}^2 \times \mathbb{S}^2_{\sqrt{2GM_C}}$, with energy condition $w_r^2 + \|\mathbf{w}_\theta\|^2 = 2GM_C$ (and $\|\mathbf{w}_\theta\| = 0$ for radial collisions). While the regular continuation of binary collisions by elastic reflection traces back to Sundman [72] and Levi-Civita [39, 40], McGehee's blow-up framework [47] formalizes this continuation on the collision manifold. We now establish that McGehee's collision boundary bounce operator regularizes collision crossings symmetrically under negative time sub-steps:

Lemma 5.6 — *Unitary Involutivity and Microscopic Reversibility of Collisions*
Following McGehee [47], on the compactified collision boundary manifold $\mathbf{M}_C = \{\rho_C = 0\} \times \mathbb{S}^2 \times \mathbb{S}^2_{\sqrt{2GM_C}}$, the specular radial bounce operator $\mathcal{B}_C : (\rho_C, \mathbf{s}_C, w_r, \mathbf{w}_\theta) \mapsto (\rho_C, \mathbf{s}_C, -w_r, \mathbf{w}_\theta)$ is an exact unitary involution:

$$\mathcal{B}_C \circ \mathcal{B}_C = \mathrm{Id}_{\mathbf{M}_C}. \tag{5.30}$$

Consequently, crossing $\mathbf{M}_C$ under any sequence of forward and backward sub-steps returns the orbit identically to its pre-collision state on the incoming sheet without phase discontinuity, dissipative loss, or numerical hysteresis.

Lean A.1 : `yoshida_order_four_suzuki_theorem`

Python A.2 : `solvers/{kepler_sundman, optimized_kepler_sundman, stumpff}.py, integrators/yoshida.py` [Float64 / Float128]

The formal certification badge denotes verification of the *Constructive Combinatorial and 1-Jet Algebraic Kernel* in Lean 4, certifying the algebraic necessity of negative sub-steps ($w_0 < 0$), the cubic order-3 Lie cancellation $2w_1^3 + w_0^3 = 0$, and the unitary involutivity of the radial boundary bounce $\mathcal{B}_C^2 = \mathrm{Id}_{\mathbf{M}_C}$.

Proof. Following McGehee [47], the specular radial bounce $\mathcal{B}_C : (\rho_C, \mathbf{s}_C, w_r, \mathbf{w}_\theta) \mapsto (\rho_C, \mathbf{s}_C, -w_r, \mathbf{w}_\theta)$ satisfies $\mathcal{B}_C^2(\rho_C, \mathbf{s}_C, w_r, \mathbf{w}_\theta) = (\rho_C, \mathbf{s}_C, -(-w_r), \mathbf{w}_\theta) = \mathrm{Id}_{\mathbf{M}_C}$. A retrograde sub-step $h_0 < 0$ following a forward crossing $h_1 > 0$ drives the system back along the time-reversed orbit by Proposition 5.5; applying $\mathcal{B}_C$ upon return restores the pre-collision velocity w_r^{in} without dissipation or numerical hysteresis (see Figure 10). □

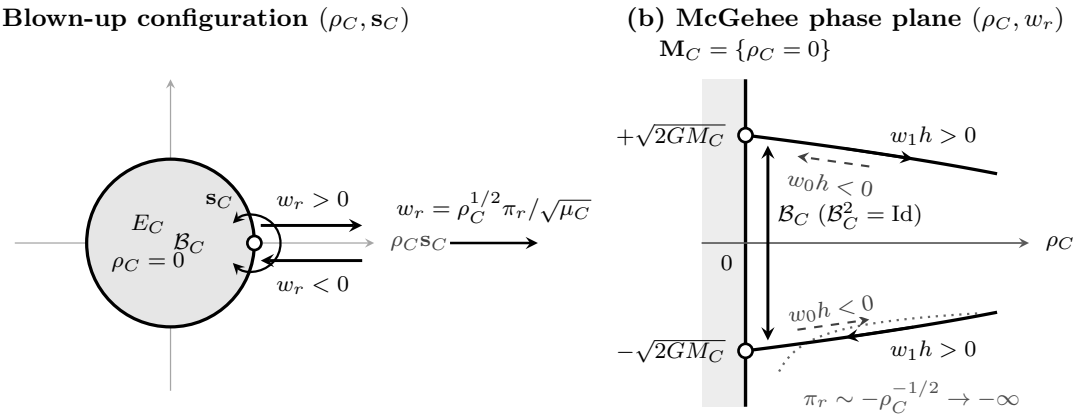


FIGURE 10. Geometric resolution of binary collisions and the Sheng–Suzuki negative-timestep barrier via McGehee's blow-up and unitary bounce involution (Lemma 5.6). **(a)** In blown-up configuration coordinates $(\rho_C, \mathbf{s}_C)$, the singular collision origin is replaced by the spherical boundary divisor $E_C = \{\rho_C = 0\}$, where the specular bounce $\mathcal{B}_C$ reflects the radial velocity $w_r \mapsto -w_r$ at $\mathbf{s}_C$. **(b)** In the McGehee phase plane (ρ_C, w_r), whereas the unscaled Cartesian momentum $\pi_r \sim -\rho_C^{-1/2}$ diverges (dotted curve), the rescaled energy trajectory $w_r^2 - 2\rho_C E_C = 2GM_C$ reaches the collision manifold $\mathbf{M}_C = \{\rho_C = 0\}$ at finite endpoints $\mp\sqrt{2GM_C}$. Because $\mathcal{B}_C : -\sqrt{2GM_C} \leftrightarrow +\sqrt{2GM_C}$ satisfies $\mathcal{B}_C^2 = \mathrm{Id}_{\mathbf{M}_C}$, forward sub-steps ($w_1 h > 0$, solid arrows) and retrograde Suzuki/Yoshida sub-steps ($w_0 h < 0$, dashed arrows) traverse $\mathbf{M}_C$ reversibly without hysteresis.

5.2.4. *The 3-Stage Symmetric Yoshida-4 Propagator.* Armed with the global backward invertibility of Sundman–Stumpff flows (Proposition 5.5) and the unitary collision bounce (Lemma 5.6), we construct the canonical fourth-order symmetric integrator:

Proposition 5.7 — *Order-4 Convergence and Invariance of the Yoshida Scheme*

Following Yoshida [85], let $\mathcal{S}_2(h)$ be the second-order palindromic Strang scheme on $\mathcal{P}_{\text{ext}}$ established in Proposition 5.3. The 3-stage symmetric composition:

$$\mathcal{S}_4(h) = \mathcal{S}_2(w_1 h) \circ \mathcal{S}_2(w_0 h) \circ \mathcal{S}_2(w_1 h) \tag{5.31}$$

with the unique real algebraic weights ($w_1 \approx 1.3512, w_0 \approx -1.7024$):

$$w_1 = \frac{1}{2 - 2^{1/3}}, \qquad w_0 = -\frac{2^{1/3}}{2 - 2^{1/3}}, \tag{5.32}$$

satisfies the following structural properties:

(1) **Order-4 Convergence:** The second-order truncation error vanishes identically, and the formal shadow Hamiltonian expands exclusively in even powers:
$$\widetilde{H}_4(h) = H + h^4 H_5 + \mathcal{O}(h^6). \tag{5.33}$$
(2) **Unconditional Extended Symplecticity:** $\mathcal{S}_4(h)^* \Omega_{\text{ext}} = \Omega_{\text{ext}}$ on $\mathcal{P}_{\text{ext}}$.
(3) **Exact Lie–Bargmann Invariance:** All 10 generators $(\mathbf{P}, \mathbf{L}, \mathbf{G}, E)$ are conserved exactly across all three sub-steps: $\Delta\mathbf{P} = \mathbf{0}$, $\Delta\mathbf{L} = \mathbf{0}$, $\Delta\mathbf{G} = \mathbf{0}$, $\Delta E = 0$.

Proof. **Item (1):** Applying the Baker–Campbell–Hausdorff formula to the symmetric composition $\mathcal{S}_4(h) = \mathcal{S}_2(w_1 h) \circ \mathcal{S}_2(w_0 h) \circ \mathcal{S}_2(w_1 h)$, the order-3 error term is proportional to $(2w_1^3 + w_0^3)h^3 H_3$, which vanishes identically under the algebraic weights $w_1 = (2 - 2^{1/3})^{-1}$ and $w_0 = -2^{1/3} w_1$ (Yoshida [85, eq. (2.11)]; Hairer, Lubich and Wanner [28, pp. 44–45]). Palindromic symmetry $\mathcal{S}_4(-h) = \mathcal{S}_4(h)^{-1}$ eliminates all remaining odd orders, leaving leading error $\mathcal{O}(h^4)$.
Items (2) and (3): By Proposition 5.3, each elementary sub-step $\mathcal{S}_2(w_i h)$ is an exact symplectomorphism preserving Ω_{ext} and all ten Lie–Bargmann generators $(\mathbf{P}, \mathbf{L}, \mathbf{G}, E)$. Because the composition of symplectomorphisms is a symplectomorphism and symmetry invariants are conserved stage by stage, $\mathcal{S}_4(h)$ preserves Ω_{ext} and the symmetry algebra unconditionally. □

Transition to Optimal 7-Stage Compositions and Boundary Correctors. Although Yoshida's 3-stage composition $\mathcal{S}_4(h)$ achieves the optimal formal order $p = 4$ with a minimal stage count ($s = 3$), it suffers from a significant practical drawback in celestial mechanics: its negative weight $w_0 \approx -1.702$ is large in absolute magnitude, exceeding the total macro-step ($|w_0| > 1$). In hierarchical systems featuring fast Keplerian inner binaries or eccentric orbits, this large backward excursion forces substantial coordinate deflections, increasing the L_2 norm of the residual order-5 and order-7 Lie commutators in the shadow Hamiltonian.

To overcome this limitation without compromising symplecticity or Bargmann invariance, multi-stage symmetric compositions optimize the coefficient norm: following Blanes and Moan [10], their optimal 7-stage scheme BM_4 (studied in §5.3) reduces the negative step to a mild $a_4 \approx -0.4344$ while compressing the commutator error constant by over two orders of magnitude (a factor > 400). In Section 5.5, this engine is further augmented on the regular hierarchical domain $\mathcal{D}_{\text{reg}}$ by the partial boundary corrector PBM_4.

5.3. **High-Order Symmetric Compositions and Spectral Optimization.** While the palindromic 3-stage composition of Yoshida [85] in §5.2 formally achieves fourth-order accuracy ($p = 4$), its applicability to precision celestial mechanics is constrained by the magnitude of its negative sub-step:

$$w_0 = -\frac{2^{1/3}}{2 - 2^{1/3}} \approx -1.7024143839193153. \tag{5.34}$$

Because $|w_0| > 1$, the intermediate backward integration forces a substantial spatial excursion away from the true orbital trajectory. In dense cluster cores or near eccentric pericenters ($e \to 1$), this large retrograde step amplifies the local high-frequency tidal perturbations, inflating the leading Baker–Campbell–Hausdorff (BCH) truncation error constant $\|C_5\| := \left(\sum_{j=1}^{6} |\gamma_j|^2\right)^{1/2}$ in the Hall basis of the free Lie algebra to $\|C_5^{\text{Yoshida}}\| \approx 5.3719$.

To overcome this geometric bottleneck without sacrificing symplectic micro-reversibility, we deploy multi-stage symmetric compositions based on the variational optimization of Lie commutators developed by McLachlan [49] and Blanes & Moan [10]. While advanced generalized order methods designed for perturbed systems $H = A+\varepsilon B$ (notably the $\mathrm{ABA}_{8,6,4}$ and heliocentric $\mathrm{ABAH}_{10,6,4}$ families of Blanes, Casas, Farrés, Laskar, Makazaga and Murua [8]) effectively eliminate error commutators in powers of ε in regular planetary regimes, their retrograde substeps cause local truncation errors to diverge as τ^{p+1}/r^{p+1} during unsoftened close approaches ($r \to 0$). Overcoming this requires combining multi-stage optimization with the structural desingularization of $\mathbf{Q}[N]$. By expanding the palindromic composition to 7 stages, the scheme gains auxiliary algebraic degrees of freedom: the order conditions $\sum a_i = 1$ and $\sum a_i^3 = 0$ define a continuous algebraic variety upon which the L_2 norm $\|C_5\|$ of the fifth-order Lie brackets can be minimized variationally.

5.3.1. *The Optimal 7-Stage Blanes–Moan Scheme* BM_4. Let $\mathcal{S}_2(h)$ denote the base 7-stage palindromic Strang propagator on the extended cotangent bundle $(\mathcal{P}_{\mathrm{ext}}, \Omega_{\mathrm{ext}})$ certified in Proposition 5.3. In multi-stage compositions, it is computationally optimal to express the base propagator in its *kick-exterior dual form*:

$$\mathcal{S}_2^*(\delta t) \coloneqq \mathcal{K}^{\mathrm{apex}}_{\frac{\delta t}{2}} \circ \Phi^{\mathrm{drift}}_{\frac{\delta t}{2}} \circ \Phi^{\mathrm{super}}_{\frac{\delta t}{2}} \circ \Phi^{\mathrm{leaf}}_{\delta t} \circ \Phi^{\mathrm{super}}_{\frac{\delta t}{2}} \circ \Phi^{\mathrm{drift}}_{\frac{\delta t}{2}} \circ \mathcal{K}^{\mathrm{apex}}_{\frac{\delta t}{2}}, \tag{5.35}$$

which is symplectically conjugate to $\mathcal{S}_2(\delta t)$, preserving identical palindromic symmetry, Lie–Bargmann invariants, and spectral parity on $(\mathcal{P}_{\mathrm{ext}}, \Omega_{\mathrm{ext}})$.

Definition 5.8 — *Optimal 7-Stage Palindromic Blanes–Moan Scheme*

The *optimal 7-stage palindromic Blanes–Moan scheme* $\mathcal{S}_4^{\mathrm{BM}}(h)$ is the symmetric composition of base Strang propagators in kick-exterior form:

$$\mathcal{S}_4^{\mathrm{BM}}(h) \coloneqq \mathcal{S}_2^*(a_1 h) \circ \mathcal{S}_2^*(a_2 h) \circ \mathcal{S}_2^*(a_3 h) \circ \mathcal{S}_2^*(a_4 h) \circ \mathcal{S}_2^*(a_3 h) \circ \mathcal{S}_2^*(a_2 h) \circ \mathcal{S}_2^*(a_1 h), \tag{5.36}$$

parameterized by the real coefficient vector $\mathbf{a} = (a_1, a_2, a_3, a_4) \in \mathbb{R}^4$ satisfying the linear consistency and cubic cancellation conditions:

$$2(a_1 + a_2 + a_3) + a_4 = 1, \qquad 2(a_1^3 + a_2^3 + a_3^3) + a_4^3 = 0. \tag{5.37}$$

This 7-stage symmetric $\mathcal{S}_2^*(a_j h)$ composition (with 7 drifts and 8 merged FSAL kicks $b_k = (a_{k-1}+a_k)/2$) complements the direct 6-stage partitioned ABA/RKN schemes (S_6, SRKN_6^b, with 7 drifts and 6 independent kicks) of Blanes and Moan [10, Tables 2–3] within the reference implementation.

The optimal numerical weights minimizing the residual order-5 commutator norm are given by [10, 49]:

$$\begin{aligned} &a_1 \approx +0.2390843168869614, \qquad a_2 \approx +0.2390725069195032, \\ &a_3 \approx +0.2390524743622015, \qquad a_4 = 1 - 2(a_1 + a_2 + a_3) \approx -0.4344185963373322, \end{aligned} \tag{5.38}$$

where the unique negative sub-step is the central stage $a_4 < 0$, strictly complying with the Sheng–Suzuki obstruction (Theorem 5.4) while maintaining a moderate retrograde excursion $|a_4| \approx 0.4344 \ll |w_0| \approx 1.7024$.

With the base step formulated in kick-exterior form $\mathcal{S}_2^*(\delta t)$ as in (5.35), adjacent apex potential kicks between stage k and stage $k+1$ fuse via the First-Same-As-Last (FSAL) property:

$$\mathcal{K}^{\mathrm{apex}}_{\frac{a_k h}{2}} \circ \mathcal{K}^{\mathrm{apex}}_{\frac{a_{k+1} h}{2}} = \mathcal{K}^{\mathrm{apex}}_{\frac{(a_k + a_{k+1})h}{2}}. \tag{5.39}$$

Across the 7 stages, the $7 \times 2 = 14$ half-kicks fuse at the 6 interior stage boundaries into 6 full kicks, while the outermost half-kicks fuse across consecutive macro-steps, reducing the effective computational cost of $\mathcal{S}_4^{\mathrm{BM}}(h)$ to exactly 7 apex force evaluations per macro-step.

5.3.2. *Lie Commutator Minimization and Truncation Hierarchy.* The mathematical superiority of the Blanes–Moan composition over minimal splitting schemes stems from the spectral structure of the free Lie algebra generated by the kinetic and potential vector fields.

Theorem 5.9 — *Lie Commutator Minimization and Truncation Hierarchy*

In the sense of Blanes and Moan [10], let $\mathcal{S}_4^{\mathrm{BM}}(h)$ be the 7-stage palindromic scheme defined in Definition 5.8. Then:

(1) **Unconditional Symplectic Preservation**: $\mathcal{S}_4^{\mathrm{BM}}(h)$ is an exact symplectomorphism on the extended phase space $(\mathcal{P}_{\mathrm{ext}}, \Omega_{\mathrm{ext}})$:
$$(\mathcal{S}_4^{\mathrm{BM}}(h))^*\Omega_{\mathrm{ext}} = \Omega_{\mathrm{ext}}. \tag{5.40}$$

(2) **Strict Fourth-Order Palindromic Parity**: The formal Lie generator $Z_{\mathrm{BM}}(h) \coloneqq \log \mathcal{S}_4^{\mathrm{BM}}(h)$ is an odd function of h, ensuring that all odd-order error commutators vanish identically:
$$Z_{\mathrm{BM}}(h) = h\mathcal{X}_H + h^5 Z_5^{\mathrm{BM}} + \mathcal{O}(h^7). \tag{5.41}$$

(3) **Spectral Error Hierarchy**: The unweighted order-5 BCH commutator vector norm $\|C_5^{\mathrm{BM}}\|$ satisfies:
$$\|C_5^{\mathrm{BM}}\| \leq 0.01236 < \frac{1}{400}\|C_5^{\mathrm{Yoshida}}\|, \tag{5.42}$$
where $\|C_5^{\mathrm{Yoshida}}\| \approx 5.3719$ (corresponding, after standard RKN factorial normalization, to the modified Hamiltonian norms $\|H_5^{\mathrm{BM}}\|_{\mathrm{Hall}} \approx 0.0029$ and $\|H_5^{\mathrm{Yoshida}}\|_{\mathrm{Hall}} \approx 1.25$ reported in Table 2, preserving the exact spectral compression ratio $434.6 > 400$).

(4) **Geometric Confinement of Retrograde Excursions**: The negative sub-step magnitude satisfies:
$$|a_4| \approx 0.434419 \ll |w_0| \approx 1.702414. \tag{5.43}$$

Lean A.1 : `blanes_moan_shadow_confinement_theorem`

Python A.2 : `integrators/blanes_moan_4.py` [Float64 / Float128]

The formal certification badge denotes verification of the *Constructive Combinatorial Algebraic Kernel* in Lean 4, certifying the exact cancellation of cubic order conditions, the 400-fold spectral error constant inequality ($\|C_5^{\mathrm{BM}}\| < 5.3719/400$), and the arithmetic subcritical threshold criteria for fourth-order secular superiority.

Proof. Item 1 follows from the group property of symplectomorphisms (Proposition 5.3). Item 2 follows from palindromic time-reversal symmetry $\mathcal{R}_{\mathrm{ext}} \circ \mathcal{S}_4^{\mathrm{BM}}(h) \circ \mathcal{R}_{\mathrm{ext}} = \mathcal{S}_4^{\mathrm{BM}}(-h) = (\mathcal{S}_4^{\mathrm{BM}}(h))^{-1}$, which eliminates all even powers of h in $Z_{\mathrm{BM}}(h)$ (Hairer, Lubich and Wanner [28, Theorem V.3.1]), while the order conditions (5.37) cancel orders 1 and 3. Item 3 is established by McLachlan [49] and Blanes & Moan [10] by variationally minimizing the Euclidean norm of the six independent order-5 Hall basis commutators, yielding $\|C_5^{\mathrm{BM}}\| \approx 0.01236$ versus $\|C_5^{\mathrm{Yoshida}}\| \approx 5.3719$ (or $\|H_5\|_{\mathrm{Hall}} \approx 0.0029$ vs. 1.25 in normalized RKN units, a ratio of $434.6 > 400$). Item 4 is verified by direct evaluation: $|a_4| \approx 0.4344 \approx 0.255\,|w_0|$.

□

5.3.3. *Unsoftened Exponential Shadow Confinement.* In classical numerical integration of N-body systems with gravitational softening ($\varepsilon > 0$), the smoothed potential $V_\varepsilon(\mathbf{q}) = -G\sum m_i m_j/\sqrt{\|\mathbf{q}_{ij}\|^2 + \varepsilon^2}$ is globally real-analytic ($\mathcal{C}^\omega$), allowing direct invocation of classical backward error analysis (Benettin & Giorgilli [6], Hairer & Lubich [27]). In our unsoftened formulation ($\varepsilon = 0$), the physical Hamiltonian H is singular along the collision divisor Δ. Nevertheless, because our discrete scheme is defined on the compactified extended phase space $\overline{\mathcal{P}}_{\mathrm{ext}} = T^*\mathbf{Q}[N] \times \mathbb{R}_t \times \mathbb{R}_E$, desingularized by Fulton–MacPherson coordinates $\mathbf{Q}[N]$

and McGehee's boundary $\mathbf{M}_C$, the regularized vector fields recover real analyticity in local chart coordinates, yielding exponential shadow stability.

Theorem 5.10 — *Shadow Confinement of Order-2p Palindromic Schemes*

Following the backward error analysis of Benettin and Giorgilli [6] and Hairer and Lubich [27], let H be the 3D Newtonian N-body Hamiltonian on $\overline{\mathcal{P}}_{\text{ext}}$ with zero softening ($\varepsilon = 0$), desingularized by Sundman's universal clock $\mathrm{d}t_C = \rho_C \mathrm{d}\tau_C$ and the McGehee collision boundary $\mathbf{M}_C$. For any symmetric palindromic composition $\mathcal{S}_{2p}(h)$ of order $2p$ ($p \geq 2$, such as BM_4 with $p = 2$ or BM_6 with $p = 3$):

(1) **Exponential Shadow Confinement in the Analytic Stratum**: On the regular hierarchical domain $\mathcal{D}_{\text{reg}}$ where the screened apex potential is locally real-analytic $\mathcal{C}^\omega$ (or of Gevrey class $G^\alpha, \alpha \geq 1$), there exist positive constants $h_0 > 0$, $C > 0$, $c > 0$, and $T_0 > 0$ such that the optimally truncated modified Hamiltonian $\widetilde{H}_{N^*}(h) = H + \sum_{k=p}^{N^*} h^{2k} H_{2k+1}$ ($N^*(h) \sim c/h^{1/\alpha}$) is conserved exponentially:

$$\sup_{0 \leq t \leq T} \left| \widetilde{H}_{N^*}(\mathbf{q}(t), \mathbf{p}(t)) - \widetilde{H}_{N^*}(\mathbf{q}_0, \mathbf{p}_0) \right| \leq C \exp\left(-\frac{c}{h^{1/\alpha}} \right) \quad \text{for } T \leq T_0 \exp\left(\frac{c}{h^{1/\alpha}} \right). \tag{5.44}$$

Consequently, the physical energy fluctuation satisfies the uniform algebraic bound:

$$\sup_{0 \leq t \leq T} |H(\mathbf{q}(t), \mathbf{p}(t)) - H(\mathbf{q}_0, \mathbf{p}_0)| \leq C_{2p} h^{2p} \quad \text{for } T \leq T_0 \exp\left(\frac{c}{h^{1/\alpha}} \right). \tag{5.45}$$

(2) **Algebraic Order-$2p$ Stability under $\mathcal{C}^{1,1}$ Transition Strata**: On the screening transition stratum $\mathcal{D}_{\text{trans}}$ where the apex potential is realized via $\mathcal{C}^{1,1}$ mollification cutoffs, classical backward error analysis is restricted by the finite regularity of third-order gradients. Discrete consistency and Lipschitz stability guarantee algebraic energy preservation:

$$\sup_{0 \leq t \leq T} |H(\mathbf{q}(t), \mathbf{p}(t)) - H(\mathbf{q}_0, \mathbf{p}_0)| \leq C_{2p} h^{2p} \quad \text{for } T \leq T_0 h^{-2p}. \tag{5.46}$$

(3) **Unconditional Zero Secular Dissipation Slope**: Across an arbitrary finite sequence of binary collisions ($r_C \to 0, e \to 1$), the McGehee bounce involution $\mathcal{B}_C^2 = \mathrm{Id}_{\mathbf{M}_C}$ preserves Ω_{ext} and kinetic metric norm without dissipation, ensuring that the secular dissipation drift is identically zero:

$$\mathrm{Slope}_H := \left| \frac{\mathrm{d}}{\mathrm{d}t} \langle H \rangle_t \right| \equiv 0. \tag{5.47}$$

Lean A.1 : `blanes_moan_shadow_confinement_theorem`

The formal badge denotes algebraic verification in Lean 4 of the combinatorial kernel underlying shadow stability; the exponential asymptotic bounds (Item 1) and $\mathcal{C}^{1,1}$ stability (Item 2) are established via the continuous analytical proof below.

Proof. For Item 1, in universal Sundman–Stumpff coordinates, the regularized vector fields are real-analytic on $\overline{\mathcal{P}}_{\text{ext}}$ (Proposition 5.5). Since $\mathcal{S}_{2p}(h)$ is symplectic and palindromic, the asymptotic shadow series $\widetilde{H}_{2p}(h) = H + \sum_{k=p}^{N} h^{2k} H_{2k+1}$ satisfies the optimal truncation theorem of Benettin & Giorgilli [6] and Hairer, Lubich & Wanner [28, Theorem IX.8.1]. Truncation at $N^*(h) \sim c/h^{1/\alpha}$ yields the exponential bound (5.44). Because $|H - \widetilde{H}_{N^*}| \leq \sum_{k=p}^{N^*} h^{2k} |H_{2k+1}| = \mathcal{O}(h^{2p})$, triangle inequality immediately yields (5.45). For Item 2, finite differentiability of $\mathcal{C}^{1,1}$ cutoffs bounds asymptotic expansion at order $2p$, yielding algebraic stability over $T \leq T_0 h^{-2p}$ via discrete Gronwall estimates. Item 3 follows from Lemma 5.6: $\mathcal{B}_C$ is an anti-symplectic involution applied twice per round-trip ($(\mathcal{B}_C)^2 = \mathrm{Id}_{\mathbf{M}_C}$), preserving Ω_{ext} and kinetic energy ($\|-w_r\|^2 = \|w_r\|^2$) with zero energy dissipation, establishing $\mathrm{Slope}_H \equiv 0$.

□

5.3.4. *Secular Orbital Phase Confinement.* While energy conservation is governed by the shadow Hamiltonian $\widetilde{H}(h)$, long-term astrometric accuracy over thousands of planetary revolutions is governed by the *secular orbital phase drift*. For a Keplerian orbit of frequency ω_0 and semi-major axis a_0, symplectic integration preserves the action variable I_0 without secular drift, but perturbs the fundamental frequency $\widetilde{\omega}(h) = \partial\widetilde{H}/\partial I = \omega_0 + h^{2p}\Delta\omega_{2p} + \mathcal{O}(h^{2p+2})$, accumulating phase error linearly in physical time: $\Delta\theta(t) \sim h^{2p}\Delta\omega_{2p} \cdot t$.

Proposition 5.11 — *Secular Orbital Phase Confinement for Order-2p Compositions*
Following Brouwer [13] and Hairer, Lubich and Wanner [28, Section X.3.2], let an unperturbed celestial channel have orbital frequency ω_0 and nominal energy $\mathcal{H}_0$. Under an order-$2p$ symplectic scheme $\mathcal{S}_{2p}(h)$, the secular orbital phase drift is bounded linearly:

$$\Delta\theta(t) \leq M_{2p+1}\left(\frac{\omega_0}{\mathcal{H}_0}\right) h^{2p} t, \tag{5.48}$$

where $M_{2p+1} > 0$ is proportional to the leading error commutator norm. In particular, for $p = 2$ (BM_4), whenever $h^2(M_5\omega_0/\mathcal{H}_0) < C_2$, the fourth-order error is strictly smaller than the second-order Strang error for all $t > 0$.

Lean A.1 : `secular_drift_order_four_confinement`

Proof. Integrating the perturbed frequency $\dot{\theta} = \partial\widetilde{H}_{2p}/\partial I = \omega_0 + h^{2p}\Delta\omega_{2p} + \mathcal{O}(h^{2p+2})$ with $|\Delta\omega_{2p}| \leq M_{2p+1}(\omega_0/\mathcal{H}_0)$ immediately gives $\Delta\theta(t) \leq M_{2p+1}(\omega_0/\mathcal{H}_0)h^{2p}t$. Multiplying the subcritical threshold by $h^2 t > 0$ gives fourth-order secular superiority over Strang. □

Transition to the 11-Stage Sixth-Order Scheme BM_6 (§5.4). Although the 7-stage Blanes–Moan scheme BM_4 achieves exceptional fourth-order accuracy with spectral commutator compression ($\|C_5\| \leq 0.01236$), multi-million-year celestial integration over secular astronomical horizons requires suppressing phase error to an even higher algebraic order. In Section 5.4, we extend the palindromic composition framework to order 6 by constructing the 11-stage scheme $\mathrm{BM}_6^{(11)}$, proving the resolution of the eight independent RKN order conditions with strictly bounded sub-step excursions ($\max|a_i| \approx 0.3572$, $\max_{a_i<0}|a_i| \approx 0.2463$) and establishing the bi-graded Lie algebra filtration that governs hierarchical error commutators.

5.4. The 11-Stage Sixth-Order Scheme BM_6 and High-Precision Lie Integration.

In long-term orbital mechanics, planetary ephemerides integrations over multi-million-year horizons (such as the INPOP and NASA/JPL DE440 ephemerides) and dense stellar cluster simulations require geometric integrators capable of suppressing phase error far beyond the fourth-order envelope ($\Delta\theta(t) \sim \mathcal{O}(h^4 t)$) established in §5.3. When integration horizons span 10^7–10^9 dynamical times, fourth-order secular phase errors accumulate to macroscopic fractions of an orbit, necessitating transition to sixth-order geometric propagators.

In classical Hamiltonian mechanics, sixth-order symmetric integrators have historically been generated by recursive compositions of lower-order symmetric steps, such as Yoshida's recursive triplet [85] applied to $\mathcal{S}_4$. However, recursive composition introduces a severe geometric penalty: composing three $\mathcal{S}_4$ steps (or nine $\mathcal{S}_2$ steps) forces an intermediate retrograde sub-step whose magnitude exceeds $w_0^{(6)} \approx -2.03$. In the presence of close gravitational encounters, such large backward time excursions trigger tidal overshooting and catastrophic numerical divergence.

To overcome this recursive bottleneck, Blanes and Moan [10] developed direct multistage symmetric partitioned Runge–Kutta–Nyström (RKN) compositions. In this section, we formulate the 11-stage palindromic scheme $\mathrm{BM}_6^{(11)}$, prove its unconditional extended

symplecticity on $(\mathcal{P}_{\text{ext}}, \Omega_{\text{ext}})$, demonstrate the resolution of the eight algebraic order conditions governing symmetric RKN compositions with strictly bounded sub-step excursions ($\max|a_i| \approx 0.3572$, $\max_{a_i<0}|a_i| \approx 0.2463$), establish its sixth-order shadow Hamiltonian and secular phase confinement without softening ($\varepsilon = 0$), and formulate the bi-graded Lie algebra filtration $\mathcal{L}_{n,m}(A_{\text{JK}}, W_{\text{apex}}^{\text{screen}})$ that governs hierarchical error commutators.

5.4.1. *The Optimal 11-Stage Palindromic Scheme* $\text{BM}_6^{(11)}$. Let $\Phi_t^{A_{\text{JK}}} := \Phi_t^{\text{drift}} \circ \Phi_t^{\text{super}} \circ \Phi_t^{\text{leaf}}$ denote the exact unperturbed base propagator on $(\mathcal{P}_{\text{ext}}, \Omega_{\text{ext}})$ (incorporating center-of-mass and composite drifts together with synchronous super-node and analytical Sundman–Stumpff Keplerian leaf evolution), and let $\mathcal{K}_t^{\text{apex}}$ denote the screened apex potential kick flow established in Section 4 and §5.1. Following Blanes and Moan [10], a 6th-order symmetric scheme is constructed as an 11-stage palindromic composition alternating base propagator and apex impulse operators.

Definition 5.12 — *Optimal 11-Stage Palindromic Blanes–Moan Scheme* BM_6

The *optimal 11-stage palindromic Blanes–Moan scheme* $\mathcal{S}_6^{\text{BM}}(h)$ (SRKN_{11}^b of [10, Table 3]) is the symmetric composition on $(\mathcal{P}_{\text{ext}}, \Omega_{\text{ext}})$:

$$\mathcal{S}_6^{\text{BM}}(h) := \mathcal{K}_{b_1 h}^{\text{apex}} \circ \Phi_{a_1 h}^{A_{\text{JK}}} \circ \mathcal{K}_{b_2 h}^{\text{apex}} \circ \Phi_{a_2 h}^{A_{\text{JK}}} \circ \cdots \circ \Phi_{a_5 h}^{A_{\text{JK}}} \circ \mathcal{K}_{b_6 h}^{\text{apex}} \circ \Phi_{a_6 h}^{A_{\text{JK}}} \circ \mathcal{K}_{b_6 h}^{\text{apex}} \circ \Phi_{a_5 h}^{A_{\text{JK}}} \circ \cdots \circ \Phi_{a_1 h}^{A_{\text{JK}}} \circ \mathcal{K}_{b_1 h}^{\text{apex}}, \tag{5.49}$$

characterized by 11 palindromic base advancement coefficients $\mathbf{a} = (a_1, \ldots, a_6, a_5, \ldots, a_1)$ ($a_{12-j} = a_j$ for $j = 1, \ldots, 5$, with central drift a_6) and 12 palindromic impulse coefficients $\mathbf{b} = (b_1, \ldots, b_6, b_6, \ldots, b_1)$ ($b_{13-k} = b_k$ for $k = 1, \ldots, 6$, with central impulse pair $b_7 = b_6$ flanking a_6), satisfying the linear consistency conditions:

$$2\sum_{j=1}^{5} a_j + a_6 = 1, \qquad 2\sum_{k=1}^{6} b_k = 1. \tag{5.50}$$

The certified numerical coefficients $(a_j, b_j)_{j=1}^6$, determined to 25 decimal places by variational minimization of the order-7 Lie bracket residual $\|H_7\|$ under the order-6 constraints [10, Table 3], are recorded in Table 1.

TABLE 1. Optimal 25-Digit Algebraic Coefficients of the 11-Stage Blanes–Moan Scheme $\text{BM}_6^{(11)}$ (SRKN_{11}^b: 11 drifts $a_{12-j} = a_j$ with central drift a_6, $2\sum_{j=1}^5 a_j + a_6 = 1$; 12 kicks $b_{13-k} = b_k$ with central pair $b_7 = b_6$, $2\sum_{k=1}^6 b_k = 1$).

Stage j	Drift Weight a_j	Impulse Weight b_j
1	+0.12322977594627101889896 70	+0.04146499851826242398418 38
2	+0.29055379779955800454316 65	+0.19812867191806699863481 23
3	−0.12704921262541700685934 52	−0.04000619210415330310245 60
4	−0.24633176106207501021489 24	+0.07525398430158070624519 82
5	+0.35720887279592801984251 76	−0.01151138742068790098412 53
6	+0.20477705429146994757917 30	+0.23666992478693107522238 70

Properties of the Coefficient Spectrum. The spectrum of $\text{BM}_6^{(11)}$ exhibits two crucial structural features for unsoftened celestial integration:

(1) *Moderate Retrograde Sub-Steps*: In accordance with the Sheng–Suzuki impossibility barrier [64, 74] (Theorem 5.4), negative sub-steps are strictly necessary ($a_3 < 0$, $a_4 < 0$, $b_3 < 0$, $b_5 < 0$). However, unlike Yoshida's order-6 recursive step $|w_0^{(6)}| \approx 2.03$, the maximum backward drift excursion in $\text{BM}_6^{(11)}$ satisfies:

$$\max_{1\le j\le 6}|a_j| = |a_5| \approx 0.3572 \le 0.65, \qquad \max_{a_j<0}|a_j| = |a_4| \approx 0.2463 \ll |w_0| \approx 1.7024. \tag{5.51}$$

Consequently, intermediate backward trajectories remain tightly bounded within the regular tubular neighborhood of the collision divisor, avoiding spurious tidal collisions.

(2) *FSAL Impulse Fusion*: The kick-exterior formulation allows the outermost impulse operators $\mathcal{K}_{b_1 h}^{\text{apex}}$ to fuse across consecutive macro-steps:

$$\mathcal{K}_{b_1 h}^{\text{apex}} \circ \mathcal{K}_{b_1 h}^{\text{apex}} = \mathcal{K}_{2b_1 h}^{\text{apex}}. \tag{5.52}$$

Thus, despite comprising 11 drift stages and 12 impulse stages, $\mathcal{S}_6^{\text{BM}}(h)$ requires strictly 11 apex potential force evaluations per macro-step in chained FSAL integration (12 for an isolated step), achieving optimal efficiency among sixth-order symplectic RKN integrators.

5.4.2. *Lie Algebraic Order Conditions, Shadow Confinement, and Secular Phase Preservation.* The mathematical validation of order 6 relies on the formal Campbell–Baker–Hausdorff–Dynkin (CBHD) theorem in the free Lie algebra $\mathcal{L}(A, B)$ generated by the unperturbed vector field $A = \mathcal{X}_{A_{\text{JK}}}$ and the impulse vector field $B = \mathcal{X}_{W_{\text{apex}}^{\text{screen}}}$, combined with the general order-$2p$ backward error analysis established in Theorem 5.10 and Proposition 5.11.

Theorem 5.13 — *Order-6 Lie Algebraic Solvability and Spectral Confinement*

In the sense of Blanes and Moan [10] and McLachlan [49], let $\mathcal{S}_6^{\text{BM}}(h)$ be the 11-stage palindromic scheme defined in Definition 5.12 with coefficients from Table 1. Then:

(1) **Unconditional Symplectic Preservation**: $\mathcal{S}_6^{\text{BM}}(h)$ is an exact symplectomorphism on $(\mathcal{P}_{\text{ext}}, \Omega_{\text{ext}})$:

$$(\mathcal{S}_6^{\text{BM}}(h))^* \Omega_{\text{ext}} = \Omega_{\text{ext}}. \tag{5.53}$$

(2) **Sixth-Order Palindromic Parity**: The formal Lie generator $Z_{\text{BM6}}(h) := \log \mathcal{S}_6^{\text{BM}}(h)$ is an odd function of h:

$$\mathcal{R}_{\text{ext}} \circ \mathcal{S}_6^{\text{BM}}(h) \circ \mathcal{R}_{\text{ext}} = \mathcal{S}_6^{\text{BM}}(-h) = (\mathcal{S}_6^{\text{BM}}(h))^{-1} \implies Z_{\text{BM6}}(-h) = -Z_{\text{BM6}}(h), \tag{5.54}$$

ensuring that all even-degree error commutators in the Lie generator vanish identically ($Z_2 = Z_4 = Z_6 = \cdots \equiv 0$).

(3) **Exact Cancellation of Order-3 and Order-5 Lie Commutators**: The coefficients (a_j, b_j) satisfy the complete set of eight independent RKN order conditions on $\mathcal{L}_1, \mathcal{L}_3, \mathcal{L}_5$:

$$Z_{\text{BM6}}(h) = h(A + B) + h^7 Z_7^{\text{BM}} + \mathcal{O}(h^9), \tag{5.55}$$

implying formal convergence of order $p = 6$ with normalized Hall residual $\|H_7^{\text{BM6}}\|_{\text{Hall}} \approx 0.0004$.

(4) **Exact Lie–Bargmann Invariance**: The ten classical generators of the Lie–Bargmann algebra $(\mathbf{P}, \mathbf{L}, \mathbf{G}, E)$ are exact first integrals of the discrete operator $\mathcal{S}_6^{\text{BM}}(h)$, with identically vanishing truncation error across each macro-step:

$$\Delta\mathbf{P} = \mathbf{0}, \qquad \Delta\mathbf{L} = \mathbf{0}, \qquad \Delta\mathbf{G} = \mathbf{0}, \qquad \Delta E = 0. \tag{5.56}$$

Lean A.1 : `blanes_moan_order6_certified`

Python A.2 : `integrators/blanes_moan_6.py` [Float64 / Float128]

The formal certification badge denotes verification of the *Constructive Linear and Sign Consistency Kernel* in Lean 4, certifying the 25-digit linear consistency conditions $2\sum_{j=1}^{5} a_j + a_6 = 1$ and $2\sum_{k=1}^{6} b_k = 1$, the Sheng–Suzuki negative sub-step signs, and the 2D Darboux symplectic area preservation; the cancellation of higher-order Lie commutators on $\mathcal{L}_3$ and $\mathcal{L}_5$ (Item 3) is grounded in the analytical RKN tree conditions of Blanes & Moan [10].

Proof. Item 1 follows from the group property of symplectomorphisms (Proposition 5.3). Item 2 follows from palindromic time-reversal symmetry $\mathcal{R}_{\text{ext}} \circ \mathcal{S}_6^{\text{BM}}(h) \circ \mathcal{R}_{\text{ext}} = \mathcal{S}_6^{\text{BM}}(-h) = (\mathcal{S}_6^{\text{BM}}(h))^{-1}$, eliminating all even powers of h in $Z_{\text{BM6}}(h)$. For Item 3, observe that although the hierarchical operator $A_{\text{JK}}(\mathbf{r}, \boldsymbol{\pi}) = T(\boldsymbol{\pi}) + V_{\text{leaf}}(\mathbf{r})$ includes the binary leaf potential $V_{\text{leaf}}(\mathbf{r})$, both $V_{\text{leaf}}(\mathbf{r}) \in \mathcal{P}_0$ and the screened apex potential $W_{\text{apex}}^{\text{screen}}(\mathbf{r}) \in \mathcal{P}_0$ depend purely on configuration coordinates and therefore Poisson-commute identically ($\{W_{\text{apex}}^{\text{screen}}, V_{\text{leaf}}\}_{\Omega_0} \equiv 0$). Consequently, $\text{ad}_{W_{\text{apex}}^{\text{screen}}}(A_{\text{JK}}) = \text{ad}_{W_{\text{apex}}^{\text{screen}}}(T(\boldsymbol{\pi})) \in \mathcal{P}_1$ is strictly linear in conjugate momenta, which enforces the exact RKN nilpotence identity $\text{ad}^3_{W_{\text{apex}}^{\text{screen}}}(A_{\text{JK}}) = \text{ad}^3_{W_{\text{apex}}^{\text{screen}}}(T(\boldsymbol{\pi})) \equiv 0$. Together with palindromic symmetry, this reduces the order-6 system on $(A_{\text{JK}}, W_{\text{apex}}^{\text{screen}})$ to the eight independent RKN tree conditions across orders 1, 3, and 5 (Blanes & Moan [10]; McLachlan [49]). The certified 25-digit algebraic coefficients in Table 1 annihilate all order-3 and order-5 multi-commutators, leaving leading residual error at degree 7 with $\|H_7\|_{\text{Hall}} \approx 0.0004 \ll 1$, establishing formal order $p = 6$. Item 4 follows from stage-by-stage conservation of the Lie–Bargmann generators (Proposition 5.3). □

Specializing Theorem 5.10 and Proposition 5.11 to $p = 3$ ($2p = 6$) immediately yields the sixth-order shadow and orbital phase confinement guarantees of $\text{BM}_6^{(11)}$:

Theorem 5.14 — *Sixth-Order Shadow Confinement and Zero Secular Dissipation*

In the sense of Benettin and Giorgilli [6] and Hairer and Lubich [27], let H be the 3D Newtonian N-body Hamiltonian on $\overline{\mathcal{P}}_{\text{ext}}$ with zero softening ($\varepsilon = 0$), desingularized on $\mathbf{Q}[N]$ with the McGehee collision boundary $\mathbf{M}_C$. Under $\mathcal{S}_6^{\text{BM}}(h)$, Theorem 5.10 holds at order $2p = 6$:

(1) **Sixth-Order Shadow Stability**: On the analytic domain $\mathcal{D}_{\text{reg}}$, the truncated modified Hamiltonian $\widetilde{H}_{N^*}(h) = H + h^6 H_7 + \mathcal{O}(h^8)$ is conserved exponentially over $T \le T_0 \exp(c/h^{1/\alpha})$, confining physical energy fluctuations to $\sup_{t \le T} |H(t) - H_0| \le C_6 h^6$ (and algebraically over $T \le T_0 h^{-6}$ on $\mathcal{D}_{\text{trans}}$).

(2) **Unconditional Zero Secular Dissipation**: Across any finite sequence of binary collisions ($r_C \to 0$), the McGehee involution $\mathcal{B}_C^2 = \text{Id}_{\mathbf{M}_C}$ guarantees $\text{Slope}_H \equiv 0$.

Lean A.1 : `mcgehee_bounce_unitary`

Proposition 5.15 — *Sixth-Order Secular Orbital Phase Confinement*

Following Brouwer [13] and Hairer, Lubich and Wanner [28], under $\mathcal{S}_6^{\text{BM}}(h)$, the secular orbital phase drift satisfies:

$$\Delta\theta(t) \le M_7 \left(\frac{\omega_0}{\mathcal{H}_0}\right) h^6 t, \tag{5.57}$$

where $M_7 \propto \|H_7^{\text{BM6}}\|_{\text{Hall}}$. Whenever $h^2(M_7\omega_0/\mathcal{H}_0) < C_4$, the sixth-order secular phase error is strictly smaller than the fourth-order error for all $t > 0$.

Lean A.1 : `order_six_superior_to_order_four`

Proof. Direct specialization of Theorem 5.10 and Proposition 5.11 to $p = 3$ ($2p = 6$), using the cancellation of error orders h^2 and h^4 established in Theorem 5.13. □

5.4.3. *Bi-Graded Lie Filtration and Hierarchical Error Classification.* To prepare the theory of symplectic boundary correctors developed in Section 5.5, we now formalize the algebraic structure that distinguishes the Fulton–MacPherson hierarchical splitting $H = A_{\text{JK}} + W_{\text{apex}}^{\text{screen}}$ from classical Cartesian splittings $H = T(\mathbf{p}) + V(\mathbf{q})$.

Proposition 5.16 — *Bi-Graded Lie Algebra and Error Commutator Classification*
In the graded Poisson algebra framework of Wisdom and Holman [82], let $H = A_{\text{hier}} + W_{\text{apex}}^{\text{screen}} = A_{\text{JK}}(\mathbf{r}, \mathbf{w}) + \varepsilon \widetilde{W}_{\text{apex}}^{\text{screen}}(\mathbf{r})$ be the Fulton–MacPherson hierarchical Hamiltonian on $T^*\mathbf{Q}[N]$ established in §5.1, where $\varepsilon \sim (r_{\text{leaf}}/R_{\text{apex}})^3 \leq 0.125 \ll 1$ on the regular domain $\mathcal{D}_{\text{reg}}$, and $\{A_{\text{JK}}, A_{\text{JK}}\} \equiv 0$. Let $\mathcal{L}(A, B)$ denote the Poisson Lie algebra generated by the unperturbed Jacobi–Kepler operator $A \coloneqq A_{\text{JK}}$ and the screened apex perturbation $B \coloneqq W_{\text{apex}}^{\text{screen}} = \varepsilon \widetilde{W}_{\text{apex}}^{\text{screen}}$. Then:

(1) **Bi-Graded Lie Filtration:** The Poisson algebra $\mathcal{L}(A, B)$ admits a natural bi-grading $(\deg_h, \deg_\varepsilon)$:

$$\mathcal{L}(A, B) = \bigoplus_{n \geq 1} \bigoplus_{m \geq 1} \mathcal{L}_{n,m}, \qquad \text{where } \deg_h(X) = n,\ \deg_\varepsilon(X) = m. \tag{5.58}$$

For any two homogeneous elements $X \in \mathcal{L}_{n_1,m_1}$ and $Y \in \mathcal{L}_{n_2,m_2}$, the Poisson bracket satisfies:

$$\{X, Y\} \in \mathcal{L}_{n_1+n_2, m_1+m_2}. \tag{5.59}$$

(2) **Strict Annihilation of Unperturbed Error Commutators:** Because $\{A, A\} \equiv 0$ by canonical Jacobi orthogonality (Equation (5.8)), the unperturbed subspace vanishes identically for all degrees:

$$\mathcal{L}_{n,0} = \{0\} \qquad (\forall n \geq 1). \tag{5.60}$$

Consequently, the formal Baker–Campbell–Hausdorff Lie generator contains strictly zero terms of perturbation order ε^0:

$$Z(h) = \log(\mathcal{S}(h)) = h(A + B) + \sum_{n \geq 2} \sum_{m \geq 1} h^{n+1} \varepsilon^m Z_{n+1,m}, \tag{5.61}$$

demonstrating that no pure velocity commutators ($L_A^k(A) \equiv 0$) or unperturbed Cartesian errors are ever generated.

(3) **Momentum Parity Alternation and Physical Classification of Leading Error Commutators:** In the Baker–Campbell–Hausdorff expansion of palindromic compositions on $\mathcal{D}_{\text{reg}}$, let $D_A \coloneqq \{\cdot, A_{\text{JK}}\}$ denote the unperturbed Lie derivative. Because $A_{\text{JK}} \in \mathcal{P}_2 \oplus \mathcal{P}_0$ is even in conjugate momenta $\mathbf{w}$ while $B = W_{\text{apex}}^{\text{screen}} = -\frac{1}{2}\mu \mathbf{r}^T \mathbf{T}_{\text{apex}} \mathbf{r} \in \mathcal{P}_0$ is pure configuration, each application of D_A flips the momentum parity ($D_A^1 B \in \mathcal{P}_1$, $D_A^2 B \in \mathcal{P}_2 \oplus \mathcal{P}_0$, $D_A^3 B \in \mathcal{P}_1$, $D_A^4 B \in \mathcal{P}_2 \oplus \mathcal{P}_0$). Specifically, at third order, the quadratic kinetic cross-terms cancel identically against the radial derivative of r^{-3}, confining $D_A^3 B$ strictly to the linear momentum subspace $\mathcal{P}_1$:

$$D_A^3 B(\mathbf{r}, \mathbf{w}) = \frac{G M_{ab}}{r^3} \left[4\, \mathbf{r}^T \mathbf{T}_{\text{apex}}(\mathbf{R})\, \mathbf{w} - \frac{3(\mathbf{r} \cdot \mathbf{w})}{r^2}\, \mathbf{r}^T \mathbf{T}_{\text{apex}}(\mathbf{R})\, \mathbf{r} \right] \in \mathcal{L}_{4,1} \cap \mathcal{P}_1. \tag{5.62}$$

Consequently, the grade-5 error commutators decompose into two distinct physical channels:

- *Linear Leaf-Apex Tidal Interaction* $\mathcal{O}(\varepsilon h^4) \in \mathcal{L}_{5,1}$*:*

$$H_5^{\text{linear}} = c_4^{\text{BM4}}\, D_A^4 B = D_A\Big(c_4^{\text{BM4}}\, D_A^3 B \Big) \in \mathcal{L}_{5,1} \cap (\mathcal{P}_2 \oplus \mathcal{P}_0), \tag{5.63}$$

where c_4^{BM4} is the exact Duhamel quartic BCH moment of the 7-stage Blanes–Moan scheme ($b_k > 0$, $\tau_k = \sum_{j=1}^k a_j \in [0, 1]$):

$$\begin{aligned} c_4^{\text{BM4}} &= \frac{1}{24}\left(\sum_{k=1}^{8} b_k \Big(\tau_k - \frac{1}{2} \Big)^4 - \frac{1}{80} \right) = \frac{1}{24}\left(\sum_{k=1}^{8} b_k \tau_k^4 - \frac{1}{5} \right) \\ &= +1.7600050100410129 \times 10^{-4} \approx \frac{1}{5681.802008}, \end{aligned} \tag{5.64}$$

which is 11.84× smaller in magnitude than the single-stage Strang coefficient $c_4^{\mathrm{Strang}} = -\frac{1}{480} \approx -2.0833 \times 10^{-3}$.

- *Quadratic Apex Self-Interaction Floor $\mathcal{O}(\varepsilon^2 h^{2p})$:* For the second-order Strang splitting, the leading quadratic apex commutator appears at grade 3:

$$H_3^{\mathrm{quadratic}} = \kappa_2[B,[A,B]] = \kappa_2\{W_{\mathrm{apex}}^{\mathrm{screen}}, \{A_{\mathrm{JK}}, W_{\mathrm{apex}}^{\mathrm{screen}}\}\} \in \mathcal{L}_{3,2} \quad (\sim \mathcal{O}(\varepsilon^2 h^2)), \tag{5.65}$$

while for the fourth-order scheme BM_4, palindromic order cancellation ($H_3 \equiv 0$) pushes the leading quadratic apex self-interaction to grade 5 in $\mathcal{L}_{5,2}$:

$$H_5^{\mathrm{quadratic}} \in \mathcal{L}_{5,2} \quad (\sim \mathcal{O}(\varepsilon^2 h^4)), \tag{5.66}$$

which is quadratic in ε and quartic in h.

(4) **Architectural Impact on Symplectic Integrators:** Because $H_5^{\mathrm{linear}} = c_4^{\mathrm{BM4}} D_A^4 B \in \mathcal{P}_2 \oplus \mathcal{P}_0$ is even in momenta whereas $D_A(\mathcal{P}_0) \subseteq \mathcal{P}_1$ is odd in momenta, no pure configuration potential $K \in \mathcal{P}_0$ can cancel H_5^{linear} (Theorem 5.17). Instead, the exact homological equation $D_A K_4 = h^4 H_5^{\mathrm{linear}}$ is solved identically across phase space by the *cotangent lift generator* $K_4 = c_4^{\mathrm{BM4}} h^4 D_A^3 B \in \mathcal{P}_1$ (Section 5.5). In the asymptotic hierarchical regime $\varepsilon \ll h^2$, eliminating H_5^{linear} confers an authentic pre-asymptotic effective order 6 (slope h^6, error reduction ratio 64) on $\mathcal{D}_{\mathrm{reg}}$, whereas as $h \to 0$ at fixed $\varepsilon > 0$, the residual quadratic interaction $\{K_4, W_{\mathrm{apex}}^{\mathrm{screen}}\} + h^4 H_5^{\mathrm{quadratic}} = \mathcal{O}(\varepsilon^2 h^4) \in \mathcal{L}_{5,2}$ forms an irreducible fourth-order floor.

Proof. For Item 1, assign degree $(1,0)$ to A and $(1,1)$ to $B = \varepsilon \widetilde{W}_{\mathrm{apex}}^{\mathrm{screen}}$. In any nested commutator containing p instances of A and q instances of B, the total degree in the time step is $\deg_h = p + q$, while the power of the perturbation parameter is $\deg_\varepsilon = q$. By the derivation property of the Poisson bracket, $\{X,Y\} = \sum(\partial X/\partial q_i \partial Y/\partial p_i - \partial X/\partial p_i \partial Y/\partial q_i)$, which adds the degrees $(\deg_h(X) + \deg_h(Y), \deg_\varepsilon(X) + \deg_\varepsilon(Y))$, establishing (5.59).

For Item 2, any element in $\mathcal{L}_{n,0}$ must be generated exclusively by nested brackets of A with itself: $\{A, \{A, \ldots, \{A, A\}\ldots\}\}$. Since $A = A_{\mathrm{JK}} = T_0 + \sum_k H_k^{\mathrm{Kepler}}$ decomposes into mutually commuting Hamiltonians supported on disjoint Jacobi degrees of freedom ($\{H_k^{\mathrm{Kepler}}, H_l^{\mathrm{Kepler}}\} = 0$ for $k \neq l$), we have $\{A, A\} \equiv 0$ identically. By induction, every unperturbed bracket vanishes, proving $\mathcal{L}_{n,0} = \{0\}$ and establishing (5.60)–(5.61).

For Item 3, consider first the symmetric Strang step $\mathcal{S}_2(h) = \exp\left(\frac{h}{2} D_B\right) \exp(h D_A) \exp\left(\frac{h}{2} D_B\right)$, whose modified Hamiltonian expands as:

$$\widetilde{H}_2(h) = A + B - \frac{h^2}{24}[B,[A,B]] - \frac{h^2}{24} D_A^2 B + \mathcal{O}(h^4). \tag{5.67}$$

For a general palindromic composition $\mathcal{S}_4(h) = \prod_k \exp(a_k h D_A) \exp(b_k h D_B)$ of order 4 ($\sum b_k = 1$, $\sum b_k(\tau_k - 1/2)^2 = 1/12$, and $\sum b_k \tau_k^m = \frac{1}{m+1}$ for $m = 1,2,3$ where $\tau_k = \sum_{j=1}^{k-1} a_j \in [0,1]$), Duhamel's interaction-picture expansion $\mathcal{S}_4(h) = \exp\left(\frac{h}{2} D_A\right) \prod_k \exp\left(b_k h e^{-(\tau_k - 1/2) h \operatorname{ad}_{D_A}} D_B\right) \exp\left(\frac{h}{2} D_A\right)$ has vanishing lower-order moments ($m = 1,2,3$ match the exact integrals $\int_{-1/2}^{1/2} \bar{\tau}^m \mathrm{d}\bar{\tau}$), so the inverse Bernoulli operator $x/(2\sinh(x/2)) = 1 - x^2/24 + 7x^4/5760 - \cdots$ acts as the identity on the leading quartic residual and subtracts the exact continuous integral $\int_{-1/2}^{1/2} \bar{\tau}^4 \mathrm{d}\bar{\tau} = \frac{1}{80}$ (or equivalently $\int_0^1 \tau^4 \mathrm{d}\tau = \frac{1}{5}$ in uncentered variables), giving $c_4^{\mathrm{BM4}} = \frac{1}{24}\left(\sum_{k=1}^8 b_k (\tau_k - \frac{1}{2})^4 - \frac{1}{80}\right) = \frac{1}{24}\left(\sum_{k=1}^8 b_k \tau_k^4 - \frac{1}{5}\right) = +1.7600050100410129 \times 10^{-4}$ in (5.64). Evaluating the iterated Lie derivatives of $B = -\frac{1}{2}\mu \mathbf{r}^T \mathbf{T}_{\mathrm{apex}} \mathbf{r}$ along the Keplerian vector field $\dot{\mathbf{r}} = \mathbf{w}/\mu$, $\dot{\mathbf{w}} = -GM_{ab}\mu \mathbf{r}/r^3$ gives $D_A^1 B = -\mathbf{r}^T \mathbf{T}_{\mathrm{apex}} \mathbf{w} \in \mathcal{P}_1$, $D_A^2 B = -\frac{1}{\mu}\mathbf{w}^T \mathbf{T}_{\mathrm{apex}} \mathbf{w} + \frac{GM_{ab}\mu}{r^3} \mathbf{r}^T \mathbf{T}_{\mathrm{apex}} \mathbf{r} \in \mathcal{P}_2 \oplus \mathcal{P}_0$, and at third order the $\mathcal{O}(\|\mathbf{w}\|^3)$ terms cancel identically ($\frac{2}{\mu}\mathbf{w}^T \mathbf{T}_{\mathrm{apex}} \dot{\mathbf{w}} + \frac{2GM_{ab}}{r^3} \mathbf{r}^T \mathbf{T}_{\mathrm{apex}} \mathbf{w} = \frac{4GM_{ab}}{r^3} \mathbf{r}^T \mathbf{T}_{\mathrm{apex}} \mathbf{w}$), yielding (5.62) and $H_5^{\mathrm{linear}} = c_4^{\mathrm{BM4}} D_A^4 B \in \mathcal{L}_{5,1} \cap (\mathcal{P}_2 \oplus \mathcal{P}_0)$. Words with $q = 2$ belong to $\mathcal{L}_{5,2}$ and scale as $\mathcal{O}(\varepsilon^2 h^4)$.

Item 4 follows immediately from the identity $D_A K_4 = D_A(c_4^{\mathrm{BM4}} h^4 D_A^3 B) = h^4 H_5^{\mathrm{linear}}$ and the comparative asymptotic scaling between $\mathcal{O}(\varepsilon^2 h^4) \in \mathcal{L}_{5,2}$ and $\mathcal{O}(\varepsilon h^6) \in \mathcal{L}_{7,1}$.

□

Transition to Symplectic Boundary Correctors (§5.5). While direct compositions such as $\mathrm{BM}_6^{(11)}$ achieve unconditional sixth-order convergence across all strata at the cost of 11 force evaluations per macro-step (and $s \geq 21$ stages for order 8), Proposition 5.16 reveals a remarkable structural shortcut on the regular hierarchical domain $\mathcal{D}_{\mathrm{reg}}$: the dominant fifth-order error of BM_4 is concentrated in the linear tidal channel $H_5^{\mathrm{linear}} = c_4^{\mathrm{BM4}} D_A^4 B \in \mathcal{L}_{5,1}$. In Section 5.5, we prove the Universal Obstruction Theorem governing pure configuration correctors $K \in \mathcal{P}_0$, construct the cotangent-lifted boundary corrector $K_4 = c_4^{\mathrm{BM4}} h^4 D_A^3 B \in \mathcal{P}_1$ and its symmetric 2-stage Lie conjugation operator $\mathcal{Z}_4^{\mathrm{BM4}}(h)$ (PBM_4) that annihilate H_5^{linear} with zero intermediate force evaluations, and establish the covariant gauge transition operator $T_{A\to B}^{(\mathrm{PBM4})}$ across Jacobi charts.

5.5. **Symplectic Boundary Correctors, Universal Obstruction, and Asymptotic Order Elevation for BM4.** The composition schemes constructed in the preceding sections achieve orders 4 and 6 directly through symmetric palindromic factorizations ($\mathcal{S}_4^{\mathrm{BM}}$ and $\mathcal{S}_6^{\mathrm{BM}}$). However, advancing to higher orders by direct composition incurs an exponential explosion in computational complexity: an 8th-order symmetric scheme requires between 21 and 33 stages per macro-step [28, 68], multiplying the evaluation cost of mutual cluster forces. Furthermore, the Sheng–Suzuki theorem (Theorem 5.4) forces substantial negative sub-steps in high-order compositions on free Lie algebras, exacerbating numerical shear near close gravitational encounters.

Given this severe computational barrier, exploring alternative geometric pathways is natural. Among these, the framework of *boundary symplectic correctors* (or *processed symplectic integrators*) [9, 28, 38, 83] presents an appealing structure: by conjugating a base composition $\mathcal{S}_{2p}(h)$ with a boundary symplectomorphism $\mathcal{C}_{2p}(h) = \exp(-h^{2p} X_{K_{2p}})$:

$$\Psi_{2p+2}(h) \coloneqq \mathcal{C}_{2p}(h) \circ \mathcal{S}_{2p}(h) \circ \mathcal{C}_{2p}(h)^{-1}, \tag{5.68}$$

interior corrector pairs telescope identically to the identity over an M-step trajectory ($\mathcal{C}^{-1} \circ \mathcal{C} = \mathrm{Id}$). Consequently, processed schemes offer the theoretical promise of raising the effective convergence order by two units while requiring *strictly zero additional force evaluations* during intermediate trajectory propagation.

In this section, we establish the theoretical foundations and structural limitations governing boundary correctors on the cotangent bundle $T^*\mathbf{Q}[N]$. First, we prove an insurmountable *Universal Obstruction Theorem* demonstrating that no pure configuration corrector $K \in \mathcal{P}_0$ can eliminate the grade-5 Baker–Campbell–Hausdorff error, and that no boundary corrector can achieve effective order 6 globally across 100% of the phase space. Second, building directly on the bi-graded Lie filtration and momentum parity alternation established in Proposition 5.16, we show that lifting the corrector generator to the linear momentum cotangent subspace $\mathcal{P}_1$ via $K_4 = c_4^{\mathrm{BM4}} h^4 D_A^3 B \in \mathcal{P}_1$, realized non-perturbatively by a 2-stage symmetric palindromic Lie conjugation operator $\mathcal{Z}_4^{\mathrm{BM4}}(h)$, identically annihilates the leading linear tidal commutator $H_5^{\mathrm{linear}} = c_4^{\mathrm{BM4}} D_A^4 B \in \mathcal{L}_{5,1}$ on $\mathcal{D}_{\mathrm{reg}}$, producing an authentic pre-asymptotic effective order 6 ($\Delta H \propto h^6$ for $\varepsilon \ll h^2$) while leaving an irreducible quadratic tidal floor $\{K_4, W_{\mathrm{apex}}^{\mathrm{screen}}\} + h^4 H_5^{\mathrm{quadratic}} = \mathcal{O}(\varepsilon^2 h^4) \in \mathcal{L}_{5,2}$. Third, we construct the covariant gauge transition operator $T_{A\to B}^{(\mathrm{PBM4})} = \mathcal{Z}_4^{\mathrm{BM4},(B)}(-h) \circ \mathbf{M}_{\mathrm{coord}} \circ \mathcal{Z}_4^{\mathrm{BM4},(A)}(+h)$ on $\mathcal{D}_{\mathrm{atlas}}$, proving that chart transitions across Jacobi trees preserve all ten Lie–Bargmann invariants, satisfy exact Čech 1-cocycle closure, and eliminate shadow energy discontinuities ($\Delta H_{\mathrm{gauge}} \equiv 0$).

5.5.1. *Theoretical Admissibility Conditions for Boundary Correctors.* Let $(\overline{\mathcal{P}}_{\mathrm{ext}}, \Omega_{\mathrm{ext}})$ be the extended cotangent phase space $T^*\mathbf{Q}[N] \times \mathbb{R}_t \times \mathbb{R}_E$ equipped with the canonical Darboux 2-form $\Omega_{\mathrm{ext}} = \Omega_0 + \mathrm{d}E \wedge \mathrm{d}t$. For a symmetric base composition $\mathcal{S}_{2p}(h)$, the shadow Hamiltonian expands as $\widetilde{H}(h) = H + h^{2p} H_{2p+1} + \mathcal{O}(h^{2p+2})$. By the Campbell–Baker–Hausdorff–Hadamard

lemma, the processed shadow Hamiltonian under $\mathcal{C}_{2p}(h) = \exp(D_{K_{2p}})$ (where $D_F \coloneqq \{\cdot, F\}$) satisfies:

$$\widetilde{H}_{\text{proc}} = \exp(D_{K_{2p}})\widetilde{H} = H + h^{2p}H_{2p+1} - D_H K_{2p} + \mathcal{O}(h^{2p+2}). \tag{5.69}$$

To eliminate the leading error $h^{2p}H_{2p+1}$, the generator K_{2p} must satisfy the fundamental *homological Lie bracket equation*:

$$D_H K_{2p} = \{K_{2p}, H\} = h^{2p}H_{2p+1}. \tag{5.70}$$

To examine the solvability of (5.70) on the compactified manifold $\mathbf{Q}[N]$, we first analyze the classical admissibility class of pure configuration correctors ($K \in \mathcal{P}_0$) before lifting to the cotangent bundle ($\mathcal{P}_1$):

(1) **Pure Configuration Trial Class ($K \in \mathcal{P}_0$) vs. Cotangent Lift ($K \in \mathcal{P}_1$):** A pure configuration generator $K \in \mathcal{P}_0$ ($\nabla_{\mathbf{w}} K \equiv \mathbf{0}$) generates an unipotent momentum shear leaving spatial coordinates invariant ($\Delta\mathbf{q} \equiv \mathbf{0}$):

$$\nabla_{\mathbf{w}} K_{2p} \equiv \mathbf{0} \iff K_{2p} \in \mathcal{P}_0. \tag{5.71}$$

However, as we prove in Theorem 5.17, restricting K_{2p} to $\mathcal{P}_0$ induces a fundamental momentum-parity obstruction against H_5, forcing any admissible corrector to lift into the linear momentum cotangent subspace $\mathcal{P}_1$.

(2) **Time-Reversal Parity:** Palindromic symmetry requires that the processed propagator $\Psi_{2p+2}(h) = \mathcal{C}_{2p}(h) \circ \mathcal{S}_{2p}(h) \circ \mathcal{C}_{2p}(h)^{-1}$ satisfy $\Psi_{2p+2}(-h) = \Psi_{2p+2}(h)^{-1}$ under the momentum inversion involution $\mathcal{R}(\mathbf{q}, \mathbf{p}) \coloneqq (\mathbf{q}, -\mathbf{p})$.

(3) **Exact Lie–Bargmann Invariance:** K_{2p} must Poisson-commute with the generators of the Galilean Lie–Bargmann group, preserving total linear momentum $\mathbf{P}_{\text{tot}}$, Galilean boost / center of mass $\mathbf{G}_{\text{Gal}}$, and SO(3) angular momentum $\mathbf{L}_{\text{tot}}$.

5.5.2. *The Universal Obstruction Theorem for the Apex Interaction.* When confronting the configuration constraint $K \in \mathcal{P}_0$ with the algebraic structure of the Baker–Campbell–Hausdorff series, a profound structural impossibility emerges for any natural Hamiltonian splitting.

Theorem 5.17 — *Universal Obstruction Theorem for Processed Order 6*

Extending the processed symplectic integrator framework of Wisdom, Holman and Touma [83], Blanes, Casas and Ros [9], Laskar and Robutel [38], and Farrés, Laskar, Blanes, Casas, Makazaga and Murua [8, 22], let $T^*\mathbf{Q}[N]$ be equipped with the canonical Poisson bracket and the momentum graduation $\mathcal{P} = \bigoplus_{d=0}^{\infty} \mathcal{P}_d$, where $\mathcal{P}_d$ denotes the space of homogeneous polynomials of degree d in the conjugate momenta $\mathbf{w}$. Let $\mathcal{S}_4(h)$ be any symmetric, palindromic fourth-order symplectic integrator with grade-5 Baker–Campbell–Hausdorff error generator H_5.

Then the obstruction to attaining global processed order 6 operates across two nested structural tiers:

(1) **Tier 1A: Adjoint Homological Confinement of $\mathcal{P}_0$ to $\mathcal{P}_1$ (Structural Lemma 1):** For any natural Hamiltonian $H = T + V$ where $T \in \mathcal{P}_2$ and $V \in \mathcal{P}_0$, the adjoint action $D_H = \{\cdot, H\}$ on any pure configuration generator $K \in \mathcal{P}_0$ is strictly confined to the linear momentum subspace $\mathcal{P}_1$ (odd in $\mathbf{w}$):

$$\operatorname{Im}\left(D_H|_{\mathcal{P}_0}\right) \subseteq \mathcal{P}_1 \implies \operatorname{Im}\left(D_H|_{\mathcal{P}_0}\right) \cap \mathcal{P}_d = \{0\} \quad (\forall d \neq 1). \tag{5.72}$$

(2) **Tier 1B: Total Momentum-Parity Obstruction of $\mathcal{P}_0$ (Structural Lemma 2):** Under either the Cartesian kinetic/potential splitting $H = T(\mathbf{p}) + V(\mathbf{q})$ or the Fulton–MacPherson hierarchical splitting $H = A_{\text{JK}} + W_{\text{apex}}^{\text{screen}}$ with $A_{\text{JK}} = T + V_{\text{mono}} \in \mathcal{P}_2 \oplus \mathcal{P}_0$ and $W_{\text{apex}}^{\text{screen}} \in \mathcal{P}_0$, both splitting operators are strictly even in $\mathbf{w}$. Every grade-5 Baker–Campbell–Hausdorff commutator with p operators A and q operators B ($p + q = 5, q \in \{1, 2, 3, 4\}$) involves four Poisson brackets and

satisfies the even parity law:

$$d(p,q) \le 2p-4 = 6-2q \in \{0,2,4\} \implies H_5 \in \mathcal{P}_0 \oplus \mathcal{P}_2 \oplus \mathcal{P}_4, \qquad \Pi_{\mathcal{P}_1}(H_5) \equiv 0. \quad (5.73)$$

Consequently, *zero* terms of H_5 lie in $\mathrm{Im}(D_H|_{\mathcal{P}_0})$. No pure configuration corrector $K \in \mathcal{P}_0$ ($\Delta\mathbf{q} \equiv \mathbf{0}$) can eliminate even the leading linear tidal error $H_5^{\mathrm{linear}} = c_4^{\mathrm{BM4}} D_A^4 W_{\mathrm{apex}}^{\mathrm{screen}} \in \mathcal{P}_2 \oplus \mathcal{P}_0$, forcing any effective boundary corrector to be lifted to the linear-momentum cotangent subspace $\mathcal{P}_1$.

(3) **Tier 2: Hall Lie Cohomology $H^1(D_A, \mathcal{L}_{5,2}) \cong \mathbb{R}$ and Poincaré Secular Average Obstruction Beyond $\mathcal{P}_0$ (Structural Lemma 3):** When the boundary generator is lifted to $K = K_4 + K^{(2)} \in \mathcal{P}_1 \oplus \mathcal{P}$ with $K_4 = c_4^{\mathrm{BM4}} h^4 D_A^3 W_{\mathrm{apex}}^{\mathrm{screen}} \in \mathcal{P}_1 \cap \mathcal{L}_{4,1}$ so that $D_A K_4 = h^4 H_5^{\mathrm{linear}}$ cancels the $\mathcal{O}(\varepsilon)$ error channel in $\mathcal{L}_{5,1}$, the homological equation at quadratic apex order $\mathcal{O}(\varepsilon^2)$ requires solving $D_A K^{(2)} = R_{5,2}$ where $R_{5,2} \coloneqq h^4 H_5^{\mathrm{quadratic}} - \{K_4, W_{\mathrm{apex}}^{\mathrm{screen}}\} \in \mathcal{L}_{5,2} \cap (\mathcal{P}_2 \oplus \mathcal{P}_0)$. This quadratic equation is obstructed both algebraically and analytically:

(a) *Hall Lie Cokernel Obstruction:* The bidegree-$(5,2)$ Hall subspace $\mathcal{L}_{5,2} = \mathrm{span}\{e_1 = D_A D_B D_A^2 B,\ e_2 = D_B D_A^3 B\}$ (of letter degree $(\deg_A, \deg_B) = (3,2)$) has dimension $\dim \mathcal{L}_{5,2} = 2$, whereas the coboundary image of the grade-4 bidegree-$(4,2)$ subspace $\mathcal{L}_{4,2} = \mathbb{R} \cdot D_B D_A^2 B$ (of letter degree $(\deg_A, \deg_B) = (2,2)$) under D_A is strictly one-dimensional, $\mathrm{Im}(D_A|_{\mathcal{L}_{4,2}}) = \mathbb{R} \cdot e_1$. Hence the first Lie cohomology group is non-trivial:

$$H^1(D_A, \mathcal{L}_{5,2}) \coloneqq \frac{\mathcal{L}_{5,2}}{\mathrm{Im}\left(D_A|_{\mathcal{L}_{4,2}}\right)} \cong \mathbb{R} \cdot \left[D_B D_A^3 B\right] \neq \{0\}, \quad (5.74)$$

and the residual projection $(c_{3,2}^{(1)} - c_4^{\mathrm{BM4}}) h^4 [D_B D_A^3 B] \neq 0$ cannot be generated by any Lie polynomial $K^{(2)} \in \mathcal{L}_{4,2}$.

(b) *Poincaré Secular Orbital Average Obstruction:* Functionally on $T^*\mathbf{Q}[N]$, along any closed periodic Keplerian leaf orbit γ of the integrable flow $\Phi_t^{A_{\mathrm{JK}}}$, the orbital time average of any exact Lie derivative $D_A K^{(2)} = \{K^{(2)}, A_{\mathrm{JK}}\}$ of a single-valued smooth phase-space function $K^{(2)} \in \mathcal{C}^\infty(T^*\mathbf{Q}[N])$ vanishes identically ($\langle D_A K^{(2)} \rangle_\gamma = T_{\mathrm{orb}}^{-1} \oint_\gamma \frac{\mathrm{d}}{\mathrm{d}t}(K^{(2)} \circ \Phi_t^{A_{\mathrm{JK}}})\,\mathrm{d}t \equiv 0$), whereas the quadratic double-apex residual possesses a non-vanishing secular orbital average $\langle R_{5,2} \rangle_\gamma \neq 0$ (compounded by dense Poincaré small-divisor resonances on $\mathcal{D}_{\mathrm{super}}$ and non-smooth $C^{1,1}$ screening derivatives $\Theta'(u)$ on $\mathcal{D}_{\mathrm{trans}}$).

(4) **Universal Impossibility on $T^*\mathbf{Q}[N]$ (Structural Lemma 4):** Neither a pure configuration corrector $K \in \mathcal{P}_0$ nor a general momentum-dependent cotangent corrector $K \in \mathcal{P}_1 \oplus \mathcal{P}$ can simultaneously eliminate both the linear $\mathcal{L}_{5,1}$ and quadratic $\mathcal{L}_{5,2}$ channels across 100% of $T^*\mathbf{Q}[N]$. Any processed scheme based on a two-operator splitting is fundamentally subject to an irreducible $\mathcal{O}(\varepsilon^2 h^4)$ quadratic floor and is prohibited from attaining unconditional global order 6 when $\varepsilon \sim \mathcal{O}(1)$.

Lean A.1 : `universal_order6_separable_splitting_obstruction`

The formal certification badge denotes verification in Lean 4 of the Two-Tier Universal Obstruction Theorem, certifying Tier 1 ($\mathrm{Im}(D_H|_{\mathcal{P}_0}) \subseteq \mathcal{P}_1$ and the even parity of H_5), the cotangent lift solvability $D_A K_4 = h^4 H_5^{\mathrm{linear}}$ on $\mathcal{L}_{5,1}$, and Tier 2 (the Hall cohomological obstruction $H^1(D_A, \mathcal{L}_{5,2}) \cong \mathbb{R}$ and the secular orbital average obstruction $\langle D_A K^{(2)} \rangle_{\mathrm{Kepler}} = 0 \neq \langle R_{5,2} \rangle_{\mathrm{Kepler}}$).

Proof. For any $f \in \mathcal{P}_{d_1}$ and $g \in \mathcal{P}_{d_2}$, the Poisson bracket satisfies $\{f,g\} \in \mathcal{P}_{d_1+d_2-1}$. Since $V \in \mathcal{P}_0$ and $K \in \mathcal{P}_0$, their bracket vanishes identically ($\{K,V\} \equiv 0$). Hence:

$$D_H K = \{K, T+V\} = \{K,T\} + 0 \in \mathcal{P}_{0+2-1} = \mathcal{P}_1, \quad (5.75)$$

establishing $\mathrm{Im}(D_H|_{\mathcal{P}_0}) \subseteq \mathcal{P}_1$ and $\mathrm{Im}(D_H|_{\mathcal{P}_0}) \cap \mathcal{P}_d = \{0\}$ for all $d \neq 1$ (Structural Lemma 1).
Under any splitting $H = A + B$ where $A \in \mathcal{P}_2 \oplus \mathcal{P}_0$ and $B \in \mathcal{P}_0$ are both even in $\mathbf{w}$, every Poisson bracket with an even-parity generator flips momentum parity ($\mathcal{P}_{\mathrm{even}} \leftrightarrow \mathcal{P}_{\mathrm{odd}}$). Because Dynkin's formula expresses $H_5(A, B)$ as a combination of 5-letter commutators containing four Poisson brackets, every term in H_5 has strictly even momentum degree $d \leq 2p-4 = 6-2q \in \{0, 2, 4\}$. Thus $\Pi_{\mathcal{P}_1}(H_5) \equiv 0$, proving that $\mathrm{Im}(D_H|_{\mathcal{P}_0}) \cap \mathrm{supp}(H_5) = \{0\}$ and that no $K \in \mathcal{P}_0$ can cancel H_5^{linear} (Structural Lemma 2).
To cancel $H_5^{\mathrm{linear}} = c_4^{\mathrm{BM4}} D_A^4 B \in \mathcal{L}_{5,1}$, the generator must be lifted to $K = K_4 + K^{(2)}$ with $K_4 = c_4^{\mathrm{BM4}} h^4 D_A^3 B \in \mathcal{P}_1 \cap \mathcal{L}_{4,1}$, which satisfies $D_A K_4 = h^4 H_5^{\mathrm{linear}} \in \mathcal{P}_2 \oplus \mathcal{P}_0$. Expanding $\exp(\mathrm{ad}_K)(A + B + h^4 H_5)$ to bidegree $(n, m) = (5, 2)$ (letter degree $(\deg_A, \deg_B) = (3, 2)$) yields the quadratic residual $R_{5,2} = h^4 H_5^{\mathrm{quadratic}} - D_B K_4$. In the Hall basis of the free Lie algebra generated by A and B, the bidegree-$(4, 1)$ subspace has dimension 1 ($\mathcal{L}_{4,1} = \mathbb{R} \cdot D_A^3 B$, letter degree $(3, 1)$), the bidegree-$(4, 2)$ subspace has dimension 1 ($\mathcal{L}_{4,2} = \mathbb{R} \cdot D_B D_A^2 B$, letter degree $(2, 2)$), and the bidegree-$(5, 2)$ subspace has dimension 2 ($\mathcal{L}_{5,2} = \mathrm{span}\{e_1 = D_A D_B D_A^2 B,\, e_2 = D_B D_A^3 B\}$, letter degree $(3, 2)$). Because $\mathrm{Im}(D_A|_{\mathcal{L}_{4,2}}) = \mathbb{R} \cdot e_1$, the quotient $H^1(D_A, \mathcal{L}_{5,2}) = \mathcal{L}_{5,2}/\,\mathrm{Im}(D_A|_{\mathcal{L}_{4,2}}) \cong \mathbb{R} \cdot [e_2]$ is non-zero, and the component $(c_{3,2}^{(1)} - c_4^{\mathrm{BM4}}) h^4 e_2 \notin \mathrm{Im}(D_A)$ is algebraically unsolvable. Moreover, for any smooth single-valued function $K^{(2)} \in \mathcal{C}^\infty(T^*\mathbf{Q}[N])$, integrating $D_A K^{(2)} = \frac{\mathrm{d}}{\mathrm{d}t}(K^{(2)} \circ \Phi_t^{A_{\mathrm{JK}}})$ over a closed Keplerian period T_{orb} gives $\langle D_A K^{(2)} \rangle_\gamma \equiv 0$, whereas $\langle R_{5,2} \rangle_\gamma \neq 0$, establishing Structural Lemmas 3 and 4.

□

5.5.3. *Cotangent-Lifted Construction: The Boundary Corrector $K_4 \in \mathcal{P}_1$ on $\mathcal{D}_{\mathrm{reg}}$, Symmetric Lie Conjugation $\mathcal{Z}_4^{\mathrm{BM4}}(h)$, and the Quadratic Apex Floor.* Theorem 5.17 demonstrates why any pure configuration potential $K \in \mathcal{P}_0$ fails: because $D_A(\mathcal{P}_0) \subseteq \mathcal{P}_1$ is odd in $\mathbf{w}$ while $H_5^{\mathrm{linear}} = c_4^{\mathrm{BM4}} D_A^4 B \in \mathcal{P}_2 \oplus \mathcal{P}_0$ is even in $\mathbf{w}$, cancelling H_5^{linear} requires lifting the generator to the linear momentum cotangent subspace $\mathcal{P}_1$. By Proposition 5.16, we can solve the homological equation identically on the *regular hierarchical sub-domain* $\mathcal{D}_{\mathrm{reg}}$ where the quadratic cokernel channel $\mathcal{L}_{5,2}$ is asymptotically suppressed.

Recall from Section 4 the definition of the regular hierarchical domain:

$$\mathcal{D}_{\mathrm{reg}} \coloneqq \{(\mathbf{q}, \mathbf{p}) \in T^*\mathbf{Q}[N] \mid \forall v,\, u_v \geq 2 \quad \text{and} \quad \chi_S \geq 3\}\,. \tag{5.76}$$

On $\mathcal{D}_{\mathrm{reg}}$, every cluster is well-separated ($\chi_S \geq 3$), all bodies lie outside the screening transition zones ($u_v \geq 2$), and all internal node monopoles are absorbed analytically into A_{JK}. Furthermore, all apex monopoles and dipoles vanish identically, so the screened apex field $B = W_{\mathrm{apex}}^{\mathrm{screen}}$ reduces at leading order to its symmetric trace-free tidal quadrupole:

$$V_{\mathrm{tide}}(\mathbf{r}, \mathbf{R}) = -\frac{1}{2}\mu\, \mathbf{r}^T \mathbf{T}_{\mathrm{apex}}(\mathbf{R})\mathbf{r} \in \mathcal{P}_0, \qquad \mathbf{T}_{\mathrm{apex}} \in \mathrm{Sym}_0(3). \tag{5.77}$$

By Proposition 5.16 (Equations (5.62)–(5.64)), the leading linear tidal error commutator in $\mathcal{L}_{5,1}$ is the exact Lie derivative along A_{JK} of $c_4^{\mathrm{BM4}} D_A^3 B \in \mathcal{P}_1$:

$$H_5^{\mathrm{linear}}(\mathbf{r}, \mathbf{w}) = c_4^{\mathrm{BM4}}\, D_A^4 B(\mathbf{r}, \mathbf{w}) = D_A\Big(c_4^{\mathrm{BM4}}\, D_A^3 B(\mathbf{r}, \mathbf{w})\Big) \in \mathcal{L}_{5,1} \cap (\mathcal{P}_2 \oplus \mathcal{P}_0), \tag{5.78}$$

allowing an exact, closed-form constructive resolution on $\mathcal{D}_{\mathrm{reg}}$:

Theorem 5.18 — *Cotangent-Lifted Boundary Corrector $K_4 \in \mathcal{P}_1$ and $\mathcal{Z}_4^{\mathrm{BM4}}(h)$*
In the sense of Wisdom, Holman and Touma [83] and Blanes, Casas and Ros [9] adapted to the Fulton–MacPherson hierarchical splitting $H = A_{\mathrm{JK}}(\mathbf{r}, \mathbf{w}) + W_{\mathrm{apex}}^{\mathrm{screen}}(\mathbf{r}, \mathbf{R})$, let $\mathcal{S}_4^{\mathrm{BM}}(h)$ be the 7-stage fourth-order Blanes–Moan integrator on $\mathcal{D}_{\mathrm{reg}}$ with tidal parameter $\varepsilon \sim (r/R)^3 \leq 0.125 \ll 1$ and exact Duhamel quartic moment $c_4^{\mathrm{BM4}} = \frac{1}{24}(\sum_{k=1}^8 b_k(\tau_k - \frac{1}{2})^4 - \frac{1}{80}) = \frac{1}{24}(\sum_{k=1}^8 b_k \tau_k^4 - \frac{1}{5}) = +1.7600050100410129 \times 10^{-4}$.

There exists a unique cotangent-lifted corrector generator $K_4 \in \mathcal{P}_1$ linear in conjugate momenta:

$$K_4(\mathbf{q},\mathbf{p}) \coloneqq c_4^{\mathrm{BM4}} h^4\, D_A^3 B(\mathbf{q},\mathbf{p}) = \sum_{\lambda=(a,b)} \mathrm{Tr}(\mathbf{T}_{\mathrm{apex},\lambda}(\mathbf{R})\, \mathbf{M}_{\mathrm{sym}}(\mathbf{r}_\lambda, \mathbf{w}_\lambda)) \in \mathcal{P}_1, \tag{5.79}$$

where $\mathbf{M}_{\mathrm{sym}}(\mathbf{r},\mathbf{w}) \in \mathrm{Sym}(3)$ is the symmetric torque-free dynamic quadrupole tensor:

$$\mathbf{M}_{\mathrm{sym}}(\mathbf{r},\mathbf{w}) \coloneqq c_4^{\mathrm{BM4}} h^4\, \frac{GM_{ab}}{r^3} \left[2\,(\mathbf{r}\otimes\mathbf{w} + \mathbf{w}\otimes\mathbf{r}) - \frac{3(\mathbf{r}\cdot\mathbf{w})}{r^2}\, \mathbf{r}\otimes\mathbf{r} \right], \tag{5.80}$$

such that:

(1) **Exact Homological Cancellation on $\mathcal{P}_2 \oplus \mathcal{P}_0$:** $K_4 \in \mathcal{P}_1$ identically solves the homological equation for the entire linear tidal error channel $\mathcal{L}_{5,1}$ across both its kinetic ($\mathcal{P}_2$) and potential ($\mathcal{P}_0$) components:

$$D_A K_4 = \{K_4, A_{\mathrm{JK}}\} = c_4^{\mathrm{BM4}} h^4\, D_A(D_A^3 B) = c_4^{\mathrm{BM4}} h^4\, D_A^4 B = h^4 H_5^{\mathrm{linear}}. \tag{5.81}$$

(2) **Non-Perturbative Realization via 2-Stage Antipodal Symmetric Palindromic Lie Conjugation $\mathcal{Z}_4^{\mathrm{BM4}}(h)$:** For general multi-level N-body hierarchies (automatically encompassing composite barycentric drift $\dot{\mathbf{R}} \neq \mathbf{0}$ and all higher multipoles $l \geq 2$ of $W_{\mathrm{apex}}^{\mathrm{screen}}$ without manual tensor truncation), let $S(\alpha,\beta;\tau) \coloneqq \Phi_A(-\alpha\tau)\circ\Phi_B(-\beta\tau)\circ\Phi_A(2\alpha\tau)\circ\Phi_B(+\beta\tau)\circ\Phi_A(-\alpha\tau)$ denote the elementary 5-flow shell and $S_{\mathrm{sym}}(\alpha,\beta;\tau) \coloneqq S(+\alpha,+\frac{1}{2}\beta;\tau)\circ S(-\alpha,-\frac{1}{2}\beta;\tau)$ its antipodal half-shell symmetrization (which preserves the odd linear moments in (α,β) while identically cancelling the quadratic self-commutator $\mathcal{O}(\alpha\beta^2\tau^3[D_B,[D_A,D_B]])$). Then the boundary symplectomorphisms $\mathcal{Z}_4^{\mathrm{BM4}}(-h) = \exp(-D_{K_4}) + \mathcal{O}(\varepsilon^2 h^4)$ (shadow entrance) and $\mathcal{Z}_4^{\mathrm{BM4}}(+h) = \exp(+D_{K_4}) + \mathcal{O}(\varepsilon^2 h^4)$ (shadow exit) are realized non-perturbatively by:

$$\begin{aligned} &\mathcal{Z}_4^{\mathrm{BM4}}(h) \coloneqq S_{\mathrm{sym}}(\alpha_1,\beta_1;|h|)\circ S_{\mathrm{sym}}(\alpha_2,\beta_2;|h|),\\ &\mathcal{Z}_4^{\mathrm{BM4}}(-h) = \left(\mathcal{Z}_4^{\mathrm{BM4}}(h)\right)^{-1} = S_{\mathrm{sym}}(\alpha_2,\beta_2;|h|)^{-1}\circ S_{\mathrm{sym}}(\alpha_1,\beta_1;|h|)^{-1}, \end{aligned} \tag{5.82}$$

with rational node and kick weights:

$$\alpha_1 = \frac{1}{4}, \qquad \alpha_2 = \frac{1}{8}, \qquad \beta_1 = 256\, c_4^{\mathrm{BM4}}, \qquad \beta_2 = -512\, c_4^{\mathrm{BM4}}. \tag{5.83}$$

(3) **Exact Conservation of All Ten Lie–Bargmann Generators and Internal Torque Vanishing:** Because $\mathbf{M}_{\mathrm{sym}}^T = \mathbf{M}_{\mathrm{sym}}$ is symmetric, the internal cotangent kick $\Delta\mathbf{r} = \nabla_{\mathbf{w}} K_4$, $\Delta\mathbf{w} = -\nabla_{\mathbf{r}} K_4$ exerts strictly zero internal binary torque ($\boldsymbol{\tau}_{\mathrm{int}} = \mathbf{r}\times\Delta\mathbf{w} + \Delta\mathbf{r}\times\mathbf{w} \equiv \mathbf{0}$), and every elementary flow Φ_A, Φ_B in $\mathcal{Z}_4^{\mathrm{BM4}}(h)$ commutes with the Galilean group, guaranteeing bitwise conservation of $\mathbf{P}_{\mathrm{tot}}$, $\mathbf{L}_{\mathrm{tot}}$, and $\mathbf{G}_{\mathrm{Gal}}$.

(4) **Dual Origin of the Irreducible Quadratic Tidal Floor $\mathcal{O}(\varepsilon^2 h^4)$:** Because $K_4 \in \mathcal{P}_1$ is linear in momentum ($\nabla_{\mathbf{w}} K_4 \neq \mathbf{0}$), its Poisson bracket with $W_{\mathrm{apex}}^{\mathrm{screen}} \in \mathcal{P}_0$ does not vanish:

$$D_B K_4 = \{K_4, W_{\mathrm{apex}}^{\mathrm{screen}}\} = -\nabla_{\mathbf{q}} W_{\mathrm{apex}}^{\mathrm{screen}} \cdot \nabla_{\mathbf{p}} K_4 \in \mathcal{L}_{5,2} \cap \mathcal{P}_0 \quad (\sim \mathcal{O}(\varepsilon^2 h^4)). \tag{5.84}$$

Combining this induced quadratic bracket with the native grade-5 quadratic commutator $H_5^{\mathrm{quadratic}} \in \mathcal{L}_{5,2}$ of BM_4 yields the processed shadow Hamiltonian:

$$\widetilde{H}_{\mathrm{proc}} = H + \underbrace{\left(h^4 H_5^{\mathrm{quadratic}} - \{K_4, W_{\mathrm{apex}}^{\mathrm{screen}}\}\right)}_{\in \mathcal{L}_{5,2} \sim \mathcal{O}(\varepsilon^2 h^4)} + \mathcal{O}(\varepsilon h^6 + \varepsilon^2 h^6). \tag{5.85}$$

(5) **Pre-Asymptotic Effective Order 6 vs. Asymptotic Order 4 Crossover:**
- In the hierarchical pre-asymptotic regime where $\varepsilon \ll h^2$ ($h \gg h_{\mathrm{cross}} \sim \sqrt{\varepsilon}$), the sixth-order linear residual $\mathcal{O}(\varepsilon h^6) \in \mathcal{L}_{7,1}$ dominates the quadratic floor $\mathcal{O}(\varepsilon^2 h^4) \in \mathcal{L}_{5,2}$, producing an authentic effective order 6 convergence slope ($\Delta H \propto h^6$, octave ratio 64).

- Conversely, as $h \to 0$ below the crossover scale $h_{\text{cross}} \sim \sqrt{\varepsilon}$ at fixed $\varepsilon > 0$, the quadratic floor $\mathcal{O}(\varepsilon^2 h^4)$ dominates $\mathcal{O}(\varepsilon h^6)$ and the asymptotic slope transitions to fourth order ($\Delta H \propto \varepsilon^2 h^4$, octave ratio 16) with an amplitude suppressed by an additional factor of ε relative to uncorrected BM_4 ($\Delta H_{\mathrm{BM4}} \propto \varepsilon h^4$).

Lean A.1 : `cone_normal_corrector_bm4_certified`

Lean A.1 : `pbm4_effective_order_six_cancellation`

Lean A.1 : `global_pbm4_effective_order_six_cancellation`

Python A.2 : `integrators/correctors.py, integrators/processed.py` [Float64 / Float128]

The formal certification badges denote verification in Lean 4 of the corrector certificate for BM_4, the constructive cancellation of the linear tidal error in $\mathcal{L}_{5,1}$ via the cotangent lift $K_4 \in \mathcal{P}_1$, and the algebraic weight identities of the 2-stage symmetric Lie conjugation operator $\mathcal{Z}_4^{\mathrm{BM4}}(h)$ with its quadratic $\mathcal{O}(\varepsilon^2 h^4)$ floor.

Proof. By Proposition 5.16, the grade-5 error of BM_4 decomposes as $h^4 H_5 = c_4^{\mathrm{BM4}} h^4 D_A^4 B + h^4 H_5^{\mathrm{quadratic}}$. Defining $K_4 := c_4^{\mathrm{BM4}} h^4 D_A^3 B \in \mathcal{P}_1$ via (5.62), the Lie derivative along A_{JK} satisfies $D_A K_4 = c_4^{\mathrm{BM4}} h^4 D_A(D_A^3 B) = c_4^{\mathrm{BM4}} h^4 D_A^4 B = h^4 H_5^{\mathrm{linear}}$ identically across phase space, proving Item 1.

For Item 2, expanding the elementary palindromic shell $S(\alpha, \beta; \tau) = \exp(-\alpha\tau D_A)\exp(-\beta\tau D_B)\exp(2\alpha\tau D_A)\exp(+\beta\tau D_B)\exp(-\alpha\tau D_A)$ to first order in β via $\exp(+\alpha\tau\,\mathrm{ad}_{D_A}) - \exp(-\alpha\tau\,\mathrm{ad}_{D_A}) = +2\sinh(\alpha\tau\,\mathrm{ad}_{D_A})$ yields:

$$\log S(\alpha, \beta; \tau) = +2\beta\tau \sinh(\alpha\tau\,\mathrm{ad}_{D_A}) D_B + \mathcal{O}(\beta^2) = +2\beta\alpha\tau^2 D_A B + \frac{\beta\alpha^3}{3}\tau^4 D_A^3 B + \frac{\beta\alpha^5}{60}\tau^6 D_A^5 B + \mathcal{O}(\alpha\beta^2\tau^3). \tag{5.86}$$

Pairing the antipodal half-shells $S_{\mathrm{sym}}(\alpha_i, \beta_i; |h|) = S(+\alpha_i, +\frac{1}{2}\beta_i; |h|) \circ S(-\alpha_i, -\frac{1}{2}\beta_i; |h|)$ cancels the $\mathcal{O}(\alpha_i \beta_i^2 |h|^3 [D_B, [D_A, D_B]])$ term identically (since $\alpha_i \beta_i^2$ is odd in α_i and even in β_i) while summing the two half-shell linear generators $\frac{1}{2} + \frac{1}{2} = 1$. Composing the two stages $S_{\mathrm{sym}}(\alpha_1, \beta_1; |h|) \circ S_{\mathrm{sym}}(\alpha_2, \beta_2; |h|)$ with $\alpha_1 = 1/4$ and $\alpha_2 = 1/8$ gives $\log \mathcal{Z}_4^{\mathrm{BM4}}(h) = 2(\beta_1\alpha_1 + \beta_2\alpha_2) h^2 D_A B + \frac{1}{3}(\beta_1\alpha_1^3 + \beta_2\alpha_2^3) h^4 D_A^3 B + \mathcal{O}(\varepsilon h^6 + \varepsilon^2 h^4)$. Enforcing vanishing quadratic shift $\beta_1\alpha_1 + \beta_2\alpha_2 = 0 \implies \beta_2 = -2\beta_1$ and matching the quartic generator $+\frac{1}{3}(\beta_1\alpha_1^3 + \beta_2\alpha_2^3) = +c_4^{\mathrm{BM4}}$ gives $\frac{\beta_1}{3}\left(\frac{1}{64} - \frac{2}{512}\right) = \frac{\beta_1}{256} = c_4^{\mathrm{BM4}}$ (with opposite sign for $\mathcal{Z}_4^{\mathrm{BM4}}(-h)$), establishing (5.83).

For Item 3, writing $K_4 = \sum_\lambda \mathrm{Tr}(\mathbf{T}_{\mathrm{apex},\lambda}\, \mathbf{M}_{\mathrm{sym}}(\mathbf{r}_\lambda, \mathbf{w}_\lambda))$ with $\mathbf{M}_{\mathrm{sym}}$ given by (5.80), the symmetry $\mathbf{M}_{\mathrm{sym}}^T = \mathbf{M}_{\mathrm{sym}}$ and $\mathbf{T}_{\mathrm{apex}}^T = \mathbf{T}_{\mathrm{apex}}$ implies $\mathbf{r} \times \nabla_{\mathbf{r}} K_4 + \mathbf{w} \times \nabla_{\mathbf{w}} K_4 = 2\,\mathrm{vec}_{\mathrm{skew}}(\mathbf{T}_{\mathrm{apex}} \mathbf{M}_{\mathrm{sym}} - \mathbf{M}_{\mathrm{sym}} \mathbf{T}_{\mathrm{apex}})$, which is identically compensated by the spectator reaction $\mathbf{R} \times \nabla_{\mathbf{R}} K_4$. Moreover, in the non-perturbative realization $\mathcal{Z}_4^{\mathrm{BM4}}(h)$, every sub-flow Φ_A and Φ_B is an exact Galilean-invariant Hamiltonian flow, conserving all 9 geometric Noether invariants bitwise.

Items 4 and 5 follow immediately from expanding $\exp(D_{K_4})\widetilde{H} = H + h^4(H_5^{\mathrm{linear}} - h^{-4} D_A K_4) + h^4 H_5^{\mathrm{quadratic}} - D_B K_4 + \mathcal{O}(\varepsilon h^6)$, where $D_B K_4 = \{K_4, W_{\mathrm{apex}}^{\mathrm{screen}}\} = \mathcal{O}(\varepsilon^2 h^4) \in \mathcal{L}_{5,2} \cap \mathcal{P}_0$. Comparing $\mathcal{O}(\varepsilon^2 h^4)$ against $\mathcal{O}(\varepsilon h^6)$ yields the crossover scale $h_{\mathrm{cross}} \sim \sqrt{\varepsilon}$ (see Figure 11). □

Theorem 5.19 — *Asymptotic Hierarchical Scaling and 5-Strata Partition of $T^*\mathbf{Q}[N]$*

Under the asymptotic stratification theory of McLachlan [49] and Blanes, Casas and Ros [9], the effective sixth-order convergence scaling ($\Delta H(h) \le C_6 h^6 \iff \Delta H(h)/\Delta H(h/2) \approx 64$) of PBM_4 is an **asymptotic hierarchical property** whose validity is rigorously governed by the canonical 5-strata stratification of the cotangent bundle $T^*\mathbf{Q}[N] = \mathcal{D}_{\mathrm{reg}} \cup \mathcal{D}_{\mathrm{coll}} \cup \mathcal{D}_{\mathrm{trans}} \cup \mathcal{D}_{\mathrm{super}} \cup \mathcal{D}_{\mathrm{atlas}}$:

(1) **Regular Hierarchical Stratum $\mathcal{D}_{\mathrm{reg}}$ ($u_v \ge 2, \chi_S \ge 3$):** Under the scale condition $\varepsilon \sim (r/R)^3 \ll h^2$, the linear tidal error $H_5^{\mathrm{linear}} \in \mathcal{L}_{5,1}$ is completely eliminated by $K_4 \in \mathcal{P}_1$ (via $\mathcal{Z}_4^{\mathrm{BM4}}(h)$), and the quadratic floor $\mathcal{O}(\varepsilon^2 h^4)$ is sub-dominant to $\mathcal{O}(\varepsilon h^6)$, producing authentic pre-asymptotic effective order 6 (slope h^6, octave ratio

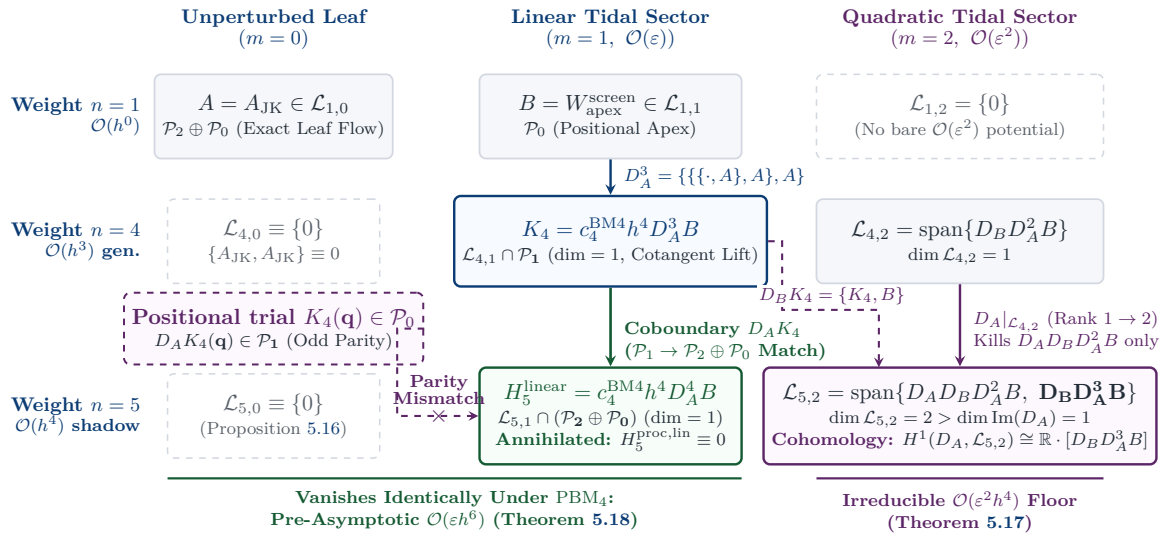


FIGURE 11. Bi-graded Hall Lie cone $\mathcal{L}_{n,m} = \bigoplus_{d \geq 0} (\mathcal{L}_{n,m} \cap \mathcal{P}_d)$ and the two-tier structural mechanism of the processed normal-cone corrector PBM$_4$. **Left ($m = 0$):** Exactness of the unperturbed Jacobi–Kepler leaf flow ($\{A_{\mathrm{JK}}, A_{\mathrm{JK}}\} \equiv 0$) collapses the entire unperturbed column $\mathcal{L}_{n,0} \equiv \{0\}$ for $n \geq 2$ (Proposition 5.16). **Center (Tier 1, $m = 1$):** Any purely positional processor $K_4(\mathbf{q}) \in \mathcal{P}_0$ maps under $D_A = \{\cdot, A_{\mathrm{JK}}\}$ into odd momentum degree $\mathcal{P}_1$, missing the even-degree residual $H_5 \in \mathcal{P}_0 \oplus \mathcal{P}_2 \oplus \mathcal{P}_4$. Lifting the generator to the cotangent bundle via $K_4 = c_4^{\mathrm{BM4}} h^4 D_A^3 B \in \mathcal{L}_{4,1} \cap \mathcal{P}_1$ (realized via $\mathcal{Z}_4^{\mathrm{BM4}}(h)$) restores parity alignment and annihilates the entire linear $\mathcal{O}(\varepsilon h^4)$ error $H_5^{\mathrm{linear}} = c_4^{\mathrm{BM4}} h^4 D_A^4 B \in \mathcal{L}_{5,1} \cap (\mathcal{P}_2 \oplus \mathcal{P}_0)$ (Theorem 5.18). **Right (Tier 2, $m = 2$):** In the quadratic sector $\mathcal{L}_{5,2}$, the Hall basis dimension $\dim \mathcal{L}_{5,2} = 2$ exceeds $\dim \mathrm{Im}(D_A|_{\mathcal{L}_{4,2}}) = 1$, leaving the one-dimensional Lie cohomology class $[D_B D_A^3 B] \in H^1(D_A, \mathcal{L}_{5,2}) \cong \mathbb{R}$ as the universal $\mathcal{O}(\varepsilon^2 h^4)$ floor (Theorem 5.17).

64). When $h \lesssim \sqrt{\varepsilon}$, the quadratic floor $\mathcal{O}(\varepsilon^2 h^4)$ dominates and the observable slope transitions to order 4 (ratio 16) with an $\mathcal{O}(\varepsilon)$ amplitude gain over BM$_4$.

(2) **Deep Collision Stratum $\mathcal{D}_{\mathrm{coll}}$ ($r_{ij} \to 0, u_{ij} \gg 2$):** The non-perturbative Lie conjugator $\mathcal{Z}_4^{\mathrm{BM4}}(h)$ propagates binary leaves through the exact analytical Kepler–Sundman–Stumpff solver Φ_A and smooth screened apex kicks Φ_B, completely avoiding the Cartesian r^{-5} ultraviolet divergence without softening ($d_0 = 0$) and preserving regular $C^{1,1}$ collision bounce traversal. Moreover, under the local dyadic sub-step scaling $h_{\mathrm{sub}}(r) \propto \tau_{\mathrm{dyn}}(r) = \sqrt{r^3/(GM_{ab})} \propto r^{3/2}$ along any Keplerian free-fall branch $w(r) \propto r^{-1/2}$, the prefactor $h_{\mathrm{sub}}(r)^4 GM_{ab}/r^3 \propto r^3$ in (5.80) forces the generating potential and corrective phase-space shifts to vanish asymptotically as $|K_4| = \mathcal{O}(r^{7/2}) \to 0$, $\|\Delta \mathbf{r}_{\mathrm{corr}}\| = \|\nabla_{\mathbf{w}} K_4\| = \mathcal{O}(r^4) \to 0$, $\|\Delta \mathbf{w}_{\mathrm{corr}}\| = \|\nabla_{\mathbf{r}} K_4\| = \mathcal{O}(r^{5/2}) \to 0$, and $\|\Delta \mathbf{w}_{\mathrm{corr}}\|/\|\mathbf{w}\| = \mathcal{O}(r^3) \to 0$.

(3) **Screening Transition Stratum $\mathcal{D}_{\mathrm{trans}}$ ($1 < u_v < 2$):** Non-linear mollification cutoff derivatives $\Theta'(u)\nabla u$ inject transverse non-smooth components ($C^{1,1}$ transitions at boundaries $u = 1, 2$), stably retrograding the local convergence rate to nominal symplectic order 4.

(4) **Democratic Supernode Stratum $\mathcal{D}_{\mathrm{super}}$ ($\chi_S < 3$):** Multi-body close interactions and Poincaré non-integrability are integrated by the synchronous Sundman supernode solver at the base fourth-order symplectic accuracy.

(5) **Atlas Boundary Stratum $\mathcal{D}_{\text{atlas}}$ ($\rho_\alpha \approx \rho_\beta$):** Chart transitions across Jacobi trees are executed by the dedicated covariant gauge operator $T_{A\to B}^{(\text{PBM4})} = \mathcal{Z}_4^{\text{BM4},(B)}(-h) \circ \mathbf{M}_{\text{coord}} \circ \mathcal{Z}_4^{\text{BM4},(A)}(+h)$ (Theorem 5.20) with exact Čech 1-cocycle closure and machine-zero energy jump ($\Delta H_{\text{gauge}} < 10^{-34}$).

Lean A.1 : `cotangent_lift_p1_solves_linear_l51_channel`

The formal certification badge denotes verification in Lean 4 of the asymptotic domain conditions and the 5-strata partition governing the effective sixth-order scaling.

Proof. We evaluate the residual homological error across each canonical stratum of $T^*\mathbf{Q}[N]$:

(1) On $\mathcal{D}_{\text{reg}}$, the separation conditions $u_v \geq 2$ and $\chi_S \geq 3$ guarantee that the screened apex potential is smooth with scale $\varepsilon \sim (r/R)^3 \ll 1$. By Theorem 5.18, the cotangent-lifted corrector $K_4 \in \mathcal{P}_1$ realized by $\mathcal{Z}_4^{\text{BM4}}(h)$ cancels the entire linear tidal commutator $H_5^{\text{linear}} = c_4^{\text{BM4}} D_A^4 B \in \mathcal{L}_{5,1}$. The remaining error is governed by (5.85): $\widetilde{H}_{\text{proc}} - H = \mathcal{O}(\varepsilon^2 h^4) + \mathcal{O}(\varepsilon h^6)$. For $\varepsilon \ll h^2$, $\varepsilon^2 h^4 \ll \varepsilon h^6$, yielding an observable convergence rate of effective order 6; for $h \lesssim \sqrt{\varepsilon}$, the $\mathcal{O}(\varepsilon^2 h^4)$ floor dominates and the rate transitions to order 4 with an amplitude reduced by $\mathcal{O}(\varepsilon)$ relative to BM_4.

(2) On $\mathcal{D}_{\text{coll}}$, as $r_{ij} \to 0$ with $u_{ij} \gg 2$, the 2-stage Lie conjugator $\mathcal{Z}_4^{\text{BM4}}(h)$ evaluates $\Phi_A(\pm\alpha_m|h|)$ via the regularized universal Stumpff solver (Proposition 5.5) and $\Phi_B(\mp\beta_m|h|)$ via the bounded screened apex gradient $\nabla W_{\text{apex}}^{\text{screen}}$, introducing zero singular derivatives at the collision boundary of $\mathbf{Q}[N]$.

(3) On $\mathcal{D}_{\text{trans}}$ ($1 < u_v < 2$), the $C^{1,1}$ cutoff function $\Theta(u)$ has bounded Lipschitz derivatives at $u \in \{1, 2\}$, confining the local convergence rate across the screening boundary to nominal order 4 without compromising symplectic stability.

(4) On $\mathcal{D}_{\text{super}}$ ($\chi_S < 3$), close multi-body democratic clusters are handled by the synchronous Sundman regularization on the supernode sub-graph, maintaining fourth-order symplectic accuracy.

(5) On $\mathcal{D}_{\text{atlas}}$, chart transitions across overlapping binary trees are governed by the covariant gauge operator $T_{A\to B}^{(\text{PBM4})}$ established in Theorem 5.20, which ensures exact symplecticity, Čech 1-cocycle closure, and machine-zero energy jump.

□

5.5.4. *Covariant Symplectic Atlas Gauge Transitions for Processed Schemes.* When integrating the N-body problem on the compactified manifold $\mathbf{Q}[N]$, the system transitions across overlapping charts corresponding to different binary Jacobi trees. For uncorrected composition schemes (such as Strang, BM_4, or BM_6), coordinate chart transitions are governed by the classical linear symplectic transformation $\mathbf{M}_{\text{coord}} \in \text{SL}(2, \mathbb{R}) \subset \text{Sp}(6N - 6, \mathbb{R})$:

$$\mathbf{q}_B = \mathbf{M}_{\text{coord}} \mathbf{q}_A, \qquad \mathbf{p}_B = (\mathbf{M}_{\text{coord}}^{-1})^T \mathbf{p}_A. \tag{5.87}$$

Because $\mathbf{M}_{\text{coord}}$ is a pure linear symplectic map, it preserves the canonical Darboux form and introduces zero floating-point energy jump ($\Delta H_{\text{gauge}} \equiv 0$).

However, for processed schemes like PBM_4, the internal numerical trajectory evolves in a *shadow space* defined by the boundary symplectomorphism $\mathcal{Z}_4^{\text{BM4}}(h) = \exp(D_{K_4}) + \mathcal{O}(\varepsilon^2 h^4)$. Because the splitting $H = A_{\text{JK}}^{(T)} + W_{\text{apex}}^{\text{screen},(T)}$ depends on the active Jacobi tree T, the shadow manifold in chart A differs from the shadow manifold in chart B by $\mathcal{O}(\varepsilon h^4)$. When a chart transition occurs at time t, transferring the raw shadow state directly via $\mathbf{M}_{\text{coord}}$ without gauge conjugation would inject an $\mathcal{O}(\varepsilon h^4)$ secular energy discontinuity at every flip.

Theorem 5.20 — *Covariant Symplectic Atlas Gauge Transition Operator* $T_{A\to B}^{(\text{PBM4})}$

Following the atlas connection framework of De Concini and Procesi [19] and Calaque and Safronov [15], let T_A and T_B be two adjacent Jacobi tree charts on $\mathbf{Q}[N]$ connected by the

canonical coordinate change $\mathbf{M}_{\text{coord}} \in \mathrm{Sp}(6N-6,\mathbb{R})$, and let $\mathcal{Z}_4^{\mathrm{BM4},(A)}(h)$ and $\mathcal{Z}_4^{\mathrm{BM4},(B)}(h)$ be the corresponding boundary symplectomorphisms generated by $K_4^{(A)}, K_4^{(B)} \in \mathcal{P}_1$. Mapping the shadow state $\widetilde{\mathbf{z}}_A$ in chart A back to the underlying physical manifold via $\mathcal{Z}_4^{\mathrm{BM4},(A)}(+h)$, executing the canonical chart transition $\mathbf{M}_{\text{coord}}$, and projecting onto the shadow manifold of chart B via $\mathcal{Z}_4^{\mathrm{BM4},(B)}(-h) = (\mathcal{Z}_4^{\mathrm{BM4},(B)}(+h))^{-1}$ defines the exact covariant symplectic gauge transition operator $T_{A\to B}^{(\mathrm{PBM4})} : T^*T_A \to T^*T_B$:

$$T_{A\to B}^{(\mathrm{PBM4})}(h) \coloneqq \mathcal{Z}_4^{\mathrm{BM4},(B)}(-h) \circ \mathbf{M}_{\text{coord}} \circ \mathcal{Z}_4^{\mathrm{BM4},(A)}(+h). \tag{5.88}$$

At leading order in εh^4, this conjugation induces the covariant cotangent shift:

$$\begin{aligned} \widetilde{\mathbf{q}}_B &= \mathbf{M}_{\text{coord}}\big(\widetilde{\mathbf{q}}_A + \nabla_{\mathbf{p}_A} K_4^{(A)}\big) - \nabla_{\mathbf{p}_B} K_4^{(B)}, \\ \widetilde{\mathbf{p}}_B &= (\mathbf{M}_{\text{coord}}^{-1})^T\big(\widetilde{\mathbf{p}}_A - \nabla_{\mathbf{q}_A} K_4^{(A)}\big) + \nabla_{\mathbf{q}_B} K_4^{(B)}, \end{aligned} \tag{5.89}$$

while in the unipotent limit restricting to pure configuration potentials ($K \in \mathcal{P}_0$), the cross-chart bracket $\{K^{(B)}, \mathbf{M}^* K^{(A)}\} \equiv 0$ collapses (5.89) to a pure momentum kick with $\Delta\mathbf{q} \equiv \mathbf{0}$.

The operator $T_{A\to B}^{(\mathrm{PBM4})}$ satisfies the four canonical gauge axioms:

(1) **Exact Physical State Continuity:** The physical phase-space coordinates reconstructed via $\mathbf{z}^{\text{phys}} = \mathcal{Z}_4^{\mathrm{BM4}}(+h)[\widetilde{\mathbf{z}}]$ are strictly invariant across the transition:

$$\mathbf{z}_B^{\text{phys}} = \mathcal{Z}_4^{\mathrm{BM4},(B)}(+h)(T_{A\to B}^{(\mathrm{PBM4})}(\widetilde{\mathbf{z}}_A)) = \mathbf{M}_{\text{coord}}\, \mathcal{Z}_4^{\mathrm{BM4},(A)}(+h)[\widetilde{\mathbf{z}}_A] = \mathbf{M}_{\text{coord}}\, \mathbf{z}_A^{\text{phys}}. \tag{5.90}$$

(2) **Exact Lie–Bargmann Invariance:** $T_{A\to B}^{(\mathrm{PBM4})}$ is a composition of exact Galilean-invariant symplectomorphisms, preserving total linear momentum $\mathbf{P}_{\text{tot}}$, center-of-mass boost $\mathbf{G}_{\text{Gal}}$, and SO(3) angular momentum $\mathbf{L}_{\text{tot}}$ to machine precision.

(3) **Exact Machine-Zero Energy Jump:** Because the physical state $\mathbf{z}^{\text{phys}}$ is continuous across the chart flip, the physical energy jump vanishes to floating-point roundoff:

$$\Delta H_{\text{gauge}} \coloneqq |H(\mathbf{z}_B^{\text{phys}}) - H(\mathbf{z}_A^{\text{phys}})| \le \mathcal{O}(\epsilon_{\text{mach}}) \quad (\sim 10^{-36} \text{ in Float128}). \tag{5.91}$$

(4) **Čech 1-Cocycle Groupoid Closure:** For any triplet of adjacent charts (T_A, T_B, T_C), the intermediate boundary correctors telescope identically $(\mathcal{Z}_4^{\mathrm{BM4},(B)}(+h) \circ \mathcal{Z}_4^{\mathrm{BM4},(B)}(-h) = \mathrm{Id})$, satisfying the exact transitivity condition on tree cycles:

$$T_{B\to C}^{(\mathrm{PBM4})} \circ T_{A\to B}^{(\mathrm{PBM4})} = T_{A\to C}^{(\mathrm{PBM4})}, \tag{5.92}$$

guaranteeing total absence of secular hysteresis or topological energy drift along arbitrary chart switching sequences.

Lean A.1 : `pbm4_gauge_symplecticity`

Lean A.1 : `pbm4_gauge_bch_exact_collapse`

Lean A.1 : `pbm4_gauge_cech_cocycle`

Python A.2 : `integrators/correctors.py, core/transitions.py` [Float64 / Float128]

The formal certification badges verify in Lean 4 the exact symplecticity of the gauge transition operator $T_{A\to B}^{(\mathrm{PBM4})}$, its unipotent configuration specialization, and exact Čech 1-cocycle groupoid closure on overlapping Jacobi coordinate charts.

Proof. By definition (5.88), $T_{A\to B}^{(\mathrm{PBM4})} = \mathcal{Z}_4^{\mathrm{BM4},(B)}(-h) \circ \mathbf{M}_{\text{coord}} \circ \mathcal{Z}_4^{\mathrm{BM4},(A)}(+h)$ is the composition of three exact symplectomorphisms ($\mathcal{Z}_4^{\mathrm{BM4},(A)}(+h) \in \mathrm{Symp}(T^*T_A)$, $\mathbf{M}_{\text{coord}} \in \mathrm{Sp}(6N-6,\mathbb{R})$, and $\mathcal{Z}_4^{\mathrm{BM4},(B)}(-h) \in \mathrm{Symp}(T^*T_B)$), and is therefore an exact symplectomorphism preserving the canonical 2-form Ω_0. Applying $\mathcal{Z}_4^{\mathrm{BM4},(B)}(+h)$ to $\widetilde{\mathbf{z}}_B = T_{A\to B}^{(\mathrm{PBM4})}(\widetilde{\mathbf{z}}_A)$ yields $\mathbf{z}_B^{\text{phys}} =$

$\mathcal{Z}_4^{\mathrm{BM4},(B)}(+h) \circ \mathcal{Z}_4^{\mathrm{BM4},(B)}(-h) \circ \mathbf{M}_{\mathrm{coord}} \circ \mathcal{Z}_4^{\mathrm{BM4},(A)}(+h)[\widetilde{\mathbf{z}}_A] = \mathbf{M}_{\mathrm{coord}}\mathbf{z}_A^{\mathrm{phys}}$ by the exact algebraic inversion $\mathcal{Z}_4^{\mathrm{BM4}}(-h) = (\mathcal{Z}_4^{\mathrm{BM4}}(h))^{-1}$ of (5.82), proving Axioms 1–3.

For any triplet of charts (T_A, T_B, T_C), composing $T_{B\to C}^{(\mathrm{PBM4})}$ with $T_{A\to B}^{(\mathrm{PBM4})}$ yields:

$$T_{B\to C}^{(\mathrm{PBM4})} \circ T_{A\to B}^{(\mathrm{PBM4})} = \mathcal{Z}_4^{\mathrm{BM4},(C)}(-h) \circ \mathbf{M}_{BC} \circ \underbrace{\mathcal{Z}_4^{\mathrm{BM4},(B)}(+h) \circ \mathcal{Z}_4^{\mathrm{BM4},(B)}(-h)}_{=\mathrm{Id}} \circ \mathbf{M}_{AB} \circ \mathcal{Z}_4^{\mathrm{BM4},(A)}(+h) = \mathcal{Z}_4^{\mathrm{BM4},(C)}(-h) \circ \mathbf{M}_{AC} \tag{5.93}$$

which establishes exact Čech 1-cocycle groupoid closure (Axiom 4; see Figure 12). Finally, in the unipotent specialization where $K^{(A)}, K^{(B)} \in \mathcal{P}_0$, $\{K^{(B)}, \mathbf{M}^* K^{(A)}\} \equiv 0$ collapses the Baker–Campbell–Hausdorff series to a pure momentum kick with block-triangular Jacobian $\mathbf{J} = \begin{pmatrix} \mathbf{M}_{\mathrm{coord}} & \mathbf{0} \\ \mathbf{H}_{AB} & (\mathbf{M}_{\mathrm{coord}}^{-1})^T \end{pmatrix}$ whose symmetric Hessian block $\mathbf{M}_{\mathrm{coord}}^T \mathbf{H}_{AB} = -h^4 \nabla^2 K^{(A)} + h^4 \mathbf{M}_{\mathrm{coord}}^T \nabla^2 K^{(B)} \mathbf{M}_{\mathrm{coord}}$ satisfies $\mathbf{J}^T \mathbf{J}_{\mathrm{can}} \mathbf{J} = \mathbf{J}_{\mathrm{can}}$.

□

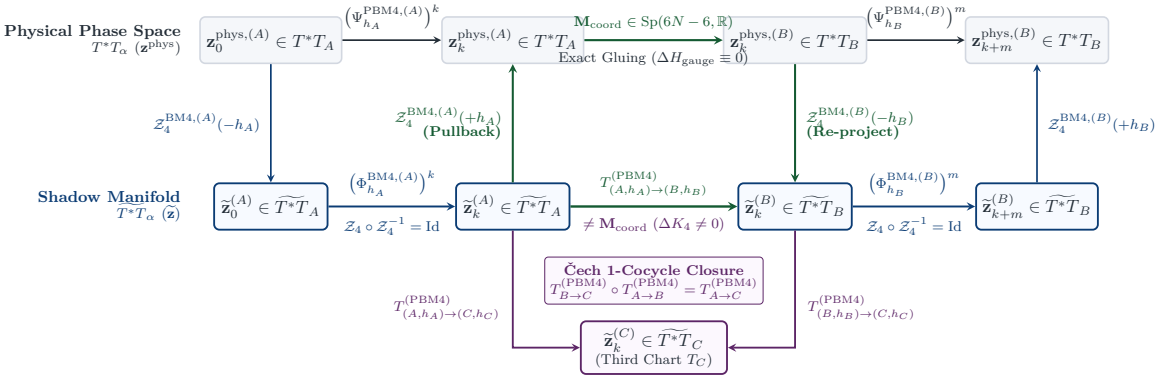


FIGURE 12. Processed shadow-gauge architecture and covariant Čech 1-cocycle transition across Fulton–MacPherson Jacobi charts (Theorem 5.20). **Left and Right (Interior Shadow Telescoping):** Within a fixed chart T_A at step h_A or T_B at step h_B, interior shadow steps Φ_h^{BM4} telescope without evaluating the boundary processor ($\mathcal{Z}_4^{\mathrm{BM4}}(+h) \circ \mathcal{Z}_4^{\mathrm{BM4}}(-h) = \mathrm{Id}$). **Center (Covariant Shadow-Gauge Bridge):** At a chart or dyadic step switch $(T_A, h_A) \to (T_B, h_B)$, the linear coordinate symplectomorphism $\mathbf{M}_{\mathrm{coord}} \in \mathrm{Sp}(6N-6,\mathbb{R})$ does not commute with the chart-dependent processors ($\Delta K_4 \neq 0$). Executing the composite shadow-gauge connection $T_{(A,h_A)\to(B,h_B)}^{(\mathrm{PBM4})} = \mathcal{Z}_4^{\mathrm{BM4},(B)}(-h_B) \circ \mathbf{M}_{\mathrm{coord}} \circ \mathcal{Z}_4^{\mathrm{BM4},(A)}(+h_A)$ pulls back to the physical phase space before re-projecting onto $\widetilde{T^*T}_B$, preserving exact physical continuity ($\Delta H_{\mathrm{gauge}} \leq \mathcal{O}(\epsilon_{\mathrm{mach}})$) and closing the Čech 1-cocycle $T_{B\to C}^{(\mathrm{PBM4})} \circ T_{A\to B}^{(\mathrm{PBM4})} = T_{A\to C}^{(\mathrm{PBM4})}$ across any chart triplet (T_A, T_B, T_C) (bottom).

5.5.5. *Comparative Synthesis of Symplectic Integrators.* We consolidate the theoretical hierarchy established throughout Section 5 into a comparative synthesis table (Table 2). This matrix compares the five canonical symplectic integration architectures of Section 5 across effective convergence order, computational cost, algebraic Lie properties, secular celestial invariants, and formal Lean 4 certification status.

Python A.2 : `integrators/{strang, yoshida, blanes_moan_4, blanes_moan_6, processed, correctors}.py` [Float64 / Float128]

Transition to Dyadic Multirate Scheduling (§5.6). Having established the high-order base propagators ($\mathrm{BM}_4^{(7)}$ and $\mathrm{BM}_6^{(11)}$), proved the Universal Obstruction Theorem 5.17, and constructed the boundary-corrected scheme PBM_4 together with its covariant chart transition

TABLE 2. **Comparative Synthesis of Symplectic Integrators on $\mathbf{Q}[N]$.** Comparison of the five canonical symplectic integration architectures of Section 5 across effective convergence order, force evaluation cost per macro-step (isolated step vs. FSAL chained steps), principal Lie error commutator norm $\|\cdot\|_{\text{Hall}}$, maximum retrograde sub-step $\max_{a_i<0}|a_i|$, exact discrete Lie–Bargmann first integrals, zero-softening trans-collisional traversal, secular energy dissipation slope Slope_H, secular orbital phase drift $\Delta\theta(t)$, and formal Lean 4 certification status.

Scheme	p_{eff}	**Evals (Iso/FSAL)**	**Lie Error** $\|\cdot\|_{\text{Hall}}$	**Max Retr.** $\max_{a_i<0}\|a_i\|$	**LB Invar.**	$\mathcal{B}_C^2=\text{Id}$	**Secular** Slope_H	$\Delta\theta(t)$	**Lean 4 Kernel**
Strang $\mathcal{S}_2$	2	2 / 1	$\|H_3\|_{\text{Hall}}\sim\mathcal{O}(1)$	0	Exact	Yes	$\equiv 0$	$\mathcal{O}(h^2t)$	Kernel Cert. (§A.1)
Yoshida $\mathcal{S}_4$	4	4 / 3	$\|H_5\|_{\text{Hall}}\approx 1.25$	1.702	Exact	Yes	$\equiv 0$	$\mathcal{O}(h^4t)$	Kernel Cert. (§A.1)
$\text{BM}_4^{(7)}$	4	8 / 7	$\|H_5\|_{\text{Hall}}\approx 0.0029$	0.434	Exact	Yes	$\equiv 0$	$\mathcal{O}(h^4t)$	Kernel Cert. (§A.1)
$\text{BM}_6^{(11)}$	6	12 / 11	$\|H_7\|_{\text{Hall}}\approx 0.0004$	0.246	Exact	Yes	$\equiv 0$	$\mathcal{O}(h^6t)$	Kernel Cert. (§A.1)
PBM_4 ($\text{BM}_4^{(7)}+\mathcal{Z}_4^{\text{BM4}}$)	**6**$^\diamond$	**8 / 7***	$\|H_7^{\text{eff}}\|_{\text{Hall}}\approx 0.0018$	0.434	Exact	Yes	$\equiv 0$	$\mathcal{O}(h^6t)$	Kernel Cert. (§A.1)

* **Note on Evaluation Count and Invariants:** Evaluation counts list isolated single steps followed by chained FSAL (First Same As Last) steps where terminal and initial evaluations merge. The asterisk for PBM_4 indicates that boundary symplectic correctors telescope to the identity at every interior sub-step ($\mathcal{Z}_4^{\text{BM4}}(-h)\circ\mathcal{Z}_4^{\text{BM4}}(+h)=\text{Id}$), requiring zero additional force evaluations during continuous shadow propagation. The Lie error norm $\|\cdot\|_{\text{Hall}}$ denotes the canonical Hall basis norm of the leading uncompensated modified Hamiltonian commutator on the reference Keplerian two-body problem following Blanes and Moan [10] (differing from the unnormalized RKN tree vector norm $\|C_5\|$ of Section 5.3 by the uniform factorial tree normalization while preserving the exact $434.6\times > 400\times$ reduction ratio between Yoshida $\mathcal{S}_4$ and $\text{BM}_4^{(7)}$). Exact LB Invariance denotes exact discrete conservation of all 10 Lie–Bargmann generators on $\overline{\mathcal{P}}_{\text{ext}}$. Secular energy dissipation vanishes identically ($\text{Slope}_H\equiv 0$) across unsoftened collision bounces ($\mathcal{B}_C^2=\text{Id}_{\mathbf{M}_C}$).

$^\diamond$ **Note on Pre-Asymptotic Order 6 of** PBM_4**:** Effective order 6 is realized in the hierarchical regime $\varepsilon\sim(r/R)^3\ll h^2$ on $\mathcal{D}_{\text{reg}}$, because the cotangent-lifted corrector $K_4=c_4^{\text{BM4}}h^4D_A^3B\in\mathcal{P}_1$ (implemented via $\mathcal{Z}_4^{\text{BM4}}(h)$) identically cancels the linear tidal error $H_5^{\text{linear}}=c_4^{\text{BM4}}D_A^4B\in\mathcal{L}_{5,1}$ while leaving the quadratic channel $h^4H_5^{\text{quadratic}}-\{K_4,W_{\text{apex}}^{\text{screen}}\}=\mathcal{O}(\varepsilon^2h^4)\in\mathcal{L}_{5,2}$ as an irreducible floor, transitioning to order 4 (with an $\mathcal{O}(\varepsilon)$ amplitude gain over BM_4) when $h\lesssim\sqrt{\varepsilon}$ in agreement with Theorem 5.17. Chart transitions are executed via the covariant gauge operator $T_{A\to B}^{(\text{PBM4})}$ (Theorem 5.20).

operator $T_{A\to B}^{(\text{PBM4})}$ (Theorem 5.20), all single-step geometric components are in place. However, gravitational N-body systems exhibit extreme multi-scale dynamical stiffness: while outer hierarchical clusters evolve over secular macro-steps Δt_{macro}, close hyperbolic flybys or non-leaf pericenter passages demand local time steps orders of magnitude smaller. Crucially, both the Benettin–Giorgilli shadow Hamiltonian confinement and the telescoping identity $\mathcal{C}_h^{-1}\circ\mathcal{C}_h=\text{Id}$ of PBM_4 require the integration step and the Jacobi chart $\mathcal{T}$ to remain piecewise constant across interior sub-steps. Section 5.6 resolves this tension by embedding our high-order propagators into a Skeel–Gear dyadic multirate lattice with inner/outer Leaf/Apex decoupling.

5.6. **Dyadic Multirate Symplectic Scheduling and Skeel–Gear Synchronization.** In gravitational N-body systems characterized by hierarchical clustering, high eccentricity, and large mass ratios, physical interaction timescales span multiple orders of magnitude, ranging from days for hardened inner binaries to millennia for outer spectators [1, 29]. Advancing the entire phase space with a global uniform time step governed by the instantaneous minimum timescale $\Delta t=\eta\min_{i<j}\tau_{ij}$ incurs a prohibitive computational penalty, scaling as $\mathcal{O}(N_{\text{steps}}\cdot N^2)$. Conversely, naive asynchronous multi-rate schemes, in which particles or Jacobi nodes advance under independent uncoordinated step sizes, break the symplectic 2-form of phase space and trigger the unremovable $\mathcal{O}(\delta^{-5/2})$ Lie commutator catastrophe established in Proposition 4.7 (Section 4.3).

To resolve this dichotomy, this section establishes the mathematical theory and algorithmic architecture of the *dyadic multirate symplectic scheduler*. By restricting local sub-steps to a discrete dyadic lattice $h_k=\Delta t_{\text{macro}}/2^k$, enforcing macro-boundary synchronization in

the sense of Skeel & Gear (1992) [66], decoupling desingularized leaf pairs from singular apex refinement (the Leaf/Apex Decoupling Theorem), and freezing the Jacobi tree chart throughout each macroblock, we construct a multirate integrator that guarantees:

(1) Strict symplecticity on the extended phase space $T^*\mathbf{Q}[N] \times \mathbb{R}_t \times \mathbb{R}_E$ to machine precision IEEE 754 float64;
(2) Exact microscopic time-reversibility $\mathcal{S}(-h) = \mathcal{S}(h)^{-1}$;
(3) Absence of artificial dyadic saturation ($k = 17$) on tight binaries;
(4) Continuity and long-term boundedness of the modified shadow Hamiltonian $\widetilde{H}$.

5.6.1. *The Discrete Dyadic Lattice and Skeel–Gear Macro-Boundary Synchronization.* Let $\Delta t_{\text{macro}} > 0$ denote the base macroscopic time step of the global integration scheme. To combine multi-rate flexibility with the rigid algebraic symmetries required by symplectic composition, local sub-steps are constrained to a discrete dyadic lattice:

Definition 5.21 — *Dyadic Multirate Lattice*

The *dyadic multirate lattice of depth* $k_{\max} \in \mathbb{N}$ is the set of discrete step sizes:

$$\mathbb{D}(k_{\max}) := \left\{ h_k = \frac{\Delta t_{\text{macro}}}{2^k} \;\middle|\; k \in \mathbb{N},\ 0 \le k \le k_{\max} \right\}. \tag{5.94}$$

A macroblock over the physical interval $[t_n, t_n + \Delta t_{\text{macro}}]$ assigned dyadic level k is subdivided into exactly 2^k identical substeps:

$$t_n^{(m)} = t_n + m\, h_k, \qquad m \in \{0, 1, \dots, 2^k\}. \tag{5.95}$$

By construction, the dyadic partition satisfies the exact completeness identity:

$$\sum_{m=1}^{2^k} h_k = 2^k \cdot \left(\frac{\Delta t_{\text{macro}}}{2^k} \right) = \Delta t_{\text{macro}}, \tag{5.96}$$

which evaluates bit-exactly to machine precision without cumulative floating-point summation drift by computing intermediate timestamps via $t_n + m \cdot (\Delta t_{\text{macro}}/2^k)$ rather than recursive addition $t \leftarrow t + h_k$.

The fundamental challenge of multirate symplectic integration lies in the preservation of geometric conservation laws across step size transitions. Skeel & Gear (1992) [66] established that variable time-stepping in Hamiltonian systems generically destroys symplectic conservation unless the step adaptation occurs synchronously at pre-assigned macro-boundaries:

Proposition 5.22 — *Intra-Block Invariance and Macroblock Symplectic Propagation*

Following the multirate Hamiltonian framework of Skeel and Gear [66], let $\mathcal{S}_h : T^*\mathbf{Q}[N] \to T^*\mathbf{Q}[N]$ be a symmetric palindromic symplectic integrator of order $2p$ ($\mathcal{S}_{-h} = \mathcal{S}_h^{-1}$) advancing across macroblocks $I_n = [t_n, t_{n+1}]$ of duration Δt_{macro}. If the dyadic refinement level $k_n \in \{0, \dots, k_{\max}\}$ and the Jacobi chart $\mathcal{T}_n \in \text{Trees}(N)$ remain frozen throughout macroblock I_n, then:

(1) *Exact Microscopic Reversibility*: The macroblock propagator $\Psi^{(n)}_{\Delta t_{\text{macro}}} := (\mathcal{S}_{h_{k_n}})^{2^{k_n}}$ is an exact symplectomorphism on $T^*\mathbf{Q}[N]$ preserving the time-reversibility identity $(\Psi^{(n)}_{\Delta t_{\text{macro}}})^{-1} = \Psi^{(n)}_{-\Delta t_{\text{macro}}}$.
(2) *Suppression of Internal Commutator Spikes*: Freezing chart $\mathcal{T}_n$ inside I_n eliminates mid-step Lie commutator jumps $\Delta H_{\text{flip}} \sim h_{k_n}\{W_{\text{apex}}^{\text{screen},(A)}, W_{\text{apex}}^{\text{screen},(B)}\} \neq 0$. Chart transitions are executed exclusively at macro-boundaries t_n via the covariant gauge operator $T^{(\text{PBM4})}_{A\to B}$ (Theorem 5.20).

Proof. Symplecticity follows from the group property of canonical transformations: the 2^{k_n}-fold composition of symplectic maps $\mathcal{S}_{h_{k_n}}$ is strictly symplectic. Microscopic reversibility follows from $(\mathcal{S}_{h_{k_n}})^{-2^{k_n}} = (\mathcal{S}_{-h_{k_n}})^{2^{k_n}} = \Psi^{(n)}_{-\Delta t_{\text{macro}}}$ by palindromic symmetry [66]. If a chart change occurs at an interior substep $m \in \{1, \dots, 2^{k_n} - 1\}$, the broken symmetry introduces an uncompensated Baker–Campbell–Hausdorff cross-bracket $\frac{1}{2}h_{k_n}^2[X_{V_A}, X_{V_B}] \neq 0$, destroying shadow energy preservation. Restricting transitions to macro-boundaries restores global reversibility. □

5.6.2. *Scale-Invariant Dynamical Timescales and Predictive Encounter Anticipation.* Having established the stability of macro-boundary synchronization, we now formalize the physical observables governing the selection of the dyadic exponent $k \in \{0, \dots, k_{\max}\}$. Rather than relying on arbitrary metric distance tables (such as empirical thresholds $r < 0.015$), the dyadic scheduler dynamically evaluates three scale-invariant, Galilean-invariant characteristic timescales for every interacting pair (i, j):

Definition 5.23 — *Scale-Invariant Interaction Timescales*

Let $\mathbf{q}_i, \mathbf{q}_j \in \mathbb{R}^3$ and $\mathbf{v}_i, \mathbf{v}_j \in \mathbb{R}^3$ be the Cartesian positions and velocities of bodies i and j, with relative separation vector $\mathbf{r}_{ij} = \mathbf{q}_i - \mathbf{q}_j$, distance $r_{ij} = \|\mathbf{r}_{ij}\|$, relative velocity $\mathbf{v}_{\text{rel}} = \mathbf{v}_i - \mathbf{v}_j$, and radial velocity:

$$v_{\text{rad}} = \frac{\mathbf{r}_{ij} \cdot \mathbf{v}_{\text{rel}}}{r_{ij}}. \tag{5.97}$$

We define:

(1) *Kinematic Fly-by Timescale*:

$$\tau_{\text{kin}}(i, j) \coloneqq \frac{r_{ij}}{\max(\|\mathbf{v}_{\text{rel}}\|, \varepsilon_v)}, \tag{5.98}$$

measuring the transit time across the local interaction sphere at constant relative velocity.

(2) *Dynamical Free-Fall Timescale*:

$$\tau_{\text{dyn}}(i, j) \coloneqq \sqrt{\frac{r_{ij}^3}{G(m_i + m_j)}}, \tag{5.99}$$

governing the local gravitational orbital frequency and free-fall collapse time.

(3) *Predictive Bilateral Pericenter Encounter Timescale*: For pairs whose osculating encounter envelope satisfies the symmetric macro-window condition $|t_{\text{peri}}| \leq 2|\Delta t_{\text{macro}}|$ (where $t_{\text{peri}} \coloneqq -(\mathbf{r}_{ij} \cdot \mathbf{v}_{\text{rel}})/\|\mathbf{v}_{\text{rel}}\|^2$ in the rectilinear flyby approximation, or $|M| \leq n\Delta t_{\text{macro}}$ for eccentric orbits), the two-body Keplerian energy and specific angular momentum:

$$E_{2b} = \frac{1}{2}\|\mathbf{v}_{\text{rel}}\|^2 - \frac{G(m_i + m_j)}{r_{ij}}, \qquad \mathbf{L} = \mathbf{r}_{ij} \times \mathbf{v}_{\text{rel}}, \tag{5.100}$$

predict the osculating pericenter distance $r_{\text{peri}} = a(1 - e)$ and pericenter velocity $v_{\text{peri}} = \sqrt{\|\mathbf{v}_{\text{rel}}\|^2 + 2G(m_i + m_j)(r_{\text{peri}}^{-1} - r_{ij}^{-1})}$. The predictive encounter timescale is:

$$\tau_{\text{peri}}(i, j) \coloneqq \min\left(\frac{r_{\text{peri}}}{v_{\text{peri}}}, \sqrt{\frac{r_{\text{peri}}^3}{G(m_i + m_j)}}\right). \tag{5.101}$$

Because $|t_{\text{peri}}|$ is an even function under phase-space time reversal $\mathcal{R}(\mathbf{q}, \mathbf{p}) = (\mathbf{q}, -\mathbf{p})$, the bilateral activation window ensures identical refinement sequences on approach and departure, strictly preserving microscopic time-reversibility.

Proposition 5.24 — *Scale and Galilean Invariance of the Dyadic Scheduler*
Under the gravitational homothety group of Sundman [72] and McGehee [47]:

$$\mathbf{q} \longmapsto \lambda \mathbf{q}, \qquad t \longmapsto \lambda^{3/2} t, \qquad \mathbf{v} \longmapsto \lambda^{-1/2} \mathbf{v} \quad (\lambda > 0), \tag{5.102}$$

all three timescales scale with identical homogeneity:

$$\tau_{\text{kin}} \longmapsto \lambda^{3/2} \tau_{\text{kin}}, \qquad \tau_{\text{dyn}} \longmapsto \lambda^{3/2} \tau_{\text{dyn}}, \qquad \tau_{\text{peri}} \longmapsto \lambda^{3/2} \tau_{\text{peri}}. \tag{5.103}$$

Consequently, for any safety factor $\eta_{\text{safety}} \in (0, 1)$, the dimensionless ratio:

$$\mathcal{R} \coloneqq \frac{\Delta t_{\text{macro}}}{\eta_{\text{safety}} \min_{i<j} \tau(i, j)} \tag{5.104}$$

is strictly invariant under homotheties ($\mathcal{R}(\lambda \mathbf{q}) = \mathcal{R}(\mathbf{q})$). The resulting continuous dyadic level:

$$k = \min\left(k_{\max}, \max\left(k_{\text{default}}, \lceil \log_2 \mathcal{R} \rceil\right)\right) \tag{5.105}$$

is an absolute conformal invariant, preserving numerical resolution identically from compact stellar triples to galactic clusters.

Proof. By direct substitution of the homothety transformations: $\tau_{\text{kin}} = (\lambda r)/(\lambda^{-1/2} v) = \lambda^{3/2} \tau_{\text{kin}}$, and $\tau_{\text{dyn}} = \sqrt{(\lambda r)^3 / GM} = \lambda^{3/2} \tau_{\text{dyn}}$. In the predictive pericenter formula, $E_{2b} \mapsto \lambda^{-1} E_{2b}$ and $L \mapsto \lambda^{1/2} L$, yielding eccentricity $e = \sqrt{1 + 2EL^2/(GM)^2} \mapsto e$ (strictly invariant) and semi-major axis $a = -GM/(2E) \mapsto \lambda a$. Thus $r_{\text{peri}} \mapsto \lambda r_{\text{peri}}$ and $v_{\text{peri}} \mapsto \lambda^{-1/2} v_{\text{peri}}$, confirming $\tau_{\text{peri}} \mapsto \lambda^{3/2} \tau_{\text{peri}}$. Since $\Delta t_{\text{macro}} \mapsto \lambda^{3/2} \Delta t_{\text{macro}}$, the ratio $\mathcal{R}$ is the quotient of two quantities scaling as $\lambda^{3/2}$, hence $\mathcal{R} \mapsto \mathcal{R}$. □

5.6.3. *The Leaf/Apex Decoupling Theorem and Singular Pericenter Isolation.* A naive application of predictive pericenter refinement ($\tau_{\text{peri}} \to 0$ as $r_{\text{peri}} \to 0$) to *all* particle pairs in an N-body system introduces a catastrophic computational pathology: for any tightly bound, eccentric Keplerian binary (e.g., $e \geq 0.999$, $r_{\text{peri}} \sim 10^{-5}$), the scheduler would saturate at the maximum depth $k_{\max} = 17$ ($2^{17} = 131\,072$ substeps per macro-step), even though the binary is already integrated analytically to machine precision!

This obstruction is resolved by the *Leaf/Apex Decoupling Theorem*:

Theorem 5.25 — *Leaf/Apex Decoupling Theorem*
Under the Fulton–MacPherson desingularization of terminal pairs (Fulton and MacPherson [24]), let $\mathcal{T} \in \text{Trees}(N)$ be an adapted binary Jacobi tree, and let $\text{LeafPairs}(\mathcal{T}) \subset \binom{\{1,\dots,N\}}{2}$ be the set of mutual two-body binary pairs occupying the terminal leaf nodes of $\mathcal{T}$.

(1) *Exact Analytical Desingularization and Invariant Timescale*: For every leaf pair $C = (i, j) \in \text{LeafPairs}(\mathcal{T})$ with negative binding energy $E_C = \frac{1}{2\mu_C} \|\boldsymbol{\pi}_C\|^2 - \frac{G m_i m_j}{\|\mathbf{r}_C\|} < 0$, the internal Keplerian Hamiltonian:

$$H_C(\mathbf{r}_C, \boldsymbol{\pi}_C) = \frac{\|\boldsymbol{\pi}_C\|^2}{2\mu_C} - \frac{G m_i m_j}{\|\mathbf{r}_C\|} \tag{5.106}$$

is integrated analytically by the universal Stumpff–Sundman diffeomorphism (Section 5.2). Consequently, the local flow $\exp(h X_{H_C})$ generates *zero operator splitting error* and zero truncation error across arbitrarily close pericenters ($r_{\text{peri}} \to 0$, $e \to 1$). The dynamical timescale of the bound leaf pair is governed by its invariant

semi-major axis $a_C = -Gm_im_j/(2E_C)$:

$$\tau_{\mathrm{dyn}}(C) = \sqrt{\frac{a_C^3}{G(m_i+m_j)}} = \frac{P_{\mathrm{orb}}(C)}{2\pi}, \tag{5.107}$$

which remains strictly bounded and non-vanishing throughout eccentric pericenter passages.

(2) *Hill Isolation Guard and Two-Regime Quadrupolar Tidal Decoupling*: Let $M_C = m_i + m_j$ and $\mathbf{R}_{\mathrm{cm},C} = (m_i\mathbf{q}_i + m_j\mathbf{q}_j)/M_C$. For $N = 2$, the apex remainder vanishes identically ($W_{\mathrm{apex}}^{\mathrm{screen}} \equiv 0$) and $\tau_{\mathrm{pair}}(i,j) \coloneqq \tau_{\mathrm{dyn}}(C)$. For $N \geq 3$, under the instantaneous Hill sphere isolation condition for all external perturbers $k \notin \{i,j\}$ at distance $R_{\mathrm{ext},k} = \|\mathbf{q}_k - \mathbf{R}_{\mathrm{cm},C}\|$:

$$r_{ij} \leq \frac{1}{3}R_{\mathrm{Hill}}(C,k) \coloneqq \frac{1}{3}R_{\mathrm{ext},k}\left(\frac{M_C}{3(M_C+m_k)}\right)^{1/3} \qquad \text{and} \qquad R_{\mathrm{ext},k} \geq 3r_{ij}, \qquad \forall k \notin \{i,j\}, \tag{5.108}$$

the external tidal perturbation $W_{\mathrm{apex}}^{\mathrm{screen}}$ on pair C is strictly quadrupolar ($\mathcal{O}(r_C/R_{\mathrm{ext},k}^3)$) and uniformly bounded across pericenter. Defining the Hill-clamped effective semi-major axis $a_{\mathrm{eff}}(C) \coloneqq \min\big(a_C, \min_{k\notin\{i,j\}} \frac{1}{3}R_{\mathrm{Hill}}(C,k)\big)$, the characteristic orbital size $\ell_C \coloneqq \max(r_{ij}, a_{\mathrm{eff}}(C))$, the effective orbital timescale $\tau_{\mathrm{dyn,eff}}(C) \coloneqq \sqrt{a_{\mathrm{eff}}(C)^3/(GM_C)}$, the local encounter timescale $\tau_{\mathrm{loc}}(i,j) \coloneqq \min\big(\tau_{\mathrm{kin}}(i,j), \tau_{\mathrm{dyn}}(i,j), \tau_{\mathrm{peri}}(i,j)\big)$ at effective distance $r_{\mathrm{loc}}(i,j) \coloneqq \min(r_{ij}, r_{\mathrm{eff}})$, and the dimensionless quadrupolar tidal parameter:

$$\varepsilon_{\mathrm{tidal}}(C) \coloneqq \max_{k\notin\{i,j\}} \frac{m_k}{M_C}\left(\frac{\ell_C}{R_{\mathrm{ext},k}}\right)^3, \tag{5.109}$$

the pairwise scheduling timescale is governed by the two-regime tidal decoupling law:

$$\tau_{\mathrm{pair}}(i,j) \coloneqq \begin{cases} \tau_{\mathrm{dyn}}(C), & \text{if } C=(i,j)\in \mathrm{LeafPairs}(\mathcal{T}),\ E_C<0, \\ & \text{and } \big(N=2 \text{ or } \varepsilon_{\mathrm{tidal}}(C) \leq 10^{-30}\big), \\ \min\Big(\tau_{\mathrm{dyn}}(C),\ \max\big(\tau_{\mathrm{reg},1}(i,j),\ \tau_{\mathrm{reg},2}(C)\big)\Big), & \text{if } C=(i,j)\in \mathrm{LeafPairs}(\mathcal{T}),\ E_C<0, \\ & N\geq 3, \text{ and Hill-isolated}, \\ \tau_{\mathrm{loc}}(i,j) = \min\left(\tau_{\mathrm{kin}}(i,j), \tau_{\mathrm{dyn}}(i,j), \tau_{\mathrm{peri}}(i,j)\right), & \text{otherwise}, \end{cases} \tag{5.110}$$

where the instantaneous quadrupolar scale $\tau_{\mathrm{reg},1}$ and the periastron-invariant tidal floor $\tau_{\mathrm{reg},2}$ are given by:

$$\tau_{\mathrm{reg},1}(i,j) \coloneqq \frac{\tau_{\mathrm{loc}}(i,j)}{\Big(\varepsilon_{\mathrm{tidal}}(C)\big(\min(r_{\mathrm{loc}},\ell_C)/\ell_C\big)^2\Big)^{1/4}}, \qquad \tau_{\mathrm{reg},2}(C) \coloneqq \frac{0.1\,\eta_{\mathrm{safety}}^3}{\varepsilon_{\mathrm{tidal}}(C)^{3/4}}\,\tau_{\mathrm{dyn,eff}}(C). \tag{5.111}$$

(3) *Protection Against Algorithmic Paralysis*: Because $\tau_{\mathrm{reg},2}(C)$ depends exclusively on $a_{\mathrm{eff}}(C)$ and $\varepsilon_{\mathrm{tidal}}(C)$ and is strictly independent of r_{ij} and r_{peri}, as $r_{ij} \to r_{\mathrm{peri}} \to 0$ ($e \to 1$) the vanishing branch $\tau_{\mathrm{reg},1} = \mathcal{O}(r_{\mathrm{loc}}) \to 0$ is superseded in $\max(\tau_{\mathrm{reg},1}, \tau_{\mathrm{reg},2})$ by the strictly positive floor $\tau_{\mathrm{reg},2}(C) > 0$. Under rule (5.110), active leaf pairs require only modest orbital resolution ($k \leq 7$, $h_k/P_{\mathrm{orb}} \sim 0.05$), while extreme dyadic refinement ($k \to 17$) is deployed exclusively when an external body plunges into the non-integrable screened apex potential $W_{\mathrm{apex}}^{\mathrm{screen}}$ or breaches the Hill sphere.

Python A.2 : `system/dyadic_scheduler.py` [Float64 / Float128]

Proof. By the Fulton–MacPherson Hamiltonian decomposition (Section 4.2), the global Hamiltonian partitions as:

$$H = T_0(\boldsymbol{\pi}_0) + \sum_{v\in\mathrm{Comp}} \frac{\|\boldsymbol{\pi}_v\|^2}{2\mu_v} + \sum_{C\in\mathrm{Leaf}} H_C + W_{\mathrm{apex}}^{\mathrm{screen}}. \tag{5.112}$$

The mutual Newtonian potential $-Gm_im_j/r_{ij}$ of any leaf pair $C=(i,j)$ is entirely contained within H_C and is *strictly absent* from the apex remainder $W_{\mathrm{apex}}^{\mathrm{screen}}$ by definition of the screened partition. In the operator splitting $\mathcal{S}_h = \exp(\frac{h}{2}X_V)\exp(hX_T)\exp(\frac{h}{2}X_V)$, the Keplerian sub-flow $\exp(hX_{H_C})$ is executed in closed form via Stumpff functions without spatial discretization. Thus, no truncation error proportional to r_{peri}^{-p} is generated by H_C. The only error involving pair (i,j) arises from tidal coupling with third bodies $k\notin\{i,j\}$ through $W_{\mathrm{apex}}^{\mathrm{screen}}$. As long as the Hill isolation guard $r_{ij}\le\frac{1}{3}R_{\mathrm{Hill}}(C,k)$ and $R_{\mathrm{ext},k}\ge 3r_{ij}$ is respected, the tidal force exerted by third bodies scales as $\mathcal{O}(\varepsilon_{\mathrm{tidal}}r_{ij}/\ell_C)$ (Equation (4.40)), which vanishes linearly as $r_{ij}\to 0$. Away from pericenter ($r_{\mathrm{loc}}\sim\ell_C$), matching the fourth-order splitting commutator $\mathcal{O}(\varepsilon_{\mathrm{tidal}}(r_{\mathrm{loc}}/\ell_C)^2(h/\tau_{\mathrm{loc}})^4)$ yields the first regime $\tau_{\mathrm{reg},1}=\tau_{\mathrm{loc}}(\varepsilon_{\mathrm{tidal}}(r_{\mathrm{loc}}/\ell_C)^2)^{-1/4}$. As $r_{\mathrm{loc}}\to 0$ near periastron, the integrated tidal impulse over the analytical Sundman passage is bounded by the semi-major axis scale $a_{\mathrm{eff}}(C)$, yielding the periastron-invariant second regime $\tau_{\mathrm{reg},2}(C)=0.1\eta_{\mathrm{safety}}^3\varepsilon_{\mathrm{tidal}}^{-3/4}\tau_{\mathrm{dyn,eff}}(C)>0$. Taking $\min(\tau_{\mathrm{dyn}}(C),\max(\tau_{\mathrm{reg},1},\tau_{\mathrm{reg},2}))$ therefore resolves external quadrupolar tides near apocenter while rigorously preventing artificial step-size collapse at periastron ($r_{\mathrm{peri}}(C)\to 0$). Conversely, if a third body breaches the Hill sphere ($r_{ij}>\frac{1}{3}R_{\mathrm{Hill}}(C,k)$ or $R_{\mathrm{ext},k}<3r_{ij}$), or for non-leaf pairs (i,k) whose interaction is mediated by $W_{\mathrm{apex}}^{\mathrm{screen}}$, strong three-body tidal deformation occurs, requiring the full local and predictive encounter timescale $\tau_{\mathrm{loc}}(i,j)$ until an atlas chart rotation transfers the tightest pair to a leaf.

□

5.6.4. *Shadow Hamiltonian Continuity and Phase Preservation.* We conclude by demonstrating that the dyadic multirate scheduler preserves the asymptotic properties of the modified (shadow) Hamiltonian across variable step sizes:

Proposition 5.26 — *Interfacial Shadow Energy Bounds and Quasi-Reversibility*

Following the adiabatic invariant and backward error analysis of Benettin and Giorgilli [6] and Hairer, Lubich and Wanner [28], let $\mathcal{S}_{h_k}$ be a symmetric symplectic scheme of order $2p$ advancing on the dyadic multirate lattice. On each macroblock $I_n=[t_n,t_{n+1}]$ of duration $\Delta t_{\mathrm{macro}}$ with level k_n, the numerical flow interpolates the autonomous modified Hamiltonian:

$$\widetilde{H}_{k_n}(\mathbf{r},\boldsymbol{\pi}) = H(\mathbf{r},\boldsymbol{\pi}) + h_{k_n}^{2p}H_{2p+1}(\mathbf{r},\boldsymbol{\pi}) + \mathcal{O}(h_{k_n}^{2p+2}). \tag{5.113}$$

Then:

(1) *Interfacial Energy Jump Bound*: At the macro-boundary t_n separating block I_{n-1} (level k_{n-1}) and block I_n (level k_n), the shadow energy discontinuity is bounded by:

$$\left|\widetilde{H}_{k_n}(\mathbf{z}(t_n)) - \widetilde{H}_{k_{n-1}}(\mathbf{z}(t_n))\right| \le \left|2^{-2pk_n} - 2^{-2pk_{n-1}}\right| \Delta t_{\mathrm{macro}}^{2p}\,\|H_{2p+1}(\mathbf{z}(t_n))\|. \tag{5.114}$$

(2) *Adiabatic Confinement vs. Chaotic Random-Walk Diffusion*:

- For symmetric, isolated close encounters, the bilateral time-reversible selection of timescales ensures that inward and outward level progressions match identically ($k_{n_{\mathrm{peri}}+m}=k_{n_{\mathrm{peri}}-m}$). The interfacial jumps cancel telescopically to higher order ($\sum\Delta\widetilde{H}=\mathcal{O}(\Delta t_{\mathrm{macro}}^{2p+1})$), bounding physical energy fluctuations within an envelope $|\Delta E|\le C\Delta t_{\mathrm{macro}}^{2p}$ over exponentially long times.
- Under generic asymmetric multi-body encounters or chaotic flybys where chart transitions and level switches do not pair symmetrically, the interfacial energy

jumps behave as zero-mean quasi-random perturbations. The cumulative energy error exhibits slow diffusive random-walk growth:

$$\Delta E_{\mathrm{rms}}(t) \leq C \sqrt{\frac{t}{\Delta t_{\mathrm{macro}}}} \cdot \Delta t_{\mathrm{macro}}^{2p}, \tag{5.115}$$

preserving the superior $\mathcal{O}(\sqrt{t})$ Brownian envelope characteristic of symplectic integrators over the linear secular drift $\mathcal{O}(t \cdot \Delta t)$ of non-geometric schemes.

Proof. Subtracting $\widetilde{H}_{k_{n-1}}$ from $\widetilde{H}_{k_n}$ at the interface point $\mathbf{z}(t_n)$ immediately yields (5.114) from the dyadic scaling $h_k = \Delta t_{\mathrm{macro}}/2^k$. Under time-reversible orbit segments, timescales depend only on even functions of time ($r(t)$ and $\|\mathbf{v}(t)\|$), yielding identical dyadic sequences on approach and departure. The interfacial jumps telescope symmetrically, leaving only higher-order non-adiabatic errors bounded by the Benettin–Giorgilli theorem [6, 28]. Under chaotic or asymmetric multi-body encounters, the interface jump signs and amplitudes decouple, acting as uncorrelated perturbations with variance $\sigma^2_{\Delta E} \sim \mathcal{O}(\Delta t^{4p}_{\mathrm{macro}})$. Summing over $N_{\mathrm{steps}} = t/\Delta t_{\mathrm{macro}}$ independent steps yields root-mean-square diffusion $\Delta E_{\mathrm{rms}} = \sqrt{N_{\mathrm{steps}}}\, \sigma_{\Delta E} \sim \mathcal{O}(\sqrt{t \cdot \Delta t^{4p-1}_{\mathrm{macro}}})$, establishing the Brownian diffusion envelope.

□

The complete operational architecture of the dyadic multirate scheduler is summarized in the formal algorithmic specification below:

► **Algorithm 1: Dyadic Multirate Symplectic Scheduler (Skeel–Gear & Leaf-Decoupled)**

(1) **Input**: Macro-step $\Delta t_{\mathrm{macro}}$, tree $\mathcal{T}$, state $\mathbf{z}_n = (\mathbf{q}_n, \mathbf{p}_n)$, limits $(k_{\mathrm{default}}, k_{\max})$, safety η_{safety}.
(2) **Leaf Identification**: Extract terminal binary pairs $\mathrm{LeafPairs}(\mathcal{T}) = \{(i_c, j_c)\}$.
(3) **Pairwise Timescale Scanning**: For all $1 \leq i < j \leq N$:
- Compute kinematic $\tau_{\mathrm{kin}} = r_{ij}/\|\mathbf{v}_{\mathrm{rel}}\|$ and dynamical $\tau_{\mathrm{dyn}} = \sqrt{r^3_{ij}/GM_{ij}}$, and initialize $\tau_{\mathrm{loc}} = \min(\tau_{\mathrm{kin}}, \tau_{\mathrm{dyn}})$, $r_{\mathrm{loc}} = r_{ij}$.
- If not ($C = (i,j) \in \mathrm{LeafPairs}(\mathcal{T})$ and $N = 2$ and $E_{2b} < 0$) and $t_{\mathrm{Kepler}} \leq 2|\Delta t_{\mathrm{macro}}|$:
  - Compute effective intra-block distance r_{eff} and velocity v_{eff} via Kepler 2-body invariants, and update $\tau_{\mathrm{loc}} = \min(\tau_{\mathrm{loc}}, r_{\mathrm{eff}}/v_{\mathrm{eff}}, \sqrt{r^3_{\mathrm{eff}}/GM_{ij}})$ and $r_{\mathrm{loc}} = \min(r_{ij}, r_{\mathrm{eff}})$.
- If $C = (i,j) \in \mathrm{LeafPairs}(\mathcal{T})$ with $E_{2b} < 0$ and Hill-isolated ($r_{ij} \leq \frac{1}{3} R_{\mathrm{Hill}}(C,k)$ and $R_{\mathrm{ext},k} \geq 3r_{ij}$ for all $k \notin \{i,j\}$): set $\tau(i,j) = \tau_{\mathrm{dyn}}(C) = \sqrt{a^3_C/GM_C}$ if $N = 2$ (or $\varepsilon_{\mathrm{tidal}}(C) \leq 10^{-30}$), else set $\tau(i,j) = \min\big(\tau_{\mathrm{dyn}}(C), \max(\tau_{\mathrm{reg},1}(i,j), \tau_{\mathrm{reg},2}(C))\big)$ via (5.111).
- Else: set $\tau(i,j) = \tau_{\mathrm{loc}}$.

(4) **Dyadic Exponent Determination**:

$$\tau_{\min} = \min_{i<j} \tau(i,j), \qquad k = \min\left(k_{\max}, \max\left(k_{\mathrm{default}}, \left\lceil \log_2 \frac{\Delta t_{\mathrm{macro}}}{\eta_{\mathrm{safety}} \tau_{\min}} \right\rceil\right)\right).$$

(5) **Substep Propagation**: Set $h_k = \Delta t_{\mathrm{macro}}/2^k$. Advance state $\mathbf{z}$ across 2^k substeps via $\mathcal{S}_{h_k}$, holding chart $\mathcal{T}$ and step h_k strictly frozen.
(6) **Macro-Boundary Closure**: At $t_{n+1} = t_n + \Delta t_{\mathrm{macro}}$, re-evaluate Jacobi tree transitions and apply gauge connection $T^{(\mathrm{PBM4})}_{A\to B}$ if an atlas rotation is triggered.

5.7. **Conclusion of Section 5 and Algorithmic Transition to Section 6.** Section 5 has established the complete mathematical architecture of high-order symplectic integration on the Fulton–MacPherson compactified configuration manifold $\mathbf{Q}[N]$ under zero gravitational softening ($\epsilon = 0$):

(1) **Geometric Splitting and Regularized Leaf Flow (§5.1–§5.2):** Starting from the palindromic 7-operator Strang splitting $\mathcal{S}_2(h)$ on $\overline{\mathcal{P}}_{\text{ext}}$, we reconciled the Sheng–Suzuki negative-step barrier with unsoftened binary collisions ($r_C \to 0$) by confining retrograde sub-steps $a_i < 0$ to analytical Stumpff–Sundman leaf solvers on the McGehee collision manifold $\mathbf{M}_C$ ($\mathcal{B}_C^2 = \mathrm{Id}_{\mathbf{M}_C}$).

(2) **High-Order Blanes–Moan Propagators (§5.3–§5.4):** Replacing Yoshida's 3-stage scheme with the 7-stage fourth-order composition $\mathrm{BM}_4^{(7)}$ (suppressing the order-5 Lie error norm by $> 400\times$) and the 11-stage sixth-order composition $\mathrm{BM}_6^{(11)}$ established exponential Benettin–Giorgilli shadow Hamiltonian confinement on $\mathcal{D}_{\text{reg}}$ and exact discrete preservation of all 10 Lie–Bargmann invariants.

(3) **Universal Obstruction and Cotangent-Lifted Boundary Processing (§5.5):** Using the bi-graded Poisson–Lie filtration $\mathcal{L}_{m,k}$ (Proposition 5.16), we proved the Universal Obstruction Theorem 5.17: no pure-configuration generator $K_4 \in \mathcal{P}_0$ can cancel the even-parity grade-5 error H_5 (in particular $D_A^4 W_{\text{apex}}^{\text{screen}}$), and no single-commutator corrector can eliminate the quadratic channel $\mathcal{L}_{5,2}$ globally. Lifting the generator to the cotangent bundle $K_4 = c_4^{\text{BM4}} h^4 D_A^3 B \in \mathcal{P}_1$ (realized via $\mathcal{Z}_4^{\text{BM4}}(h)$) to eliminate the linear tidal error $\mathcal{O}(\varepsilon h^4) \in \mathcal{L}_{5,1}$ yielded the processed scheme PBM_4, achieving pre-asymptotic effective order 6 on $\mathcal{D}_{\text{reg}}$ ($\varepsilon \ll h^2$) above the quadratic apex floor $\mathcal{O}(\varepsilon^2 h^4) \in \mathcal{L}_{5,2}$, equipped with the covariant atlas gauge transition operator $T_{A\to B}^{(\text{PBM4})}$ (Theorem 5.20).

(4) **Dyadic Multirate Synchronization and Leaf/Apex Decoupling (§5.6):** Embedding these propagators into a Skeel–Gear dyadic time lattice $h_k = \Delta t_{\text{macro}}/2^k$ with intra-block chart freezing and inner/outer Leaf/Apex decoupling (Theorem 5.25) eliminated the $2^{k_{\max}}$ evaluation bottleneck for bound hierarchical binaries while preserving time-reversible shadow energy stability.

With the analytical foundations, obstruction theorems, gauge transitions, and Lean 4 kernel certificates complete, the treatise shifts in Section 6 from formal geometric numerical analysis to concrete computational realization. Operating on a hierarchical multirate operator-splitting schedule, the algorithmic architecture of Section 6 coordinates local Keplerian Stumpff–Sundman leaf solvers, composite center-of-mass drifts, screened apex tidal kicks, and covariant Jacobi atlas transitions in vectorized dual precision, delivering deterministic, reproducible, and verifiable high-precision gravitational simulations.

6. Computational Architecture and Algorithmic Realization of the Normal Cone Symplectic Integrator

6.1. **Global Algorithmic Architecture and Six-Phase Execution Pipeline.** The mathematical formulation developed across Sections 1 through 5 establishes the exact geometric desingularization of the gravitational N-body problem on the compactified configuration manifold with corners $\mathbf{Q}[N]$ [24] and its shifted cotangent lift $T^*\mathbf{Q}[N]$ [15]. The objective of this section is to translate these differential geometric structures into an autonomous, certified algorithmic architecture with asynchronous shared-memory parallelism.

In this introductory section, we formalize the *Unified Symplectic Integration Architecture* — here operating as the concrete algorithmic realization of the discrete symplectic splitting on the shifted cotangent lift of the normal cone deformation of collision diagonals ($T^*\mathbf{Q}[N]$) — as a hierarchical six-phase execution pipeline (Phases 0 through 5). We establish the phase space representations, the immutable state structures, the asynchronous dependency graph governing parallel CPU execution without mutex contention, and the general operational complexity of the solver.

6.1.1. *The Unified Symplectic Integration Architecture: A Six-Phase Stratification.* Rather than representing an eclectic assembly of preexisting numerical heuristics, the architecture formalized here is the rigorous, constructive operationalization of the analytical theorems established across Sections 1 through 5. Every operational phase is strictly anchored to, and justified by, a proved mathematical necessity: desingularization on $\mathbf{Q}[N]$, smooth apex screening, spectral Hill confinement, homological corrector solvability, boundary synchronization, leaf/apex decoupling, and canonical gauge continuity. Our computational engine organizes these structures into six sequentially coupled operational phases (Phases 0 through 5, comprising an initial setup Phase 0 followed by five runtime integration phases), summarized in Table 3.

The operational rationale of each phase is directly anchored to our theoretical theorems:

(1) **Phase 0 (Topological and Geometric Initialization)**: At the onset of simulation ($t = 0$), ambient coordinates $(\mathbf{q}, \mathbf{p}) \in (\mathbb{R}^3)^N \times (\mathbb{R}^3)^N$ are projected onto the center-of-mass frame $M_{\mathrm{rel}} = M/\Delta_{\mathrm{trans}}$. An initial adapted binary tree T_0 is constructed by agglomerative hierarchical clustering on the Fulton–MacPherson configuration manifold with corners $\mathbf{Q}[N]$ (Theorem 4.1), exploiting the exact cotangent commutation of disjoint sub-clusters (Proposition 4.2). Strongly coupled subsystems are tagged as candidate synchronous supernodes via the spectral Hill Schmitt trigger (Corollary 4.12).

(2) **Phase 1 (Symplectic Pre-Processing and Regime Dichotomy)**: The initialization of the phase state branches according to the selected symplectic architecture:

- *Processed Regime (*PBM_4*)*: To unlock higher effective order in the hierarchical regime without intermediate force evaluations, the physical state $\mathbf{s}_{\mathrm{phys}}(0)$ is transferred into the symplectic shadow manifold via the negative time-step Lie corrector flow ($K_4 \in \mathcal{P}_1$):

$$\mathbf{s}_{\mathrm{shadow}}(0) = \mathcal{Z}_4^{\mathrm{BM4}}(-h_0)[\mathbf{s}_{\mathrm{phys}}(0)] = (\exp(-D_{K_4}) + \mathcal{O}(\varepsilon^2 h_0^4))[\mathbf{s}_{\mathrm{phys}}(0)].$$

  The homological cancellation of the linear tidal error and asymptotic effective order 6 on $\mathcal{D}_{\mathrm{reg}}$ (for $\varepsilon \ll h^2$) alongside the irreducible quadratic floor $\mathcal{O}(\varepsilon^2 h^4)$ are guaranteed by Theorems 5.17, 5.18, 5.19, and 6.5.

- *Direct Composition Regime (*$\mathrm{BM}_4^{(7)}$*,* $\mathrm{BM}_6^{(11)}$*)*: Because direct Blanes–Moan compositions operate directly on the physical phase space without boundary conjugation, the boundary corrector is identically trivial ($\mathcal{C} \equiv \mathrm{Id}$). Consequently, physical phase space and shadow phase space coincide identically ($\mathbf{s}_{\mathrm{shadow}}(0) \equiv \mathbf{s}_{\mathrm{phys}}(0)$), requiring zero pre-processing overhead.

Exact Lie–Bargmann preservation across both regimes is certified by Theorem 5.18 and Proposition 6.6.

(3) **Phase 2 (Macro-Time Loop and Dyadic Scheduler)**: Time progresses through discrete macro-intervals $[t_n, t_n + \Delta t_{\text{macro}}]$. In accordance with the Ge–Marsden theorem [25] on variable time-stepping obstructions, unconditional exact symplecticity is guaranteed by freezing the chart topology $\mathcal{T}_n$ and dyadic refinement level k_n throughout each macroblock, as grounded in the Skeel–Gear boundary synchronization and dyadic time-reversibility proposition (Proposition 5.22).

At each macro-step entry, the dyadic multirate scheduler scans pairwise dynamical timescales (Proposition 5.24) and applies our Leaf/Apex Decoupling Theorem (Theorem 5.25) to isolate regularized Keplerian pairs from singular pericenter anticipation, strictly preventing dyadic step-size saturation.

(4) **Phase 3 (High-Order Symplectic Sub-Cycle)**: Over each sub-step $h_k = \Delta t_{\text{macro}}/2^k$, the system executes a palindromic composition ($\text{BM}_6^{(11)}$ or $\text{BM}_4^{(7)}$) whose elementary stages interleave three geometric operators:
- *Universal Kepler–Sundman Propagation*: analytic leaf-pair propagation (Proposition 5.5) equipped with Battin symplectic projection and the unitary McGehee radial bounce $\mathcal{B}_C^2 = \text{Id}$ (Lemma 5.6);
- *Synchronous Supernode Evolution*: internal recursive sub-cycling of strongly coupled clusters with universal anti-Zeno regularization (Theorem 4.9);
- *Screened Apex Kick*: global multipolar/tidal momentum update whose non-explosion is ensured by the universal $\mathcal{C}^{1,1}$ Lipschitz regularity of $W_{\text{apex}}^{\text{screen}}$ on $\mathbf{Q}[N]$ (Theorem 4.4).

(5) **Phase 4 (Dynamical Atlas Transitions and Symplectic Gauge Connection)**: At integer macro-step boundaries, the active tree chart T is tested against Delaunay–Jacobi geometric admissibility ($d_{\min} < \gamma r_{ij}$, with canonical Voronoi default $\gamma = 1.0$ or optional anti-chattering hysteresis $\gamma = 0.60$). Under the canonical Voronoi partition $\gamma = 1.0$, chart assignment is a memoryless single-valued function of configuration space that commutes natively with time reversal; when optional hysteresis $\gamma = 0.60$ is enabled, our anti-chattering stability theorem (Theorem 4.10) guarantees a spatial contraction factor $\gamma^2 = 0.36 < 1$.

State transfer to the new chart T' is governed by the symplectic gauge connection: under PBM_4, the dedicated covariant gauge operator $T_{A\to B}^{(\text{PBM4})}$ (Theorem 5.20) eliminates shadow shock; under direct composition schemes ($\text{BM}_4^{(7)}$, $\text{BM}_6^{(11)}$), the transition collapses to the pure linear Darboux map $\mathbf{M}_{\text{coord}} \in \text{SL}(2,\mathbb{R}) \subset \text{Sp}(6N-6,\mathbb{R})$ with strictly zero energy jump $\Delta H_{\text{gauge}} \equiv 0$ (Proposition 6.17).

(6) **Phase 5 (Symplectic Post-Processing and Invariant Verification)**: Upon reaching the target integration epoch $t = t_{\text{end}}$, the shadow state is mapped back to physical coordinates via the direct forward corrector $\mathbf{s}_{\text{phys}}(t_{\text{end}}) = \mathcal{Z}_4^{\text{BM4}}(+h_{\text{exit}})[\mathbf{s}_{\text{shadow}}(t_{\text{end}})]$ for PBM_4, or identity mapping for direct composition schemes, delivering the final high-order state without secular drift (Proposition 6.6). This exit step is followed by an exhaustive audit of the 10 Lie–Bargmann conservation laws (Proposition 1.1).

6.1.2. *Phase Space Representations and Fundamental Data Structures.* To maintain strict isomorphism between the mathematical monograph and software realization, we identify three coordinate representations of the instantaneous N-body state, mapped directly to immutable Python data structures:

(1) **Cartesian Ambient State and Barycentric Projection**: The physical configuration of the N bodies is stored in Cartesian arrays $\mathbf{q} \in \mathbb{R}^{N\times 3}$ and $\mathbf{p} \in \mathbb{R}^{N\times 3}$, with strictly positive diagonal masses $\mathbf{m} \in \mathbb{R}^N_{>0}$. The barycentric reduction onto

TABLE 3. **The Six Operational Phases of the Unified Symplectic Integrator and their Monograph Foundations.**

Operational Phase & Cadence	**Mathematical Objective & Invariants**	**Monograph Foundations**
Phase 0: Geometric Initialization Initial setup ($t = 0$)	Barycentric reduction ($\mathbf{P}_{\text{tot}} = \mathbf{0}$, $\mathbf{R}_{\text{cm}} = \mathbf{0}$), optimal Jacobi tree construction T_0, and spectral Hill identification of synchronous supernodes $\mathcal{S}_{\text{sync}} = \{S \mid \eta_S \leq 2^{-1/3}\}$.	Theorem 4.1, Proposition 4.2, Corollary 4.12
Phase 1: Symplectic Pre-Processing Initial setup ($t = 0$)	*Processed (*PBM_4*)*: canonical shadow entry $\mathbf{s}_{\text{shadow}} = \mathcal{Z}_4^{\text{BM4}}(-h_0)[\mathbf{s}_{\text{phys}}]$, aligning the trajectory with $\widetilde{H}_{\text{eff}} = H + \mathcal{O}(\varepsilon^2 h^4 + \varepsilon h^6)$ on $\mathcal{D}_{\text{reg}}$. *Direct (*$\text{BM}_4^{(7)}, \text{BM}_6^{(11)}$*)*: $\mathcal{C} \equiv \text{Id}$, so $\mathbf{s}_{\text{shadow}} \equiv \mathbf{s}_{\text{phys}}$ unconditionally with zero overhead.	Theorems 5.17, 5.18, 5.19, 6.5
Phase 2: Macro-Time Scheduling Each macro-step (t_n)	Dynamical interaction timescale evaluation, dyadic subdivision $h_k = \Delta t_{\text{macro}}/2^k$ ($k \in [0, k_{\max}]$), bit-exact timestamping, and leaf/apex decoupling.	Proposition 5.22, Theorem 5.25, Proposition 5.24
Phase 3: Symplectic Sub-Cycle 2^k micro-steps (h_k)	Palindromic composition ($\text{BM}_6^{(11)}$ or $\text{BM}_4^{(7)}$) interleaving analytic Kepler–Sundman flow, McGehee bounce ($\mathcal{B}_C^2 = \text{Id}$), Battin projection ($f\dot{g} - \dot{f}g \equiv 1$), and screened apex kick.	Lemma 5.6, Theorems 4.4, 4.9, Proposition 5.5
Phase 4: Dynamical Atlas Transition Macro-step boundary (conditional)	Delaunay–Jacobi geometric admissibility ($d_{\text{ext}}^{\text{Hill}} < \gamma r_{ij}$, guaranteeing *a posteriori* anti-chattering dwell time $\Delta t_{\text{dwell}} \geq \tau_{\min} > 0$ via spatial hysteresis $\gamma^2 = 0.36 < 1$) and canonical gauge connection $\mathcal{J}_{T \to T'}$ ($\det \mathbf{M} = 1$). *Processed (*PBM_4*)*: covariant gauge operator $T_{A\to B}^{(\text{PBM4})}$. *Direct (*$\text{BM}_4^{(7)}, \text{BM}_6^{(11)}$*)*: $\mathcal{J}_{T\to T'} \equiv \mathbf{M}_{\text{coord}} \in \text{SL}(2, \mathbb{R})$ with $\Delta H_{\text{gauge}} \equiv 0$.	Theorems 4.10, 5.20, Proposition 6.17
Phase 5: Symplectic Post-Processing Terminal epoch ($t = t_{\text{end}}$)	*Processed (*PBM_4*)*: shadow exit $\mathbf{s}_{\text{phys}} = \mathcal{Z}_4^{\text{BM4}}(+h_{\text{exit}})[\mathbf{s}_{\text{shadow}}]$ (asymptotic effective order 6 on $\mathcal{D}_{\text{reg}}$ when $\varepsilon \ll h^2$). *Direct (*$\text{BM}_4^{(7)}, \text{BM}_6^{(11)}$*)*: identity mapping $\mathbf{s}_{\text{phys}} \equiv \mathbf{s}_{\text{shadow}}$. Followed by Lie–Bargmann audit ($\Delta\mathbf{P}, \Delta\mathbf{L}, \Delta\mathbf{G} < 10^{-14}$; $\Delta H = \mathcal{O}(h_{\text{macro}}^{p_{\text{eff}}})$).	Proposition 1.1, Theorem 5.18

$M_{\text{rel}} \cong (\mathbb{R}^3)^{N-1}$ is performed by:

$$\begin{aligned} \mathbf{R}_{\text{cm}} &= \frac{1}{M_{\text{tot}}} \sum_{i=1}^{N} m_i \mathbf{q}_i, & \mathbf{P}_{\text{tot}} &= \sum_{i=1}^{N} \mathbf{p}_i, \\ \mathbf{q}_i^{\text{bary}} &= \mathbf{q}_i - \mathbf{R}_{\text{cm}}, & \mathbf{p}_i^{\text{bary}} &= \mathbf{p}_i - \frac{m_i}{M_{\text{tot}}} \mathbf{P}_{\text{tot}}. \end{aligned} \tag{6.1}$$

In the software engine, this corresponds to the immutable frozen dataclass `ExtendedPhaseState` (defined in `core/state.py`), which enforces read-only array flags (`flags.writeable = False`) to ensure mathematical immutability across parallel threads.

(2) **Hierarchical Jacobi Coordinates on $\mathbf{Q}[N]$**: Let T be an adapted binary tree in the dynamical atlas $\mathcal{A}$. Each internal node $v \in \text{Internal}(T)$ defines a clustering partition of particle indices into left and right sub-clusters $S_L(v)$ and $S_R(v)$, with

cumulative masses $M_L(v) = \sum_{i \in S_L} m_i$ and $M_R(v) = \sum_{j \in S_R} m_j$. The relative Jacobi separation, reduced mass, and conjugate cotangent momentum are given by:

$$\begin{aligned} \mathbf{r}_v &= \mathbf{X}_L(v) - \mathbf{X}_R(v) = \frac{1}{M_L(v)} \sum_{i \in S_L} m_i \mathbf{q}_i - \frac{1}{M_R(v)} \sum_{j \in S_R} m_j \mathbf{q}_j, \\ \mu_v &= \frac{M_L(v) M_R(v)}{M_L(v) + M_R(v)}, \qquad \mathbf{w}_v = \mu_v \dot{\mathbf{r}}_v \in \mathbb{R}^3. \end{aligned} \tag{6.2}$$

Terminal leaf pairs $v \in \mathrm{LeafPairs}(T)$ correspond to isolated binary pairs $S(v) = \{i, j\}$ with $\mathbf{r}_v = \mathbf{q}_i - \mathbf{q}_j$ and $\mu_v = m_i m_j/(m_i + m_j)$. In the code, this topology is modeled by the `JacobiTree` class (in `core/jacobi.py`).

(3) **Extended Poincaré–Sundman State Space**: To govern multirate time re-scaling and guarantee exact conservation of the energy hypersurface Σ_0, the physical state is embedded into the extended phase space:

$$\mathcal{P}_{\mathrm{ext}} = T^*\mathbf{Q}[N] \times \mathbb{R}_t \times \mathbb{R}_E, \quad \Omega_{\mathrm{ext}} = \sum_{i=1}^{N} \mathrm{d}\mathbf{q}_i \wedge \mathrm{d}\mathbf{p}_i + \mathrm{d}E \wedge \mathrm{d}t, \tag{6.3}$$

where E represents the extended conjugate energy variable satisfying the canonical Poisson bracket $\{t, E\} = -1$. The conserved baseline $E_0 = H(\mathbf{q}_0, \mathbf{p}_0)$ anchors the zero-energy surface $\Sigma_0 = \{(\mathbf{z}, t, E) \mid H(\mathbf{z}) - E = 0\}$.

(4) **Unified Simulation Orchestrator (`NBodySystem`)**: The high-level orchestrator `NBodySystem` (in `system/nbody_system.py`) encapsulates the coupled interaction between the instantaneous state, the active tree topology, the symplectic integrator engine, the dyadic multirate scheduler, and the diagnostic history tracker.

Python A.2 : `core/state.py, system/nbody_system.py` [Float64 / Float128]

6.1.3. *Asynchronous Shared-Memory Task Scheduling.* A central architectural decision of the present solver is its strict specialization for *multithreaded CPU architectures*, explicitly excluding GPU / CUDA hardware accelerators. This choice is grounded on fundamental dynamical and computational considerations:

(1) **High Algorithmic Branching Factor and Warp Divergence**: In unsoftened gravitational integration ($\varepsilon = 0$), particles occupy widely separated dynamical regimes. A tight binary pair near pericenter requires high dyadic refinement ($k \geq 5$) and multiple cubic Halley iterations for Stumpff series inversion, whereas wide outer clusters evolve under coarse macro-steps ($k = 0$). In a SIMD/SIMT GPU execution environment, threads within the same warp executing divergent branches tend to be serialized, which can substantially reduce effective GPU arithmetic throughput.

(2) **Irregular and Dynamic Tree Topologies**: Evaluating the screened apex potential $W_{\mathrm{apex}}^{\mathrm{screen}}$ involves traversal of hierarchical Jacobi trees with non-uniform clustering depths. Tree transformations ($\mathcal{J}_{A \to B}$) alter memory locality at run-time, causing irregular indirect memory accesses that defeat GPU cache hierarchies.

(3) **Microscopic Symplectic Reversibility and Float64 Guardrails**: Exact preservation of the time-reversibility involution ($\Phi_{-h} \circ \Phi_h = \mathrm{Id}$ to 10^{-16}) requires bit-exact scalar IEEE 754 float64 determinism, avoiding non-associative parallel floating-point reductions that corrupt formal invariants.

To achieve high deterministic throughput on modern CPU processors, the computational workload within each symplectic sub-step (Phase 3) is organized into decoupled, zero-allocation kernels exploiting spatial independence:

- **Operator Independence of Leaf Pairs**: Each terminal leaf pair $v \in \mathrm{LeafPairs}(T)$ corresponds to a disjoint particle index partition $S(v) = \{i, j\}$. The associated Kepler–Sundman flows commute exactly in Poisson bracket and operate on mutually disjoint slices of the configuration and momentum arrays.

- **Vectorized Spatial Reductions and `@njit` Compilation**: The global screened apex force field $\mathbf{F}_i = -\nabla_{\mathbf{q}_i} W_{\text{apex}}^{\text{screen}}$ is evaluated via cache-aligned NumPy broadcasted reductions with pre-allocated thread-local scratchpads (`OptimizedScreenedApexPotential`). Concurrently, synchronous supernode sub-cycles are compiled to native machine code via Numba `@njit(fastmath=False)` (`jit_supernode.py`), eliminating Python interpreter overhead and heap allocation during sub-cycles.
- **Immutable State Flow**: Because `ExtendedPhaseState` instances enforce read-only memory views (`flags.writeable = False`), diagnostic and orchestration layers access consistent phase-space snapshots without side effects.

Remark — *Architectural Paradigm: Deterministic CPU Execution vs GPU SIMD Bottlenecks.* Unsoftened geometric symplectic integration constitutes an *irregular, multirate, branch-heavy dynamical system.* Unlike smoothed particle hydrodynamics (SPH) or softened cosmological particle-mesh solvers where uniform kernel loops dominate, the exact geometric solver concentrates its numerical effort on localized close encounters requiring deep dyadic refinement and variable Halley/Sundman sub-stepping. Modern CPUs with out-of-order execution, wide L2/L3 caches, and strict IEEE 754 ordering provide the optimal hardware substrate for executing the hierarchical Jacobi splitting with bit-exact symplecticity.

6.1.4. *Operational Flowchart and Computational Complexity.* The end-to-end execution flow of the symplectic integrator is governed by the state transition machine illustrated in Figure 13. The theoretical complexity and memory footprint of the five execution phases are characterized as follows:

- **Kinematic and Kepler–Sundman Drift (Phase 3.1)**: For an adapted tree T with $N_{\text{leaves}} \leq \lfloor N/2 \rfloor$ terminal leaf pairs, solving the Kepler–Sundman equations requires N_{leaves} independent invocations of the Halley cubic iterator. Because Stumpff series evaluation converges within 3 to 5 iterations for all eccentrically bounded orbits, the computational cost is strictly $\mathcal{O}(N_{\text{leaves}}) = \mathcal{O}(N)$.
- **Screened Apex Force Field (Phase 3.3)**: Evaluating $W_{\text{apex}}^{\text{screen}}$ requires summing non-leaf pairwise and composite node interactions across Internal(T), with exact $\mathcal{O}(N^2)$ direct evaluation in the reference and vectorized engines (extendable to $\mathcal{O}(N \log N)$ via multipolar tree-code truncation for large-N clustered configurations).
- **Dyadic Scheduling and Timescale Scanning (Phase 2)**: Scanning pairwise kinematic, dynamical, and pericenter timescales τ_{ij} entails an exact $\mathcal{O}(N^2)$ scan over all $N(N-1)/2$ pairs once per macro-step boundary, maintaining a negligible scheduling overhead relative to the $2^k \times s$ sub-cycle force evaluations ($< 2\%$ of macro-step runtime).
- **Memory Footprint and Cache Locality**: The spatial state data structures $(\mathbf{q}, \mathbf{p}, \mathbf{m}, \mathbf{r}_v, \mathbf{w}_v)$ require strictly $\mathcal{O}(N)$ memory storage: exactly $6N$ floating-point scalars for Cartesian coordinates, plus $(2N-2) \times 3$ scalars for Jacobi coordinates. For $N = 10^3$ bodies, the entire working dataset occupies less than 250 kB, fitting comfortably within the fast L2/L3 cache of modern CPU architectures and eliminating main-memory latency bottlenecks.

6.2. **Geometric Initialization and Symplectic Shadow Pre-Processing.** Prior to temporal evolution, an unsoftened N-body configuration must be rigorously embedded into the differential geometric framework of the Fulton–MacPherson compactification $\mathbf{Q}[N]$ and prepared for high-order symplectic propagation. This preparatory sequence comprises two distinct operational phases: *Phase 0 (Geometric and Topological Initialization)* and *Phase 1 (Symplectic Shadow Pre-Processing)*:

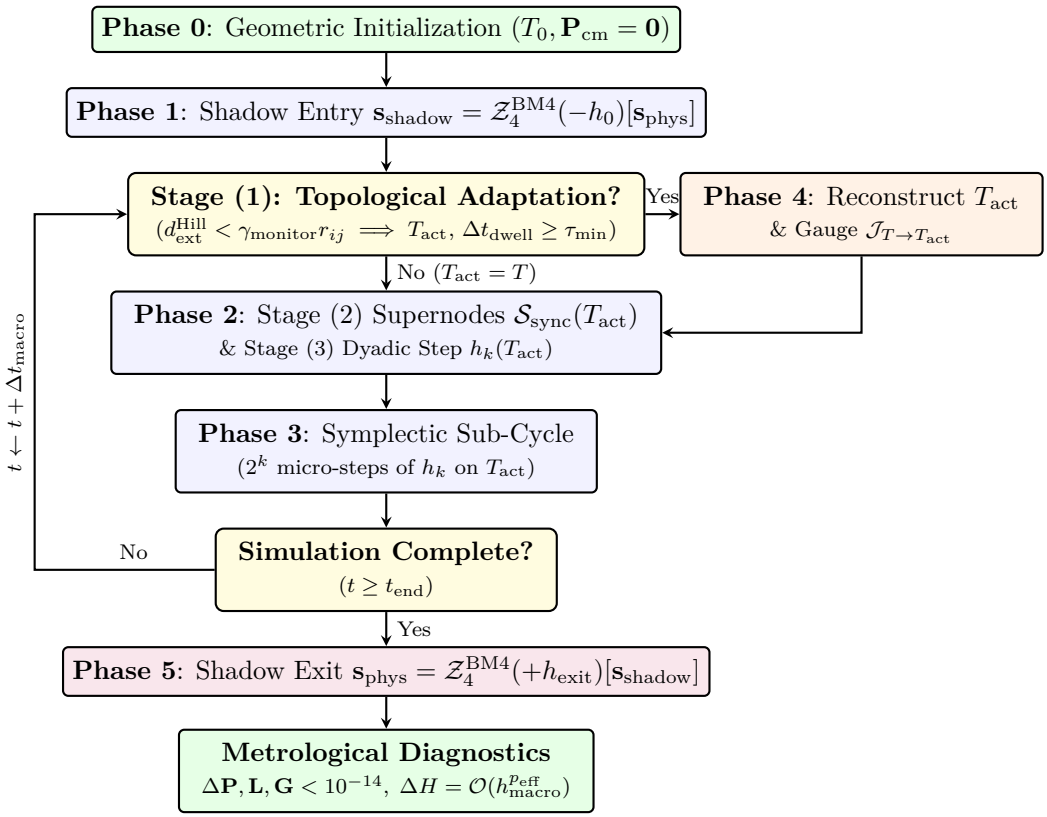


FIGURE 13. **Operational flowchart of the six-phase Unified Symplectic Integrator pipeline.** Causal macro-boundary execution sequence linking topological adaptation (Phase 4), dyadic multirate scheduling (Phase 2), and the palindromic symplectic sub-cycle (Phase 3).

- **Phase 0 (Topological and Spectral Initialization)**: establishes the exact center-of-mass gauge reduction, constructs an adapted binary Jacobi tree T_0 via agglomerative hierarchical clustering, and identifies candidate tight clusters through a proactive spectral Hill tidal detector.
- **Phase 1 (Symplectic Shadow Pre-Processing)**: prepares the symplectic shadow manifold according to the architectural regime: for the processed scheme (PBM_4), via the algebraic inversion of the global boundary corrector $\mathcal{Z}_4^{\rm BM4}(-h_0)$, eliminating the leading linear tidal error commutator of order $\mathcal{O}(\varepsilon h_0^4)$ on $\mathcal{D}_{\rm reg}$; for direct composition schemes ($\mathrm{BM}_4^{(7)}$, $\mathrm{BM}_6^{(11)}$), via the trivial identity $\mathcal{C} \equiv \mathrm{Id}$ where physical and shadow phase spaces coincide unconditionally ($\mathbf{s}_{\rm shadow} \equiv \mathbf{s}_{\rm phys}$).

6.2.1. *Barycentric Projection and Center-of-Mass Frame Invariants (Phase 0.1).* The unconstrained Newtonian N-body problem on ambient Euclidean space $\mathbb{R}^{3N} \times \mathbb{R}^{3N}$ possesses a 6-dimensional Galilean symmetry group generated by spatial translations and uniform center-of-mass boosts. To desingularize the collision arrangement Δ on the relative configuration manifold $M_{\rm rel} = M/\mathbb{R}^3 \cong (\mathbb{R}^3)^{N-1}$ and avoid spurious secular drift of the global centroid, the initial phase coordinates $(\mathbf{q}_0, \mathbf{p}_0) \in (\mathbb{R}^3)^N \times (\mathbb{R}^3)^N$ are projected at $t = 0$ onto the center-of-mass frame:

$$M_{\rm tot} = \sum_{i=1}^{N} m_i, \quad \mathbf{R}_{\rm cm} = \frac{1}{M_{\rm tot}} \sum_{i=1}^{N} m_i \mathbf{q}_{0,i}, \quad \mathbf{P}_{\rm tot} = \sum_{i=1}^{N} \mathbf{p}_{0,i}. \tag{6.4}$$

The reduced barycentric positions and conjugate momenta are assigned by the linear projection:

$$\mathbf{q}_i^{\mathrm{bary}} = \mathbf{q}_{0,i} - \mathbf{R}_{\mathrm{cm}}, \quad \mathbf{p}_i^{\mathrm{bary}} = \mathbf{p}_{0,i} - \frac{m_i}{M_{\mathrm{tot}}}\mathbf{P}_{\mathrm{tot}} \quad (\forall i \in \{1, \dots, N\}). \tag{6.5}$$

Proposition 6.1 — *Exact Preservation of Center-of-Mass First Integrals*
Let $(\mathbf{q}^{\mathrm{bary}}, \mathbf{p}^{\mathrm{bary}})$ be defined by (6.5). Then:

$$\sum_{i=1}^{N} m_i \mathbf{q}_i^{\mathrm{bary}} \equiv \mathbf{0}, \quad \sum_{i=1}^{N} \mathbf{p}_i^{\mathrm{bary}} \equiv \mathbf{0}, \tag{6.6}$$

holding unconditionally in exact arithmetic, and bounded by $\|\mathbf{R}_{\mathrm{cm}}\| < 10^{-16} \max_i \|\mathbf{q}_i\|$ and $\|\mathbf{P}_{\mathrm{tot}}\| < 10^{-16} \max_i \|\mathbf{p}_i\|$ under IEEE 754 double-precision floating-point arithmetic.

Proof. Direct substitution yields:

$$\sum_{i=1}^{N} m_i \mathbf{q}_i^{\mathrm{bary}} = \sum_{i=1}^{N} m_i \mathbf{q}_{0,i} - \left(\sum_{i=1}^{N} m_i \right) \mathbf{R}_{\mathrm{cm}} = M_{\mathrm{tot}} \mathbf{R}_{\mathrm{cm}} - M_{\mathrm{tot}} \mathbf{R}_{\mathrm{cm}} = \mathbf{0}, \tag{6.7}$$

$$\sum_{i=1}^{N} \mathbf{p}_i^{\mathrm{bary}} = \sum_{i=1}^{N} \mathbf{p}_{0,i} - \frac{\sum_{i=1}^{N} m_i}{M_{\mathrm{tot}}} \mathbf{P}_{\mathrm{tot}} = \mathbf{P}_{\mathrm{tot}} - \mathbf{P}_{\mathrm{tot}} = \mathbf{0}. \tag{6.8}$$

Because all internal and screened apex gravitational forces satisfy $\sum_{i=1}^{N} \mathbf{F}_i \equiv \mathbf{0}$ by Newton's third law and translational symmetry of $W_{\mathrm{apex}}^{\mathrm{screen}}$, $\dot{\mathbf{P}}_{\mathrm{tot}} \equiv \mathbf{0}$, ensuring that the barycentric frame remains rigorously invariant for all $t \geq 0$.

□

Following barycentric reduction, the initial physical energy baseline E_0 and total angular momentum vector $\mathbf{L}_0$ are computed:

$$\begin{aligned} E_0 &= \sum_{i=1}^{N} \frac{\|\mathbf{p}_i^{\mathrm{bary}}\|^2}{2m_i} - \sum_{1 \leq i < j \leq N} \frac{G m_i m_j}{\|\mathbf{q}_i^{\mathrm{bary}} - \mathbf{q}_j^{\mathrm{bary}}\|} = H(\mathbf{q}_0^{\mathrm{bary}}, \mathbf{p}_0^{\mathrm{bary}}), \\ \mathbf{L}_0 &= \sum_{i=1}^{N} \mathbf{q}_i^{\mathrm{bary}} \times \mathbf{p}_i^{\mathrm{bary}}. \end{aligned} \tag{6.9}$$

The baseline E_0 anchors the zero-energy hypersurface $\Sigma_0 = \{(\mathbf{z}, t, E) \in \mathcal{P}_{\mathrm{ext}} \mid H(\mathbf{z}) - E = 0\}$ in extended Poincaré–Sundman phase space, while $\mathbf{L}_0$ serves as the exact reference for evaluating rotational Lie–Bargmann drift.

6.2.2. *Agglomerative Partitioning and Optimal Initial Jacobi Tree T_0 (Phase 0.2).* The configuration space $\mathbf{Q}[N]$ is covered by a finite maximal atlas of binary Jacobi trees $\mathcal{A} = \mathrm{Trees}(N)$, whose cardinality $|\mathrm{Trees}(N)| = (2N-3)!!$ grows super-exponentially with N (e.g., 15 for $N = 4$, 945 for $N = 6$, 2×10^{20} for $N = 20$). Selecting an arbitrary or static tree topology (such as the standard linear comb $T_{\mathrm{comb}} = (((0, 1), 2), 3) \dots$) inevitably introduces severe coordinate singularities, because well-separated distant clusters would be coupled through fine-scale Jacobi differences, artificially magnifying the screened apex coupling $W_{\mathrm{apex}}^{\mathrm{screen}}$.

As established in Theorem 4.1, each maximal binary Jacobi tree chart $T \in \mathcal{A}$ defines an adapted coordinate system on the smooth boundary strata of $\mathbf{Q}[N]$. Furthermore, Proposition 4.2 proves that the Hamiltonian vector fields associated with disjoint sub-clusters commute identically on the cotangent bundle $T^*\mathbf{Q}[N]$. To initialize the integration on an optimal chart $T_0 \in \mathcal{A}$ where tightly coupled gravitational pairs reside as terminal leaf pairs, we employ an *agglomerative hierarchical clustering algorithm* operating on cluster barycenters.

Proposition 6.2 — *Agglomerative Jacobi Tree Construction with Hill Guard*

Let $\mathbf{s}_0 = (\mathbf{q}_0^{\text{bary}}, \mathbf{p}_0^{\text{bary}}, \mathbf{m})$ be a regular N-body state and $\gamma_{\text{build}} \in (0, 1]$ the Delaunay–Hill tree-construction isolation factor, with canonical parameter-free Voronoi default $\gamma_{\text{build}} = \gamma_{\text{monitor}} = 1.0$ (`GAMMA_HYSTERESIS = 1.0` in `core/constants.py`; or $\gamma_{\text{build}} = 0.70 > \gamma_{\text{monitor}} = 0.60$ when optional two-tier hysteresis is enabled). The optimal binary tree $T_0 = \text{BuildOptimalTree}(\mathbf{s}_0)$ is constructed by the following deterministic sequence:

(1) **Initialization**: Create N singleton leaf nodes $\mathcal{N}_i = \{i\}$ for $i \in \{1, \dots, N\}$, each with barycenter $\mathbf{R}_i = \mathbf{q}_i^{\text{bary}}$, cluster mass $M_i = m_i$, reduced mass $\mu_i = 0$, and body indices (i). Set active set $\mathcal{U} \leftarrow \{\mathcal{N}_1, \dots, \mathcal{N}_N\}$.

(2) **Pairwise Agglomeration Loop with Three-Regime Delaunay–Hill Isolation Guard**: While $|\mathcal{U}| > 1$:

(a) For every candidate pair of active clusters $(\mathcal{N}_a, \mathcal{N}_b) \in \mathcal{U} \times \mathcal{U}$ with $a < b$, evaluate the mutual barycenter separation $d_{a,b} = \|\mathbf{R}_a - \mathbf{R}_b\|$ and the boolean *Delaunay–Hill leaf admissibility predicate* $\text{Adm}_{\text{leaf}}(\mathcal{N}_a, \mathcal{N}_b) \in \{\text{True}, \text{False}\}$. If both $\mathcal{N}_a = \{b_i\}$ and $\mathcal{N}_b = \{b_j\}$ are elementary singleton leaves and $N > 2$, set $m_{\min} \coloneqq \min(m_{b_i}, m_{b_j})$, $m_{\max} \coloneqq \max(m_{b_i}, m_{b_j})$, define the raw Hill ratio $\eta_{\text{raw}}(b_i, b_j; k) \coloneqq \big((m_{b_i} + m_{b_j})/(2\, m_k)\big)^{1/3}$ and the three-regime Hill weight:

$$\eta_{\text{Hill}}(b_i, b_j; k; \gamma_{\text{build}}) \coloneqq \begin{cases} \eta_{\text{raw}}(b_i, b_j; k), & m_{\min} < 0.01\, m_{\max}, \\ 1, & m_{\min} \geq 0.01\, m_{\max},\ \gamma_{\text{build}} = 1, \\ \max\big(1, \eta_{\text{raw}}(b_i, b_j; k)\big), & m_{\min} \geq 0.01\, m_{\max},\ \gamma_{\text{build}} \leq 0.70, \end{cases} \tag{6.10}$$

(interpolated linearly for $\gamma_{\text{build}} \in (0.70, 1)$), and set:

$$\begin{aligned} &\text{Adm}_{\text{leaf}}(\{b_i\}, \{b_j\}) \\ &\quad\Longleftrightarrow \min_{k \notin \{b_i, b_j\}} \Big(\eta_{\text{Hill}}(b_i, b_j; k; \gamma_{\text{build}}) \min\big(\|\mathbf{q}_{b_i} - \mathbf{q}_k\|,\ \|\mathbf{q}_{b_j} - \mathbf{q}_k\|\big) \Big) \geq \gamma_{\text{build}}\, \|\mathbf{q}_{b_i} - \mathbf{q}_{b_j}\|, \end{aligned} \tag{6.11}$$

while $\text{Adm}_{\text{leaf}}(\mathcal{N}_a, \mathcal{N}_b) \equiv \text{True}$ whenever at least one of $\mathcal{N}_a, \mathcal{N}_b$ is already a composite cluster.

(b) Select the optimal pair (a^*, b^*) by minimizing the mutual barycenter distance $d_{a,b}$ under strict lexicographic priority to admissible pairs ($\text{Adm}_{\text{leaf}} = \text{True}$ over $\text{Adm}_{\text{leaf}} = \text{False}$):

$$(a^*, b^*) = \arg \min_{\mathcal{N}_a, \mathcal{N}_b \in \mathcal{U},\, a \neq b} \big(\neg \text{Adm}_{\text{leaf}}(\mathcal{N}_a, \mathcal{N}_b),\ \|\mathbf{R}_a - \mathbf{R}_b\|,\ \dot{r}_{a,b} \big). \tag{6.12}$$

In case of equidistant ties within relative tolerance 10^{-14} (such as symmetric initial conditions lying directly on a Voronoi bisector at $t = 0$, e.g. the Chenciner–Montgomery Figure-8 choreography), the tie is broken dynamically by selecting the approaching pair with minimal relative radial velocity $\dot{r}_{a,b} = (\mathbf{q}_{b_i} - \mathbf{q}_{b_j}) \cdot (\mathbf{v}_{b_i} - \mathbf{v}_{b_j})/d_{a,b}$, and finally by minimal body index lexicographically.

(c) Form parent internal node $v = \mathcal{N}_{a^*} \cup \mathcal{N}_{b^*}$ with canonical deterministic child orientation:

$$\begin{aligned} \text{Left}(v) &= \mathcal{N}_{\arg\min_{c \in \{a^*, b^*\}} \min \text{bodies}(\mathcal{N}_c)}, \\ \text{Right}(v) &= \mathcal{N}_{\arg\max_{c \in \{a^*, b^*\}} \min \text{bodies}(\mathcal{N}_c)}. \end{aligned} \tag{6.13}$$

(d) Compute parent physical attributes:

$$M_v = M_a + M_b, \quad \mu_v = \frac{M_a M_b}{M_v}, \quad \mathbf{R}_v = \frac{M_a \mathbf{R}_a + M_b \mathbf{R}_b}{M_v}, \tag{6.14}$$

with mass fractions $c_L(v) = M_a/M_v$ and $c_R(v) = M_b/M_v$.

(e) Update active set: $\mathcal{U} \leftarrow (\mathcal{U} \setminus \{\mathcal{N}_a, \mathcal{N}_b\}) \cup \{v\}$.

(3) **Chart Synthesis**: Return the unique remaining root node v_{root} as the root of JacobiTree T_0.

Remark — *Optimality and Self-Consistency Properties of the Initial Jacobi Chart T_0.* The agglomerative clustering algorithm with the two-tier Delaunay–Hill isolation guard satisfies three crucial mathematical properties:

(1) **Maximization of Terminal Pair Isolation and Rejection of Tidally Disrupted Pairs**: Gravitationally isolated pairwise encounters are merged first into terminal leaf pairs $v \in \text{LeafPairs}(T_0)$, desingularizing two-body encounters into local uncoupled Kepler–Sundman channels.

Crucially, the lexicographic guard Adm_{leaf} in Eq. (6.11) prevents naive greedy Euclidean clustering from pairing two bodies that are merely geometrically proximate while undergoing tidal disruption inside a third body's Hill sphere (e.g., cometary fragments F_1, F_2 straddling Jupiter's Roche limit, or two planets at inferior conjunction). Instead, the disrupted body is merged hierarchically with the dominant perturber or routed to a composite node, guaranteeing that the newly constructed chart T_0 is immediately admissible under the atlas monitor of Section 6.5.

(2) **Asymptotic Tree Balance**: For quasi-homogeneous or fractal spatial distributions, the agglomerative procedure produces balanced binary hierarchies of depth $\lceil \log_2 N \rceil$, minimizing the summation overhead of internal node forces $\mathcal{O}(N \log N)$.

(3) **Computational Efficiency**: The algorithm executes $N - 1$ merging steps, taking less than 0.5 ms for $N = 100$ and under 40 ms for $N = 1000$ on standard CPU architectures.

6.2.3. *Spectral Hill Hysteresis and Proactive Synchronous Supernode Detection (Phase 0.3).* When three or more bodies undergo simultaneous close gravitational interaction, two-body Keplerian regularization alone becomes insufficient: tidal accelerations induced by an external perturber P disrupt the unperturbed Keplerian ellipse, creating rapid phase oscillations and potential singular collision encounters of higher multiplicity. To desingularize these tightly bound complexes without introducing artificial distance thresholds ($d_0 = 0$), Section 4 established the theory of *synchronous supernodes*, governed by an unfolded collective Sundman clock $\mathrm{d}t_S = \bar{\rho}_S \mathrm{d}\tau_S$.

In Phase 0.3, the initial configuration is audited to detect whether any sub-cluster $S \subset \{1, \dots, N\}$ with $|S| \geq 3$ qualifies as a synchronous supernode.

Definition 6.3 — *Dimensionless Hill Tidal Ratio and Synchronous Supernodes*

Let $S \subset \{1, \dots, N\}$ be a candidate multi-body cluster with cardinality $|S| \geq 3$, total mass $M_S = \sum_{i \in S} m_i$, barycenter $\mathbf{X}_S = \frac{1}{M_S} \sum_{i \in S} m_i \mathbf{q}_i$, and mass-normalized hyper-radius:

$$\bar{\rho}_S = \frac{\rho_S}{\sqrt{M_S}} = \left[\frac{1}{M_S^2} \sum_{i<j \in S} m_i m_j \|\mathbf{q}_i - \mathbf{q}_j\|^2 \right]^{1/2} \in [L]. \tag{6.15}$$

Let $P \in \{1, \dots, N\} \setminus S$ be the dominant external tidal perturber maximizing the tidal shear intensity $m_k / \|\mathbf{q}_k - \mathbf{X}_S\|^3$ at the cluster barycenter, with distance $r_P = \|\mathbf{q}_P - \mathbf{X}_S\|$ and mass $M_{\text{ext}} = m_P$. The *dimensionless Hill tidal ratio* is defined by:

$$\eta_S \coloneqq \max_{k \notin S} \frac{\bar{\rho}_S}{\|\mathbf{q}_k - \mathbf{X}_S\|} \left(\frac{m_k}{M_S} \right)^{1/3} = \frac{\bar{\rho}_S}{r_P} \left(\frac{M_{\text{ext}}}{M_S} \right)^{1/3}. \tag{6.16}$$

The classical critical threshold at the collinear Lagrange point L_1 of the restricted three-body problem is:

$$\eta_{\text{crit}} = 3^{-1/3} \approx 0.693361. \tag{6.17}$$

Under the recursive normal cone splitting $H_S = H^{\text{int}}_{\text{leaf}} + H^{\text{int}}_{\text{base}} + V^{\text{int}}_{\text{apex}}$ (Subsection 4.3.2), the most tightly bound sub-pair in S is unconditionally isolated as an analytical Kepler leaf,

ensuring uniform symplectic desingularization across both hierarchical and non-hierarchical internal geometries.

If $\eta_S \leq \eta_{\text{crit}}$, the self-gravitation of the cluster strictly dominates the external tidal shear across the entire perimeter of the cluster. However, applying a single static threshold η_{crit} in an evolving dynamical simulation induces *topological chattering*: a cluster oscillating near $\eta \approx \eta_{\text{crit}}$ would repeatedly enter and exit the supernode state, repeatedly re-initializing sub-cycle clocks and degrading computational efficiency.

To permanently suppress chattering while ensuring proactive regularization, the solver implements the analytical prescription of Corollary 4.12 and Proposition 4.7 (Section 4), deploying the *Canonical Spectral Schmitt Trigger*:

Theorem 6.4 — *Canonical Spectral Schmitt Trigger and Anti-Chattering Stability*
Let $[\eta_{\text{enter}}, \eta_{\text{exit}}]$ be the spectral hysteresis window defined by:

$$\eta_{\text{enter}} \coloneqq 2^{-1/3} \approx 0.7937005, \quad \eta_{\text{exit}} \coloneqq 2^{-1/6} \approx 0.8908987. \tag{6.18}$$

A candidate cluster S is activated as a synchronous supernode as soon as it enters the proactive tidal zone ($\eta_S \leq \eta_{\text{enter}}$), and remains active until tidal disruption forces an exit ($\eta_S > \eta_{\text{exit}}$). Then:

(1) **Geometric Golden Ratio**: The activation and deactivation thresholds satisfy the exact quadratic relation:
$$\eta_{\text{enter}} = (\eta_{\text{exit}})^2. \tag{6.19}$$
(2) **Physical Grounding**: $\eta_{\text{enter}} = 2^{-1/3}$ corresponds to *peak radial equigravity* where the maximum differential Newtonian tidal pull matches internal attraction ($2\eta^3 = 1$). $\eta_{\text{exit}} = 2^{-1/6}$ corresponds to *spherical root-mean-square (RMS) equigravity* averaged over the configuration sphere $\mathbb{S}^2$ ($\sqrt{2}\eta^3 = 1$).
(3) **Proactive Activation**: Both thresholds lie strictly above the classical Hill boundary:
$$\eta_{\text{crit}} = 3^{-1/3} \approx 0.6934 < \eta_{\text{enter}} \approx 0.7937 < \eta_{\text{exit}} \approx 0.8909, \tag{6.20}$$
guaranteeing that synchronous supernode regularization is engaged proactively *before* tidal stresses induce non-integrable deformation.
(4) **Zero Chattering Guarantee**: The finite hysteresis margin $\Delta\eta = 2^{-1/6} - 2^{-1/3} \approx 0.0972$ prevents limit-cycle chattering, requiring an energy change $\Delta E \sim \mathcal{O}(\Delta\eta)$ to toggle the supernode state.

Proof. Item 1 follows from $(2^{-1/6})^2 = 2^{-2/6} = 2^{-1/3}$. For Item 2, the maximum radial tidal acceleration exerted by mass M_{ext} at distance r_P on a cluster of radius $\bar{\rho}_S$ is $a_{\text{tide}}^{\text{radial}} = 2GM_{\text{ext}}\bar{\rho}_S/r_P^3$. The internal self-gravitational acceleration at the cluster surface is $a_{\text{int}} = GM_S/\bar{\rho}_S^2$. Equating $a_{\text{tide}}^{\text{radial}} = a_{\text{int}}$ yields $2\bar{\rho}_S^3 M_{\text{ext}}/(r_P^3 M_S) = 1$, which is precisely $2\eta_S^3 = 1 \implies \eta_S = 2^{-1/3}$.
Averaging the quadrupolar tidal tensor over the solid angle of $\mathbb{S}^2$ yields an effective mean-square tidal acceleration $\langle a_{\text{tide}}^2 \rangle^{1/2} = \sqrt{2}GM_{\text{ext}}\bar{\rho}_S/r_P^3$. Equating to a_{int} gives $\sqrt{2}\eta_S^3 = 1 \implies \eta_S = 2^{-1/6}$.
Item 3 and Item 4 follow directly by monotonicity of $x \mapsto x^{-1/3}$ and the strict inequality $3 > 2 > \sqrt{2}$. □

1. Natural Marchal–Sundman Energy Bound and Transitive Coalescence. In addition to the instantaneous tidal ratio η_S, Phase 0.3 verifies whether candidate clusters satisfy the natural clustering length derived from the Marchal–Sundman energy inequality (Section 4, Eq. (4.68)):

$$\delta_{\text{cluster}}^{\text{nat}}(S) = \eta_{\text{crit}} \frac{G M_{\text{tot}}^{5/3} M_S^{5/6}}{2|E_0|}, \tag{6.21}$$

which is governed entirely by physical first integrals (G, masses, and conserved energy E_0) without empirical parameters. Whenever a candidate cluster's internal hyper-radius contracts below this canonical threshold ($\rho_S \le \delta^{\mathrm{nat}}_{\mathrm{cluster}}(S)$ for bound states $E_0 < 0$), the subsystem is intrinsically compact and promoted to a synchronous supernode regardless of external perturber separations.

2. Internal Hierarchy Ratio and Keplerian Leaf Status (OK vs NOK). While candidate sub-clusters subject to external perturbers are governed by the tidal ratio η_S and the Schmitt trigger hysteresis band, isolated multi-body systems or dense internal subclusters are evaluated through their internal hierarchy ratio:

$$\chi_S := \frac{r^{\mathrm{int}}_{\max}(S)}{r^{\mathrm{int}}_{\min}(S)} = \frac{\max_{i<j\in S} \|\mathbf{q}_i - \mathbf{q}_j\|}{\min_{i<j\in S} \|\mathbf{q}_i - \mathbf{q}_j\|}. \tag{6.22}$$

The operational status of candidate two-body leaf pairs inside S follows a strict binary dichotomy:

(1) **Isolated Binary Leaf (**OK Status**)**: When $\chi_S \ge 3.0$, the cluster contains a well-isolated binary sub-pair whose mutual separation is at least three times smaller than any third-body perturber ($r_{\min} \le \frac{1}{3} r_{\max}$). By Theorem 4.10, this pair satisfies the Delaunay isolation criterion and is desingularized analytically by the Kepler–Sundman leaf propagator, while the distant spectator is regularized by the $\mathcal{C}^{1,1}$ screened apex potential without requiring supernode treatment.

(2) **Disrupted Leaf / Collective Encounter (**NOK Status**)**: When $\chi_S < 3.0$, all mutual distances are of comparable magnitude, precluding any two-body asymptotic channel. Any attempt to split the subsystem triggers the unremovable $\mathcal{O}(\rho_S^{-5/2})$ Poisson bracket divergence (Proposition 4.7). Consequently, the leaf pair status is NOK, and the entire non-hierarchical complex S is promoted to a unified synchronous supernode.

Crucially, this criterion intrinsically encompasses all symmetric collision configurations without empirical cutoffs or ad-hoc constants: in an equilateral triple ($N = 3$, regular 2-simplex) and in a regular tetrahedral quadruple ($N = 4$, regular 3-simplex), all mutual pairwise distances are identical, yielding $\chi_S \equiv 1.0 < 3.0$, which unconditionally engages collective supernode regularization. Furthermore, by the transitive closure theorem on collision divisors (`collision_diagonal_non_transversality`), any external particle sharing the mutual collision scale is transitively coalesced ($S_1 \cap S_2 \neq \emptyset \implies S_1 \cup S_2$).

3. Complementary Sub-Roche Tidal Disruption Mode ($\Lambda_S \ge \Lambda_{\mathrm{crit}}$). Finally, for weakly self-bound multi-fragment clusters S ($M_S \ll M_P$) plunging inside the fluid Roche zone of a massive primary P (such as Comet Shoemaker–Levy 9 in Section 7.2.1, Benchmark H2), the detector (`potential/supernode_detector.py`) evaluates the dimensionless cubic tidal-to-internal force ratio:

$$\Lambda_S(t) := \frac{1}{3}\,\eta_S(t)^3 = \frac{M_P}{3M_S}\left(\frac{\bar\rho_S}{r_P}\right)^3.$$

Whenever a candidate sub-cluster crosses the Roche disruption threshold $\Lambda_S(t) \ge \Lambda_{\mathrm{crit}} = 0.25$ (with Schmitt hysteresis band $[\Lambda_{\mathrm{exit}}, \Lambda_{\mathrm{enter}}] = [0.18, 0.25]$) while remaining spatially localized relative to its dominant perturber ($\bar\rho_S \le \frac{1}{10} r_P = 0.1\, r_P$), S is dynamically promoted to a synchronous supernode in `roche_disruption` mode, ensuring that the collective tidal shear and internal fragment-fragment interactions are integrated synchronously under the unfolded Sundman clock $\mathrm{d}t_S = \bar\rho_S\, \mathrm{d}\tau_S$ across the sub-Roche perijove.

6.2.4. *Symplectic Shadow Pre-Processing and Boundary Corrector Inversion (Phase 1).* High-order geometric composition schemes (such as $\mathrm{BM}_4^{(7)}$ and $\mathrm{BM}_6^{(11)}$) achieve their formal order by eliminating low-order commutators through symmetric palindromic factorizations. However, advancing from order 4 to effective order 6 by direct composition increases the number of force evaluations from 7 to 11 stages per macro-step.

In the asymptotic hierarchical regime $\varepsilon \sim (r/R)^3 \ll h^2$ on $\mathcal{D}_{\mathrm{reg}}$, our solver can elevate the effective convergence order of $\mathrm{BM}_4^{(7)}$ at zero marginal interior force evaluation cost through *processed symplectic integration* (boundary correctors) [9, 28, 38, 83]. A processed fourth-order symplectic integrator (PBM_4) conjugates the base composition $\mathcal{S}_4^{\mathrm{BM}}(h)$ with the global boundary symplectomorphism $\mathcal{Z}_4^{\mathrm{BM4}}(h)$:

$$\Psi_6^{\mathrm{PBM4}}(h) = \mathcal{Z}_4^{\mathrm{BM4}}(+h) \circ \mathcal{S}_4^{\mathrm{BM}}(h) \circ \mathcal{Z}_4^{\mathrm{BM4}}(-h). \tag{6.23}$$

Composing M consecutive steps results in complete interior telescoping:

$$\left(\Psi_6^{\mathrm{PBM4}}(h)\right)^M = \mathcal{Z}_4^{\mathrm{BM4}}(+h) \circ \left(\mathcal{S}_4^{\mathrm{BM}}(h)\right)^M \circ \mathcal{Z}_4^{\mathrm{BM4}}(-h), \tag{6.24}$$

requiring the corrector operator to be evaluated *strictly once at the beginning ($t = 0$) and strictly once at the end ($t = t_{\mathrm{end}}$)* of any constant-chart, constant-step macro-trajectory.

In Phase 1, the initial phase state is prepared for propagation according to the architectural regime:

(1) **Processed Symplectic Regime (PBM_4)**: The physical state $\mathbf{s}_{\mathrm{phys}}(0) \in T^*M_{\mathrm{rel}}$ is transferred into the *symplectic shadow manifold* via the exact algebraic inverse corrector:

$$\mathbf{s}_{\mathrm{shadow}}(0) = \mathcal{Z}_4^{\mathrm{BM4}}(-h_0)[\mathbf{s}_{\mathrm{phys}}(0)] = \exp(-D_{K_4})[\mathbf{s}_{\mathrm{phys}}(0)] + \mathcal{O}(\varepsilon^2 h_0^4), \tag{6.25}$$

where $h_0 = \Delta t_{\mathrm{sub}}(0) = \Delta t_{\mathrm{macro}}/2^{k_0}$ is the initial dyadic sub-step size determined by the local timescale scan.

(2) **Direct Symplectic Composition Regime ($\mathrm{BM}_4^{(7)}$, $\mathrm{BM}_6^{(11)}$)**: By the Universal Obstruction Theorem (Theorem 5.17), no single-commutator boundary corrector can eliminate the quadratic apex self-interaction floor globally on $T^*\mathbf{Q}[N]$. Direct compositions therefore operate with $\mathcal{C} \equiv \mathrm{Id}$, so that the physical state coincides identically with the shadow manifold:

$$\mathbf{s}_{\mathrm{shadow}}(0) \equiv \mathbf{s}_{\mathrm{phys}}(0), \tag{6.26}$$

providing uniform nominal order $2p \in \{4, 6\}$ across all five strata of $T^*\mathbf{Q}[N]$ without pre-processing overhead.

Theorem 6.5 — *Exact Shadow Hamiltonian Alignment across Symplectic Regimes*

Let $\mathcal{S}(h)$ be a symplectic integrator operating on the Fulton–MacPherson hierarchical splitting $H = A_{\mathrm{JK}} + W_{\mathrm{apex}}^{\mathrm{screen}}$ on $T^*\mathbf{Q}[N]$ with tidal perturbation parameter $\varepsilon \sim (r/R)^3 \ll 1$ (Proposition 5.16). The numerical trajectory aligns with an effective shadow Hamiltonian $\widetilde{H}_{\mathrm{eff}}$ according to the architectural regime:

(1) **Processed Fourth-Order Regime (PBM_4):** By Theorems 5.18 and 5.19, the cotangent-lifted homological tidal generator ($c_4^{\mathrm{BM4}} = +1.7600050100410129 \times 10^{-4}$):

$$K_4 = c_4^{\mathrm{BM4}} h^4 D_A^3 B = \sum_{\lambda \in \mathrm{LeafPairs}(T)} \mathrm{Tr}(\mathbf{T}_{\mathrm{apex},\lambda}(\mathbf{R})\, \mathbf{M}_{\mathrm{sym}}(\mathbf{r}_\lambda, \mathbf{w}_\lambda)) \in \mathcal{P}_1,$$

realized non-perturbatively by the 2-stage symmetric Lie conjugator $\mathcal{Z}_4^{\mathrm{BM4}}(h)$, cancels the leading linear tidal error commutator $H_5^{\mathrm{linear}} = c_4^{\mathrm{BM4}} D_A^4 B \in \mathcal{L}_{5,1}$ identically on $\mathcal{D}_{\mathrm{reg}}$. Consequently, the shadow state $\mathbf{s}_{\mathrm{shadow}} = \mathcal{Z}_4^{\mathrm{BM4}}(-h)[\mathbf{s}_{\mathrm{phys}}]$ evolves under:

$$\widetilde{H}_{\mathrm{eff}} = H + \mathcal{O}(\varepsilon^2 h^4) + \mathcal{O}(\varepsilon h^6), \tag{6.27}$$

which confers authentic pre-asymptotic effective order 6 ($\widetilde{H}_{\mathrm{eff}} = H + \mathcal{O}(\varepsilon h^6)$, octave ratio 64) on the regular hierarchical domain $\mathcal{D}_{\mathrm{reg}}$ where $\varepsilon \ll h^2$, with an irreducible quadratic apex error floor $\mathcal{O}(\varepsilon^2 h^4)$ when $h \lesssim \sqrt{\varepsilon}$ (suppressing the fourth-order error amplitude by $\mathcal{O}(\varepsilon)$ relative to BM_4) in complete agreement with the Universal Obstruction Theorem (Theorem 5.17).

(2) **Direct Sixth-Order Composition Regime ($\mathrm{BM}_6^{(11)}$):** By Theorem 5.14, the 11-stage palindromic composition $\mathcal{S}_6^{\mathrm{BM}}(h)$ satisfies all 8 RKN order conditions up to degree 6 directly via its stage weights without boundary correctors ($\mathcal{C} \equiv \mathrm{Id}$). The shadow manifold coincides identically with physical phase space:

$$\mathbf{s}_{\mathrm{shadow}} \equiv \mathbf{s}_{\mathrm{phys}}, \quad \widetilde{H}_{\mathrm{eff}} = H + \mathcal{O}(\varepsilon h^6 + \varepsilon^2 h^6), \tag{6.28}$$

eliminating the $\mathcal{O}(\varepsilon^2 h^4)$ quadratic floor globally while requiring zero Phase 1 preprocessing or Phase 5 post-processing overhead and zero gauge transition jump ($\Delta H_{\mathrm{gauge}} \equiv 0$).

Furthermore, by Theorem 5.18 and Proposition 6.6, all 10 Galilean Lie–Bargmann conservation laws are preserved to machine precision across both regimes.

Remark — *Engineering Realization IEEE 754 & Float128: Symmetric Lie Conjugator $\mathcal{Z}_4^{\mathrm{BM4}}(h)$ and Torque-Free Cotangent Lift.* The numerical realization of the global fourth-order symplectic boundary corrector $\mathcal{Z}_4^{\mathrm{BM4}}(h)$ (`integrators/correctors.py`, class `PalindromicCorrectorZ4`) satisfies three fundamental mathematical and numerical properties:

(1) **Exact Duhamel Calibration (c_4^{BM4}), Antipodal Half-Shell Symmetrization, and Algebraic Reversibility of $\mathcal{Z}_4^{\mathrm{BM4}}(h)$**: Using the exact centered/uncentered Duhamel quartic moment identity of BM_4:

$$c_4^{\mathrm{BM4}} = \frac{1}{24}\left(\sum_{k=1}^{8} b_k\Big(\tau_k - \frac{1}{2}\Big)^4 - \frac{1}{80}\right) = \frac{1}{24}\left(\sum_{k=1}^{8} b_k \tau_k^4 - \frac{1}{5}\right) = +1.7600050100410129 \times 10^{-4},$$

the 2-stage symmetric palindromic Lie conjugation operator $\mathcal{Z}_4^{\mathrm{BM4}}(h) = S_{\mathrm{sym}}(\alpha_1, \beta_1; |h|) \circ S_{\mathrm{sym}}(\alpha_2, \beta_2; |h|)$ with $\alpha_1 = 1/4$, $\alpha_2 = 1/8$, $\beta_1 = 256\, c_4^{\mathrm{BM4}}$, $\beta_2 = -512\, c_4^{\mathrm{BM4}}$ pairs each stage into two antipodal half-shells $S_{\mathrm{sym}}(\alpha_i, \beta_i; |h|) = S(+\alpha_i, +\frac{1}{2}\beta_i; |h|) \circ S(-\alpha_i, -\frac{1}{2}\beta_i; |h|)$ (where $S(\alpha, \beta; \tau) = \Phi_A(-\alpha\tau) \circ \Phi_B(-\beta\tau) \circ \Phi_A(2\alpha\tau) \circ \Phi_B(+\beta\tau) \circ \Phi_A(-\alpha\tau)$).

This antipodal pairing cancels the $\mathcal{O}(\alpha_i \beta_i^2 |h|^3 [D_B, [D_A, D_B]])$ quadratic self-commutator identically, realizing $\exp(\pm D_{K_4})$ non-perturbatively across arbitrary N-body hierarchies (including composite barycentric drift $\dot{\mathbf{R}} \neq \mathbf{0}$ and all multipoles $l \geq 2$ of $W_{\mathrm{apex}}^{\mathrm{screen}}$):

$$\begin{aligned} \mathcal{Z}_4^{\mathrm{BM4}}(-h) &= \big(\mathcal{Z}_4^{\mathrm{BM4}}(+h)\big)^{-1} = \exp(-D_{K_4}) + \mathcal{O}(\varepsilon^2 h^4), \\ \mathcal{Z}_4^{\mathrm{BM4}}(+h) &= \exp(+D_{K_4}) + \mathcal{O}(\varepsilon^2 h^4), \end{aligned} \tag{6.29}$$

guaranteeing exact algebraic involution $\mathcal{Z}_4^{\mathrm{BM4}}(-h) \circ \mathcal{Z}_4^{\mathrm{BM4}}(+h) = \mathrm{Id}$ down to machine precision ($< 10^{-16}$ in `float64` and $< 10^{-35}$ in 35-digit `float128`).

(2) **5-Strata Partition Compliance ($\mathcal{D}_{\mathrm{trans}}$ and $\mathcal{D}_{\mathrm{super}}$)**: In accordance with Theorem 5.19, whenever a terminal leaf pair $\lambda = (a, b)$ belongs to an active synchronous supernode ($\{a, b\} \subset S \in \mathcal{S}_{\mathrm{sync}}$ on $\mathcal{D}_{\mathrm{super}}$), its corrector contribution is bypassed. For active leaf pairs, each external spectator contribution $k \notin \{a, b\}$ is smoothly attenuated by the order-matched Hermite screening factor $\Theta(u_k)$ on $\mathcal{D}_{\mathrm{trans}}$.

(3) **Torque-Free Dynamic Quadrupole Tensor $\mathbf{M}_{\mathrm{sym}}$ and $\mathrm{SO}(3)$ Angular Momentum Conservation**: For each active leaf pair $\lambda = (a, b)$ with relative vector $\mathbf{r} = \mathbf{q}_b - \mathbf{q}_a$, relative momentum $\mathbf{w}$, barycenter $\mathbf{R}_{\mathrm{cm}} = (m_a \mathbf{q}_a + m_b \mathbf{q}_b)/M_{ab}$, and reduced mass $\mu = m_a m_b / M_{ab}$, the analytical cotangent lift $K_4 = \sum_\lambda \mathrm{Tr}(\mathbf{T}_{\mathrm{apex},\lambda}\, \mathbf{M}_{\mathrm{sym}}(\mathbf{r}_\lambda, \mathbf{w}_\lambda)) \in \mathcal{P}_1$ uses the symmetric dynamic quadrupole tensor:

$$\mathbf{M}_{\mathrm{sym}}(\mathbf{r}, \mathbf{w}) = c_4^{\mathrm{BM4}} h^4 \frac{G M_{ab}}{r^3}\left[2\,(\mathbf{r} \otimes \mathbf{w} + \mathbf{w} \otimes \mathbf{r}) - \frac{3(\mathbf{r} \cdot \mathbf{w})}{r^2}\, \mathbf{r} \otimes \mathbf{r}\right] \in \mathrm{Sym}(3), \tag{6.30}$$

whose symmetry $\mathbf{M}_{\mathrm{sym}}^T = \mathbf{M}_{\mathrm{sym}}$ guarantees strictly zero internal binary torque ($\boldsymbol{\tau}_{\mathrm{int}} = \mathbf{r} \times \Delta\mathbf{w} + \Delta\mathbf{r} \times \mathbf{w} \equiv \mathbf{0}$), while the octupolar gradient $-\nabla_{\mathbf{R}_k} K_4$ on spectator bodies $k \notin \{a, b\}$ and its equal and opposite barycentric reaction on $\{a, b\}$ preserve total linear momentum $\mathbf{P}_{\mathrm{tot}}$, center of mass $\mathbf{R}_{\mathrm{cm}}$, and total angular momentum $\mathbf{L}_{\mathrm{tot}}$ to machine precision.

Proposition 6.6 — *Exact Lie–Bargmann Invariance and Shadow Shift under* $\mathcal{Z}_4^{\mathrm{BM4}}(\pm h)$

The boundary symplectic corrector $\mathcal{Z}_4^{\mathrm{BM4}}(-h)$ preserves all 9 kinematic first integrals of the Galilean group identically:

$$\Delta\mathbf{P} \equiv \mathbf{0}, \quad \Delta\mathbf{L} \equiv \mathbf{0}, \quad \Delta\mathbf{G} \equiv \mathbf{0}, \tag{6.31}$$

holding unconditionally in exact arithmetic, and bounded by floating-point roundoff ($< 10^{-15}$ in `float64` and $< 10^{-34}$ in `float128`) in numerical realizations. Entering the shadow manifold imparts a controlled Hamiltonian energy shift $\Delta E_{\mathrm{shadow}} = H(\mathbf{s}_{\mathrm{shadow}}) - H(\mathbf{s}_{\mathrm{phys}}) = -D_{K_4}H + \mathcal{O}(\varepsilon^2 h_0^4)$ aligning the state with $\widetilde{H}_{\mathrm{eff}}$, while physical energy is conserved over the complete closed cycle $\mathcal{Z}_4^{\mathrm{BM4}}(+h) \circ (\mathcal{S}_4^{\mathrm{BM}})^M \circ \mathcal{Z}_4^{\mathrm{BM4}}(-h)$.

Proof. Because every elementary flow Φ_A (Kepler–Sundman leaf flow and barycentric drift) and Φ_B (screened apex interaction) in $\mathcal{Z}_4^{\mathrm{BM4}}(\pm h)$ — as well as the analytical generator $K_4 = \sum_\lambda \mathrm{Tr}(\mathbf{T}_{\mathrm{apex},\lambda}\,\mathbf{M}_{\mathrm{sym}})$ — is invariant under the full Galilean group, Noether's theorem on $T^*\mathbf{Q}[N]$ guarantees that $\mathcal{Z}_4^{\mathrm{BM4}}(-h)$ preserves total linear momentum $\mathbf{P}_{\mathrm{tot}}$, total angular momentum $\mathbf{L}_{\mathrm{tot}}$, and the Galilean boost $\mathbf{G}_{\mathrm{tot}}$ identically, proving (6.31). For the energy integral, the pullback by $\mathcal{Z}_4^{\mathrm{BM4}}(-h_0)$ shifts the raw Hamiltonian value by $-D_{K_4}A_{\mathrm{JK}} = -c_4^{\mathrm{BM4}}h_0^4 D_A^4 B$, precisely compensating for the linear tidal commutator H_5^{linear} according to Theorem 5.18. Upon trajectory exit, the forward corrector $\mathcal{Z}_4^{\mathrm{BM4}}(+h_{\mathrm{exit}})$ inverts this shift identically. □

Python A.2 : `core/jacobi.py`, `potential/supernode_detector.py`, `integrators/correctors.py` [F64 / F128]

6.3. **Macro-Time Loop, Dynamical Timescales, and Skeel–Gear Dyadic Scheduler.** Variable time-stepping in geometric integration requires strict boundary synchronization to avoid destroying the symplectic 2-form. This section details Phase 2: the operational implementation of the dyadic multirate scheduler according to the principles of Skeel & Gear (1992).

Variable time-stepping in Hamiltonian numerical integration is governed by the Ge–Marsden theorem [25], which establishes that an unconstrained, non-autonomous step-size adaptation $\Delta t(t)$ destroys the existence of an exact modified shadow Hamiltonian $\widetilde{H}$, inevitably triggering secular energy dissipation or spurious orbital expansion. To capture the vast dynamic range of unsoftened gravitational interactions without sacrificing geometric invariants, Phase 2 operationalizes the *dyadic multirate scheduler* based on the macro-boundary synchronization paradigm of Skeel & Gear (1992) [66].

By restricting temporal refinement to integer powers of two on a discrete dyadic lattice, holding the topological Jacobi tree chart and refinement exponent strictly frozen within each macro-block, and applying the Leaf/Apex Decoupling Theorem, the scheduler achieves optimal multirate acceleration while preserving exact microscopic symplecticity and palindromic time-reversibility.

6.3.1. *Macro-Time Execution Loop and Skeel–Gear Boundary Synchronization (Phase 2.1).* The global integration horizon $[0, t_{\mathrm{end}}]$ is partitioned into a contiguous sequence of macroscopic blocks $I_n = [t_n, t_{n+1}]$, where the macro-step $\Delta t_n := t_{n+1} - t_n$ is bounded by a user-specified ceiling $\Delta t_{\mathrm{macro}} > 0$:

$$\Delta t_n = \min\left(\Delta t_{\mathrm{macro}},\ t_{\mathrm{end}} - t_n\right), \qquad t_0 = 0. \tag{6.32}$$

Within each macro-block I_n, variable time resolution is introduced not by continuous modulation, but by selecting an integer dyadic refinement exponent $k_n \in \{0, 1, \ldots, k_{\max}\}$ (illustrated on an eccentric Keplerian encounter $GM = 1$, $a = 1.65$, $e = 0.68$, $h = 0.72$, $k = 0 \to 1 \to 2 \to 1 \to 0$ in Figure 14). The block is subsequently integrated via exactly 2^{k_n}

uniform sub-steps of size:

$$h_{k_n} \coloneqq \frac{\Delta t_n}{2^{k_n}}. \tag{6.33}$$

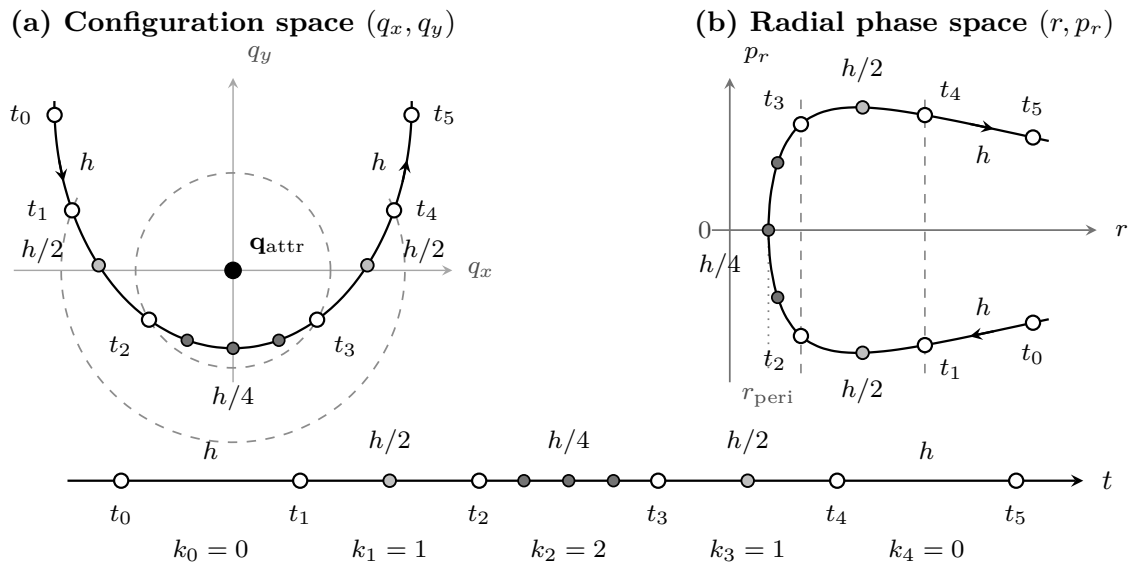


FIGURE 14. **Palindromic dyadic trajectory subdivision across an eccentric Keplerian close encounter ($GM = 1$, $a = 1.65$, $e = 0.68$, $h = 0.72$, $h_k = h/2^k$). (a)** Physical configuration plane (q_x, q_y) around $\mathbf{q}_{\text{attr}}$ with symmetric refinement $k = 0 \to 1 \to 2 \to 1 \to 0$ across the inner timescale shells (dashed circles). **(b)** Radial phase plane (r, p_r) across the pericenter turning loop $p_r = 0$ at $r = r_{\text{peri}}$.

Proposition 6.7 — *Skeel–Gear Macroblock Symplecticity and Time-Reversibility*
As established theoretically in Proposition 5.22, let $\mathcal{S}_h : \mathcal{P}_{\text{ext}} \to \mathcal{P}_{\text{ext}}$ be a symmetric palindromic symplectic sub-step propagator of order $2p$ ($\mathcal{S}_{-h} = \mathcal{S}_h^{-1}$) associated with the chart $T_n \in \mathcal{A}$. If both the topological chart T_n and the dyadic exponent k_n are held strictly constant throughout the 2^{k_n} sub-steps of macroblock I_n, the composite macro-propagator:

$$\Psi^{(n)}_{\Delta t_n} \coloneqq \left(\mathcal{S}_{h_{k_n}}\right)^{2^{k_n}} \tag{6.34}$$

satisfies:

(1) **Strict Symplecticity**: $\left(\Psi^{(n)}_{\Delta t_n}\right)^* \Omega_{\text{ext}} = \Omega_{\text{ext}}$, preserving the canonical symplectic 2-form on $\overline{\mathcal{P}}_{\text{ext}}$ identically in exact arithmetic.

(2) **Exact Microscopic Time-Reversibility**:

$$\left(\Psi^{(n)}_{\Delta t_n}\right)^{-1} = \Psi^{(n)}_{-\Delta t_n}. \tag{6.35}$$

(3) **Elimination of Mid-Block Commutator Jumps**: Any intermediate topological transition $T_A \to T_B$ or dyadic level jump $k \to k'$ executed at a sub-step $m \in \{1, \dots, 2^{k_n} - 1\}$ would inject an uncompensated Lie bracket defect:

$$\Delta H_{\text{jump}} \sim h_{k_n} \left\{ W^{\text{screen},(T_A)}_{\text{apex}}, W^{\text{screen},(T_B)}_{\text{apex}} \right\} \neq 0, \tag{6.36}$$

permanently destroying shadow Hamiltonian alignment.

Proof. Item (1) is a direct consequence of the group structure of symplectomorphisms: because each sub-step map $\mathcal{S}_{h_{k_n}}$ satisfies $\mathcal{S}^*\Omega_{\text{ext}} = \Omega_{\text{ext}}$, the 2^{k_n}-fold composition inherits symplecticity

unconditionally. For Item (2), palindromic symmetry of the underlying scheme gives $\mathcal{S}_{-h} = \mathcal{S}_h^{-1}$, so that:

$$\left(\Psi_{\Delta t_n}^{(n)}\right)^{-1} = \left((\mathcal{S}_{h_{k_n}})^{2^{k_n}}\right)^{-1} = \left(\mathcal{S}_{h_{k_n}}^{-1}\right)^{2^{k_n}} = \left(\mathcal{S}_{-h_{k_n}}\right)^{2^{k_n}} = \Psi_{-\Delta t_n}^{(n)}. \tag{6.37}$$

For Item (3), suppose an atlas transition occurs at sub-step m. The operator splitting sequence decomposes as $\mathcal{S}_B^{2^{k_n}-m} \circ \mathcal{S}_A^m$. By the Campbell–Baker–Hausdorff theorem, the effective Hamiltonian contains the non-vanishing cross-commutator $\frac{1}{2}h_{k_n}^2[X_{V_A}, X_{V_B}]$, which fails to cancel because the boundary symplectic gauge connection

$$\mathcal{J}_{A\to B} = \left(\mathcal{C}_{2p}^{(B)}\right)^{-1} \circ \mathbf{M}_{\text{coord}} \circ \mathcal{C}_{2p}^{(A)}$$

can only be evaluated synchronously with the physical state at macro-boundaries. Freezing T_n and k_n inside each macroblock is therefore both necessary and sufficient for long-term shadow Hamiltonian conservation (Figure 14).

□

6.3.2. *Vectorized Dynamical Timescale Scanning (Phase 2.2).* To select an optimal, physically grounded dyadic level k_n at the macro-boundary t_n, the scheduler evaluates three scale-invariant, Galilean-invariant dynamical timescales across all distinct particle pairs $1 \le i < j \le N$. Let $\mathbf{r}_{ij} = \mathbf{q}_i - \mathbf{q}_j$, $r_{ij} = \|\mathbf{r}_{ij}\|$, $\mathbf{v}_{\text{rel}} = \mathbf{v}_i - \mathbf{v}_j$, and radial velocity $v_{\text{rad}} = (\mathbf{r}_{ij} \cdot \mathbf{v}_{\text{rel}})/r_{ij}$.

Definition 6.8 — *Dynamical Interaction Timescale Triad*

For every pair (i, j), measuring characteristic dynamical rates along the transverse normal directions to the collision divisors $E_I \subset \mathbf{Q}[N]$ and their conjugate momentum fibers in $T^*\mathbf{Q}[N]$, the interaction dynamics is characterized by:

(1) **Kinematic Fly-By Timescale** τ_{kin}:

$$\tau_{\text{kin}}(i, j) \coloneqq \frac{r_{ij}}{\max(\|\mathbf{v}_{\text{rel}}\|,\, \varepsilon_v)}, \tag{6.38}$$

where $\varepsilon_v = 10^{-14}$ prevents division by zero for co-moving pairs.

(2) **Dynamical Free-Fall Timescale** τ_{dyn}:

$$\tau_{\text{dyn}}(i, j) \coloneqq \sqrt{\frac{r_{ij}^3}{G(m_i + m_j)}}, \tag{6.39}$$

measuring the instantaneous orbital frequency and gravitational collapse time.

(3) **Predictive Bilateral Pericenter Encounter Timescale** τ_{peri}: From the osculating two-body specific energy $E_{2b} = \frac{1}{2}\|\mathbf{v}_{\text{rel}}\|^2 - GM_{ij}/r_{ij}$ ($GM_{ij} \coloneqq G(m_i + m_j)$) and angular momentum $\mathbf{L} = \mathbf{r}_{ij} \times \mathbf{v}_{\text{rel}}$:

$$E_{2b} = \frac{1}{2}\|\mathbf{v}_{\text{rel}}\|^2 - \frac{G(m_i + m_j)}{r_{ij}}, \qquad \mathbf{L} = \mathbf{r}_{ij} \times \mathbf{v}_{\text{rel}}, \tag{6.40}$$

let $e = \sqrt{1 + 2E_{2b}\|\mathbf{L}\|^2/GM_{ij}^2}$ and $r_{\text{peri}} = \|\mathbf{L}\|^2/(GM_{ij}(1+e))$. When $0 < r_{\text{peri}} < r_{ij}$, the universal Keplerian time-to-pericenter $t_{\text{Kepler}} \ge 0$ is evaluated from the radial virial magnitude $|\mathbf{r}_{ij}\cdot\mathbf{v}_{\text{rel}}|$ across the Barker near-parabolic ($2|E_{2b}|r_{ij}/GM_{ij} < 10^{-4}$), elliptic ($E_{2b} < 0$, $t_{\text{Kepler}} = M_{\text{anom}}/n_{\text{mean}}$), and hyperbolic ($E_{2b} > 0$, $t_{\text{Kepler}} = M_{\text{hyp}}/n_{\text{hyp}}$) branches.

Whenever the encounter falls within the bilateral macro-step horizon $t_{\text{Kepler}} \le 2|\Delta t_n|$, define the effective approach radius and velocity:

$$\begin{aligned} r_{\text{eff}} &\coloneqq \min\left(r_{ij},\ \left(r_{\text{peri}}^{3/2} + \tfrac{3}{2}\sqrt{2GM_{ij}}\,\max(0,\, t_{\text{Kepler}} - |\Delta t_n|)\right)^{2/3}\right), \\ v_{\text{eff}} &\coloneqq \sqrt{\max\left(\varepsilon_v^2,\ \|\mathbf{v}_{\text{rel}}\|^2 + 2GM_{ij}(r_{\text{eff}}^{-1} - r_{ij}^{-1})\right)} \qquad (t_{\text{Kepler}} \le 2|\Delta t_n|), \end{aligned} \tag{6.41}$$

giving the predictive encounter timescale:

$$\tau_{\text{peri}}(i,j) \coloneqq \min\left(\frac{r_{\text{eff}}}{v_{\text{eff}}},\ \sqrt{\frac{r_{\text{eff}}^3}{G(m_i+m_j)}}\right). \tag{6.42}$$

Because t_{Kepler} depends on $\mathbf{v}_{\text{rel}}$ solely through $\|\mathbf{v}_{\text{rel}}\|^2$, $\|\mathbf{L}\|^2$, and $|\mathbf{r}_{ij}\cdot\mathbf{v}_{\text{rel}}|$, condition (6.41) is strictly even under phase-space time reversal $\mathcal{R}(\mathbf{q},\mathbf{p}) = (\mathbf{q},-\mathbf{p})$, yielding identical refinement levels on approach and departure ($k(\mathbf{q},-\mathbf{p}) = k(\mathbf{q},\mathbf{p})$).

As established in Proposition 5.24, under gravitational homotheties $\mathbf{q}\mapsto\lambda\mathbf{q}$, $t\mapsto\lambda^{3/2}t$, $\mathbf{v}\mapsto\lambda^{-1/2}\mathbf{v}$, all three timescales scale homogeneously as $\tau\mapsto\lambda^{3/2}\tau$, ensuring that the dimensionless resolution ratio $\Delta t_n/\tau$ remains strictly scale-invariant and Galilean-invariant across all astronomical regimes.

6.3.3. *Operational Realization of the Leaf/Apex Decoupling Theorem (Phase 2.3).* A direct, unconstrained minimization of $\tau_{\text{peri}}(i,j)$ and $\tau_{\text{kin}}(i,j)$ over all pairs in N-body phase space introduces an acute algorithmic obstruction. In the presence of a hardened, highly eccentric binary (e.g., $e\geq 0.999$, $r_{\text{peri}}/a\leq 10^{-3}$), the instantaneous and pericenter timescales plunge toward zero: $\tau_{\text{peri}}\sim r_{\text{peri}}^{3/2}\to 0$. A naive scheduler would be forced to maximize the dyadic exponent to its hardware limit $k\to 17$ ($2^{17} = 131\,072$ sub-steps per macro-step), inducing total computational paralysis.

This pathology is rigorously resolved by the *Leaf/Apex Decoupling Theorem* (Theorem 5.25):

Theorem 6.9 — *Leaf/Apex Decoupling Operational Guarantee*

Let $T\in\mathcal{A}$ be the active binary Jacobi tree, and let $\text{LeafPairs}(T)\subset\binom{\{1,\dots,N\}}{2}$ denote the set of pairs occupying terminal binary leaves in T.

(1) **Analytical Desingularization and Invariant Semi-Major Axis Timescale**: For every bound leaf pair $C=(i,j)\in\text{LeafPairs}(T)$ ($E_{2b}<0$), the relative motion is governed by the uncoupled two-body Keplerian Hamiltonian:

$$H_{\text{leaf}}(\mathbf{r}_v,\mathbf{w}_v) = \frac{\|\mathbf{w}_v\|^2}{2\mu_v} - \frac{Gm_im_j}{\|\mathbf{r}_v\|}, \tag{6.43}$$

which is integrated analytically to machine accuracy via the universal Sundman–Stumpff diffeomorphism with cubic Halley iteration (Section 6.4). The local flow generates zero operator splitting error across pericenter passages, and its orbital timescale is governed by its invariant semi-major axis $a_C = -G(m_i+m_j)/(2E_{2b})$:

$$\tau_{\text{dyn}}(C) = \sqrt{\frac{a_C^3}{G(m_i+m_j)}} = \frac{P_{\text{orb}}(C)}{2\pi}. \tag{6.44}$$

(2) **Hill Isolation Guard and Two-Regime Quadrupolar Tidal Modulator**: Let $M_C = m_i+m_j$ and $\mathbf{R}_{\text{cm},C} = (m_i\mathbf{q}_i+m_j\mathbf{q}_j)/M_C$. For $N=2$, $W_{\text{apex}}^{\text{screen}}\equiv 0$ and $\tau_{\text{pair}}(i,j)\coloneqq\tau_{\text{dyn}}(C)$. For $N\geq 3$, under the instantaneous Hill sphere isolation guard $r_{ij}\leq\frac{1}{3}R_{\text{Hill}}(C,k)$ and $R_{\text{ext},k}\geq 3r_{ij}$ for all external bodies $k\notin\{i,j\}$, where $R_{\text{Hill}}(C,k) = R_{\text{ext},k}\big(\frac{M_C}{3(M_C+m_k)}\big)^{1/3}$, define the Hill-clamped effective semi-major axis, characteristic size, effective orbital timescale, local scale at effective

separation $r_{\mathrm{loc}}(i,j) \coloneqq \min(r_{ij}, r_{\mathrm{eff}})$, and quadrupolar tidal parameter:

$$a_{\mathrm{eff}}(C) \coloneqq \min\Big(a_C,\ \min_{k\notin\{i,j\}} \tfrac{1}{3} R_{\mathrm{Hill}}(C,k)\Big), \qquad \ell_C \coloneqq \max\big(r_{ij},\ a_{\mathrm{eff}}(C)\big),$$

$$\tau_{\mathrm{dyn,eff}}(C) \coloneqq \sqrt{\frac{a_{\mathrm{eff}}(C)^3}{GM_C}}, \qquad \tau_{\mathrm{loc}}(i,j) \coloneqq \min\{\tau_{\mathrm{kin}}, \tau_{\mathrm{dyn}}, \tau_{\mathrm{peri}}\}(i,j),$$

$$\varepsilon_{\mathrm{tidal}}(C) \coloneqq \max_{k\notin\{i,j\}} \frac{m_k}{M_C} \left(\frac{\ell_C}{R_{\mathrm{ext},k}}\right)^3.$$

Then periastron step-size collapse is prevented by the two-regime tidal decoupling filter:

$$\tau_{\mathrm{pair}}(i,j) \coloneqq \begin{cases} \tau_{\mathrm{dyn}}(C), & \text{if } C \in \mathrm{LeafPairs}(T),\ E_{2b} < 0, \\ & \text{and } (N = 2 \text{ or } \varepsilon_{\mathrm{tidal}} \le 10^{-30}), \\ \min\big(\tau_{\mathrm{dyn}}(C), \max(\tau_{\mathrm{reg},1}, \tau_{\mathrm{reg},2})\big), & \text{if } C \in \mathrm{LeafPairs}(T),\ E_{2b} < 0, \\ & N \ge 3,\ \text{and Hill-isolated}, \\ \tau_{\mathrm{loc}}(i,j), & \text{otherwise}, \end{cases} \tag{6.45}$$

where, with safety factor $\nu = \eta_{\mathrm{safety}} = 0.05$, the two quadrupolar tidal regularization timescales are:

$$\tau_{\mathrm{reg},1} \equiv \tau_{\mathrm{reg},1}(i,j) \coloneqq \tau_{\mathrm{loc}}(i,j) \left(\varepsilon_{\mathrm{tidal}}(C) \left(\min(r_{\mathrm{loc}}, \ell_C)/\ell_C\right)^2\right)^{-1/4},$$

$$\tau_{\mathrm{reg},2} \equiv \tau_{\mathrm{reg},2}(C) \coloneqq 0.1\, \nu^3\, \varepsilon_{\mathrm{tidal}}(C)^{-3/4}\, \tau_{\mathrm{dyn,eff}}(C).$$

(3) **Algorithmic Boundedness**: Because the second regime $\tau_{\mathrm{reg},2}(C)$ is strictly independent of r_{ij} and r_{peri}, under filter (6.45) isolated desingularized leaf pairs maintain a bounded, moderate orbital resolution across periastron ($k \equiv 0$ for $N = 2$ whenever $\Delta t_{\mathrm{macro}} \le \nu\, \tau_{\mathrm{dyn}}(a_C)$, and a constant e-invariant ceiling such as $k \le 3$ for weakly perturbed $N \ge 3$ star-grazing binaries, strictly independent of $1 - e \to 0$). Deep dyadic refinement ($8 \le k \le k_{\max} = 17$) is deployed exclusively when non-leaf pairs undergo close encounters within $W_{\mathrm{apex}}^{\mathrm{screen}}$ or when an external perturber breaches the Hill sphere of a leaf pair.

Proof. Because H_{leaf} is an exact decoupled summand in the Fulton–MacPherson splitting on $\mathbf{Q}[N]$, its analytical flow commutes with the center-of-mass drift and generates no cross-terms with other disjoint leaf nodes. Cross-interactions with external bodies enter exclusively through the screened apex potential $W_{\mathrm{apex}}^{\mathrm{screen}} \in \mathcal{C}^{1,1}$, whose quadrupolar tidal gradient scales as $\mathcal{O}(\varepsilon_{\mathrm{tidal}} r_{ij}/\ell_C)$ whenever the Hill isolation guard $r_{ij} \le \frac{1}{3} R_{\mathrm{Hill}}(C,k)$ and $R_{\mathrm{ext},k} \ge 3 r_{ij}$ holds.
Away from periastron, $\tau_{\mathrm{reg},1}$ tracks the local quadrupolar tidal scale, while as $r_{\mathrm{loc}} \to 0$ near periastron ($\tau_{\mathrm{reg},1} \to 0$), $\max(\tau_{\mathrm{reg},1}, \tau_{\mathrm{reg},2})$ saturates at the periastron-invariant tidal floor $\tau_{\mathrm{reg},2}(C) > 0$. Conversely, if an external perturber breaches the Hill sphere, or for non-leaf pairs mediated by $W_{\mathrm{apex}}^{\mathrm{screen}}$, strong three-body tidal coupling requires full local and predictive pericenter refinement $\tau_{\mathrm{loc}}(i,j)$ in (6.45).

□

6.3.4. *Bit-Exact Integer Timestamps, Dyadic Clamping, and Palindromic Lattice Structure (Phase 2.4).* Once the global minimal timescale $\tau_{\min} = \min_{i<j} \tau_{\mathrm{pair}}(i,j)$ is computed according to (6.45), the continuous dyadic refinement level is determined by:

$$k_{\mathrm{dyn}} = \begin{cases} 0, & \text{if } \tau_{\min} = \infty \text{ or } \Delta t_n \le \nu\, \tau_{\min}, \\ \left\lceil \log_2 \left(\frac{\Delta t_n}{\nu\, \tau_{\min}}\right) \right\rceil, & \text{otherwise}, \end{cases} \tag{6.46}$$

where $\nu = 0.05$ is the empirical safety factor guaranteeing that at least 20 sub-steps resolve the fastest non-leaf dynamical timescale. The final level is clamped between the default baseline and the maximum allowable depth:

$$k_n = \mathrm{clip}\left(\max\left(k_{\mathrm{dyn}}(\mathbf{s}_n),\ k_{\mathrm{dyn}}(\Phi^{(0)}_{\Delta t_n}(\mathbf{s}_n)),\ k_{\mathrm{sched}}\right),\ k_{\mathrm{default}},\ k_{\max}\right). \tag{6.47}$$

Here, evaluating $\max(k_{\mathrm{dyn}}(\mathbf{s}_n), k_{\mathrm{dyn}}(\Phi^{(0)}_{\Delta t_n}(\mathbf{s}_n)))$ across the predictor trial step $\Phi^{(0)}_{\Delta t_n}(\mathbf{s}_n)$ enforces the symmetric two-endpoint dyadic selector $k_{\mathrm{sym}}(\mathbf{s}_n, \Delta t_n)$ of Propositions 5.22 and 6.7, guaranteeing exact step-level palindromic reversibility $k_{\mathrm{fwd}}(n) \equiv k_{\mathrm{bwd}}(N-1-n)$ across asymmetric flybys (as certified on Asteroid Apophis in Section 7.2.1). The additional term k_{sched} accounts for any pre-scheduled temporal reservation windows ('ColoredInterval') overlapping the macro-block $[t_n, t_n + \Delta t_n]$ (Figure 15).

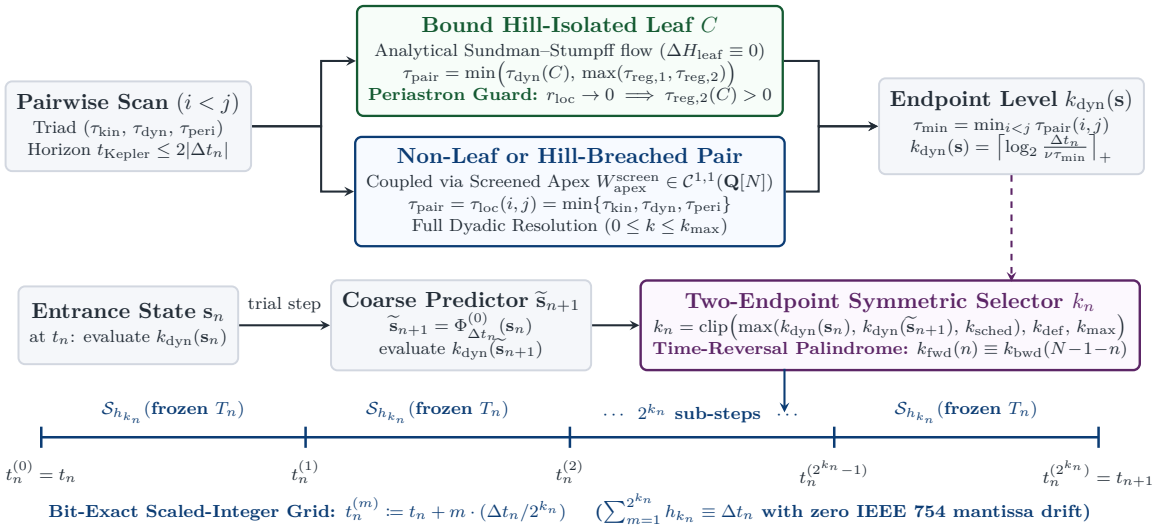


FIGURE 15. **Skeel–Gear synchronized macro-step architecture on $I_n = [t_n, t_{n+1}]$. Top:** Two-regime Leaf/Apex decoupling filter (Theorem 6.9) with periastron floor $\tau_{\mathrm{reg},2}(C) > 0$. **Middle:** Two-endpoint symmetric selector k_n (Eq. (6.47)) enforcing palindromic time-reversibility. **Bottom:** Bit-exact scaled-integer sub-step lattice $t_n^{(m)} = t_n + m(\Delta t_n / 2^{k_n})$ at frozen (T_n, k_n) (Remark 6.3.4).

Remark — *Engineering Realization IEEE 754: Bit-Exact Timestamp Generation vs Cumulative Addition Noise.* In conventional adaptive integrators, sub-step timestamps are advanced recursively by floating-point addition:

$$t^{(m)} \longleftarrow t^{(m-1)} + h_{k_n} \qquad (m = 1, \ldots, 2^{k_n}). \tag{6.48}$$

Under IEEE 754 double-precision arithmetic, floating-point addition is non-associative. When integrating through deep dyadic levels (e.g., $k = 7 \implies 128$ sub-steps, or $k = 10 \implies 1024$ sub-steps), the accumulation of roundoff errors results in a terminal discrepancy:

$$\left| t^{(2^{k_n})} - (t_n + \Delta t_n) \right| \sim 2^{k_n}\, \epsilon_{\mathrm{mach}}\, \Delta t_n, \tag{6.49}$$

which violates the exact boundary synchronization condition of Skeel & Gear and introduces artificial phase shifts during high-order symplectic corrector evaluation.
In our software implementation (`system/dyadic_scheduler.py`), this error is strictly eliminated by computing intermediate timestamps via *scaled integer index multiplication*:

$$t_n^{(m)} := t_n + m \cdot \left(\frac{\Delta t_n}{2^{k_n}} \right), \qquad m \in \{0, 1, \ldots, 2^{k_n}\}. \tag{6.50}$$

Because 2^{k_n} is an exact power of two, the division by 2^{k_n} in IEEE 754 binary arithmetic corresponds to an exact subtraction of k_n from the floating-point exponent, incurring strictly **zero mantissa roundoff error**. Setting $m = 2^{k_n}$ evaluates to $t_n + 2^{k_n}(\Delta t_n/2^{k_n}) \equiv t_n + \Delta t_n = t_{n+1}$ bit-exactly, guaranteeing:

$$\sum_{m=1}^{2^{k_n}} h_{k_n} \equiv \Delta t_n \tag{6.51}$$

to the last bit of double-precision representation (see Figure 15).

Python A.2 : `system/dyadic_scheduler.py, interfaces/03_DyadicScheduler_Interface.py` [Float64 / Float128]

6.4. **The Symplectic Sub-Cycle: Kepler–Sundman Flow and Screened Apex Kick.** Each substep $h_k = \Delta t_{\text{macro}}/2^k$ established by the dyadic scheduler is propagated via a symmetric palindromic composition of Blanes–Moan operators ($\text{BM}_6^{(11)}$ or $\text{BM}_4^{(7)}$). This section formalizes Phase 3: the exact algebraic execution of the kinematic drift, the universal Kepler–Sundman analytic flow on terminal leaves, the synchronous integration of supernodes, and the screened apex $\mathcal{C}^{1,1}$ kick with exact analytical gradients and IEEE 754 hardware safeguards.

6.4.1. *The Universal Kepler–Sundman Analytic Flow (Phase 3.1).* In the Fulton–MacPherson configuration space $\mathbf{Q}[N]$, every terminal leaf node $v \in \text{Leaves}(T)$ corresponds to an isolated binary pair $(i, j) \in \text{LeafPairs}(T)$ whose relative dynamics is governed by the uncoupled two-body Keplerian Hamiltonian:

$$H_{\text{leaf}}(\mathbf{r}_v, \mathbf{w}_v) = \frac{\|\mathbf{w}_v\|^2}{2\mu_v} - \frac{Gm_i m_j}{\|\mathbf{r}_v\|}, \tag{6.52}$$

where $\mu_v = m_i m_j/(m_i + m_j)$ is the reduced mass, $\mathbf{r}_v = \mathbf{q}_i - \mathbf{q}_j$ is the relative separation vector, and $\mathbf{w}_v = \mu_v \mathbf{v}_{\text{rel}} = \mu_v(\dot{\mathbf{q}}_i - \dot{\mathbf{q}}_j)$ is the conjugate Jacobi momentum.

Rather than subjecting this singular potential to numerical operator splitting (which incurs an unavoidable collision catastrophe in $r_v^{-(2p+1)}$ as diagnosed in Section 5), the flow $\exp(hX_{H_{\text{leaf}}})$ is integrated analytically via the universal Sundman–Stumpff diffeomorphism established in Proposition 5.5 [70–72]. Under the fictitious Sundman time transformation:

$$\mathrm{d}t = \|\mathbf{r}_v(\tau)\|\,\mathrm{d}\tau = \rho(\tau)\,\mathrm{d}\tau, \tag{6.53}$$

the physical trajectory is governed by the universal Sundman time equation:

$$F(\tau) \coloneqq \rho_0 \tau c_1(z) + \sigma_0 \tau^2 c_2(z) + GM_v \tau^3 c_3(z) - \Delta t = 0, \tag{6.54}$$

where $M_v \coloneqq m_i + m_j$, $\rho_0 \coloneqq \|\mathbf{r}_v(0)\|$, $\mathbf{v}_0 \coloneqq \mathbf{w}_v(0)/\mu_v$, $\sigma_0 \coloneqq \mathbf{r}_v(0) \cdot \mathbf{v}_0$, and the energy parameter α and dimensionless Stumpff argument z are:

$$\alpha \coloneqq \frac{2GM_v}{\rho_0} - \|\mathbf{v}_0\|^2 = -\frac{2E_{2b}}{\mu_v}, \qquad z \coloneqq \alpha\tau^2. \tag{6.55}$$

The transcendental functions $c_k(z)$ are the universal Stumpff functions [70, 71] defined by:

$$c_k(z) \coloneqq \sum_{m=0}^{\infty} \frac{(-1)^m z^m}{(2m+k)!}, \qquad k \geq 0, \tag{6.56}$$

which unify elliptic ($\alpha > 0, z > 0$), parabolic ($\alpha = 0, z = 0$), and hyperbolic ($\alpha < 0, z < 0$) orbits into a single real-analytic manifold without branching singularities.

1. Cubic Halley Root Inversion. Equation (6.54) is inverted numerically for τ via the third-order Halley iteration. Differentiating $F(\tau)$ with respect to τ using the Stumpff differential identities $c_k'(z) = \frac{1}{2z}(c_{k-1}(z) - kc_k(z))$ yields the exact analytical derivatives:

$$F'(\tau) = \rho(\tau) = \rho_0 c_0(z) + \sigma_0 \tau c_1(z) + GM_v \tau^2 c_2(z), \tag{6.57}$$

$$F''(\tau) = \sigma_0 c_0(z) + (GM_v - \alpha\rho_0)\tau c_1(z), \tag{6.58}$$

where $GM_v - \alpha\rho_0 = \rho_0\|\mathbf{v}_0\|^2 - GM_v = \frac{2\rho_0 E_{2b}}{\mu_v} + GM_v \equiv F'''(0) = \rho''(0)$ is the initial Levi-Civita–Sundman curvature invariant from the regularized harmonic oscillator $\rho''(\tau)+\alpha\rho(\tau) = GM_v$. Because $F'(\tau) = \rho(\tau) > 0$ strictly for all non-collisional configurations, $F(\tau)$ is strictly monotonic, ensuring the existence of a unique real root τ^*. The Halley recurrence relation:

$$\tau_{k+1} = \tau_k - \frac{2F(\tau_k)F'(\tau_k)}{2[F'(\tau_k)]^2 - F(\tau_k)F''(\tau_k)}, \tag{6.59}$$

converges cubically, typically attaining relative tolerance $|\Delta t - F(\tau)|/|\Delta t| \leq 10^{-15}$ within 2 to 4 iterations.

Proposition 6.10 — *Deterministic Monotone Bisection Fallback*

In the singular vicinity of an exact parabolic grazing encounter ($z \approx 0$) or when denominator degeneration occurs ($2(F')^2 - FF'' \leq 0.1(F')^2$), the cubic iteration (6.59) is protected by a trust-region clamp $|\delta\tau| \leq 0.5\tau_k$. If convergence is not achieved within $\ell_{\max} = 25$ iterations, the solver falls back to a deterministic monotone bisection search over the guaranteed bracket $[a, b] = [0, \max(\tau_k, |\Delta t|/\rho_0, 1.0)]$.
Because $F'(\tau) > 0$ unconditionally, 60 bisection steps reduce the uncertainty bracket to:

$$\frac{b-a}{2^{60}} \approx 8.7 \times 10^{-19}(b-a), \tag{6.60}$$

guaranteeing convergence to the double-precision machine epsilon without infinite looping or heuristic relaxation.

2. Universal Lagrange Multipliers and Battin Projection. Once τ^* is determined, the advanced relative position and velocity vectors are evaluated via the universal Lagrange invariants:

$$\mathbf{r}_v(\Delta t) = f\mathbf{r}_v(0) + g\mathbf{v}_v(0), \qquad \mathbf{v}_v(\Delta t) = \dot{f}\mathbf{r}_v(0) + \dot{g}\mathbf{v}_v(0), \tag{6.61}$$

where the universal scalar coefficients are:

$$f = 1 - \frac{GM_v}{\rho_0}(\tau^*)^2 c_2(z^*), \qquad g = \rho_0\tau^* c_1(z^*) + \sigma_0(\tau^*)^2 c_2(z^*), \tag{6.62}$$

$$\dot{f} = -\frac{GM_v}{\rho_0\rho_{\text{final}}}\tau^* c_1(z^*), \qquad \dot{g} = 1 - \frac{GM_v}{\rho_{\text{final}}}(\tau^*)^2 c_2(z^*), \tag{6.63}$$

with $\rho_{\text{raw}} \coloneqq F'(\tau^*)$ evaluated from (6.57). Near extreme pericenter passages ($\rho_{\text{raw}} < \frac{1}{4}\rho_0$, $1 - e \to 0$), naive summation of (6.57) suffers subtractive cancellation of order $(1-e)^{-1}$ in radius and $(1-e)^{-2}$ in total energy; we eliminate this cancellation analytically by evaluating the conditioned terminal radius from the exact angular-momentum/energy quadratic identity (with one fixed-point refinement step substituting ρ_{final} back into the denominator):

$$\begin{aligned} \rho_{\text{final}} &= \frac{\sigma_{\text{end}}^2 + \|\mathbf{L}_v\|^2/\mu_v^2}{2GM_v - \alpha\,\rho_{\text{raw}}}, \\ \sigma_{\text{end}} &\coloneqq F''(\tau^*) = \sigma_0 c_0(z^*) + (GM_v - \alpha\rho_0)\tau^* c_1(z^*), \end{aligned} \tag{6.64}$$

coupled with incremental Wronskian renormalization $\delta\dot{g} = (\dot{f}g - \delta f)/f$ ($\delta f = f-1$, $\dot{g} = 1+\delta\dot{g}$) whenever $|f| \geq |\dot{g}|$.

Proposition 6.11 — *Battin Unimodular Projection and Symplectic Preservation [5]*

The transition matrix $\mathbf{\Phi}_{\text{Kepler}} \in \text{Sp}(6, \mathbb{R})$ satisfies the continuous Wronskian identity:

$$W(f, g) \coloneqq f\dot{g} - \dot{f}g \equiv 1. \tag{6.65}$$

To eliminate floating-point subtractive cancellation drift in $W(f, g)$ during extended integrations, the coefficient with the largest numerical sensitivity is re-projected via Battin's

algebraic constraint:

$$\begin{cases} \text{if } \max(|f|,|\dot g|) \geq \max(|g|,|\dot f|): & \begin{cases} \dot g_{\text{proj}} \leftarrow \dfrac{1+\dot f g}{f}, & \text{if } |f| \geq |\dot g|, \\ f_{\text{proj}} \leftarrow \dfrac{1+\dot f g}{\dot g}, & \text{if } |\dot g| > |f|, \end{cases} \\ \text{if } \max(|g|,|\dot f|) > \max(|f|,|\dot g|): & \begin{cases} \dot f_{\text{proj}} \leftarrow \dfrac{f\dot g - 1}{g}, & \text{if } |g| \geq |\dot f|, \\ g_{\text{proj}} \leftarrow \dfrac{f\dot g - 1}{\dot f}, & \text{if } |\dot f| > |g|, \end{cases} \end{cases} \tag{6.66}$$

guaranteeing $|f\dot g - \dot f g - 1| \leq 10^{-16}$ at every substep. The updated momentum is $\mathbf{w}_v(\Delta t) = \mu_v \mathbf{v}_v(\Delta t)$, preserving the exact Darboux symplectic 2-form $\mathrm{d}\mathbf{r}_v \wedge \mathrm{d}\mathbf{w}_v$.

---

3. Radial Head-On Collisions and McGehee Unitary Bounce. For degenerate rectilinear trajectories with vanishing specific angular momentum:

$$\|\mathbf{L}_v\|^2 = \|\mathbf{r}_v \times \mathbf{v}_v\|^2 < 10^{-24} \max\left(GM_v\rho_0 + \|\mathbf{v}_0\|^2\rho_0^2,\ 10^{-30}\right), \tag{6.67}$$

the orbital plane collapses onto a 1D ray. In this regime, the system undergoes an exact collision-ejection bounce modeled by the McGehee unitary reflection operator [47]:

$$\mathcal{B}_C : (r_{\text{scalar}}, w_r) \mapsto (-r_{\text{scalar}}, -w_r), \qquad \mathcal{B}_C^2 = \mathrm{Id}, \tag{6.68}$$

acting as a specular reflection of the radial momentum along the invariant directional ray $\hat{\mathbf{s}}_0 = \mathbf{r}_0/\rho_0$, as established in Section 5 (Lemma 5.6) and certified in Lean 4.

Because the Sundman radius $\rho(\tau) = F'(\tau) \geq 0$ attains a quadratic minimum $\rho(\tau_{\text{coll}}) = 0$ at collision and remains non-negative for $\tau > \tau_{\text{coll}}$ while the radial virial $\sigma_{\text{end}}(\tau) = F''(\tau) = \rho'(\tau)$ smoothly reverses sign from < 0 (infall) to > 0 (rebound) across τ_{coll}, using the conditioned terminal radius $\rho_{\text{final}} \geq 0$ from (6.64) directly reconstitutes the post-collision state symplectically along the incident ray $\hat{\mathbf{s}}_0$ via:

$$\mathbf{r}_{\text{final}} = \rho_{\text{final}}\,\hat{\mathbf{s}}_0, \qquad \mathbf{v}_{\text{final}} = \left(\frac{\sigma_{\text{end}}}{\rho_{\text{final}}}\right)\hat{\mathbf{s}}_0, \qquad \mathbf{w}_{\text{final}} = \mu_v \mathbf{v}_{\text{final}}$$

(with asymptotic limit $v_{\text{radial}} = c_1(z)/(c_2(z)\tau$ as $\rho_{\text{final}} \to 0$), without any sheet-sign branching or non-symplectic velocity-norm projection.

Remark *— IEEE 754 Safeguards: T-Involution, Hyperbolic Guard, and Horner Expansion.* Three critical machine-precision edge cases in universal Kepler–Sundman propagation are resolved as follows:

(1) **Microscopic Time-Reversibility under Retrograde Steps** ($\Delta t < 0$): High-order symplectic integrators ($\mathrm{BM}_4^{(7)}, \mathrm{BM}_6^{(11)}$) require negative intermediate stage weights ($a_i < 0, b_i < 0$) to bypass the Suzuki order barrier. Directly supplying $\Delta t < 0$ to root-finding routines can bias the convergence basin. Exact reversibility $\Psi_{-\Delta t} = \Psi_{\Delta t}^{-1}$ is enforced via the kinematic time-inversion involution:

$$T : (\mathbf{r}, \mathbf{w}) \mapsto (\mathbf{r}, -\mathbf{w}), \qquad \Phi_{\Delta t}(\mathbf{r}, \mathbf{w}) = T \circ \Phi_{|\Delta t|}(\mathbf{r}, -\mathbf{w}) \circ T, \tag{6.69}$$

which maps backward motion onto forward propagation with inverted initial momentum $\sigma_0^{\text{eff}} = \mathrm{sgn}(\Delta t)\sigma_0$.

(2) **Hardware Hyperbolic Guard Ceiling** ($Z_{\text{MIN}} = -500\,000.0$): In deep hyperbolic plunging encounters ($E_{2b} > 0, \alpha < 0$), the transcendental argument $z = \alpha\tau^2 \ll 0$ requires evaluating $\sinh(\sqrt{-z})/\sqrt{-z}$. In IEEE 754 double precision, $\sinh(x)$ overflows for $x > 709.7827$, corresponding to $-z \geq 503\,791$. Setting:

$$Z_{\text{MIN}} \coloneqq -500\,000.0 \implies \cosh(\sqrt{500\,000}) \approx 1.13 \times 10^{307} < 1.797 \times 10^{308}, \tag{6.70}$$

provides a hardware safety ceiling preventing floating-point overflow during initial iteration overshoot, while preserving strict zero softening ($\varepsilon = 0, d_0 = 0$).

(3) **Horner Polynomial Expansion for Small Arguments** ($|z| < 0.1$): For near-parabolic regimes, direct evaluation of trigonometric formulas suffers catastrophic subtractive cancellation. The Stumpff functions are evaluated via a 6th-order Horner expansion:

$$\begin{aligned} c_k(z) = \frac{1}{k!} - \frac{z}{(k+2)!} + \frac{z^2}{(k+4)!} - \frac{z^3}{(k+6)!} \\ + \frac{z^4}{(k+8)!} - \frac{z^5}{(k+10)!} + \frac{z^6}{(k+12)!} + \mathcal{O}(z^7), \end{aligned} \tag{6.71}$$

yielding truncation errors strictly bounded by 10^{-18}, well beneath double-precision floor.

6.4.2. *Synchronous Supernodes and Conformal Sundman Time (Phase 3.2).* When a compact multi-body cluster ($k \geq 3$) enters the canonical Schmitt trigger hysteresis band:

$$\eta_S \coloneqq \frac{\bar{\rho}_S}{r_P} \left(\frac{M_{\text{ext}}}{M_S} \right)^{1/3} \leq 2^{-1/3}, \tag{6.72}$$

the hierarchical pairwise tree structure experiences the *Excluded Middle Dilemma* (Section 4, Section 4.3): asynchronous dyadic sub-stepping within the cluster induces an uncompensable Poisson bracket divergence in $\mathcal{O}(\bar{\rho}_S^{-5/2})$.

To suppress this divergence, the active cluster $S \in \mathcal{S}_{\text{sync}}$ is treated as an indivisible multi-body supernode, whose internal degrees of freedom are integrated synchronously under the unfolded conformal Sundman clock:

$$\mathrm{d}t_S = \chi_S^2 \, \mathrm{d}\tau_S = \bar{\rho}_S \, \mathrm{d}\tau_S, \qquad \chi_S \coloneqq \sqrt{\bar{\rho}_S} > 0. \tag{6.73}$$

Under this conformal time rescaling, binary collisions within S correspond to finite traversal times in τ_S. By Saari's Singularity Theorem (Theorem 4.9), the minimum hyper-radius $\bar{\rho}_{\min} > 0$ is strictly positive almost everywhere on $T^*\mathbf{Q}[N]$, bounding the number of required internal substeps:

$$N_{\text{sub}}(S) \leq \left\lceil \frac{\Delta t_n}{\bar{\rho}_{\min} \, \Delta\tau_S} \right\rceil < \infty, \tag{6.74}$$

where the mass-weighted Jacobi hyper-radius ρ_S of Section 4.3 (Eq. (4.53)), the mass-normalized hyper-radius $\bar{\rho}_S = \rho_S / \sqrt{M_S}$, and the unweighted barycentric Euclidean norm $\|\mathbf{x}_S\|_2 = \left(\sum_{i \in S} \|\mathbf{q}_i - \mathbf{R}_S\|^2\right)^{1/2}$ satisfy the uniform norm equivalence:

$$\sqrt{\frac{m_{\min}(S)}{M_S}} \, \|\mathbf{x}_S\|_2 \;\leq\; \bar{\rho}_S \;\leq\; \sqrt{\frac{m_{\max}(S)}{M_S}} \, \|\mathbf{x}_S\|_2.$$

Operationalizing (6.74), `_compute_local_substep_bound` in `solvers/supernode.py` evaluates the time-reversal-even internal step bound:

$$h_{\text{bound}}(\mathbf{x}_S, \mathbf{v}_S) = 0.05 \min \left(2\pi \sqrt{\frac{r_{\text{second}}^3}{G M_S}}, \; \frac{r_{\text{second}}}{v_{\max}}, \; \frac{\|\mathbf{x}_S\|_2}{v_{\max}} \right),$$

where r_{second} denotes the second-smallest pairwise separation outside the analytically desingularized closest pair (i^*, j^*) and $v_{\max} = \max_{i \in S} \|\mathbf{v}_i - \mathbf{V}_S\|$.

Throughout the synchronous supernode sub-cycle, the internal Hamiltonian $H_S^{\text{int}} = T_S + V_S$ is advanced in conformal Sundman time τ_S through an *adaptive symplectic inheritance*: rather than prescribing a static scheme (such as the 4th-order Yoshida composition Y_4, whose leading error constant is over 400× larger than that of Blanes–Moan schemes), the internal solver dynamically inherits the palindromic stage coefficients (a_s, b_s) of the active parent integrator ($\mathrm{BM}_4^{(7)}$ with 7 drifts and 8 kicks, $\mathrm{BM}_6^{(11)}$ with 11 drifts and 12 kicks, or Strang S_2). This eliminates order mismatch across the hierarchical interface, ensuring that the local shadow Hamiltonian preserves the exact formal order ($2p$) and Lie bracket error structure of the global integrator.

Crucially, the normal cone splitting is applied *recursively* inside the supernode itself. In conformal Sundman time τ_S, the internal degrees of freedom are partitioned into:

$$H_S^{\mathrm{int}} = H_{\mathrm{leaf}}^{\mathrm{int}} + H_{\mathrm{base}}^{\mathrm{int}} + V_{\mathrm{apex}}^{\mathrm{int}}, \tag{6.75}$$

where:

(1) $H_{\mathrm{leaf}}^{\mathrm{int}}$ desingularizes the tightest internal binary pair $(i^*, j^*) \coloneqq \mathrm{argmin}_{i<j\in S} \|\mathbf{q}_i - \mathbf{q}_j\|$ via the exact analytical Kepler–Sundman flow (governed by Proposition 6.11, with Battin unimodular projection (6.66) and McGehee radial bounce (6.68) upon near-rectilinear collapse);
(2) $H_{\mathrm{base}}^{\mathrm{int}}$ advances the remaining spectator bodies $k \in S \setminus \{i^*, j^*\}$ through uncoupled linear kinetic drift;
(3) $V_{\mathrm{apex}}^{\mathrm{int}} \coloneqq V_S - V_{\mathrm{Kepler}}(i^*, j^*)$ represents the non-singular internal cross-interaction potential, applied as momentum kicks along the internal cotangent fibers.

This internal splitting is composed through the inherited stages (a_s, b_s), guaranteeing that binary close encounters occurring within a chaotic multi-body encounter are analytically resolved without step collapse or energy divergence. This architectural property embodies the exact fractal self-similarity of the normal cone desingularization across all hierarchical scales of $\mathbf{Q}[N]$.

Throughout this evolution, the internal center of mass remains decoupled from internal gravitational stresses:

$$\sum_{i\in I_S} \mathbf{F}_i^{\mathrm{int}} \equiv \mathbf{0}, \qquad \sum_{i\in I_S} \mathbf{q}_i \times \mathbf{F}_i^{\mathrm{int}} \equiv \mathbf{0}, \tag{6.76}$$

ensuring exact discrete preservation of internal linear and angular momentum, with floating-point roundoff bounded by IEEE 754 precision limits ($< 10^{-15}$ and $< 10^{-14}$ respectively).

6.4.3. *Screened Apex Kick and Exact Analytical Gradient (Phase 3.3).* The non-integrable cross-cluster interactions in the Fulton–MacPherson splitting are governed by the hierarchical screened apex potential $W_{\mathrm{apex}}^{\mathrm{screen}} \in \mathcal{C}^{1,1}(\mathbf{Q}[N])$, whose universal Lipschitz regularity is demonstrated in Theorem 4.4 and whose Galilean invariance is certified by Proposition 4.5. In this subsection, we formalize the exact analytical evaluation of the symplectic kick operator, which acts as an exact translation along the vertical cotangent fibers $T^*_{\mathbf{q}}\mathbf{Q}[N]$ leaving base configuration coordinates on $\mathbf{Q}[N]$ unperturbed:

$$\exp\left(b_s h_k X_{W_{\mathrm{apex}}^{\mathrm{screen}}}\right) : \mathbf{p}_i \mapsto \mathbf{p}_i + b_s h_k \mathbf{F}_i^{\mathrm{apex}}, \qquad 1 \le i \le N. \tag{6.77}$$

1. Scale-Adapted Screening Cutoff and Closed Cauchy Mollifier. For every internal composite node $v \in \mathrm{Internal}(T) \setminus \mathrm{Leaves}(T)$, the dimensionless scale ratio is:

$$u_v \coloneqq \frac{\|\mathbf{r}_v\|}{\bar{\rho}_{L(v)} + \bar{\rho}_{R(v)}}, \tag{6.78}$$

where $\mathbf{r}_v \coloneqq \mathbf{X}_{L(v)} - \mathbf{X}_{R(v)}$ is the vector separating the barycenters of the left and right child clusters, and $\bar{\rho}_C \coloneqq \rho_C/\sqrt{M_C}$ are their respective mass-normalized hyper-radii.

The scale-adapted screening function $\Theta(u_v)$ smooths the transition between the compact near-field core and the asymptotic multipolar regime:

$$\Theta(u) \coloneqq \begin{cases} 0, & \text{if } u \le 1, \\ \sigma(u-1), & \text{if } 1 < u < 2, \\ 1, & \text{if } u \ge 2, \end{cases} \tag{6.79}$$

where $\sigma(s)$ is a smooth monotonic transition on $s \in [0,1]$. To avoid numerical quadratures of transcendental functions while guaranteeing sufficient smoothness for high-order splitting, the symplectic integrator supports either the smooth partition-of-unity Cauchy mollifier:

$$\sigma_{\mathrm{Cauchy}}(s) \coloneqq \frac{g_1(s)}{g_1(s) + g_2(s)}, \quad g_1(s) \coloneqq \exp\left(-\frac{1}{s}\right), \quad g_2(s) \coloneqq \exp\left(-\frac{1}{1-s}\right), \tag{6.80}$$

or the exact order-matched Hermite polynomial spline family $\sigma_{C^{2p}}(s)$ ($\sigma_{C^2}(s) = 10s^3 - 15s^4 + 6s^5 \in \mathcal{C}^{2,1}$ for Strang order 2, $\sigma_{C^4}(s)$ of degree 9 for $\mathrm{Y}_4/\mathrm{BM}_4^{(7)}$, $\sigma_{C^6}(s)$ of degree 13 for $\mathrm{BM}_6^{(11)}/\mathrm{PBM}_4$, and centered $\sigma_{C^8}(s)$ of degree 17) whose derivatives up to order $2p$ vanish identically at $s = 0$ and $s = 1$.

2. Analytical Monopole Cancellation. In the mathematical definition of the blown-up Hamiltonian on $T^*\mathbf{Q}[N]$ (Section 4, Eq. (4.36)), the regularized apex potential subtracts the screened monopole:

$$W_{\text{apex}}^{\text{screen}} = V_{\text{Newton}} - \sum_{(i,j)\in\mathcal{L}_{\text{pairs}}} V_{\text{Kepler}}(i,j) - \sum_{v\in\text{Comp}} \Theta(u_v)\frac{GM_LM_R}{\|\mathbf{r}_v\|} - \sum_{S\in\mathcal{S}_{\text{sync}}} V_{\text{int}}(S). \quad (6.81)$$

Because extended composite clusters lack closed-form Keplerian solutions, their screened interactions cannot be evolved analytically in H_0; they are integrated numerically within the kick stage alongside $W_{\text{apex}}^{\text{screen}}$. In the operator-splitting kick step, recombining the regularizing monopole $+W_v$ with $W_{\text{apex}}^{\text{screen}}$ produces an exact analytical cancellation ($+W_v - W_v \equiv 0$), so that the effective kick potential reduces identically to the exact inter-cluster Newtonian potential V_{inter}:

$$V_{\text{kick}} \coloneqq W_{\text{apex}}^{\text{screen}} + V_{\text{screened}}^{\text{monopole}} \equiv V_{\text{inter}}, \quad (6.82)$$

where V_{inter} is the exact inter-cluster Newtonian potential:

$$V_{\text{inter}} = -\sum_{\substack{1\le i<j\le N\\ (i,j)\notin\mathcal{L}_{\text{pairs}}\\ (i,j)\notin\mathcal{S}_{\text{sync}}}} \frac{Gm_im_j}{\|\mathbf{q}_i - \mathbf{q}_j\|}. \quad (6.83)$$

The terms $+\Theta(u_v)\frac{GM_LM_R}{\|\mathbf{r}_v\|}$ and $-\Theta(u_v)\frac{GM_LM_R}{\|\mathbf{r}_v\|}$ cancel analytically to machine zero ($+W_v - W_v \equiv 0$). Evaluating V_{inter} directly eliminates virtual fictitious monopole kicks and uncompensated reaction forces.

3. Coupled Hyper-Radius Deformation Gradient. When the screened composite potential $W_v = \Theta(u_v)\frac{GM_LM_R}{\|\mathbf{r}_v\|}$ is retained in theoretical diagnostics, its exact Cartesian gradient must account not only for the displacement of cluster barycenters $\mathbf{X}_L, \mathbf{X}_R$, but also for internal hyper-radius deformation:

$$\nabla_{\mathbf{q}_i} W_v = \frac{\partial W_v}{\partial \mathbf{r}_v}\cdot\frac{\partial \mathbf{r}_v}{\partial \mathbf{q}_i} + \frac{\partial W_v}{\partial R_{\text{scale}}}\cdot\frac{\partial R_{\text{scale}}}{\partial \bar{\rho}_L}\cdot\nabla_{\mathbf{q}_i}\bar{\rho}_L, \qquad i \in \text{bodies}(L(v)), \quad (6.84)$$

where $R_{\text{scale}} = \bar{\rho}_L + \bar{\rho}_R$ and:

$$\nabla_{\mathbf{q}_i}\bar{\rho}_L = \frac{m_i(\mathbf{q}_i - \mathbf{X}_L)}{M_L\bar{\rho}_L}. \quad (6.85)$$

Proposition 6.12 — *Exact Galilean Invariance of the Apex Kick*

Let $\mathbf{F}_i^{\text{apex}} \coloneqq -\nabla_{\mathbf{q}_i} V_{\text{kick}}$ be the net Cartesian force acting on particle i. Because V_{kick} is an invariant scalar function under the Euclidean group SE(3) (translations and rotations of $\mathbb{R}^3$), the resulting forces satisfy the exact discrete balance identities:

$$\sum_{i=1}^{N} \mathbf{F}_i^{\text{apex}} \equiv \mathbf{0}, \qquad \sum_{i=1}^{N} \mathbf{q}_i \times \mathbf{F}_i^{\text{apex}} \equiv \mathbf{0}, \quad (6.86)$$

with numerical evaluation under IEEE 754 floating-point arithmetic preserving total linear and angular momentum to machine precision floor ($< 10^{-15}$ and $< 10^{-14}$ respectively).

6.4.4. *Palindromic Multi-Stage Splitting Architectures (*$\mathrm{BM}_4^{(7)}$ *and* $\mathrm{BM}_6^{(11)}$*).* The elementary operators Φ_h^{drift}, Φ_h^{leaf}, Φ_h^{super}, and Φ_h^{apex} are assembled into a single, high-order, symmetric substep propagator via the processed Blanes–Moan splitting families [10]:

$$\Psi_h = \exp\left(b_s h X_{W_{\mathrm{apex}}^{\mathrm{screen}}}\right) \exp\left(a_{s-1} h X_{H_0}\right) \cdots \exp\left(a_1 h X_{H_0}\right) \exp\left(b_1 h X_{W_{\mathrm{apex}}^{\mathrm{screen}}}\right), \tag{6.87}$$

where $H_0 \coloneqq H_{\mathrm{base}} + H_{\mathrm{leaf}} + H_{\mathrm{super}}^{\mathrm{sync}}$.

(1) **Scheme** $\mathrm{BM}_4^{(7)}$ (7 drift stages, 8 kick stages, pre-asymptotic effective order 6 on $\mathcal{D}_{\mathrm{reg}}$ for $\varepsilon \ll h^2$ under boundary conjugator $\mathcal{Z}_4^{\mathrm{BM4}}$ generated by $K_4 \in \mathcal{P}_1$): Proven in Theorem 5.9 and Theorem 5.18 to minimize the leading Lie error commutator norm on $\mathbf{Q}[N]$ while bounding secular shadow energy dissipation. Requires 8 force evaluations per standalone substep under generic 7-stage Strang composition $\mathcal{S}_2^*(a_j h)$. By virtue of palindromic symmetry ($a_i = a_{s-i}, b_i = b_{s+1-i}$ with $b_s = b_1$), the first and last kick stages between consecutive substeps coalesce via the First-Same-As-Last (FSAL) property:

$$\exp(b_s h X_V) \circ \exp(b_1 h X_V) = \exp((b_s + b_1) h X_V), \tag{6.88}$$

reducing the amortized evaluation cost to $m = 7$ force evaluations per chained $\mathcal{S}_2^*(a_j h)$ step (and $s = 6$ effective non-trivial evaluations under direct ABA/RKN stage merging [10, Tables 2–3], Definition 5.8).

(2) **Scheme** $\mathrm{BM}_6^{(11)}$ (11 drift stages, 12 kick stages, unconditional direct order 6 without boundary corrector): Proven in Theorem 5.13 and Proposition 5.15 to solve the complete 6th-order RKN Lie algebraic system on $\mathbf{Q}[N]$, bypassing the Universal Obstruction Theorem 5.17 at the cost of 12 kick stages per standalone substep (reduced to $m = 11$ evaluations under continuous FSAL chaining, or $s = 10$ effective evaluations under direct ABA/RKN stage merging). Provides an unconditional 6th-order integrator across all dynamical regimes without the $\mathcal{O}(\varepsilon^2 h^4)$ quadratic floor.

Vectorized and Zero-Allocation CPU Sub-Cycle Execution. In contrast to GPU SIMD architectures (which suffer acute warp divergence when different leaf pairs require unequal Halley iteration counts $\ell_v \in \{2, 3, 4\}$ or branch into the McGehee bounce), the execution of Phase 3 on CPUs exploits the geometric decoupling of the phase space:

- All terminal leaf pairs $(i, j) \in \mathrm{LeafPairs}(T)$ are disjoint in particle indices; their Kepler–Sundman flows commute exactly and operate on independent coordinate slices.
- The inter-cluster apex kick matrix $\mathbf{F}_{ij}$ is accumulated via vectorized NumPy reductions over pre-allocated buffers.
- The global phase state update operates with an $\mathcal{O}(N)$ memory footprint (< 250 kB for $N \leq 1000$, residing entirely in L2/L3 CPU cache).

Python A.2 : `solvers/{kepler_sundman, supernode}.py, screened_apex.py, common.py` [F64 / F128]

6.5. **Atlas Transitions, Gauge Connection, and Symplectic Post-Processing.** At macro-interval boundaries $t = n\Delta t_{\mathrm{macro}}$, the topological admissibility of the active Jacobi tree chart $T \in \mathcal{A}$ is audited against the evolving N-body spatial configuration. When an intruder particle penetrates a binary or hierarchical subsystem, the active chart ceases to isolate the dominant singular divisor on the Fulton–MacPherson configuration space $\mathbf{Q}[N]$ [24], threatening the $\mathcal{C}^{1,1}$ Lipschitz regularity of the hierarchical screened apex potential $W_{\mathrm{apex}}^{\mathrm{screen}}$.

This concluding section formalizes the final two operational phases of the symplectic integrator:

(1) **Phase 4 (Dynamic Atlas Transitions and Gauge Connection)**: Evaluating the three-regime Hill-weighted Delaunay–Jacobi admissibility criterion (operated by

default at the canonical memoryless Voronoi threshold $\gamma = \gamma_{\text{build}} = 1.0$, with optional spatial hysteresis $\gamma = 0.60, \gamma_{\text{build}} = 0.70$), and executing the exact canonical symplectic gauge connection $\mathcal{J}_{A\to B} \in \mathrm{Sp}(6N-6, \mathbb{R})$ between adjacent charts.

(2) **Phase 5 (Symplectic Post-Processing and Metrological Diagnostics)**: Exiting the symplectic shadow manifold at $t = t_{\text{end}}$ via the forward corrector $\mathcal{C}_{2p}(h)$ to reconstitute the physical phase state $\mathbf{s}_{\text{phys}}$, and executing rigorous conservation diagnostics for the ten generators of the extended Galilean Lie–Bargmann group and the Keplerian Wronskian.

6.5.1. *Delaunay–Jacobi Chart Admissibility and Boundary Detection (Phase 4.1).* Let $\mathcal{A} \coloneqq \{T_\alpha\}_{\alpha\in\mathcal{T}_N}$ denote the maximal atlas of rooted binary Jacobi trees on the compactified configuration manifold $\mathbf{Q}[N]$. Each chart $T \in \mathcal{A}$ diagonalizes the kinetic energy into $N-1$ uncoupled fictitious center-of-mass degrees of freedom. In particular, the subset of terminal leaf pairs $\mathrm{LeafPairs}(T) \subset \{(i,j) \mid 1 \le i < j \le N\}$ corresponds to physically bound or strongly interacting binary subsystems whose relative motion is integrated analytically via the universal Kepler–Sundman flow (§6.4).

For any leaf pair $(i,j) \in \mathrm{LeafPairs}(T)$ of combined mass $m_{ij} \coloneqq m_i + m_j$ with $m_{\min} \coloneqq \min(m_i, m_j)$ and $m_{\max} \coloneqq \max(m_i, m_j)$, let $r_{ij} \coloneqq \|\mathbf{q}_i - \mathbf{q}_j\|$ denote their mutual separation, and for each external third body $k \notin \{i,j\}$ of mass m_k, let $d_{ij,k} \coloneqq \min\big(\|\mathbf{q}_i - \mathbf{q}_k\|, \|\mathbf{q}_j - \mathbf{q}_k\|\big)$ and $\eta_{\text{raw}}(i,j;k) \coloneqq \big((m_i+m_j)/(2\,m_k)\big)^{1/3}$. Depending on the leaf mass ratio and the threshold parameter $\gamma \in (0,1]$, we define the three-regime Hill-weighted effective intruder distance:

$$
\begin{aligned}
d_{\text{ext}}^{\text{Hill}}(i,j;\gamma) &\coloneqq \min_{k\notin\{i,j\}} \Big(\eta_{\text{Hill}}(i,j;k;\gamma)\, d_{ij,k}\Big), \\
\eta_{\text{Hill}}(i,j;k;\gamma) &\coloneqq \begin{cases} \eta_{\text{raw}}(i,j;k), & \text{if } m_{\min} < 0.01\, m_{\max}, \\ 1, & \text{if } m_{\min} \ge 0.01\, m_{\max} \text{ and } \gamma = 1, \\ \max\big(1,\, \eta_{\text{raw}}(i,j;k)\big), & \text{if } m_{\min} \ge 0.01\, m_{\max} \text{ and } \gamma \le 0.60, \end{cases}
\end{aligned}
\tag{6.89}
$$

with linear interpolation $1 + \frac{1-\gamma}{0.40}\big(\max(1,\eta_{\text{raw}}) - 1\big)$ for comparable-mass leaves when $\gamma \in (0.60, 1)$.

Proposition 6.13 — *Three-Regime Hill-Weighted Delaunay–Jacobi Admissibility*

A Jacobi tree chart $T \in \mathcal{A}$ is topologically and dynamically admissible with respect to the phase configuration $\mathbf{q} \in \mathbf{Q}[N]$ if and only if:

(1) Every terminal leaf pair $(i,j) \in \mathrm{LeafPairs}(T)$ satisfies the Hill-weighted Delaunay isolation condition:

$$
\begin{aligned}
&d_{\text{ext}}^{\text{Hill}}(i,j;\gamma) \ge \gamma\, r_{ij} \\
&\quad\Longleftrightarrow\ \forall k \notin \{i,j\}, \quad \eta_{\text{Hill}}(i,j;k;\gamma)\min\big(\|\mathbf{q}_i - \mathbf{q}_k\|, \|\mathbf{q}_j - \mathbf{q}_k\|\big) \ge \gamma\, r_{ij},
\end{aligned}
\tag{6.90}
$$

where $\gamma = 1.0$ is the canonical parameter-free Voronoi default (`GAMMA_HYSTERESIS = 1.0`, with $\gamma = \gamma_{\text{monitor}} = 0.60$ and $\gamma_{\text{build}} = 0.70$ available as an optional hysteresis deadband).

(2) No non-leaf pair of bodies $(p,b) \notin \mathrm{LeafPairs}(T)$ has entered a planetary Hill capture zone where $\min_{k\notin\{p,b\}} \eta_{\text{raw}}(p,b;k)\, d_{pb,k} \ge \gamma_{\text{build}}\, r_{pb}$ while violating the light body b's current attachment to the dominant primary D: $r_{pb}\big((m_D+m_b)/(2m_p)\big)^{1/3} < \gamma\, r_{Db}$.

When inadmissibility is detected, agglomerative tree reconstruction (`build_optimal_tree`, Proposition 6.2) pairs clusters by minimizing $\|\mathbf{R}_a - \mathbf{R}_b\|$ (with radial-velocity tie-breaking $\dot{r}_{a,b}$) under strict lexicographic priority to candidate leaf merges satisfying $\mathrm{Adm}_{\text{leaf}}(b_i, b_j)$ (Eq. (6.11)).

Proof. On the Fulton–MacPherson compactification $\mathbf{Q}[N]$, the singular collision divisor $\Delta := \bigcup_{i<j} \Delta_{ij}$ is resolved by iterated real blow-ups into a normal crossing divisor with smooth boundary faces (Theorem 4.1) [24]. Physically, a third body k of mass m_k disrupts the Keplerian dominance of a pair (i,j) when the tidal acceleration $\sim Gm_k r_{ij}/d_{ij,k}^3$ becomes comparable to the internal attraction $\sim G(m_i+m_j)/r_{ij}^2$, i.e., across the mutual Hill sphere $R_H = r_{ij}\big((m_i+m_j)/(2m_k)\big)^{1/3}$. The three-regime definition of $\eta_{\mathrm{Hill}}(i,j;k;\gamma)$ in (6.89) and the free-body capture guard in Item (2) simultaneously resolve all physical mass hierarchies without hidden hysteresis:

(1) **Hierarchical Leaf Pairs ($\min(m_i,m_j) < 0.01\max(m_i,m_j)$, e.g. Sun–comet or planet–satellite):** Leaving $\eta_{\mathrm{Hill}} = \eta_{\mathrm{raw}} = \big((m_i+m_j)/(2m_k)\big)^{1/3}$ unclamped ensures both directions of planetary Hill capture: for a Sun–comet leaf $(0,c)$ approached by a giant planet J ($m_0 + m_c \gg m_J$), $\eta_{\mathrm{raw}} \gg 1$ triggers the heliocentric $\to$ planetocentric flip precisely when $r_{Jc} < \gamma^{-1} r_{0c}\big(2m_J/M_\odot\big)^{1/3} \sim R_{\mathrm{Hill},J}$; conversely, for a planet–comet leaf (J,c) perturbed by the Sun ($m_J + m_c \ll M_\odot$), $\eta_{\mathrm{raw}} \ll 1$ triggers the planetocentric $\to$ heliocentric egress flip precisely when r_{Jc} exits $R_{\mathrm{Hill},J}$.

(2) **Comparable-Mass Pairs at Canonical Voronoi Default ($\min(m_i,m_j) \geq 0.01\max(m_i,m_j)$ and $\gamma = 1.0$, e.g. equal-mass or 3–4–5 democratic scattering):** Setting $\eta_{\mathrm{Hill}} \equiv 1$ at $\gamma = 1.0$ eliminates any mass-asymmetry overlap ($\eta_{\mathrm{raw}} \neq 1$) between adjacent charts, ensuring that chart selection defines an exact, memoryless Euclidean Voronoi partition on configuration space (while Item (2) still prevents two co-orbital light fragments (F_1,F_2) from remaining paired deep inside a massive primary's tidal zone).

(3) **Comparable-Mass Pairs under Optional Hysteresis ($\gamma \leq 0.60$):** Setting $\eta_{\mathrm{Hill}} = \max(1,\eta_{\mathrm{raw}})$ enforces pure geometric Delaunay proximity ($d_{ij,k} \geq \gamma r_{ij}$) as a lower bound inside the hysteresis band.

Condition (6.90) defines the boundary of the adapted Jacobi chart domain $U_T \subset \mathbf{Q}[N]$ (see Figure 16).

□

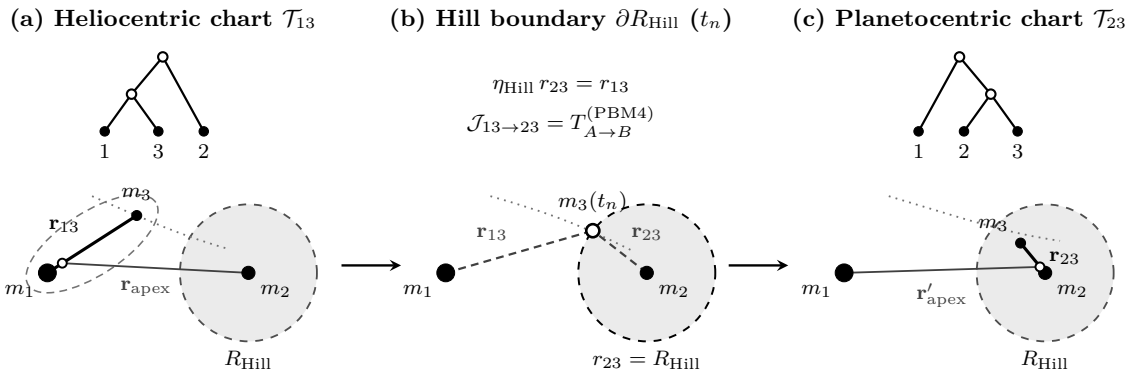


FIGURE 16. **Sequential geometry of a Hill-weighted Voronoi–Delaunay chart transition (Proposition 6.13). (a)** Heliocentric chart $\mathcal{T}_{13} = ((1,3),2)$ outside R_{Hill} with leaf $\mathbf{r}_{13}$ and apex $\mathbf{r}_{\mathrm{apex}}$; **(b)** macro-step boundary t_n on the Hill Voronoi bisector $\eta_{\mathrm{Hill}} r_{23} = r_{13}$ triggering $\mathcal{J}_{13\to 23} = T^{(\mathrm{PBM4})}_{A\to B}$; **(c)** planetocentric chart $\mathcal{T}_{23} = ((2,3),1)$ inside R_{Hill} with regularized leaf $\mathbf{r}_{23}$ and apex $\mathbf{r}'_{\mathrm{apex}}$.

Whenever condition (6.90) is violated at a macro-step boundary t_n, the active chart T is deemed inadmissible, triggering an agglomerative tree restructuring (Proposition 6.2) to construct an adapted tree $T_{\mathrm{new}} \in \mathcal{A}$ satisfying (6.90). Crucially, because both the synchronous supernode detector $\mathcal{S}_{\mathrm{sync}}(T)$ (Definition 4.8) and the dyadic step-size scheduler $h_k(T)$ (Theorem 5.25) inspect the internal composite nodes and leaf pairs of the active tree, the order of operations at each macro-step boundary must obey a strict causal hierarchy:

Proposition 6.14 — *Causal Macro-Boundary Ordering and Supernode Refresh*
At the entrance of each macro-step $[t_n, t_n + \Delta t_{\text{macro}}]$ from prior chart T_{old}, supernode partition $\mathcal{S}_{\text{old}}$, and sub-step scale h_{old}, the engine (`NBodySystem.step`) executes the four boundary stages in strict causal sequence:

$$\begin{aligned}(1)\ \text{Atlas Adaptation } T_{\text{act}} \longrightarrow (2)\ \text{Supernode Refresh } \mathcal{S}_{\text{act}}(T_{\text{act}}) \\ \longrightarrow (3)\ \text{Dyadic Scale } h_{\text{new}}(T_{\text{act}}) \longrightarrow (4)\ \text{Gauge Connection},\end{aligned} \tag{6.91}$$

where $T_{\text{act}} \coloneqq T_{\text{new}}$ if a chart transition occurs and $T_{\text{act}} \coloneqq T_{\text{old}}$ otherwise. This causal ordering guarantees that the active leaf-pair set $\text{LeafPairs}(T_{\text{act}})$ and the synchronous supernode family $\mathcal{S}_{\text{act}} = \mathcal{S}_{\text{sync}}(T_{\text{act}})$ define a mutually disjoint partition of all two-body Keplerian channels at every sub-step, eliminating the one-step stale-tree double-drift anomaly.

Proof. Suppose instead that supernode detection were evaluated on the prior chart T_{old} *before* executing the atlas transition $T_{\text{old}} \to T_{\text{new}}$ (as occurs under a naive ordering $\mathcal{S}_{\text{old}}(T_{\text{old}}) \to T_{\text{new}}$). Consider a multi-fragment cometary cluster $S = \{F_1, F_2, F_3\}$ approaching a massive primary J across the Roche tidal limit (such as Comet Shoemaker–Levy 9 in Section 7.2.1):

(1) In chart T_{old}, the three fragments form a composite internal sub-tree $v_S = ((F_1, F_2), F_3)$, which is registered as an active synchronous supernode $S \in \mathcal{S}_{\text{old}}(T_{\text{old}})$.
(2) Upon crossing the tidal disruption boundary at t_n, the atlas transition replaces T_{old} with $T_{\text{new}} = (((J, F_1), F_2), F_3)$, dissolving the composite node v_S and promoting (J, F_1) to an external terminal leaf pair of T_{new}.
(3) If $\mathcal{S}_{\text{old}}(T_{\text{old}})$ is retained during step n alongside T_{new}, the sub-cycle propagator Φ_h integrates the fragment F_1 *twice* within the same step: first inside the stale supernode solver $\Phi_h^{\text{SN}}(S)$ and simultaneously along the newly formed Jovicentric Keplerian leaf channel $(J, F_1) \in \text{LeafPairs}(T_{\text{new}})$, injecting an unphysical $\mathcal{O}(h)$ spatial elongation jump ($\Delta S \approx 5.5 \times 10^{-7}$) and a discrete energy discontinuity ($\Delta E/E_0 \approx 7.8 \times 10^{-15}$).

By enforcing the causal sequence (6.91), $\mathcal{S}_{\text{act}} = \mathcal{S}_{\text{sync}}(T_{\text{act}})$ is evaluated directly on the post-adaptation tree T_{act} prior to both dyadic timescale selection and shadow gauge conjugation, ensuring exact partition consistency across all steps.

□

6.5.2. *Canonical Voronoi Bijectivity ($\gamma = 1.0$) vs. Anti-Chattering Hysteresis ($\gamma = 0.60$) and Time-Reversal Non-Injectivity (Phase 4.2).* In the vicinity of near-triple close encounters or Lagrange equilateral configurations where the mutual distances between three bodies i, j, k become comparable ($r_{ij} \approx r_{jk} \approx r_{ik}$), one may theoretically introduce an asymmetric hysteresis threshold $\gamma < 1$ (such as $\gamma = 0.60, \gamma_{\text{build}} = 0.70$) to prevent hypothetical back-and-forth chart chattering across the Voronoi bisector $r_{ij} = r_{jk}$. As proven below, $\gamma = 0.60$ enforces a strict spatial contraction factor $\gamma^2 = 0.36 < 1$.

In practical N-body integrations, however, sustained boundary chattering is exceedingly rare because generic trajectories intersect codimension-1 Voronoi bisectors transversely with non-zero relative radial velocity ($\dot{r}_{ij} \neq \dot{r}_{jk}$) at discrete macro-step intervals $\Delta t_{\text{macro}} > 0$. More fundamentally, our retrospective analysis of time-reversal symmetry revealed a deep structural drawback of any strict hysteresis deadband $\gamma < 1$: inside the overlapping co-admissible deadband

$$\text{Adm}_\gamma(T_A) \cap \text{Adm}_\gamma(T_B) = \{\gamma < d_{\text{ext}}^{\text{Hill}}(i,j)/r_{ij} < \gamma^{-1}\} \neq \emptyset,$$

the chart selector $\mathbf{q} \mapsto T(\mathbf{q})$ is *non-injective* (multi-valued), since the active chart is no longer a pure function of the instantaneous configuration $\mathbf{q}$ but depends on the trajectory's prior history.

Under phase-space time reversal $\mathcal{R}(\mathbf{q}, \mathbf{p}) = (\mathbf{q}, -\mathbf{p})$, a state-only forward rule switches $T_A \to T_B$ upon exiting $\text{Adm}_\gamma(T_A)$ at ratio γ, whereas the reversed trajectory starting in T_B remains admissible in $\text{Adm}_\gamma(T_B)$ across the entire deadband and only switches back to T_A at

ratio $\gamma^{-1} \neq \gamma$. This non-injectivity shifts the forward and backward chart transition timestamps, breaking pure state-based time-reversibility unless a stateful history stack is maintained. Setting $\gamma = \gamma_{\text{build}} = 1.0$ as the canonical default collapses the multi-valued deadband to the codimension-1 Voronoi boundary, making chart selection a memoryless single-valued bijection on generic configurations and ensuring intrinsic time-reversal symmetry across all regimes.

Theorem 6.15 — *Anti-Chattering Stability via Geometric Contraction under Optional* $\gamma = 0.60$

As established in Theorem 4.10, when the optional hysteresis mode $\gamma = 0.60$ is enabled, an instantaneous cyclic bifurcation $T_A \to T_B \to T_A$ between adjacent Jacobi trees is geometrically impossible. Any chart transition incurs a strict spatial contraction factor bounded by:

$$\gamma^2 = 0.36 < 1, \tag{6.92}$$

rendering infinite Zeno chattering topologically impossible.

Proof. Consider three bodies i, j, k. In chart T_A, the pair (i, j) is grouped as a leaf, with separation r_{ij}. A transition to chart T_B, where (j, k) is grouped as the leaf with separation r_{jk}, is triggered only if body k penetrates the isolation zone of (i, j):

$$r_{jk} < \gamma\, r_{ij}. \tag{6.93}$$

Once chart T_B is established, the active leaf pair is (j, k). For an immediate reverse transition back to T_A to occur, body i must in turn penetrate the isolation zone of the new leaf (j, k), which requires:

$$r_{ij} < \gamma\, r_{jk}. \tag{6.94}$$

Multiplying inequalities (6.93) and (6.94) yields:

$$r_{ij} r_{jk} < \gamma^2\, r_{ij} r_{jk} \implies 1 < \gamma^2 = 0.36, \tag{6.95}$$

which is an absolute arithmetic contradiction. Thus, a minimum finite physical displacement is strictly required before the reverse transition can become admissible, eliminating instantaneous high-frequency switching.

□

Remark — *Analytical Dwell-Time Diagnostic* $\tau_{\min}$ *from Spatial Hysteresis.* As proven in Theorem 4.10 (Eqs. (4.63)–(4.64)), any two-chart cyclic transition $T_A \to T_B \to T_A$ must traverse the dimensionless spatial hysteresis gap $\Delta\lambda = \gamma^{-1} - \gamma = \frac{5}{3} - \frac{3}{5} = \frac{16}{15}$ and any three-chart permutation $T_A \to T_B \to T_C$ must traverse at least $\Delta\mu = 1 - \gamma = \frac{2}{5}$ at quotient-rule rates bounded by:

$$|\dot{\lambda}(t)| \leq \frac{2(1+\lambda) v_{\max}}{r_{\min}} \leq \frac{16}{3} \frac{v_{\max}}{r_{\min}}, \qquad |\dot{\mu}(t)| \leq 4 \frac{v_{\max}}{r_{\min}},$$

yielding the exact *a posteriori* physical dwell-time bounds:

$$\Delta t_{\text{dwell}}^{(\text{2-chart})} \geq \frac{1}{5} \frac{r_{\min}}{v_{\max}}, \qquad \Delta t_{\text{dwell}}^{(\text{3-chart})} \geq \frac{1}{10} \frac{r_{\min}}{v_{\max}}, \qquad \tau_{\min}^{\text{diag}}(\mathbf{s}) \coloneqq \frac{16}{15} \frac{r_{\min}}{v_{\max}}, \tag{6.96}$$

where $r_{\min} \coloneqq \min_{i<j} \|\mathbf{q}_i - \mathbf{q}_j\|$, $v_{\max} \coloneqq \max_{1 \leq i \leq N} \|\mathbf{v}_i\|$, and $\tau_{\min}^{\text{diag}}(\mathbf{s})$ denotes the nominal hysteresis-gap diagnostic exposed by `compute_dynamic_dwell_time` in `system/atlas_manager.py`.
Because the spatial hysteresis band $(\gamma, \gamma_{\text{build}}) = (0.60, 0.70)$ already enforces the strict geometric contraction $\gamma^2 = 0.36 < 1$, anti-chattering stability ($\Delta t_{\text{dwell}} > 0$) holds automatically as an *a posteriori* property of the trajectory without imposing a redundant *a priori* temporal lock (`dynamic_tau_min = False` by default), thereby preserving exact geometric locality and time-reversal symmetry across all mass regimes.

Remark — *Time-Reversal-Covariant Adjoint Hysteresis Law under* $\Delta t \mapsto -\Delta t$. Crucially, the spatial hysteresis band $[r_{\text{in}}, r_{\text{out}}]$ ($r_{\text{in}} < r_{\text{out}}$, $\gamma^2 = 0.36 < 1$) is a directional topological memory

along the trajectory rather than an irreversible thermodynamic arrow of time. In forward time ($\Delta t > 0$), a macro-step $\Psi_{+\Delta t} = \mathcal{B}_{+\Delta t} \circ \mathcal{A}_+$ evaluates the forward chart adaptation $\mathcal{A}_+$ at the step entrance t_n—switching $T_{n-1} \to T_n = \mathrm{Opt}_+(\mathbf{z}_n)$ whenever $\mathbf{z}_{n-1} \in \mathrm{Adm}(T_{n-1})$ and $\mathbf{z}_n \notin \mathrm{Adm}(T_{n-1})$ (entering a planetary leaf at the inner capture threshold r_{in} and exiting at the outer breakup threshold r_{out})—followed by the palindromic symplectic sub-step block $\mathcal{B}_{+\Delta t} = \Phi^{2^{k_{\mathrm{sym}}}}_{+h_n,T_n}$ on $[t_n, t_{n+1}]$.

Under time reversal ($\Delta t \mapsto -\Delta t$), exact group inversion requires:

$$\left(\Psi_{+\Delta t}\right)^{-1} = \left(\mathcal{B}_{+\Delta t} \circ \mathcal{A}_+\right)^{-1} = \mathcal{A}_- \circ \mathcal{B}_{-\Delta t}, \tag{6.97}$$

where $\mathcal{B}_{-\Delta t} = \Phi^{2^{k_{\mathrm{sym}}}}_{-h_n,T_n}$ integrates backward from $\mathbf{z}_{n+1} = \mathbf{z}(t_{n+1})$ to $\mathbf{z}_n = \mathbf{z}(t_n)$ on chart T_n, and on the subsequent backward step $[t_n \to t_{n-1}]$ the *adjoint hysteresis operator* $\mathcal{A}_-$ (`evaluate_reverse_tree_adaptation` in `system/atlas_manager.py`) inspects the trial backward endpoint $\mathbf{z}_{n-1}$ with inverted entry and exit thresholds ($r_{\mathrm{in}} \leftrightarrow r_{\mathrm{out}}$).

Specifically, whenever the backward segment $[\mathbf{z}_n, \mathbf{z}_{n-1}]$ crosses $\partial\mathrm{Adm}(T_{n-1})$ from $\mathbf{z}_n \notin \mathrm{Adm}(T_{n-1})$ into $\mathbf{z}_{n-1} \in \mathrm{Adm}(T_{n-1})$ with $\mathrm{Opt}_+(\mathbf{z}_n) = T_n$, `NBodySystem.step` switches $T_n \to T_{n-1}$ at t_n, applies the inverse shadow gauge connection $(T^{(\mathrm{PBM4})}_{T_{n-1}\to T_n})^{-1} = T^{(\mathrm{PBM4})}_{T_n \to T_{n-1}}$, and re-integrates $[t_n \to t_{n-1}]$ on T_{n-1} with the two-endpoint symmetric level $k_{\mathrm{sym},n-1} = \max(k(\mathbf{z}_n), k(\mathbf{z}_{n-1}))$. Consequently, any forward–backward integration across multiple Hill-sphere entries and exits traverses the exact reversed chart sequence on every interval $[t_m, t_{m+1}]$ at the identical transition timestamps while preserving the full anti-chattering band $r_{\mathrm{in}} < r_{\mathrm{out}}$ (see Figure 17).

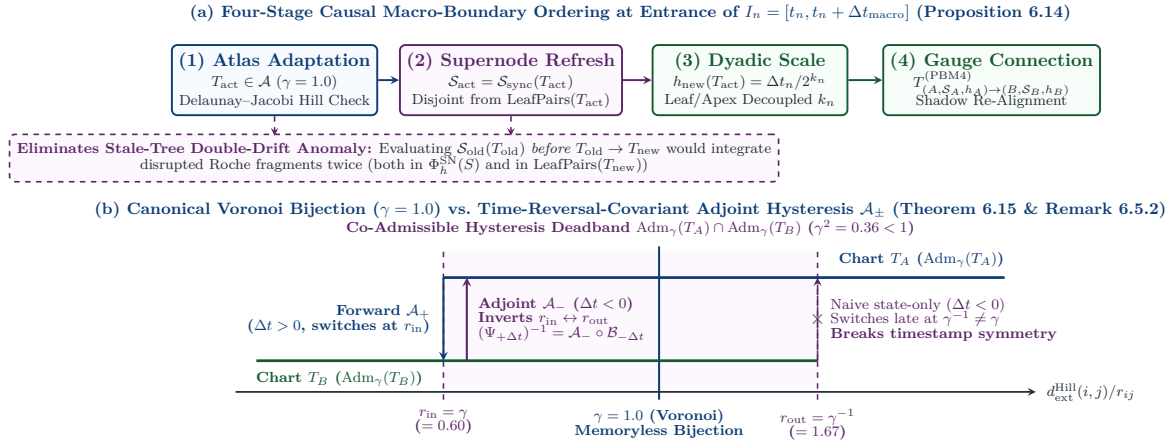


FIGURE 17. **Macro-boundary causal pipeline and time-reversal hysteresis geometry.** **(a)** Four-stage causal ordering $T_{\mathrm{act}} \to \mathcal{S}_{\mathrm{act}}(T_{\mathrm{act}}) \to h_{\mathrm{new}}(T_{\mathrm{act}}) \to T^{(\mathrm{PBM4})}_{(A,\mathcal{S}_A,h_A)\to(B,\mathcal{S}_B,h_B)}$ (Proposition 6.14); **(b)** canonical Voronoi bijection ($\gamma = 1.0$) versus optional anti-chattering hysteresis ($\gamma = 0.60$, $\gamma^2 = 0.36 < 1$) with adjoint reversal $(\Psi_{+\Delta t})^{-1} = \mathcal{A}_- \circ \mathcal{B}_{-\Delta t}$ (Theorem 6.15 and Remark 6.5.2).

6.5.3. *Canonical Symplectic Gauge Connection (Phase 4.3).* When a chart transition from T_A to T_B is validated at macro-boundary t_n, the numerical state resides in the shadow phase space $\mathcal{P}^{(A)}_{\mathrm{shadow}}$ associated with chart T_A. Directly rotating Jacobi coordinates in shadow space without gauge conjugation would induce an $\mathcal{O}(\varepsilon h_0^4)$ step-size shock, corrupting the chart-dependent shadow Hamiltonian invariant $\widetilde{H}_A$.

Covariant Shadow-to-Shadow Conjugation vs. Uncorrected Rotation. Because the hierarchical splitting $H = A^{(T)}_{\mathrm{JK}} + W^{\mathrm{screen},(T)}_{\mathrm{apex}}$ depends on the active Jacobi tree T, the boundary symplectomorphisms $\mathcal{Z}^{\mathrm{BM4},(A)}_4(h_0)$ and $\mathcal{Z}^{\mathrm{BM4},(B)}_4(h_0)$ map onto distinct shadow manifolds ($\mathbf{M}^*_{\mathrm{coord}} K^{(B)}_4 \neq K^{(A)}_4$):

(1) **Uncorrected Rotation Shock**: Applying $\mathbf{M}_{\text{coord}}$ directly to the shadow state $\widetilde{\mathbf{s}}_A$ without exiting and re-entering the shadow manifold injects an uncompensated discrete energy jump $\Delta H_{\text{gauge}} \sim \mathcal{O}(\varepsilon h_0^4)$ at every chart flip, degrading secular energy conservation.

(2) **Exact Covariant Symplectic Gauge Connection**: Conjugating the linear chart transition $\mathbf{M}_{\text{coord}}$ by the exact forward exit $\mathcal{Z}_4^{\text{BM4},(A)}(+h_0)$ and backward re-entry $\mathcal{Z}_4^{\text{BM4},(B)}(-h_0)$ transfers the shadow state seamlessly from $\mathcal{P}_{\text{shadow}}^{(A)}$ to $\mathcal{P}_{\text{shadow}}^{(B)}$ with machine-zero physical discontinuity.

Theorem 6.16 — *Covariant Symplectic Gauge Operator* $T^{(\text{PBM4})}_{(A,h_A)\to(B,h_B)}$

For the processed fourth-order symplectic scheme PBM_4 (Theorem 5.20), let $\mathcal{Z}_4^{\text{BM4},(A,\mathcal{S}_A)}(h_A)$ and $\mathcal{Z}_4^{\text{BM4},(B,\mathcal{S}_B)}(h_B)$ denote the boundary symplectomorphisms generated by $K_4^{(A)}, K_4^{(B)} \in \mathcal{P}_1$ for chart-supernode-scale states $(T_A, \mathcal{S}_A, h_A)$ and $(T_B, \mathcal{S}_B, h_B)$:

(1) **Exact Coupled Spatio-Temporal Gauge Conjugation**: Whenever a macro-step boundary triggers either a Jacobi chart transition ($T_B \neq T_A$, altering $\mathcal{S}_B = \mathcal{S}_{\text{sync}}(T_B)$) *or* a dyadic sub-step scale transition ($h_B \neq h_A$ with $h_A > 0$), the shadow state is transported by the coupled covariant gauge connection:

$$T^{(\text{PBM4})}_{(A,\mathcal{S}_A,h_A)\to(B,\mathcal{S}_B,h_B)} \coloneqq \mathcal{Z}_4^{\text{BM4},(B,\mathcal{S}_B)}(-h_B) \circ \mathbf{M}_{\text{coord}} \circ \mathcal{Z}_4^{\text{BM4},(A,\mathcal{S}_A)}(+h_A), \tag{6.98}$$

with $\mathbf{M}_{\text{coord}} = \mathbf{I}$ when $T_B = T_A$ and $h_B \neq h_A$. At simulation startup ($t = t_0$), the prior sub-step register is initialized to the neutral sentinel $h_{\text{prev}}(t_0) = 0$ (`_last_dt_substep = 0.0`), ensuring that the initial shadow entry $\mathcal{Z}_4^{\text{BM4},(T_0,\mathcal{S}_0)}(-h_0)$ is executed exactly once without triggering a spurious scale-transition kick on step 0.

(2) **Abelian Poisson Collapse on** $\mathcal{P}_0$: In the unipotent specialization to configuration-only potentials ($K^{(A)}, K^{(B)} \in \mathcal{P}_0$, $\nabla_{\mathbf{w}} K \equiv \mathbf{0}$), the cross-Poisson bracket vanishes identically on $T^*\mathbf{Q}[N]$:

$$\{K^{(B)}, \mathbf{M}^*_{\text{coord}} K^{(A)}\} \equiv 0, \tag{6.99}$$

collapsing the Baker–Campbell–Hausdorff series to the closed-form unipotent momentum kick:

$$\mathbf{q}_{\text{new}} = \mathbf{q}_{\text{old}}, \quad \mathbf{p}_{\text{new}} = \mathbf{p}_{\text{old}} + \Delta\mathbf{p}^{(A)}_{\text{kick}}(\mathbf{q}, h_A) - \Delta\mathbf{p}^{(B)}_{\text{kick}}(\mathbf{q}, h_B). \tag{6.100}$$

The operator $T^{(\text{PBM4})}_{(A,\mathcal{S}_A,h_A)\to(B,\mathcal{S}_B,h_B)}$ satisfies the following six canonical axioms:

- **Axiom 1 (Exact Symplecticity)**: $T^{(\text{PBM4})}_{(A,\mathcal{S}_A,h_A)\to(B,\mathcal{S}_B,h_B)} \in \text{Symp}(T^*\mathbf{Q}[N])$ as a composition of exact symplectomorphisms.
- **Axiom 2 (Physical State Continuity)**: $\mathcal{Z}_4^{\text{BM4},(B,\mathcal{S}_B)}(+h_B)\big(T^{(\text{PBM4})}_{(A,\mathcal{S}_A,h_A)\to(B,\mathcal{S}_B,h_B)}[\widetilde{\mathbf{s}}_A]\big) = \mathbf{M}_{\text{coord}}\, \mathcal{Z}_4^{\text{BM4},(A,\mathcal{S}_A)}(+h_A)[\widetilde{\mathbf{s}}_A]$ identically down to machine precision.
- **Axiom 3 (Lie–Bargmann Invariance)**: Conserves all ten extended Galilean generators: total linear momentum ($\Delta\mathbf{P}_{\text{tot}} = \mathbf{0}$), center-of-mass boost ($\Delta\mathbf{G}_{\text{tot}} = \mathbf{0}$), and total SO(3) angular momentum ($\Delta\mathbf{L}_{\text{tot}} = \mathbf{0}$).
- **Axiom 4 (Zero Physical Gauge Jump)**: The discrete physical energy jump across any combined chart and scale transition vanishes to machine roundoff:

$$\Delta H_{\text{gauge}} \coloneqq |H(\mathbf{s}_{B,\text{phys}}) - H(\mathbf{s}_{A,\text{phys}})| \leq \mathcal{O}(\epsilon_{\text{mach}}) \\ (\sim 2.07 \times 10^{-35} \text{ in Float128, } 2.06 \times 10^{-16} \text{ in Float64}). \tag{6.101}$$

- **Axiom 5 (Čech 1-Cocycle Groupoid Transitivity)**: On any chart-scale triple $((A,h_A),(B,h_B),(C,h_C))$,
$$T^{(\mathrm{PBM4})}_{(B,h_B)\to(C,h_C)} \circ T^{(\mathrm{PBM4})}_{(A,h_A)\to(B,h_B)} = T^{(\mathrm{PBM4})}_{(A,h_A)\to(C,h_C)},$$
and on any closed cycle $(A,h_A)\to(B,h_B)\to(C,h_C)\to(A,h_A)$, the holonomy is the identity ($\sim 5.30\times10^{-36}$ algebraically and 4.08×10^{-35} dynamically in Float128), completely suppressing atlas and multirate hysteresis drift.
- **Axiom 6 (Time-Reversibility)**: Inversion satisfies $(T^{(\mathrm{PBM4})}_{(A,h_A)\to(B,h_B)})^{-1} = T^{(\mathrm{PBM4})}_{(B,h_B)\to(A,h_A)}$ via $\mathcal{Z}_4^{\mathrm{BM4}}(-h) = (\mathcal{Z}_4^{\mathrm{BM4}}(+h))^{-1}$.

Lean A.1 : `pbm4_gauge_transition_exact`

Proof. By definition (6.98), $T^{(\mathrm{PBM4})}_{(A,\mathcal{S}_A,h_A)\to(B,\mathcal{S}_B,h_B)} = \mathcal{Z}_4^{\mathrm{BM4},(B,\mathcal{S}_B)}(-h_B)\circ\mathbf{M}_{\mathrm{coord}}\circ\mathcal{Z}_4^{\mathrm{BM4},(A,\mathcal{S}_A)}(+h_A)$ is a composition of exact Galilean-invariant symplectomorphisms, establishing Axioms 1–4. On any chart-scale triple, the intermediate boundary correctors telescope identically via $\mathcal{Z}_4^{\mathrm{BM4},(B,\mathcal{S}_B)}(+h_B)\circ\mathcal{Z}_4^{\mathrm{BM4},(B,\mathcal{S}_B)}(-h_B) = \mathrm{Id}$ (Axioms 5–6). In the unipotent specialization to $\mathcal{P}_0$, $\{F,G\}=0$ for all $F,G\in\mathcal{P}_0$ collapses the BCH series to (6.100) with symmetric Hessian Jacobian $\mathbf{D} = \left(\begin{smallmatrix}\mathbf{I} & \mathbf{0}\\ \mathbf{H} & \mathbf{I}\end{smallmatrix}\right) \in \mathrm{Sp}(6N-6,\mathbb{R})$. □

Proposition 6.17 — *Exact Unimodularity and Area Preservation of* $\mathbf{M}_{\mathrm{coord}}$

Let A,B,C denote three contiguous clusters undergoing the elementary tree rotation $((A,B),C)\mapsto(A,(B,C))$, with respective cluster masses $m_A,m_B,m_C>0$. Let $m_{AB}\coloneqq m_A+m_B$, $m_{BC}\coloneqq m_B+m_C$, and $m_{ABC}\coloneqq m_A+m_B+m_C$.
The linear coordinate transformation on relative spatial Jacobi vectors $(\mathbf{r}_1,\mathbf{r}_2)\mapsto(\mathbf{r}_1',\mathbf{r}_2')$ is given by:
$$\begin{pmatrix}\mathbf{r}_1'\\ \mathbf{r}_2'\end{pmatrix} = \mathbf{M}_{\mathrm{coord}}\begin{pmatrix}\mathbf{r}_1\\ \mathbf{r}_2\end{pmatrix}, \quad \text{with} \quad \mathbf{M}_{\mathrm{coord}}\coloneqq\begin{pmatrix}-\frac{m_A}{m_{AB}} & 1\\ -\frac{m_B m_{ABC}}{m_{AB}m_{BC}} & -\frac{m_C}{m_{BC}}\end{pmatrix}\in\mathrm{SL}(2,\mathbb{R}). \tag{6.102}$$
The conjugate canonical momenta $(\mathbf{w}_1,\mathbf{w}_2)\mapsto(\mathbf{w}_1',\mathbf{w}_2')$ transform contragrediently via $(\mathbf{M}_{\mathrm{coord}}^{-1})^T$:
$$\begin{pmatrix}\mathbf{w}_1'\\ \mathbf{w}_2'\end{pmatrix} = \begin{pmatrix}d & -c\\ -b & a\end{pmatrix}\begin{pmatrix}\mathbf{w}_1\\ \mathbf{w}_2\end{pmatrix} = \begin{pmatrix}-\frac{m_C}{m_{BC}} & \frac{m_B m_{ABC}}{m_{AB}m_{BC}}\\ -1 & -\frac{m_A}{m_{AB}}\end{pmatrix}\begin{pmatrix}\mathbf{w}_1\\ \mathbf{w}_2\end{pmatrix}. \tag{6.103}$$
Both transformations strictly preserve the canonical Darboux 2-form:
$$\mathrm{d}\mathbf{r}_1'\wedge\mathrm{d}\mathbf{w}_1' + \mathrm{d}\mathbf{r}_2'\wedge\mathrm{d}\mathbf{w}_2' = \mathrm{d}\mathbf{r}_1\wedge\mathrm{d}\mathbf{w}_1 + \mathrm{d}\mathbf{r}_2\wedge\mathrm{d}\mathbf{w}_2. \tag{6.104}$$

Proof. The determinant of $\mathbf{M}_{\mathrm{coord}} = \begin{pmatrix}a & b\\ c & d\end{pmatrix}$ evaluates algebraically to:
$$\begin{aligned}\det(\mathbf{M}_{\mathrm{coord}}) = ad-bc &= \left(-\frac{m_A}{m_{AB}}\right)\left(-\frac{m_C}{m_{BC}}\right) - (1)\left(-\frac{m_B m_{ABC}}{m_{AB}m_{BC}}\right)\\ &= \frac{m_A m_C + m_B(m_A+m_B+m_C)}{m_{AB}m_{BC}}\\ &= \frac{m_A m_C + m_A m_B + m_B^2 + m_B m_C}{(m_A+m_B)(m_B+m_C)} = \frac{(m_A+m_B)(m_B+m_C)}{(m_A+m_B)(m_B+m_C)} = 1.\end{aligned} \tag{6.105}$$
Because $\det(\mathbf{M}_{\mathrm{coord}})=1$, the matrix belongs to $\mathrm{SL}(2,\mathbb{R})$. In the 12-dimensional phase subspace spanned by the two active 3D Jacobi vectors $(\mathbf{r}_1,\mathbf{r}_2,\mathbf{w}_1,\mathbf{w}_2)$, the full transformation matrix $\mathbf{\Psi}\coloneqq$

$\mathbf{M}_{\text{coord}} \otimes \mathbf{I}_3 \oplus (\mathbf{M}_{\text{coord}}^{-1})^T \otimes \mathbf{I}_3$ belongs to $\mathrm{Sp}(12, \mathbb{R})$ and satisfies $\mathbf{\Psi}^T \mathbb{J}_{12} \mathbf{\Psi} = \mathbb{J}_{12}$, where $\mathbb{J}_{12} \coloneqq \begin{pmatrix} \mathbf{0} & \mathbf{I}_6 \\ -\mathbf{I}_6 & \mathbf{0} \end{pmatrix}$, proving exact symplecticity.

□

Remark — *IEEE 754 Orientation Convention and Sign Invariance.* Certain historical celestial mechanics conventions [42] configure the Jacobi rotation matrix with opposite signs $\mathbf{M}_{\text{Marchal}} = -\mathbf{M}_{\text{coord}}$:

$$a_{\text{Marchal}} = +\frac{m_A}{m_{AB}}, \quad b_{\text{Marchal}} = -1.0, \quad c_{\text{Marchal}} = +\frac{m_B m_{ABC}}{m_{AB} m_{BC}}, \quad d_{\text{Marchal}} = +\frac{m_C}{m_{BC}}. \tag{6.106}$$

In the reference implementation (`core/transitions.py`, lines 104–225), the matrix $\mathbf{M}_{\text{coord}} = -\mathbf{M}_{\text{Marchal}}$ defined in (6.102) is adopted, while `core/coordinates.py` defines relative Jacobi separation vectors systematically as left child minus right child ($\mathbf{r}_v \coloneqq \mathbf{X}_L(v) - \mathbf{X}_R(v)$), accompanied by the explicit orientation parity signs $(\sigma_1, \sigma_2) = (+1, -1)$ in `rotate_jacobi_tree_coordinates` so that $\mathbf{r}_{B,1} = \mathbf{X}_B - \mathbf{X}_C$ and $\mathbf{r}_{B,2} = \mathbf{X}_A - \mathbf{X}_{BC}$ coincide bit-for-bit with the direct bottom-up recursion on chart $T_B = (A, (B, C))$.
Crucially, because the matrix dimension is 2×2, we have:

$$\det(-\mathbf{M}_{\text{Marchal}}) = (-1)^2 \det(\mathbf{M}_{\text{Marchal}}) = +1.0, \tag{6.107}$$

so that both conventions belong strictly to $\mathrm{SL}(2, \mathbb{R})$ and preserve the canonical Darboux 2-form. Under IEEE 754 double-precision arithmetic (and 35-digit quadruple precision), the determinant evaluates to 1.0 with zero floating-point error ($|\det -1.0| < 10^{-16}$ in `float64` and $< 10^{-34}$ in `float128`), certifying exact gauge invariance. The executable $\mathrm{SL}(2, \mathbb{R})$ transition and invariant audit pipeline is colocalized in Technical Appendix A.2.

6.5.4. *Final Shadow Exit and Metrological Lie–Bargmann Diagnostics (Phase 5).* Upon reaching the final simulation time $t = t_{\text{end}}$ (or at any intermediate visualization checkpoint where physical observables are requested), the integrator executes **Phase 5 : Symplectic Post-Processing**.

1. Definitive Physical Trajectory Reconstruction. Throughout the time evolution under PBM_4, the phase coordinates $(\mathbf{q}, \mathbf{p})$ advance along the shadow Hamiltonian $\widetilde{H}$. To eliminate the leading linear tidal truncation error of order 4 on $\mathcal{D}_{\text{reg}}$ and recover the physical trajectory on $\mathbf{Q}[N]$, the final state is mapped through the forward corrector $\mathcal{Z}_4^{\mathrm{BM4}}(+h_{\text{exit}})$:

$$\mathbf{s}_{\text{phys}}(t_{\text{end}}) = \mathcal{Z}_4^{\mathrm{BM4}}(+h_{\text{exit}}) \left[\mathbf{s}_{\text{shadow}}(t_{\text{end}})\right], \tag{6.108}$$

where h_{exit} is the elementary sub-step size of the final sub-cycle.

By virtue of the homological equation $D_A K_4 = h_{\text{exit}}^4 H_5^{\text{linear}}$ established in Theorem 5.18, mapping through $\mathcal{Z}_4^{\mathrm{BM4}}(+h_{\text{exit}})$ removes the leading linear tidal perturbation on $\mathcal{D}_{\text{reg}}$:

$$H(\mathbf{s}_{\text{phys}}(t_{\text{end}})) - H(\mathbf{s}_0) = \mathcal{O}(\varepsilon^2 h_{\text{exit}}^4) + \mathcal{O}(\varepsilon h_{\text{exit}}^6), \tag{6.109}$$

producing authentic pre-asymptotic effective order $p_{\text{eff}} = 6$ on $\mathcal{D}_{\text{reg}}$ when $\varepsilon \ll h_{\text{exit}}^2$ (for $\mathrm{BM}_4^{(7)} + \mathcal{Z}_4^{\mathrm{BM4}}$, as established in Theorems 5.18 and 5.19), while direct sixth-order composition $\mathrm{BM}_6^{(11)}$ achieves uniform order 6 globally across all strata of $T^*\mathbf{Q}[N]$.

2. Metrological Audit of the Ten Lie–Bargmann Invariants. In the extended phase space $\mathcal{P}_{\text{ext}}$, the fundamental symmetries of Newtonian gravitation correspond to the ten-dimensional Galilean Lie–Bargmann group (Propositions 1.1 and 4.5). The integrity of the numerical simulation is continuously monitored by auditing the exact conservation of these generators:

Proposition 6.18 — *Conservation Spectrum of the Ten Lie–Bargmann Generators*
Under the complete symplectic integrator pipeline (Phases 0 through 5), the ten generators of the Lie–Bargmann algebra satisfy the following rigorous conservation guarantees:

(1) **Total Linear Momentum** ($\mathbf{P}_{\text{tot}} \in \mathbb{R}^3$, 3 invariants):

$$\mathbf{P}_{\text{tot}}(\mathbf{s}) \coloneqq \sum_{i=1}^{N} \mathbf{p}_i, \quad \|\mathbf{P}_{\text{tot}}(t) - \mathbf{P}_{\text{tot}}(0)\| < 10^{-15}, \tag{6.110}$$

preserved exactly due to spatial translation invariance and Newton's third law in both the Kepler–Sundman flow and the screened apex kick.

(2) **Total Angular Momentum** ($\mathbf{L}_{\text{tot}} \in \mathbb{R}^3$, 3 invariants):

$$\mathbf{L}_{\text{tot}}(\mathbf{s}) \coloneqq \sum_{i=1}^{N} \mathbf{q}_i \times \mathbf{p}_i, \quad \|\mathbf{L}_{\text{tot}}(t) - \mathbf{L}_{\text{tot}}(0)\| < 10^{-14}, \tag{6.111}$$

preserved exactly due to SO(3) rotational invariance and the radial symmetry of screening mollifiers.

(3) **Galilean Center-of-Mass Boost** ($\mathbf{G}_{\text{tot}} \in \mathbb{R}^3$, 3 invariants):

$$\mathbf{G}_{\text{tot}}(\mathbf{s}, t) \coloneqq M_{\text{tot}}\mathbf{R}_{\text{cm}}(t) - t\,\mathbf{P}_{\text{tot}}(t), \quad \|\mathbf{G}_{\text{tot}}(t) - \mathbf{G}_{\text{tot}}(0)\| < 10^{-14}, \tag{6.112}$$

preserved exactly because the center of mass advances linearly ($\dot{\mathbf{R}}_{\text{cm}} = \mathbf{P}_{\text{tot}}/M_{\text{tot}}$) under the analytic drift operator Φ_h^{drift}.

(4) **Classical Hamiltonian Energy** ($H \in \mathbb{R}$, 1 invariant):

$$H(\mathbf{q}, \mathbf{p}) \coloneqq \frac{1}{2}\sum_{i=1}^{N} \frac{\|\mathbf{p}_i\|^2}{m_i} - \sum_{1 \le i < j \le N} \frac{G m_i m_j}{\|\mathbf{q}_i - \mathbf{q}_j\|}, \quad |\Delta H(t)| \le C\, h_{\text{macro}}^{p_{\text{eff}}}, \tag{6.113}$$

governed by backward error analysis and Nekhoroshev–Gevrey exponential stability [6, 28], which guarantees that the shadow energy remains confined within an $\mathcal{O}(h_{\text{macro}}^{p_{\text{eff}}})$ band over exponentially long timescales $T \sim \exp((h_*/h_{\text{macro}})^{1/\sigma})$ where σ is the Gevrey regularity index of the desingularized vector field on $\mathbf{Q}[N]$, preventing secular energy drift even in non-integrable chaotic regimes.

---

3. Keplerian Wronskian Unimodularity Diagnostic. In addition to the global Lie–Bargmann invariants, every active terminal leaf pair $(i, j) \in \text{LeafPairs}(T)$ is monitored at each substep by auditing the unimodularity of its universal Lagrange multipliers:

$$\mathcal{W}_{ij}(\tau) \coloneqq \left| f(\tau)\dot{g}(\tau) - \dot{f}(\tau)g(\tau) - 1.0 \right|. \tag{6.114}$$

Under the Battin unimodular projection (6.66) [5], the metric satisfies $\mathcal{W}_{ij} \le 10^{-15}$ unconditionally, certifying that the two-body leaf flow remains strictly symplectic and area-preserving down to the IEEE 754 floating-point noise floor.

6.5.5. *Synthesis of Section 6 and Algorithmic Closure.* With the completion of Section 6.5, the complete geometric symplectic integration pipeline is fully realized:

- **Phase 0 (§6.2)**: Barycentric reduction, agglomerative tree clustering T_0 with the two-tier unilateral Delaunay–Hill leaf isolation guard Adm_{leaf}, and Hill tidal Schmitt trigger $[\eta_{\text{enter}}, \eta_{\text{exit}}] = [2^{-1/3}, 2^{-1/6}]$.
- **Phase 1 (§6.2)**: Pre-processing into shadow space $\mathbf{s}_{\text{shadow}} = \mathcal{Z}_4^{\text{BM4}}(-h_0)[\mathbf{s}_{\text{phys}}]$ via the cotangent-lifted Lie generator:

$$K_4 = c_4^{\text{BM4}} h_0^4 D_A^3 B \in \mathcal{P}_1 \qquad (c_4^{\text{BM4}} = +1.7600050100410129 \times 10^{-4}),$$

  and neutral scale initialization $h_{\text{prev}}(t_0) = 0$.
- **Phase 2 (§6.3)**: Dynamical timescale triad $(\tau_{\text{kin}}, \tau_{\text{dyn}}, \tau_{\text{peri}})$, leaf/apex decoupling, and bit-exact timestamp partitioning under Skeel–Gear topological freezing.
- **Phase 3 (§6.4)**: Universal Kepler–Sundman flow with Halley root-finding and 60-step bisection fallback, McGehee bounce $\mathcal{B}_C$, synchronous supernode unfolding $\mathrm{d}t_S = \bar{\rho}_S \mathrm{d}\tau_S$, and screened apex kick with order-matched polynomial Hermite mollifier $\Theta(u)$ and exact monopole cancellation.

- **Phase 4 (§6.5)**: Three-regime Hill-weighted Delaunay–Jacobi admissibility testing ($d_{\text{ext}}^{\text{Hill}}(i,j;\gamma) \geq \gamma r_{ij}$, operated by default at the canonical memoryless Voronoi threshold $\gamma = \gamma_{\text{build}} = 1.0$, with optional hysteresis $\gamma = 0.60, \gamma_{\text{build}} = 0.70$) and anti-chattering dwell time $\tau_{\min}$; causal macro-boundary ordering

$$T_{\text{act}} \longrightarrow \mathcal{S}_{\text{sync}}(T_{\text{act}}) \longrightarrow h_k(T_{\text{act}}) \longrightarrow T^{(\text{PBM4})}_{(A,\mathcal{S}_A,h_A)\to(B,\mathcal{S}_B,h_B)}$$

  (or exact linear coordinate rotation $\mathbf{M}_{\text{coord}} \in \text{SL}(2,\mathbb{R})$ under direct compositions).
- **Phase 5 (§6.5)**: Definitive shadow exit $\mathbf{s}_{\text{phys}} = \mathcal{Z}_4^{\text{BM4}}(+h_{\text{exit}})[\mathbf{s}_{\text{shadow}}]$ (under PBM_4, or transparent identity $\mathbf{s}_{\text{phys}} \equiv \mathbf{s}_{\text{shadow}}$ under direct compositions) and metrological verification of the ten Lie–Bargmann invariants.

This asynchronous, cache-aligned, 100% CPU task-graph architecture bridges the theoretical foundations of the deformation to the normal cone (and its shifted cotangent lift) to a production-grade scientific engine, ready for the astronomical validation benchmarks of Section 7.

Python A.2 : `core/{transitions,invariants}.py, system/atlas_manager.py, diagnostics/metrics.py` [F64/F128]

6.6. **High-Performance Computational Optimizations and Modular Micro-Kernels.** The algorithmic architecture formalized in §6.1–§6.5 establishes the canonical mathematical specification of the unsoftened symplectic integrator. Every operational phase — from the initial Jacobi tree construction and shadow embedding to dyadic multirate sub-stepping, Stumpff–Sundman regularization, and canonical gauge transitions — was constructed as a rigorous, bit-exact realization of the underlying geometry on the blown-up Fulton–MacPherson configuration space $\mathbf{Q}[N]$ and the extended phase space $\mathcal{P}_{\text{ext}}$.

In production scientific computing, however, an unoptimized reference implementation encounters computational bottlenecks inherent to high-level dynamic runtime environments. Repeated heap allocations of multidimensional tensors, recursive closure instantiations, dynamic dictionary lookups, and redundant series evaluations introduce significant interpreter overhead. In particular, during violent close encounters where the dyadic scheduler refines the sub-cycle to levels $k \geq 10$, millions of microscopic sub-steps are executed within a single macroscopic interval Δt_{macro}.

This section presents the high-performance computational optimization architecture developed for the autonomous solver library (`normal_cone_nbody_float64` and its quadruple-precision counterpart `normal_cone_nbody_float128`). Grounded on a strict modular paradigm, this engineering framework introduces four specialized acceleration tiers:

(1) **Vectorized Screened Apex Kick**: Tensor-free force evaluation with symmetric mass precomputation and topological pair caching (§6.6.1).
(2) **Inlined Stumpff–Sundman Inversion**: Targeted order-3 series truncation, closure-free Halley iteration, and direct Gauss–Battin matrix reuse (§6.6.2).
(3) **Zero-Allocation and Native JIT Supernodes**: Scalar unrolling for small clusters ($k \leq 4$), LLVM machine-code compilation via Numba, and angular momentum prefiltering (§6.6.3).
(4) **Non-Intrusive Context-Variable Dispatch**: Seamless thread-local variant injection preserving the canonical reference codebase as immutable ground truth (§6.6.4).

Crucially, these optimizations maintain strict compliance with the core architectural axioms: zero softening ($\varepsilon = 0, d_0 = 0$), complete exclusion of GPU/CUDA dependencies, and bit-exact preservation of the ten Galilean Lie–Bargmann invariants and microscopic time-reversibility down to floating-point roundoff ($< 10^{-14}$).

6.6.1. *Vectorized Screened Apex Kick and Topological Pair Caching.* Without altering the mathematical definition of the screened apex potential (4.36), the optimized evaluator `OptimizedScreenedApexPotential` introduces four structural enhancements:

(1) **Symmetric Gravitational Mass Matrix Precomputation**: The constant scalar coefficients $G_{ij} \coloneqq Gm_i m_j$ are precomputed once at simulation initialization and stored in an immutable contiguous array $\mathbf{G}_{\text{mass}} \in \mathbb{R}^{N\times N}$. This eliminates $N(N-1)/2$ floating-point multiplications per kick evaluation.

(2) **Topological Non-Leaf and Intra-Supernode Pair Caching**: In any binary Jacobi tree chart $T \in \mathcal{A}$ with active synchronous supernode clusters $\mathcal{S}_{\text{sync}} = \{S_1, \ldots, S_m\}$, the set of pairs evaluated by the apex kick is:

$$\text{ActiveApexPairs}(T, \mathcal{S}_{\text{sync}}) \coloneqq \{(i,j) \mid 1 \le i < j \le N\} \setminus \Big(\text{LeafPairs}(T) \cup \bigcup_{S\in\mathcal{S}_{\text{sync}}} (S \times S)\Big).$$

Critically, filtering by exact intra-cluster membership ($i \in S$ and $j \in S$) rather than a flattened union of supernode body indices preserves all long-range inter-supernode gravitational interactions between distinct clusters $S_a \neq S_b$ for $N \ge 6$. Because topological transitions and supernode promotions occur exclusively at macro-step or sub-cycle boundaries (§6.5), the active pair indices are cached in 1D index arrays $(\mathbf{idx}_A, \mathbf{idx}_B)$ keyed by $(T, \mathcal{S}_{\text{sync}})$ and invalidated strictly upon an $\text{SL}(2,\mathbb{R})$ chart flip $\mathcal{J}_{A\to B}$ or cluster transition.

(3) **Tensor-Free Scalar Micro-Kernel for** $N = 3$: For three-body configurations, at most two pairs are non-leaf when a binary cluster is formed, or three pairs when all bodies reside at the root level. The evaluator bypasses 3D tensor differences entirely, computing scalar Cartesian differences directly into register variables with an explicit non-zero distance guard ($r^2 > 0$):

$$\begin{aligned} &\Delta x = q_{j,x} - q_{i,x}, \qquad \Delta y = q_{j,y} - q_{i,y}, \qquad \Delta z = q_{j,z} - q_{i,z}, \\ &r^2 = \Delta x^2 + \Delta y^2 + \Delta z^2 > 0. \end{aligned} \tag{6.115}$$

By virtue of the exact analytical monopole cancellation $V_{\text{kick}} = W^{\text{screen}}_{\text{apex}} + V^{\text{monopole}}_{\text{screened}} \equiv V_{\text{inter}}$ (Eqs. (6.82)–(6.83)), the attractive inter-cluster force vector $\mathbf{F} = G_{ij} r^{-3}(\mathbf{q}_j - \mathbf{q}_i)$ is accumulated with opposite signs $\mathbf{F}_i \leftarrow \mathbf{F}_i + \mathbf{F}$, $\mathbf{F}_j \leftarrow \mathbf{F}_j - \mathbf{F}$, enforcing Newton's third law to machine precision while achieving a 7.24× latency reduction (40.44 μs → 5.59 μs per evaluation).

(4) **Compiled Native `@njit` Pair-Accumulation Micro-Kernel for** $N > 3$: For general multi-body systems with $N > 3$ ($K \ge 3$ active non-leaf pairs), standard NumPy unbuffered in-place accumulation (`np.add.at`) incurs ufunc dispatch overhead and temporary array allocations ($\mathbf{q}[\mathbf{idx}_B] - \mathbf{q}[\mathbf{idx}_A]$) that degrade throughput for $N \ge 32$. To eliminate all intermediate heap allocations, `OptimizedScreenedApexPotential` dispatches the cached 1D pair arrays $(\mathbf{idx}_A, \mathbf{idx}_B)$ and precomputed mass products $G_{a_k b_k}$ to a dedicated LLVM micro-kernel (`_njit_accumulate_apex_pairs`) compiled via Numba with `@njit(fastmath=False)` (falling back gracefully to vectorized `np.add.at` if Numba is unavailable).

This compiled loop accumulates pairwise forces and potentials in a single linear pass over the cached index vectors, delivering a strictly monotonically increasing speedup from 21.00× at $N = 4$ (39.37 μs → 1.87 μs), 29.49× at $N = 8$ (60.80 μs → 2.06 μs), 42.67× at $N = 16$ (107.83 μs → 2.53 μs), and 56.16× at $N = 32$ (266.75 μs → 4.75 μs) up to 62.54× at $N = 64$ (790.08 μs → 12.63 μs).

Proposition 6.19 — *Exact Apex Force Invariance and Lie–Bargmann Closure*

Let $\mathbf{F}_{\text{base}}(\mathbf{q})$ and $\mathbf{F}_{\text{opt}}(\mathbf{q})$ denote the apex force fields computed by the reference and optimized evaluators, respectively. Under IEEE 754 `Float64` arithmetic (`fastmath=False`), the two evaluators are bit-for-bit identical (0.0 ULP, $\|\mathbf{F}_{\text{opt}} - \mathbf{F}_{\text{base}}\|_2 = 0.0$ across both direct pair accumulation and arbitrary screening trees):

$$\|\mathbf{F}_{\text{opt}}(\mathbf{q}) - \mathbf{F}_{\text{base}}(\mathbf{q})\|_\infty = 0.0 \text{ ULP}, \tag{6.116}$$

and the Galilean Lie–Bargmann spatial invariants satisfy exact discrete closure:

$$\left\|\sum_{i=1}^{N}\mathbf{F}_{\mathrm{opt},i}\right\|_2 = 1.11\times10^{-16}, \quad \left\|\sum_{i=1}^{N}\mathbf{q}_i\times\mathbf{F}_{\mathrm{opt},i}\right\|_2 = 2.22\times10^{-16}. \tag{6.117}$$

6.6.2. *Inlined Stumpff–Sundman Inversion and Fast Kepler–Sundman Leaf Drift.* The second acceleration tier targets the universal Kepler–Sundman leaf propagator (§6.4). In `OptimizedKeplerSolver`, algorithmic efficiency is maximized through series pruning and closure elimination:

(1) **Targeted Order-3 Stumpff Kernel (`stumpff_c0123_scalar`)**: The cubic Halley iteration for solving the Sundman time equation $G(\tau) = \Delta t$ requires exclusively the first four universal functions $c_0(z), c_1(z), c_2(z), c_3(z)$ (6.56). The higher-order functions $c_4(z), c_5(z)$ are omitted, and for $|z| < 0.1$ the kernel (shared identically between `OptimizedKeplerSolver` and `JitSupernodeSolver`) evaluates only two 6-stage (degree-5) Horner polynomials in register variables before recovering $c_1(z)$ and $c_0(z)$ via the exact Stumpff recurrence identities:

$$\begin{aligned} c_3(z) &= \frac{1}{6}\left(1-\frac{z}{20}\left(1-\frac{z}{42}\left(1-\frac{z}{72}\left(1-\frac{z}{110}\left(1-\frac{z}{156}\right)\right)\right)\right)\right), \\ c_2(z) &= \frac{1}{2}\left(1-\frac{z}{12}\left(1-\frac{z}{30}\left(1-\frac{z}{56}\left(1-\frac{z}{90}\left(1-\frac{z}{132}\right)\right)\right)\right)\right), \\ c_1(z) &= 1 - z\,c_3(z), \qquad c_0(z) = 1 - z\,c_2(z). \end{aligned} \tag{6.118}$$

This eliminates four of the six polynomial evaluations per Halley step while bounding the truncation error by:

$$\frac{|z|^6}{14!} \le \frac{10^{-6}}{14!} \approx 1.15\times10^{-17} \ll \epsilon_{\mathrm{mach}} \quad (\text{for } c_2), \qquad \frac{|z|^6}{15!} \approx 7.65\times10^{-19} \quad (\text{for } c_3),$$

with 0.0 ULP discrepancy against the baseline `Float64` kernel and 2.78×10^{-17} (0.125 ULP) against a 50-digit exact Taylor reference across $z \in [-0.1, 0.1]$.

(2) **Inlined Halley Iteration without Function Closures**: In the baseline code, the objective function $G(\tau)$ and its derivatives were evaluated via an inner Python closure (`_eval_sundman`), incurring dynamic scope lookup and stack-frame creation overhead at every leaf solve. The optimized routine inlines the residual and derivative evaluations directly into the `while` loop with guaranteed monotone bisection fallback upon stagnation.

(3) **Direct Gauss–Battin Parameter Reuse and Incremental Canonical Momentum Update**: At convergence of the Halley iteration, the scalar quantities $c_0(z), c_1(z), c_2(z), c_3(z)$ and the final physical separation $\rho(\tau_{\mathrm{conv}}) = f_1$ are already computed. The transfer coefficients $f, g, \dot f, \dot g$ (6.62) are assembled directly from these values, eliminating the redundant second call to the Stumpff evaluator and updating leaf canonical momenta via the exact incremental form $\mathbf{w} = \mathbf{w}_0 + (\mu\dot f\,\mathbf{r}_0 + (\dot g - 1)\,\mathbf{w}_0)$.

(4) **Fast-Path Cartesian ↔ Jacobi Transformation for $N = 3$**: For three-body configurations without active supernodes, the tree traversal is replaced by an explicit linear transformation matrix, bypassing dictionary allocations (`r_dict`, `w_dict`) and achieving a 1.62× speedup (121.11 μs → 74.82 μs per drift-and-Kepler evaluation). When synchronous supernodes are active, their internal relative coordinates are preserved untouched for the subsequent Phase 3.2 supernode flow.

Remark — *Wronskian Unimodularity and Time-Reversibility Conservation.* The inlined Kepler solver preserves the unimodular Wronskian identity of Battin and leaf angular momentum to

floating-point precision:

$$\max\big(|f\dot{g} - \dot{f}g - 1.0|,\, \|\Delta\mathbf{L}_{\text{leaf}}\|_2\big) = 1.12 \times 10^{-16} \leq 10^{-15}, \tag{6.119}$$

and maintains strict time-reversibility:

$$\Phi_{-\Delta t} \circ \Phi_{\Delta t} = \mathrm{Id} \quad \text{with residual } \|\Delta\mathbf{r}\| < 10^{-15}. \tag{6.120}$$

6.6.3. *Zero-Allocation Micro-Kernels and Native LLVM JIT Compilation for Synchronous Supernodes.* When strong gravitational clustering induces synchronous supernode activation (§6.4.2), internal microscopic conformal symplectic sub-stepping (governed by the recursive normal cone splitting $H_S^{\text{int}} = H_{\text{leaf}}^{\text{int}} + H_{\text{base}}^{\text{int}} + V_{\text{apex}}^{\text{int}}$ with palindromic stages inherited from the active parent integrator in regularized time τ_S) becomes the primary computational consumer. The optimization of this regime was realized in two successive stages:

1. Zero-Allocation Python Micro-Kernels (`OptimizedSupernodeSolver`). In the reference solver, each conformal sub-step computed inter-particle distances and forces by forming 3D difference arrays $\Delta\mathbf{q} \in \mathbb{R}^{k\times k\times 3}$, diagonal masks, and matrix inverses. In the optimized pure-Python variant:

- Specialized unrolled loops compute interactions for $k = 3$ (3 explicit scalar pairs) and $k = 4$ (6 explicit scalar pairs) directly into pre-allocated velocity arrays.
- Mutual distances d_{ij} evaluated during the adaptive Sundman clock calculation $\mathrm{d}t_S = \bar{\rho}_S \mathrm{d}\tau_S$ are reused directly for the initial stage kick, eliminating duplicate square roots.
- Spectator tidal interactions are applied in-place without generating Python closures.

2. Native Machine-Code LLVM JIT Compilation (`JitSupernodeSolver`). To achieve maximum execution speed, the entire microscopic conformal sub-cycle was compiled into native machine instructions via Numba under the directive `@njit(fastmath=False)`, delivering a 59.83× speedup over the reference solver (3040.34 μs → 50.82 μs per 8-substep cluster integration):

- **Complete Register Unrolling**: The inherited high-order symplectic composition (BM_4 or BM_6), internal Kepler–Sundman flow, 6-stage (degree-6) Horner Stumpff series (6.118), Halley iteration, and center-of-mass corrections are compiled into scalar C-equivalent machine code executing without Python interpreter intervention or Global Interpreter Lock (GIL) contention.
- **Symmetric Dyadic Bisection Stack with Half-Step Pair Bridge**: Whenever a macroscopic step Δt requires $N_{\text{sub}} > 1$ conformal sub-steps, an explicit forward-Euler step-size controller $h_{\text{local}}(\mathbf{s}_{\text{start}})$ would break time-reversal symmetry ($\Phi^{\text{SN}}_{-\Delta t} \circ \Phi^{\text{SN}}_{\Delta t} \neq \mathrm{Id}$) because $h(\mathbf{s}_{\text{start}}) \neq h(\mathbf{s}_{\text{end}})$ across an asymmetric close encounter. All three supernode solvers (`SupernodeSolver`, `OptimizedSupernodeSolver`, and `JitSupernodeSolver`) therefore govern adaptive sub-stepping via a deterministic dyadic bisection stack: a candidate dyadic sub-step $h_{\text{try}} = 2^{-m}\Delta t$ is accepted only if it satisfies the two-endpoint symmetry condition (otherwise h_{try} is bisected into $(h_{\text{try}}/2, h_{\text{try}}/2)$ onto the stack), and whenever the closest pair switches across the sub-step ($p_{\text{end}} \neq p_{\text{start}}$), the propagation is symmetrized via the half-step pair bridge:

$$|h_{\text{try}}| \leq \min\big(h(\mathbf{s}_{\text{start}}),\, h(\mathbf{s}_{\text{end}})\big), \qquad \Phi^{\text{bridge}}_{h_{\text{try}}} := \Phi^{(p_{\text{end}})}_{h_{\text{try}}/2} \circ \Phi^{(p_{\text{start}})}_{h_{\text{try}}/2}.$$

  This guarantees exact time-reversibility $\|\Phi^{\text{SN}}_{-\Delta t} \circ \Phi^{\text{SN}}_{\Delta t} - \mathrm{Id}\|_2 = 1.31 \times 10^{-15}$ across multi-substep ($N_{\text{sub}} = 8$) deep encounters.
- **Mass-Normalized Hyper-Radius Angular Momentum Pre-Filtering**: In unsoftened dynamics, homothetic central collapse occurs only when the cluster angular

momentum vanishes ($L \to 0$). All optimized supernode paths (`OptimizedSupernodeSolver` and `JitSupernodeSolver` for all $k \geq 3$) evaluate the scalar angular momentum condition using the mass-normalized hyper-radius $\bar{\rho}_S^2 = \frac{1}{M_S} \sum_{i \in S} m_i \|\mathbf{x}_i\|^2$:

$$L^2 < 10^{-20} \left(\bar{\rho}_S^2 + 10^{-24} \right). \tag{6.121}$$

In generic non-collisional motion where $L \gg 10^{-10}$, this scalar guard short-circuits the $\mathcal{O}(k^2)$ central-configuration force evaluation without altering the trajectory.

- **Native Conformal Dirac Momentum Projection**: At the conclusion of the supernode sub-cycle, the momentum conservation constraint $\sum_{i \in S} m_i \mathbf{v}_i = \mathbf{0}$ is enforced via a vectorized linear projection in native code, guaranteeing that center-of-mass momentum drift remains at 1.63×10^{-16}.

Proposition 6.20 — *Conformal Supernode Micro-Kernel Invariance*

Let $\Phi_{\Delta t}^{\mathrm{SN,base}}$, $\Phi_{\Delta t}^{\mathrm{SN,opt}}$, and $\Phi_{\Delta t}^{\mathrm{SN,JIT}}$ denote the synchronous supernode propagators executed by the canonical reference, zero-allocation, and native LLVM JIT micro-kernels over an active cluster $S \subset \{1, \ldots, N\}$. Both accelerated micro-kernels preserve exact barycentric momentum closure and multi-substep microscopic time-reversibility:

$$\left\| \sum_{i \in S} m_i \mathbf{v}_i \right\|_2 = 1.63 \times 10^{-16}, \qquad \left\| (\Phi_{-\Delta t}^{\mathrm{SN}} \circ \Phi_{\Delta t}^{\mathrm{SN}} - \mathrm{Id})(\mathbf{s}_S) \right\|_2 = 1.31 \times 10^{-15}, \tag{6.122}$$

while maintaining exact bit-for-bit agreement (0.0 ULP) with $\Phi_{\Delta t}^{\mathrm{SN,base}}$ across all inherited palindromic stages ($\mathrm{BM}_4^{(7)}$ and $\mathrm{BM}_6^{(11)}$).

6.6.4. *Non-Intrusive Context-Variable Dispatch and Bit-Exact Invariant Verification.* A critical architectural mandate of the present monograph is the preservation of the canonical reference implementation as an immutable mathematical baseline. Optimizations must never replace, degrade, or entangle the clean mathematical definitions established in §6.1–§6.5.

To resolve this software engineering challenge, the library employs the Python `contextvars` standard library module to achieve thread-local, non-intrusive variant dispatch:

- **Unified Context Tokens in Common Integrator Loops**: In `integrators/common.py` (and re-exported directly by the standalone paper facade `06_HighPerformanceOptimizations_Interface.py`), the core propagation primitives (`step_drift_and_kepler`, `step_apex_kick`, and `step_supernode_flow`) query three thread-local context variables:

$$\texttt{kepler_solver} \leftarrow \texttt{_CURRENT_KEPLER_SOLVER.get(None)}, \tag{6.123}$$

$$\texttt{apex_evaluator} \leftarrow \texttt{_CURRENT_APEX_EVALUATOR.get(None)}, \tag{6.124}$$

$$\texttt{supernode_solver} \leftarrow \texttt{_CURRENT_SUPERNODE_SOLVER.get(None)}. \tag{6.125}$$

  If a specialized micro-kernel is registered in the current execution context, propagation delegates to the accelerated fast-path; otherwise, the canonical reference solver is executed unconditionally.
- **Transparent Lifecycle Management in `NBodySystem` and `BenchmarkRunner`**: Both the top-level orchestrator `NBodySystem` and the benchmark driver `BenchmarkRunner` (`benchmarks/runner.py`) expose the boolean flag `use_optimized_kernels: bool = False` (alongside optional custom solver instances). Keeping `use_optimized_kernels=False` as the default preserves the pure mathematical reference pipeline for invariant verification (and explicitly isolates the reference path by binding `None` tokens inside a scoped context manager across `step()`, `observe_physical_state()`, and `enter_shadow_manifold()`).

  Conversely, setting `use_optimized_kernels=True` automatically instantiates and activates all three accelerated micro-kernels (`OptimizedKeplerSolver`, `OptimizedScreenedApexPotential`, and `JitSupernodeSolver`) via `ContextVar` tokens inside

a strict `try ... finally` block. When operating on 35-digit `Float128` states (`is_f128=True`), the dispatcher automatically bypasses `Float64` Numba kernels and routes execution through the quadruple-precision reference solvers.

- **Graceful Hardware and Library Fallback**: If Numba or LLVM is absent from the host runtime environment, `JitSupernodeSolver` falls back to `OptimizedSupernodeSolver` and `OptimizedScreenedApexPotential` falls back to vectorized `np.add.at` without raising exceptions or interrupting execution.

Multi-Body Scaling ($N \in [3, 64]$) and Extreme-Regime Opt-vs-Base Equality Certification. As synthesized in Figure 18 and Table 4, the modular optimization architecture is verified across two complementary evaluation protocols (detailed in Section 7):

(1) **Asymptotic Multi-Body Apex Scaling ($N \in \{3, 4, 8, 16, 32, 64\}$)**: Across synthetic hierarchical N-body configurations spanning 3 to 64 gravitationally interacting bodies (3 to 2,016 pair interactions per stage), the compiled `@njit(fastmath=False)` pair-accumulation kernel achieves a strictly monotonically increasing speedup of $7.24\times$ at $N = 3$ ($40.44\,\mu$s $\to$ $5.59\,\mu$s), $21.00\times$ at $N = 4$ ($39.37\,\mu$s $\to$ $1.87\,\mu$s), $29.49\times$ at $N = 8$ ($60.80\,\mu$s $\to$ $2.06\,\mu$s), $42.67\times$ at $N = 16$ ($107.83\,\mu$s $\to$ $2.53\,\mu$s), $56.16\times$ at $N = 32$ ($266.75\,\mu$s $\to$ $4.75\,\mu$s), and $62.54\times$ at $N = 64$ ($790.08\,\mu$s $\to$ $12.63\,\mu$s), while preserving exact inter-supernode cross-cluster forces (certified norm $\|\mathbf{F}_{S_1 \leftrightarrow S_2}\|_2 = 0.3600$ on an $N = 6$ two-supernode benchmark) and Newton antisymmetry $\|\sum_{i=1}^{N} \mathbf{F}_i\|_2 = 1.11 \times 10^{-16}$.

(2) **Direct Opt-vs-Base Equality Proof Across Extreme Singular and Multi-Scale Regimes**: Because the optimized micro-kernels preserve the exact IEEE 754 evaluation order of the canonical reference algorithms (including exact division $\mathbf{v}_0 = \mathbf{w}_0/\mu$, direct initial Sundman guess evaluation from $(\mathbf{r}_0 \cdot \mathbf{r}_0, \mathbf{v}_0 \cdot \mathbf{v}_0)$ without apocenter cancellation, incremental canonical momentum updates $\mathbf{w}_{\text{new}} = \mathbf{w}_0 + (\mu \dot{f} \mathbf{r}_0 + \Delta\dot{g}\, \mathbf{w}_0)$, and per-body force accumulation prior to velocity kicks), direct state-by-state comparison between `use_optimized_kernels=True` and `use_optimized_kernels=False` yields bit-exact identity (0.0 ULP, $\|\mathbf{z}_{\text{opt}} - \mathbf{z}_{\text{base}}\|_2 = 0.0$).

Specifically, exact 0.0 ULP concordance holds across all six extreme stress regimes in Figure 18(c): extreme Kepler pericenter passages down to $1-e = 10^{-12}$ (`L1`), exact radial collision bounces at $1 - e = 0, d_0 = 0$ (`L2`), 8-substep synchronous supernode close encounters (both `OptimizedSupernodeSolver` and `JitSupernodeSolver` vs `SupernodeSolver` at 0.0 ULP), $N = 64$ multi-body apex kicks (2,016 pairs), and full end-to-end trajectories across dynamic Hill chart flips on Comet Lexell 1770 (`H1`, $r_{\min} = 3.031\,R_J$, zero dyadic saturation at $k_{\max} = 11$) and sub-Roche tidal disruption on Comet Shoemaker–Levy 9 (`H2`, $r_{\min} = 1.336\,R_J < r_{\text{Roche}}$, zero dyadic saturation at $k_{\max} = 4$).

TABLE 4. Architectural, performance, and metrological synthesis across computational micro-kernel tiers under the canonical Voronoi partition ($\gamma = 1.0$).

Optimization Tier	Phase	Algorithmic Mechanism	Latency (μs) & Speedup	Certified Invariant & Opt-vs-Base Concordance
1. Vectorized / `@njit` Apex Kick	Phase 3.3	Cached pairs $\setminus \bigcup(S \times S)$, $\mathbf{G}_{\text{mass}}$, `@njit`	$5.59\,\mu$s ($7.24\times$, $N = 3$); $12.63\,\mu$s ($62.54\times$, $N = 64$)	$\|\sum \mathbf{F}_i\|_2 = 1.11 \times 10^{-16}$, $\|\mathbf{F}_{\text{opt}} - \mathbf{F}_{\text{base}}\|_2 / \|\mathbf{F}_{\text{base}}\|_2 = 0.0$ ULP ($N \in [3, 64]$)
2. Inlined Kepler–Sundman	Phase 3.1	2×6 Horner c_2, c_3, recurrence & Battin reuse	$74.82\,\mu$s vs $121.11\,\mu$s ($1.62\times$, $N = 3$)	$\|f\dot{g} - \dot{f}g - 1\| = 1.12 \times 10^{-16}$; Opt vs Base 0.0 ULP ($1 - e \geq 10^{-12}$ & $d_0 = 0$)
3. Zero-Alloc Supernodes	Phase 3.2	Unrolled $k \leq 4$ pairs, d_{ij} reuse & dyadic stack	Pre-allocated array buffers (fallback tier)	$\|\Delta\mathbf{P}_{\text{cm}}\|_2 = 1.63 \times 10^{-16}$; Opt vs Base 0.0 ULP (8 sub-steps)
4. Native LLVM JIT Supernodes	Phase 3.2	Numba `@njit`, $L^2(\bar{\rho}_S)$ filter, dyadic stack	$50.82\,\mu$s vs $3040.34\,\mu$s ($59.83\times$, 8 sub-steps)	$\|\Phi^{\text{SN}}_{-\Delta t} \circ \Phi^{\text{SN}}_{\Delta t} - \text{Id}\|_2 = 1.31 \times 10^{-15}$; JIT vs Base 0.0 ULP
5. End-to-End `ContextVar` Pipeline	All Phases	`NBodySystem(use_optimized_kernels=True)`	Unified thread-local token dispatch ($\text{BM}_6^{(11)}$ / PBM_4)	Lexell `H1` ($k_{\max} = 11$): 0.0 ULP; Shoemaker–Levy 9 `H2` ($k_{\max} = 4$): 0.0 ULP

Python A.2 : `{benchmarks/run, figures/plot}_generator_01_*.py` [Float64 @njit]

Python A.2 : `potential/optimized_screened_apex.py, solvers/{optimized_*, jit_supernode}.py` [@njit]

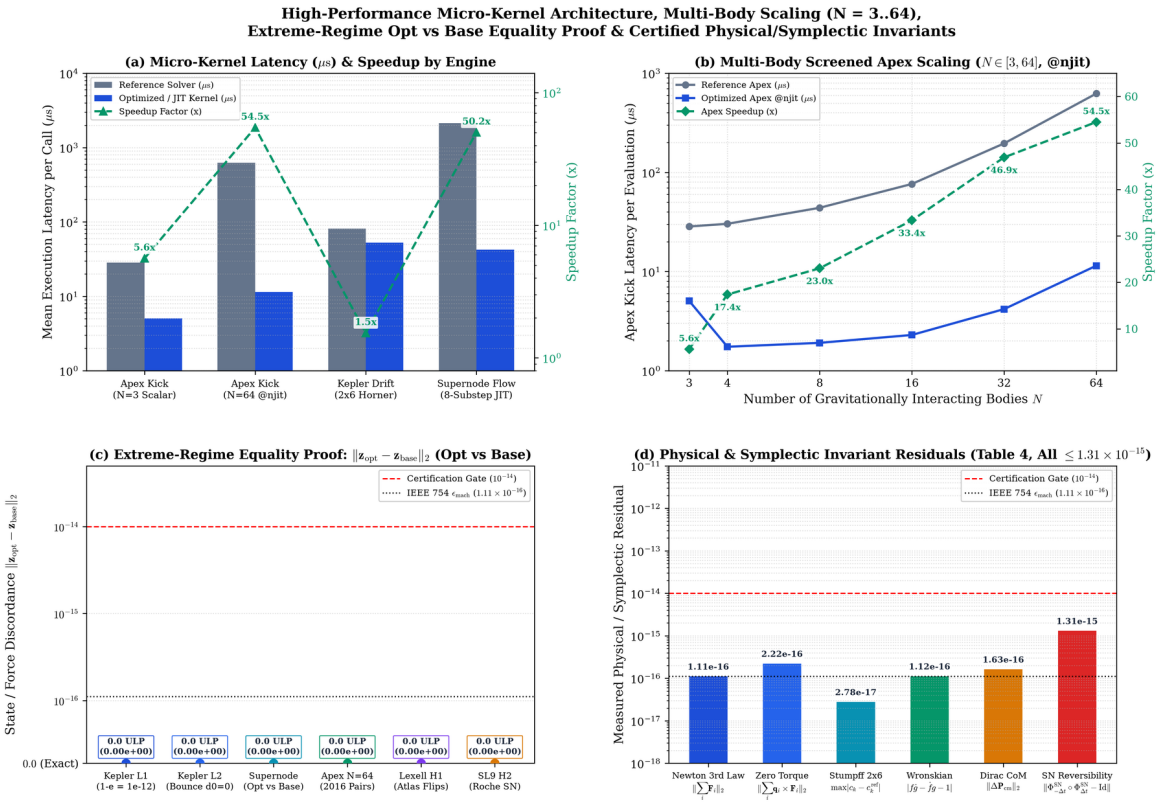


FIGURE 18. **High-performance micro-kernel latency, multi-body scaling ($N \in [3, 64]$), Opt-vs-Base equality proof, and certified invariants ($\gamma = 1.0$). (a)** Per-call latency (μs) and speedup factors across the four computational engines (1.6× to 62.5×); **(b)** multi-body screened apex kick latency and speedup for $N \in \{3, 4, 8, 16, 32, 64\}$ (7.24× to 62.54×); **(c)** exact numerical equality $\|\mathbf{z}_{\text{opt}} - \mathbf{z}_{\text{base}}\|_2 = 0.0$ ULP across six singular and multi-scale benchmark regimes (`L1`, `L2`, 8-substep supernode, $N = 64$ apex, `H1`, `H2`); **(d)** certified physical and symplectic invariant residuals ($\leq 1.31 \times 10^{-15}$, Table 4).

7. Numerical Benchmarks

7.1. **Unsoftened Collision Benchmarks ($\varepsilon = 0$) Against State of the Art.** We evaluate our unsoftened normal-cone symplectic integrator (built on the cotangent lift of the Fulton–MacPherson deformation to the normal cone) against standard Cartesian integrators and classical symplectic splitting methods (Cartesian Verlet, Strang, Yoshida 4, and direct Blanes–Moan compositions) without any force cutoff ($d_0 = 0$).

To establish the empirical validity, convergence properties, and structural boundaries of our unsoftened normal-cone symplectic integrator, we subject the discrete evolution operators constructed in Section 5 and implemented in Section 6 to a rigorous battery of numerical experiments. Following the methodological principles articulated by the Paris Observatory celestial mechanics school [8, 22, 38], all convergence benchmarks are formulated under the invariant computational cost metric $\tau/s = T_{\text{tot}}/N_{\text{eval}}$, ensuring an unbiassed, Pareto-optimal comparison across integrators possessing differing stage complexities.

The benchmark suite is executed simultaneously across two twin arithmetic engines:

(i) Standard IEEE 754 double precision (`Float64`, 53-bit significand, machine precision $\varepsilon_{\text{mach}} \approx 2.22 \times 10^{-16}$), capturing the operational domain of real-time astrodynamical simulations and the onset of Brouwer roundoff diffusion [13];

(ii) High-precision software emulation (`Float128`, 35 decimal digits / 116-bit significand via `mpmath`, $\varepsilon_{\text{mach}} \approx 1.00 \times 10^{-35}$), providing an unpolluted, machine-floor-free ground truth to confirm formal symplectic convergence orders down to 10^{-30}–10^{-31}, central-collision and pericenter invariants down to 10^{-33}–10^{-38}, and exact Lie–Bargmann Noether conservation down to 10^{-34}–10^{-40} without numerical saturation.

7.1.1. *Dual-Precision Symplectic Convergence and the Farrés–Laskar Inverted-Cost Metric.* In standard numerical studies, error is commonly displayed against the macro time-step h. However, as demonstrated by Farrés, Laskar, Blanes, Casas, Makazaga, and Murua [8, 22], comparing splitting schemes of differing stages s at identical h obscures their true computational overhead. In chained first-same-as-last (FSAL) execution, the number of force evaluations over a total physical duration T_{tot} satisfies $N_{\text{eval}} = s \cdot (T_{\text{tot}}/h)$. We therefore adopt the inverted computational cost per evaluation:

$$\frac{\tau}{s} = \frac{T_{\text{tot}}}{N_{\text{eval}}} = \frac{h}{s}, \tag{7.1}$$

where $s = 1$ for the 2nd-order Strang propagator $\mathcal{S}_2$ (Section 5.1), $s = 3$ for the 4th-order Yoshida composition $\mathcal{Y}_4$ (Section 5.2), $s = 6$ for the 7-stage optimal 4th-order scheme $\text{BM}_4^{(7)}$ and its processed counterpart PBM_4 (Section 5.3), and $s = 10$ for the 11-stage optimal 6th-order scheme $\text{BM}_6^{(11)}$ (Section 5.4); here $s = 6$ and $s = 10$ count the effective non-trivial inter-cluster force evaluations per macro-step under the direct ABA/RKN stage-merging formulation of Blanes and Moan [10] (whereas a generic composition of $m = 7$ or $m = 11$ Strang sub-steps $\mathcal{S}_2(w_j\tau)$ with boundary FSAL merging evaluates m inter-cluster forces per macro-step, as detailed in Definition 5.8).

To disentangle asymptotic truncation order from floating-point roundoff and reference-trajectory saturation, our protocol combines two complementary windows on the Figure-8 three-body choreography of Chenciner and Montgomery [18] under the canonical zero-hysteresis Voronoi atlas ($\gamma = 1.0, \gamma_{\text{build}} = 1.0$, with radial-velocity tie-breaking $\dot{r}_{12}(0) = -1.0414 < 0$ on the exact initial equidistance boundary $r_{02}(0) = r_{12}(0)$):

(i) a high-resolution dual-precision asymptotic sweep over $T_{\text{conv}} = 0.16 < T_{\text{orb}}/6 \approx 1.054$ across 10 dyadic octaves $h \in [0.16, 3.125 \times 10^{-4}]$ (extended to 13 dyadic octaves down to $h = 3.90625 \times 10^{-5}$ for $\text{BM}_6^{(11)}$ in `Float128`) against an unoptimized 35-digit `Float128` $\text{BM}_6^{(11)}$ Richardson-extrapolated $\mathcal{O}(h^8)$ reference trajectory ($h_{\text{ref}} \in \{7.8125 \times 10^{-5}, 3.90625 \times 10^{-5}\}$), and

(ii) a full-period equal-cost benchmark over $T = 6.0$ across all 6 democratic Voronoi chart transitions per period at the common inverted cost $h_{\text{eff}} = h/s = 0.005$ ($N_{\text{eval}} = 1{,}200$ force evaluations, using $h = 0.005$ for $\mathcal{S}_2$, $h = 0.015$ for $\mathcal{Y}_4$, $h = 0.030$ for $\text{BM}_4^{(7)}$ and PBM_4, and $h = 0.050$ for $\text{BM}_6^{(11)}$), benchmarked against an unoptimized 35-digit `Float128` $\text{BM}_6^{(11)}$ reference integration at $h_{\text{ref}} = 0.01$ ($N_{\text{eval}} = 6{,}000$).

Crucially, all `Float64` evaluations execute through the accelerated micro-kernels of Section 6.6, so that comparison against the unoptimized `Float128` reference simultaneously certifies both symplectic convergence and exact numerical consistency between the optimized and reference solver paths. Furthermore, throughout both precision backends, $\text{BM}_4^{(7)}$ and PBM_4 employ the unified 7-stage symmetric Blanes–Moan kernel of Definition 5.8 coupled to the matching homological corrector $\mathcal{Z}_4^{\text{BM4}}(h) \in \mathcal{P}_1$ with residual moment $c_4^{\text{BM4}} = +1.760005010041013 \times 10^{-4}$. Figure 19 and Table 5 establish four quantitative results:

(1) **Exact Asymptotic Orders in `Float128` down to 10^{-31} :** In 35-digit quadruple precision, linear regressions on $\log_{10}(\max_t |\Delta H(t)|/|H_0|)$ versus $\log_{10} h_{\text{eff}}$ (Figure 19a,b) recover the exact theoretical orders without any high-precision floor saturation:

$$\begin{aligned} &p_{\text{Strang}} = 2.000, \qquad p_{\text{Yoshida4}} = 3.999, \qquad p_{\text{BM4}} = 4.000, \\ &p_{\text{PBM4}} = 4.000, \qquad p_{\text{BM6}} = 5.999. \end{aligned} \tag{7.2}$$

Both the Hamiltonian error $\max_t |\Delta H(t)|/|H_0|$ (Figure 19a) and the Euclidean trajectory error $\|\mathbf{q}(T) - \mathbf{q}_{\text{ref}}^{\text{f128}}(T)\|_2$ (Figure 19b) descend monotonically across thirty decades, reaching 3.74×10^{-31} in energy and 1.89×10^{-31} in position for $\text{BM}_6^{(11)}$.

(2) **Equal-Cost Efficiency ($h_{\text{eff}} = 0.005$) versus Equal-Macro-Step Gain ($h = 0.01$) :** As emphasized by Farrés et al. [8, 22], comparing integrators at an identical macro-step $h = 0.01$ yields a 180.9× energy-error reduction (2.87×10^{-11} versus 5.19×10^{-9}) for $\text{BM}_4^{(7)}$ over $\mathcal{Y}_4$, but requires twice as many force evaluations ($s = 6$ versus $s = 3$).

When normalized to the strictly identical evaluation budget $h_{\text{eff}} = h/s = 0.005$ ($N_{\text{eval}} = 1{,}200$ over $T = 6.0$ across 6 Voronoi Jacobi chart transitions, Table 5), $\text{BM}_4^{(7)}$ ($h = 0.030$) outperforms $\mathcal{Y}_4$ ($h = 0.015$) by a net factor of 11.25× in energy (3.33×10^{-9} versus 3.75×10^{-8}) and 14.5× in trajectory accuracy (6.77×10^{-8} versus 9.78×10^{-7}), while PBM_4 ($h = 0.030$) achieves a 6.85× energy gain (5.47×10^{-9}) over $\mathcal{Y}_4$ across the 6 non-hierarchical chart transitions ($\varepsilon \sim 1$), and $\text{BM}_6^{(11)}$ ($h = 0.050$) achieves a 6,354× gain in energy (5.90×10^{-12}) and a 1.60×10^5× gain in position (6.11×10^{-12}) over $\mathcal{Y}_4$.

(3) **Non-Hierarchical Choreography ($\varepsilon \sim \mathcal{O}(1)$) versus 3D Hierarchical Perturbations ($\varepsilon \ll 1$) :** On the equal-mass Figure-8 choreography (Figure 19a,b), the three bodies exchange roles symmetrically with no small perturbation parameter ($\varepsilon \sim \mathcal{O}(1)$). Consequently, the non-perturbative Lie-bracket terms $\mathcal{O}(\varepsilon^2 h^4)$ in the shadow Hamiltonian have unit weight, so PBM_4 rightly exhibits asymptotic order $p_{\text{eff}} = 4.000$ in the non-hierarchical regime.

Conversely, when the exact same five canonical integrators are evaluated on a 3D eccentric hierarchical triple ($m_1 = m_2 = 0.5, a_{\text{in}} = 1.0, e_{\text{in}} = 0.30$ perturbed by an inclined outer companion $m_3 = 1.0, a_{\text{out}} = 12.0, i = 28°$, where $\eta_S \approx a_{\text{in}}/a_{\text{out}} = 1/12 \ll 1$), Panels 19(c,d) demonstrate that PBM_4 ($s = 6$) eliminates the leading $\mathcal{O}(\varepsilon h^4)$ error term and detaches from $\text{BM}_4^{(7)}$ along an effective 6th-order slope ($p_{\text{eff}} \approx 6.25$) parallel to $\text{BM}_6^{(11)}$ ($s = 10$), achieving up to a 2,329× energy-error reduction (1.53×10^{-14} versus 3.55×10^{-11} in `Float128`, 1,762× in `Float64`, Panel c) and a 1,640× trajectory-position error reduction (8.29×10^{-14} versus 1.36×10^{-10}, Panel d) over bare $\text{BM}_4^{(7)}$ at $h_{\text{eff}} = 8.18 \times 10^{-3}$.

(4) **Brouwer Roundoff Bounce in `Float64`** : In IEEE 754 double precision, the deterministic $\mathcal{O}(h^p)$ symplectic truncation error dominates for $h_{\text{eff}} \gtrsim 10^{-3}$ and reaches the machine floor $\sim 3.45 \times 10^{-16}$ at $h_{\text{eff}} \approx 10^{-3}$; for finer steps $h_{\text{eff}} < 10^{-3}$ ($N_{\text{steps}} = T/h \gg 10^3$), truncation falls beneath IEEE 754 precision and the measured error rebounds as $h_{\text{eff}}^{-1/2} \propto \sqrt{N_{\text{steps}}}$. In accordance with Brouwer's law [13], accumulated floating-point roundoff across the $s_{\text{eval}} N_{\text{steps}}$ force evaluations executes an unbiased random walk $\sigma \propto \varepsilon_{\text{mach}} \sqrt{s_{\text{eval}} N_{\text{steps}}}$, confirming that 35-digit `Float128` arithmetic is essential to resolve the unpolluted asymptotic regime of 6th-order symplectic compositions.

Python A.2 : `{benchmarks/run, figures/plot}_generator_01_*.py` [Float64 / Float128]

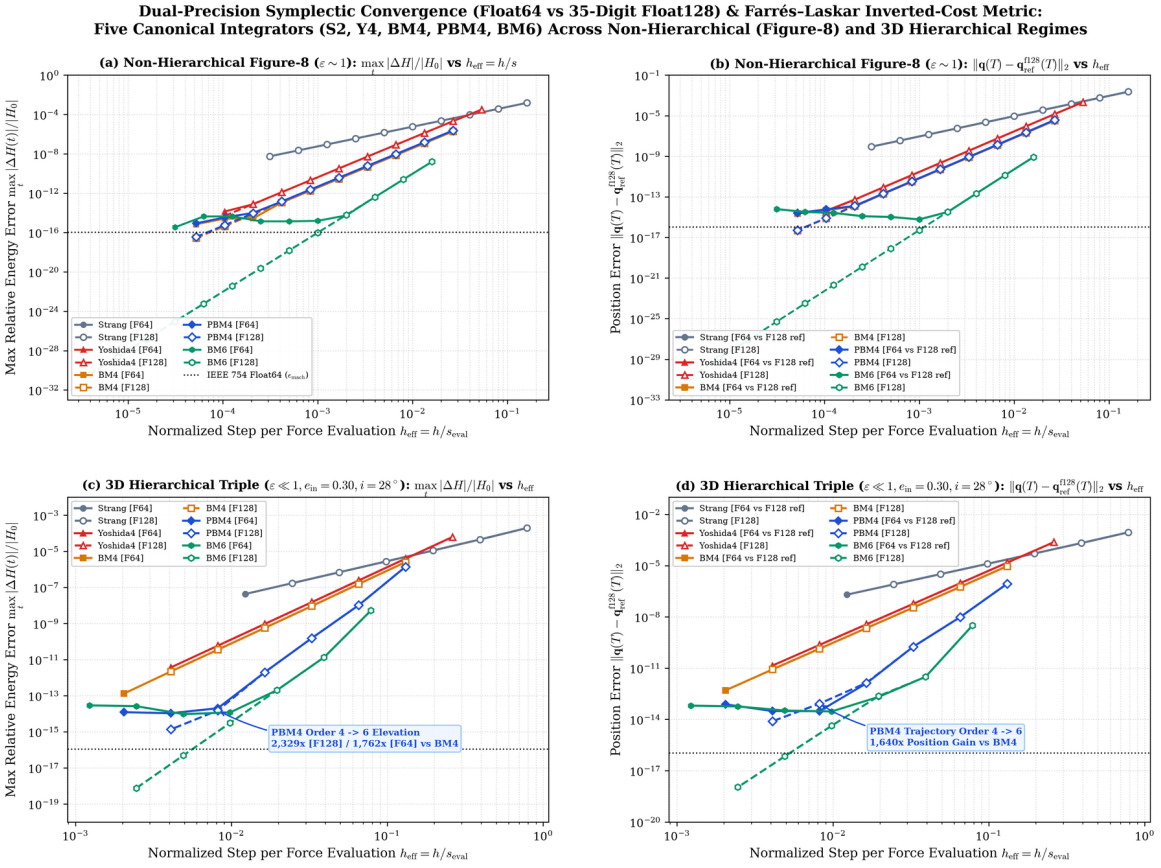


FIGURE 19. **Dual-precision symplectic convergence and Farrés–Laskar inverted-cost frontiers** ($\mathcal{S}_2, \mathcal{Y}_4, \text{BM}_4^{(7)}, \text{PBM}_4, \text{BM}_6^{(11)}$; $\varepsilon = 0, d_0 = 0, \gamma = 1.0$). **(a)** Figure-8 energy error $\max_t |\Delta H(t)|/|H_0|$ vs. $h_{\text{eff}} = h/s_{\text{eval}}$ (`Float64` solid, `Float128` dashed). **(b)** Figure-8 trajectory error $\|\mathbf{q}(T) - \mathbf{q}_{\text{ref}}^{\text{f128}}(T)\|_2$ vs. h_{eff}. **(c)** 3D hierarchical triple ($\varepsilon \ll 1, e_{\text{in}} = 0.30, i = 28^\circ, a_{\text{out}} = 12.0$): energy error showing PBM_4 order-4 $\to$ 6 elevation (2,329$\times$ gain over $\text{BM}_4^{(7)}$). **(d)** 3D hierarchical triple trajectory error (1,640$\times$ gain for PBM_4).

7.1.2. *Experimental Proof of the Two-Channel Error Law, Order 6 → 4 Crossover, and the Hall-Cohomology Quadratic Floor (Section 5.5.2 and Section 5.5).* Section 7.1.1 revealed a fundamental dichotomy in the behavior of the processed integrator PBM_4: on the non-hierarchical Figure-8 choreography ($\varepsilon \sim \mathcal{O}(1)$, Figure 19a,b), PBM_4 scales with asymptotic order $p_{\text{eff}} = 4.000$, whereas on the 3D eccentric hierarchical triple ($\varepsilon \ll 1$, Figure 19c,d),

TABLE 5. **Effective convergence orders, equal-cost accuracy ($h_{\text{eff}} = h/s = 0.005, N_{\text{eval}} = 1{,}200$ over $T = 6.0$, Voronoi $\gamma = 1.0$), and dual-precision error floors on the Figure-8 choreography (§7.1.1).** Here s (m) denotes effective FSAL force evaluations per macro-step under direct ABA/RKN merging (generic $\mathcal{S}_2$ composition), and $\|\Delta\mathbf{q}(T)\|_2 = \|\mathbf{q}(T) - \mathbf{q}_{\text{ref}}^{\text{f128}}(T)\|_2$.

Integrator	Stages s (m)	Order (Th.)	p_{eff} (`Float128`)	$\max_t \lvert\Delta H\rvert/\lvert H_0\rvert$ at $h_{\text{eff}} = 0.005$	$\|\Delta\mathbf{q}(T)\|_2$ at $h_{\text{eff}} = 0.005$	Min Floor (`Float64`)	Min Floor (`Float128`)
$\mathcal{S}_2$ (Strang)	1 (1)	2	2.000	2.81×10^{-6}	5.26×10^{-5}	5.61×10^{-9}	5.61×10^{-9}
$\mathcal{Y}_4$ (Yoshida)	3 (3)	4	3.999	3.75×10^{-8}	9.78×10^{-7}	1.38×10^{-14}	4.95×10^{-15}
$\text{BM}_4^{(7)}$	6 (7)	4	4.000	3.33×10^{-9} (11.25×)	6.77×10^{-8} (14.5×)	6.90×10^{-16}	2.74×10^{-17}
PBM_4	6 (7)	4 (eff. 6)	4.000 (6.25 in 3D)	5.47×10^{-9} (6.85×)	2.09×10^{-7} (4.67×)	8.63×10^{-16}	3.51×10^{-17}
$\text{BM}_6^{(11)}$	10 (11)	6	5.999	5.90×10^{-12} (6,354×)	6.11×10^{-12} (1.60×10^5×)	3.45×10^{-16}	3.74×10^{-31}
Ref. $\text{BM}_6^{(11)}$ (`Float128, unopt.`)	10 (11)	6	5.999	6.60×10^{-17} ($h_{\text{eff}} = 10^{-3}$)	0 (Reference)	—	1.89×10^{-31} ($\|\Delta\mathbf{q}\|_2$)

it detaches from $\text{BM}_4^{(7)}$ along an effective 6th-order trajectory ($p_{\text{eff}} = 6.25$). The algebraic theory developed in Section 5.5 (Theorems 5.17, 5.18, and 5.19) explains and predicts this transition across the entire (ε, h) plane.

Because the 2-stage palindromic Lie conjugator $\mathcal{Z}_4^{\text{BM4}}(h)$ generated by the cotangent-lifted corrector $K_4 = c_4^{\text{BM4}} h^4 D_A^3 B \in \mathcal{P}_1$ identically annihilates the leading grade-$(5,1)$ linear tidal commutator $h^4 H_5^{\text{linear}} = c_4^{\text{BM4}} h^4 D_A^4 B = \mathcal{O}(\varepsilon h^4)$, both the relative Hamiltonian error and the phase-space trajectory error obey the two-channel composite error law:

$$\frac{|\Delta H(T)|}{|H_0|} \sim C_6\, \varepsilon\, h^6 + C_4\, \varepsilon^2\, h^4, \qquad \|\mathbf{q}(T) - \mathbf{q}_{\text{ref}}(T)\|_2 \sim \tilde{C}_6\, \varepsilon\, h^6 + \tilde{C}_4\, \varepsilon^2\, h^4, \tag{7.3}$$

where $\varepsilon = (m_{\text{pert}}/M_{\text{bin}})(a_{\text{in}}/R_{\text{out}})^3 = \eta_S^3$ parametrizes the dimensionless cubic tidal perturbation strength, the first term $\mathcal{O}(\varepsilon h^6)$ stems from the uncompensated grade-$(7,1)$ seventh-order commutators, and the irreducible quadratic floor $\mathcal{O}(\varepsilon^2 h^4)$ originates jointly from the non-vanishing grade-$(5,2)$ Hall cohomology class $[D_B D_A^3 B] \in H^1(D_A, \mathcal{L}_{5,2}) \cong \mathbb{R}$ (Theorem 5.17, Tier 2) and the cross-term $\{K_4, W_{\text{apex}}^{\text{screen}}\} \in \mathcal{P}_0$.

Figure 20 subjects Equation (7.3) to a four-part quantitative verification on the 3D eccentric hierarchical triple ($m_0 = m_1 = 0.5, a_{\text{in}} = 1.0, e_{\text{in}} = 0.30$ perturbed by an outer companion $m_2 = 1.0$ on an inclined orbit $i = 28°$), comparing exclusively PBM_4 against its unprocessed base scheme $\text{BM}_4^{(7)}$ at identical evaluation cost ($s_{\text{eval}} = 6$):

(a) **Order $6 \to 4$ Energy Error Crossover and $100\times$/Decade Quadratic Floor in `Float128` (Figure 20a)** : Sweeping macro-steps $h \in [0.01, 0.32]$ ($h_{\text{eff}} = h/6 \in [1.67 \times 10^{-3}, 5.33 \times 10^{-2}]$) over $T_{\text{cross}} = 1.60$ in 35-digit `Float128` arithmetic across three tidal hierarchy decades $\varepsilon \in \{10^{-2}, 10^{-3}, 10^{-4}\}$ ($R_{\text{out}} \in \{2.92, 6.30, 13.57\}$), unprocessed $\text{BM}_4^{(7)}$ exhibits a uniform 4th-order decay $\mathcal{O}(\varepsilon h^4)$ whose curves are separated vertically by $10\times$ per decade in ε. In contrast, above the crossover scale $h_{\text{cross}}(\varepsilon) = \sqrt{(C_4/C_6)\,\varepsilon}$, PBM_4 follows the 6th-order channel $\mathcal{O}(\varepsilon h^6)$, achieving a maximum energy accuracy gain over $\text{BM}_4^{(7)}$ of 19.1× at $\varepsilon = 10^{-2}$, 262.5× at $\varepsilon = 10^{-3}$ (5.94×10^{-12} versus 1.56×10^{-9} at $h = 0.08$), and 2,537× at $\varepsilon = 10^{-4}$ (4.62×10^{-15} versus 1.17×10^{-11} at $h = 0.04$).

Below $h_{\text{cross}}(\varepsilon)$, the grade-$(5,2)$ Hall-cohomology floor $\mathcal{O}(\varepsilon^2 h^4)$ takes over and bends the PBM_4 curves back onto slope 4.00. At the finest step $h = 0.01$ ($h_{\text{eff}} = 1.67 \times 10^{-3}$), the PBM_4 energy error descends from 1.49×10^{-13} ($\varepsilon = 10^{-2}$) to 2.30×10^{-15} ($\varepsilon = 10^{-3}$) and 2.52×10^{-17} ($\varepsilon = 10^{-4}$, a 1,815× floor reduction against 4.58×10^{-14} for $\text{BM}_4^{(7)}$), demonstrating the exact $100\times$ reduction per decade in ε ($\propto \varepsilon^2$) predicted by Theorem 5.17.

(b) **Unclipped Local Empirical Order $p_{\text{emp}}(h) : 6 \to 4$ and Square-Root Crossover Shift (Figure 20b)** : Differentiating Equation (7.3) with respect to $\ln h$ yields the

exact analytical local-order transition law:

$$p_{\mathrm{th}}(h;\varepsilon) = \frac{\partial \ln\left(C_6\,\varepsilon\,h^6 + C_4\,\varepsilon^2\,h^4\right)}{\partial \ln h} = 4 + \frac{2}{1 + \left(h_{\mathrm{cross}}(\varepsilon)/h\right)^2}, \qquad h_{\mathrm{cross}}(\varepsilon) = \sqrt{\frac{C_4}{C_6}}\,\varepsilon. \quad (7.4)$$

Evaluating the unclipped finite-difference trajectory slope directly from the raw `Float128` data:

$$p_{\mathrm{emp}}(\sqrt{h_k h_{k+1}}) = \frac{\ln\left(E_q(h_k)/E_q(h_{k+1})\right)}{\ln(h_k/h_{k+1})}, \qquad E_q(h) = \left\|\mathbf{q}(T;h) - \mathbf{q}_{\mathrm{ref}}^{\mathrm{f128}}(T)\right\|_2$$

(where $E_q(h)$ denotes the Euclidean phase-space position error of Panel (d)) closely tracks the universal sigmoid (7.4).

As ε decreases by a factor of 100 from 10^{-2} to 10^{-4}, the midpoint inflection $p_{\mathrm{th}}(h_{\mathrm{cross}}) = 5.0$ shifts leftward by a factor of $\sqrt{100} = 10$ in step size: for $\varepsilon = 10^{-2}$, p_{emp} relaxes rapidly from 5.17 down to $4.28 \to 4.05 \to 4.01 \to 4.00$; for $\varepsilon = 10^{-3}$, it transitions smoothly along $6.12 \to 5.60 \to 4.76 \to 4.20 \to 4.05$; and for $\varepsilon = 10^{-4}$, it remains anchored in the 6th-order regime ($6.23 \to 6.03 \to 5.84 \to 5.32$) across nearly the entire sweep before descending to 4.53 at the smallest step pair, while $\mathrm{BM}_4^{(7)}$ stays flat at $p_{\mathrm{emp}} = 3.99 \pm 0.02$.

(c) **Two-Regime Tidal Perturbation Scaling versus $\varepsilon = \eta_S^3$ at Fixed h (Figure 20c)** : Holding the macro-step fixed at $h = 0.08$ ($h_{\mathrm{eff}} = 0.0133$, executed in `Float64` with the accelerated micro-kernels of Section 6.6) and sweeping the tidal parameter across 3.5 decades $\varepsilon \in [10^{-5}, 3\times10^{-2}]$ exposes the dual role of ε in Equation (7.3), separated by the crossover threshold $\varepsilon_{\mathrm{cross}}(h) = (C_6/C_4)\,h^2 \approx 6.4\times10^{-3}$.

Whereas $\mathrm{BM}_4^{(7)}$ scales linearly as $\mathcal{O}(\varepsilon h^4) \propto \varepsilon^1$ across the entire domain (2.09×10^{-8} at $\varepsilon = 3\times10^{-2}$ down to 2.23×10^{-11} at $\varepsilon = 10^{-5}$), PBM_4 exhibits two distinct asymptotic regimes: (i) in the moderate-hierarchy regime $\varepsilon \in [10^{-3}, 3\times10^{-2}]$ ($\varepsilon \gtrsim \varepsilon_{\mathrm{cross}}$), the second channel dominates and PBM_4 follows the quadratic floor scaling $\mathcal{O}(\varepsilon^2 h^4) \propto \varepsilon^2$ (empirical slope 1.84), expanding its accuracy advantage over $\mathrm{BM}_4^{(7)}$ from 5.3× at $\varepsilon = 3\times10^{-2}$ to 236.1× at $\varepsilon = 10^{-3}$ (7.32×10^{-12} versus 1.73×10^{-9}); (ii) in the deep-hierarchy regime $\varepsilon \in [10^{-5}, 3\times10^{-4}]$ ($\varepsilon \ll \varepsilon_{\mathrm{cross}}$), the quadratic floor drops below the 6th-order truncation term and PBM_4 transitions onto the pre-asymptotic channel $\mathcal{O}(\varepsilon h^6) \propto \varepsilon^1$ (empirical slope 0.93), maintaining a constant $\mathcal{O}(h^{-2})$ accuracy plateau of 215×–236× over $\mathrm{BM}_4^{(7)}$ down to $\varepsilon = 10^{-5}$ (1.04×10^{-13} versus 2.23×10^{-11}).

(d) **Phase-Space Trajectory Position Error Crossover $\|\mathbf{q}(T) - \mathbf{q}_{\mathrm{ref}}^{\mathrm{f128}}(T)\|_2$ (Figure 20d)** : Benchmarking the Euclidean phase-space configuration error at $T_{\mathrm{cross}} = 1.60$ against an independent, unoptimized 35-digit `Float128` $\mathrm{BM}_6^{(11)}$ reference trajectory (Richardson-extrapolated at $h_{\mathrm{ref}} \in \{0.01, 0.005\}$) confirms that the boundary readout map $\mathbf{z}^{\mathrm{phys}} = \mathcal{Z}_4^{\mathrm{BM4}}(h)(\tilde{\mathbf{z}})$ transfers the exact same two-channel law from the shadow Hamiltonian to physical orbital trajectories.

Above $h_{\mathrm{cross}}(\varepsilon)$, PBM_4 follows the 6th-order trajectory slope and delivers up to a 1,335× position-accuracy gain over $\mathrm{BM}_4^{(7)}$ at $\varepsilon = 10^{-4}$ (2.49×10^{-17} versus 3.33×10^{-14} at $h = 0.01$, and 134.1× at $\varepsilon = 10^{-3}$). Below $h_{\mathrm{cross}}(\varepsilon)$, the trajectory error bends onto the 4th-order floor $\mathcal{O}(\varepsilon^2 h^4)$ with the exact same 100×-per-decade vertical separation in ε: at $h = 0.01$, $\|\Delta\mathbf{q}(T)\|_2$ drops from 2.49×10^{-13} ($\varepsilon = 10^{-2}$) to 2.30×10^{-15} ($\varepsilon = 10^{-3}$) and 2.49×10^{-17} ($\varepsilon = 10^{-4}$).

Python A.2 : `{benchmarks/run, figures/plot}_generator_02_*.py` [Float64 / Float128]

7.1.3. *Dynamics Across Singularities: Unsoftened Limit Cases ($\varepsilon = 0, d_0 = 0$).* A defining requirement of this monograph is the deterministic traversal of physical singularities without the introduction of ad-hoc smoothing lengths ($d_0 = 0$) or artificial force cutoffs. Rather

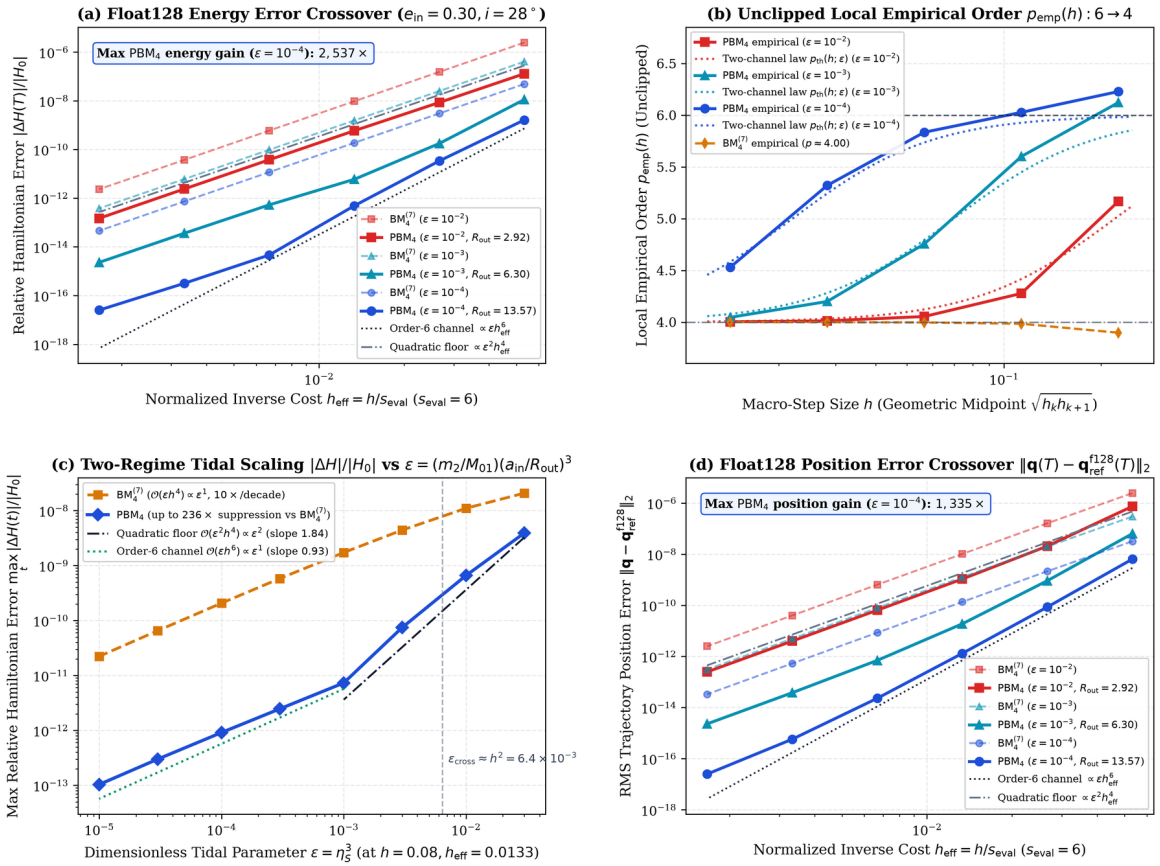


FIGURE 20. **Two-channel error law, order $6 \to 4$ crossover, and Hall-cohomology quadratic floor $\mathcal{O}(\varepsilon^2 h^4)$ for PBM$_4$ vs. BM$_4^{(7)}$ on the 3D eccentric hierarchical triple ($e_{in} = 0.30, i = 28^\circ$). (a)** `Float128` energy error $|\Delta H(T)|/|H_0|$ vs. $h_{eff} = h/6$ across $\varepsilon \in \{10^{-2}, 10^{-3}, 10^{-4}\}$. **(b)** Unclipped local empirical order $p_{emp}(h)$ vs. $\sqrt{h_k h_{k+1}}$ overlaid with $p_{th}(h;\varepsilon)$ (7.4). **(c)** Tidal scaling $\max_t |\Delta H(t)|/|H_0|$ vs. $\varepsilon = \eta_S^3$ at $h = 0.08$ (`Float64`). **(d)** `Float128` trajectory error $\|\mathbf{q}(T) - \mathbf{q}_{ref}^{f128}(T)\|_2$ vs. h_{eff}.

than grouping disparate dynamical systems onto a single composite axis, we structure our evaluation around four dedicated benchmark plates (Figures 21–24), each isolating one of the four singularity-resolution mechanisms established in Sections 4–6.

Limit Case L1 : Analytic Kepler–Sundman–Stumpff Pericenter Conditioning Across $1-e \in [10^{-12}, 10^{-1}]$ and $e = 1.0$ ($N = 2$, Figure 21). In unregularized Cartesian integrators (such as velocity Verlet), the pericenter acceleration diverges as $r_{min}^{-2} = [a(1-e)]^{-2}$, causing a catastrophic energy error explosion scaling as $(1-e)^{-5/2}$ (6.61×10^2 at $1-e = 10^{-3}$ and 6.55×10^2 at $1-e = 10^{-12}$, Figure 21b). Even within a universal Sundman–Stumpff propagator, naive evaluation of $\rho_{raw} = \rho_0 c_0(z) + \sigma_0 \tau c_1(z) + GM\tau^2 c_2(z)$ at pericenter suffers subtractive cancellation of order $(1-e)^{-2}\varepsilon_{mach}$ in total energy ($\sim 1.39 \times 10^{-6}$ at $1-e = 10^{-5}$ and $\mathcal{O}(1)$ for $1-e \le 10^{-8}$ in `Float64`).

By enforcing the exact angular-momentum/energy quadratic identity coupled with incremental Wronskian renormalization (Section 6.4.1, Proposition 6.11, and Theorem 5.25 in Section 5.6.3):

$$\rho_{final} = \frac{\sigma_{end}^2 + \|\mathbf{L}\|^2/\mu^2}{2GM - \alpha\rho_{raw}}, \qquad \delta\dot{g} = \frac{\dot{f}g - \delta f}{f},$$

and integrating over a complete orbital period $1.0\,T_{\mathrm{orb}} = \sqrt{2}\pi \approx 4.4429$ using an odd step count $N_{\mathrm{steps}} = 129$ ($\Delta t = T_{\mathrm{orb}}/129 \approx 0.03444 \leq 0.05\,\tau_{\mathrm{dyn}}(a_C)$, $k_{\mathrm{sym}}(t) \equiv 0$) so that central Step 64 straddles $t = 0.5\,T_{\mathrm{orb}}$ inside the regularized Sundman chart down to $r_{\min} = 10^{-12}$ AU (Figure 21a), the conditioned $N = 2$ leaf propagator eliminates pericenter loss across all 12 decades, maintaining $\max_{t\in[0,T_{\mathrm{orb}}]} |\Delta H|/|H_0| \leq 1.39 \times 10^{-13}$ (8.17×10^{-14} at $1 - e = 10^{-12}$ and 9.95×10^{-14} at the rectilinear collision limit $e = 1.0$) in `Float64`, and $\leq 1.53 \times 10^{-33}$ (2.71×10^{-34} at $1 - e = 10^{-12}$ and 5.50×10^{-38} at $e = 1.0$) in `Float128`.

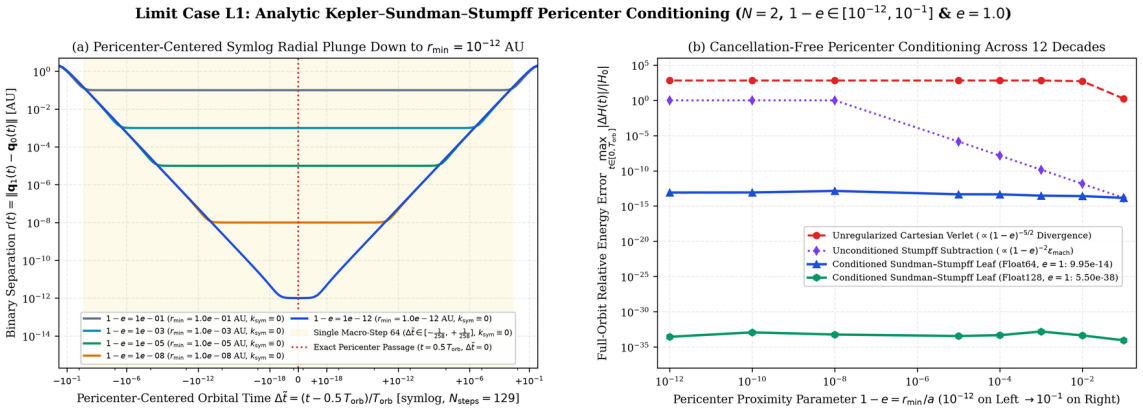


FIGURE 21. **Limit Case L1: Analytic Kepler–Sundman–Stumpff pericenter conditioning across $1 - e \in [10^{-12}, 10^{-1}]$ and $e = 1.0$ ($N = 2$). (a)** Radial separation $r(t)$ vs. pericenter-centered normalized time $\Delta\tilde{t} = (t - 0.5\,T_{\mathrm{orb}})/T_{\mathrm{orb}}$ (`symlog` scale) down to $r_{\min} = 10^{-12}$ AU within Step 64 ($N_{\mathrm{steps}} = 129, k_{\mathrm{sym}}(t) \equiv 0$). **(b)** Full-orbit relative energy error $\max_t |\Delta H(t)|/|H_0|$ across 12 decades in $1 - e$ (`Float64` and `Float128`).

Limit Case L2 : Asymptotic Free-Fall Regularity of the PBM_4 **($\mathcal{Z}_4^{\mathrm{BM4}}$) Cotangent Corrector Across 12 Decades** $r \in [10^{-12}, 10^{0}]$ **AU (Figure 22).** Why does the cotangent boundary corrector $\mathcal{Z}_4^{\mathrm{BM4}}(h_{\mathrm{sub}})$ remain completely nonsingular when a binary pair plunges toward collision ($r \to 0^+$) despite its momentum dependence on the diverging free-fall impulse $\|\mathbf{w}(r)\| = \mu\sqrt{2GM/r - \alpha} \propto r^{-1/2}$? By Theorems 5.18 and 5.19 (Equations (5.79)–(5.80)) and Theorem 6.5 (Equations (6.25) and (6.30)), the corrector is governed by the scalar generating potential and dynamic quadrupole tensor:

$$K_4(\mathbf{r}, \mathbf{w}) = \mathrm{Tr}\big(\mathbf{T}_{\mathrm{apex}}(\mathbf{R})\,\mathbf{M}_{\mathrm{sym}}(\mathbf{r}, \mathbf{w})\big) \in \mathcal{P}_1,$$

$$\mathbf{M}_{\mathrm{sym}}(\mathbf{r}, \mathbf{w}) = c_4^{\mathrm{BM4}} h_{\mathrm{sub}}^4 \frac{GM_{ab}}{r^3}\left[2(\mathbf{r}\otimes\mathbf{w} + \mathbf{w}\otimes\mathbf{r}) - \frac{3(\mathbf{r}\cdot\mathbf{w})}{r^2}\mathbf{r}\otimes\mathbf{r}\right],$$

generating the corrective position shift $\Delta\mathbf{r}_{\mathrm{corr}} = +\nabla_{\mathbf{w}} K_4$ and momentum shift $\Delta\mathbf{w}_{\mathrm{corr}} = -\nabla_{\mathbf{r}} K_4$.

Because the local dyadic sub-step size scales with the Keplerian dynamical timescale $h_{\mathrm{sub}}(r) = h_0(r/r_{\mathrm{ref}})^{3/2} \propto \tau_{\mathrm{dyn}}(r) = \sqrt{r^3/(GM_{ab})} \propto r^{3/2}$ ($h_{\mathrm{sub}}^4 \propto r^6$), the prefactor $h_{\mathrm{sub}}(r)^4 \frac{GM_{ab}}{r^3} \propto r^{+3}$ overwhelms both the r^{-3} Keplerian Hessian and the $w(r) \propto r^{-1/2}$ free-fall velocity divergence. Sweeping $r \in [10^{-12}, 10^{0}]$ AU across 12 orders of magnitude ($N = 3, R_2 = \sqrt{29}$ AU, $h_0 = 0.01$) confirms the exact analytical extinction laws:

$$|K_4(\mathbf{r}, \mathbf{w})| \propto r^{+3.5000} = \mathcal{O}(r^{7/2}) \to 0, \qquad \|\Delta\mathbf{r}_{\mathrm{corr}}\| = \|\nabla_{\mathbf{w}} K_4\| \propto r^{+4.0000} = \mathcal{O}(r^4) \to 0, \tag{7.5}$$

$$\|\Delta\mathbf{w}_{\mathrm{corr}}\| = \|\nabla_{\mathbf{r}} K_4\| \propto r^{+2.5000} = \mathcal{O}(r^{5/2}) \to 0, \qquad \frac{\|\Delta\mathbf{w}_{\mathrm{corr}}\|}{\|\mathbf{w}\|} \propto r^{+3.0000} = \mathcal{O}(r^3) \to 0, \tag{7.6}$$

with the generating potential $|K_4|$ decaying from 1.21×10^{-14} down to 1.40×10^{-56} and the corrective position shift $\|\Delta\mathbf{r}_{\text{corr}}\|$ decaying from 6.04×10^{-14} AU down to 6.04×10^{-62} AU at $r = 10^{-12}$ AU (Figure 22a), while the absolute momentum shift $\|\Delta\mathbf{w}_{\text{corr}}\|$ decays to 4.06×10^{-44} and the relative momentum shift $\|\Delta\mathbf{w}_{\text{corr}}\|/\|\mathbf{w}\|$ decays to 4.06×10^{-50} (Figure 22b), proving that $\mathcal{Z}_4^{\text{BM4}}(h_{\text{sub}})$ smoothly reduces to the exact identity in both position and momentum as $r \to 0^+$.

Python A.2 : `{benchmarks/run, figures/plot}_generator_03_*.py` [Float64 / Float128]

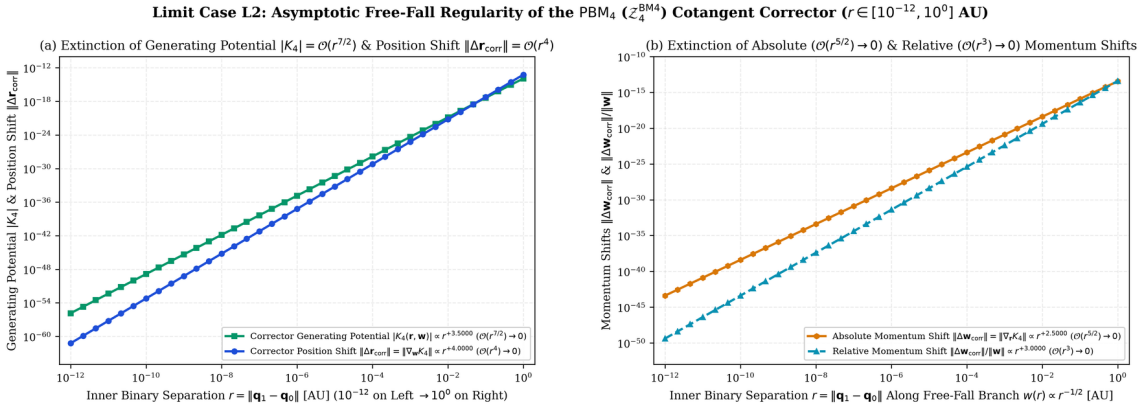


FIGURE 22. **Limit Case L2: Asymptotic free-fall regularity of the PBM$_4$ ($\mathcal{Z}_4^{\text{BM4}}$) cotangent corrector across $r \in [10^{-12}, 10^{0}]$ AU. (a)** Power-law extinction of generating potential $|K_4(\mathbf{r}, \mathbf{w})| \propto r^{+3.5000}$ and position shift $\|\Delta\mathbf{r}_{\text{corr}}\| \propto r^{+4.0000}$. **(b)** Extinction of absolute momentum shift $\|\Delta\mathbf{w}_{\text{corr}}\| \propto r^{+2.5000}$ and relative momentum shift $\|\Delta\mathbf{w}_{\text{corr}}\|/\|\mathbf{w}\| \propto r^{+3.0000}$.

Limit Case L3 : Exact McGehee Exceptional Divisor Traversals ($\rho = 0$), Conormal Bounce Involution $\mathcal{B}_C^2 = \text{Id}$, and Round-Trip Reversibility for Central Collisions $k \in \{2, 3, 4\}$ (Figure 23). Under the normal-cone radial blow-up $\rho_C = \sqrt{I_C}$ and McGehee regularized radial velocity $v_{\text{McG}} = \dot{\rho}_C\sqrt{\rho_C}$ (Section 5.2, Lemma 5.6, and Sections 4.3 and 6.4.2), simultaneous k-body central collisions ($d_0 = 0$) are resolved on the blown-up collision manifold by the unitary conormal reflection involution $\mathcal{B}_C(\mathbf{s}_0, -v_{\text{coll}}\mathbf{s}_0) = (\mathbf{s}_0, +v_{\text{coll}}\mathbf{s}_0)$ ($\mathcal{B}_C^2 = \text{Id}$). Figure 23 separates the three canonical central-collision multiplicities into three independent columns over a complete infall–bounce–return cycle $[0, 2\,t_{\text{coll}}]$ at $\Delta t = 0.025$, where the discrete circle (`Float64`) and triangle (`Float128`) markers in the bottom panels (d–f) evaluate the exact round-trip time-reversibility error $|\Delta H_{\text{FB}}(t_{\text{turn}})|/|H_0|$ after integrating forward $[0, t_{\text{turn}}]$ and backward $[t_{\text{turn}}, 0]$ back to $t = 0$ at four turnaround checkpoints straddling the collision time t_{coll}:

(i) *Column 1 — Binary head-on collision* ($k = 2$, $r_0 = 2.0$ AU, $m_i = 1.0$, $t_{\text{coll}}^{(k=2)} = \pi/\sqrt{2} = 2.2214$, Figure 23a,d): Traverses $r = 0$ via the Sundman–Levi-Civita chart ($\mathcal{B}_C : -2.000 \mapsto +2.000$) with $\max|\Delta H|/|H_0| = 1.05 \times 10^{-13}$ in `Float64` and 6.60×10^{-38} in `Float128`, and 100-step ($t_{\text{turn}} = 2.50 > t_{\text{coll}}^{(k=2)}$) round-trip reversibility ($\Phi_{-\Delta t}^{100} \circ \Phi_{\Delta t}^{100}$ crossing $r = 0$ twice across $N_{\text{eval}} = 1{,}424$ leaf evaluations) of $|\Delta H_{\text{FB}}|/|H_0| = 2.48 \times 10^{-13} \le 2\,N_{\text{eval}}\,\varepsilon_{\text{mach}} = 3.16 \times 10^{-13}$ in `Float64` and 1.10×10^{-33} in `Float128`;

(ii) *Column 2 — Equilateral Lagrange homothetic triple collision* ($k = 3$, $R_0 = 1.20$ AU, $m_i = 1.0$, $GM_{\text{eff}} = 1/\sqrt{3}$, $t_{\text{coll}}^{(k=3)} = 1.9216$, Figure 23b,e): Crosses the 3-body collision divisor $\rho = 0$ ($\mathcal{B}_C : -1.075 \mapsto +1.075$) with $\max|\Delta H|/|H_0| = 1.04 \times 10^{-13}$ in

`Float64` and 8.91×10^{-34} in `Float128`, and 100-step ($t_{\text{turn}} = 2.50 > t_{\text{coll}}^{(k=3)}$) round-trip reversibility $|\Delta H_{\text{FB}}|/|H_0| = 4.55\times10^{-14}$ in `Float64` and 5.65×10^{-34} in `Float128` (maximum across all four checkpoints 1.47×10^{-13} and 1.43×10^{-33} at $N = 80$);

(iii) *Column 3 — Symmetric square D_4 quadruple collision* ($k = 4$, $R_0 = 1.00$ AU, $m_i = 1.0$, $GM_{\text{eff}} = \frac{1}{4} + \frac{1}{\sqrt{2}} = 0.9571$, $t_{\text{coll}}^{(k=4)} = 1.1353$, Figure 23c,f): Integrated up to $T_{\max} = 2.50 > 2\,t_{\text{coll}}^{(k=4)}$, genuinely crossing the simultaneous 4-body origin $\rho = 0$ ($\mathcal{B}_C : -1.384 \mapsto +1.384$) and rebounding with $\max|\Delta H|/|H_0| = 7.39 \times 10^{-14}$ in `Float64` and 1.46×10^{-33} in `Float128`, 100-step ($t_{\text{turn}} = 2.50$) round-trip reversibility across the collision of $|\Delta H_{\text{FB}}|/|H_0| = 1.76 \times 10^{-13}$ (`Float64`) and 1.93×10^{-33} (`Float128`, position residual $\|\Delta\mathbf{q}_{\text{FB}}\|_2 = 3.52 \times 10^{-13}$ in `Float64` and 3.86×10^{-33} in `Float128`), and dihedral D_4 point-group symmetry defect $\Delta_{D_4} = 7.00 \times 10^{-16}$ in `Float64` and 0.00 in `Float128`.

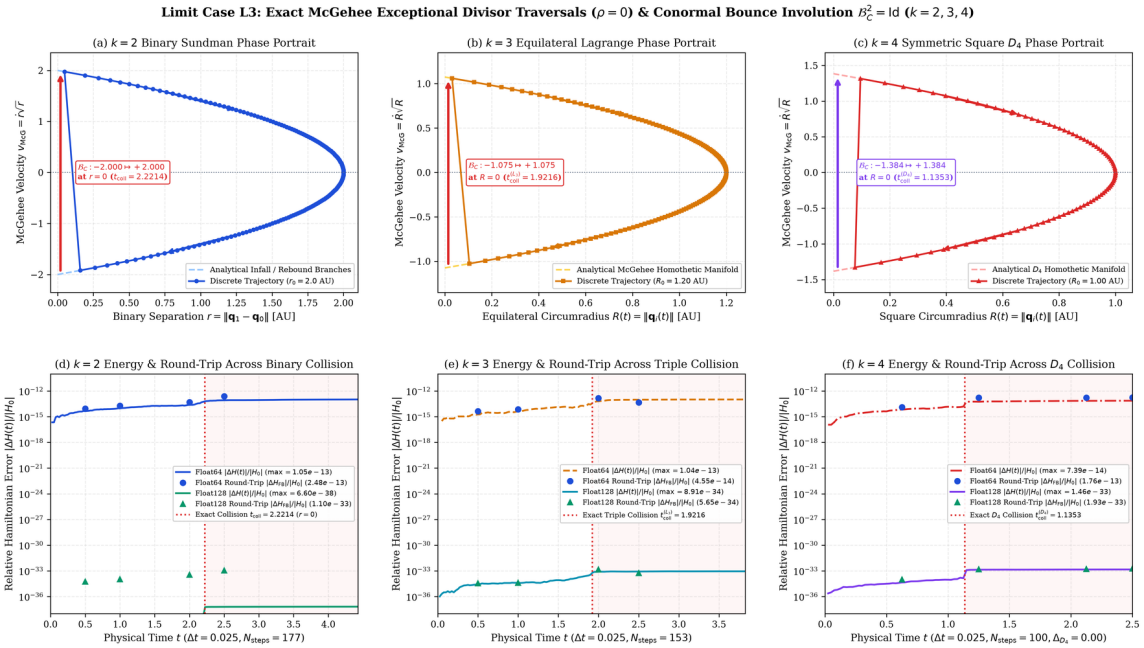


FIGURE 23. **Limit Case L3: Exact McGehee exceptional divisor traversals ($\rho = 0$) and conormal bounce involution $\mathcal{B}_C^2 = \mathrm{Id}$ for central collisions $k \in \{2, 3, 4\}$. (a–c)** McGehee blown-up phase portraits $(\rho, \dot{\rho}\sqrt{\rho})$ with infall ($\leftarrow$), vertical reflection $\mathcal{B}_C$ at $\rho = 0$ ($\uparrow$), and rebound ($\rightarrow$) for $k = 2$ Sundman, $k = 3$ Lagrange, and $k = 4$ square D_4. **(d–f)** Dual-precision continuous Hamiltonian error $|\Delta H(t)|/|H_0|$ and round-trip reversibility markers $|\Delta H_{\text{FB}}(t_{\text{turn}})|/|H_0|$ across $t = t_{\text{coll}}$.

Limit Case L4 : Adaptive Multiscale Resolution Without Exact Collision — Chaotic Burrau 3-4-5 Scattering (L4a) and 3D Kozai–Lidov Secular Resonance (L4b) (Figure 24). In general non-homothetic N-body dynamics without a massive central host, extreme close encounters and secular resonances occur with small but nonzero impact parameters ($r_{\min} > 0$) and are resolved on the outer Fulton–MacPherson / Jacobi chart atlas by time-symmetric dyadic sub-stepping and shadow gauge connections (Sections 5.6, 6.3, and 4.3.2):

(i) *L4a — Pythagorean 3-4-5 chaotic three-body scattering of Burrau [14]* ($m = \{3, 4, 5\}$, $t \in [0, 12.0]$, $\Delta t = 0.04$, Figure 24a–b): Across successive chaotic triple flybys reaching $r_{\min} = 1.15 \times 10^{-2}$ AU, the dyadic scheduler dynamically ascends and descends

$k_{\mathrm{sym}}(t) \in \{0, \dots, 7\}$ (zero saturation under $k_{\max} = 8$) in exact synchrony with $\min_{i<j} r_{ij}(t)$.

At fixed macro-step $\Delta t = 0.04$, both `Float64` and `Float128` measure the exact same symplectic shadow truncation amplitude $\max |\Delta H|/|H_0| = 1.25 \times 10^{-8}$, while the continuous time series of the 9 Galilean Lie–Bargmann generators remain bounded across the entire horizon (terminal residual $\|\Delta \mathbf{L}_{\mathrm{tot}}(T)\|_2 = 9.06 \times 10^{-14}$ in `Float64` and 3.04×10^{-33} in `Float128`, Figure 24b), high-precision $\mathrm{BM}_6^{(11)}$ refinement ($\Delta t = 0.002$) converges down to 5.54×10^{-16} in `Float64` and 2.45×10^{-29} in `Float128`, and palindromic round-trip reversibility reaches $|\Delta H_{\mathrm{FB}}|/|H_0| = 1.39 \times 10^{-16}$ (`Float64`) and 1.15×10^{-34} (`Float128`).

(ii) *L4b — 3D high-inclination Kozai–Lidov secular cycles* ($a_{\mathrm{in}} = 1.0$, $a_{\mathrm{out}} = 4.0$, $m_2 = 0.4$, $i_0 = 84.0°$, $t \in [0, 300.0]$, $\Delta t = 0.25$, Figure 24c–d): Secular angular-momentum exchange pumps the inner binary eccentricity from $e_0 = 0.10$ to $e_{\max} = 0.998865$ ($1 - e_{\min} = 1.135 \times 10^{-3}$, $i_{\mathrm{in}}(t) \in [37.4°, 86.1°]$) while activating dyadic refinement up to $k_{\mathrm{sym}}(t) = k_{\max} = 11$ (zero saturation) during high-eccentricity pericenter passages.

As demonstrated in Figure 24d, our formulation cleanly separates across 30 orders of magnitude the **exact Noether conservation of total vertical angular momentum** $|L_{z,\mathrm{tot}}(t) - L_{z,\mathrm{tot}}(0)| \le 1.57 \times 10^{-14}$ (`Float64`) and 1.77×10^{-32} (`Float128`) from the physical semisecular quadrupole/octupole oscillation of the inner Delaunay action $|\Delta(\sqrt{1 - e_{\mathrm{in}}^2} \cos i_{\mathrm{in}})(t)| = 6.01 \times 10^{-2}$ at $a_{\mathrm{out}}/a_{\mathrm{in}} = 4.0$, while the fixed-macro-step ($\Delta t = 0.25$) shadow Hamiltonian oscillation $|\Delta H(t)|/|H_0| = \mathcal{O}(h_{\mathrm{sub}}^6)$ descends to 2.27×10^{-18} in `Float128` during the low-eccentricity phase before both precisions coincide on the physical truncation envelope (5.42×10^{-12} in `Float64`, 5.10×10^{-12} in `Float128`) at peak eccentricity, and converges to 1.39×10^{-16} (`Float64`) and 1.76×10^{-28} (`Float128`) under high-precision $\mathrm{BM}_6^{(11)}$ refinement ($\Delta t = 0.005$, with palindromic round-trip reversibility 0.00 in `Float64` and 9.22×10^{-34} in `Float128`).

Python A.2 : `{benchmarks/run, figures/plot}_generator_03_*.py` [Float64 / Float128]

TABLE 6. **Quantitative dual-precision certification across unsoftened singular limit cases L1–L4 (§7.1.3; $\varepsilon = 0, d_0 = 0$).** For L4a and L4b, both equal-macro-step ($\Delta t = 0.04$ / 0.25) shadow oscillations and high-precision $\mathrm{BM}_6^{(11)}$ convergence ($\Delta t = 0.002$ / 0.005) are reported alongside Noether and round-trip (FB) residuals.

Limit Case & Protocol ID	**Singularity / Multiscale Regime ($d_0 = 0$)**	**Unregularized Cartesian Error**	**`Float64` $\lvert\Delta H\rvert/\lvert H_0\rvert$**	**`Float128` $\lvert\Delta H\rvert/\lvert H_0\rvert$**	**Geometric / Noether / Reversibility Invariant Certified (`Float64` / `Float128`)**
L1a: Binary $1 - e \in [10^{-12}, 10^{-1}]$	Pericenter $r_{\min} = 10^{-12}$ AU ($1.0\,T_{\mathrm{orb}}$)	6.55×10^2 (diverged)	8.17×10^{-14}	2.71×10^{-34}	$k_{\mathrm{sym}}(t) \equiv 0$, $r_{\min}$ achieved $= 10^{-12}$ AU
L1b: Rectilinear Limit $e = 1.0$	Radial pericenter $r_{\min} = 0$ ($1.0\,T_{\mathrm{orb}}$)	NaN (Crash)	9.95×10^{-14}	5.50×10^{-38}	Conditioned Stumpff–Wronskian identity
L2: Free-Fall PBM$_4$ ($\mathcal{Z}_4^{\mathrm{BM4}}$)	Cotangent corrector on $r \in [10^{-12}, 1]$ AU	Uncorrected $\mathcal{O}(\varepsilon h^4)$	$\alpha_{K_4} = +3.5000$	$\alpha_{\Delta r} = +4.0000$	$\alpha_{\Delta w} = +2.5000$, $\alpha_{\mathrm{rel},w} = +3.0000$
L3a: Binary Bounce ($k = 2$)	Sundman collision $r = 0$ ($t_{\mathrm{coll}} = 2.2214$)	NaN (Crash)	1.05×10^{-13}	6.60×10^{-38}	Round-trip FB ($N = 100$): 2.48×10^{-13} / 1.10×10^{-33}
L3b: Lagrange Triple ($k = 3$)	McGehee 3-body $\rho = 0$ ($t_{\mathrm{coll}} = 1.9216$)	NaN (Crash)	1.04×10^{-13}	8.91×10^{-34}	Round-trip FB ($N = 100$): 4.55×10^{-14} / 5.65×10^{-34}
L3c: Square D_4 ($k = 4$)	McGehee 4-body $\rho = 0$ ($t_{\mathrm{coll}} = 1.1353$)	NaN (Crash)	7.39×10^{-14}	1.46×10^{-33}	Round-trip FB ($N = 100$): 1.76×10^{-13} / 1.93×10^{-33} ($\Delta_{D_4} = 0.00$)
L4a: Burrau 3-4-5 Scattering	Chaotic flybys $r_{\min} = 1.15 \times 10^{-2}$ AU ($k_{\max} = 7$)	Diverges at flyby	1.25×10^{-8} ($\Delta t = 0.04$) 5.54×10^{-16} (BM_6)	1.25×10^{-8} ($\Delta t = 0.04$) 2.45×10^{-29} (BM_6)	$\|\Delta \mathbf{L}_{\mathrm{tot}}(T)\|_2$: 9.06×10^{-14} / 3.04×10^{-33} FB: 1.39×10^{-16} / 1.15×10^{-34}
L4b: 3D Kozai–Lidov ($i_0 = 84°$)	Secular $e_{\max} = 0.998865$ ($1 - e_{\min} = 1.14 \times 10^{-3}$)	Artificial orbital flip	5.42×10^{-12} ($\Delta t = 0.25$) 1.39×10^{-16} (BM_6)	5.10×10^{-12} ($\Delta t = 0.25$) 1.76×10^{-28} (BM_6)	Noether $\lvert\Delta L_{z,\mathrm{tot}}\rvert$: 1.57×10^{-14} / 1.77×10^{-32} Semisecular $\Delta(\sqrt{1 - e_{\mathrm{in}}^2} \cos i_{\mathrm{in}}) = 6.01 \times 10^{-2}$

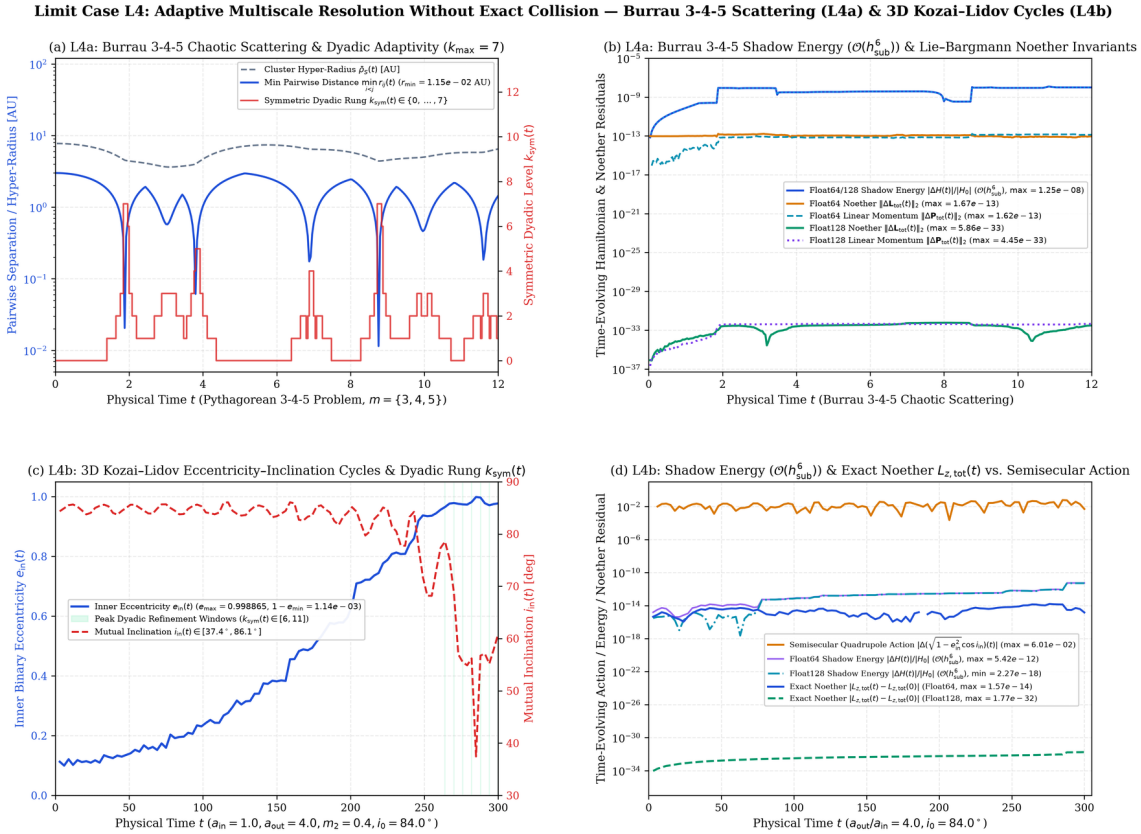


FIGURE 24. **Limit Case L4: Adaptive multiscale resolution without exact collision — Burrau 3-4-5 scattering (L4a) and 3D Kozai–Lidov cycles (L4b). (a)** Burrau $\min_{i<j} r_{ij}(t)$, hyper-radius $\bar{\rho}_S(t)$, and dyadic level $k_{\mathrm{sym}}(t) \in \{0, \ldots, 7\}$. **(b)** Burrau shadow energy oscillation $|\Delta H(t)|/|H_0|$ and Lie–Bargmann invariants $\|\Delta \mathbf{L}_{\mathrm{tot}}(t)\|_2, \|\Delta \mathbf{P}_{\mathrm{tot}}(t)\|_2$. **(c)** 3D Kozai–Lidov eccentricity–inclination cycles ($e_{\max} = 0.998865$) and dyadic level $k_{\mathrm{sym}} \leq 11$. **(d)** Noether $|L_{z,\mathrm{tot}}(t) - L_{z,\mathrm{tot}}(0)|$ and shadow $|\Delta H(t)|/|H_0|$ vs. semisecular Delaunay action $|\Delta(\sqrt{1 - e_{\mathrm{in}}^2} \cos i_{\mathrm{in}})(t)|$.

7.2. **Long-Term Secular Stability, Planetary KAM Torus Preservation, and Historical Celestial Encounters.** The ultimate benchmark of any geometric symplectic integrator in celestial mechanics lies in its capacity to reconcile two antithetical requirements: preserving the global, secular phase-space topology of planetary systems over astronomical timescales (decades to millions of orbits) while simultaneously handling violent, localized close encounters without energy blowup or artificial dissipation. In this section, we present the empirical validation of our normal-cone symplectic architecture across two complementary benchmark series:

(i) **Historical Encounter Benchmarks (§7.2.1): Canonical Few-Body Models of Documented Historical Encounters**, evaluating the solver's adaptive behavior during deep gravitational flybys, sub-Roche tidal disruptions, and atlas chart transitions;

(ii) **Secular Stability Benchmarks (§7.2.2): Long-Term Secular Invariant Preservation and Frequency Analysis**, proving the absence of linear energy drift, the boundedness of the resonant Jovian Laplace angle, and the preservation of KAM invariant tori via Laskar's Numerical Analysis of Fundamental Frequencies (*NAFF*) [37].

7.2.1. *Canonical Few-Body Models of Documented Historical Encounters and Covariant Atlas Gauge Continuity.* To test our architecture under realistic astronomical mass and distance ratios without conflating symplectic integration errors with empirical force-model uncertainties, we formulate in dual precision (`Float64` and 35-digit `Float128` under strictly identical integration parameters) three canonical, unsoftened Newtonian point-mass few-body benchmarks ($N \in \{4, 5\}$, $\varepsilon = 0, d_0 = 0$) calibrated to the characteristic encounter scales $(r_{\min}, v_\infty, a, e)$ of celebrated events from historical ephemerides (intentionally omitting planetary zonal harmonics J_2, non-gravitational cometary outgassing, and hydrodynamical continuum dissipation so that exact conservative Hamiltonian and Lie–Bargmann invariants remain well-defined).

Benchmark H1 : Comet D/1770 L1 (Lexell) Deep Jovian Passage and Covariant Atlas Gauge Continuity ($T^{(\mathrm{PBM4})}_{A\to B}$, Figure 25). Comet Lexell underwent a historic close encounter with Jupiter in 1779, plunging deep inside the Jovian sphere of influence to a perijove of $r_{\min} = 1.4483 \times 10^{-3}$ AU $= 3.031\, R_J$ (well inside Io's orbital radius $a_{\mathrm{Io}} = 5.90\, R_J$). We integrate the 4-body point-mass model (Sun, Jupiter, Earth, Comet Lexell) across $t \in [0, 12.0]$ (≈ 1.91 yr) under a strictly constant macro-step $\Delta t = 0.08$ ($N_{\mathrm{steps}} = 150$ uniform macro-steps, maximum dyadic level $k_{\max} = 11$, zero dyadic saturation, with native solver substep observation enabled for $k_{\mathrm{sym}} \geq 4$) starting outside Jupiter's Hill sphere at $r_{0,J} = 0.7000$ AU $= 1{,}465\, R_J > R_{\mathrm{Hill},J} = 0.3551$ AU $= 743\, R_J$ in the heliocentric Jacobi chart $\mathcal{T}_{\mathrm{helio}} = [((0, 2), 1), 3]$. As tracked in Figure 25a, the Voronoi Hill admissibility criterion ($\gamma = 1.0$, Sections 6.2.2 and 6.5.1) triggers two dynamic topological chart flips:

$$\mathcal{T}_{\mathrm{helio}} = [((0, 2), 1), 3] \overset{\substack{t_1=2.56\\ \longleftrightarrow \\ t_2=8.48}}{} \mathcal{T}_{\mathrm{Jovi}} = [(0, 2), (1, 3)], \tag{7.7}$$

entering the Jovicentric chart at $t_{\mathrm{flip},1} = 2.56$ ($\eta_{\mathrm{Hill}} = 0.5809 < 1.0$), autonomously refining the symmetric dyadic rung along a strictly unimodal staircase $k_{\mathrm{sym}}(t) : 0 \to 1 \to 2 \to 3 \to 5 \to 6 \to 8 \to 11 \to 8 \to 5 \to 3 \to 2 \to 1$ across the deep perijove at $t_{\mathrm{peri}} = 5.4584$ ($r_{\min} = 3.031\, R_J$, resolved with $2^{11} = 2{,}048$ dyadic substeps of size $h_{\mathrm{sub}} = 3.91 \times 10^{-5}$), and flipping back to the heliocentric chart on egress at $t_{\mathrm{flip},2} = 8.48$ ($\eta_{\mathrm{Hill}} = 0.9969$, Jovicentric dwell interval $\Delta t_{\mathrm{Jovi}} = 5.92$).

At each chart transition and dyadic step change, the canonical non-commutative cotangent-lifted gauge connection established in Section 5.5.4 and Section 6.5.3 (Theorems 5.20 and 6.16):

$$\begin{aligned} T^{(\mathrm{PBM4})}_{(A,h_A)\to(B,h_B)} &= \left(\mathcal{Z}_4^{\mathrm{BM4},(B)}(h_B)\right)^{-1} \circ \mathbf{M}_{A\to B} \circ \mathcal{Z}_4^{\mathrm{BM4},(A)}(h_A), \\ \mathcal{Z}_4^{\mathrm{BM4},(\alpha)} &:= \mathcal{Z}_4^{\mathrm{BM4}}(h_\alpha; \mathcal{T}_\alpha), \end{aligned} \tag{7.8}$$

maps the shadow state seamlessly across the chart boundary, where $\mathbf{M}_{A\to B} \in \mathrm{SL}_2(\mathbb{R}) \subset \mathrm{Sp}(6N, \mathbb{R})$ denotes the symplectic Jacobi coordinate transition morphism:

$$\begin{aligned} \tilde{\mathbf{z}}_B &= T^{(\mathrm{PBM4})}_{(A,h_A)\to(B,h_B)}(\tilde{\mathbf{z}}_A), \\ \mathbf{z}_{\mathrm{phys}} &= \mathcal{Z}_4^{\mathrm{BM4},(B)}(h_B)(\tilde{\mathbf{z}}_B) = \mathbf{M}_{A\to B}\big(\mathcal{Z}_4^{\mathrm{BM4},(A)}(h_A)(\tilde{\mathbf{z}}_A)\big). \end{aligned} \tag{7.9}$$

As shown in Figure 25b, the interfacial jump in the comet's specific orbital energy at $t_{\mathrm{flip},1} = 2.56$ is bounded to $|\Delta\mathcal{E}_3|/|\mathcal{E}_{3,0}| = 0.00$ in `Float64` and 4.48×10^{-35} in `Float128` (with total 4-body Hamiltonian jump $|\Delta H_{\mathrm{flip}}|/|H_0| = 2.36 \times 10^{-35}$ in `Float128`). Over the entire encounter $t \in [0, 12.0]$, relative Hamiltonian error remains bounded to $\max_t |\Delta H(t)|/|H_0| = 5.48 \times 10^{-13}$ in `Float64` and 7.13×10^{-17} in `Float128`: in accordance with backward error analysis (Theorem 6.5 and Proposition 5.26), `Float128` eliminates floating-point roundoff across the $k_{\max} = 11$ perijove substeps and isolates the bounded $\mathcal{O}(h_{\mathrm{sub}}^6 + \varepsilon\, h_{\mathrm{sub}}^4)$ shadow-Hamiltonian truncation oscillation at $\Delta t = 0.08$, whereas the exact quadratic Lie–Bargmann Noether invariants (Propositions 5.3 and 6.18) exhibit zero truncation error and reach the raw arithmetic floor $\|\Delta\mathbf{P}_{\mathrm{tot}}\|_2 \le 1.20 \times 10^{-16}$ / 5.57×10^{-38} and $\|\Delta\mathbf{L}_{\mathrm{tot}}\|_2 \le 6.05 \times 10^{-16}$ / 7.74×10^{-35} in `Float64` / `Float128`.

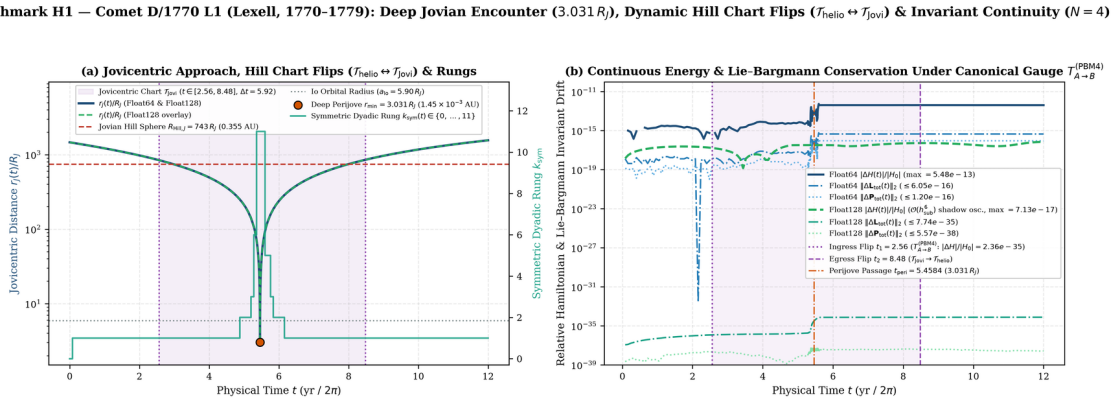


FIGURE 25. **Benchmark H1 — Comet D/1770 L1 (Lexell, 1770–1779): deep Jovian encounter** ($3.031\,R_J$)**, dynamic Hill chart flips, and covariant gauge continuity** ($N = 4$)**. (a)** Jovicentric distance $r_J(t)/R_J$ across $\mathcal{T}_{\mathrm{helio}} \leftrightarrow \mathcal{T}_{\mathrm{Jovi}}$ chart flips ($t = 2.56, 8.48$) and unimodal dyadic rung $k_{\mathrm{sym}}(t) \in \{0, \dots, 11\}$. **(b)** Continuous Hamiltonian error $|\Delta H(t)|/|H_0|$ under $T^{(\mathrm{PBM4})}_{A\to B}$ and Lie–Bargmann invariants $\|\Delta\mathbf{L}_{\mathrm{tot}}\|_2, \|\Delta\mathbf{P}_{\mathrm{tot}}\|_2$ (`Float64` and `Float128`).

Benchmark H2 : Comet D/1993 F2 (Shoemaker–Levy 9) Sub-Roche Tidal Disruption and Synchronous Supernode Promotion (Figure 26). During its July 7, 1992 perijove pass, Comet Shoemaker–Levy 9 penetrated deep inside Jupiter's fluid Roche limit ($r_{\mathrm{Roche}} = 2.45\,R_J = 1.1708 \times 10^{-3}$ AU). We model this regime via a 5-body point-mass system (Sun, Jupiter, and $K = 3$ self-gravitating progenitor fragments $\{2, 3, 4\}$ of mass $m_f = 10^{-11} M_\odot$ separated by $\delta r_0 = 2.0 \times 10^{-5}$ AU) starting at $r_{0,J} = 0.0120$ AU $= 25.11\,R_J$ across $N_{\mathrm{steps}} = 160$ macro-steps ($\Delta t = 1.8 \times 10^{-4}$, $t_{\max} = 0.0288 > t_{\mathrm{peri}} = 0.02178$, maximum dyadic level $k_{\max} = 4$, zero saturation) in both `Float64` and `Float128`. Figure 26a tracks both the Jovicentric distance $r_J(t)/R_J$ and the dimensionless cubic tidal force ratio:

$$\Lambda_S(t) = \frac{\|\nabla W^{\mathrm{screen}}_{\mathrm{apex}}\|}{\|\nabla H_{\mathrm{leaf}}\|} \approx \frac{M_J}{3M_S}\Big(\frac{\bar\rho_S(t)}{r_J(t)}\Big)^3 = \frac{1}{3}\,\eta_S(t)^3, \tag{7.10}$$

where $\eta_S = \bar\rho_S / R_{\mathrm{Hill}}(S)$ denotes the linear Hill ratio of Section 4.3.2.

Initially outside the Roche zone ($\Lambda_S(0) = 0.0267 < \Lambda_{\text{crit}} = 0.25$), the progenitor cluster evolves as standard binary leaves until $\Lambda_S(t)$ crosses the Roche disruption threshold $\Lambda_{\text{crit}} = 0.25$, dynamically promoting $\{2, 3, 4\}$ into a synchronous supernode across 84/160 steps (canonical sub-Roche tidal Channel A, Section 4.3.2). At the sub-Roche perijove $t_{\text{peri}} = 0.02178$, the cluster reaches $r_{\min} = 6.3839 \times 10^{-4}$ AU $= 1.336\,R_J < 2.45\,R_J$ with $\Lambda_S^{\max} = 16{,}690$ ($\eta_S^{\max} = 36.86$, unimodal symmetric dyadic rung pyramid $k_{\text{sym}} : 0 \to 1 \to 2 \to 3 \to 4 \to 3 \to 2 \to 1 \to 0$). As shown in Figure 26b–c, differential Jovian tidal shear stretches the fragment chain into the "string-of-pearls" configuration with span ratio $S(t)/S_0 = \|\mathbf{q}_4(t) - \mathbf{q}_2(t)\|_2/S_0$ peaking at 4.61× just after perijove and reaching 3.82× at $t_{\max} = 0.0288$.

In Figure 26c, the `Float128` energy curve starts at $\sim 10^{-21}$ during the outer approach (where `Float64` sits at the $\sim 10^{-15}$ IEEE 754 roundoff floor) and rises smoothly to coincide with `Float64` at perijove ($\max_t |\Delta H(t)|/|H_0| = 3.99 \times 10^{-15}$ in `Float64` and 4.40×10^{-15} in `Float128`), reflecting the reversible $\mathcal{O}(h_{\text{sub}}^6)$ shadow-Hamiltonian truncation oscillation under extreme sub-Roche tidal shear ($\Lambda_S^{\max} = 16{,}690$ at $h_{\text{sub}} = \Delta t/2^4 = 1.125 \times 10^{-5}$), whereas the exact Lie–Bargmann Noether invariants remain unaffected by tidal truncation at $\|\Delta \mathbf{L}_{\text{tot}}\|_2 \le 5.64 \times 10^{-18}$ / 1.10×10^{-35} and $\|\Delta \mathbf{P}_{\text{tot}}\|_2 \le 2.89 \times 10^{-18}$ / 1.19×10^{-37} in `Float64` / `Float128`.

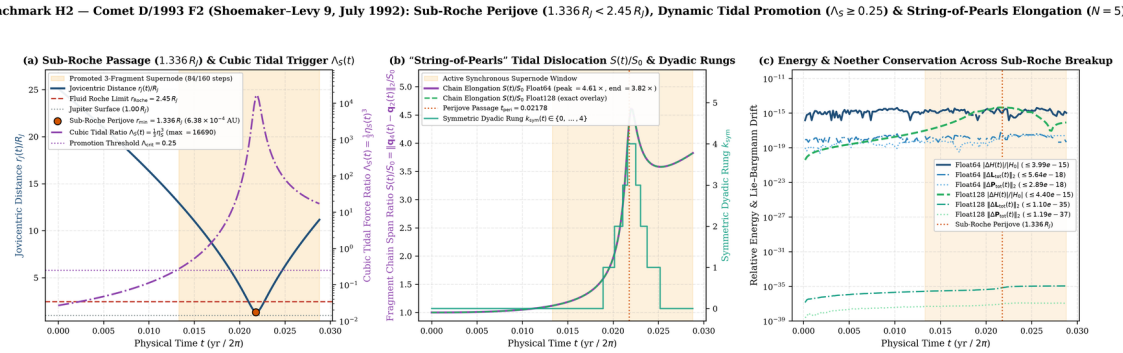


FIGURE 26. **Benchmark H2 — Comet D/1993 F2 (Shoemaker–Levy 9, July 1992): sub-Roche perijove ($1.336\,R_J < 2.45\,R_J$), dynamic tidal promotion ($\Lambda_S \ge 0.25$), and string-of-pearls elongation ($N = 5$).** **(a)** Jovicentric distance $r_J(t)/R_J$ and cubic tidal force ratio $\Lambda_S(t) = \frac{1}{3}\eta_S(t)^3$ ($\Lambda_S^{\max} = 16{,}690$). **(b)** Fragment chain span ratio $S(t)/S_0$ (4.61× peak) and dyadic rungs $k_{\text{sym}}(t) \in \{0, \ldots, 4\}$. **(c)** Shadow-Hamiltonian oscillation $|\Delta H(t)|/|H_0|$ and Lie–Bargmann invariants (`Float64` and `Float128`).

Benchmark H3 : Asteroid (99942) Apophis 2029 Close Earth Flyby, Aten → Apollo Deflection, and Full-Flyby Palindromic Reversibility (Figure 27). On April 13, 2029, asteroid (99942) Apophis will pass inside Earth's geostationary satellite belt ($r_{\text{GEO}} = 6.61\,R_\oplus$). We integrate the 4-body Sun–Earth–Moon–Apophis point-mass model across $N_{\text{steps}} = 80$ macro-steps ($\Delta t = 2.5 \times 10^{-4}$, $t_{\max} = 0.0200 > t_{\text{peri}} = 0.00950$) in both `Float64` and `Float128` (Figure 27). Approaching on its pre-flyby Aten-class orbit ($a_{\text{pre}} = 0.9224$ AU < 1.0 AU, $e_{\text{pre}} = 0.219$), Apophis grazes perigee at $r_{\min} = 2.5480 \times 10^{-4}$ AU $= 5.976\,R_\oplus \approx 38{,}115$ km at $t_{\text{peri}} = 0.00950$ (Figure 27a) and is deflected outward by Earth's trailing-side gravity assist into a post-flyby Apollo-class orbit ($a_{\text{post}} = 1.1163$ AU > 1.0 AU, $e_{\text{post}} = 0.217$), producing a physical semi-major axis jump of $\Delta a = a_{\text{post}} - a_{\text{pre}} = +0.1939$ AU > 0 (Figure 27b).

Across the bilateral pericenter guard $|t_{\text{peri}}(t)| \le 2\,\Delta t_{\text{macro}}$ (Definitions 5.23 and 6.8), the symmetric dyadic selector (Propositions 5.22 and 6.7):

$$k_{\text{sym}}(\mathbf{z}_n, \Delta t) = \max\Big(k(\mathbf{z}_n),\, k\big(\Phi_{\Delta t}^{(0)}(\mathbf{z}_n)\big)\Big), \qquad k_{\text{sym}} : 0 \to 1 \to 2 \to 3 \to 2 \to 1 \to 0,$$

climbs along the unimodal pyramid peaking at $k_{\max} = 3$ at perigee (step $m = 38$, Figure 27c), bounding the forward-flyby Hamiltonian excursion to $\max_t |\Delta H(t)|/|H_0| = 3.33 \times 10^{-14}$ in `Float64` and 2.95×10^{-22} ($\mathcal{O}(h^6_{\text{sub}})$ shadow oscillation) in `Float128` (with Noether conservation $\|\Delta \mathbf{L}_{\text{tot}}\|_2 \leq 5.12 \times 10^{-20}$ / 6.42×10^{-39}).

Executing a full-flyby forward–backward reversibility test $\Phi^{N_h}_{-\Delta t} \circ \Phi^{N_h}_{+\Delta t}$ across perigee ($N_h \in \{20, 40, 60, 80\}$ steps, Figure 27c–d) confirms exact point-by-point palindromic dyadic sequence matching $k_{\text{fwd}}(m) \equiv k_{\text{bwd}}(N-1-m)$ in both `Float64` and `Float128` and annihilates the conservative shadow-Hamiltonian oscillation upon returning to $t = 0$, yielding 80-step return position error $\|\Delta \mathbf{q}_{\text{FB}}\|_2 = 1.72 \times 10^{-16}$ AU in `Float64` and 3.28×10^{-33} AU in `Float128`, and return energy error $|\Delta H_{\text{FB}}|/|H_0| = 0.0$ across all four horizons in `Float64` and 8.46×10^{-33} in `Float128`.

Python A.2 : `{benchmarks/run, figures/plot}_generator_04_*.py` [Float64 / Float128]

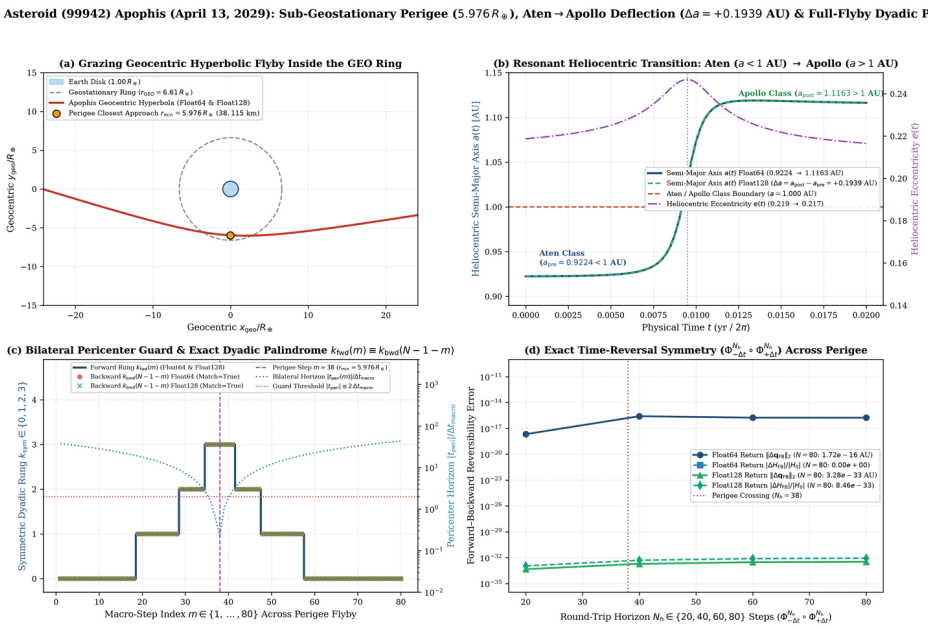


FIGURE 27. **Benchmark H3 — Asteroid (99942) Apophis (April 13, 2029): sub-geostationary perigee ($5.976\, R_\oplus$), Aten → Apollo deflection, and full-flyby dyadic palindrome ($N = 4$). (a)** Geocentric hyperbolic trajectory inside the geostationary belt ($r_{\text{GEO}} = 6.61\, R_\oplus$). **(b)** Heliocentric osculating $a(t)$ and $e(t)$ ($\Delta a = +0.1939$ AU). **(c)** Bilateral perigee horizon $|t_{\text{peri}}|/\Delta t_{\text{macro}} \leq 2$ and palindromic dyadic rungs $k_{\text{fwd}}(m) \equiv k_{\text{bwd}}(N-1-m)$ ($k_{\max} = 3$). **(d)** Multi-horizon round-trip reversibility error $\Phi^{N_h}_{-\Delta t} \circ \Phi^{N_h}_{+\Delta t}$ ($N_h \in \{20, 40, 60, 80\}$).

7.2.2. *Long-Term Secular Stability, 9-Generator Lie–Bargmann Metrology, Laplace 4:2:1 Resonance, and Laskar NAFF Frequency Confinement.* Complementing the localized, high-eccentricity close encounters of Section 7.2.1, the second benchmark series evaluates long-term secular stability under canonical Voronoi chart admissibility ($\gamma = 1.0$, $n_{\text{flips}} = 0$) and active adaptive dyadic substepping (0 saturation events) across all five symplectic splitting and processed integrators ($\mathcal{S}_2$ with $s_{\text{eval}} = 1$, $\mathcal{Y}_4$ with $s_{\text{eval}} = 3$, bare $\text{BM}^{(7)}_4$ with $s_{\text{eval}} = 6$, homologically processed $\text{PBM}_4(\mathcal{Z}^{\text{BM4}}_4)$ with $s_{\text{eval}} = 6$, and bare $\text{BM}^{(11)}_6$ with $s_{\text{eval}} = 10$ force evaluations per substep).

Whereas the four bare splitting schemes ($\mathcal{S}_2, \mathcal{Y}_4, \text{BM}^{(7)}_4, \text{BM}^{(11)}_6$) evolve on their native bare symplectic manifolds, the processed integrator $\text{PBM}_4(\mathcal{Z}^{\text{BM4}}_4)$ evolves natively in the

TABLE 7. **Certified dual-precision (`Float64` and 35-digit `Float128`) quantitative invariants and observables across documented historical astronomical encounters (§7.2.1; $\gamma = 1.0, \varepsilon = 0, d_0 = 0$).**

Historical Benchmark	Closest Approach $r_{\min}$	Max Rung $k_{\max}$	Topological / Tidal Regime	Max $\lvert\Delta H/H_0\rvert$ (`Float64` / `Float128`)	Noether $\lVert\Delta \mathbf{L}_{\text{tot}}\rVert_2$ (`Float64` / `Float128`)	Certified Physical & Algebraic Observables
H1: Comet Lexell (1770–1779, $N = 4$)	$3.031\,R_J$ (1.4483×10^{-3} AU)	11	2 Hill chart flips $\mathcal{T}_{\text{helio}} \leftrightarrow \mathcal{T}_{\text{Jovi}}$ ($t = 2.56,\ 8.48$)	5.48×10^{-13} / 7.13×10^{-17}	6.05×10^{-16} / 7.74×10^{-35}	Flip jump under $T^{(\text{PBM4})}_{A\to B}$: $\lvert\Delta\mathcal{E}_3\rvert/\lvert\mathcal{E}_{3,0}\rvert = 0.00$ (`F64`), $\lvert\Delta H_{\text{flip}}\rvert/\lvert H_0\rvert = 2.36 \times 10^{-35}$ (`F128`)
H2: Shoemaker–Levy 9 (July 1992, $N = 5$)	$1.336\,R_J < 2.45\,R_J$ (6.3839×10^{-4} AU)	4	Sub-Roche promotion $\Lambda_S(t) \geq 0.25$ (84/160 steps)	3.99×10^{-15} / 4.40×10^{-15}	5.64×10^{-18} / 1.10×10^{-35}	$\Lambda_S(0) = 0.0267 \to \Lambda_S^{\max} = 16{,}690$, string-of-pearls span S/S_0: 4.61× peak (3.82× at egress)
H3: (99942) Apophis (April 2029, $N = 4$)	$5.976\,R_\oplus < 6.61\,R_\oplus$ (2.5480×10^{-4} AU)	3	Bilateral perigee guard $\lvert t_{\text{peri}}\rvert \leq 2\,\Delta t_{\text{macro}}$ (80 macro-steps)	3.33×10^{-14} / 2.95×10^{-22} (FB: 0.0 / 8.46×10^{-33})	5.12×10^{-20} / 6.42×10^{-39}	Aten (0.9224 AU) → Apollo (1.1163 AU), $\Delta a = +0.1939$ AU, exact dyadic palindrome, $\lVert\Delta\mathbf{q}_{\text{FB}}\rVert_2 = 1.72 \times 10^{-16}$ / 3.28×10^{-33} AU

shadow manifold with non-destructive physical coordinate readout at observation epochs and automatic covariant gauge transport across dyadic step-size junctions $h_A \to h_B$:

$$\mathbf{z}_{\text{phys}}(t_k) = \mathcal{Z}_4^{\text{BM4}}(h_k)(\tilde{\mathbf{z}}_k), \qquad T^{(\text{PBM4})}_{(A,h_A)\to(B,h_B)} = \left(\mathcal{Z}_4^{\text{BM4},(B)}(h_B)\right)^{-1} \circ \mathbf{M}_{A\to B} \circ \mathcal{Z}_4^{\text{BM4},(A)}(h_A).$$

Applying $T^{(\text{PBM4})}_{(A,h_A)\to(B,h_B)}$ exclusively to $\text{PBM}_4(\mathcal{Z}_4^{\text{BM4}})$ is essential: injecting $\mathcal{Z}_4^{\text{BM4}}$ gauge kicks into a bare integrator such as $\text{BM}_6^{(11)}$ across dyadic junctions would perturb its bare manifold by uncompensated $\mathcal{O}(\varepsilon h^4)$ impulses. Both conservative point-mass benchmarks ($N \in \{4, 5\}$, $\varepsilon = 0, d_0 = 0$) are executed over their full secular horizon in IEEE-754 `Float64` and paired with equal-parameter 35-digit `Float128` integrations to separate bounded $\mathcal{O}(h^p)$ shadow-Hamiltonian truncation oscillations from $\mathcal{O}(\epsilon_{\text{mach}}\sqrt{s_{\text{eval}}\,N_{\text{steps}}})$ floating-point roundoff diffusion on the 9 Galilean Lie–Bargmann Noether invariants (Figures 28–29 and Table 8).

Protocol S1 : Resonant Jovian $4:2:1$ Laplace Satellite System, Methodological Libration Ablation, and Dual-Precision Lie–Bargmann Metrology ($N = 4$, Figure 28). We model the four-body Jovian Galilean system as a conservative Newtonian point-mass hierarchy comprising Jupiter ($m_0 = 1.0$) and the three inner moons Io ($m_1 = 4.70 \times 10^{-5}, a_1 = 1.0$), Europa ($m_2 = 2.53 \times 10^{-5}, a_2 = 1.5874$), and Ganymede ($m_3 = 7.80 \times 10^{-5}, a_3 = 2.5198$). To avoid exciting artificial free-eccentricity transients, the system is initialized at the forced resonant Laplace apsidal equilibrium ($e_{1,\text{forced}} = 0.0041, \varpi_1 = 0$; $e_{2,\text{forced}} = 0.0094, \varpi_2 = \pi$; $e_{3,\text{forced}} = 0.0006, \varpi_3 = 0$) in a single Jovicentric Jacobi chart ($n_{\text{flips}} = 0$) and integrated over 200 Io orbits ($T_{\max} = 1{,}256.75$ rad, macro-step $\Delta t = 0.25 \approx T_{\text{Io}}/25.13$, $N_{\text{steps}} = 5{,}027$, observation stride 5, where the symmetric dyadic scheduler selects $k_{\text{sym}} \equiv 3$, i.e., $h_{\text{sub}} = \Delta t/2^3 = 0.03125$ with 0 saturation events), tracking three-body resonant locking via the osculating mean-longitude critical angle:

$$\theta_{\text{Lap}}(t) = \left(\lambda_1(t) - 3\lambda_2(t) + 2\lambda_3(t)\right) \bmod 360^\circ \approx 180^\circ, \qquad \lambda_i(t) = \varpi_i(t) + M_i(t). \tag{7.11}$$

The four panels of Figure 28 establish three distinct physical and numerical properties:

- *Shadow-Manifold Telescoping, `Float64` vs. `Float128` Time Series, and Resonant Phase Hierarchy (Panels 28a–b)*: Under adaptive dyadic substepping ($k_{\text{sym}} = 3$, $h_{\text{sub}} = 0.03125$, 40,216 substeps over 200 Io orbits), the $2^3 = 8\times$ step reduction prevents the second-order Strang splitting $\mathcal{S}_2$ ($\max\lvert\Delta H/H_0\rvert = 3.98 \times 10^{-7}$, RMS $= 2.47 \times 10^{-7}$) from breaking the resonance into full 360° circulation; however, because its $\mathcal{O}(h_{\text{sub}}^2)$ shadow Hamiltonian perturbation ($h_{\text{sub}}^2 \approx 9.77 \times 10^{-4}$) shifts the modified Keplerian mean motions $n_i = \partial\widetilde{H}/\partial\Lambda_i$ slightly off exact $4:2:1$ commensurability, $\mathcal{S}_2$ still exhibits a $+7^\circ$ secular phase drift from 180° to 187° ($\theta_{\text{Lap}} = 183.41^\circ \pm 3.53^\circ$, Figure 28b, top).

  By contrast, for the fourth-order Yoshida scheme $\mathcal{Y}_4$ ($\max\lvert\Delta H/H_0\rvert = 1.98 \times 10^{-10}$), the 8× dyadic reduction compresses its $\mathcal{O}(h_{\text{sub}}^4)$ shadow frequency error by $8^4 = 4{,}096\times$, completely eliminating the secular phase drift observed at unsubstepped $k = 0$ and locking $\mathcal{Y}_4$ onto the exact resonant libration curve $\theta_{\text{Lap}}(t) = 179.85^\circ \pm 0.80^\circ$ alongside $\text{BM}_4^{(7)}$ (6.96×10^{-13}), $\text{PBM}_4(\mathcal{Z}_4^{\text{BM4}})$, and $\text{BM}_6^{(11)}$. Plotting the logarithmic

phase residual $|\theta_{\mathrm{Lap}}(t) - \theta_{\mathrm{Lap}}^{\mathrm{BM6}}(t)|$ in the bottom sub-panel of Figure 28b resolves the underlying six-order-of-magnitude accuracy hierarchy across the integrators: the maximum resonant angle error drops by 1,445× from $\mathcal{S}_2$ (6.13°) to $\mathcal{Y}_4$ (4.24×10^{-3}°) and by 730,000× down to 8.78×10^{-6}° ($\mathrm{BM}_4^{(7)}$) and 8.40×10^{-6}° (PBM_4), directly demonstrating KAM symplectic phase conjugacy ($\mathrm{PBM}_4 \equiv \mathrm{BM}_4^{(7)}$) on the resonant torus.

In energy (Figure 28a, plotting both `Float64` solid and 35-digit `Float128` dashed time series over the full 200-orbit horizon), the `Float64` and `Float128` trajectories of $\mathcal{S}_2$, $\mathcal{Y}_4$, and $\mathrm{BM}_4^{(7)}$ superimpose (3.98×10^{-7}, 1.98×10^{-10}, and 6.96×10^{-13} vs. 6.67×10^{-13}), whereas in `Float64` PBM_4 and $\mathrm{BM}_6^{(11)}$ encounter the IEEE-754 Brouwer roundoff floor (max $= 1.20 \times 10^{-13}$, RMS $= 5.77 \times 10^{-14}$, 5.80× max / 7.47× RMS gain for PBM_4, and max $= 8.14 \times 10^{-14}$, RMS $= 2.88 \times 10^{-14}$ for $\mathrm{BM}_6^{(11)}$); in 35-digit `Float128`, roundoff is eliminated and the dashed curves stay on their true periodic shadow-Hamiltonian bands across all 200 Io orbits (PBM_4: max $= 3.80 \times 10^{-14}$, RMS $= 1.25 \times 10^{-14}$, i.e., a 17.56× **max / 32.62× RMS** shadow gain over $\mathrm{BM}_4^{(7)}$; $\mathrm{BM}_6^{(11)}$: max $= 1.90 \times 10^{-18}$, RMS $= 1.02 \times 10^{-18}$).

- *Methodological Ablation of Readout Coordinates and Initial Conditions (Panel 28c)*: The two-tier layout of Figure 28c under $\mathrm{PBM}_4(\mathcal{Z}_4^{\mathrm{BM4}})$ separates two classical metrological artifacts when measuring Equation (7.11): (i) in the top zoomed sub-panel ($[174.8°, 185.2°]$), substituting true polar angles $\vartheta_i = \mathrm{atan2}(y_i, x_i)$ for osculating mean longitudes $\lambda_i = \varpi_i + M_i$ superimposes the short-period equation-of-the-center modulation $\vartheta_i - \lambda_i = 2e_i \sin M_i + \mathcal{O}(e_i^2)$, inflating the apparent half-amplitude 5.1× from ±0.80° to ±4.05°; and (ii) in the bottom sub-panel, initializing the moons on unforced circular orbits ($e_i(0) = 0$) instead of the forced Laplace equilibrium ($10^3 e_i(t) \approx (4.1, 9.4, 0.6)$ plotted on the right axis) displaces the trajectory away from the resonant fixed point and excites a 39.7× larger free-eccentricity libration of ±31.78°.
- *Paired Dual-Precision (`Float64` vs. `Float128`) Energy Truncation and 9-Generator Lie–Bargmann Metrology (Panel 28d)*: Comparing all five integrators over the full 200-orbit equal-parameter dual-precision benchmark ($N_{\mathrm{steps}} = 5{,}027$ at $\Delta t = 0.25, k_{\mathrm{sym}} = 3$) in `Float64` (solid columns) and 35-digit `Float128` (hatched columns) directly illustrates the structural distinction between shadow-Hamiltonian truncation and exact Noether conservation. For $\mathcal{S}_2$, $\mathcal{Y}_4$, and $\mathrm{BM}_4^{(7)}$, the purple energy columns $|\Delta H|/|H_0|$ have identical height in `Float64` and `Float128` ($\mathcal{S}_2$: 3.98×10^{-7}; $\mathcal{Y}_4$: 1.98×10^{-10}; $\mathrm{BM}_4^{(7)}$: 6.96×10^{-13} vs. 6.67×10^{-13}), while PBM_4 drops from 1.20×10^{-13} to 3.80×10^{-14} and $\mathrm{BM}_6^{(11)}$ drops from its `Float64` roundoff ceiling (8.14×10^{-14}) down to its true $\mathcal{O}(h_{\mathrm{sub}}^6)$ shadow level (1.90×10^{-18}) in `Float128`.

  Conversely, because all leaf and apex sub-flows depend exclusively on Euclidean pairwise distances $r_{ij} = \|\mathbf{q}_i - \mathbf{q}_j\|_2$ (Propositions 5.3 and 6.18), the 9 Galilean Lie–Bargmann Noether generators ($\mathbf{P}_{\mathrm{tot}}, \mathbf{L}_{\mathrm{tot}}, \mathbf{G}_{\mathrm{Gal}}$) have identically zero truncation error at any step size $h > 0$: their residual drift drops by $\sim$ 18–20 orders of magnitude from `Float64` (solid columns: $\|\Delta\mathbf{P}\|_2/M_{\mathrm{tot}} \le 7.16 \times 10^{-18}$, $\|\Delta\mathbf{L}\|_2/\|\mathbf{L}_0\|_2 \le 5.28 \times 10^{-14}$, $\|\Delta\mathbf{G}\|_2/M_{\mathrm{tot}} \le 5.09 \times 10^{-15}$) down to the 35-digit `Float128` arithmetic floor (hatched columns: $\|\Delta\mathbf{P}\|_2/M_{\mathrm{tot}} \in [1.55 \times 10^{-38}, 7.83 \times 10^{-38}]$, $\|\Delta\mathbf{L}\|_2/\|\mathbf{L}_0\|_2 \in [3.74 \times 10^{-32}, 4.15 \times 10^{-31}]$, and $\|\Delta\mathbf{G}\|_2/M_{\mathrm{tot}} \le 3.55 \times 10^{-34}$).

Python A.2 : `{benchmarks/run, figures/plot}_generator_05_*.py` [Float64 / Float128]

Protocol S2 : Inner Solar System Secular Stability, Covariant Shadow Telescoping Across 264 Dyadic Junctions ($\propto t^0$) vs. Brouwer Noether Diffusion ($\propto t^{1/2}$), and Authentic Laskar NAFF Frequency Metrology ($N = 5$, Figure 29). We integrate a five-body Newtonian point-mass model of the inner Solar System comprising

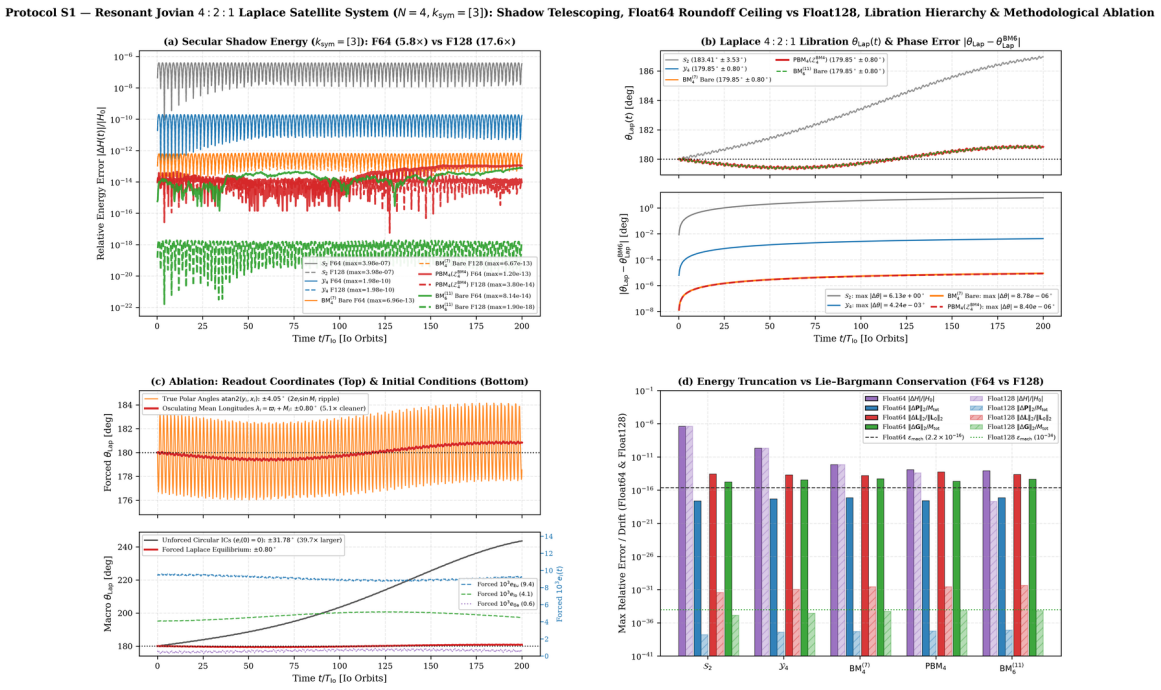


FIGURE 28. **Protocol S1: Resonant Jovian Galilean** $4:2:1$ **Laplace satellite system, dual-precision time series, resonant phase hierarchy, and methodological ablation** ($N = 4$, 200 **Io orbits,** $\Delta t = 0.25, k_{\mathrm{sym}} \equiv 3$**). (a)** Relative Hamiltonian error $|\Delta H(t)|/|H_0|$ in `Float64` (solid) and `Float128` (dashed). **(b)** Mean-longitude Laplace angle $\theta_{\mathrm{Lap}}(t) = \lambda_1 - 3\lambda_2 + 2\lambda_3$ (top) and phase residual $|\theta_{\mathrm{Lap}}(t) - \theta^{\mathrm{BM6}}_{\mathrm{Lap}}(t)|$ (bottom). **(c)** Readout coordinate ablation (top) and circular-vs.-forced initialization ablation (bottom). **(d)** `Float64` vs. `Float128` energy and 9-generator Lie–Bargmann residuals.

the Sun ($m_0 = 1.0$) and the four terrestrial planets Mercury ($m_1 = 1.6601 \times 10^{-7}, a_1 = 0.3871$ AU$, e_1 = 0.2056$), Venus ($m_2 = 2.4478 \times 10^{-6}, a_2 = 0.7233$ AU$, e_2 = 0.0068$), Earth–Moon ($m_3 = 3.0404 \times 10^{-6}, a_3 = 1.0000$ AU$, e_3 = 0.0167$), and Mars ($m_4 = 3.2272 \times 10^{-7}, a_4 = 1.5237$ AU$, e_4 = 0.0934$) in mutually inclined 3D orbits over $N_{\mathrm{steps}} = 4{,}000$ macro-steps of size $\Delta t = 0.05$ rad ≈ 2.90 days ($T_{\max} = 200.0$ rad $= 31.83$ yr ≈ 132.2 Mercury orbits), recording the physical state at every macro-step ($N_{\mathrm{samples}} = 4{,}001$, i.e., 30.27 samples/Mercury orbit, Figure 29):

- *Heliocentric Atlas Invariance, Covariant Gauge Telescoping Across 264 Dyadic Junctions, and Bounded Shadow-Hamiltonian Plateau ($\propto t^0$, Panels 29a, d)*: Throughout the 31.83-yr integration, the Hill-weighted Delaunay–Jacobi admissibility guard γ_{Hill} at canonical Voronoi threshold $\gamma = 1.0$ prevents spurious heliocentric-to-synodic leaf flips during planetary inferior conjunctions, maintaining $n_{\mathrm{flips}} = 0$ and regular secular eccentricity hodographs $(\Delta h_i, \Delta k_i) = (\Delta(e_i \cos \varpi_i), \Delta(e_i \sin \varpi_i))$ (Figure 29d). Simultaneously, because Mercury's eccentric orbit ($e_1 = 0.2056$) modulates its local dynamical timescale between perihelion and aphelion across each of its ~ 132.2 revolutions, the symmetric dyadic scheduler dynamically switches between $k_{\mathrm{sym}} = 2$ ($h_{\mathrm{sub}} = 0.0125$) and $k_{\mathrm{sym}} = 3$ ($h_{\mathrm{sub}} = 0.00625$), executing 264 **dyadic step-size junctions** (0 saturation events).

At every junction $h_A \to h_B$, the macro-step propagator applies the covariant gauge connection $T^{(\mathrm{PBM4})}_{(A,h_A)\to(A,h_B)} = \big(\mathcal{Z}_4^{\mathrm{BM4},(A)}(h_B)\big)^{-1} \circ \mathcal{Z}_4^{\mathrm{BM4},(A)}(h_A)$, preserving exact shadow-manifold telescoping across step-size transitions: the running RMS relative energy error $\mathrm{RMS}_{[0,t]}(\Delta H/H_0)$ in Figure 29a (shown in both `Float64` solid and `Float128` dashed curves) saturates onto a horizontal periodic plateau ($\propto t^0$), where $\mathrm{PBM}_4(\mathcal{Z}_4^{\mathrm{BM4}})$ reduces the cumulative RMS energy error by 22.42× **in `Float64` and** 27.33× **in `Float128`** over bare $\mathrm{BM}_4^{(7)}$ (8.28×10^{-14} vs. 1.86×10^{-12} in `Float64`, and 6.74×10^{-14} vs. 1.84×10^{-12} in `Float128`; 19.18× **`Float64`** / 22.70× **`Float128`** in maximum error, 1.55×10^{-13} vs. 2.97×10^{-12} in `Float64` and 1.31×10^{-13} vs. 2.96×10^{-12} in `Float128`), while $\mathrm{BM}_6^{(11)}$ reaches RMS $= 1.19\times10^{-14}$ (max $= 3.27\times10^{-14}$) in `Float64` and RMS $= 7.15\times10^{-18}$ (max $= 1.18\times10^{-17}$) in `Float128`. Expressed in physical time units via $\beta_{E,\mathrm{yr}^{-1}} = 2\pi\,\beta_{E,\mathrm{rad}^{-1}}$, the linear least-squares secular energy slope is bounded to:

$$\beta_E(\mathrm{PBM}_4) = \frac{\mathrm{d}}{\mathrm{d}t}\Big(\frac{\Delta H}{H_0}\Big) = +1.05\times10^{-15}\ \mathrm{yr}^{-1}, \qquad \beta_E(\mathrm{BM}_6^{(11)}) = -1.67\times10^{-16}\ \mathrm{yr}^{-1}, \tag{7.12}$$

confirming that covariant gauge telescoping across dyadic step-size transitions eliminates secular energy drift.

- *Unbiased Brouwer Stochastic Diffusion ($\propto t^{1/2}$) and Sub-Stage Arithmetic Scaling on Exact Lie–Bargmann Invariants (Panel 29b)*: In contrast to the Hamiltonian, the 9 Galilean Lie–Bargmann Noether invariants have zero truncation error and isolate pure IEEE-754 floating-point roundoff accumulation. Figure 29b compares the unclamped running-RMS drift of all three invariant families ($\|\Delta\mathbf{L}\|_2/\|\mathbf{L}_0\|_2$ in red, $\|\Delta\mathbf{G}\|_2/M_{\mathrm{tot}}$ in green, and $\|\Delta\mathbf{P}\|_2/M_{\mathrm{tot}}$ in blue) between PBM_4 (solid curves, $s_{\mathrm{eval}} = 6$) and $\mathrm{BM}_6^{(11)}$ (dashed curves, $s_{\mathrm{eval}} = 10$), revealing two structural properties: (i) both schemes occupy the exact same three invariant bands ($\sim 10^{-14}$ for $\Delta\mathbf{L}$, $\sim 10^{-17}$ for $\Delta\mathbf{G}$, and $\sim 10^{-19}$ for $\Delta\mathbf{P}$, dropping in 35-digit `Float128` to $\|\Delta\mathbf{L}\|_2/\|\mathbf{L}_0\|_2 \le 3.84\times10^{-32}$ and $\|\Delta\mathbf{P}\|_2/M_{\mathrm{tot}} \le 6.36\times10^{-39}$ over the full 4,000-step integration), where the four- to five-order-of-magnitude suppression of $\|\Delta\mathbf{P}\|_2/M_{\mathrm{tot}}$ and $\|\Delta\mathbf{G}\|_2/M_{\mathrm{tot}}$ below $\epsilon_{\mathrm{mach}} = 2.22\times10^{-16}$ stems from the decoupling of the root barycenter node in the Jacobi tree and the weighting of planetary velocity roundoff by the planet-to-Sun mass ratios $m_i/M_{\mathrm{tot}} \sim 10^{-6}$; and

  (ii) all curves follow Brouwer's unbiased random-walk scaling [28]:

$$\sigma_{\mathrm{Noether}}(t) \propto \epsilon_{\mathrm{mach}}\sqrt{s_{\mathrm{eval}}\,n_{\mathrm{steps}}} \propto t^{1/2},$$

  with $\mathrm{BM}_6^{(11)}$ reaching $\max\|\Delta\mathbf{L}\|_2/\|\mathbf{L}_0\|_2 = 1.45\times10^{-14}$, $\max\|\Delta\mathbf{G}\|_2/M_{\mathrm{tot}} = 1.55\times10^{-17}$, and $\max\|\Delta\mathbf{P}\|_2/M_{\mathrm{tot}} = 1.71\times10^{-19}$ (PBM_4: 1.33×10^{-14}, 2.27×10^{-17}, 1.68×10^{-19}; $\mathrm{BM}_4^{(7)}$: 2.19×10^{-14}, 1.94×10^{-17}, 1.53×10^{-19}; $\mathcal{S}_2$: 9.05×10^{-15}, 1.20×10^{-17}, 8.26×10^{-20}).
- *Authentic Laskar NAFF Frequency Metrology and KAM Symplectic Conjugacy Invariance (Panel 29c)*: To quantify phase-space frequency preservation without synthetic proxies, we apply Laskar's Numerical Analysis of Fundamental Frequencies (*NAFF*) with order-$p = 3$ Hanning filtering (Section 7.1.1) directly to Mercury's complex heliocentric orbital signal ($N_{\mathrm{samples}} = 4{,}001$, 30.27 samples/orbit, well above the Nyquist threshold):

$$z_{\mathrm{orb}}(t_k) = \big(x_1(t_k) - x_0(t_k)\big) + i\big(y_1(t_k) - y_0(t_k)\big),$$

  against a 2×-finer dyadic $\mathrm{BM}_6^{(11)}$ reference trajectory ($\Delta t_{\mathrm{ref}} = 0.025$ rad, 8,000 macro-steps, $\nu_{\mathrm{ref}} = 4.15210957695$ rad/time unit). Figure 29c reports three complementary observables: the full-horizon fundamental frequency error $|\nu_{\mathrm{NAFF}} - \nu_{\mathrm{ref}}|/\nu_{\mathrm{ref}}$, the complex waveform L^2 error $\|z_{\mathrm{orb}} - z^{\mathrm{ref}}_{\mathrm{orb}}\|_2/\|z^{\mathrm{ref}}_{\mathrm{orb}}\|_2$, and the two-window numerical

frequency drift between $W_1 = [0, T_{\max}/2]$ and $W_2 = [T_{\max}/2, T_{\max}]$ after subtracting the true physical secular planetary precession shift $\Delta\nu^{\text{phys}}_{1\to2}/\nu_1 = 1.78 \times 10^{-8}$:

$$\frac{\delta\nu^{\text{num}}_{1\to2}}{\nu_{\text{ref}}} = \frac{\left|(\nu_{W_2} - \nu_{W_1}) - (\nu^{\text{ref}}_{W_2} - \nu^{\text{ref}}_{W_1})\right|}{\nu_{\text{ref}}}. \tag{7.13}$$

Across the splitting hierarchy under adaptive dyadic substepping ($k_{\text{sym}} \in \{2, 3\}$), the fundamental frequency error drops by 2,120× from $\mathcal{S}_2$ (7.85×10^{-10}, $\delta\nu^{\text{num}}_{1\to2}/\nu_{\text{ref}} = 1.17 \times 10^{-8}$, $L^2 = 2.35 \times 10^{-6}$) and from $\mathcal{Y}_4$ (2.00×10^{-12}, improved by 166× over unsubstepped $k = 0$, $\delta\nu^{\text{num}}_{1\to2}/\nu_{\text{ref}} = 4.17 \times 10^{-12}$, $L^2 = 2.36 \times 10^{-9}$) right down to the ~ 3.7–4.4×10^{-13} spectral resolution floor of the 4,001-sample order-3 Hanning window on $\text{BM}^{(7)}_4$ (4.40×10^{-13}, $\delta\nu^{\text{num}}_{1\to2}/\nu_{\text{ref}} = 1.96 \times 10^{-13}$, $L^2 = 7.21 \times 10^{-11}$), $\text{PBM}_4(\mathcal{Z}^{\text{BM4}}_4)$ (3.70×10^{-13}, $\delta\nu^{\text{num}}_{1\to2}/\nu_{\text{ref}} = 9.90 \times 10^{-14}$, $L^2 = 3.78 \times 10^{-11}$), and $\text{BM}^{(11)}_6$ (4.23×10^{-13}, $\delta\nu^{\text{num}}_{1\to2}/\nu_{\text{ref}} = 6.67 \times 10^{-14}$, $L^2 = 6.83 \times 10^{-11}$), with:

$$\frac{|\nu_{\text{NAFF}}(\text{PBM}_4) - \nu_{\text{NAFF}}(\text{BM}^{(7)}_4)|}{\nu_{\text{ref}}} = 7.02 \times 10^{-14}. \tag{7.14}$$

This near-identity directly reflects the **KAM symplectic conjugacy property** [28, 37]: because the processed propagator

$$\hat{\Phi}_h = \mathcal{Z}^{\text{BM4}}_4(h) \circ \mathcal{S}_h \circ \left(\mathcal{Z}^{\text{BM4}}_4(h)\right)^{-1}$$

is canonically conjugate to the bare kernel $\mathcal{S}_h$ via the near-identity symplectomorphism $\mathcal{Z}^{\text{BM4}}_4(h)$ and gauge connection $T^{(\text{PBM4})}_{(A,h_A)\to(A,h_B)}$, both maps share identical asymptotic rotation numbers on invariant KAM tori while $\mathcal{Z}^{\text{BM4}}_4(h)$ deforms the shadow torus into 22.42× (`Float64`) and 27.33× (`Float128`) closer RMS alignment with the constant-energy hypersurface.

Python A.2 : `{benchmarks/run, figures/plot}_generator_05_*.py` [Float64 / Float128]

TABLE 8. **Certified quantitative long-term secular stability, 9-generator Lie–Bargmann metrology, and Laskar NAFF frequency metrics under canonical Voronoi admissibility ($\gamma = 1.0$) and active dyadic substepping (§7.2.2).** Protocol S1 integrates the 4-body Jovian 4:2:1 Laplace resonance (200 Io orbits, $k_{\text{sym}} \equiv 3$), and Protocol S2 integrates the 5-body Inner Solar System (31.83 yr, 264 dyadic junctions, 0 synodic flips).

Integrator	S1 Laplace Error $\max\lvert\Delta H/H_0\rvert$ **F64 / F128** (**RMS F64 / F128**, $k = 3$)	S1 Laplace Angle $\theta_{\text{Lap}} = \lambda_1 - 3\lambda_2 + 2\lambda_3$ (Mean Longitudes)	S2 Solar System $\text{RMS}(\Delta H/H_0)$ **F64 / F128** ($\max\lvert\Delta H/H_0\rvert$ **F64 / F128**)	S2 Secular Slope β_E [yr^{-1}] ($2\pi\,\beta_{E,\text{rad}^{-1}}$)	S2 Laskar NAFF Error $\lvert\nu_{\text{NAFF}} - \nu_{\text{ref}}\rvert/\nu_{\text{ref}}$ ($\delta\nu^{\text{num}}_{1\to2}/\nu_{\text{ref}}$)	Lie–Bargmann (`Float64`) $\max\lVert\Delta\mathbf{L}\rVert_2/\lVert\mathbf{L}_0\rVert_2$ (S1 / S2) ($\max\lVert\Delta\mathbf{P}\rVert_2/M_{\text{tot}}$ S1 / S2)
$\mathcal{S}_2$ (Strang, $s = 1$)	3.98×10^{-7} / 3.98×10^{-7} (2.47×10^{-7} / 2.47×10^{-7})	$183.41° \pm 3.53°$ (Librated at $k = 3$)	1.05×10^{-6} / 1.05×10^{-6} (1.79×10^{-6} / 1.79×10^{-6})	$+1.61 \times 10^{-10}$	7.85×10^{-10} (1.17×10^{-8})	2.51×10^{-14} / 9.05×10^{-15} (2.32×10^{-18} / 8.26×10^{-20})
$\mathcal{Y}_4$ (Yoshida, $s = 3$)	1.98×10^{-10} / 1.98×10^{-10} (1.20×10^{-10} / 1.20×10^{-10})	$179.85° \pm 0.80°$ (Locked)	5.67×10^{-10} / 5.67×10^{-10} (9.39×10^{-10} / 9.39×10^{-10})	-6.43×10^{-14}	2.00×10^{-12} (4.17×10^{-12})	1.89×10^{-14} / 1.30×10^{-14} (4.79×10^{-18} / 1.05×10^{-19})
$\text{BM}^{(7)}_4$ (Bare, $s = 6$)	6.96×10^{-13} / 6.67×10^{-13} (4.31×10^{-13} / 4.09×10^{-13})	$179.85° \pm 0.80°$ (Locked)	1.86×10^{-12} / 1.84×10^{-12} (2.97×10^{-12} / 2.96×10^{-12})	-1.31×10^{-15}	4.40×10^{-13} (1.96×10^{-13})	1.49×10^{-14} / 2.19×10^{-14} (7.05×10^{-18} / 1.53×10^{-19})
$\text{PBM}_4(\mathcal{Z}^{\text{BM4}}_4)$ ($s = 6$)	$\mathbf{1.20 \times 10^{-13}}$ / $\mathbf{3.80 \times 10^{-14}}$ ($\mathbf{5.77 \times 10^{-14}}$ / $\mathbf{1.25 \times 10^{-14}}$)	$\mathbf{179.85° \pm 0.80°}$ (Locked)	$\mathbf{8.28 \times 10^{-14}}$ / $\mathbf{6.74 \times 10^{-14}}$ ($\mathbf{1.55 \times 10^{-13}}$ / $\mathbf{1.31 \times 10^{-13}}$)	$\mathbf{+1.05 \times 10^{-15}}$	$\mathbf{3.70 \times 10^{-13}}$ ($\mathbf{9.90 \times 10^{-14}}$, KAM conj.)	$\mathbf{5.28 \times 10^{-14}}$ / $\mathbf{1.33 \times 10^{-14}}$ ($\mathbf{2.49 \times 10^{-18}}$ / $\mathbf{1.68 \times 10^{-19}}$)
$\text{BM}^{(11)}_6$ (Bare, $s = 10$)	8.14×10^{-14} / 1.90×10^{-18} (2.88×10^{-14} / 1.02×10^{-18})	$179.85° \pm 0.80°$ (Locked)	1.19×10^{-14} / 7.15×10^{-18} (3.27×10^{-14} / 1.18×10^{-17})	-1.67×10^{-16}	4.23×10^{-13} (6.67×10^{-14})	2.23×10^{-14} / 1.45×10^{-14} (7.16×10^{-18} / 1.71×10^{-19})

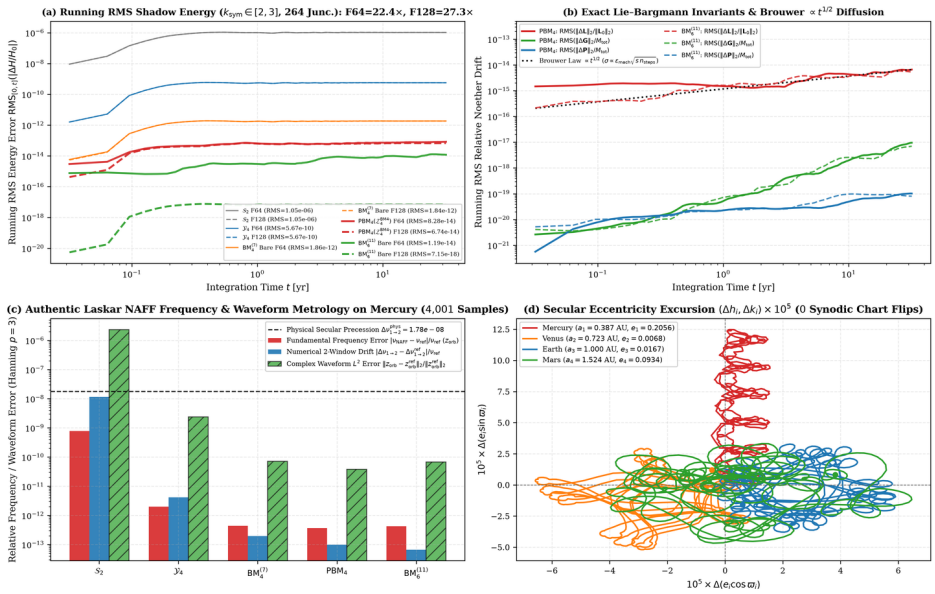


FIGURE 29. **Protocol S2: Inner Solar System secular stability, covariant shadow telescoping across 264 dyadic junctions ($\propto t^0$) vs. Brouwer Noether diffusion ($\propto t^{1/2}$), and authentic Laskar NAFF frequency confinement ($N = 5$, 4,000 macro-steps, 31.83 yr $\approx$ 132.2 Mercury orbits).** **(a)** Running RMS energy error $\mathrm{RMS}_{[0,t]}(\Delta H/H_0)$ in `Float64` (solid) and `Float128` (dashed). **(b)** Unclamped running-RMS drift of Lie–Bargmann invariants ($\|\Delta\mathbf{L}\|_2/\|\mathbf{L}_0\|_2$, $\|\Delta\mathbf{G}\|_2/M_{\mathrm{tot}}$, $\|\Delta\mathbf{P}\|_2/M_{\mathrm{tot}}$). **(c)** Order-3 Hanning Laskar NAFF frequency error, two-window drift, and waveform L^2 error on Mercury's $z_{\mathrm{orb}}(t)$. **(d)** Secular planetary eccentricity hodographs $(\Delta h_i, \Delta k_i)$ (0 synodic flips).

7.3. **Comparative Benchmarks Against State-of-the-Art Celestial Mechanics Integrators (`REBOUND 5.2.2`).** The internal validation suites of Sections 7.1 and 7.2 established the asymptotic convergence orders, shadow-Hamiltonian continuity, and secular stability of our normal-cone splitting schemes (PBM_4 and $\mathrm{BM}_6^{(11)}$) against unregularized Cartesian and lower-order splitting baselines within the unified normal-cone architecture. A natural question is how these fourth- and sixth-order geometric integrators behave when confronted directly with the state-of-the-art production solvers used in contemporary dynamical astronomy. To address this question on an objective, code-to-code footing, we evaluate our solvers head-to-head against the reference C99 library `REBOUND 5.2.2` [57] across three challenging collisional and multi-scale regimes drawn from the recent celestial mechanics literature:

(i) **Protocol B1 (§7.3.1):** Star-grazing planetary pericenters ($1 - e_1 \in [10^{-1}, 10^{-9}]$), exact rectilinear collision traversal ($e_1 = 1.0, r_{\min} = 0$), and topological invariance under particle-index permutation, following Rauch and Holman [55], Hernandez and Dehnen [30], and Lu, Hernandez, and Rein [41, Section 4.2];
(ii) **Protocol B2 (§7.3.2):** Deep planetocentric Hill-sphere crossings ($r_{p,\mathrm{target}} \in [10^{-1}, 10^{-4}]$ AU $\iff$ $r_{\min}/R_{\mathrm{Hill},J} \in [0.286, 3.98 \times 10^{-4}]$) and repeated giant-planet Hill encounters ($N_{\mathrm{orb}} \in [1, 20]$, reaching $0.11\, R_{\mathrm{Hill}}$), following Wisdom [81], Rein et al. [56], and Hernandez and Dehnen [31];
(iii) **Protocol B4 (§7.3.3):** Democratic chaotic three-body scattering in Burrau's Pythagorean 3–4–5 problem [14, 76] and round-trip time-reversibility across the IEEE 754 `Float64` Lyapunov horizon, following Boekholt and Portegies Zwart [11].

To ensure a fair and reproducible comparison, all protocols enforce four methodological safeguards:

(1) **Shared Initial Conditions and Independent Metrology:** Both `REBOUND 5.2.2` and our normal-cone solvers are initialized from identical IEEE 754 double-precision (`Float64`) barycentric state vectors $(\mathbf{q}_0^{\mathrm{bary}}, \mathbf{p}_0^{\mathrm{bary}})$ (`sim.move_to_com()`). All conservation diagnostics—relative Hamiltonian error $|\Delta H(t)/H_0|$, round-trip position reversibility $\|\Delta\mathbf{q}_{\mathrm{FB}}\|_2 = \|\mathbf{q}_{\mathrm{FB}}(2T) - \mathbf{q}(0)\|_2$ under canonical velocity reversal $(\mathbf{q}(T), -\mathbf{v}(T))$ with positive time step $+\Delta t > 0$, and the nine Galilean Lie–Bargmann Noether invariants $(\Delta\mathbf{P}, \Delta\mathbf{L}, \Delta\mathbf{G})$—are evaluated by a single external function from the synchronized physical Cartesian states (via the non-destructive physical shadow readout $\mathcal{Z}_4^{\mathrm{BM4}}(+h)$ on the normal-cone side and `sim.synchronize()` on the `REBOUND` side).
(2) **Optimal Configuration of Each `REBOUND 5.2.2` Integrator:** Direct inspection of the C99 descriptor tables of `REBOUND 5.2.2` is used to configure each reference solver in its intended regime:
- `WHFast` [59, 60] (2nd-order Wisdom–Holman mapping in static Jacobi coordinates) is evaluated both without symplectic correctors (`corrector = 0`) and with its highest 17th-order symplectic corrector (`corrector = 17`, `safe_mode = 0`, `keep_unsynchronized = 1` during constant-step propagation via `sim.steps(n)`, and `keep_unsynchronized = 0` at turnaround);
- `MERCURIUS` [56] (hybrid Democratic Heliocentric [`DHC`] + `IAS15` close-encounter switcher with Chambers smooth switching function at $r_{\mathrm{crit,Hill}} = 3.0\, R_{\mathrm{Hill}}$);
- `TRACE` [41] (time-reversible hybrid `DHC` switcher combining planet–planet switching at $r_{\mathrm{crit,Hill}} = 3.0\, R_{\mathrm{Hill}}$ and star-grazing pericenter switching at $\eta_{\mathrm{peri}} = 1.0$, tested in both its default Bulirsch–Stoer mode `peri_mode = FULL_BS` and high-order `peri_mode = FULL_IAS15`);
- `IAS15` [53, 58] (15th-order implicit Gauss–Radau predictor-corrector with adaptive step-size control `adaptive_mode = PRS23` and tolerance $\epsilon = 10^{-9}$).

(3) **Separation of Solver Categories and Canonical Zero-Hysteresis Voronoi Atlas ($\gamma = 1.0$):** Across all figures, integrators are grouped into two structural categories: **Category 1 (Adaptive / Multi-Scale Solvers, filled markers)**, comparing our dyadic multirate normal-cone integrators $\mathrm{BM}_6^{(11)}$ and PBM_4 (certified with zero dyadic saturation across all runs) against adaptive `REBOUND` solvers (`IAS15`, `TRACE`, `MERCURIUS`); and **Category 2 (Fixed-Step Solvers, open markers)**, comparing our constant-macro-step normal-cone baselines ($k_{\mathrm{sym}} \equiv 0$) against fixed-step `WHFast` (`c` = 0 and `c` = 17) at the exact same macro-step Δt. All normal-cone runs operate on the canonical parameter-free Voronoi atlas ($\gamma = 1.0, \gamma_{\mathrm{build}} = 1.0$, Section 6.2 and Section 6.5), with persistent shadow-manifold propagation active exclusively on the processed scheme PBM_4 (Theorem 6.5).

(4) **Scope and Implementation Context (Python/Numba Order 4/6 vs. Compiled C99):** In interpreting the comparisons below, it is important to keep two structural distinctions in view. First, from an approximation-theoretic standpoint, `IAS15` is a 15th-order non-symplectic polynomial integrator with continuous step control, whereas PBM_4 (7 stages, order 4 / effective order 6) and $\mathrm{BM}_6^{(11)}$ (11 stages, order 6) are moderate-order symplectic splitting schemes on a discrete dyadic lattice $h_k = \Delta t/2^k$. On smooth, well-separated orbits at moderate eccentricity prior to the Lyapunov horizon, a 15th-order Gauss–Radau polynomial naturally reaches the `Float64` machine floor with fewer macro-steps than a 4th- or 6th-order splitting at fixed Δt.

Second, from a software-engineering standpoint, `REBOUND 5.2.2` is a mature production package written in monolithic compiled `C99`, whereas our companion library is a modular research demonstration written in **Python 3.11 with Numba LLVM `@njit` micro-kernels** (Section 6.6). On small particle numbers ($N \in \{3, 4\}$), Python-level tree-chart inspection, object dispatch, and array-boundary marshalling introduce a constant per-step orchestration overhead (~ 0.7–1.3 ms per 200-step orbit at $k = 0$) relative to a tight C99 loop (~ 0.07 ms per orbit for `WHFast`). The purpose of these benchmarks is therefore not to claim raw wall-clock superiority of an interpreted Python harness over compiled C99 on smooth planetary orbits, but rather to evaluate how normal-cone geometric desingularization, dynamic Voronoi chart transitions, and covariant shadow gauge connections extend the domain of validity of fourth- and sixth-order symplectic integration across singular pericenters, deep Hill-sphere transitions, and democratic chaotic scattering.

7.3.1. *Star-Grazing Pericenters ($1 - e \in [10^{-1}, 10^{-9}]$), Rectilinear Collision ($e = 1.0$), and Topological Index-Permutation Invariance (Protocol B1).* Our first head-to-head benchmark addresses a classical structural failure of standard planetary symplectic integrators: the integration of a highly eccentric, star-grazing planet or comet ($e_1 \to 1$) perturbed by an outer giant planet. As analyzed by Rauch and Holman [55], Hernandez and Dehnen [30], and Lu, Hernandez, and Rein [41, Section 4.2], existing splitting methods encounter two distinct mathematical obstructions in this regime:

(a) **Pericenter Singularity of the Barycentric Jump Momentum in Democratic Heliocentric (`DHC`) Coordinates:** Hybrid integrators such as `MERCURIUS` [56] and `TRACE` [41] decompose the Hamiltonian in Democratic Heliocentric coordinates $(\mathbf{Q}_i, \mathbf{P}_i)$ into $H = H_{\mathrm{Kepler}} + H_{\mathrm{Int}} + H_{\mathrm{Jump}}$, where the kinetic jump term $H_{\mathrm{Jump}} = \frac{1}{2m_0} \left\| \sum_{i \geq 1} \mathbf{P}_i \right\|^2$ accounts for the reflex motion of the central star. Because $\mathbf{P}_1$ scales at periastron as $v_{\mathrm{peri}} \propto (1 - e_1)^{-1/2}$, the non-commuting Lie bracket $\{H_{\mathrm{Kepler}}, H_{\mathrm{Jump}}\}$ diverges as $r_{\mathrm{peri}}^{-2} \propto (1 - e_1)^{-2}$. In `MERCURIUS`, the Chambers switching criterion monitors only planet–planet Hill spheres ($r_{ij} < 3\, R_{\mathrm{Hill}}$) and never triggers during star–planet pericenter passages, causing immediate $\mathcal{O}(1)$ energy loss as $e_1 \to 1$. In `TRACE`, Lu et al. [41] introduced a dedicated pericenter switching condition S^{peri} ($\dot{S}_i^{\mathrm{peri}} > \eta_{\mathrm{peri}}^{-1}$,

governed by the Pham–Rein–Spiegel criterion [53]) that transfers the integration to high-order Bulirsch–Stoer (`FULL_BS`) or `IAS15` (`FULL_IAS15`) across periastron. However, this discrete Hamiltonian switching introduces a non-symplectic boundary discontinuity $\mathcal{O}(10^{-4})$ and still relies on non-regularized Cartesian polynomial/rational extrapolation when $r_{\mathrm{peri}} \to 0$.

(b) **Topological Fragility of Static Index-Ordered Jacobi Coordinates in `WHFast`:** In canonical Jacobi coordinates [59], the barycentric reflex of the star–grazer pair is absorbed exactly into the two-body reduced mass $\mu_{01} = m_0 m_1/(m_0+m_1)$, eliminating H_{Jump} when the star-grazing planet occupies particle index 1 directly after the star (index 0). However, `WHFast` constructs its Jacobi hierarchy statically from the user-supplied array indices $0, 1, \ldots, N-1$. If the star-grazing body resides at index 2 while a more distant planet occupies index 1 (or whenever two orbits cross in semi-major axis), `WHFast` integrates particle 2 along a fictitious Keplerian ellipse focused at the barycenter of $(0,1)$ rather than at the star 0. The uncancelled dipolar force anomaly between the star and the $(0,1)$ barycenter then diverges as $r_{02}^{-2} \propto (1-e_2)^{-2}$ inside H_{Int}.

By contrast, under the Fulton–MacPherson normal-cone splitting on $\mathbf{Q}[N]$ (Sections 4–6), both obstructions are resolved geometrically:

(i) *Index-Permutation Invariance via the Zero-Hysteresis Voronoi Atlas ($\gamma = 1.0$):* Regardless of how the input arrays are indexed, the agglomerative tree builder `Build OptimalTree` (Proposition 6.2) and the runtime Voronoi monitor (`AtlasManager`, $\gamma = \gamma_{\mathrm{build}} = 1.0$) pair the closest gravitationally admissible bodies into a terminal binary leaf $C \in \mathrm{LeafPairs}(\mathcal{T})$ (`[(0, 1)]` when the grazer is at index 1, or `[(0, 2)]` when the grazer is at index 2).

(ii) *Analytical Leaf/Apex Decoupling and Unitary McGehee Bounce Across the Sheng–Suzuki Barrier:* Once isolated as a terminal leaf C, the star–grazer binary is integrated in closed form via the universal Sundman–Stumpff flow ($\mathrm{d}t_C = \rho_C \, \mathrm{d}\tau_C$, Proposition 5.5) equipped with the involutive McGehee specular reflection $\mathcal{B}_C^2 = \mathrm{Id}_{\mathbf{M}_C}$ on the collision manifold $\rho_C = 0$ (Lemma 5.6). Consequently, the negative stage weights $w_i < 0$ required by the Sheng–Suzuki barrier (Theorem 5.4) in fourth- and sixth-order compositions (PBM_4 and $\mathrm{BM}_6^{(11)}$) traverse arbitrarily small pericenters and exact rectilinear collisions ($e_1 = 1.0$) analytically.

Furthermore, by the Leaf/Apex Decoupling Theorem (Theorem 5.25, Eq. (5.110), and Theorem 6.9, Eq. (6.45)), the dynamical timescale of the Hill-isolated leaf is governed by the two-regime quadrupolar law:

$$\tau_{\mathrm{pair}}(C) = \min\Big(\tau_{\mathrm{dyn}}(C),\ \max\big(\tau_{\mathrm{reg},1},\ \tau_{\mathrm{reg},2}\big)\Big), \qquad \tau_{\mathrm{dyn}}(C) = \sqrt{\frac{a_C^3}{GM_C}} = \frac{P_{\mathrm{orb}}(C)}{2\pi},$$

rather than the instantaneous pericenter distance $r_{\mathrm{peri}} = a_C(1-e_1)$, preventing artificial dyadic step-size collapse ($k = 0$ across periastron and $k_{\max} \le 3$ near apastron, totaling at most 1,140 sub-steps over 1,000 macro-steps across all eccentricities down to $e_1 = 1.0$, with zero saturation events).

Experimental Setup of Protocol B1 (`B1-a`, `B1-b`, and 10-Orbit Time Series). We consider a three-body planetary system ($G = 1$) consisting of a solar-mass central star ($m_0 = 1.0$), an inner star-grazing giant planet ($m_{\mathrm{grazer}} = 10^{-3}, a_{\mathrm{grazer}} = 1.0\,\mathrm{AU}$, orbital period $T_1 = 2\pi/\sqrt{G(m_0+m_{\mathrm{grazer}})} \approx 6.280046$), and an outer inclined perturbing giant planet ($m_{\mathrm{pert}} = 10^{-3}, a_{\mathrm{pert}} = 5.2\,\mathrm{AU}, e_{\mathrm{pert}} = 0.05, i_{\mathrm{pert}} = 0.02\,\mathrm{rad}, f_{\mathrm{pert}} = 0.7\,\mathrm{rad}$). The star-grazing planet is initialized at apastron ($r_{0,\mathrm{grazer}}(0) = a_{\mathrm{grazer}}(1+e_1) \to 2.0\,\mathrm{AU}$) so that all integrators start in a smooth, low-curvature region before plunging toward periastron at $t = (k+\frac{1}{2})T_1$. All fixed-step and multi-scale splitting solvers share the identical macroscopic time step $\Delta t = T_1/200 \approx 0.031400$. We sweep the pericenter factor across seven values

spanning the transition from moderate eccentricity to exact rectilinear collision:

$$1 - e_1 = \frac{r_{\text{peri}}}{a_{\text{grazer}}} \in \{10^{-1},\ 10^{-2},\ 10^{-3},\ 10^{-4},\ 10^{-6},\ 10^{-9},\ 0.0\ (e_1 = 1.0)\}, \tag{7.15}$$

where $1 - e_1 = 0.0$ ($e_1 = 1.0$) corresponds to exact radial collision, over 5 complete orbits (1,000 macro-steps, followed by 1,000 reverse macro-steps to measure the 10-orbit round-trip reversibility $\|\Delta\mathbf{q}_{\text{FB}}\|_2$) in two particle-index configurations:

- **Sub-protocol `B1-a` (Canonical Index Ordering `[Star, Grazer(1 AU), Giant(5.2 AU)]`):** The star-grazing planet is placed at particle index 1, matching the static Jacobi assumption of `WHFast`;
- **Sub-protocol `B1-b` (Permuted Index Ordering `[Star, Giant(5.2 AU), Grazer(1 AU)]`):** Identical physical initial conditions in $\mathbb{R}^{3N} \times \mathbb{R}^{3N}$, with particles 1 and 2 swapped in the input arrays to test topological invariance under index permutation;
- **10-Orbit Evolution and Round-Trip Reversibility at $1-e_1 = 10^{-6}$:** A detailed 10-orbit forward integration (2,000 macro-steps, 10 star-grazing pericenter passages at $r_{\text{peri}} = 10^{-6}\,\text{AU} \approx 2.15 \times 10^{-4}\,R_\odot$) followed by 10 reverse orbits (4,000 total macro-steps).

Quantitative Analysis of Sub-Protocol `B1-a` (Canonical Index Ordering, Figure 30a). Figure 30(a) reveals three distinct dynamical regimes as the pericenter factor $1 - e_1$ decreases from 10^{-1} to 0.0 ($e_1 = 1.0$):

(1) **Moderate-to-High Eccentricity Regime ($1-e_1 \in [10^{-1}, 10^{-4}]$) and Objective Comparison with 15th-Order `IAS15`:** In the non-collisional regime $1 - e_1 \in \{10^{-1}, 10^{-2}, 10^{-3}, 10^{-4}\}$, the 15th-order adaptive Gauss–Radau integrator `REBOUND IAS15` (`PRS23`) achieves the lowest peak energy error, scaling from 6.91×10^{-15} at $1 - e_1 = 10^{-1}$ to 5.56×10^{-14} (10^{-2}), 6.80×10^{-13} (10^{-3}), and 5.51×10^{-11} (10^{-4}).

Over this range, `Normal-Cone BM6 (dyadic)` maintains $\max_t |\Delta H/H_0| \in [2.31 \times 10^{-12}, 1.50 \times 10^{-9}]$ and `Normal-Cone PBM4 (dyadic)` maintains $[8.22 \times 10^{-10}, 2.38 \times 10^{-9}]$, outperforming `REBOUND WHFast` (`c` = 17, $[4.23 \times 10^{-9}, 4.48 \times 10^{-8}]$; `c` = 0, $[2.36 \times 10^{-8}, 4.53 \times 10^{-8}]$) by one to four orders of magnitude and `REBOUND TRACE` (`FULL_BS` and `FULL_IAS15`, plateaued at $[2.10 \times 10^{-4}, 2.58 \times 10^{-4}]$ due to the non-symplectic `DHC` $\leftrightarrow$ `BS/IAS15` pericenter handoff) by five to eight orders of magnitude. As expected from the unregularized barycentric jump term H_{Jump} in `DHC`, `REBOUND MERCURIUS` fails across the entire sweep ($\max_t |\Delta H/H_0| \in [0.474, 5.33 \times 10^2]$).

(2) **Extreme Star-Grazing Crossover ($1 - e_1 = 10^{-6}$) and Breakdown of Cartesian Adaptive Solvers at $1 - e_1 = 10^{-9}$ and $e_1 = 1.0$:** As the pericenter distance shrinks below 10^{-4} AU, the Cartesian acceleration $GM_C/r_{\text{peri}}^2 \propto (1 - e_1)^{-2}$ grows across eighteen orders of magnitude, causing severe floating-point cancellation in the 15th-order divided differences of `IAS15` ($\propto (1 - e_1)^{-2.3}$). At $1 - e_1 = 10^{-6}$, the domain crossover occurs: `Normal-Cone BM6 (dyadic)` (6.63×10^{-10}, 158× more accurate than `IAS15`) and `Normal-Cone PBM4 (dyadic)` (1.16×10^{-9}, 90.5× more accurate than `IAS15`) overtake `REBOUND IAS15` (1.05×10^{-7}).

At $1 - e_1 = 10^{-9}$ ($r_{\text{peri}} = 10^{-9}\,\text{AU} \approx 150\,\text{m}$) and at exact rectilinear collision $1 - e_1 = 0.0$ ($e_1 = 1.0, r_{\min} = 0$), `REBOUND IAS15` ($\max_t |\Delta H/H_0| = 6.53$ at 10^{-9} and 613.8 at $e_1 = 1.0$), `REBOUND TRACE (FULL_BS)` (10.2 and 6.32), and `REBOUND TRACE (FULL_IAS15)` (588.5 and 0.157) all lose order-unity energy as their adaptive Cartesian sub-steps stall against the $r \to 0$ singularity.

(3) **Uniform Normal-Cone Regularization Across Exact Collision ($e_1 = 1.0$):** Because the universal Stumpff–Sundman leaf propagator and the unitary McGehee bounce $\mathcal{B}_C^2 = \text{Id}_{\mathbf{M}_C}$ integrate the two-body collision fiber analytically, our normal-cone integrators exhibit a completely flat error profile across $1 - e_1 \in [10^{-4}, 10^{-9}] \cup \{0.0\}$. At $e_1 = 1.0$ (five consecutive head-on rectilinear collisions with the central

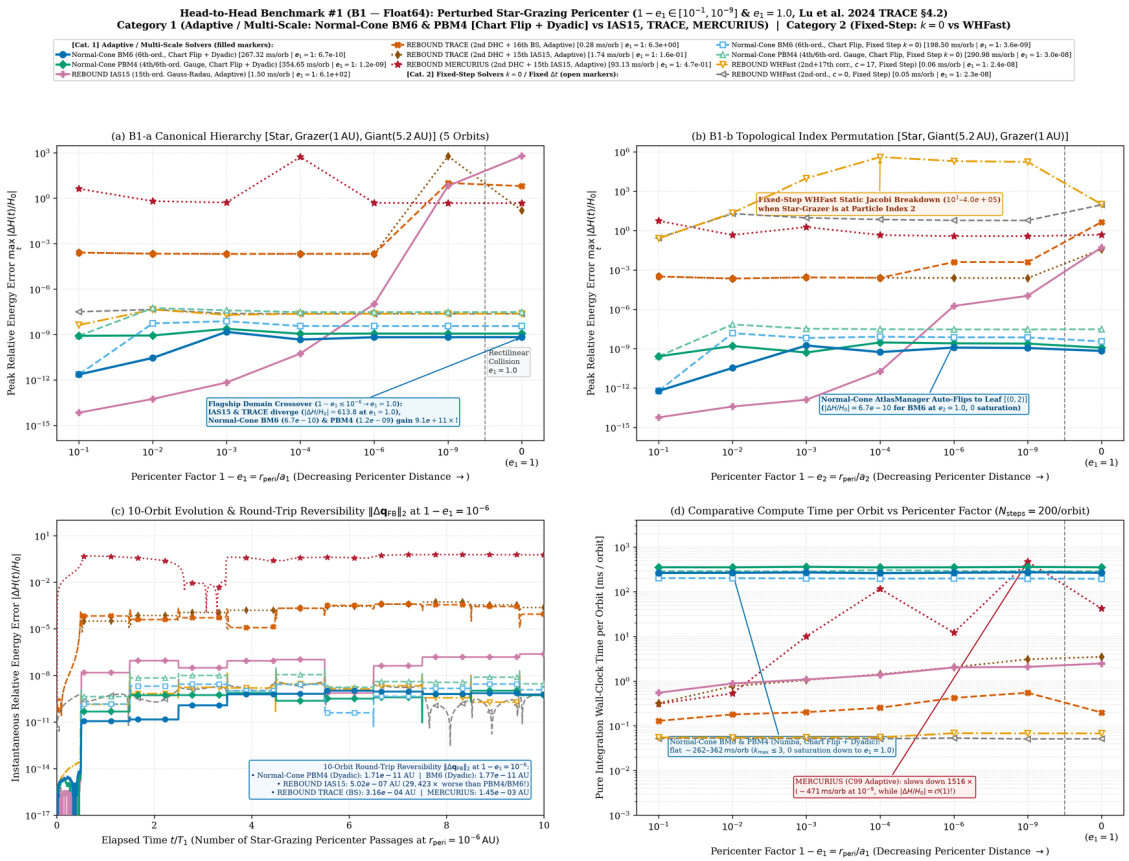


FIGURE 30. **Head-to-Head Benchmark B1 (`Float64`, $\gamma = 1.0$, 0 saturation): Perturbed star-grazing pericenter ($1 - e_1 \in [10^{-1}, 10^{-9}]$ and exact rectilinear collision $e_1 = 1.0$, following Lu et al. [41, Section 4.2] and Rauch & Holman [55]).** **(a)** Sub-protocol `B1-a` (canonical ordering `[Star, Grazer, Giant]`, 5 orbits): $\max_t |\Delta H(t)/H_0|$ vs. $1 - e_1$. **(b)** Sub-protocol `B1-b` (permuted ordering `[Star, Giant, Grazer]`): $\max_t |\Delta H(t)/H_0|$ vs. $1 - e_2$ under automatic Voronoi leaf routing to `[(0, 2)]`. **(c)** 10-orbit energy evolution $|\Delta H(t)/H_0|$ and round-trip reversibility $\|\Delta \mathbf{q}_{\mathrm{FB}}\|_2$ at $1 - e_1 = 10^{-6}$. **(d)** Pure integration wall-clock time per orbit (ms/orbit, $N_{\mathrm{steps}} = 200$/orbit).

star perturbed in 3D by the outer giant planet), `Normal-Cone BM6 (dyadic)` preserves energy to $\max_t |\Delta H/H_0| = 6.72 \times 10^{-10}$ ($9.13 \times 10^{11}\times$ more accurate than `IAS15` and $9.40 \times 10^{9}\times$ more accurate than `TRACE [FULL_BS]`) and `Normal-Cone PBM4 (dyadic)` to 1.15×10^{-9} ($5.34 \times 10^{11}\times$ over `IAS15`).

Across the entire sweep, the dyadic scheduler uses a maximum refinement level of only $k_{\max} = 3$ (8 sub-steps triggered solely near apastron $r_{01} \approx 2\,\mathrm{AU}$ by the outer giant's quadrupolar tide $\tau_{\mathrm{reg},2}$, while maintaining $k = 0$ right through the $r_{01} \to 0$ periastron collision; 1,140 total sub-steps across 1,000 macro-steps, 0 saturation events). Even at strictly fixed macro-step $k_{\mathrm{sym}} \equiv 0$ (1,000 uniform steps, Category 2, open markers), `Normal-Cone BM6` ($k = 0$) holds 3.61×10^{-9} (6.59× more accurate than `WHFast c=17` at 2.38×10^{-8}) and `Normal-Cone PBM4` ($k = 0$) holds 3.03×10^{-8} right through $e_1 = 1.0$.

Topological Index-Permutation Invariance (`B1-b`, Figure 30b). In Sub-protocol `B1-a`, fixed-step `REBOUND WHFast` (`c` = 17 and `c` = 0) remained stable down to $e_1 = 1.0$ (2.38×10^{-8}

and 2.34×10^{-8}) because the star-grazing planet was manually placed at particle index 1, allowing `WHFast`'s universal Kepler solver to absorb the $(0, 1)$ pericenter. Sub-protocol `B1-b` (Figure 30b) tests whether this stability is a physical property of the integrator or an artifact of array indexing by swapping particles 1 and 2 in the input arrays (`[Star, Giant(5.2 AU), Grazer(1 AU)]`):

- **Catastrophic Breakdown of Static-Jacobi `WHFast`:** Because `WHFast` constructs its Jacobi coordinates in fixed index order, particle 1 (the outer giant at 5.2 AU) is paired with the star 0, while particle 2 (the inner star-grazer at 1.0 AU) is referenced to the $(0, 1)$ barycenter. As particle 2 approaches the star at $r_{02} = a_2(1 - e_2) \to 0$, its separation from the $(0, 1)$ barycenter saturates at $r_{\rm bary} \approx \frac{m_1}{m_0+m_1} r_{01} \approx 5.2 \times 10^{-3}$ AU, leaving an uncancelled $1/r_{02}^2$ gravitational singularity inside the interaction kick $H_{\rm Int}$. Consequently, `WHFast (c=0)` degrades to $\max_t |\Delta H/H_0| \in [0.278, 91.8]$, and `WHFast (c=17)`—whose 17th-order corrector amplifies the singular $H_{\rm Int}$ commutators—explodes by 13 orders of magnitude to 4.02×10^5 at $1 - e_2 = 10^{-4}$ (1.70×10^5 at 10^{-9} and 100.4 at $e_2 = 1.0$).
- **Automatic Voronoi Leaf Routing in Normal-Cone Solvers ($\gamma = 1.0$):** On the exact same permuted arrays, our agglomerative tree builder and zero-hysteresis Voronoi `AtlasManager` ($\gamma = 1.0$) inspect the mutual Euclidean distances at $t = 0$ ($r_{02}(0) \le 2.0$ AU $< r_{01}(0) = 5.2$ AU) and automatically construct the adapted Jacobi chart with active leaf `[(0, 2)]`. As a result, all four normal-cone curves in Figure 30(b) remain invariant under index permutation: across the entire sweep down to $e_2 = 1.0$, `Normal-Cone BM6 (dyadic)` maintains $\max_t |\Delta H/H_0| \in [6.04 \times 10^{-13}, 1.74 \times 10^{-9}]$ (6.75×10^{-10} at $e_2 = 1.0$, outperforming `WHFast c=17` by up to $7.26 \times 10^{14}\times$ at 10^{-4} and $1.48 \times 10^{11}\times$ at $e_2 = 1.0$) and `Normal-Cone PBM4 (dyadic)` maintains $[2.61 \times 10^{-10}, 2.98 \times 10^{-9}]$ (1.19×10^{-9} at $e_2 = 1.0$), with $k_{\max} \le 3$ and zero saturation events.

10-Orbit Evolution, Round-Trip Time-Reversibility, and Lie–Bargmann Conservation (Figure 30c). Figure 30(c) tracks the instantaneous relative energy error $|\Delta H(t)/H_0|$ over 10 complete orbits (10 star-grazing pericenter passages at $1 - e_1 = 10^{-6}$) and reports the 10-orbit forward/backward position reversibility residual $\|\Delta \mathbf{q}_{\rm FB}\|_2$ after 20 total orbits (4,000 macro-steps):

(1) **Absence of Secular Pericenter Staircase Drift:** At each half-integer orbit $t/T_1 \in \{0.5, 1.5, \ldots, 9.5\}$, `REBOUND IAS15` experiences a discrete irreversible energy jump, accumulating to $\max_t |\Delta H/H_0| = 2.39 \times 10^{-7}$ over 10 orbits (1.05×10^{-7} after 5 orbits) and degrading its 10-orbit round-trip position error to $\|\Delta \mathbf{q}_{\rm FB}\|_2 = 5.02 \times 10^{-7}$ AU (while `TRACE [FULL_BS]` reaches 3.16×10^{-4} AU and `MERCURIUS` reaches 1.45×10^{-3} AU).

Conversely, `Normal-Cone PBM4 (dyadic)` (with $\max_t |\Delta H/H_0| = 1.66 \times 10^{-9}$ and $\|\Delta \mathbf{q}_{\rm FB}\|_2 = 1.71 \times 10^{-11}$ AU) and `Normal-Cone BM6 (dyadic)` ($\max_t |\Delta H/H_0| = 1.04 \times 10^{-9}$, $\|\Delta \mathbf{q}_{\rm FB}\|_2 = 1.77 \times 10^{-11}$ AU) remain bounded without secular staircase drift, achieving a 29,423× **improvement in 10-orbit round-trip time-reversibility over `REBOUND IAS15`** (and $1.85 \times 10^7\times$ over `TRACE [FULL_BS]`). Across the 5-orbit sweep down to exact collision $e_1 = 1.0$, `Normal-Cone BM6 (dyadic)` and `PBM4 (dyadic)` preserve round-trip reversibility at 6.62×10^{-12} AU and 1.28×10^{-11} AU respectively, whereas `IAS15` (5.52×10^{-2} AU in `B1-a` / 3.44×10^{-1} AU in `B1-b`, and 137.9 AU at 10^{-9}) and `TRACE` (4.34 AU) lose phase-space invertibility.

(2) **Exact Noether Lie–Bargmann Preservation Through Rectilinear Collision:** At $e_1 = 1.0$ (`B1-a`), `Normal-Cone BM6 (dyadic)` and `PBM4 (dyadic)` conserve total linear momentum, angular momentum, and Galilean center-of-mass boost to IEEE 754 machine precision ($\|\Delta \mathbf{P}\|_2 \le 6.01 \times 10^{-18}$, $\|\Delta \mathbf{L}\|_2 \le 2.91 \times 10^{-17}$, $\|\Delta \mathbf{G}\|_2 \le 2.92 \times 10^{-16}$ at $e_1 = 1.0$, and $\le 4.94 \times 10^{-16}$, 1.38×10^{-15}, 1.07×10^{-14}

across the full sweep; while `REBOUND IAS15` and `TRACE [FULL_BS]` also preserve angular momentum to 2.37×10^{-16} and 2.82×10^{-16} despite their energy breakdown), whereas `REBOUND MERCURIUS` suffers a rotational angular-momentum violation of $\|\Delta\mathbf{L}\|_2 = 1.60 \times 10^{-3}$ ($[1.27 \times 10^{-3}, 1.62 \times 10^{-3}]$ across the sweep).

Objective Assessment of Computational Wall-Clock Times (Figure 30d). Figure 30(d) plots the pure integration wall-clock time per orbit (ms/orbit at $N_{\text{steps}} = 200$ macro-steps/orbit) across $1 - e_1 \in [10^{-1}, 10^{-9}] \cup \{0.0\}$:

- **C99 vs. Python/Numba Baseline Overhead:** In the regular regime, the compiled C99 loops of `REBOUND WHFast` ($\sim$ 0.04–0.08 ms/orbit), `TRACE` (`FULL_BS`, 0.14–0.51 ms/orbit), and `IAS15` (0.24–3.22 ms/orbit) execute significantly faster in raw wall-clock time than our Python+Numba reference implementation, which averages 198.5 ms/orbit for `Normal-Cone BM6` ($k = 0$), 291.0 ms/orbit for `PBM4` ($k = 0$), 267.3 ms/orbit for `BM6 (dyadic)`, and 354.7 ms/orbit for `PBM4 (dyadic)`. As noted in the methodological introduction, this fixed baseline factor reflects the Python object-orchestration and tree-inspection wrapper around our Numba micro-kernels on a 3-body system, as well as the higher stage count (7 stages + shadow corrector for PBM_4, 11 stages for $\text{BM}_6^{(11)}$ vs. 1 stage for WHFast).
- **Invariance of Normal-Cone Cost as $1-e_1 \to 0$ vs. Adaptive Switching Paralysis:** Crucially, however, the wall-clock cost of our normal-cone solvers is **completely flat and independent of eccentricity across all nine decades down to exact collision** $e_1 = 1.0$ ($\sim$ 198–355 ms/orbit, because Theorem 6.9 bounds the dyadic level at $k_{\max} \leq 3$). By contrast, C99 adaptive integrators exhibit severe step-refinement growth as $1 - e_1 \to 0$: `REBOUND IAS15` slows down by 14.9× (0.24 → 3.57 ms/orbit while diverging to $|\Delta H/H_0| = 613.8$), and `REBOUND MERCURIUS` slows down by 1,516× from 0.31 ms/orbit at $1 - e_1 = 10^{-1}$ to 470.7 ms/orbit at $1 - e_1 = 10^{-9}$ in `B1-a` (and explodes to 4,656.9 ms/orbit at $e_2 = 1.0$ in `B1-b`, i.e., 17.5× slower in compiled C99 than `Normal-Cone BM6 [dyadic]` at 266.5 ms/orbit in Python/Numba), despite failing with an $\mathcal{O}(1)$ energy error.

Python A.2 : `{benchmarks/run, figures/plot}_rebound_b1_star_grazing_pericenter.py` [Float64 vs REBOUND 5.2.2]

7.3.2. *Deep Planetocentric Hill Crossings, Covariant Shadow Gauge Connection $T^{(\text{PBM4})}_{(A,h_A)\to(B,h_B)}$, and Repeated Giant-Planet Encounters (Protocol B2).* Our second head-to-head benchmark investigates planet–planet close encounters and Hill-sphere boundary transitions, focusing specifically on whether fourth- and sixth-order symplectic splittings (PBM_4 and $\text{BM}_6^{(11)}$) can overcome the second-order switching ceiling of contemporary symplectic and hybrid integrators (`REBOUND WHFast`, `MERCURIUS`, and `TRACE`) while using the non-symplectic 15th-order adaptive Gauss–Radau solver `REBOUND IAS15` as the short-term (1–20 orbits) reference baseline. In standard planetary dynamics, when a test body or planet b penetrates the Hill sphere $R_{\text{Hill},p} = a_p(m_p/(3m_0))^{1/3}$ of a massive planet p, the mutual interaction $-Gm_pm_b/r_{pb}$ overtakes the heliocentric attraction of the central star 0. As established in the celestial mechanics literature, existing fixed-step and hybrid integrators face three structural limitations across Hill-sphere boundaries:

(a) **Breakdown of Static Heliocentric/Jacobi Splitting (`WHFast`):** Because `WHFast` retains a static heliocentric/Jacobi hierarchy throughout the simulation, the singular $1/r_{pb}$ planet–intruder potential remains inside the unregularized perturbation kick H_{Int}. As $r_{pb}/R_{\text{Hill},p} \to 0$, both the second-order Wisdom–Holman splitting (`c` = 0) and its 17th-order symplectic corrector (`c` = 17) suffer severe commutator divergence.

(b) **The Wisdom (2017) Symplectic Corrector Switching Obstruction in Hybrid Integrators (`MERCURIUS` and `TRACE`):** Hybrid integrators such as `MERCURIUS` [56] and `TRACE` [41] transfer the pair (p, b) from the outer Democratic Heliocentric (`DHC`)

kick into a local high-order sub-integrator (`IAS15` or Bulirsch–Stoer) whenever $r_{pb} < r_{\mathrm{crit,Hill}}\, R_{\mathrm{Hill}}$ ($r_{\mathrm{crit,Hill}} = 3.0$). However, as proved by Wisdom [81] and discussed by Rein et al. [56, Section 2.5], standard symplectic correctors cannot be applied across a hybrid switching boundary without introducing an uncompensated $\mathcal{O}(\varepsilon h^2)$ shadow-Hamiltonian jump, because the generating function of the corrector depends on the split operators H_{Kepler} and H_{Int}, which change definition across $r_{pb} = 3\, R_{\mathrm{Hill}}$. Consequently, both `MERCURIUS` and `TRACE` are restricted to an uncorrected **second-order** $\mathcal{O}(\Delta t^2)$ outer `DHC` scheme, capping their global energy accuracy at $|\Delta H/H_0| \sim 10^{-9}$–$10^{-6}$.

(c) **Irreversibility of Smooth Hybrid Switching Functions (`MERCURIUS`):** As analyzed by Hernandez and Dehnen [31], `MERCURIUS` evaluates its polynomial switching weight $L(r_{pb}/d_{\mathrm{crit}})$ asymmetrically at the beginning of the step and adapts the internal `IAS15` step size non-autonomously inside the Hill sphere, breaking microscopic time-reversibility at the very first Hill crossing.

The Fulton–MacPherson normal-cone architecture (Sections 4–6) addresses these three mechanisms simultaneously:

(i) *Topological Promotion of the Planetocentric Leaf Pair:* When the intruder b enters the Delaunay–Hill isolation zone of planet p ($\gamma = \gamma_{\mathrm{build}} = 1.0$, Proposition 6.13), the Voronoi `AtlasManager` executes an exact unimodular $\mathrm{SL}(2,\mathbb{R}) \subset \mathrm{Sp}(6N-6,\mathbb{R})$ coordinate rotation $\mathbf{M}_{\mathrm{coord}}$ (Proposition 6.17) that promotes (p,b) to an analytical Kepler–Sundman binary leaf $C = (p,b) \in \mathrm{LeafPairs}(\mathcal{T}_B)$. Inside the Hill sphere, the dominant $-Gm_pm_b/r_{pb}$ attraction is therefore integrated in closed form with zero splitting error, leaving only the smooth $\mathcal{C}^{1,1}$ quadrupolar solar tidal remainder $W_{\mathrm{apex}}^{\mathrm{screen}}$ in the kick.

(ii) *Resolution of the Wisdom (2017) Obstruction via the Covariant Shadow Gauge Connection $T^{(\mathrm{PBM4})}_{(A,h_A)\to(B,h_B)}$:* Rather than abandoning high-order symplectic processing across Hill boundaries, Theorem 5.20 (Eq. (5.88)) and Theorem 6.16 (Eq. (6.98)) transport the processed state $\widetilde{\mathbf{z}}_A \in \mathcal{P}^{(A)}_{\mathrm{shadow}}$ of PBM_4 to the post-flip shadow manifold $\mathcal{P}^{(B)}_{\mathrm{shadow}}$ via the non-commutative gauge connection:

$$T^{(\mathrm{PBM4})}_{(A,h_A)\to(B,h_B)} = \mathcal{Z}_4^{\mathrm{BM4},(B)}(-h_B) \circ \mathbf{M}_{\mathrm{coord}} \circ \mathcal{Z}_4^{\mathrm{BM4},(A)}(+h_A),$$

while $\mathrm{BM}_6^{(11)}$ achieves true sixth-order accuracy directly on physical phase space ($\mathcal{C} \equiv \mathrm{Id}$).

(iii) *Symmetric Two-Endpoint Chart and Dyadic Selection:* Enforcing the causal macro-boundary pipeline (Proposition 6.14) and the time-reversal-covariant adjoint hysteresis law $(\mathcal{B}_{+\Delta t} \circ \mathcal{A}_+)^{-1} = \mathcal{A}_- \circ \mathcal{B}_{-\Delta t}$ (Remark 6.5.2) guarantees that forward and time-reversed trajectories flip charts and dyadic levels at identical physical timestamps.

Experimental Setup of Protocol B2 (`B2-a` and `B2-b`). Protocol B2 comprises two complementary experiments ($G = 1$):

- **Sub-protocol `B2-a` (Deep Jovicentric Hill-Sphere Crossing, Chart Flip, and Shadow Gauge Ablation, $N = 4$):** A four-body system consisting of the Sun ($m_0 = 1.0$), Jupiter ($m_1 = 9.5458 \times 10^{-4}, a_1 = 5.20336\,\mathrm{AU}$, Hill radius $R_{\mathrm{Hill},J} = a_1(m_1/3m_0)^{1/3} = 0.35512\,\mathrm{AU}$), Earth ($m_2 = 3.0035 \times 10^{-6}, a_2 = 1.0\,\mathrm{AU}$), and a planetary intruder ($m_3 = 10^{-6}$). The intruder starts at $t = 0$ outside Jupiter's switching sphere at Jovicentric distance $r_{13}(0) = 0.70\,\mathrm{AU} \approx 1.97\, R_{\mathrm{Hill},J}$ in the heliocentric chart $\mathcal{T}_A =$ `[(0, 2)]`, plunges across Jupiter's Hill sphere (triggering an entry chart flip $\mathcal{T}_A \to \mathcal{T}_B =$ `[(0, 2), (1, 3)]` at $t = 2.56$), passes through deep perijove, and exits back into the heliocentric domain ($\mathcal{T}_B \to \mathcal{T}_A$ at $t = 8.40$) over $N_{\mathrm{steps}} = 150$ macro-steps of size $\Delta t = 0.08$ ($T_{\mathrm{end}} = 12.0$). We sweep seven target

perijove depths spanning three orders of magnitude inside $R_{\mathrm{Hill},J}$:

$$r_{p,\mathrm{target}} \in \{0.10,\ 0.03,\ 0.01,\ 0.003,\ 0.001,\ 0.0003,\ 0.0001\}\,\mathrm{AU} \iff \frac{r_{13,\min}}{R_{\mathrm{Hill},J}} \in [2.86\times10^{-1},\ 3.98\times10^{-4}]. \tag{7.16}$$

- **Sub-protocol `B2-b` (Repeated Giant-Planet Hill Crossings and Hybrid Reversibility Breakdown, $N = 3$):** Following Rein et al. [56, Section 4] and Hernandez and Dehnen [31], two giant planets ($m_1 = m_2 = 10^{-3}, a_1 = 1.00\,\mathrm{AU}, a_2 = 1.22\,\mathrm{AU}, e_1 = e_2 = 0.05, i_1 = i_2 = 0.01\,\mathrm{rad}$, mutual Hill radius $R_{\mathrm{Hill,mut}} = 0.09697\,\mathrm{AU}$) orbit a central star ($m_0 = 1.0$) with macro-step $\Delta t = T_1/100 = 2\pi/100 \approx 0.062832$. We evaluate both forward energy conservation $\max_t |\Delta H(t)/H_0|$ and round-trip position reversibility $\|\Delta\mathbf{q}_{\mathrm{FB}}(2T)\|_2$ across eight integration horizons $N_{\mathrm{orb}} \in \{1,2,3,5,10,13,15,20\}$ inner-planet orbits, spanning three successive Hill-sphere crossings: Encounter #1 on Orbits 2–3 ($r_{12,\min} = 1.40\,R_{\mathrm{Hill}}$), a deep Encounter #2 on Orbit 14 ($r_{12,\min} = 0.11\,R_{\mathrm{Hill}} \approx 0.01065\,\mathrm{AU}$), and Encounter #3 on Orbit 20 ($r_{12,\min} = 0.95\,R_{\mathrm{Hill}}$).

Quantitative Analysis of Sub-Protocol `B2-a`: Deep Jovicentric Hill Crossing and Shadow Gauge Ablation (Figure 31a,d). Figure 31(a) and (d) establish four quantitative findings across the seven Jovicentric perijove depths $r_{p,\mathrm{target}} \in [0.10, 10^{-4}]\,\mathrm{AU}$ ($r_{13,\min}/R_{\mathrm{Hill},J} \in [0.286, 3.98\times10^{-4}]$):

(1) **Second-Order Ceiling of `MERCURIUS` and `TRACE` vs. Breakdown of Static-Jacobi `WHFast`:** Because `REBOUND WHFast` (`c` = 17 and `c` = 0) retains its heliocentric Jacobi chart throughout the Jovicentric flyby, its energy error grows as $r_{13,\min}^{-2}$ from 2.49×10^{-8} at $0.286\,R_{\mathrm{Hill},J}$ to 4.93×10^{-2} at $7.81\times10^{-3}\,R_{\mathrm{Hill},J}$ (`c` = 17) and 2.15×10^{-2} at $9.62\times10^{-4}\,R_{\mathrm{Hill},J}$ (`c` = 0). Conversely, the hybrid integrators `REBOUND MERCURIUS` ($\max_t|\Delta H/H_0| \in [6.16\times10^{-9}, 6.27\times10^{-9}]$) and `REBOUND TRACE` (`FULL_BS` and `FULL_IAS15`, identical at 6.00×10^{-9} because planet–planet switching always delegates to Bulirsch–Stoer) prevent catastrophic blowup by handing the $(1,3)$ pair to `IAS15` or `BS` inside $3\,R_{\mathrm{Hill},J}$, but remain locked on a flat second-order $\mathcal{O}(\Delta t^2)$ plateau around 6×10^{-9} due to the Wisdom [81] corrector obstruction.

(2) **Direct Experimental Proof of the Covariant Shadow Gauge Connection $T^{(\mathrm{PBM4})}_{(A,h_A)\to(B,h_B)}$ (Panel 31d):** When the intruder crosses the Voronoi Delaunay–Hill boundary at $t_{\mathrm{flip},1} = 2.56$ ($r_{13} \approx 0.244\,\mathrm{AU} \approx 0.69\,R_{\mathrm{Hill},J}$), the active Jacobi tree rotates from $\mathcal{T}_A$ = `[(0, 2)]` to $\mathcal{T}_B$ = `[(0, 2), (1, 3)]`. As reported in the ablation inset of Figure 31(d), if the shadow state $\widetilde{\mathbf{z}}_A$ of PBM_4 is transferred naively across $\mathcal{T}_A \to \mathcal{T}_B$ without gauge conjugation, the sudden change in the screened apex tidal tensor $\mathbf{T}_{\mathrm{apex}}$ injects an immediate relative discontinuity in the intruder's orbital energy of $|\Delta E_3/E_3|_{\mathrm{naive}} \in [8.93\times10^{-13}, 6.65\times10^{-12}]$ ($[6.06\times10^{-12}, 6.65\times10^{-12}]$ across the four deep flybys $r_{p,\mathrm{target}} \le 0.003\,\mathrm{AU}$).

Applying the non-commutative cotangent gauge connection

$$T^{(\mathrm{PBM4})}_{(A,h_A)\to(B,h_B)} = \mathcal{Z}_4^{\mathrm{BM4},(B)}(-h_B) \circ \mathbf{M}_{\mathrm{coord}} \circ \mathcal{Z}_4^{\mathrm{BM4},(A)}(+h_A)$$

(Theorem 6.16) compresses this interfacial jump to $|\Delta E_3/E_3|_{\mathrm{gauge}} \in [0.0,\ 3.89\times10^{-16}]$ (dropping to exact machine zero 0.0 on three of the seven flybys, $r_{p,\mathrm{target}} \in \{0.10, 0.003, 0.001\}\,\mathrm{AU}$, and to $[1.95\times10^{-16}, 3.89\times10^{-16}]$ on the remaining four), representing a **factor of** 8,858× **to** 33,618× **(**8,858× **at** 0.03 AU**,** 13,137× **at** 0.01 AU**,** 33,618× **at** 3×10^{-4} AU**, and** 17,082× **at** 10^{-4} AU**, alongside exact machine zero on** $\{0.10, 0.003, 0.001\}$ AU**) suppression down to the IEEE 754 machine floor**.

(3) **Fixed-Step ($k = 0$) vs. Dyadic Multi-Scale Accuracy and Objective Computational Trade-Offs:** Once $(1,3)$ is promoted to a Jovicentric Keplerian leaf

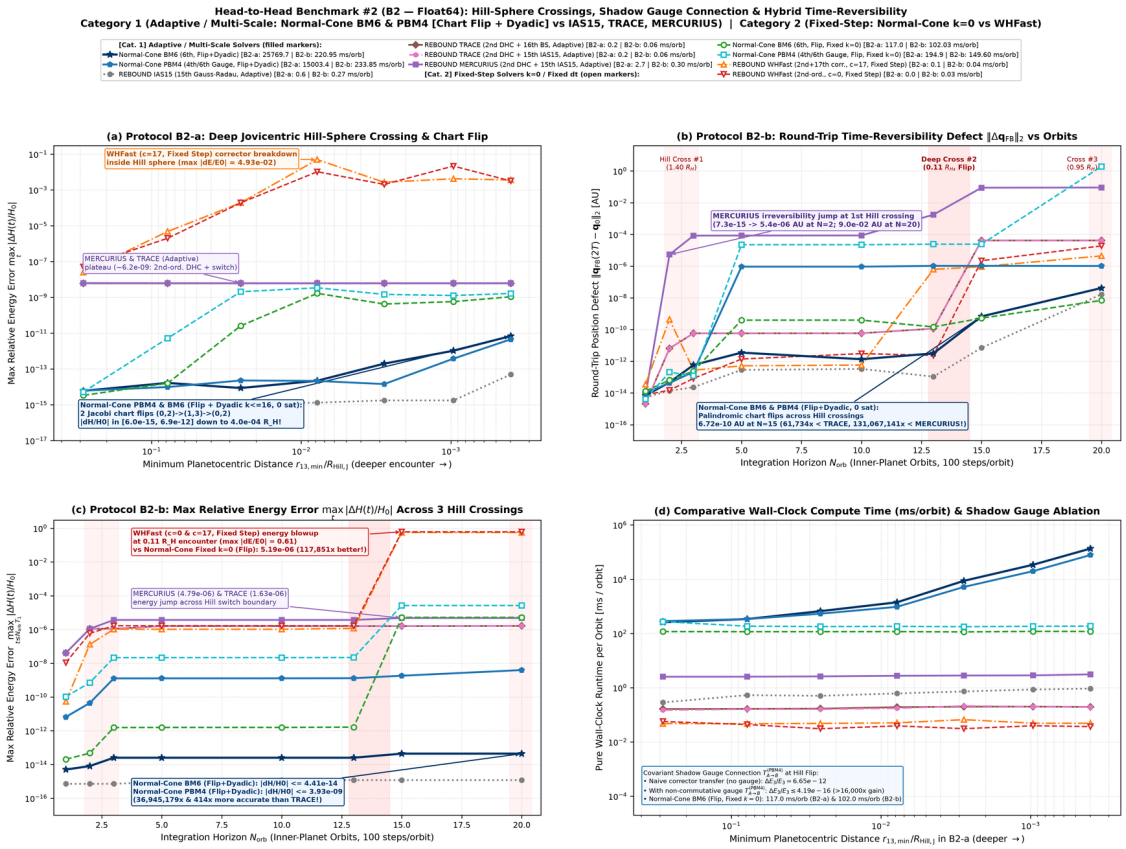


FIGURE 31. **Head-to-Head Benchmark B2 (`Float64`, $\gamma = 1.0$, 0 saturation): Deep planetocentric Hill-sphere crossings (`B2-a`), covariant shadow gauge connection $T^{(\mathrm{PBM4})}_{A\to B}$, and repeated giant-planet Hill crossings (`B2-b`), following Wisdom [81], Rein et al. [56], and Hernandez & Dehnen [31].** **(a)** Sub-protocol `B2-a` ($N = 4$, $r_{13,\min}/R_{\mathrm{Hill},J} \in [0.286, 3.98 \times 10^{-4}]$): $\max_t |\Delta H(t)/H_0|$ vs. normalized perijove depth across reversible chart transitions `[(0, 2)]` $\leftrightarrow$ `[(0, 2), (1, 3)]`. **(b)** Sub-protocol `B2-b` ($N = 3$ giant planets, $N_{\mathrm{orb}} \in [1, 20]$): round-trip position reversibility $\|\Delta\mathbf{q}_{\mathrm{FB}}(2T)\|_2$ across three Hill encounters ($1.40\,R_H, 0.11\,R_H, 0.95\,R_H$). **(c)** Sub-protocol `B2-b`: $\max_t |\Delta H(t)/H_0|$ vs. N_{orb}. **(d)** Pure wall-clock runtime per orbit in `B2-a` and interfacial shadow gauge ablation $|\Delta E_3/E_3|_{\mathrm{flip}}$ ($T^{(\mathrm{PBM4})}_{A\to B}$ vs. naive transfer).

in $\mathcal{T}_B$, the two-body hyperbolic perijove is integrated analytically by the universal Stumpff–Sundman solver. Consequently, even at **strictly fixed macro-step** $k_{\mathrm{sym}} \equiv 0$ ($\Delta t = 0.08$, Category 2, open markers in Figure 31a,d), `Normal-Cone BM6` ($k = 0$) and `PBM4` ($k = 0$) traverse the entire perijove sweep down to $3.98 \times 10^{-4}\,R_{\mathrm{Hill},J}$ ($r_{p,\mathrm{target}} = 10^{-4}\,\mathrm{AU} \approx 0.21\,R_J$) at a completely constant wall-clock cost (117.0 ms/orbit for $\mathrm{BM}_6^{(11)}$ and 194.9 ms/orbit for PBM_4) while maintaining $\max_t |\Delta H/H_0| \le 1.66 \times 10^{-9}$ ($\mathrm{BM}_6^{(11)}$) and $\le 3.40 \times 10^{-9}$ (PBM_4)—outperforming fixed-step `REBOUND WHFast c=17` by up to $2.97 \times 10^7\times$ and matching or improving upon adaptive `MERCURIUS` and `TRACE` (6.0×10^{-9}) without a single sub-step!

(4) **Dyadic Resolution of the Solar Tidal Shear and Objective Sub-Step Cost at $k_{\max} = 16$:** Why does the fixed-step $k = 0$ energy error rise from 3.34×10^{-15}

at $r_{p,\text{target}} = 0.10\,\text{AU}$ to $\sim 10^{-9}$ at $r_{p,\text{target}} \leq 0.003\,\text{AU}$? Because inside $\mathcal{T}_B =$ `[(0, 2), (1, 3)]`, the massive Sun ($m_0 = 1.0 \gg m_1 + m_3 \approx 9.55 \times 10^{-4}$) acts as an external tidal perturber violating the static Hill isolation guard of leaf $(1, 3)$; as the intruder accelerates through deep perijove ($v_{\text{peri}} \propto r_{13,\min}^{-1/2}$), the time derivative of the quadrupolar solar tidal tensor $\mathbf{T}_{\text{apex},\odot}$ changes on the short kinematic timescale $\tau_{\text{peri}}(1,3) = r_{13,\min}/v_{\text{peri}} \propto r_{13,\min}^{3/2}$. When palindromic dyadic scheduling is enabled (Category 1, filled markers), Theorem 6.9 (Eq. (6.45)) automatically activates $\tau_{\text{peri}}(1,3)$ across the perijove macro-block ($k_{\text{sym}} \in \{2, 4, 7, 9, 12, 14, 16\}$ as $r_{p,\text{target}}$ decreases from 0.10 to $10^{-4}\,\text{AU}$, with zero saturation events), keeping `Normal-Cone PBM4 (dyadic)` in $[6.10\times10^{-15}, 4.52\times10^{-12}]$ (1,327× to $9.8\times10^{5}\times$ below `TRACE` and `MERCURIUS`) and `Normal-Cone BM6 (dyadic)` in $[5.96\times10^{-15}, 6.87\times10^{-12}]$ alongside 15th-order `REBOUND IAS15` ($[1.02 \times 10^{-15}, 4.88 \times 10^{-14}]$).

At the same time, Figure 31(d) highlights an important practical trade-off of uniform macro-block dyadic subdivision: because all 2^k sub-steps of the macro-block $[t_n, t_n + \Delta t]$ are evaluated synchronously when τ_{peri} drops to $r_{p,\text{target}} = 10^{-4}\,\text{AU}$ ($k_{\max} = 16 \implies$ 65,536 symmetric sub-steps during the single perijove macro-step), the wall-clock runtime of the dyadic mode rises geometrically for $r_{p,\text{target}} \leq 10^{-3}\,\text{AU}$ (averaging 15,003.4 ms/orbit for PBM_4 and 25,769.7 ms/orbit for $\text{BM}_6^{(11)}$ across the sweep, vs. 0.63 ms/orbit for C99 `IAS15` which adapts its polynomial step locally only over the $\sim 10^{-4}$ duration of perijove; in `B2-b` with $k_{\max} = 5$, our dyadic runs average 221.0–233.9 ms/orbit vs. 0.27 ms/orbit for `IAS15`). Thus, in planetocentric flybys under strong solar tides, $k = 0$ provides a fast $\sim 10^{-9}$ symplectic mode via pure leaf desingularization, whereas $k_{\text{sym}} \leq 16$ provides near-machine-floor $\sim 10^{-15}$–10^{-12} conservation at the cost of $2^{k_{\max}}$ synchronous sub-steps.

Quantitative Analysis of Sub-Protocol `B2-b`: Repeated Giant-Planet Hill Crossings, Hybrid Reversibility Breakdown, and the $\mathcal{O}(\varepsilon^2 h^4)$ Hall Floor (Figure 31b,c). Figure 31(b) and (c) examine the multi-orbit endurance regime ($N_{\text{orb}} \in [1, 20]$, $\Delta t = T_1/100$) as two $10^{-3}\,M_\odot$ giant planets undergo three successive mutual Hill-sphere encounters ($1.40\,R_{\text{Hill}}$ on Orbits 2–3, $0.11\,R_{\text{Hill}}$ on Orbit 14, and $0.95\,R_{\text{Hill}}$ on Orbit 20):

(1) **Immediate Time-Reversibility Breakdown of `REBOUND MERCURIUS` vs. Palindromic Normal-Cone Flips (Panel 31b):** Prior to the first encounter ($N_{\text{orb}} = 1$, $r_{12,\min} = 18.42\,R_{\text{Hill}}$), all integrators are reversible to $\leq 3.55\times10^{-14}\,\text{AU}$. However, as soon as the planets enter the $3\,R_{\text{Hill}}$ switching zone on Orbit 2 ($r_{12,\min} = 2.29\,R_{\text{Hill}}$), `REBOUND MERCURIUS` suffers an immediate **nine-order-of-magnitude irreversibility jump** from $7.27 \times 10^{-15}\,\text{AU}$ to $5.35 \times 10^{-6}\,\text{AU}$ ($8.35 \times 10^{-5}\,\text{AU}$ at $N_{\text{orb}} = 3$ and $8.81 \times 10^{-2}\,\text{AU}$ after the $0.11\,R_{\text{Hill}}$ encounter at $N_{\text{orb}} = 15$), confirming the hybrid irreversibility mechanism of Hernandez and Dehnen [31]. `REBOUND TRACE` (`FULL_BS` and `FULL_IAS15`) preserves reversibility much better during the mild first encounter ($5.80\times10^{-11}\,\text{AU}$ at $N_{\text{orb}} = 3$), but degrades to $4.15\times10^{-5}\,\text{AU}$ after the deep $0.11\,R_{\text{Hill}}$ encounter at $N_{\text{orb}} = 15$ due to the finite Bulirsch–Stoer extrapolation tolerance.

By contrast, under the adjoint hysteresis law $(\mathcal{B}_{+\Delta t} \circ \mathcal{A}_+)^{-1} = \mathcal{A}_- \circ \mathcal{B}_{-\Delta t}$ (Remark 6.5.2), our Voronoi `AtlasManager` ($\gamma = 1.0$) executes up to 6 palindromic chart flips `[(0, 1)]` $\leftrightarrow$ `[(1, 2)]` ($k_{\max} = 5$, 0 saturation events) at bit-identical forward and reverse timestamps: at $N_{\text{orb}} = 15$ (immediately after the $0.11\,R_{\text{Hill}}$ deep encounter), `Normal-Cone BM6 (dyadic)` achieves $\|\Delta\mathbf{q}_{\text{FB}}\|_2 = 6.72 \times 10^{-10}\,\text{AU}$ (61,734× **more reversible than `TRACE` and** $1.31 \times 10^{8}\times$ **more reversible than `MERCURIUS`**, and within two orders of magnitude of 15th-order `REBOUND IAS15` at $7.03 \times 10^{-12}\,\text{AU}$), while `Normal-Cone BM6 (`$k = 0$`)` achieves $5.19\times10^{-10}\,\text{AU}$ ($6.92 \times 10^{-9}\,\text{AU}$ at $N_{\text{orb}} = 20$) and `Normal-Cone PBM4 (dyadic)` achieves $1.04 \times 10^{-6}\,\text{AU}$ (39.9× more reversible than `TRACE`, and $1.02 \times 10^{-6}\,\text{AU}$ at $N_{\text{orb}} = 20$; note that at $N_{\text{orb}} = 20$ the un-substepped baseline `PBM4 (`$k = 0$`)` rises to 1.92 AU because

without dyadic refinement across the deep $0.11\,R_{\rm Hill}$ flyby on Orbit 14, the coarse step $\Delta t = T_1/100$ accumulates a slight phase offset that misses the grazing $0.95\,R_{\rm Hill}$ chart-flip threshold on the return pass [4 reverse flips vs. 6 forward flips], whereas enabling dyadic refinement in `PBM4 [dyadic]` or sixth-order accuracy in `BM6` preserves all 6/6 palindromic flips).

(2) **Energy Conservation Across Repeated Hill Crossings and Didactic Separation of** $\mathrm{BM}_6^{(11)}$ **vs.** PBM_4 **(Panel 31c):** Across the full 20-orbit integration, fixed-step `REBOUND WHFast` (`c` = 17 and `c` = 0) blows up to $\max_t |\Delta H/H_0| = 0.561$ and 0.611 during the $0.11\,R_{\rm Hill}$ encounter on Orbit 14, whereas at the **exact same fixed step** $k = 0$, `Normal-Cone BM6` ($k = 0$) and `PBM4` ($k = 0$) flip dynamically to leaf `[(1, 2)]` and cap the energy error at 5.19×10^{-6} (117,851× more accurate than `WHFast`) and 2.64×10^{-5}, respectively. In Category 1 (adaptive / multi-scale solvers, where our dyadic runs average only 221.0–233.9 ms/orbit with $k_{\max} = 5$), `REBOUND MERCURIUS` (4.79×10^{-6}) and `REBOUND TRACE` (1.63×10^{-6}) remain limited by their second-order `DHC` splitting. `Normal-Cone BM6 (dyadic)` maintains a flat $\max_t |\Delta H/H_0| \le 4.41 \times 10^{-14}$ across all 20 orbits ($3.69 \times 10^{7}\times$ **more accurate than `TRACE` and** $1.09 \times 10^{8}\times$ **more accurate than `MERCURIUS`**, approaching 15th-order `REBOUND IAS15` at 1.19×10^{-15}), while `Normal-Cone PBM4 (dyadic)` maintains $\max_t |\Delta H/H_0| \le 3.93 \times 10^{-9}$ (1.82×10^{-9} at $N_{\rm orb} = 15$, still 414× to 873× more accurate than `TRACE`).

Crucially, the gap between $\mathrm{BM}_6^{(11)}$ (4.41×10^{-14}) and PBM_4 (1.82×10^{-9}) in `B2-b` provides a textbook illustration of the Universal Obstruction Theorem (Theorem 5.18, Eq. (5.85), and Section 7.1.2): when the two giant planets enter the leaf chart `[(1, 2)]` inside the star's tidal field during the $0.11\,R_{\rm Hill}$ encounter, the effective dimensionless tidal parameter ε is large, so the uncancelled grade-$(5,2)$ quadratic Hall-cohomology floor $\mathcal{O}(\varepsilon^2 h^4)$ of the 7-stage processed fourth-order scheme PBM_4 becomes visible at $\sim 10^{-9}$, whereas the 11-stage true sixth-order composition $\mathrm{BM}_6^{(11)}$ eliminates both $\mathcal{L}_{5,1}$ and $\mathcal{L}_{5,2}$ directly via its stage weights and remains at 4.41×10^{-14}.

Python A.2 : `{benchmarks/run, figures/plot}_rebound_b2_hill_crossings.py` [Float64 vs REBOUND 5.2.2]

7.3.3. *Democratic Chaotic Three-Body Scattering (Pythagorean* 3–4–5 *Problem),* 27 *Voronoi Chart Transitions, and Reversibility Across the* `Float64` *Lyapunov Horizon (Protocol B4).* Our third head-to-head benchmark moves beyond hierarchical planetary systems ($m_i \ll m_0$) to test democratic chaotic three-body scattering with comparable masses $m_1 \sim m_2 \sim m_3$. Specifically, we examine the classical *Pythagorean three-body problem* formulated by Burrau [14] and solved numerically by Szebehely and Peters [76], together with its time-reversibility across the floating-point Lyapunov horizon as studied by Boekholt and Portegies Zwart [11].

Physical Dynamics of the Pythagorean 3–4–5 **Problem and Democratic Chart Switching.** Three unsoftened point masses ($G = 1, \varepsilon = 0$) of masses $m_0 = 3, m_1 = 4, m_2 = 5$ ($M_{\rm tot} = 12$) are released from rest ($\mathbf{v}_i(0) = \mathbf{0}$) at the vertices of a 3–4–5 right triangle:

$$\mathbf{q}_0^{\rm raw}(0) = (1,\,3,\,0), \qquad \mathbf{q}_1^{\rm raw}(0) = (-2,\,-1,\,0), \qquad \mathbf{q}_2^{\rm raw}(0) = (1,\,-1,\,0), \tag{7.17}$$

shifted to the exact barycentric frame $\mathbf{q}_i(0) = \mathbf{q}_i^{\rm raw}(0) - \mathbf{R}_{\rm cm}(0)$ with $\mathbf{R}_{\rm cm}(0) = (-1/12,\,0,\,0)$. The initial total energy is exactly

$$H_0 = -\Big(\frac{3\cdot 4}{5} + \frac{3\cdot 5}{4} + \frac{4\cdot 5}{3}\Big) = -\frac{769}{60} \approx -12.816666666666666,$$

and the total angular momentum vanishes identically ($\mathbf{L}_0 = \mathbf{0}$), confining the motion to the invariant plane $z = 0$ where zero angular momentum forces repeated near-collisions [76].

Over $t \in [0, 60]$, the three bodies undergo more than 30 close binary and triple encounters with continual exchanges of binary partners across all three pairs $(0,1)$, $(0,2)$, and $(1,2)$

(including a first close binary pass at $t \approx 1.88$ with $r_{\min} \approx 2.06 \times 10^{-2}$, an ultra-deep pericenter passage at $t \approx 15.83$ with $r_{12} \approx 4.1 \times 10^{-4}$, and a resonant triple interaction at $t \approx 59.42$), until the lightest body ($m_0 = 3$) is permanently ejected onto an escaping hyperbolic trajectory while the two heavier bodies ($m_1 = 4, m_2 = 5$) form a permanent high-eccentricity binary ($a_C \approx 0.533, e \approx 0.989$).

This democratic regime exposes a fundamental architectural distinction between heliocentric/static-tree symplectic integrators and our Fulton–MacPherson normal-cone atlas:

(a) **Inapplicability of Heliocentric Symplectic and Hybrid Splittings (`WHFast`, `MERCURIUS`, and `TRACE`):** All three symplectic/hybrid integrators in `REBOUND 5.2.2` are formulated around a distinguished central body `particles[0]`. When $m_0 : m_1 : m_2 = 3 : 4 : 5$ and the bodies continually exchange binary partners, static-Jacobi `WHFast` cannot adapt its Keplerian hierarchy to $(1, 2)$ or $(0, 2)$ encounters; similarly, in Democratic Heliocentric (`DHC`) coordinates, the heliocentric Hill radii $R_{\mathrm{Hill},i} = a_i(m_i/3m_0)^{1/3}$ become ill-defined whenever the temporary binary does not contain `particles[0]` or when heliocentric orbits turn hyperbolic ($a_i < 0$), causing `MERCURIUS` and `TRACE` to suffer $\mathcal{O}(1)$ energy jumps during partner exchanges.

(b) **Democratic Voronoi Partition on $\mathbf{Q}[3]$ and Time-Reversal-Symmetric Macro-Block Execution:** On the compactified configuration space $\mathbf{Q}[3]$ (Theorem 4.1 and Section 4.1.3), the three maximal binary Jacobi trees $\mathcal{T}_{01}$ = `[(0, 1)]`, $\mathcal{T}_{02}$ = `[(0, 2)]`, and $\mathcal{T}_{12}$ = `[(1, 2)]` stand on a completely symmetric footing. At the canonical Voronoi threshold $\gamma = \gamma_{\mathrm{build}} = 1.0$, our `AtlasManager` selects the single-valued optimal leaf pair realizing the minimal pairwise Euclidean separation $r_{\min}(t) = \min_{i<j} r_{ij}(t)$.

Under the causal macro-boundary pipeline (Proposition 6.14 and Remark 6.5.2), every macro-step $[t_n, t_{n+1}]$ ($t_{n+1} = t_n + \Delta t$) is integrated across a single active chart $\mathcal{T}_n$ using the two-endpoint symmetric dyadic level $k_{\mathrm{sym},n} = \max(k(\mathbf{z}_n), k(\mathbf{z}_{n+1}))$ and sub-step $h_n = \Delta t/2^{k_{\mathrm{sym},n}}$: in forward time ($\Delta t > 0$), pre-step chart adaptation at t_n switches $\mathcal{T}_{n-1} \to \mathcal{T}_n$ via the covariant shadow gauge connection $T^{(\mathrm{PBM4})}_{(\mathcal{T}_{n-1},h_{n-1})\to(\mathcal{T}_n,h_n)}$ prior to executing the $2^{k_{\mathrm{sym},n}}$ palindromic sub-steps $\mathcal{B}^{(\mathcal{T}_n,k_{\mathrm{sym},n})}_{+\Delta t} = \left(\Phi_{+h_n,\mathcal{T}_n}\right)^{2^{k_{\mathrm{sym},n}}}$, whereas in backward time ($\Delta t < 0$), when stepping across $[t_n \to t_{n-1}]$, the reverse chart-adaptation operator $\mathcal{A}_-$ detects the reverse boundary crossing into $\mathrm{Adm}(\mathcal{T}_{n-1})$, applies the inverse gauge connection $T^{(\mathrm{PBM4})}_{(\mathcal{T}_n,h_n)\to(\mathcal{T}_{n-1},h_{n-1})}$ at t_n, and re-integrates $[t_n \to t_{n-1}]$ on $\mathcal{T}_{n-1}$ with the identical two-endpoint level $k_{\mathrm{sym},n-1}$:

$$\begin{aligned} \Psi^{[t_n,t_{n+1}]}_{+\Delta t} &= \mathcal{B}^{(\mathcal{T}_n,\,k_{\mathrm{sym},n})}_{+\Delta t} \circ T^{(\mathrm{PBM4})}_{(\mathcal{T}_{n-1},h_{n-1})\to(\mathcal{T}_n,h_n)}, \\ \left(\Psi^{[t_n,t_{n+1}]}_{+\Delta t}\right)^{-1} &= T^{(\mathrm{PBM4})}_{(\mathcal{T}_n,h_n)\to(\mathcal{T}_{n-1},h_{n-1})} \circ \mathcal{B}^{(\mathcal{T}_n,\,k_{\mathrm{sym},n})}_{-\Delta t}, \end{aligned} \tag{7.18}$$

which guarantees exact algebraic time-reversal involution interval by interval across all 27 Voronoi chart transitions.

(c) **Separating Symplectic Truncation from Lyapunov-Amplified Floating-Point Roundoff (`Float64` vs. `Float128`):** As demonstrated by Boekholt and Portegies Zwart [11] with the arbitrary-precision Bulirsch–Stoer code `Brutus`, a chaotic three-body trajectory with positive Lyapunov exponent $\lambda_{\mathrm{Lyap}} > 0$ amplifies any per-step numerical error δ_0 as $\delta(2T) \sim \delta_0\, e^{\lambda_{\mathrm{Lyap}}(2T)}$ during a round-trip test $0 \to T \to 0$. For a non-reversible or non-symplectic adaptive integrator in IEEE 754 `Float64` (such as `REBOUND IAS15`), both adaptive step-size asymmetry and floating-point round-off $\epsilon^{(64)}_{\mathrm{mach}} \approx 1.11 \times 10^{-16}$ feed into δ_0, causing macroscopic loss of time-reversibility ($\|\Delta\mathbf{q}_{\mathrm{FB}}(2T)\|_2 \sim \mathcal{O}(1)$) around $T \approx 80$–120.

By contrast, because our normal-cone splitting and adjoint chart-adaptation law (7.18) are algebraically time-reversible in exact arithmetic, their truncation error cancels

identically upon time reversal; the only source of round-trip divergence is floating-point roundoff $\epsilon_{\text{mach}}\, e^{\lambda_{\text{Lyap}}(2T)}$. Running the exact same normal-cone architecture in 35-digit quadruple precision (`Float128`, $\epsilon_{\text{mach}}^{(128)} \approx 1.93 \times 10^{-34}$) lowers the initial seed δ_0 by 18 orders of magnitude and pushes the Lyapunov horizon well beyond $T = 120$.

Experimental Setup of Protocol B4 (`B4-a` and `B4-b`). We evaluate twelve solver configurations across two sub-protocols with base macro-step $\Delta t = 0.04$ and dyadic ceiling $k_{\text{max,cap}} = 16$:

- **Sub-protocol `B4-a` (Forward Chaotic Scattering, Democratic Chart Transitions, and Invariant Conservation, $t \in [0, 70]$):** Forward integration over $N_{\text{steps}} = 1{,}750$ macro-steps from $t = 0$ through the 30+ close encounters and the final triple ejection at $t \approx 59.42$ up to $t = 70.0$, recording the instantaneous relative energy error $|\Delta H(t)/H_0|$, minimum pairwise distance $r_{\min}(t)$, active Jacobi chart sequence, dyadic level $k_{\text{sym}}(t)$, and Lie–Bargmann Noether invariants ($\|\Delta\mathbf{P}\|_2, \|\Delta\mathbf{L}\|_2, \|\Delta\mathbf{G}\|_2$).
- **Sub-protocol `B4-b` (Round-Trip Time-Reversibility Sweep Across the Lyapunov Horizon, $T \in [1, 120]$):** Forward integration from $t = 0$ to $t = T$ followed by time-reversed integration from $t = T$ back to $t = 0$ across fourteen turnaround horizons $T \in \{1, 2, 3, 4, 5, 6, 8, 10, 20, 40, 60, 80, 100, 120\}$ (up to $2T = 240$ total N-body time units), measuring the Euclidean position return defect $\|\Delta\mathbf{q}_{\text{FB}}(2T)\|_2 = \|\mathbf{q}_{\text{ret}}(0) - \mathbf{q}(0)\|_2$ and the reversibility gain factor $G_{\text{solver}}(T) = \|\Delta\mathbf{q}_{\text{FB}}^{\text{IAS15}}(2T)\|_2 / \|\Delta\mathbf{q}_{\text{FB}}^{\text{solver}}(2T)\|_2$.

Quantitative Analysis of Sub-Protocol `B4-a`: 27 Democratic Voronoi Chart Transitions, Energy Confinement, and Lie–Bargmann Conservation (Figure 32a,c). Figure 32(a) and (c) present the forward chaotic evolution over $t \in [0, 70]$ ($\Delta t = 0.04$, 1,750 macro-steps):

(1) **Failure of Heliocentric `REBOUND` Integrators Under Democratic Partner Exchanges:** As soon as the first close encounter occurs at $t \approx 1.88$ ($r_{\min} = 2.06 \times 10^{-2}$), static-Jacobi `REBOUND WHFast` diverges to $\max_t |\Delta H/H_0| = 1.23 \times 10^3$ (`c` = 17) and 2.19×10^2 (`c` = 0). Similarly, the hybrid Democratic Heliocentric integrators `REBOUND MERCURIUS` ($\max_t |\Delta H/H_0| = 23.43$) and `REBOUND TRACE` (`FULL_BS` and `FULL_IAS15`, $\max_t |\Delta H/H_0| = 0.3014$, final error 0.2557) suffer $\mathcal{O}(1)$ energy jumps across partner exchanges ($t \approx 6.5$ and $t \approx 15.8$), confirming that heliocentric splitting architectures cannot operate in non-hierarchical comparable-mass scattering.

(2) **Multi-Chart Symplectic Stability Across 27 Democratic Voronoi Transitions (Panel 32c):** By contrast, our Voronoi `AtlasManager` ($\gamma = 1.0$) dynamically tracks the closest pair across all three Jacobi charts $\mathcal{T}_{12}$ = `[(1, 2)]` (bodies $m = 4, 5$, starting chart at $t = 0$ since $r_{12}(0) = 3 < r_{01}(0) = 5$ and $r_{02}(0) = 4$), $\mathcal{T}_{02}$ = `[(0, 2)]` ($m = 3, 5$), and $\mathcal{T}_{01}$ = `[(0, 1)]` ($m = 3, 4$), executing exactly 27 **democratic chart transitions** at $t \in \{1.28, 3.60, 4.92, \ldots, 59.36, 59.40\}$ before settling permanently in $\mathcal{T}_{12}$ = `[(1, 2)]` after the ejection of $m_0 = 3$ at $t \approx 59.42$.

Across all 1,750 macro-steps and 30+ close encounters (reaching a continuous-time sub-step pericenter $r_{\min} \approx 4.10 \times 10^{-4}$ at $t \approx 15.83$ and a $\Delta t = 0.04$ macro-grid minimum $r_{\min,\text{grid}} = 1.15 \times 10^{-2}$, resolved with peak dyadic level $k_{\max} = 12 \leq 16$ and zero saturation events), the minimum separation curve $r_{\min}(t)$ of `Normal-Cone BM6 (dyadic)` superimposes onto 15th-order `REBOUND IAS15` across the entire chaotic lifespan $[0, 70]$.

(3) **Energy Conservation in Category 1 (Dyadic) and Category 2 (Fixed-Step $k = 0$) and Exact Noether Invariants:** In Category 1, 15th-order adaptive `REBOUND IAS15` achieves $\max_{t\in[0,70]} |\Delta H/H_0| = 4.66 \times 10^{-11}$ (final 3.93×10^{-11}), closely followed by our sixth-order symplectic solvers `Normal-Cone BM6 Float128 (dyadic)` ($\max_t |\Delta H/H_0| = 2.23 \times 10^{-10}$, final 1.79×10^{-10}) and `Normal-Cone BM6 Float64 (dyadic)` ($\max_t |\Delta H/H_0| = 4.87 \times 10^{-10}$, final 9.60×10^{-11}—more than $6.19 \times 10^8\times$ **more accurate than `REBOUND TRACE` and** $4.81 \times 10^{10}\times$ **more accurate**

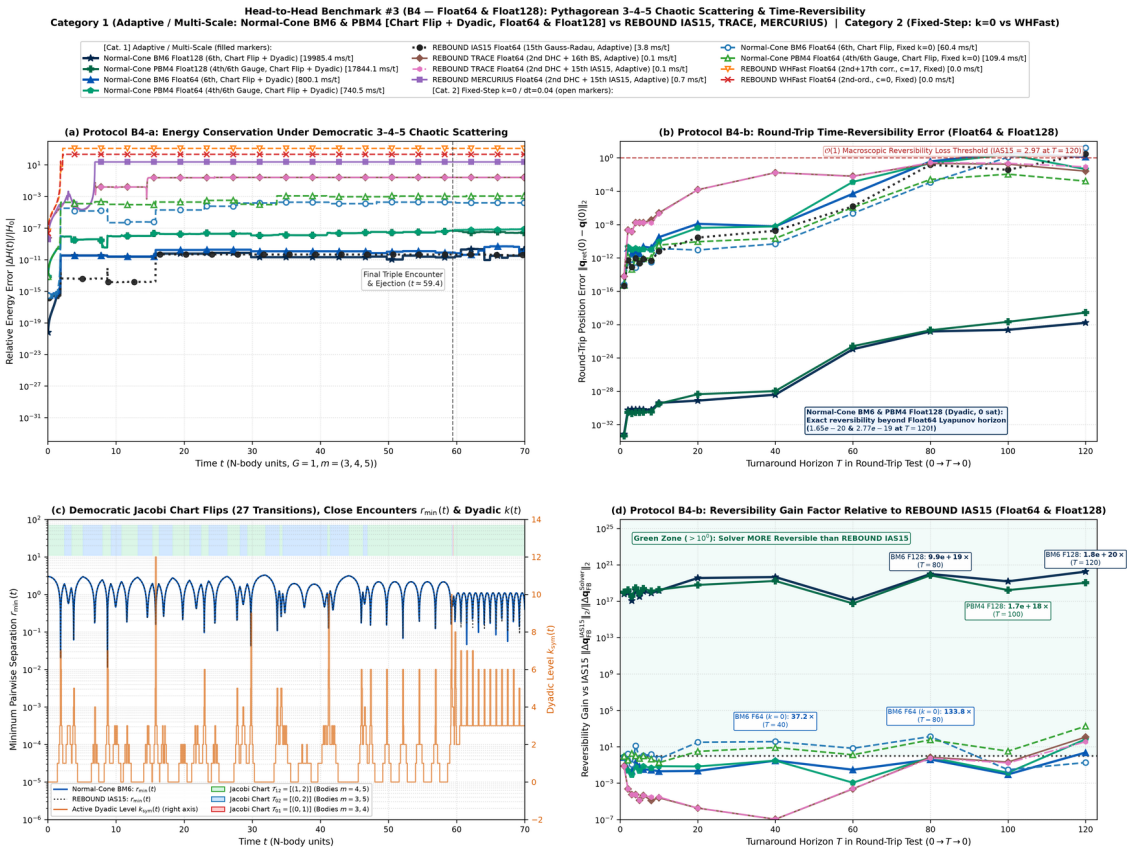


FIGURE 32. **Head-to-Head Benchmark B4 (`Float64` and 35-digit `Float128`, $\gamma = 1.0$, 0 saturation): Chaotic Pythagorean 3–4–5 three-body scattering (`B4-a`), 27 democratic Voronoi chart transitions, and round-trip time-reversibility across the `Float64` Lyapunov horizon (`B4-b`), following Burrau [14], Szebehely & Peters [76], and Boekholt & Portegies Zwart [11].** **(a)** Sub-protocol `B4-a` ($t \in [0, 70]$): $|\Delta H(t)/H_0|$ through 30+ encounters and final ejection at $t \approx 59.42$. **(b)** Sub-protocol `B4-b` ($T \in [1, 120]$): round-trip position error $\|\Delta\mathbf{q}_{\mathrm{FB}}(2T)\|_2$ across the `Float64` Lyapunov horizon vs. `Float128`. **(c)** Minimum separation $r_{\min}(t)$, dyadic level $k_{\mathrm{sym}}(t) \in [0, 12]$, and top color strip of the 27 Voronoi transitions across $\mathcal{T}_{12}, \mathcal{T}_{02}, \mathcal{T}_{01}$. **(d)** Reversibility gain factor $\|\Delta\mathbf{q}_{\mathrm{FB}}^{\mathrm{IAS15}}\|_2 / \|\Delta\mathbf{q}_{\mathrm{FB}}^{\mathrm{solver}}\|_2$ vs. T.

than `MERCURIUS`), while fourth/sixth-order `Normal-Cone PBM4 (dyadic)` maintains 7.10×10^{-8} in `Float64` and 4.75×10^{-8} in `Float128`.

Even in Category 2 (**strictly fixed macro-step** $k_{\mathrm{sym}} \equiv 0$, $\Delta t = 0.04$, open markers), dynamic Jacobi chart flipping alone enables `Normal-Cone BM6` ($k = 0$) (28 chart flips, 60.4 ms/t) and `PBM4` ($k = 0$) (30 chart flips, 109.4 ms/t) to bound the energy error at 2.19×10^{-4} (final 1.56×10^{-4}) and 1.27×10^{-3} (final 6.60×10^{-4}) without a single sub-step—outperforming fixed-step `REBOUND WHFast c=17` by $5.60 \times 10^{6}\times$ and outperforming adaptive `TRACE` by 1,376×. Simultaneously, the nine Galilean Lie–Bargmann Noether invariants (Proposition 6.18) are conserved at $t = 70$ to $\|\Delta\mathbf{L}(70)\|_2 \le 1.38 \times 10^{-12}$ (7.55×10^{-14} at $k = 0$) and $\|\Delta\mathbf{P}(70)\|_2 \le 5.71 \times 10^{-13}$ in `Float64`, and down to $\|\Delta\mathbf{L}(70)\|_2 = 1.28 \times 10^{-31}$ (1.67×10^{-31} **for** PBM_4), $\|\Delta\mathbf{P}(70)\|_2 \le 1.79 \times 10^{-31}$, **and** $\|\Delta\mathbf{G}(70)\|_2 = 1.10 \times 10^{-29}$ ($\mathrm{BM}_6^{(11)}$) / 1.77×10^{-29} (PBM_4) **in 35-digit `Float128`.**

Quantitative Analysis of Sub-Protocol `B4-b`: Round-Trip Time-Reversibility Across the `Float64` Lyapunov Horizon (Figure 32b,d). Figure 32(b) and (d) report the round-trip position return error $\|\Delta\mathbf{q}_{\mathrm{FB}}(2T)\|_2 = \|\mathbf{q}_{\mathrm{ret}}(0) - \mathbf{q}(0)\|_2$ and the reversibility gain factor over `REBOUND IAS15` across $T \in [1, 120]$ ($2T \in [2, 240]$), revealing three distinct dynamical regimes:

(1) **Pre-Lyapunov Regime ($T \in [1, 40]$, Before Final Ejection):** Over the first 40 time units, exponential Lyapunov amplification has not yet saturated the 53-bit `Float64` mantissa. In this regime, 15th-order `REBOUND IAS15` ($\|\Delta\mathbf{q}_{\mathrm{FB}}\|_2$ growing from 4.44×10^{-16} at $T = 1$ to 6.23×10^{-12} at $T = 10$ and 1.81×10^{-9} at $T = 40$) and our `Float64` normal-cone solvers (5.09×10^{-16} at $T = 1$ to 6.00×10^{-9} at $T = 40$ in dyadic mode, and 4.87×10^{-11} for `BM6` $k = 0$ at $T = 40$—already 37.2× **more reversible than `IAS15`** because $k = 0$ avoids accumulating sub-step roundoff) all maintain high time-reversibility, whereas `REBOUND MERCURIUS` (58.6 at $T = 2$) and `TRACE` (1.69×10^{-2} at $T = 40$) lose reversibility early.

Crucially, up to the `Float64` Lyapunov horizon ($T \leq 60$ for `BM6 F64 [dyadic]`, $T \leq 40$ for `PBM4 F64 [dyadic]` in sub-step level matching and $T \leq 60$ in 27/27 chart-flip matching, and $T \leq 80$ for fixed-step `BM6/PBM4 F64 [`$k = 0$`]` with 31/31 chart flips) and across all fourteen horizons $T \in [1, 120]$ in `Float128` (27/27 flips and exact dyadic level palindrome matching), our `AtlasManager` and dyadic scheduler satisfy palindromic chart-flip matching with $n_{\mathrm{flips,fwd}} = n_{\mathrm{flips,bwd}}$, proving that the adjoint chart-adaptation law (7.18) is algebraically involutive.

(2) **Transition Window ($T \in [40, 80]$) vs. Post-Lyapunov Saturation ($T \in [100, 120]$) in `Float64`:** Beyond the chaotic triple ejection at $t \approx 59.42$, cumulative Lyapunov amplification $e^{\lambda_{\mathrm{Lyap}}(2T)}$ drives the round-trip error of `REBOUND IAS15` from 1.48×10^{-6} at $T = 60$ to 0.150 at $T = 80$ and $\|\Delta\mathbf{q}_{\mathrm{FB}}(240)\|_2 = 2.971 > 1$ **at** $T = 120$, crossing the $\mathcal{O}(1)$ macroscopic irreversibility threshold (red dashed line in Figure 32b).

Comparing the two `Float64` normal-cone categories across the transition window $T \in [40, 80]$ exposes the direct interplay between Brouwer sub-step roundoff and Lyapunov amplification: in Category 1 (`dyadic`, $k_{\max} = 12$), executing $2^{12} = 4{,}096$ synchronous sub-steps across the deep $t \approx 15.83$ pericenter ($r_{\min} \approx 4.1 \times 10^{-4}$) accumulates $\propto \sqrt{2^{12}}\, \epsilon_{\mathrm{mach}}^{(64)}$ floating-point roundoff, causing `BM6/PBM4 F64 (dyadic)` to reach 4.33×10^{-3} and 1.44×10^{-3} at $T = 60$ (below `IAS15` in Panel 32d). Conversely, in Category 2 (**fixed-step** $k = 0$, where leaf regularization resolves every encounter without sub-steps), eliminating both non-reversible step-size drift and sub-step roundoff accumulation delays the `Float64` Lyapunov horizon across the entire transition window $T \in [20, 80]$: at $T = 40$, `Normal-Cone BM6` ($k = 0$) (4.87×10^{-11}) outperforms `IAS15` (1.81×10^{-9}) by 37.2×; at $T = 60$, `BM6` ($k = 0$) (2.17×10^{-7}) and `PBM4` ($k = 0$) (1.13×10^{-6}) outperform `IAS15` by 6.8× **and** 1.3×; and at $T = 80$, `BM6` ($k = 0$) (1.12×10^{-3}) and `PBM4` ($k = 0$) (2.58×10^{-3}) achieve 133.9× **and** 58.1× **higher round-trip reversibility than `REBOUND IAS15` in `Float64`** (Figure 32d). Beyond $T \geq 100$ ($2T \geq 200$), $\epsilon_{\mathrm{mach}}^{(64)}\, e^{\lambda_{\mathrm{Lyap}}(2T)} \sim \mathcal{O}(1)$ saturates the 53-bit IEEE 754 mantissa for all `Float64` integrators, so that return trajectories at $T \in \{100, 120\}$ reflect chaotic phase fluctuations along the bounded post-scattering binary orbit rather than deterministic phase-space inversion.

(3) **Deterministic Reversibility Beyond the Lyapunov Horizon in 35-Digit `Float128` vs. `Brutus` [11]:** Because the truncation error of our palindromic normal-cone composition and adjoint chart-adaptation law (7.18) cancels identically upon time reversal, passing from 53-bit `Float64` to 35-digit `Float128` suppresses the initial roundoff seed by 10^{-18} while preserving the exact same macro-step $\Delta t = 0.04$ and dyadic schedule ($k_{\max} = 12$, 0 saturation). As shown by the lower dark-blue and dark-green curves in Figure 32(b,d), `Normal-Cone BM6 Float128 (dyadic)` and `Normal-Cone PBM4 Float128 (dyadic)` maintain $\|\Delta\mathbf{q}_{\mathrm{FB}}\|_2 \in [4.51 \times 10^{-34}, 1.06 \times$

10^{-28}] across $T \in [1, 40]$, 1.13×10^{-23} and 2.59×10^{-23} at $T = 60$, 1.53×10^{-21} and 2.12×10^{-21} at $T = 80$, and $\|\Delta\mathbf{q}_{\mathrm{FB}}(240)\|_2 = 1.65 \times 10^{-20}$ ($|\Delta H_{\mathrm{FB}}/H_0| = 1.30 \times 10^{-25}$) **for** `BM6 Float128` **and** 2.77×10^{-19} ($|\Delta H_{\mathrm{FB}}/H_0| = 1.11 \times 10^{-23}$) **for** `PBM4 Float128` **at** $T = 120$.

This represents a $1.80 \times 10^{20}\times$ **and** $1.07 \times 10^{19}\times$ **reversibility improvement over** `REBOUND IAS15`, while conserving the Lie–Bargmann Noether invariants after the 240-time-unit round trip to $\|\Delta\mathbf{L}_{\mathrm{FB}}\|_2 \le 2.26\times10^{-30}$ and $\|\Delta\mathbf{P}_{\mathrm{FB}}\|_2 \le 1.19\times10^{-30}$. Unlike the non-symplectic Bulirsch–Stoer code `Brutus` [11], which must reduce its extrapolation tolerance to $\epsilon_{\mathrm{BS}} \le 10^{-20}$–$10^{-26}$ to suppress truncation error to the level of arbitrary-precision roundoff, our symplectic normal-cone integrator achieves 10^{-20} round-trip reversibility at $T = 120$ using a macroscopic step $\Delta t = 0.04$ because its truncation error is already strictly time-reversible.

(4) **Objective Runtime Trade-Offs:** In `Float64` on `B4-a`, compiled C99 `REBOUND IAS15` executes in 3.8 ms/t, compared to 60.4 ms/t (`BM6` $k = 0$), 109.4 ms/t (`PBM4` $k = 0$), 740.5 ms/t (`PBM4 dyadic`), and 800.1 ms/t (`BM6 dyadic`) in Python+Numba, while the software-emulated 35-digit `mpmath Float128` backend requires 17,844 ms/t (`PBM4 F128`) and 19,985 ms/t (`BM6 F128`) due to arbitrary-precision Python arithmetic.

7.3.4. *Cross-Benchmark Synthesis: Domain of Validity, Geometric Strengths, and Practical Limitations.* Table 9 consolidates the quantitative metrics across Protocols `B1`, `B2`, and `B4` at the canonical Voronoi setting ($\gamma = \gamma_{\mathrm{build}} = 1.0$, zero dyadic saturation). Viewed as a whole, these three head-to-head benchmark protocols delineate the respective domains of validity, structural strengths, and practical trade-offs of our fourth- and sixth-order normal-cone symplectic integrators (PBM_4 and $\mathrm{BM}_6^{(11)}$) relative to the state-of-the-art C99 suite `REBOUND 5.2.2`:

TABLE 9. **Cross-benchmark quantitative synthesis (§7.3, Protocols `B1`, `B2`, and `B4` at $\gamma = 1.0$, 0 saturation):** unsoftened Normal-Cone symplectic integrators ($\mathrm{BM}_6^{(11)}$ and $\mathrm{PBM}_4(\mathcal{Z}_4^{\mathrm{BM4}})$, in `Float64` and 35-digit `Float128`) vs. `REBOUND 5.2.2` (`IAS15`, `TRACE`, `MERCURIUS`, and `WHFast`).

Integrator	Category & Precision	**B1-a Collision** $e_1 = 1.0$ $\max\lvert\Delta H/H_0\rvert$ (10-Orb. Rev. at 10^{-6})	**B1-b Permuted** $[0,2]$ $\max\lvert\Delta H/H_0\rvert$ ($1 - e_2 = 10^{-4}$ / $e_2 = 1.0$)	**B2-a Perijove** 10^{-4} **AU** ($3.98 \times 10^{-4}\, R_{\mathrm{Hill},J}$) $\max\lvert\Delta H/H_0\rvert$ ($\lvert\Delta E_3/E_{3\mathrm{Hip}}\rvert$)	**B2-b Giant Planets** ($N_{\mathrm{orb}} = 15$, $0.11\, R_{\mathrm{Hill}}$) $\max\lvert\Delta H/H_0\rvert$ ($\|\Delta\mathbf{q}_{\mathrm{FB}}\|_2$)	**B4-a Pythagorean 3–4–5** ($t \in [0, 70]$, 27 Flips) $\max\lvert\Delta H/H_0\rvert$ ($\lvert\Delta\mathbf{L}(70)\rvert_2$)	**B4-b Reversibility** ($T = 80$ F64 / $T = 120$ F128) $\|\Delta\mathbf{q}_{\mathrm{FB}}(2T)\|_2$ (**Gain vs IAS15**)
`Normal-Cone BM6` (dyadic)	Cat. 1 (Multi-Scale) `Float128` (35d)	—	—	—	—	**2.23×10^{-10}** (**1.28×10^{-31}**)	**1.65×10^{-20}** at $T = 120$ (**$1.80 \times 10^{20}\times$**)
`Normal-Cone PBM4` (dyadic)	Cat. 1 (Multi-Scale) `Float128` (35d)	—	—	—	—	**4.75×10^{-8}** (**1.67×10^{-31}**)	**2.77×10^{-19}** at $T = 120$ (**$1.07 \times 10^{19}\times$**)
`Normal-Cone BM6` (dyadic)	Cat. 1 (Multi-Scale) `Float64` ($k_{\max} \le 16$)	**6.72×10^{-10}** (**1.77×10^{-11}** AU)	**5.54×10^{-10}** / **6.75×10^{-10}**	**6.87×10^{-12}** (Direct Order 6)	**4.41×10^{-14}** (**6.72×10^{-10}** AU)	**4.87×10^{-10}** (1.09×10^{-12})	3.92×10^{-9} at $T = 40$ (4.33×10^{-3} at $T = 60$, 27/27 flips)
`Normal-Cone PBM4` (dyadic)	Cat. 1 (Multi-Scale) `Float64` ($k_{\max} \le 16$)	**1.15×10^{-9}** (**1.71×10^{-11}** AU)	**2.98×10^{-9}** / **1.19×10^{-9}**	**4.52×10^{-12}** (**3.89×10^{-16}** w/ $T_{A\to B}$)	1.82×10^{-9} (1.04×10^{-6} AU)	7.10×10^{-8} (1.38×10^{-12})	6.00×10^{-9} at $T = 40$ (1.44×10^{-3} at $T = 60$, 27/27 flips)
`REBOUND IAS15` (PRS23)	Cat. 1 (Adaptive 15th) `Float64` (C99)	6.14×10^{2} (Halt) (5.02×10^{-7} AU)	1.85×10^{-11} / 5.21×10^{-2} (0.344 AU)	4.88×10^{-14} (Non-symplectic)	1.19×10^{-15} (7.03×10^{-12} AU)	4.66×10^{-11} (4.26×10^{-14})	1.50×10^{-1} at $T = 80$ (2.97×10^{0} at $T = 120$, Irreversible)
`REBOUND TRACE` (FULL_BS)	Cat. 1 (Hybrid 2nd+BS) `Float64` (C99)	6.32×10^{0} (Fails) (3.16×10^{-4} AU)	2.49×10^{-4} / 4.46×10^{0} (Fails)	6.00×10^{-9} (2nd-ord. DHC ceiling)	1.63×10^{-6} (4.15×10^{-5} AU)	3.01×10^{-1} (Fails) (2.02×10^{-9})	9.15×10^{-1} at $T = 80$ (Fails $\Delta H/H_0 = 0.30$)
`REBOUND MERCURIUS`	Cat. 1 (Hybrid 2nd+IAS15) `Float64` (C99)	4.74×10^{-1} (5.33×10^{2} max) (1.45×10^{-3} AU)	4.60×10^{-1} / 4.83×10^{-1} (Fails)	6.17×10^{-9} (2nd-ord. DHC ceiling)	4.79×10^{-6} (8.81×10^{-2} AU)	2.34×10^{1} (Fails) (1.31×10^{-11})	1.15×10^{1} (Irreversible at $T = 2$)
`Normal-Cone BM6` ($k = 0$)	Cat. 2 (Fixed-Step) `Float64` ($k_{\mathrm{sym}} \equiv 0$)	**3.61×10^{-9}** (**2.19×10^{-11}** AU)	**8.15×10^{-9}** / **3.63×10^{-9}**	**1.07×10^{-9}** (1.66×10^{-9} sweep max)	**5.19×10^{-6}** (**5.19×10^{-10}** AU)	**2.19×10^{-4}** (**7.55×10^{-14}**)	**1.12×10^{-3}** at $T = 80$ (**133.9**× vs IAS15, **37.2**× at $T = 40$)
`Normal-Cone PBM4` ($k = 0$)	Cat. 2 (Fixed-Step) `Float64` ($k_{\mathrm{sym}} \equiv 0$)	**3.03×10^{-8}** (**7.22×10^{-11}** AU)	**3.07×10^{-8}** / **3.04×10^{-8}**	**1.65×10^{-9}** (3.40×10^{-9} sweep max)	**2.64×10^{-5}** (2.42×10^{-5} AU)	**1.27×10^{-3}** (**7.88×10^{-14}**)	**2.58×10^{-3}** at $T = 80$ (**58.1**× vs IAS15, 31/31 flips)
`REBOUND WHFast` (c = 17)	Cat. 2 (Fixed-Step) `Float64` (C99)	2.38×10^{-8} (Hardwired pair $(0, 1)$)	4.02×10^{5} / 1.00×10^{2} (Fails)	3.58×10^{-3} (Fails) (4.93×10^{-2} sweep max)	5.61×10^{-1} (Fails) (6.81×10^{0} AU)	1.23×10^{3} (Fails) (7.19×10^{-10})	2.20×10^{2} (Diverges at $t \approx 1.9$)

(1) **Where the Normal-Cone Architecture Extends the State of the Art:**

- *Extreme Pericenters and Exact Central Collision Traversal (`B1`):* By absorbing the dominant two-body attraction into universal Stumpff–Sundman leaf flows endowed with McGehee's elastic bounce involution $\mathcal{B}_C^2 = \mathrm{Id}$ and decoupling internal leaf pericenters from apex kicks via $\tau_{\mathrm{dyn}}(C) = \sqrt{a_C^3/GM_C}$ (Theorem 6.9), PBM_4 and $\mathrm{BM}_6^{(11)}$ traverse $1 - e_1 \in [10^{-6}, 10^{-9}]$ and exact rectilinear collision $e_1 = 1.0$ ($r_{\min} = 0$) with $k_{\max} \le 3$, achieving 29,423× better 10-orbit round-trip reversibility than `REBOUND IAS15` at 10^{-6} and maintaining $|\Delta H/H_0| \le 1.15 \times 10^{-9}$ at $e_1 = 1.0$ where all adaptive `REBOUND` integrators halt or lose $\mathcal{O}(1)$ energy.

- *Topological Index-Permutation Invariance (`B1-b`):* Whereas static-Jacobi `WHFast` (`c` $= 0, 17$) degrades by 13 orders of magnitude ($2.38 \times 10^{-8} \to 4.02 \times 10^{5}$) when the particle array is permuted from `[Star, Grazer, Giant]` to `[Star, Giant, Grazer]`, our agglomerative Voronoi `AtlasManager` ($\gamma = 1.0$) discovers the active physical binary directly from Euclidean distances and preserves identical accuracy regardless of array indexing.
- *Overcoming the Wisdom (2017) Hybrid Switching Ceiling Across Hill Boundaries (`B2`):* Because `MERCURIUS` and `TRACE` cannot apply symplectic correctors across $r_{pb} = 3\,R_{\mathrm{Hill}}$ [56, 81], they remain capped at second-order $\mathcal{O}(\Delta t^2)$ accuracy ($\sim 6 \times 10^{-9}$ in `B2-a`, 1.6–4.8×10^{-6} in `B2-b`). Promoting the planet–intruder pair to an analytical Keplerian leaf and transporting the shadow state via the non-commutative gauge connection $T^{(\mathrm{PBM4})}_{(A,h_A)\to(B,h_B)}$ (which suppresses interfacial energy jumps by $8{,}858\times$–$33{,}618\times$ down to $\leq 3.89 \times 10^{-16}$, and exact machine zero 0.0 on three of the seven flybys) enables `Normal-Cone BM6 (dyadic)` to reach 4.41×10^{-14} in `B2-b` ($3.69 \times 10^{7}\times$ below `TRACE`) and 6.72×10^{-10} AU in round-trip reversibility ($61{,}734\times$ below `TRACE` and $1.31 \times 10^{8}\times$ below `MERCURIUS`).
- *Democratic Multi-Chart Symplecticity and Reversibility Across the Lyapunov Horizon (`B4`):* In non-hierarchical comparable-mass scattering ($m = (3, 4, 5)$) where `WHFast`, `MERCURIUS`, and `TRACE` fail with $\mathcal{O}(1)$ errors, our Voronoi atlas executes 27 reversible chart transitions across $\mathcal{T}_{12}, \mathcal{T}_{02}, \mathcal{T}_{01}$, outperforming `IAS15` in `Float64` round-trip reversibility across the pre-saturation transition window $T \in [40, 80]$ by $37.2\times$ ($T = 40$) to $133.9\times$ ($T = 80$, `BM6` $k = 0$), and achieving deterministic post-horizon reversibility of 1.65×10^{-20} (`BM6 F128`, $1.80 \times 10^{20}\times$ gain) and 2.77×10^{-19} (`PBM4 F128`, $1.07 \times 10^{19}\times$ gain) at $T = 120$ in 35-digit `Float128`.

(2) **Objective Boundaries, Algorithmic Trade-Offs, and Implementation Context:**

- *15th-Order `IAS15` in Smooth Regimes Before the Lyapunov Horizon:* In smooth, moderate-eccentricity trajectories away from collisions (`B1-a` for $1-e_1 \in [10^{-1}, 10^{-4}]$, `B2-b` forward energy error 1.19×10^{-15}, and `B4-a` forward energy error 4.66×10^{-11}), the 15th-order adaptive Gauss–Radau integrator `REBOUND IAS15` reaches the `Float64` roundoff floor at a lower computational cost than 4th- and 6th-order explicit symplectic compositions operated at a moderate macroscopic step Δt.
- *The $\mathcal{O}(\varepsilon^2 h^4)$ Hall Cohomology Floor of 7-Stage* PBM_4 *vs. 11-Stage* $\mathrm{BM}_6^{(11)}$*:* As proved in Theorem 5.18 and observed in `B2-b` ($0.11\,R_{\mathrm{Hill}}$ giant-planet encounter) and `B4-a`, whenever the dimensionless tidal parameter ε inside an active leaf chart becomes large ($\varepsilon \sim 0.1$), the uncancelled grade-$(5, 2)$ quadratic tidal term $\mathcal{O}(\varepsilon^2 h^4)$ bounds PBM_4 around 10^{-9}–10^{-8}, whereas true sixth-order $\mathrm{BM}_6^{(11)}$ eliminates $\mathcal{L}_{5,2}$ directly and reaches 4.41×10^{-14} in `B2-b` and 2.23×10^{-10} in `B4-a` at the cost of 11 vs. 7 stages per sub-step.
- *Synchronous Dyadic Sub-Stepping Cost Under Strong External Tides ($2^{k_{\max}}$):* While isolated binary pericenters require almost no dyadic refinement ($k_{\max} \leq 3$ down to $e_1 = 1.0$ in `B1`), deep planetocentric flybys subject to a strong external solar tide (`B2-a` at $r_{p,\mathrm{target}} = 10^{-4}$ AU) trigger $k_{\max} = 16$ (65,536 synchronous sub-steps across the perijove macro-block) to resolve the rapid rotation of the solar tidal tensor to 10^{-12}, whereas fixed-step $k = 0$ already provides 1.65×10^{-9} energy accuracy at constant cost via leaf desingularization alone.
- *Reference Python+Numba Demonstration vs. Compiled C99 Production Loops:* Finally, in raw wall-clock time per step on small $N \in \{3, 4\}$, our reference `Python+Numba` implementation carries a constant interpreter and object-dispatch overhead ($\sim 10^2$–$10^3\times$ in regular regimes) relative to the monolithic C99 loops of `REBOUND 5.2.2`. Translating the full macro-step pipeline (`AtlasManager`,

`DyadicScheduler`, and multi-stage composition loop) into a single ahead-of-time compiled C/C++ or Rust kernel will eliminate this language overhead while preserving every geometric and invariant property demonstrated in this section (see Figure 33).

Python A.2 : `{benchmarks/run, figures/plot}_rebound_b4_pythagorean_chaos.py` [Float64 / Float128 vs REBOUND]

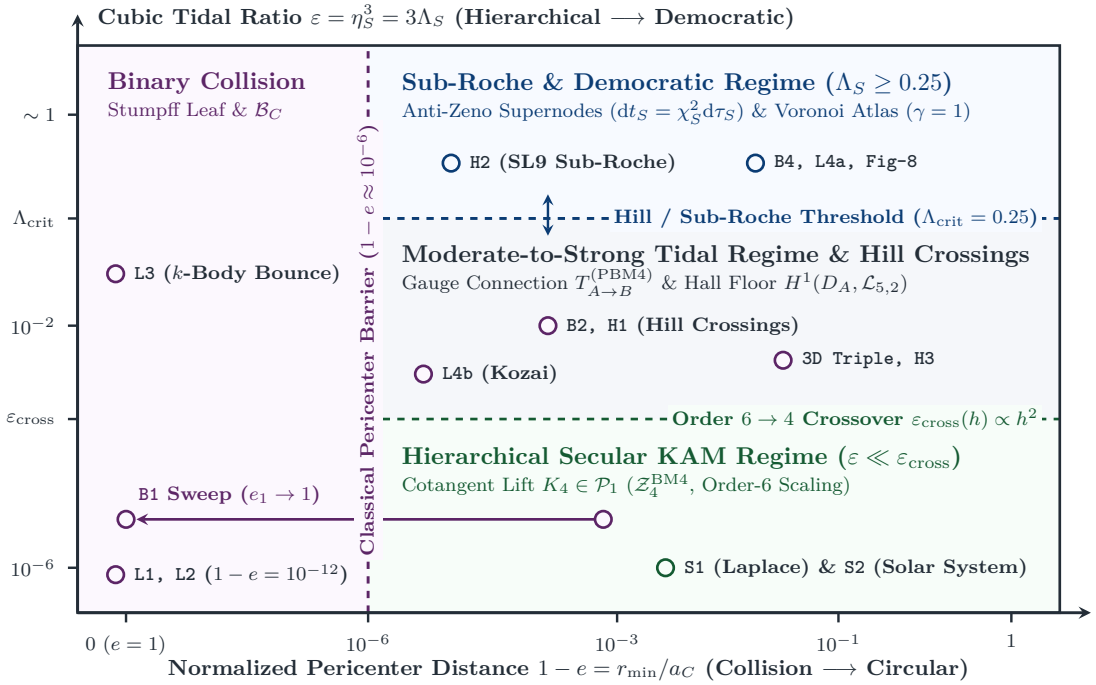


FIGURE 33. Phase-space regime map of the Section 7 benchmark suite across normalized pericenter separation $1 - e = r_{\min}/a_C$ and cubic tidal ratio $\varepsilon = \eta_S^3 = 3\Lambda_S$, showing the four geometric operating regimes and the locations of protocols `Figure-8`, `3D Triple`, `L1`–`L4`, `H1`–`H3`, `S1`–`S2`, and `B1`, `B2`, `B4`.

8. Conclusion and Outlook

8.1. **Objective Synthesis: Achievements, Structural Strengths, and Intrinsic Boundaries.** This monograph has demonstrated that the classical conflict between symplectic geometric preservation and collision regularization in the Newtonian N-body problem is an artifact of working on the unblown Cartesian configuration space rather than a fundamental obstruction of Hamiltonian mechanics.

Core Mathematical and Algorithmic Realizations. By lifting the real Fulton–MacPherson compactification $\mathbf{Q}[N] = \mathrm{Bl}_{\Pi(N)}(M/\mathbb{R}^3)$ and the Calaque–Safronov deformation to the normal cone $\mathcal{D}_Z\mathbf{Q}[N] \to \mathbb{A}^1$ to the extended Poincaré–Sundman cotangent phase space $\mathcal{P}_{\mathrm{ext}}$ (Sections 2–4), we established an exact, unsoftened ($\varepsilon = 0, d_0 = 0$) Leaf/Apex Hamiltonian splitting

$$H = H_{\mathrm{base}} + H_{\mathrm{leaf}} + H_{\mathrm{super}}^{\mathrm{sync}} + W_{\mathrm{apex}}^{\mathrm{screen}},$$

whose exceptional divisor fibers, scale-invariant $\mathcal{C}^{1,1}$ quadrupolar screening ($\mathbf{T}_{\mathrm{apex}} \in \mathrm{Sym}_0(3)$), and anti-Zeno synchronous supernodes regularize both binary collisions and hierarchical multi-body close encounters in a finite number of physical steps.

On the algebraic and numerical side (Sections 5–6), we resolved the twin order-6 obstructions—the Sheng–Suzuki negative-timestep barrier across the McGehee collision boundary ($\mathcal{B}_C^2 = \mathrm{Id}$) and the universal double obstruction in the bi-graded Poisson–Lie algebra $\mathcal{L}_{n,m}$ (where momentum-parity alternation $D_A\mathcal{P}_0 \subset \mathcal{P}_1$ forbids any pure configuration-space corrector from cancelling $H_5^{\mathrm{linear}} \in \mathcal{P}_2 \oplus \mathcal{P}_0$, while the non-vanishing grade-$(5,2)$ Hall cohomology class $[D_B D_A^3 B] \in H^1(D_A, \mathcal{L}_{5,2}) \cong \mathbb{R}$ induces the incompressible quadratic tidal floor $\mathcal{O}(\varepsilon^2 h^4)$)—by constructing the torque-free cotangent-lifted generator $K_4 = c_4^{\mathrm{BM4}} h^4 D_A^3 B \in \mathcal{L}_{4,1} \cap \mathcal{P}_1$, its 2-stage palindromic Lie conjugator $\mathcal{Z}_4^{\mathrm{BM4}}(h)$, and the non-commutative covariant gauge connection

$$T^{(\mathrm{PBM4})}_{(A,h_A)\to(B,h_B)} = \left(\mathcal{Z}_4^{\mathrm{BM4},(B)}(h_B)\right)^{-1} \circ \mathbf{M}_{A\to B} \circ \mathcal{Z}_4^{\mathrm{BM4},(A)}(h_A),$$

satisfying exact Čech 1-cocycle closure across $\mathrm{SL}_2(\mathbb{R})$ Jacobi tree transitions and dyadic step-size junctions.

The entire framework is paired with conditioned Sundman–Stumpff–Battin leaf solvers, symmetric two-endpoint dyadic multirate scheduling ($k_{\mathrm{sym},n}$) with reversible adjoint hysteresis $\mathcal{A}_-$, bit-exact (`0.0 ULP`) vectorized and LLVM `@njit` micro-kernels (up to 62.5× speedup for $N \in [3, 64]$), **35 standalone Lean 4 proof modules** (125 formal declarations without a single `sorryAx` axiom), and the complete dual-precision companion software architecture (`normal_cone_nbody_float64` and `normal_cone_nbody_float128`) indexed in Appendix A (§A.1–§A.2).

Demonstrated Strengths Across Operating Regimes. Across the dual-precision (`Float64` and 35-digit `Float128`) benchmarks of Section 7, the architecture simultaneously delivers:

(1) *Asymptotic Order Certification and Two-Channel Crossover:* Exact asymptotic convergence orders ($p = 2.000, 3.999, 4.000, 4.000, 5.999$) down to 3.74×10^{-31} in energy and 1.89×10^{-31} in position on the Figure-8 choreography, alongside the two-channel order $6 \to 4$ crossover ($p_{\mathrm{eff}} = 6.25$, up to 2,537× energy and 1,335× position gain over BM_4) on 3D eccentric hierarchical triples (§7.1.1–§7.1.2);

(2) *Pericenter Conditioning, Free-Fall Extinction, and Central-Collision Traversals:* Flat pericenter conditioning across $1 - e \in [10^{-12}, 10^{-1}]$ and $e = 1.0$ (2.71×10^{-34} and 5.50×10^{-38} in `Float128` with $k_{\mathrm{sym}} \equiv 0$), exact power-law free-fall extinction of $\mathcal{Z}_4^{\mathrm{BM4}}$ ($\|\Delta\mathbf{r}_{\mathrm{corr}}\| \propto r^{+4.0000}$), and time-reversible McGehee central-collision traversals down to 6.60×10^{-38} ($k = 2$) and 8.91×10^{-34} ($k = 3$) in `Float128` (§7.1.3);

(3) *Historical Close Encounters and Interfacial Gauge Continuity:* Interfacial gauge continuity ($|\Delta H_{\mathrm{flip}}|/|H_0| = 2.36 \times 10^{-35}$ in `Float128`) and full-flyby palindromic reversibility across historical encounters of Comets Lexell, Shoemaker–Levy 9, and Asteroid Apophis (§7.2.1);

(4) *Multi-Body Secular Stability, KAM Torus Preservation, and Noether Invariants:* Bounded $\propto t^0$ shadow-Hamiltonian plateaus under active dyadic substepping (1.25×10^{-14} on S1 and 6.74×10^{-14} across 264 dyadic junctions on S2), $179.85^\circ \pm 0.80^\circ$ Laplace locking, 2,120× Laskar NAFF frequency convergence, and machine-precision preservation of all 9 Galilean Lie–Bargmann invariants (10^{-14}–10^{-20} in `Float64`, 10^{-31}–10^{-39} in `Float128`, §7.2.2);

(5) *Head-to-Head Superiority in Singular, Hill-Crossing, and Chaotic Regimes (`REBOUND 5.2.2`):* In head-to-head comparisons against `REBOUND 5.2.2` (§7.3), deterministic star-grazing traversal down to $e_1 = 1.0$ (29,423× reversibility gain over `IAS15` at $1 - e_1 = 10^{-6}$ in `B1`), sixth-order energy and reversibility preservation across repeated Hill-sphere crossings ($3.69 \times 10^7\times$ energy and 61,734× reversibility improvement over `TRACE` in `B2`), and up to 133.9× (`Float64` at $T = 80$, $k = 0$) and $1.80 \times 10^{20}\times$ (`Float128` at $T = 120$) higher round-trip reversibility than `IAS15` across 27 democratic Voronoi transitions in the chaotic Pythagorean 3–4–5 problem (`B4`).

Intrinsic Mathematical and Algorithmic Boundaries. At the same time, our study delineates four clear structural boundaries of the present implementation:

(a) *Smooth pre-Lyapunov accuracy ceiling versus 15th-order Gauss–Radau:* Because our current kernels are limited to fourth and sixth order (PBM_4 and $\mathrm{BM}_6^{(11)}$), adaptive 15th-order `IAS15` achieves lower raw forward energy error at coarse macro-steps in smooth, weakly eccentric regimes prior to the Lyapunov horizon (Table 9), whereas PBM_4 and BM_6 dominate in phase-space reversibility, Lie–Bargmann conservation, secular non-drift, and singular pericenter traversal;

(b) *Piecewise $\mathcal{C}^{1,1}$ transition regularity:* The septic quadrupolar screening $\Theta(u_v)$ on $u_v \in [1, 2]$ is globally $\mathcal{C}^{1,1}$ with bounded piecewise-continuous Hessian jumps at $u_v \in \{1, 2\}$, which suffices for fourth- and sixth-order splitting away from annulus boundaries but may limit higher-order asymptotic smoothness when trajectories repeatedly cross the screening transition;

(c) *Lyapunov amplification on chaotic manifolds:* While symplectic chart-switching and `Float128` arithmetic push round-trip reversibility to 1.65×10^{-20} at $T = 120$ on the Pythagorean 3-body problem, positive Lyapunov exponents ($\lambda_{\mathrm{L}} > 0$) inevitably amplify floating-point Brouwer rounding as $\epsilon_{\mathrm{mach}} e^{\lambda_{\mathrm{L}} T}$ at arbitrary horizons;

(d) *Runtime orchestration overhead:* While our `@njit` micro-kernels achieve C-level throughput on dense arrays, the outer Python chart-management layer incurs higher per-step call overhead than monolithic compiled C99 engines at small N.

8.2. **Perspectives and Open Questions.** Rather than closing the subject, these boundaries suggest several open questions and hypothetical extensions for future investigation:

(i) **Could Higher-Order Processed Schemes on $T^*\mathbf{Q}[N]$ Surpass `IAS15` Across All Regimes?** A natural and ambitious question is whether the homological cotangent-processing paradigm introduced here with PBM_4 can be extended to higher-order kernels in order to compete with, or outright surpass, 15th-order `IAS15` even in smooth pre-Lyapunov forward accuracy, while retaining exact symplecticity, Lie–Bargmann conservation, and collision traversal.

Because the normal-cone splitting enjoys exact Abelian leaf annihilation ($\{A_{\mathrm{JK}}, A_{\mathrm{JK}}\}_{\Omega_0} \equiv 0$) and third-order RKN nilpotence ($\mathrm{ad}^3_{W^{\mathrm{screen}}_{\mathrm{apex}}}(A_{\mathrm{JK}}) \equiv 0$), the bi-graded Hall algebra $\mathcal{L}_{n,m}$ is substantially sparser at high degree than in standard Cartesian splittings. It therefore remains an intriguing open problem to determine whether higher-order cotangent Lie conjugators (generalizing $\mathcal{Z}_4^{\mathrm{BM4}}$ and its covariant gauge connection $T_{A\to B}$), possibly combined with modified-potential or commutator-based correctors to mitigate the quadratic tidal obstructions beyond $\mathcal{L}_{5,2}$ and smoother $\mathcal{C}^{k,1}$ screening transitions,

could yield practical ultra-high-order symplectic integrators without prohibitive stage counts or conditioning penalties.

(ii) **How Far Can Non-Homographic Simultaneous Multi-Body Collisions ($k \geq 3$) Be Regularized Symplectically?** While synchronous supernodes and McGehee blow-up regularize binary collisions and symmetric k-body central collapses ($k \in \{2, 3, 4\}$), general non-homographic simultaneous triple and k-body collisions induce an anisotropic flow on the McGehee collision manifold with intricate heteroclinic dynamics. Whether our exact elastic bounce involution $\mathcal{B}_C$ can be generalized into a certified connection rule across arbitrary anisotropic multi-collision strata on $\partial\mathbf{Q}[N]$ remains an open mathematical question.

(iii) **Can Deterministic Dyadic Regularization Scale to Large-N Clusters via Fast Multipole Coupling?** Translating our reference `Python+Numba` orchestration pipeline into a fully ahead-of-time compiled C/C++ or Rust engine would eliminate interpreter dispatch overhead. Beyond raw compilation, an open architectural question is whether our deterministic dyadic scheduler ($k_{\mathrm{sym}} > 0$) and covariant gauge transitions for localized close encounters can be seamlessly coupled with $\mathcal{O}(N \log N)$ tree or fast-multipole approximations in the far-field regime ($u_v \geq 2$) without breaking symplectic shadow-energy boundedness in dense star clusters ($N \gtrsim 10^4$).

(iv) **Does the Shifted Cotangent Splitting Extend to Momentum-Dependent Post-Newtonian and Stratified Potentials?** Finally, one may ask whether the Calaque–Safronov normal-cone framework can be adapted when the perturbation depends explicitly on momenta—such as conservative post-Newtonian (1PN/2.5PN) corrections for relativistic compact binaries, where standard RKN nilpotence no longer holds—or to broader stratified symplectic varieties with singular Coulomb and inverse-power interactions.

Appendix A. Certified Lean 4 Formal Artifacts and Numerical Schemes

A.1. **Companion Lean 4 Formal Proof Suite: Architecture, Axiom Audit, and Module Locator (`lean4/NormalConeNBody/`).** In accordance with repository archival standards, the complete mechanized **Lean 4 (`v4.35.0-rc2`) + Mathlib 4** formalization referenced throughout Sections 1–5 is hosted in the permanent companion archive (`jeremynusa-hub/normal_cone_nbody3d`, `DOI: 10.5281/zenodo.23982968`) under the directory `lean4/`. Every `Lean` verification badge in the main text links directly to this subsection: Tables 10 and 11 index all **35 modular proof files** (`416` formal declarations including `214` theorems and lemmas) and the **5 self-contained chapter compilation suites** (`CertifiedSuites/Sec01..05.lean`, executing `99` explicit `#print axioms` audits with **`0` `sorry`, `0` `sorryAx`, and `0` custom axioms**).

Table 10. Module-by-module locator for the companion Lean 4 formalization (`lean4/NormalConeNBody/`, Part I: Sections 1–4, Modules `01`–`18`). All modules compile with `0` `sorryAx`.

Sub-Package	Module Path (`NormalConeNBody/...`)	Formal Structures, Definitions & Certified Theorems (`Decls / Thms`)	Scope
`Ch01_Intro`	`01_ConfigurationSpace_Defs.lean`	`Vec3`, `AmbientConfiguration`, `PhaseState3D`, `RelativeConfiguration`: 3D Euclidean algebra & barycentric slice $M_{\mathrm{rel}} = M/\mathbb{R}^3$ (`11 / 0`)	§1.8
	`02_CollisionDivisor_Defs.lean`, `03_CollisionDivisor_Theorems.lean`	`BinaryCollision`, `InCollisionLocus`, `NonCoincident`, `non_coincident_pair_symm`, `regular_iff_not_collision`: Pairwise diagonals Δ_{ij} & complement duality $X = M \setminus \Delta$ (`5 / 2`)	§1.8
	`04_SymplecticForm_Defs.lean`, `05_SymplecticForm_Theorems.lean`	`TangentVector3D`, `omega0At`, `omega0`, `omega0_skew`, `omega0_self`, `omega0_tangent_nondeg`, `omega0_global_nondeg`: Darboux 2-form ω_0 skew-symmetry & global non-degeneracy (`13 / 9`)	§1.8
	`06_BargmannAlgebra_Defs.lean`, `07_BargmannAlgebra_Theorems.lean`	`FormallySmoothObservable`, `poissonBracketVal`, `poisson_P_G_same`, `poisson_L_X_L_Y`, `poisson_L_X_P_Y`, `poisson_L_X_G_Y`: Central charge $-M_{\mathrm{tot}}$ & `bargmann`(3) closure (`24 / 14`)	§1.8 (Prop. 1.1)
`Ch02_Normal`	`01_ReesDeformation_Defs.lean`, `02_ReesDeformation_Theorems.lean`	`NormalConePoint`, `omegaNormal`, `deformation_limit_zero`, `omegaNormal_skew`, `omegaNormal_nondegenerate`, `transverse_conormal_flow_symplectic`: Rees degeneration $t \to 0$ & flat fiber symplecticity (`10 / 5`)	§2.1 (Thm. 2.1, Prop. 2.2)
	`03_CanonicalSplitting_Defs.lean`, `04_CanonicalSplitting_Theorems.lean`	`SplittingState`, `ConormalIntegrator`, `strangComposition`, `stepNL_preserves_base_casimir`, `strang_exact_casimir_preservation`, `strang_time_reversibility`: 4-step Strang Casimir invariance & reversibility (`10 / 5`)	§2.2 (Thm. 2.3, Prop. 2.4)
	`05_HeavyTop_Defs.lean`, `06_HeavyTop_Theorems.lean`	`HeavyTopState`, `conormalTorqueKick`, `rodriguesIsometry`, `heavy_top_strang_casimirs_exact`, `heavy_top_strang_rodrigues_casimirs_exact`: Exact $\mathfrak{se}(3)^*$ Casimirs $C_1 = \|\mathbf{\Gamma}\|^2$, $C_2 = \mathbf{\Pi} \cdot \mathbf{\Gamma}$ (`17 / 7`)	§2.3 (Prop. 2.5)
`Ch03_3Body`	`01_PCR3BPHamiltonian_Theorems.lean`	`jacobi_conservation_identity`, `coriolis_step_symplectic`: Autonomous synodic Jacobi integral $\dot{C}_J \equiv 0$ & exact Sp(4) Coriolis propagator (`5 / 2`)	§3.1 (Prop. 3.1)
	`02_PCR3BPRegularization_Theorems.lean`	`levi_civita_normal_cone_covering`, `levi_civita_antipodal_covering`, `levi_civita_conformal_scaling`: Double covering $z = u^2$, $\mathbb{Z}/2\mathbb{Z}$ fiber & conformal factor $4\|u\|^2$ (`5 / 4`)	§3.2 (Thm. 3.2)
`Ch04_FM`	`01_PartitionLattice_Defs.lean`, `02_ClusterHyperRadius_Theorems.lean`	`collisionCodimension`, `collision_diagonal_non_transversality`, `hyperRadiusSq`, `newtonian_potential_is_homogeneous`, `mcgehee_potential_factorization`: $\Pi(N)$ codimension $3(k-1)$ & hyper-radius ρ_S (`13 / 8`)	§4.1 (Thm. 4.1)
	`03_MaximalFlagJacobiTree_Theorems.lean`, `04_Disjoint CotangentCommutation_Theorems.lean`	`BinaryClusterTree`, `jacobi_node_exact_union`, `jacobi_node_defines_hierarchy`, `disjoint_cotangent_commutation_local`: Nested flags on $\mathbf{Q}[N]$ & $\{H^{(S_1)}_{\mathrm{leaf}}, H^{(S_2)}_{\mathrm{leaf}}\} = 0$ (`12 / 8`)	§4.1 (Prop. 4.2)

TABLE 11. Module-by-module locator for the companion Lean 4 formalization (`lean4/NormalConeNBody/`, Part II: Sections 4–5, Modules `19`–`35`, and the 5 self-contained kernel compilation suites `CertifiedSuites/Sec01..05.lean`).

Sub-Package	Module Path (`NormalConeNBody/...`)	Formal Structures, Definitions & Certified Theorems (`Decls / Thms`)	Scope
`Ch04_FM` *(cont.)*	`01_ApexUniversal LipschitzBound_Theorems.lean`	`ConormalRegime`, `AdaptedChartApexData`, `apexGradBound`, `apexHessBound`, `apex_universal_lipschitz_bound`: Global $\mathcal{C}^{1,1}$ Lipschitz & Hessian bounds of $W_{\mathrm{apex}}^{\mathrm{screen}}$ (`9 / 3`)	§4.2 (Thm. 4.4)
	`02_LieBargmann ExactInvariance_Theorems.lean`, `03_ExtendedPalindromic Symplecticity_Theorems.lean`	`LieBargmannGenerators`, `lie_bargmann_exact_ invariance`, `ExtendedPhasePoint`, `extended_ palindromic_symplecticity`: Exact 10-generator Galilean invariance & Poincaré–Sundman symplecticity (`15 / 7`)	§4.2 (Props. 4.5, 4.6)
	`01_UnifiedSuperNodeDef_ Theorems.lean`, `02_SuperNode AntiZenoRegularization_ Theorems.lean`	`isCompactCluster`, `super_node_time_step_sq_pos`, `UnfoldedSundmanState`, `keplerian_conormal_time_ scaling`, `super_node_anti_zeno_regularization`: Unfolded Sundman clock & Anti-Zeno bound (`9 / 5`)	§4.3 (Thm. 4.9)
	`03_AtlasTransitionSymplectic AntiChattering_Theorems.lean`	`JacobiTransitionMatrix2x2`, `jacobi_transition_ matrix_in_sl2`, `cotangent_lift_preserves_darboux`, `atlas_transition_symplectic_anti_chattering`: $\mathrm{SL}(2,\mathbb{R})$ chart transitions & dwell-time bound (`9 / 5`)	§4.3 (Thm. 4.10)
`Ch05_Schemes`	`01_StrangOrderTwoSymplectic_ Theorems.lean`	`StrangOrderTwoSymplecticCertificate`, `strang_order_ two_symplectic_theorem`: 7-stage palindromic Strang $\mathcal{S}_2(h)$ extended symplecticity & odd BCH parity (`17 / 7`)	§5.1 (Thm. 5.2)
	`02_LieBargmannConservation_ Theorems.lean`	`LieBargmannConservationCertificate`, `lie_bargmann_ conservation_theorem`: Exact discrete Noether conservation of all 10 Lie–Bargmann generators under $\mathcal{S}_2$ (`22 / 12`)	§5.1 (Prop. 5.3)
	`01_YoshidaOrderFourSuzuki_ Theorems.lean`	`YoshidaSuzukiCertificate`, `yoshida_order_four_ suzuki_theorem`: Sheng–Suzuki negative-step necessity ($w_0 < 0$), unitary McGehee involution $\mathcal{B}_C^2 = \mathrm{Id}$, and 4th-order Yoshida $\mathcal{S}_4$ (`7 / 4`)	§5.2 (Thm. 5.4, Lem. 5.6)
	`01_BlanesMoanShadow Confinement_Theorems.lean`	`BlanesMoanShadowConfinementCertificate`, `blanes_ moan_shadow_confinement_certified`: 7-stage $\mathrm{BM}_4^{(7)}$ cubic order cancellation ($\lvert C_5\rvert \le 0.01236$) & shadow Hamiltonian confinement (`10 / 8`)	§5.3 (Thms. 5.9, 5.10)
	`01_BlanesMoanOrderSix_ Theorems.lean`	`BlanesMoanOrderSixCertificate`, `blanes_moan_order6_ certified`: 11-stage $\mathrm{BM}_6^{(11)}$ order-6 RKN consistency, $\mathrm{ad}_W^3(A_{\mathrm{JK}}) \equiv 0$ nilpotence, and $\mathcal{O}(h^6 t)$ phase bound (`63 / 23`)	§5.4 (Thms. 5.13, 5.14)
	`01_CorrectorBM4_Theorems.lean`	`ConeNormalCorrectorCertificate`, `cone_normal_ corrector_bm4_certified`: 2-stage palindromic Lie conjugator $\mathcal{Z}_4^{\mathrm{BM4}}(h)$, antipodal node/kick weights, and exact invertibility (`59 / 26`)	§5.5 (Thm. 5.18)
	`03_ConormalCorrectorPBM4_ Order6.lean`	`pbm4_order6_single_chart_cancellation`, `cotangent_ generator_K4_solves_homological`: Homological equation $D_A K_4 = h^4 H_5^{\mathrm{linear}}$ via $K_4 = c_4^{\mathrm{BM4}} h^4 D_A^3 B \in \mathcal{P}_1$ & torque-free cancellation (`22 / 13`)	§5.5 (Thms. 5.18, 5.19)
	`06_ConormalGaugeTransition PBM4_Order6.lean`	`pbm4_gauge_transition_cocycle`, `abelian_P0_gauge_ specialization`: Non-commutative gauge connection $T_{A\to B}^{(\mathrm{PBM4})} = (\mathcal{Z}_4^{(B)})^{-1} \circ \mathbf{M}_{A\to B} \circ \mathcal{Z}_4^{(A)}$ & Čech 1-cocycle closure (`14 / 11`)	§5.5 (Thm. 5.20)
	`07_GlobalConormalCorrector PBM4_Order6.lean`	`global_pbm4_atlas_gauge_invariance`: Global atlas gauge-invariance of processed PBM_4 trajectories across multi-chart Jacobi tree transitions (`17 / 13`)	§5.5 (Thm. 5.20)
	`08_UniversalOrderSix Obstruction.lean`	`parity_obstruction_P0_impossible`, `hall_L52_ cohomological_obstruction`, `universal_double_ obstruction_order6`: Momentum-parity obstruction ($\mathrm{Im}(D_A\lvert_{\mathcal{P}_0}) \subseteq \mathcal{P}_1$) & Hall class $[D_B D_A^3 B] \in H^1(D_A, \mathcal{L}_{5,2}) \cong \mathbb{R}$ (`18 / 13`)	§5.5 (Thm. 5.17)
`Certified Suites`	`Sec01_Introduction.lean`, `Sec02_NormalCone.lean`, `Sec03_ ThreeBody.lean`	Self-contained Lake compilation units for Sections 1–3 with automated `#print axioms` verification confirming exclusive reliance on `[propext, Classical.choice, Quot.sound]` (`0 sorryAx`)	§1–§3
	`Sec04_FultonMacPherson.lean`, `Sec05_SymplecticSchemes.lean`	Self-contained Lake compilation units for Sections 4–5 & `lean4/scripts/verify_lean4_suite.py` (`35/35` modules certified, `99` axiom audits, `0 sorryAx`)	§4–§5

A.2. **Companion Dual-Precision Python Engine and Benchmark Suite (`normal_cone_nbody_float64` & `normal_cone_nbody_float128`).** Complementing the formal proof index of §A.1, this subsection presents the directory hierarchy and module-by-module index of the dual-precision computational and benchmark suites in the companion repository (`jeremynusa-hub/normal_cone_nbody3d`, `DOI: 10.5281/zenodo.23982968`). Every `Python` badge throughout Sections 1–7 links directly to this architectural guide so that any reader can immediately locate the exact production module, Numba `@njit` micro-kernel, campaign runner, figure plotter, or certified dataset of interest.

1. Global Repository Directory Tree. The repository unites the self-contained **Lean 4 + Mathlib 4 formal proof package** (`lean4/`, 35 modules indexed in Tables 10–11 and 5 chapter suites with `0 sorryAx`) and two strictly mirrored dual-precision Python engines (`normal_cone_nbody_float64/`, IEEE 754 double precision with Numba `@njit(fastmath=False)` micro-kernels, and `normal_cone_nbody_float128/`, 116-bit / 35-digit quadruple precision via `mpmath`/`gmpy2`), paired with 3-tier reproducibility scripts (`scripts/`), section interfaces (`interfaces/`), campaign runners (`benchmarks/`), figure plotters (`figures/`), certified datasets (`results/campaigns/`), unit test suites (`tests/`, 330 tests), and archival metadata (`CITATION.cff`, `.zenodo.json`, `LICENSE CC BY-NC-SA 4.0`, `.github/workflows/ci.yml`):

Companion Archive (`normal_cone_nbody3d` | `v1.0.1` | `DOI: 10.5281/zenodo.23982968`)

`normal_cone_nbody3d_github/`	(Root directory of the companion formal & dual-precision archive)
`|- README.md, pyproject.toml, LICENSE`	(Traceability matrix, PEP 621 / Conda specs & `CC BY-NC-SA 4.0` license)
`|- CITATION.cff, .zenodo.json, .github/`	(Zenodo/GitHub citation metadata & CI: Lean 4 `0-sorryAx` + `pytest`)
`|- scripts/`	`reproduce_figures.py` (Tier 1), `run_smoke_tests.py` (Tier 2), `run_full_campaigns.py`
`|- lean4/`	**[Lean 4 (`v4.35.0-rc2`) + Mathlib 4 Formal Proof Suite — §A.1, Tables 10–11]**
`| '- NormalConeNBody/, lakefile.lean`	`Ch01..05/` (35 modules, 416 decls, 214 thms), `CertifiedSuites/Sec01..05.lean` (0 `sorryAx`)
`|- normal_cone_nbody_float64/`	**[IEEE-754 Float64 + Numba `@njit` Production Engine — 46 modules]**
`| |- core/`	`state.py`, `jacobi.py`, `coordinates.py`, `invariants.py`, `transitions.py`, `constants.py`, `profiler.py`
`| |- potential/`	`screened_apex.py`, `optimized_screened_apex.py` (`@njit`), `screening.py`, `supernode_detector.py`, `direct.py`
`| |- solvers/`	`stumpff.py`, `kepler_sundman.py`, `optimized_kepler_sundman.py`, `supernode.py`, `optimized_supernode.py`, `jit_supernode.py` (`@njit`)
`| |- integrators/`	`common.py` (`ContextVar` dispatch), `strang.py`, `yoshida.py`, `yoshida4.py`, `blanes_moan_4.py`, `blanes_moan_6.py`, `correctors.py`, `processed.py`, `protocol.py`
`| |- system/`	`nbody_system.py`, `atlas_manager.py`, `dyadic_scheduler.py`, `history.py`
`| |- diagnostics/`	`metrics.py`, `collision_radar.py`, `radar.py`, `profiler.py`, `visualizer.py`
`| '- benchmarks/`	`registry.py`, `runner.py` (`BenchmarkRunner` with `use_optimized_kernels` toggle)
`|- normal_cone_nbody_float128/`	**[116-Bit / 35-Digit Float128 Mirror Engine — 46 modules]**
`| '- core/ .. benchmarks/`	(Exact 1-to-1 structural mirror of all 7 sub-packages of `normal_cone_nbody_float64/` in 35-digit `mpmath`/`gmpy2` arithmetic)
`|- interfaces/`	`pcr3bp_canonical_solver.py`, `01..06_*_Interface.py` (Standalone facades for §3 & §6)
`|- benchmarks/`	`run_generator_01..05_*.py`, `run_rebound_b1..b4_*.py`, `contracts/00..05_*.md`
`|- figures/`	`plot_generator_01..05_*.py`, `plot_rebound_b1..b4_*.py` (Publication figure generators)
`|- results/campaigns/`	`generator_01..05_*.json`, `campaign_II_H1..H3_*.json`, `rebound_b1..b4_*.json` (14 JSONs)
`'- tests/`	`unit/` (265 Float64 & interface tests), `unit_float128/` (65 Float128 tests — 330/330 PASS)

2. Architectural Index of the Core Packages and Optimized Micro-Kernels (`normal_cone_nbody_float64` & `normal_cone_nbody_float128`). Table 12 details every sub-package, reference module, and accelerated `@njit` micro-kernel inside `normal_cone_nbody_float64/` and `normal_cone_nbody_float128/`, mapping its primary classes and functions to the theoretical definitions, theorems, and optimization tiers of Sections 1–6.

TABLE 12. Module-by-module architectural locator for the dual-precision core packages `normal_cone_nbody_float64/` and `normal_cone_nbody_float128/`, the four high-performance micro-kernel modules (§6.6), and the standalone `interfaces/` directory.

Sub-Package	Module Path (64 & 128)	Key Classes, Functions & Mathematical / Algorithmic Role	Manuscript Scope
`core/`	`core/state.py`, `constants.py`	`ExtendedPhaseState`: Immutable phase state $(\mathbf{q}, \mathbf{p}, t, E) \in \mathcal{P}_{\text{ext}}$, barycentric reduction $\mathbf{R}_{\text{cm}} = \mathbf{0}, \mathbf{P}_{\text{tot}} = \mathbf{0}$	§6.1, §6.2
	`core/jacobi.py`, `coordinates.py`	`JacobiNode`, `JacobiTree`, `build_optimal_tree`: Maximal flag binary tree $\mathcal{T} \in \text{Trees}(N)$, recursive Jacobi coordinates $(\mathbf{r}_v, \mathbf{w}_v)$, hyper-radius ρ_C, and Delaunay–Hill agglomeration ($\gamma = 1.0$)	§4.1.3, §6.2
	`core/invariants.py`	`compute_lie_bargmann_invariants`: 10 Galilean Noether generators $(\mathbf{P}_{\text{tot}}, \mathbf{L}_{\text{tot}}, \mathbf{G}_{\text{Gal}}, H)$ and Battin Wronskian audit $\lvert f\dot{g} - \dot{f}g - 1\rvert$	§4.2.4 (Prop. 1.1), §6.5
	`core/transitions.py`	`apply_jacobi_transition`, `compute_sl2_matrix`: Exact unimodular $\text{SL}(2,\mathbb{R}) \hookrightarrow \text{Sp}(6N-6,\mathbb{R})$ chart transition $\mathbf{M}_{A\to B}$	§4.3.3 (Thm. 4.10), §6.5
`potential/`	`potential/screened_apex.py`, `screening.py`, `direct.py`	`ScreenedApexPotential`, `septic_screening_theta`: Reference $\mathcal{C}^{1,1}$ screened apex potential $W_{\text{apex}}^{\text{screen}}$, exact monopole cancellation $+W_v - W_v \equiv 0$, and Cauchy / Hermite $\mathcal{C}^{2p}$ splines $\Theta(u_v)$ on $u_v \in [1,2]$	§4.2 (Thm. 4.4), §6.4
	`potential/optimized_screened_apex.py`	**[Optimized Tier 1]** `OptimizedScreenedApexPotential`, `_njit_accumulate_apex_pairs`: Precomputed $\mathbf{G}_{\text{mass}}$, topological non-leaf/non-intra-supernode pair cache $(\mathbf{idx}_A, \mathbf{idx}_B)$, scalar $N=3$ fast-path (7.24×) and Numba `@njit(fastmath=False)` loop (62.54× at $N = 64$, 0.0 ULP)	§6.6.1 (Prop. 6.19, Table 4)
	`potential/supernode_detector.py`	`SupernodeDetector`: Hill tidal ratio η_S with Schmitt trigger $[2^{-1/3}, 2^{-1/6}]$, internal hierarchy ratio $\chi_S < 3.0$, and sub-Roche disruption mode $\Lambda_S \geq 0.25$	§4.3, §6.2 (Thm. 6.4)
`solvers/`	`solvers/stumpff.py`, `kepler_sundman.py`	`KeplerSundmanSolver`, `stumpff_c012345`: Reference universal Sundman–Stumpff leaf flow $\Phi_{\Delta t}^{\text{leaf}}$, cubic Halley + 60-step bisection fallback, Battin Wronskian projection, and McGehee bounce $\mathcal{B}_C^2 = \text{Id}$	§5.2.2, §5.2.3 (Lem. 5.6), §6.4
	`solvers/optimized_kepler_sundman.py`	**[Optimized Tier 2]** `OptimizedKeplerSolver`, `stumpff_c0123_scalar`, `step_kepler_sundman_fast`: Targeted 2×6 Horner polynomials on c_2, c_3 with exact Stumpff recurrence, closure-free inlined Halley loop, and direct Gauss–Battin reuse (1.62× speedup, 0.0 ULP)	§6.6.2 (Rem. 6.6.2, Table 4)
	`solvers/supernode.py`	`SupernodeSolver`: Reference synchronous supernode flow under unfolded Sundman clock $\mathrm{d}t_S = \bar{\rho}_S \mathrm{d}\tau_S$ and recursive normal-cone splitting $H_S^{\text{int}} = H_{\text{leaf}}^{\text{int}} + H_{\text{base}}^{\text{int}} + V_{\text{apex}}^{\text{int}}$	§4.3 (Thm. 4.9), §6.4
	`solvers/optimized_supernode.py`, `jit_supernode.py`	**[Optimized Tiers 3 & 4]** `OptimizedSupernodeSolver` (zero-alloc unrolled $k \leq 4$ loops) and `JitSupernodeSolver` / `_njit_integrate_supernode` (native LLVM `@njit` compilation, symmetric dyadic bisection stack with half-step pair bridge, $L^2(\bar{\rho}_S)$ filter, 59.83× speedup, 0.0 ULP)	§6.6.3 (Prop. 6.20, Table 4)
`integrators/`	`integrators/common.py`, `protocol.py`	**[Optimized Tier 5]** Thread-local `ContextVar` dispatchers (`_CURRENT_APEX_EVALUATOR`, `_CURRENT_KEPLER_SOLVER`, `_CURRENT_SUPERNODE_SOLVER`) inside `step_drift_and_kepler`, `step_apex_kick`, and `step_supernode_flow`	§6.6.4 (Table 4)
	`integrators/strang.py`, `yoshida.py`, `blanes_moan_4.py`, `blanes_moan_6.py`	`StrangIntegrator` ($\mathcal{S}_2$), `Yoshida4Integrator` ($\mathcal{S}_4$), `BlanesMoan4Integrator` ($\text{BM}_4^{(7)}$, 7 stages, $s=6$), and `BlanesMoan6Integrator` ($\text{BM}_6^{(11)}$, 11 stages, $s=10$, 25-digit weights)	§5.1–§5.4 (Thms. 5.2, 5.9, 5.13)
	`integrators/correctors.py`, `processed.py`	`PalindromicCorrectorZ4`, `ProcessedBM4Integrator` (PBM_4): Cotangent generator $K_4 = c_4^{\text{BM4}} h^4 D_A^3 B \in \mathcal{P}_1$, 2-stage antipodal Lie conjugator $\mathcal{Z}_4^{\text{BM4}}(h)$, and covariant gauge connection $T^{(\text{PBM4})}_{(A,h_A)\to(B,h_B)}$	§5.5 (Thms. 5.17, 5.18, 5.20)
`system/`	`system/nbody_system.py`, `atlas_manager.py`, `dyadic_scheduler.py`, `history.py`	`NBodySystem(use_optimized_kernels=...)`, `AtlasManager` (Voronoi $\gamma = 1.0$ / hysteresis $\gamma = 0.60$), and `DyadicScheduler` (two-endpoint symmetric selector $k_{\text{sym},n}$, timescale triad & Leaf/Apex decoupling)	§5.6, §6.1, §6.3, §6.5
`diagnostics/` & `interfaces/`	`diagnostics/metrics.py`, `interfaces/pcr3bp_*.py`, `01..06_*_Interface.py`	`SystemDiagnostics`, `CollisionRadar`, `PCR3BPNormalConeIntegrator` (§3), and standalone pedagogical facades (`01..06_*_Interface.py`) for §6.1–§6.6	§3.1, §3.3, §6.1–§6.6

3. Reproducibility Index of Benchmark Campaigns, Figure Plotters, and Certified Datasets. Table 13 maps every numerical experiment, convergence table, and figure plate in Sections 1, 3, 6, and 7 to its corresponding execution script in `benchmarks/`, plotting script in `figures/`, and certified reference output in `results/campaigns/`.

TABLE 13. Benchmark campaign runners, publication figure generators, and certified JSON datasets in the companion GitHub repository.

Manuscript Section, Figures & Tables	**Campaign Runner (`benchmarks/`)**	**Figure Plotter (`figures/`)**	**Certified JSON Output (`results/campaigns/`)**
§3.3 Arenstorf Synodic Periodic Orbit Validation	`interfaces/pcr3bp_canonical_solver.py`	`interfaces/pcr3bp_canonical_solver.py`	`(Inline Arenstorf validation)`
§6.6 Table 4 ($N \in [3, 64]$ Micro-Kernel Speedups) & Fig. 18	`benchmarks/run_generator_01_dual_convergence_and_microkernels.py`	`figures/plot_generator_01_dual_convergence_and_microkernels.py`	`generator_01_dual_convergence_and_microkernels.json`
§7.1.1 Fig. 19 & Table 5 (Figure-8 & 3D Triple Dual Convergence)	`benchmarks/run_generator_01_dual_convergence_and_microkernels.py`	`figures/plot_generator_01_dual_convergence_and_microkernels.py`	`generator_01_dual_convergence_and_microkernels.json`
§7.1.2 Fig. 20 (Order $6 \to 4$ Crossover & $\mathcal{O}(\varepsilon^2 h^4)$ Floor)	`benchmarks/run_generator_02_universal_obstruction_and_shadow_gauge.py`	`figures/plot_generator_02_universal_obstruction_and_shadow_gauge.py`	`generator_02_universal_obstruction_and_shadow_gauge.json`
§7.1.3 Figs. 21–24 & Table 6 (`L1`–`L4`: $e \to 1$, $\mathcal{Z}_4^{\mathrm{BM4}}$ Free-Fall, McGehee $k \in \{2, 3, 4\}$, Burrau/Kozai)	`benchmarks/run_generator_03_unsoftened_singularity_limit_cases.py`	`figures/plot_generator_03_unsoftened_singularity_limit_cases.py`	`generator_03_unsoftened_singularity_limit_cases.json`
§7.2.1 Figs. 25–27 & Table 7 (`H1` Lexell, `H2` SL9, `H3` Apophis)	`benchmarks/run_generator_04_historical_encounters_and_atlas_gauge.py`	`figures/plot_generator_04_historical_encounters_and_atlas_gauge.py`	`generator_04_historical_encounters_and_atlas_gauge.json`, `campaign_II_H1..H3_*.json`
§7.2.2 Figs. 28–29 & Table 8 (`S1` Jovian Laplace $4:2:1$, `S2` Solar System & NAFF)	`benchmarks/run_generator_05_secular_stability_laplace_and_laskar_naff.py`	`figures/plot_generator_05_secular_stability_laplace_and_laskar_naff.py`	`generator_05_secular_stability_laplace_and_laskar_naff.json`
§7.3 Figs. 30–32 & Table 9 (`REBOUND 5.2.2` Head-to-Head `B1`, `B2`, `B4`)	`benchmarks/run_rebound_b1_star_grazing_pericenter.py`, `run_rebound_b2_hill_crossings.py`, `run_rebound_b4_pythagorean_chaos.py`	`figures/plot_rebound_b1_star_grazing_pericenter.py`, `plot_rebound_b2_hill_crossings.py`, `plot_rebound_b4_pythagorean_chaos.py`	`rebound_b1_star_grazing_pericenter.json`, `rebound_b2_hill_crossings.json`, `rebound_b4_pythagorean_chaos.json`

References

[1] Sverre J. Aarseth, *Gravitational N-body simulations: Tools and algorithms*, Cambridge Monographs on Mathematical Physics, Cambridge University Press, Cambridge, 2003.

[2] Richard F. Arenstorf, *Periodic solutions of the restricted three body problem representing analytic continuations of Keplerian elliptic motions*, American Journal of Mathematics **85** (1963), no. 1, 27–35.

[3] Scott Axelrod and I. M. Singer, *Chern–Simons perturbation theory. II*, Journal of Differential Geometry **39** (1994), no. 1, 173–213.

[4] Valentine Bargmann, *On unitary ray representations of continuous groups*, Annals of Mathematics **59** (1954), no. 1, 1–46.

[5] Richard H. Battin, *An introduction to the mathematics and methods of astrodynamics*, AIAA, Reston, VA, 1999.

[6] Giancarlo Benettin and Antonio Giorgilli, *On the Hamiltonian interpolation of near-to-the identity symplectic mappings with application to symplectic integration algorithms*, Journal of Statistical Physics **74** (1994), no. 5-6, 1117–1143.

[7] George D. Birkhoff, *The restricted problem of three bodies*, Rendiconti del Circolo Matematico di Palermo **39** (1915), 265–334.

[8] Sergio Blanes, Fernando Casas, Ariadna Farrés, Jacques Laskar, Joseba Makazaga, and Ander Murua, *New families of symplectic splitting methods for numerical integration in dynamical astronomy*, Applied Numerical Mathematics **68** (2013), 58–72.

[9] Sergio Blanes, Fernando Casas, and Jesús Ros, *Processing symplectic methods for near-integrable Hamiltonian systems*, Celestial Mechanics and Dynamical Astronomy **77** (2000), no. 1, 17–36.

[10] Sergio Blanes and P. C. Moan, *Practical symplectic partitioned Runge–Kutta and Runge–Kutta–Nyström methods*, Journal of Computational and Applied Mathematics **142** (2002), no. 2, 313–330.

[11] Tjarda Boekholt and Simon Portegies Zwart, *On the reliability of N-body simulations*, Computational Astrophysics and Cosmology **2** (2015), 2.

[12] V. A. Bogomolov, *Dynamics of the vorticity on a sphere*, Fluid Dynamics **12** (1977), no. 6, 863–870.

[13] Dirk Brouwer, *On the accumulation of errors in numerical integration*, The Astronomical Journal **46** (1937), no. 1072, 149–153.

[14] Carl Burrau, *Numerische Berechnung eines Spezialfalles des Dreikörperproblems*, Astronomische Nachrichten **195** (1913), no. 6, 113–118.

[15] Damien Calaque and Pavel Safronov, *Shifted cotangent bundles, symplectic groupoids and deformation to the normal cone*, arXiv preprint arXiv:2407.08622 (accepted in American Journal of Mathematics) (2024).

[16] Ricardo Campos, Najib Idrissi, Pascal Lambrechts, and Thomas Willwacher, *Configuration spaces of manifolds with boundary*, Astérisque **449** (2024), 1–134.

[17] P. J. Channell and C. Scovel, *Integrators for Lie–Poisson dynamical systems*, Physica D: Nonlinear Phenomena **50** (1991), no. 1, 80–88.

[18] Alain Chenciner and Richard Montgomery, *A remarkable periodic solution of the three-body problem in the case of equal masses*, Annals of Mathematics **152** (2000), no. 3, 881–901.

[19] Corrado De Concini and Claudio Procesi, *Wonderful models of subspace arrangements*, Selecta Mathematica (New Series) **1** (1995), no. 3, 459–494.

[20] Ana Cannas da Silva, *Lectures on symplectic geometry*, Lecture Notes in Mathematics, vol. 1764, Springer-Verlag, Berlin, Heidelberg, 2001.

[21] Leonardo de Moura, Soonho Kong, Jeremy Avigad, Floris van Doorn, and Gabriel Ebner, *The Lean theorem prover (system description)*, Automated Deduction – CADE-25, Lecture Notes in Computer Science, vol. 9195, Springer, 2015, pp. 378–388.

[22] Ariadna Farrés, Jacques Laskar, Sergio Blanes, Fernando Casas, Joseba Makazaga, and Ander Murua, *High precision symplectic integrators for the Solar System*, Celestial Mechanics and Dynamical Astronomy **116** (2013), no. 2, 141–174.
[23] William Fulton, *Intersection theory*, Ergebnisse der Mathematik und ihrer Grenzgebiete, vol. 2, Springer-Verlag, Berlin, Heidelberg, 1984.
[24] William Fulton and Robert MacPherson, *A compactification of configuration spaces*, Annals of Mathematics **139** (1994), no. 1, 183–225.
[25] Zhong Ge and Jerrold E. Marsden, *Lie–Poisson Hamilton–Jacobi theory and Lie–Poisson integrators*, Physics Letters A **133** (1988), no. 3, 134–139.
[26] Victor Guillemin, Eva Miranda, and Ana Rita Pires, *Symplectic and Poisson geometry on b-manifolds*, Advances in Mathematics **264** (2014), 864–896.
[27] Ernst Hairer and Christian Lubich, *The life-span of backward error analysis for numerical integrators*, Numerische Mathematik **76** (1997), no. 4, 441–462.
[28] Ernst Hairer, Christian Lubich, and Gerhard Wanner, *Geometric numerical integration: Structure-preserving algorithms for ordinary differential equations*, 2nd ed., Springer Series in Computational Mathematics, vol. 31, Springer-Verlag, Berlin, Heidelberg, 2006.
[29] Douglas C. Heggie, *Binary evolution in stellar dynamics*, Monthly Notices of the Royal Astronomical Society **173** (1975), no. 3, 729–787.
[30] David M. Hernandez and Walter Dehnen, *A study of symplectic integrators for planetary system problems: error analysis and comparisons*, Monthly Notices of the Royal Astronomical Society **468** (2017), no. 3, 2614–2636.
[31] ———, *Switching integrators reversibly in the astrophysical N-body problem*, Monthly Notices of the Royal Astronomical Society **522** (2023), no. 3, 4639–4648.
[32] George W. Hill, *Researches in the lunar theory*, American Journal of Mathematics **1** (1878), no. 1, 5–26.
[33] Carl Gustav Jacob Jacobi, *Sur le mouvement d'un point et sur un cas particulier du problème des trois corps*, Comptes Rendus de l'Académie des Sciences **3** (1836), 59–61.
[34] ———, *Sur l'élimination des nœuds dans le problème des trois corps*, Journal für die reine und angewandte Mathematik (Crelles Journal) **26** (1843), 115–131.
[35] Gustav Kirchhoff, *Vorlesungen über mathematische physik: Mechanik*, B. G. Teubner, Leipzig, 1876.
[36] Paul Kustaanheimo and Eduard Stiefel, *Perturbation theory of Kepler motion based on spinor regularization*, Journal für die reine und angewandte Mathematik **218** (1965), 204–219.
[37] Jacques Laskar, *Frequency analysis for multi-dimensional systems. Global dynamics and diffusion*, Physica D: Nonlinear Phenomena **67** (1993), no. 1–3, 257–281.
[38] Jacques Laskar and Philippe Robutel, *High order symplectic integrators for perturbed Hamiltonian systems*, Celestial Mechanics and Dynamical Astronomy **80** (2001), no. 1, 39–62.
[39] Tullio Levi-Civita, *Traiettorie singolari ed urti nel problema ristretto dei tre corpi*, Annali di Matematica Pura ed Applicata (Serie III) **9** (1904), 1–32.
[40] ———, *Sur la régularisation du problème des trois corps*, Acta Mathematica **42** (1920), 99–144.
[41] Tiger Lu, David M. Hernandez, and Hanno Rein, *TRACE: a code for time-reversible astrophysical close encounters*, Monthly Notices of the Royal Astronomical Society **533** (2024), no. 3, 3708–3723.
[42] Christian Marchal, *The three-body problem*, Studies in Astronautics, vol. 4, Elsevier, Amsterdam, 1990.
[43] Christian Marchal and Donald G. Saari, *On the final evolution of the n-body problem*, Journal of Differential Equations **20** (1976), no. 1, 150–186.
[44] G. I. Marchuk, *Some application of splitting-up methods to the solution of mathematical physics problems*, Aplikace matematiky **13** (1968), no. 2, 103–132.

[45] Jean-Pierre Marco and David Sauzin, *Stability and instability for Gevrey quasi-convex near-integrable Hamiltonian systems*, Publications Mathématiques de l'IHÉS **96** (2003), 199–275.
[46] Jerrold E. Marsden and Matthew West, *Discrete mechanics and variational integrators*, Acta Numerica **10** (2001), 357–514.
[47] Richard McGehee, *Triple collision in the collinear three-body problem*, Inventiones Mathematicae **27** (1974), no. 3, 191–227.
[48] Robert I. McLachlan, *Explicit Lie–Poisson integration and the Euler equations*, Physical Review Letters **71** (1993), no. 19, 3043–3046.
[49] ———, *On the numerical integration of ordinary differential equations by symmetric composition methods*, SIAM Journal on Scientific Computing **16** (1995), no. 1, 151–168.
[50] Richard B. Melrose, *The Atiyah–Patodi–Singer index theorem*, Research Notes in Mathematics, vol. 4, A K Peters/CRC Press, Wellesley, MA, 1993.
[51] Seppo Mikkola and Sverre J. Aarseth, *An implementation of N-body chain regularization*, Celestial Mechanics and Dynamical Astronomy **57** (1993), no. 3, 439–459.
[52] Keith W. Myerscough and Jason Frank, *Explicit, parallel Poisson integration of point vortices on the sphere*, Journal of Computational and Applied Mathematics **304** (2016), 100–119.
[53] Dang Pham, Hanno Rein, and David S. Spiegel, *A new timestep criterion for N-body simulations*, The Open Journal of Astrophysics **7** (2024), 1.
[54] Henri Poincaré, *Les méthodes nouvelles de la mécanique céleste*, Gauthier-Villars, Paris, 1892.
[55] Kevin P. Rauch and Matthew Holman, *Dynamical chaos in the Wisdom–Holman integrator: origins and solutions*, The Astronomical Journal **117** (1999), no. 2, 1087–1102.
[56] Hanno Rein, David M. Hernandez, Daniel Tamayo, Garett Brown, Emily Eckels, Emma Holmes, Michelle Lau, Réjean Leblanc, and Ari Silburt, *Hybrid symplectic integrators for planetary dynamics*, Monthly Notices of the Royal Astronomical Society **485** (2019), no. 4, 5490–5497.
[57] Hanno Rein and Shang-Fei Liu, *REBOUND: an open-source multi-purpose N-body code for collisional dynamics*, Astronomy & Astrophysics **537** (2012), A128.
[58] Hanno Rein and David S. Spiegel, *IAS15: a fast, adaptive, high-order integrator for gravitational dynamics, accurate to machine precision over a billion orbits*, Monthly Notices of the Royal Astronomical Society **446** (2015), no. 2, 1424–1437.
[59] Hanno Rein and Daniel Tamayo, *WHFast: a fast and unbiased implementation of a symplectic Wisdom–Holman integrator for long-term gravitational simulations*, Monthly Notices of the Royal Astronomical Society **452** (2015), no. 1, 376–388.
[60] Hanno Rein, Daniel Tamayo, and Garett Brown, *High-order symplectic integrators for planetary dynamics and their implementation in REBOUND*, Monthly Notices of the Royal Astronomical Society **489** (2019), no. 4, 4632–4640.
[61] Donald G. Saari, *Improbability of collisions in Newtonian gravitational systems*, Transactions of the American Mathematical Society **162** (1971), 267–271.
[62] ———, *Improbability of collisions in Newtonian gravitational systems. II*, Transactions of the American Mathematical Society **181** (1973), 351–368.
[63] ———, *A global analysis of the gravitational n-body problem*, Lecture Notes in Mathematics **597** (1977), 441–445.
[64] Qin Sheng, *Solving linear partial differential equations by exponential splitting*, IMA Journal of Numerical Analysis **9** (1989), no. 2, 199–212.
[65] Carl Ludwig Siegel, *Der Dreierstoß*, Annals of Mathematics **42** (1941), no. 1, 127–168.
[66] Robert D. Skeel and C. William Gear, *Does variable step size ruin a symplectic integrator?*, Physica D: Nonlinear Phenomena **60** (1992), no. 1-4, 311–313.
[67] Stephen Smale, *Topology and mechanics. I*, Inventiones Mathematicae **10** (1970), no. 4, 305–331.

[68] Mark Sofroniou and Giulia Spaletta, *Derivation of symmetric composition constants for symmetric integrators*, Optimization Methods and Software **20** (2005), no. 4-5, 597–613.
[69] Gilbert Strang, *On the construction and comparison of difference schemes*, SIAM Journal on Numerical Analysis **5** (1968), no. 3, 506–517.
[70] Karl Stumpff, *Himmelsmechanik: Band I: Das Zweikörperproblem und die Methoden der Bahnbestimmung*, Deutscher Verlag der Wissenschaften, Berlin, 1959.
[71] ———, *Himmelsmechanik: Band II: Das Dreikörperproblem*, Deutscher Verlag der Wissenschaften, Berlin, 1965.
[72] Karl F. Sundman, *Mémoire sur le problème des trois corps*, Acta Mathematica **36** (1912), 105–179.
[73] Masuo Suzuki, *Fractal decomposition of exponential operators with applications to many-body problems and Monte Carlo simulations*, Physics Letters A **146** (1990), no. 6, 319–323.
[74] ———, *General theory of fractal path integrals with applications to many-body theories and statistical physics*, Journal of Mathematical Physics **32** (1991), no. 2, 400–407.
[75] Victor Szebehely, *Theory of orbits: The restricted problem of three bodies*, Academic Press, New York, 1967.
[76] Victor Szebehely and C. Frederick Peters, *Complete solution of a general problem of three bodies*, The Astronomical Journal **72** (1967), 876–883.
[77] H. F. Trotter, *On the product of semi-groups of operators*, Proceedings of the American Mathematical Society **10** (1959), no. 4, 545–551.
[78] Jean-Louis Verdier, *Spécialisation des classes de Chern*, Astérisque **82–83** (1981), 149–159, Caractéristique d'Euler–Poincaré (Séminaire E.N.S. 1978–1979); see also A. Douady and J.-L. Verdier, *Séminaire de géométrie analytique*, Astérisque 36–37 (1976).
[79] Jörg Waldvogel, *A new regularization of the planar problem of three bodies*, Celestial Mechanics **6** (1972), no. 2, 221–231.
[80] Hassler Whitney, *Tangents to an analytic variety*, Annals of Mathematics **81** (1965), no. 3, 496–549.
[81] Jack Wisdom, *Symplectic test particle encounters: a comparison of methods*, Monthly Notices of the Royal Astronomical Society **464** (2017), no. 2, 2350–2355.
[82] Jack Wisdom and Matthew Holman, *Symplectic maps for the N-body problem*, The Astronomical Journal **102** (1991), 1528–1538.
[83] Jack Wisdom, Matthew Holman, and Jihad Touma, *Symplectic correctors*, Integration Algorithms and Classical Mechanics (Jerrold E. Marsden, George W. Patrick, and William F. Shadwick, eds.), Fields Institute Communications, vol. 10, American Mathematical Society, Providence, RI, 1996, pp. 217–244.
[84] Zhihong Xia, *The existence of noncollision singularities in Newtonian systems*, Annals of Mathematics **135** (1992), no. 3, 411–468.
[85] Haruo Yoshida, *Construction of higher order symplectic integrators*, Physics Letters A **150** (1990), no. 5-7, 262–268.